PHYSIQUE COSMOLOGIQUE AVEC LENTILLE GRAVITATIONNELLE

COSMOLOGICAL PHYSICS WITH GRAVITATIONAL LENSING

Sponsored by

- EU (*European Union*): Training and Mobility of Researchers
- CNRS (*Centre National de la Recherche Scientifique*)
- CEA (*Commissariat à l'Énergie Atomique*)
- IN2P3
- Institut d'Astrophysique de Paris
- Observatoire de Paris

XXXVth Rencontres de Moriond
Les Arcs, Savoie, France – March 11-18, 2000

Cosmological physics with gravitational lensing
Series: Moriond Astrophysics Meetings

ISBN 2-86883-531-7

Proceedings of the XXXVth RENCONTRES DE MORIOND

Series: Moriond Astrophysics Meetings

Les Arcs, France *March 11-18, 2000*

COSMOLOGICAL PHYSICS WITH GRAVITATIONAL LENSING

edited by

Jean Trân Thanh Vân
Yannick Mellier
Marc Moniez

EDP SCIENCES

7 avenue du Hoggar, PA de Courtabœuf, B.P. 112, 91944 Les Ulis cedex A, France

XXXVth Rencontres de Moriond

Cosmological physics with gravitational lensing

were organized by:

J. Trân Thanh Vân (Orsay)

with the active collaboration of:

J.-P. Kneib
R. Maoli
Y. Mellier
M. Moniez

FOREWORD

'2000 RENCONTRES DE MORIOND

The XXXVth Rencontres de Moriond were held in Les Arcs 1800, Savoie, France.

The first meeting took place at Moriond in the French Alps in 1966. There, experimental a well as theoretical physicists not only shared their scientific preoccupations but also the househol chores. The participants in the first meeting were mainly French physicists interested i electromagnetic interactions. In subsequent years, a session on high energy strong interactions wa also added.

The main purpose of these meetings is to discuss recent developments in contemporary physic and also to promote effective collaboration between experimentalists and theorists in the field o elementary particle physics. By bringing together a relatively small number of participants, th meeting helps to develop better human relations as well as a more thorough and detailed discussio of the contributions.

This concern of research and experimentation of new channels of communication and dialogu which from the start animated the Moriond meetings, inspired us to organize a simultaneou meeting of biologists on Cell Differenciation (1980) and to create the Moriond Astrophysic Meeting (1981). In the same spirit, we have started a new series on Condensed Matter Physics i January 1994. Common meetings between biologists, astrophysicists, condensed matter physicist and high energy physicists are organized to study the implications of the advances of one field int the others. I hope that these conferences and lively discussions may give birth to new analytica methods or new mathematical languages.

At the XXXVth Rencontres de Moriond in 2000, three physics sessions, one condense matter session, one astrophysics session and one biology session were held:

* January 22-29	"Energy densities in the Universe"
* March 11-18	"Electroweak Interactions and Unified Theories"
	"Cosmological physics with gravitational lensing"
* March 18-25	"QCD and High Energy Hadronic Interactions"
	"Rencontre de Biologie – Méribel"

I thank the organizers of the XXXVth Rencontres de Moriond:

- R. Ansari, J. Bartlett, T. Damour, J. Dumarchez, W. Forman, Y. Giraud-Héraud B. Guiderdoni, M. Kamionskowski, E. Kolb, O. Lahav, D. Langlois, A. Liddle an C. Magneville for the "Energy densities in the Universe" session,
- J. Bagger, A. Blondel, G. Coignet, P. Fayet, J.-M. Frère, H. Frisch, L. Krauss, S. Loucatos F. Montanet, L. Okun, L. Randall, G. Unal, D. Wood and F. Zwirner for the "Electrowea Interactions and Unified Theories" session,

- C. Alard, R. Blandford, T. Brainerd, R. Ellis, B. Fort, B. Guiderdoni, N. Kaiser, J.P. Kneib, C. Kochanek, K. Kuijken, Y. Mellier, M. Moniez, B. Paczinski, P. Schneider and R. Webster "Cosmological physics with gravitational lensing" session,
- E. Augé, E. Berger, A. Capella, S. Catani, D. Denegri, B. Klima, L. Kluberg, G. Korchemsky, L. McLerran, L. Montanet, B. Pietrzyk, Tan Chung I and C. Voltolini for the "QCD and High Energy Hadronic Interactions" session,
- F. Bonhomme, B. Godelle, T. Langin, P. Sonigo, F. A. Wollmann for the Biology meeting,

nd the conference secretariat: C. Barthélemy, I. Cossin, F. Delmas, D. Granger, H. Mauger, '. Leclercq-Ortal, F. N. Oswald, Pham Duy Tu, A. M. Renault-Perrin, F. Warin, C. Windrif and :. Wrzesinski.

I am also grateful to Mr. and Ms. E. Rocca-Serra, Ms. C. Dufourny, Ms. S. Kovalevsky who ontributed through their hospitality and cooperation to the well-being of the participants enabling iem to work in a relaxed atmosphere.

These Rencontres were sponsored by the European Union Training and Mobility of esearchers Program, the Centre National de la Recherche Scientifique (INSU, SPM and FP), the istitut National de Physique Nucléaire et de Physique des Particules (IN2P3-CNRS), the Commissariat à l'Énergie Atomique (DAPNIA), the Ministère de l'Enseignement Supérieur et de la echerche (programme ACCES) and the National Science Foundation. I would like to express my ianks for their encouraging support.

I sincerely wish that a fruitful exchange and an efficient collaboration between the hysicists, the astrophysicists and the biologists will arise from these Rencontres as from the revious ones.

J. Trân Thanh Vân

CONTENTS

Foreword V

I. Microlensing

Microlensing in a Nutshell	*M. Moniez*	3
The MOA Strategy for Microlensing Planet Searches	*I. Bond*	11
The Optical Gravitational Lensing Experiment. OGLE- II Results	*K. Żebruń*	15
Not enough Stellar Mass Machos in the Galactic Halo	*T. Lasserre*	21
Results of the EROS II Collaboration towards the Galactic Spiral Arms	*F. Derue*	25
Faint Moving Objects of the Dark Halo?	*R. Ibata*	29
EROS 2 Proper Motion Survey for Halo White Dwarfs	*B . Goldman*	33
Search for High Proper Motion White Dwarfs	*J.T.A. De Jong*	39
MACHOs and the Clouds of Uncertainty	*E. Kerins*	43
A New (Old) Component of the Milky Way	*E. Gates*	49
Binaries, Blending, and Measurements of the Microlensing Optical Depth	*R. Di Stefano*	53
Microlensing by Non-Baryonic (Non-Compact) Objects	*A.F. Zakharov*	57
Probing the Galactic Center by Gravitational Lensing	*S. Capozziello*	61
AGAPE: Results from Microlensing on Unresolved Stars	*Y. Le Du*	65
Analysis of Microlensing Observations Using Purely Differential Methods	*C. Alard*	69
Breaking the Degeneracy of Microlensing Towards the LMC	*H. Zhao*	81
Perturbative Analysis in Multiple and Planetary Gravitational Lensing	*V. Bozza*	85
Microlensing of Quasars	*J. Wambsganss*	89
Microlensing in Q2237+0305	*J. Stuart Wyithe*	95
Radio-Microlensing in B1600+434: Probing MACHOs at High-Redshifts	*L.V.E. Koopmans*	99
Constraints on the Gravitational Force on Photons from Microlensing	*J.-F. Glicenstein*	103

II. Gravitational Lensing by Galaxies, Groups and Clusters

Gravitational Lensing and Cluster of Galaxies	*J.-P. Kneib*	109
Maximum Entropy Weak Lensing Mass Reconstruction	*S. Bridle*	117
Infrared Observations of a Depletion of Distant Galaxies behind Abell 2219 with CIRSI	*M.E. Gray*	121
A combined HST/CFH12k/XMM Survey of X-Ray Luminous Clusters of Galaxies at $z \sim 0.2$	*O. Czoske*	125
Cluster Mass Profiles from Weak Lensing: Constraints from Shear and Magnification Information	*L.J. King*	129
Cluster Galaxies: Contribution to the Arc Statistics	*M. Meneghetti*	133
A Multiwavelength Study of the Cluster of Galaxies CL0016	*F.J. Castander*	137
Cluster Deprojection with Multiple Data Sets: First Applications to Simulations	*K. Reblinsky*	141
Detection of a Dark Matter Concentration near the Cluster Abell 1942 with Weak Gravitational Lensing	*T. Erben*	145

II. Weak Lensing and Large-Scale Structures

Veak Lensing Study of Low Mass Galaxy Groups: Implications for Ω_m	*H. Hoekstra*	151
Veak Weak Lensing: How Accurately Can Small Shears Be Measured?	*K. Kuijken*	157
'osmic Shear with the CFHT	*L. Van Waerbeke*	165
)etection of Cosmic Shear with the William Herschel Telescope	*D.J. Bacon*	173
'osmic Shear with the VLT	*R. Maoli*	177
tatistical Properties of the Convergence Due to Weak Gravitational ,ensing by Non-Linear Structures	*P. Valageas*	183
Jumerical Study of the Cosmic Shear	*T. Hamana*	187
\ Numerical Study of Cosmic Shear Statistics	*A. Thion*	191
'oreground-Background Galaxy Correlations in the Hubble Deep Fields	*D. Herranz*	197
iravitational Lensing Effect on Two-point Correlation Function f Hotspots in the CMB Maps	*M. Takada*	201
'ross-Correlations of CMB and Weak Lensing Surveys	*K. Benabed*	205
'osmic Strings Lens Phenomenology Revisited	*F. Bernardeau*	211

V. Quasars and H_0, Lensing and High-z Galaxies

'hotometric Redshifts and Gravitational Telescopes	*R. Pello*	219
tudy of the Depletion Effect in the Cluster MS1008-1224	*C. Mayen*	225
pectroscopic Follow Up of Arclets in ACl 14 with the VLT	*J.-F. Le Borgne*	229
hedding Light on the Dark Side of Galaxy Formation: ubmillimetre Surveys through Lensing Clusters	*R. Ivison*	233
'rospects for the Lensing of Supernovae	*R.B. Metcalf*	239
Gravitational Lens Survey with the *Planck Surveyor*	*A.W. Blain*	245
ialaxy-Galaxy Lensing Predictions from the Semi-Analytic Galaxy 'ormation Models	*J. Guzik*	253
Spectroscopic Survey for Strong Galaxy-Galaxy Lenses	*J.P. Willis*	257
'he Current Status of CLASS	*P. Helbig*	261
'ime Delays	*T. Wiklind*	265
'ime Delay in Gravitational Lens Systems and Hubble Constant	*D. Narasimha*	271
Jear-IR Spectroscopy of the Double Quasar HE 110-1805	*C. Lidman*	275
'he Lens-Redshift Test Revisited	*P. Helbig*	279
'he Statistics of Wide-Separation Lenses	*D.J. Mortlock*	283
Veak Lensing and Cosmology	*M. Lombardi*	287
'onstraining (Ω_m, Ω_λ) from Strong Lensing	*G. Golse*	291

,ist of Participants	295

MICROLENSING

MICROLENSING IN A NUTSHELL

Marc MONIEZ
Laboratoire de l'Accélérateur Linéaire, IN2P3-CNRS,
Université de Paris-Sud, B.P. 34, F-91898 Orsay Cedex, France

Microlensing is now a very popular observational technique. The investigations accessible to this technique range from the dark matter problem to the search for extrasolar planets. The microlensing principles are explained, from the simpliest approximations to the most complex configurations. The techniques for the search and the study of the microlensing effects are described, and the present limitations are discussed.

1 Introduction: the microlensing use

B. Paczyński [13] first pointed out the possibility of using the gravitational microlensing effect to detect massive compact objects of the galactic halo in the direction of the Magellanic Clouds. In september 1993, three teams, EROS [5], MACHO [2] and OGLE [15] have discovered the first microlensing events in the directions of the Large Magellanic Cloud and the Galactic Center. Since the first discoveries, hundreds of microlensing effects have been detected in the direction of the galactic bulge together with a handful of events towards the Galactic Spiral Arms and the Magellanic Clouds. Microlensing search was first intended to study Galactic structure (dark halo, disk, bar structure) and important constraints have been obtained by the OGLE, MACHO and EROS teams on this issue.

The specific networks PLANET and MPS have been setup in order to continuously monitor the possible microlensing effects, as soon as they are suspected by MACHO, OGLE or EROS. The main purpose of these networks is to search for anomalous microlensing events, and therefore use the phenomenon as a tool to probe the target star and the deflector and get informations not accessible by other means, like planet detection and stellar profiles.

2 microlensing basics

The microlensing effect occurs if a massive compact object passes close to the line of sight of a star and gives gravitational images that are not intercepted by the massive object (no eclipse), but that cannot be separated in telescopes (no multiple images)(see Fig. 1). The detection of such a coincidence is then possible only if a measurable magnification variation occurs during the observation time. In the approximation of a single point-like object acting as a deflector on a single point-like source, the total magnification of the source luminosity at a given time t is

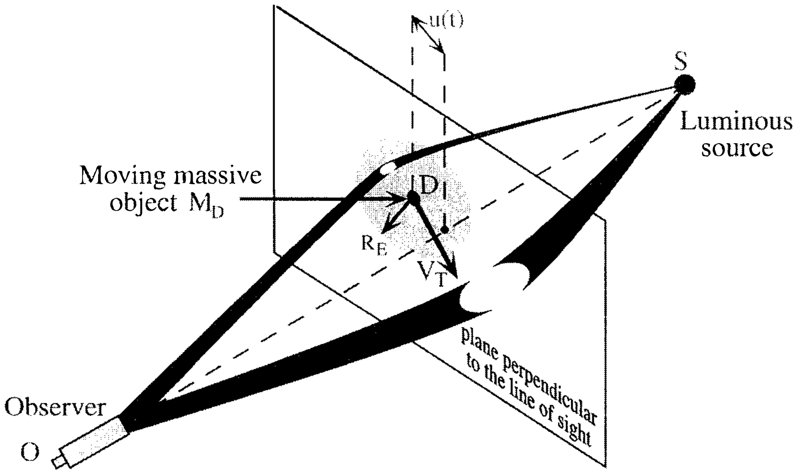

Figure 1: *Principle of the microlensing effect: As the deflector D moves with the transverse relative speed V_T, the impact parameter u(t) changes with time, and so does the magnification of the source.*

the sum of the magnifications of the two images, given by

$$A(t) = \frac{u(t)^2 + 2}{u(t)\sqrt{u(t)^2 + 4}}\,, \tag{1}$$

where $u(t)$ is the distance between the undeflected line of sight and the deflecting object, expressed in units of the "Einstein Radius" R_E

$$R_E = \sqrt{\frac{4GM_D}{c^2}\,Lx(1-x)} \simeq 970 \times R_\odot \times \left[\frac{M_D}{M_\odot}\right]^{\frac{1}{2}} \times \left[\frac{L}{10\ Kpc}\right]^{\frac{1}{2}} \times \frac{[x(1-x)]^{\frac{1}{2}}}{0.5} \tag{2}$$

$$\simeq 4.5\ A.U. \times \left[\frac{M_D}{M_\odot}\right]^{\frac{1}{2}} \times \left[\frac{L}{10\ Kpc}\right]^{\frac{1}{2}} \times \frac{[x(1-x)]^{\frac{1}{2}}}{0.5} \tag{3}$$

Here G is the gravitational constant, L is the distance to the source, xL is the distance to the deflector and M_D its mass. In eq. (1), a singularity occurs when $u(t) = 0$. The amplification of an idealized point-like source would be infinite at this position, and the image would be a ring with a radius equal to the Einstein radius. When projected on the transverse plane of the deflector, the set of positions where a point-like source would undergo an infinite magnification is called the caustic curve, and the corresponding image is called the critical curve. For simple microlensing, the caustic curve is the single point corresponding to the direction of the deflector, and the critical curve is the Einstein ring.

The angular separation of the two images is of the order of the Eintein angular radius:

$$\theta_E \sim \frac{R_E}{xL} \simeq 0.9\ milliArcSec \times \left[\frac{M_D}{M_\odot}\right]^{\frac{1}{2}} \times \left[\frac{L}{10\ Kpc}\right]^{-\frac{1}{2}} \times \left[\frac{1-x}{x}\right]^{\frac{1}{2}} \tag{4}$$

The motion of the deflector relative to the line of sight to the source makes the magnification vary with time: for deflectors of masses M_D within the interval $[10^{-7}, 1]M_\odot$ located in the galactic halo, time scales range typically from hours to months for a significant change of the magnification of a source in the Large Magellanic Cloud (LMC). Assuming a deflector moving at a constant relative transverse speed V_T, reaching its minimum distance (impact parameter) to the undeflected line of sight u_{min} at time t_0, $u(t)$ is given by $u(t) = \sqrt{u_{min}^2 + ((t-t_0)/\Delta t)^2}$, where $\Delta t = \frac{R_E}{V_T}$ the "lensing time scale" is the only measurable parameter bringing useful information on the deflector in the approximation of the simple microlensing.

$$\Delta t(days) = 39 \times \left[\frac{V_T}{200km/s}\right]^{-1} \times \left[\frac{M_D}{M_\odot}\right]^{\frac{1}{2}} \times \left[\frac{L}{10\ Kpc}\right]^{\frac{1}{2}} \times \frac{[x(1-x)]^{\frac{1}{2}}}{0.5} \tag{5}$$

2.1 microlensing event characteristics

The general properties of the gravitational lensing apply to the microlensing: the microlensing of a source *element* does not affect its colour and polarization. The magnification of a source that undergoes a simple microlensing effect (point-like source and point-like deflector with uniform relative motion with respect to the line of sight) has some very characteristic features which allow to discriminate it from any known intrinsic stellar variability :

- The magnification phase is singular in the history of the source (as well as of the deflector).
- The gravitational origin of the effect makes the magnification independent of the colour.
- The magnification is a known function of time, depending on only 3 parameters ($u_{min}, t_0, \Delta t$), with a symmetrical shape.
- As the geometric configuration of the source-deflector system is random, the dates of maximum amplification and the impact parameters of the events have to be uniformly distributed. This allows to predict the expected maximum amplification distribution which, corrected for microlensing detection efficiency, can be compared with the observed one.
- The passive role of the lensed stars implies that their population should be representative of the monitored sample, particularly with respect to the observed colour and magnitude distributions.

2.2 Optical depth and event rate

The probability for a given star to be magnified by a factor larger than 1.34 ($u < 1$) at a given time, is the probability for its line of sight to intercept the Einstein disk of radius R_E of one of the deflectors. This probability, called the optical depth τ, is independant of the deflectors mass function, because the surface of the Einstein disk is proportional to the deflectors mass. When events are detected towards a monitored population of stars, the *measured* optical depth is estimated from

$$\tau = \frac{1}{N_{obs}T_{obs}} \frac{\pi}{2} \sum_{events} \frac{\Delta t}{\epsilon(\Delta t)} \tag{6}$$

where N_{obs} is the number of monitored stars in the target, T_{obs} is the duration of the observation period and $\epsilon(\Delta t)$ is the average detection efficiency of the microlensing events with a time scale Δt, relative to the events with impact parameter $u_{min} < 1$ and time of maximum within the observation period. Similarly, the event rate corrected for the observation efficiency is computed to be $\Gamma = 1/(N_{obs}T_{obs}) \times \Sigma_{events}(1/\epsilon(\Delta t))$.

3 Microlensing configurations

3.1 intragalactic microlensing

Microlensing has been discovered towards the Milky Way center, towards the Galactic arms (deflector and source then both belong to the Galaxy) and towards the magellanic clouds. The

expected and measured typical timescale of the events is 10-100 days.
The optical depths τ towards the Galactic center and through the Galactic plane at longitude $\pm 30°$ are respectively estimated [10] to be $\sim 2.5 \times 10^{-6}$ and $\sim 0.5 \times 10^{-6}$. Assuming that the Galactic halo is described by a standard isothermal halo model [6], and that it is fully made of compact objects acting as deflectors, the optical depth is estimated to be about 5×10^{-7} up to the LMC, and 7×10^{-7} up to the SMC. Assuming that all deflectors have the same mass M_D, the rate per star for microlensing effects with amplifications greater than a threshold amplification A_T (corresponding to an impact parameter $u_{min} = u_T$) has been calculated to be $1.6\ 10^{-6}\ u_T \sqrt{M_\odot / M_D}\ yr^{-1}$ in the direction of LMC[8 11].

3.2 intergalactic microlensing

Microlensing towards M31 is actively searched through the so-called "pixel technique". The expected event characteristics are close to the characteristics of intragalactic events, given the slow variation of the parameters with the distances (as the square root).

3.3 extragalactic microlensing

Two configurations are considered here:

- The source is a quasar and the microlens is a compact object in the halo of a cluster of galaxies. The typical optical depth in this configuration could be $\tau \sim 0.001$ if the halo is fully made of compact objects, and the typical microlensing duration is a few months.
- The source is one of the images of a quasar lensed by a galaxy, and the microlens is one of the compact objects from the same galaxy. The optical depth is of order one in this case and the magnification can lasts for years. As the optical depth is very large, caustic crossing (see next section) with much shorter durations should occur, which can be more easily detected. The luminosity variation of the microlensed image can be distinguished from the intrinsic quasar variability by comparing with the variations of the other images (taking into account the time-delay between the images).

4 Beyond standard microlensing

The simple microlensing approximation can be broken in many different ways : double lens, extended source, deviations from the uniform motion due to the rotation of the earth around the sun (parallax effect), to the orbit of the source around the center of mass of a multiple system, or to a similar orbit of the acting deflector. These deviations have all been observed. Interest for these "exotics" comes from the extremely valuable extra-information that can be obtained (more constraints on the lensing configuration, or informations on the source or on the deflector...).
Three actors are involved in a microlensing effect, the source, the deflector and the observer. The microlensing event structure is sensitive to the distributions of the source light and deflector mass projected onto the corresponding transverse planes, and to the transverse speeds of each source/deflector element and of the observer (see Fig. 2). At a given time, the source plane can be described as a luminosity distribution, and the deflector plane as an amplification map. The average magnification can then be obtained by averaging over the light source elements the magnification given by the amplification map at the intercept of the line of sight. The luminosity distribution of the sources can differ from one wavelength to the other, and can evolve with time as well as the shape and orientation of the magnification map. The position of the observer (extremity of the line of sight) also describes the terrestrial orbit, for which a

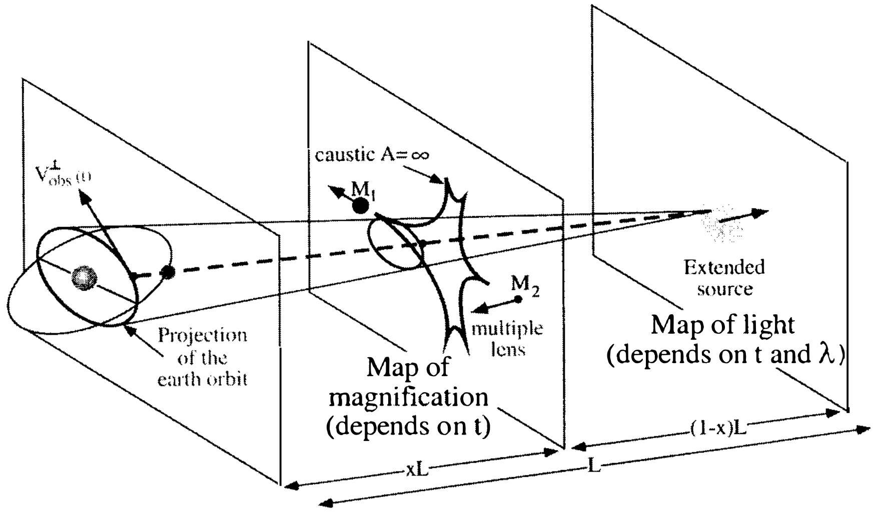

Figure 2: *The three actors of the microlensing effect:* **observer plane:** $V^{\perp}_{obs}$ *the projected speed of the observer (earth) relative to the sun changes with the season. If this speed is not small compared with the speed of the deflector projected from the source onto the observer plane, a distorsion called parallax effect can be detected.* **Deflector plane:** *the curve shown here is the caustic map due to a double deflector* (M_1, M_2)*. The masses can have different speeds, leading to variations of the map configuration with time (in addition to its global motion).* **Source plane:** *if the source is extended, different parts will undergo different magnifications. All these effects can occur simultaneously.*

uniform approximation is valid only for short durations (few weeks). The following shows the possible distorsions to the single event approximation due to each of the three actors.

Observer trajectory If the variation of the Earth's velocity rotating component around the sun is not negligible with respect to the projected transverse speed of the deflector, then the apparent trajectory of the deflector with respect to the line of sight is a cycloid instead of a straight line. The resulting amplification versus time curve is then affected by this parallax effect. This effect is more easily observable for long duration events (several months), for which the change in the Earth velocity is important [3].

Lens plane In the case of a multiple lens, the map of magnification exhibit very different features than in the simple approximation, because the caustic curve is no more a single point. Then the source elements of which the line of sight crosses the caustic curve are subject to an infinite magnification. Obviously, the average magnification of the source is always finite and its maximum is limited by the extension of the light distribution. The magnification map evolves with time, because the multiple lens system has a global motion (translation and rotation), and the projected distances between the components change with the time. The search for multiple lenses made of a main star surrounded by a planetary system is now considered as the most promising way to undoubtly discover new extra-solar planets, and as *the only way* to discover earth-like planets.

Source plane As the source is not point-like, the correct way to estimate the magnification of a finite size source by microlensing is to average the lensing effect over the light distribution projected onto the transverse plane. The light transverse distribution can change with the wavelength and vary with time, and the trajectory of each component of a multiple source can be complex. For example, considering a point-like deflector, if the angular

Table 1: The experimental devices devoted to the microlensing searches.

Set-up	location	telescope diameter	pixels $\times 10^6$	stars $\times 10^6$	remarks
EROS	ESO-Chile	1 m	64	~ 60	stop 2002
MACHO	mount Stromlo Australia	1.3 m	32	~ 30	stopped since end 1999
OGLE	Las Campanas Chile	1.3 m	$4 \rightarrow 64$ (in 2001)		driftscan mode
MOA	New Zealand	0.6 m	9	~ 2	
AGAPE	Pic du Midi-France	2 m	1		target: M31
VATT	Arizona	2 m	1		target: M31
PLANET	network	~ 1 m			targets=alerts
MPS	network	~ 1 m			EROS/OGLE

radius of a source star is not negligible with respect to the angular impact parameter, then the magnification curve is distorted from the simple approximation. In particular, the maximum amplification is limited, and chromatic effects can occur if the light distribution on the star's surface depends on the wavelength. Another example is the "Xallarap" effect (mirror of parallax), which is due to the rotation of the source around the center-of-mass of a multiple system. This effect has a characteristic time given by the period of the rotation of the source [14].

Blending effects: the detected light may also have a composite origin ; a multiple system may be lensed, with different amplifications for each component depending on the impact parameters, or with only one component being amplified [14]. The latter case is equivalent to the configuration of a single amplified star, blended by another star close to the line of sight (but not amplified). The light curve of a microlensing event is affected by this blending effect. Moreover, it can make the measurement of the optical depth very difficult, because the experimental efficiency to detect the microlensing events is difficult to control in the case of strong blending (see section 6).

5 The setups dedicated to microlensing searches

5.1 The experimental detection of microlensing events

Three types of experiments can be distinguished. The two first could be called "discovery experiments" whereas the third could be considered as "follow-up experiments". Table 5.2 lists the current devices devoted to the microlensing studies.

All the discovery setups have in common the fact that they aim at monitoring the largest possible field of view, with the shortest time-sampling. They all make use of wide field CCD-cameras, mounted on one meter class telescopes. Data analysis are also based on the same principles : Firstly, light curves (i.e. flux versus time curves) for catalogued stars or for pixels are extracted from the raw data, using automatic astrometric and photometric alignment procedures ; secondly each light curve is subjected to a microlensing search algorithm based on the expected characteristics of the events.

5.2 The discovery experiments based on star monitoring

Three dedicated devices (EROS, OGLE and MOA) are currently searching for microlensing, looking for specific patterns in the light curves of several million monitored stars.

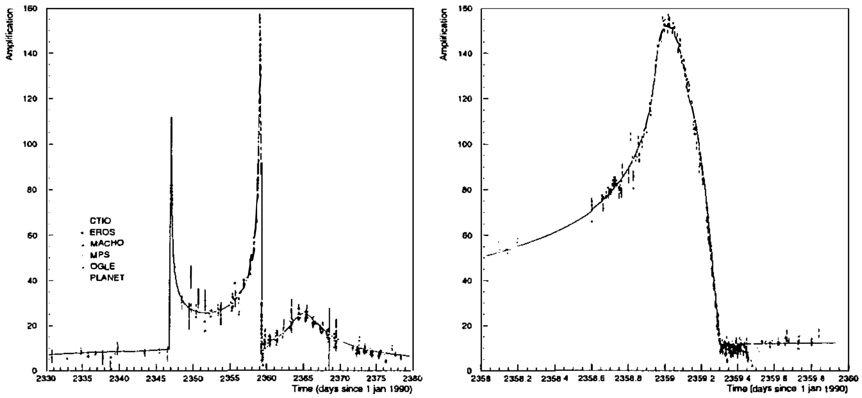

Figure 3: *The binary lens towards SMC.*

5.3 The discovery experiments based on pixel monitoring

Two teams, AGAPE (Andromeda Gravitational Amplification Pixel Experiment [4]) and VATT Microlensing Survey of M31 (Vatican Advanced Technology Telescope [7]) are monitoring pixels instead of individual stars. Those surveys take advantage of the large number of underlying stars participating to the flux of each single pixel, of which one could potentially undergo a strong microlensing effect, and then temporarily emerge from a continuum. Using this technique can increase the microlensing signal in the directions monitored by the previous experiments [12]. But the most promising issue is the possibility to search for microlensing in directions where the stars are not resolved, like M31. The AGAPE and VATT teams both use 2 meter class non-dedicated telescopes equipped with large CCDs. The MEGA (Microlensing Exploration of the Galaxy and Andromeda) survey has also started to use the KPNO 4-meter and Isaac Newton telescopes in the purpose of studying the variations of the optical depth around the center of M31. Now those teams have demonstrated their ability to detect and characterize microlensing events [1].

5.4 The follow-up experiments

Two networks (PLANET and MPS) are able to monitor the most interesting candidates found by the other experiments, which have developped the capability of on-line detection needed to start alerts well before the end of the lensing process. PLANET and MPS use one meter class telescopes located all around the world, to be able to monitor the candidates 24 hours a day. Wide field of view is not needed here, but a precise photometry has to be performed, which needs longer exposures and finer images, compared with the discovery experiments. In some cases, spectrometry has also been performed at various amplification stages.

5.5 Worldwide collaborations

The power of the discovery experiments associated with the followup networks has allowed the discovery of some very exciting deviations to the simple microlensing. The best example of the collaboration between all the search teams is the study of a binary lens acting on a star of the Small Magellanic Cloud (see Fig. 3) [9]; the MACHO collaboration first published an early alert on this on-going event, which later revealed to be a binary lens. The first caustic crossing was missed, but the second crossing was then correctly predicted and monitored by 6 different teams.

6 Experimental difficulties

After a decade of maturation, some sensible experimental aspects of the microlensing subject have been brought to the fore.

- Residual backgrounds: Unexpected backgrounds of fake microlensing events have been found ; a population of bright blue stars, named "blue bumpers", sometimes exhibit temporary moderate flux increases (typically smaller than a factor 1.6), that can mimic a microlensing effect if the photometric precision and/or the sampling are not good enough. Supernovæ located far behind the LMC have been detected and could also be accidentally selected as microlensing signal. An estimate of the residual contamination from those backgrounds in the selected sample of microlensing candidates has to be done, specially for the LMC/SMC studies where the signal is low.

- Blending of the source stars: The blending can also be a major difficulty for the efficiency calculations. In a very crowded sample of faint stars, a strong blending can occur. In such a case, the effective (or apparent) maximum magnification and duration of microlensing events can be very different than the true ones, and the real efficiency to detect them is then lower than that calculated for non-blended stars. In the other hand, the blend is due to stars not taken into account, and these stars can also be microlensed, inducing an apparent enhance of efficiency. The two effects compensate at the 10% level in the case of EROS, but they do not compensate in the case of MACHO, because the catalog of monitored stars is deeper, thus involving more blending effects.

7 Conclusion

Microlensing is now a mature domain. It has already rendered valuable services to science for the dark matter problem and for the galactic structure. The microlensing phenomenon also acts as an unhoped-for natural telescope, which has made possible for the first time the resolution of star-profiles, and great hope to detect extra-solar planets is now justified. Last but not least, the huge data-bases built by the dedicated experiments have already contributed to a better knowledge of variable stars like the cepheids. Ambitious projects exists to develop this new field, and new ways to analyse data are also explored.

References

1. AGAPE coll., 1999, A&A, 344, L49-L52
2. Alcock C., Akerlof C.W., Allsman R.A. et al. 1993, Nat 365, 621
3. Alcock C., Allsman R.A., Alves D. et al. 1995b, ApJ, 454 , L125
4. Ansari R. et al., 1997, A&A, 324, 843
5. Aubourg E., Bareyre P., Bréhin S. et al. 1993a, Nat 365, 623
6. Caldwell, J.A.R. & Ostriker, J.P. 1981, ApJ 251, 61
7. Crotts A.P.S., Tomaney A.B., 1996, ApJ, 473, L87
8. De Rujula A., Jetzer Ph. and Massó E., 1991, MNRAS 250,348 ; 1992, A&A 254, 99
9. EROS, MACHO/GMAN, MPS, OGLE and PLANET coll., 2000, ApJ, 532, 340
10. Grenacher L. & al., 1999, Paul Scherrer Institut report PSI PR-99-26 ZU-TH 23/99
11. Griest, K. 1991, ApJ 366, 412
12. Melchior A.L. et al., 1998, A&A 339, 658-670.
13. Paczyński, B. 1986, ApJ 304, 1
14. Sazhin M. V., Cherepashchuk A. M., 1994, Astron. Lett., Vol. 20, No. 5, 523
15. Udalski A., Szymański M., Kaluzny J. et al. 1993, Act. Astr. 43, 289

THE MOA STRATEGY FOR MICROLENSING PLANET SEARCHES

Ian Bond (MOA Collaboration)

Department of Physics
University of Auckland
New Zealand

Abstract

High magnification microlensing events have been identified as promising hunting grounds for extra solar planet searches. In such events excursions due to planetary microlensing events occur near the times of peak amplification and at significant detection probabilities. MOA has carried out intensive observations of two high magnification microlensing events. Starting in 2000, MOA plans to issue alerts of high magnification events in progress using online analysis based on image subraction.

1 Introduction

The MOA Collaboration carries out both survey observations of selected fields towards the Galactic Bulge and Magellanic Clouds and follow-up observations of selected microlensing events. A particular objective is to detect excursions from the single lens light curve due to the presence of planets in the lensing system.

To obtain an observational detection of a planet by microlensing, two conditions need to met. The source trajectory must intersect or pass very close to one of the caustics and one must be observing the event at the time of the caustic crossing. The characteristic crossing times range from 2–3 days for a Jupiter mass planet down to a few hours for an Earth mass planet. When compared with the typical Einstein ring crossing times of ~ 40 days, one can appreciate the difficulty in meeting these conditions. A study by Griest and Safizadeh (1997) argued that in the case of high magnification events, there is a significant chance of planetary caustic crossings occurring around the time of peak magnification.

Thanks to the online analysis capabilities of the survey groups MACHO, OGLE, and EROS, reliable estimates of the times and sizes of peak amplification of ongoing microlensing events can be determined well before the event peak. Thus if an ongoing event is known to be of high amplification, intensive observations can be planned accordingly. Such intensive observations were carried out by MOA on two high magnification events, 98-BLG-35

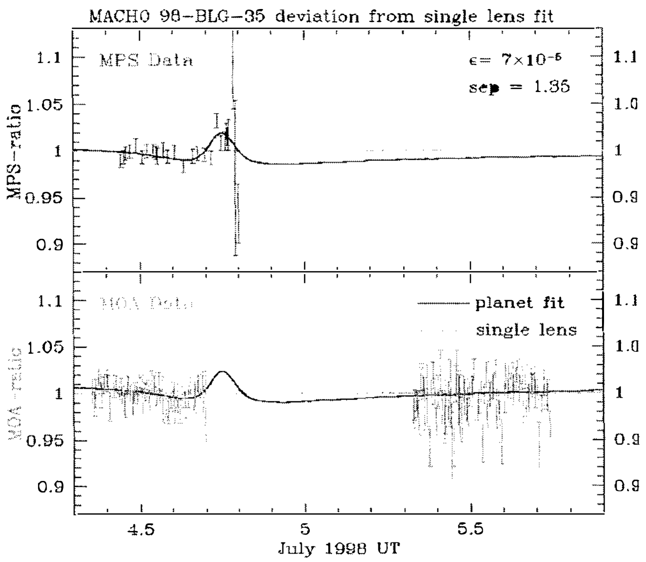

Figure 1: Deviation from a single lens fit for MPS and MOA observations of MACHO-98-BLG-35.

and 99-LMC-2, which were alerted by the MACHO Collaboration. These are described in the following sections.

2 MOA Observations of MACHO-98-BLG-35

The microlensing event MACHO-98-BLG-35 attained a peak amplification of 70.3 on 1998 July 4.6 UT. A total of 163 measurements were obtained by the MOA group over two nights around the time of peak amplification. On the night of the peak itself, 65 measurements were taken over an 8 hour period with a median sampling time of 5 minutes. This event was also observed intensely by the Microlensing Planet Search (MPS) Collaboration. The results of a detailed analysis of the combined MOA and MPS data were presented by Rhie et al (2000). Large planets of around Jupiter masses were excluded within the lensing zone. Furthermore a deviation from the single

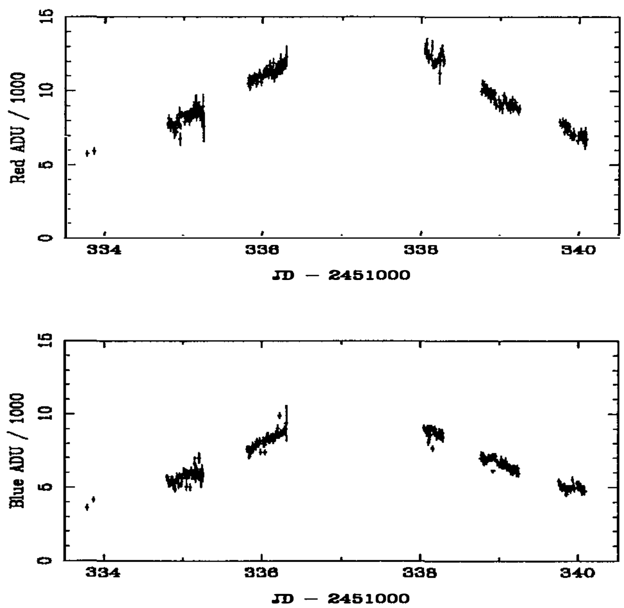

Figure 2: Light of MACHO-99-LMC-2 obtained by MOA in red and blue passbands.

lens light curve was detected (Fig. 1) and attributed to a planet in the lensing system with a mass between that of the Earth and Neptune. The detection was statistically significant at 4.5σ.

3 MOA Observations of MACHO-99-LMC-2

The microlensing event MACHO-99-LMC-2 attained a peak amplification of 43.3 on 1999 June 7.7 UT. This event was intensely observed by MOA over 5 nights around the time of peak amplification. A total of 200 measurements were made in each of the red and blue passbands with a median sampling time of 10 minutes per passband. Unfortunately, cloud prevented observations on the night of the peak. Otherwise, weather permitting, it is possible to observe targets in the Magellanic Clouds continuously for 12 hours during the Winter nights in New Zealand.

The light curve of 99-LMC-2 obtained by MOA is shown in Fig. 2. These observations will be used to determine how one can constrain the planetary configurations of the corresponding lensing system. A joint analysis of data on this event obtained by all the microlensing groups would be even more constraining. Because of its high magnification, this event is a good prospect for obtaining information on the distance to the lensing system through an analysis of parallax signatures. Furthermore, if the source star turns out to be a spectroscopic binary it may be possible to study the inverse effect of parallax in the light curve - the so-called "xallarap" effect (D. Bennett, these proceedings).

If subsequent constraints on the distance to the lensing system show 99-LMC-2 to an LMC self-lensing effect, this raises the prospect of constraining or studying the configurations of extra-galactic planetary systems.

4 MOA Planet Hunting Strategy

High amplification events appear to be the best hunting grounds for extra-solar planets through microlensing follow-up observations. The planet hunting strategy for MOA is to concentrate on agressively observing high magnification events around the times of their peak amplifications. Alerts for such events would come from the established survey groups OGLE and EROS (MACHO has now finished).

From the southern Winter of 2000, MOA began issuing alerts of ongoing "transient" events based on an online image processing pipeline using image subtraction analysis. The image subtraction procedure is our implementation of the method of Alard & Lupton (1998). The use of image subtraction analysis is potentially very powerful since it allows the detection of high magnification microlensing events whose baseline fluxes are below the detection threshold. This increases the number of potential microlensing sources. The MOA Alert Web pages can be found at:

`http://www.phys.canterbury.ac.nz/~physib/alert/alert.html.`

5 References

Alard, C. & Lupton, R.H. 1998, ApJ, 503, 325
Griest, K. & Safizadeh, N., ApJ, 500, 37
Rhie, S. et al 2000, ApJ, 532

THE OPTICAL GRAVITATIONAL LENSING EXPERIMENT OGLE-II RESULTS

K. ŻEBRUŃ, A. UDALSKI, M. SZYMAŃSKI, M. KUBIAK,
G. PIETRZYŃSKI, I. SOSZYŃSKI, P. WOŹNIAK
Warsaw University Astronomical Observatory, Al. Ujazdowskie 4, 00-478 Warsaw, Poland

KAROL ZEBRUN

We present results of observations obtained in years 1997-1999 during second phase of the OGLE experiment. Our main result is the Catalog of Microlensing events in the GB. We searched for microlensing events in database of $4 \cdot 10^9$ photometric observations of 20.5 million stars from the Galactic Bulge (GB). 214 cases of microlensing in a 11sq.deg.area. were detected. The distribution of normalized number of microlensing events in 24 lines of sight is presented. It is a crude estimate of the optical depth toward GB. Our results show that the majority of lenses are located in the Galactic Bar rather than in the Galactic disk. Details and the Catalog of Microlensing Events in GB, are available from the OGLE internet archive.

1 The Project

The idea of a search for dark matter in the Galaxy with microlensing phenomena was first proposed by Paczyński [1]. The Optical Gravitational Lensing Experiment (OGLE) main goal is to put this idea into life.

1.1 OGLE-I

First phase of the project, OGLE-I, observations (Udalski *et.al.* [2]) span the period 1992-1995. During this phase we used 1m Swope telescope located at the Las Campanas Observatory [a]. Our target was the Galactic Bulge (GB). We discovered first microlensing event toward GB (Udalski *et.al.* [3]). We also detected first binary event OGLE#7 (Udalski *et.al.* [4]). In 1994 we presented the first estimate of the optical depth to microlensing toward GB: $(3.2 \pm 1.2) \times 10^{-6}$ (Udalski *et.al* [5]). During the OGLE-I phase we succesfully implemented the Early Warning System (Udalski *et.al* [6]) to detect events in real time. An analysis of four seasons of OGLE-I observations revealed 20 microlensing events (Woźniak & Szymański [7]).

[a] Las Campanas Observatory is operated by Carnegie Institution of Washington.

1.2 OGLE-II

First phase of the project suffered from limited availability of telescope time, only about 70 nights per year. In 1997 a new 1.3m Warsaw telescope located at the Las Campanas observatory and dedicated for the OGLE microlensing search began operating. Details of instrumental setup can be found in Udalski, Kubiak & Szymański [8]. In brief, we use 2k×2k CCD detector. The pixel size is 24μm giving the scale of 0.417arcsec/pixel. The detector works in driftscan mode. This method allows us to obtain single image larger than CCD detector size. At present our images are 8k×2k and cover 0.22sq deg. Observations cover central parts of LMC and SMC bar, 4.62 and 2.42 sq. deg. respectively. GB fields cover 10.34 sq. deg. These are dense regions of smaller interstellar extinction. Their l coordinates range from -11° to +11°, around b=-3.5°. There are also a few GB fields located at positive b. Some fields are spread across Galactic disk. In 1998 we implemented the EWS system that detects events in progress (Udalski & Szymański [9]). The EWS detection technique is very similar to that used in OGLE-I phase. On-line information about microlensing events is available from our EWS web page.

2 Available data

In this paper we concentrate on analysis of GB data. We also present briefly results from Magellanic Clouds and Galactic disk. To perform our search for microlensing events in the GB we used 3 seasons of observations. Every season lasts typically from mid-February to the end of October. In years 1997-1999 we collected data for 44 GB fields. For three additional fields that were added later in 1998 we have only two seasons of observations. We collected from 142 to 324 observations for different GB fields. Whole GB databases include $4 \cdot 10^9$ photometric measurements of 20.5 million stars during 1997-1999 period. The observations were done in standard BVI bands with effective exposure time of 162, 124 and 87 seconds, respectively. The majority of observations were done in the I-band while only several epochs were collected in BV-bands. Errors of zero points of photometric calibration should not be larger than ±0.05mag. Median seeing of the presented dataset is 1"29.

3 Search algorithm

Search algorithm used for detection of microlensing events is described in detail in Udalski *et al.*[10].

4 Results

4.1 Galactic Bulge

214 microlensing events were found during our search. The majority of events in 1998 and 1999 were detected by EWS in real time. Some of these events were observed by follow-up programs, (e.g. 1998-BUL-14, Albrow [11]). The sample of 214 cases of microlensing contains 20 binary microlensing candidates. 14 of them are caustic crossing events and the remaining 6 are due to binary lens or double source star. The rate of binary microlensing, ~9.5%, is very consistent with theoretical estimates (10% Mao & Paczyński [12]).

Our sample is reasonably complete down to 19mag. Preliminary analysis of detection efficiency shows that our sample is quite complete for events longer than t_0=8days. The distribution of t_0 vs number of events peaks at t_0=17days with a longer tail of long time-scale events. The number of searched stars differs by factor of more than four in our fields. Therefore we normalized number of detected events in each field to 10^6 stars. We selected 24 lines of sight and averaged normalized numbers from overlapping fields. The fields used in each line of sight and

Table 1: Average number of microlensing events in the Galactic Bulge in 24 lines of sight.

Line of sight: BUL_SC	l	b	N per 10^6 stars	Line of sight: BUL_SC	l	b	N per 10^6 stars
5+44	359.67	−1.26	36	3+37	0.05	−1.83	17
4+39	0.48	−2.11	23	22+23	359.62	−3.15	14
6+7	359.80	−5.80	4	40+41	357.11	−3.20	18
24+25	357.62	−3.46	10	26+27	355.09	−3.51	13
28+29	353.30	−4.52	4	47+48+49	348.79	−2.88	0
1+38	1.02	−3.52	5	20+34	1.52	−2.43	9
21+30	1.87	−2.75	13	31+32	2.28	−3.04	8
35+36	3.10	−3.10	6	2+33	2.29	−3.56	7
18+19	4.03	−3.24	9	42	4.48	−3.38	9
16+17	5.19	−3.37	4	12+13	7.85	−3.48	2
10+11	9.69	−3.54	7	8+9	10.53	−3.88	0
14+15	5.30	2.72	18	43	0.37	2.95	14

number of events per 10^6 stars are shown in Table 1. Spatial distribution is shown in Figure 1. Our results can be treated in the first approximation as crude estimate of the optical depth.

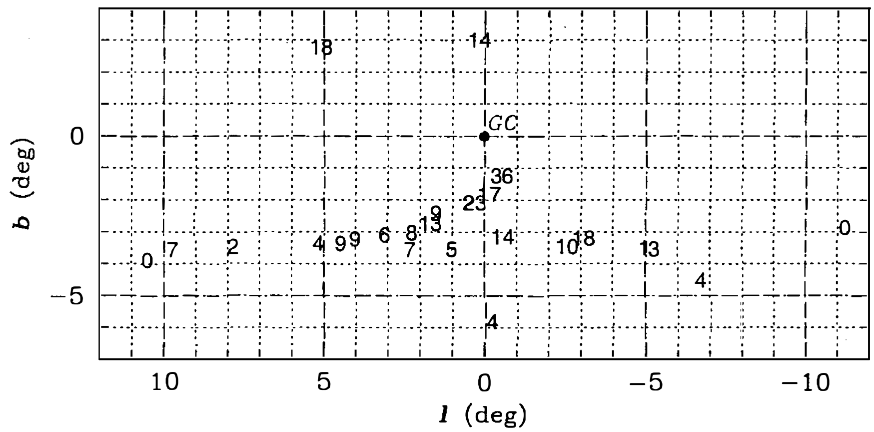

Figure 1: Frequency of microlensing in the GB. The numbers, taken from Table 1, correspond to the number of observed microlensing events per one million stars during 1997-1999 period.

When we take a closer look at a Figure 1 we can see that number of events depends on l coordinate with a noticeable assymetry toward negative l. This suggests that most of lenses are located in Galactic Bar rather than in Galactic disk. This conclusion supports the results of previous analysis of red clump population of stars in GB done by Stanek *et.al.* [13]. For details please also refer to Udalski *et.al.*[10].

4.2 Galactic Disk and LMC, SMC

The full search for microlensing events has not been performed in these fields yet. However, the EWS system discovered several very interesting events. In the Galactic disk we detected one event in Carina field OGLE-1999-CAR-01 (Udalski & Szymański [14]). Parameters of this event are τ=90days, A_{max}=3.0 I_0=18.0. This event is very likely a genuine microlensing. Effect of parralax was detected by Mao[15]. In 2000 season we detected another candidates for microlensing OGLE-2000-SCO-01 and OGLE-2000-SCO-02.

One event in the LMC was discovered with the EWS system, OGLE-1999-LMC-01 (previously detected by MACHO). In 2000 season we detected next candidate for microlensing, OGLE-2000-LMC-01.

In the SMC follow-up observations of two events were performed. For MACHO-1997-SMC-1 our photometry allowed us to deblend source star (Udalski *et.al.*[16]). For another double event MACHO-1998-SMC-1 our photometry helped to find correct double lens model (Udalski *et.al.*[17]).

5 Future prospects – OGLE-III

In the fall of 2000, after four seasons of OGLE-II Galactic Bulge observations, a large instrumental upgrade is planned. We suspend observations for several months. Old CCD camera will be replaced by new eight chip mosaic. The array will consist of thin 4k×2k detectors. The total image size will be 8k×8k. The pixel size will be 15μm giving the scale of 0.26 arcsec/pix.

Due to increased observed sky area by a factor of 5-8 we will cover larger area of the Galactic bulge and Magellanic Clouds. The number of microlensing alerts should scale similarly, now we issue about 50 alerts per year. The large observed number of microlensing events will allow us to obtain more accurate information on the optical depth distribution in GB.

It is also planned to reanalyze OGLE-II data for all targets with image substraction method. It would allow us to get rid off blending uncertainties and to obtain more precise photometry.

6 Summary

Here we presented OGLE-II results for the three seasons of the GB observations and preliminary results for other fields. We detected 214 events in the GB. Analysis of these data gives us crude estimate of the microlensing depth. Our results indicate the existence of a bar in the center of the Galaxy. The EWS system detected also events in the LMC and Galactic disk.

The Catalog of Microlensing Events in the GB is available from OGLE internet archive:

http://www.astrouw.edu.pl/~ogle/
ftp://sirius.astrouw.edu.pl/ogle/ogle2/microlensing/

or its US mirror

http://www.astro.princeton.edu/~ogle/
ftp://astro.princeton.edu/ogle/ogle2/microlensing/

Information about currently ongoing events in 2000 season and previous EWS seasons can be found on our EWS pages

http://www.astrouw.edu.pl/~ogle/ogle2/ews/ews.html
or http://www.astro.princeton.edu/~ogle/ogle2/ews/ews.html

Acknowledgments

The paper was partly suported by the Polish KBN grants 2P0300814 to A. Udalski, 2P0300916 to M. Szymański and 2P03D00717 to K. Zebrun. OGLE project is also partly supported by the NSF grant AST-9820314 to B. Paczyński.

References

1. Paczyński, B., 1986, *Astrophysical Journal*, **304**, 1

2. Udalski A., Szymański M., Kałużny J., Kubiak M., & Mateo M., 1992, *Acta Astronomica*, **42**, 253
3. Udalski A., Szymański M., Kałużny J., Kubiak M., Krzemiński W., Mateo M., Preston, G.W., & Paczyński B., 1993, *Acta Astronomica*, **43**, 289
4. Udalski A., Szymański M., Mao, S., Di Stefano, R., Kałużny J., Kubiak M., Mateo M., & Krzemiński W., 1994, *Astrophysical Journal Lett.*, **436**. L103
5. Udalski A., Szymański M., Stanek K.Z., Kałużny J., Kubiak M., Mateo M., Krzemiński W., Paczyński B., & Venkat, R., 1994, *Acta Astronomica*, **44**, 165
6. Udalski A., Szymański M., Kałużny J., Kubiak M., Mateo M., Krzemiński W., & Paczyński B., 1994, *Acta Astronomica*, **44**, 227
7. Woźniak, P., & Szymański, M., 1998, *Acta Astronomica*, **48**, 269
8. Udalski, A., Kubiak, M., & Szymański, M., 1997, *Acta Astronomica*, **47**, 319
9. Udalski, A., Szymański, M., 1998, *IAU Circ.*, **6901**, 2
10. Udalski, A., Żebruń, K., Szymański, M., Kubiak, M., Pietrzyński, G., Soszyński, I., Woźniak, P., 2000, *Acta Astronomica*, **50** 1
11. Albrow, M. D., *et.al.*, 2000, *Astrophysical Journal*, **535**, 176
12. Mao, S., & Paczyński, B., 1991, *Astrophysical Journal Lett.*, **374**, 73
13. Stanek K.Z., Udalski A., Szymański M., Kalużny J. Kubiak M., Mateo M., & Krzemiński W., 1997, *Astrophysical Journal*, **477**, 163
14. Udalski, A., & Szymański, M., *The Astronomer's Telegram*, **#39**
15. Mao, S., 2000, *Astronomy and Astrophysics*, **350**, L19
16. Udalski A., Szymański M., Kubiak M., Pietrzyński G., Woźniak P., & Żebruń K., 1997, *Acta Astronomica*, **47**, 431
17. Udalski A., Szymański M., Kubiak M., Pietrzyński G., Woźniak P., & Żebruń K., 1998, *Acta Astronomica*, **48**, 431

NOT ENOUGH STELLAR MASS MACHOS IN THE GALACTIC HALO

T. Lasserre and A. Milsztajn, on behalf the EROS collaboration
CEA, DSM, DAPNIA, Centre d'Études de Saclay, F-91191 Gif-sur-Yvette Cedex, France

We present the latest results from the EROS2 galactic dark matter search for microlensing effects towards the Large Magellanic Cloud. 25 million stars have been monitored over three years, and four candidates have been found, which is much lower than expected if MACHOs are a significant component of the galactic dark halo. We combine these new EROS2 results with those from our search towards the Small Magellanic Cloud as well as earlier ones from the EROS1 experiment. The combined data, sensitive to compact objects in the broad mass range $10^{-7} - 10 M_{\odot}$, allowed us to derived an upper limit on the abundance of stellar mass MACHOs. This combined limit rules out such objects as an important component of the galactic halo if their mass is smaller than a few solar mass.

1 Research context

Following the proposal of Paczyński[17] to use gravitational microlensing to probe the dark matter content of the galactic halo, several groups have been observing both Magellanic Clouds for a decade, and first candidates in these directions were reported in 1993 by the EROS and MACHO collaborations [9,2]. The main result from the first generation experiments is the strong limit derived by both EROS1 and MACHO groups on the fraction of galactic dark matter in planet-sized objects, from the absence of candidates with duration shorter than 10 days [10,3,20,21,6]. In 1996, based on 6 candidates discovered towards the LMC (with an average duration of about 40 days), the MACHO group estimated the optical depth at half that required to account for the dynamical mass of the standard spherical dark halo [4]. From similar observations, EROS1 found 2 candidates in the same range of timescales and decided to set an upper limit on the halo mass fraction [8].

The second phase of the EROS programme was started in 1996, with a ten-fold increase over EROS1 in the number of monitored stars in the Magellanic Clouds. The analysis of the first two years of data towards the Small Magellanic Cloud (SMC) allowed the observation of one microlensing event [19] also detected by the MACHO collaboration [5]. This single event, out of 5.3 million monitored stars, allowed EROS2 to further constrain the halo composition, at the level of 50 % for $0.01 - 0.5\,M_{\odot}$ halo objects [1]. At the same time, an optical detection of a halo white dwarf population, consistent with a galactic halo full of white dwarfs, was reported by Ibata et al. [12]. At the beginning of the year 2000, the MACHO group presented an analysis of 5.7 year light curves of 10.7 million stars in the LMC with an improved determination of their detection efficiency and a better rejection of background supernova explosions behind the LMC; they now favour a galactic halo MACHO component of 20% in the form of $0.4\ M_{\odot}$ objects [7]. A few days after, a detection of a halo white dwarf population at the level of a 10% component was reported by Ibata et al. [13]. Simultaneously, the EROS2 group presented its results from a two-year survey of 17.5 million stars in the LMC [16]. One EROS1 microlensing candidate, EROS1-LMC-2, exhibited a new variation, 8 years after the first one, and was thus eliminated from the list of microlensing candidates. Two new candidates were discovered, which is much lower than expected if MACHOs are a substantial component of the galactic halo. Furthermore, these new candidates do not show excellent agreement with simple microlensing light curves. Because of these two reasons, EROS chose to combine these results with those from previous EROS analyses, and to quote an upper limit on the fraction of the galactic halo in the form of MACHOs.

In this article, we describe an update on the EROS2 LMC data, the analysis of the three-year light curves from 25.5 million stars.

2 Experimental setup and observations

The telescope, camera, telescope operation and data reduction are described in Palanque-Delabrouille et al. (1998) [19]. Towards the LMC, 39 square degrees spread over 64 one square degree fields have been analyzed from August 1996 to May 1999, with a sampling of one measurement every 6 days in average. The exposure times range from 3 min in the LMC center to 12 min on the periphery.

3 LMC Analysis

We only give here a list of the various steps of the analysis which is very similar to that reported in Lasserre et al. (2000) [15]. A detailed description will be provided in Lasserre [14], and Lasserre et al. [16].

To begin, we select the 6% "most variable" light curves, a sample much larger than the number of detectable variable stars. This subset of our data is "enriched" in variable stars, but also and mainly in photometrically biased light curves. Working from this subset, we apply a first set of cuts to select, in each colour separately, the light curves that exhibit a smooth significant variation that is very unlikely to be a statistical fluctuation.

The second set of cuts compares the measurements with the best fit point-lens point-source constant speed microlensing light curve (hereafter "simple microlensing"). They allow us to reject intrinsic variable stars whose luminosity shape differs too much from simple microlensing. These cuts are loose enough not to reject most of the exotic microlensing events as blending, parallax, finite size of the source, and most cases of multiple lenses or sources. After this second set of cuts, stars selected separately in the two passbands represent about 0.01% of the initial sample; almost all of them are found in two thinly populated zones of the colour-magnitude diagram.

The third set of cuts deals with this physical background. The first zone contains stars brighter and much redder than those of the red giant clump; We reject variable stars in this zone if they vary by less than a factor two or have a very poor fit to simple microlensing. The second zone is the top of the main sequence, where the selected stars, known as blue bumpers [4], display variations that are almost always smaller than 60% of the base flux or at least 20% lower in the visible passband than in the red one. We thus reject all candidates from the second zone exhibiting one of these two features.

Compared to the analysis in Lasserre et al. (2000) [15], a new cut is introduced to reject cataclysmic variable stars as nova or supernova (behind the LMC). It rejects light curves which have a rise time significantly smaller than the decline time [a]. The final cuts are simply tighter cuts on the fit quality, applied to both colour.

[a] This cut is not applied to events with a timescale longer than 60 days, in order to avoid the rejection of microlensing phenomena with parallax effects that could also show such an asymmetry.

The tuning of each cut and the calculation of the microlensing detection efficiency are done with simulated simple microlensing light curves, as described in Palanque-Delabrouille et al. (1998) [19]. Only four candidates remain after all cuts, with a mean duration of about 35 days. One of the two-year candidate [15] was seen to vary in the third season and was thus rejected, and three new candidates have been detected. It is worth noting that, for each candidate, agreement with simple microlensing is not excellent.

4 Upper limits on the abundance of MACHOs

Up to now, a total of six microlensing candidates have been observed by EROS towards the Magellanic Clouds, one from EROS1, four from EROS2 towards the LMC, and one towards the SMC. As discussed in Graff (2000) [11] the lens of event EROS2-SMC-97-1 is unlikely to lie in the halo (at 98% C.L.); for that reason we do not include it in the limit computation.

The limits on the contribution of MACHOs to the galactic halo are obtained by comparing the number and durations of microlensing candidates with those expected from the so-called "standard" halo model described in Palanque-Delabrouille et al. (1998) [19]. The model predictions are computed for each EROS data set in turn and then summed; detection efficiencies of each programmes [8,21,1,14] have been taken into account. In this model, all dark objects have the same mass M; the model predictions have been computed for many trial masses M in turn, in the range $[10^{-8}\ \mathrm{M}_\odot,\ 10^{2}\ \mathrm{M}_\odot]$. Details on the method used to compute the limit are described in (Ansari et al. 1996). Figure 1 shows the 95% C.L. exclusion limit derived from this analysis on the halo mass fraction, f, for any given dark object mass, M. The EROS total sensitivity, estimated for stellar mass lenses, is proportional to the sum of $N_* T_{\rm obs}\,\epsilon(t_E = 50\mathrm{d})$ over the four EROS data sets. It is about 3.2 times larger than that of Alcock et al. (1997) [4] and two thirds that of Alcock et al. (2000) [7]. The standard spherical halo model fully comprised of objects with any mass function inside the range $[10^{-7} - 10]\ M_\odot$ is ruled out at 95% C.L., and the halo cannot be composed by more than 30% of objects with mass inside the range $[10^{-7} - 0.5]\ M_\odot$.

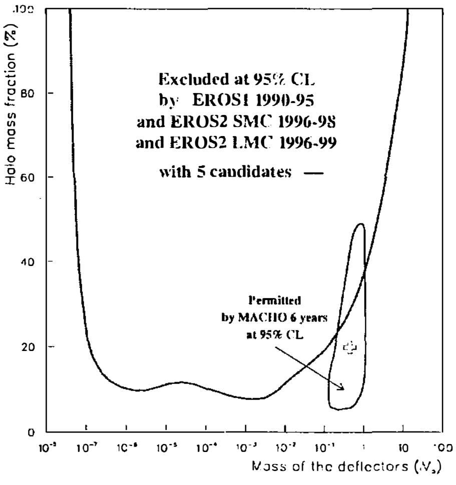

Figure 1: Combined upper limit (95% C.L) on the halo mass fraction in the form of compact objects of mass M, for the standard halo model ($4 \times 10^{11}\ \mathrm{M}_\odot$ inside 50 kpc), from all LMC and SMC EROS data 1990-99 (solid line). The closed contour represent the new MACHO 95% C.L. accepted region (the cross indicates the prefer value).

5 Discussion

There are now strong evidences, from both EROS and MACHO data sets, that MACHOs with masses less than a few solar mass are not the substantial component of the galactic dark halo[15,7]. Whereas EROS and MACHO results are consistent, their interpretations remain different, both on the variable star background and the localisation of the lenses. To be conservative, and because the agreement of our candidates with simple microlensing is not excellent, the EROS group prefer to only quote upper limits on the MACHOs content; on the contrary the MACHO collaboration reported a positive detection, which means they consider their microlensing sample to be background-free.

While the comparison of LMC and SMC events was first suggested as a way to measure the flattening of the dark halo [5], we think that the comparison of both numbers and durations of candidates should mainly be used as a test of the halo hypothesis. Indeed, since the two lines of sight are at about 20 degrees apart in the sky, the timescale distributions of microlensing candidates as well as the event rates[b] towards the two Clouds should be nearly identical if lenses belong to the galactic halo. At present, with the EROS data alone, such a comparison is not yet significant, and coming results in the direction of the SMC will provide important informations on the localisation of the lenses.

References

1. Afonso C. et al. (EROS), 1999, A&A 344, L63
2. Alcock C. et al. (MACHO), 1993, Nat 365, 621
3. Alcock C. et al. (MACHO), 1996, ApJ 471, 774
4. Alcock C. et al. (MACHO), 1997a, ApJ 486, 697
5. Alcock C. et al. (MACHO), 1997b, ApJ 491, L11
6. Alcock C. et al. (MACHO), 1998, ApJ 499, L9
7. Alcock C. et al. (MACHO), 2000, preprint astro-ph/0001272, to appear in ApJ
8. Ansari R. et al. (EROS), 1996, A&A 314, 94
9. Aubourg É. et al. (EROS), 1993, Nat 365, 623
10. Aubourg É. et al. (EROS), 1995, A&A 301, 1
11. Graff D., Lasserre T. and Milsztajn A., 2000, Nu2000 conference (Sudbury)
12. Ibata R. et al., 1999, ApJ 524, L95
13. Ibata R. et al., 2000, ApJ 532, L41
14. Lasserre T., 2000, PhD thesis, Université de Paris 6 (in French)
15. Lasserre T. et al. (EROS), 2000a, A&A 355, L39
16. Lasserre T. et al. (EROS), 2000b, in preparation
17. Paczyński B., 1986, ApJ 304, 1
18. Palanque-Delabrouille N., 1997, PhD thesis, Univ. of Chicago and Univ. de Paris 7
19. Palanque-Delabrouille N. et al. (EROS), 1998, A&A 332, 1
20. Renault C. et al. (EROS), 1997, A&A 324, L69
21. Renault C. et al. (EROS), 1998, A&A 329, 522

[b]For the standard halo model, the event rate ratio between the SMC and the LMC is about 1.4.

RESULTS OF THE EROS II COLLABORATION TOWARDS THE GALACTIC SPIRAL ARMS

Frédéric DERUE, on behalf the EROS II Collaboration
Laboratoire de l'Accélérateur Linéaire, IN2P3-CNRS, *Université de Paris-Sud, B.P. 34, 91898 Orsay*
Service de Physique des Particules, CEA-DAPNIA, *Saclay, 91191 Gif-sur-Yvette, France*

We present the analysis of the lightcurves of 9.1 million stars observed during three seasons by EROS (Expérience de Recherche d'Objets Sombres) in the Galactic plane away from the bulge. Seven stars exhibit luminosity variations compatible with gravitational microlensing effects due to unseen objects. The corresponding optical depth, averaged over the four monitored directions, is $\bar{\tau} = 0.45^{+0.25}_{-0.17} \times 10^{-6}$. The interpretation of the optical depths inferred from these observations is hindered by the imperfect knowledge of the distance to the target stars. Our measurements are compatible with expectations from simple galactic models under reasonable assumptions on the target distances.

1 Introduction

Following the suggestion of Paczyński[1] the EROS project has begun few years ago a systematic survey of the Magellanic Clouds to look for microlensing events due to MACHOs. The estimate of the disc contribution to the optical depth can be refined by investigating lines of sight that do not go through the hypothetic ellipsoidal structure in the Galactic Centre. Therefore the EROS II team has chosen to search for microlensing in four regions of the Galactic plane, located at a large angle from the Galactic Centre, corresponding to a total of 29 fields, refered as β & γ Sct, γ Nor and θ Mus. The three year data set contains 9.1 million lightcurves : 2.1 towards β Sct, 1.8 towards γ Sct, 3.0 towards γ Nor and 2.2 towards θ Mus. The data presented here have been taken between July 1996 and November 1998, except towards θ Mus (between January 1997 and November 1998), with an average of 100 measurements in each of the EROS bands V_{EROS} and R_{EROS}.

By contrast with the Magellanic Clouds, the distance distribution of the monitored stars is imperfectly known. An analysis of our colour-magnitude diagrams has shown that their content is dominated by a population of source stars located ~ 7 kpc away, undergoing an interstellar extinction of about 3 magnitudes. This distance estimate is in rough agreement with the distance to the spiral arms deduced from[2], and will be used in this paper.

2 The search for lensed stars

The selection criteria (see[3] &[4] for their description) are designed to isolate microlensing events using the expected characteristics of their lightcurves (one single peak, simultaneous in both passbands, with a known shape). To reject most of the remaining variable stars, we use the two-colours combined $\chi^2_{\mathrm{ml-out}}$ of the microlensing fit outside the peak, *i.e* limited to the periods where the magnification is lower than 10%. We remove events with low signal-to-noise ratio by requiring a significant improvement $\Delta\chi^2$ of a microlensing fit (ml) over a constant flux fit (cst) :

$$\Delta\chi^2 = \frac{\chi^2_{cst} - \chi^2_{ml}}{\chi^2_{ml}/N_{dof}} \frac{1}{\sqrt{2N_{dof}}}, \tag{1}$$

where N_{dof} is the number of degrees of freedom.

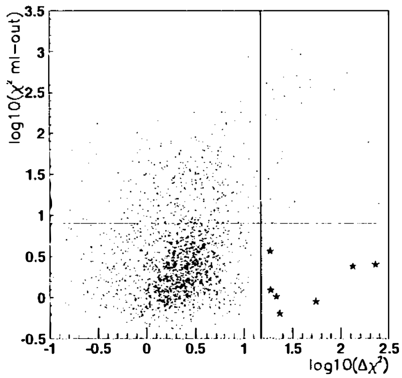

Figure 1: Distribution of $\log_{10}(\chi^2_{ml-out})$ versus $\log_{10}(\Delta\chi^2)$ for data. The two lines correspond to the adopted cut. Stars ($\star$) correspond to the seven candidates selected by our analysis.

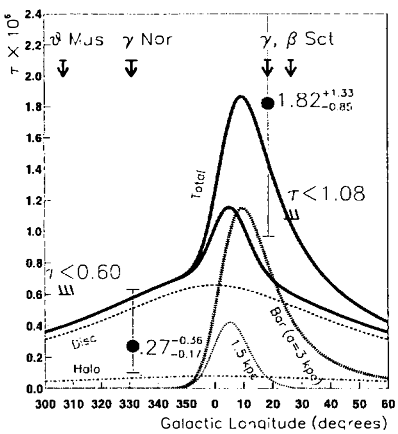

Figure 2: Expected optical depth ($\times 10^6$) up to 7 kpc for the different components of the Milky Way as a function of the Galactic longitude at $b = -2.5°$ for two values of the bar length parameter (a).

Seven lightcurves satisfy all the requirements and are hereafter named candidates and labelled GSA1 to 7. Fig. 1 shows the distribution of $\log_{10}(\chi^2_{ml-out})$ versus $\log_{10}(\Delta\chi^2)$ for lightcurves having one (and only one) significant bump. The seven candidates are isolated in a region of the diagram corresponding to lightcurves with a magnification well described by a microlensing fit and constant outside, as expected from microlensing events. The upper right side of the diagram is populated with variable stars, mostly red and bright. Table 1 contains the characteristics of the 7 candidates.

To determine the efficiency of each selection criterion, we have applied them to Monte-Carlo generated lightcurves, obtained from a representative sample of the observed stars, on which we superimpose randomly generated microlensing effects. The microlensing parameters are uniformly drawn in the following intervals: impact parameter expressed in Einstein radius unit $u_0 \in [0, 2]$, maximum magnification time in a research period T_{obs} starting 150 days before the first observations and ending 150 days after the last observations, and Einstein radius crossing time $\Delta t \in [1, 250]$ days. The analysis efficiency (or sampling efficiency) $\epsilon(\Delta t)$ reported in Table 1 is relative to a set of unblended stars, normalised to $u_0 < 1$.

Table 1: Characteristics of the 7 microlensing candidates and contribution to the optical depth.

Candidate	GSA1	GSA2	GSA3	GSA4	GSA5	GSA6	GSA7
field	γ *Sct*	γ *Nor*	γ *Nor*	γ *Sct*	γ *Sct*	γ *Sct*	γ *Sct*
α(J2000)	18:29:09	16:11:50	16:16:27	18:32:26	18:32:12	18:33:57	18:34:10
δ(J2000)	-14:15:09	-52:56:49	-54:37:49	-12:56:04	-12:55:16	-14:33:52	-14:03:40
V_{EROS} - R_{EROS}	20.7 - 17.7	19.4 - 17.8	18.6 - 17.5	17.9 - 17.1	19.9 - 17.9	18.5 - 17.2	18.7 - 17.5
Δt (days)	73.5 ± 1.4	98.3 ± 0.9	70.0 ± 2.0	23.9 ± 1.1	59.0 ± 5.5	37.9 ± 5.0	6.20 ± 0.50
Max. magnif.	26.5 ± 0.6	3.05 ± 0.02	1.89 ± 0.01	1.72 ± 0.02	1.71 ± 0.03	1.35 ± 0.02	2.70 ± 0.30
$\epsilon(\Delta t)$ (%)	10.5	30.0	25.0	6.0	10.0	8.0	2.1
contribution to τ ($\times 10^6$)	0.51	0.15	0.12	0.30	0.44	0.35	0.22

2.1 *Optical depth and event timescale*

For a given target the measured optical depth τ or a limit (when $N_{event} = 0$) can be computed using the expression :

$$\tau = \frac{1}{N_{obs} T_{obs}} \frac{\pi}{2} \sum_{events} \frac{\Delta t}{\epsilon(\Delta t)} , \tag{2}$$

where N_{obs} is the number of monitored stars in the target, T_{obs} is the duration of the search period (1170 days for this 3 year analysis, except 990 days towards θ Mus. The contribution of the candidates to the optical depth (in their own direction) is given in Table 1.

We have modeled the Galaxy using three components: a central bulge, a disc and a dark halo. The density distribution for the bulge - a bar-like triaxial model - is taken from Dwek et al.[5] model G2 (in cartesian coordinates) : $\rho_{Bulge} = \frac{M_{Bulge}}{8\pi abc} e^{-r^2/2}$, $r^4 = \left[\left(\frac{x}{a}\right)^2 + \left(\frac{y}{b}\right)^2\right]^2 + \frac{z^4}{c^4}$, where $M_{Bulge} = 2.1 \times 10^{10} M_\odot$ is the bulge mass, and a=1.5, b=0.6, c=0.4 kpc are the length scale factors. The bar major axis is inclined at an angle of 15° with respect to the Sun-Galactic Centre line. We use a standard isotropic and isothermal halo with a density distribution given in spherical coordinates by : $\rho(r) = 0.008 \frac{R_\odot^2 + R_c^2}{r^2 + R_c^2} M_\odot \mathrm{pc}^{-3}$, where $R_\odot = 8.5$ kpc is the distance Sun-Galactic Centre, and $R_c = 5$ kpc is the Halo "core radius". The matter distribution in the disc is modeled in cylindrical coordinates by a double exponential (see e.g[9]) : $\rho_{thin}(R, z) = \frac{\Sigma_{thin}}{2H_{thin}} \exp\left(\frac{-(R-R_\odot)}{R_{thin}}\right) \exp\left(\frac{-|z|}{H_{thin}}\right)$, $\Sigma_{thin} = 50 M_\odot \mathrm{pc}^{-2}$ is the column density of the disc at the Sun position, $H_{thin} = 0.325$ kpc is the height scale and $R_{thin} = 3.5$ kpc is the length scale of the disc.

Fig. 2 shows the expected optical depth up to 7 kpc as a function of longitude for this model, at the average latitude of our fields $b = -2.5°$. As the main contribution comes from the thin disc (about 90%), variations of the optical depth from field to field due to the range of 2 to 3° in latitude can reach $\simeq$ 30% in the case of γ Nor, and $\simeq$ 20% for the other targets. The expected optical depth, averaged over the four directions, is 0.55×10^{-6} for our model. This estimate varies by 30% if the parameter Σ_{thin} is changed by $10 M_\odot/\mathrm{pc}^2$, or if the parameter R_{thin} is decreased by 1 kpc.

The measured optical depth, averaged over the four directions is:

$$\bar{\tau} = 0.45^{+0.25}_{-0.17} \times 10^{-6}. \tag{3}$$

The confidence interval reported here takes into account Poisson fluctuations and the possible event timescale variations inside the observed range. In Fig. 2 we report for each target the measured optical depth. In the case of β Sct and θ Mus, where no events have been observed, we have computed a 95% confidence level upper limit on the optical depths, assuming mean event durations $\Delta t = 50$ days : $\tau(\theta$ Mus$) < 0.60 \times 10^{-6}$ and $\tau(\beta$ Sct$) < 1.08 \times 10^{-6}$. The comparison of Fig. 2 with Table 3 also shows that the measured optical depths in the four directions are compatible with the predictions of our model.

The expected event duration distribution is obtained assuming that lenses belonging to the (non-rotating) halo have the same mass ($0.5 M_\odot$); their velocities transverse to the line of sight of disc stars follow a Boltzmann distribution with a dispersion of $\sim$ 150km/s. For lenses belonging to the bulge, the mass function is taken from[6] and the velocities transverse to the line of sight of disc stars also follow a Boltzmann distribution with a dispersion of $\sim$ 110km/s. The disc lenses mass function is taken from[7], which is derived from HST observations. Disc lenses are subject to a similar global rotation as the observer and the sources[8]. The motion of the Sun relative to the Local Standard of Rest is taken as ($v_{\odot R} = 9$, $v_{\odot \theta} = 11$, $v_{\odot z} = 16$) (in km/s) ; the velocity dispersions of the lens population are expected to be ($\sigma(V_R) = 40$, $\sigma(V_\theta) = 30$, $\sigma(V_z) = 20$) (in km/s). The duration of the seven events is long ($\sim$ 55 days in average) as expected from lenses from the disc.

Results direction by direction are more puzzling - despite the very low statistics. The two targets γ Sct and γ Nor are located at nearly symmetric longitudes with respect to the Galactic Centre. Yet, we find an optical depth towards γ Sct ($1.82^{+1.23}_{-0.85} \times 10^{-6}$) higher (but not significantly) than expected (0.72×10^{-6}) and than towards γ Nor ($0.27^{+0.36}_{-0.17} \times 10^{-6}$). In addition, the average measured event timescale towards γ Sct is 40 days, half of that observed for γ Nor. Provided that this is not due to a statistical fluctuation, at least two simple hypotheses could explain the observed asymmetry :

- An increase of the bar length parameter enhances the asymmetric contribution to the optical depth. Changing this parameter from $a = 1.5$ kpc to $a = 3$ kpc (see Fig. 2) leads to an optical depth towards γ Sct $\tau(\gamma\ Sct) = 1.40 \times 10^{-6}$.

- Changing the γ *Sct* source star distance from 7 to 9 kpc increases the expected optical depth from 0.75 to 1.3×10^{-6}. However, this hypothesis alone cannot account for the shorter event durations observed towards γ Sct.

3 Conclusion

We have searched for microlensing events with durations ranging from a few days to a few months in four Galactic disc fields lying 18° to 55° from the Galactic Centre. We find seven events that can be interpreted as microlensing effects due to massive compact objects. The average optical depth measured towards the four directions is $\bar{\tau} = 0.45^{+0.25}_{-0.17} \times 10^{-6}$. Assuming the sources to be 7 kpc away, the expected optical depths from a simple galactic model is 0.55×10^{-6}, in agreement with our measurement. No events have been detected in the two farthest direction from the Galactic Centre.

1. Paczyński B., 1986, ApJ 304, 1.
2. Georgelin Y.M., Amram P., Georgelin Y.P. et al., 1994, A&AS 108,513.
3. Derue F., Afonso C., Alard C. et al. (EROS Coll.), 1999a, A&A 351:87.
4. Derue F., Afonso C., Alard C. et al. (EROS Coll.), 1999b, astro-ph/0001083.
5. Dwek E., Arendt R.G., Hauser M.G. et al., 1995, ApJ 445, 716.
6. Richer H.B., Fahlman G.G., 1992, Nature 358, 383.
7. Gould A., Bahcall J.N., Flynn C., 1997, ApJ 482, 913.
8. Brand J., Blitz J., 1993, A&A 275, 67.
9. Schaeffer R., Méra D. and Chabrier G., 1998, Acta. Phys. Polonica B., Vol. 29., 1905.

FAINT MOVING OBJECTS OF THE DARK HALO?

Rodrigo Ibata, Olivier Bienayme, Ron Gililland, Jean Guibert, Simon Hodgkin, Harvey Richer and Douglas Scott
Max-Plank Institut für Astronomie, Königstuhl 17, D-69117 Heidelberg, Germany

We discuss two recent surveys aimed at constraining the number of high proper motion Halo stars. The discovery of a small number of high proper motion objects with the colours and spectra expected of cool white dwarfs suggests the existence of a population of ancient stellar remnants, which may account for the microlensing events towards the LMC. A significant fraction, $\sim$ 10%, of the local dark matter Halo may be in the form of old, cool, white dwarfs.

1 Introduction

Does the Halo of the Milky Way contain stellar mass dark objects? Though is now clear that the Halo is certainly not dominated by such objects, they could provide up to $\sim$ 20% of the Halo's mass [1, 3]. The existence of a significant population of MACHOs is suggested by the ten to twenty microlensing event candidates that have been observed towards the LMC, though alternative explanations, that invoke self-lensing of the LMC, are also plausible. However, the self-lensing scenarios have problems of their own (they require the LMC to be more puffed up than is inferred from observations), so it is still not clear whether the existence of MACHOs can be avoided. Under both interpretations, the inferred mass of the lenses is in the stellar range.

If the lens population belongs to the Galactic Halo, it should also be present in the Solar neighborhood, and in principle could be seen in deep or wide field surveys, if the individual components are sufficiently luminous. Apart from ancient white dwarfs (WDs), all stellar MACHO candidates can be safely ruled out. Ancient WDs, which have stellar masses in the range inferred from the MACHO experiment (0.1–$1.0\,M_{\odot}$), though not yet ruled out by direct star-count observations, are difficult to envisage as a MACHO population due to several indirect constraints (see e.g., [5, 7, 6]).

A renewed interest in ancient Halo WDs has arisen, due to a theoretical reappraisal of the WD cooling function. New models with a self-consistent treatment of radiation transfer and the inclusion of H_2 opacity [9, 16] drastically change the predicted colours and magnitudes of the oldest, and hence coolest, WDs. In particular, hydrogen atmosphere (DA) WDs with ages $\gtrsim$ 10 Gyr have depressed red and NIR flux; contrary to previous expectations they become bluer in, for instance, $V - I$, with age. Striking confirmation that the new WD models are correct has recently been found [10]: the spectrum of WD0346+246 shows a large supression of the NIR flux relative to a black-body model fit to the visible radiation, as predicted [9] for ancient DA WDs. Furthermore, the proper motion of WD0346+246 and the measured parallax, indicate that it is most likely a Halo member. Therefore, Halo WDs do exist and the DA subset have bluer colours than previously expected. However, are these stars present in sufficient numbers to contribute significantly to the proposed Halo of MACHOs?

2 Hubble Deep Field proper motion survey

We have conducted [11] a proper motion analysis using two epochs of I-band imaging data in the Hubble Deep Field. Though the HDF covers a small area, it is very deep (reaching to V $\sim$ 28), so the volume probed for faint Galactic sources is considerable. The second epoch HDF exposures, obtained in the same field as the original HDF, give a baseline of almost exactly two years and have total integration of 63 Ksec in I (F814W), approximately half the integration time of the first epoch I-band exposures.

Among the population of 40 faint point sources with $V > 27$, five are observed to have PMs that exceed the measurement uncertainty by more than a factor of 3 (Figure 1). Artificial star simulations show that the measured displacements of these 5 sources cannot be due to chance occurrence, and also cannot be due to noise spikes. We find that, unless there are pathological frame distortions on the scale of 1 to 2 arcsec, object 4–551 shows significant PM, so it must be a nearby moving source, and that object 2–766 likely has measurable PM, though there is a small chance that the measured offset is an artefact of a SN superimposed on a galaxy. The faintest three candidates are low signal-to-noise photometric detections in the second epoch frames, so their PM measurements are more likely to suffer from unknown systematic errors.

The detected PMs are much too low for Solar System objects, and since the two epochs were at almost identical times of the year, parallax is also ruled out. The only plausible alternative is that at least some of this sample of five objects are Galactic stars, although no known population is expected in the colour-magnitude-PM region of parameter space they occupy.

Can the moving objects we have detected be Halo WDs? That the Halo may contain numerous such stars has been suggested naturally [13, 4] through the microlensing experiments which yield MACHO masses [2] of $0.5^{+0.3}_{-0.2}\,M_\odot$, a value similar to the mass of $0.51 \pm 0.03\,M_\odot$ inferred for old WDs in ancient star clusters [15].

If the entire dark matter Halo of the Milky Way were to be made up of such WDs there should be approximately 9 such objects in the HDF between $27 < V < 28.5$, they should have colors $-0.2 < V - I < 1.0$, and they should be situated at a mean distance of 1.2 kpc. Assuming an intrinsic one-dimensional velocity dispersion of $200\,\mathrm{km\,s^{-1}}$ for the dark Halo population in the Solar Neighborhood, with zero net rotation about the Galactic center, the expected PM distributions (after correction for the Solar Reflex Motion) in both μ_ℓ and μ_b, have a mean of -20 mas/yr and a dispersion of 35 mas/yr.

The sample of moving objects we have discovered fits reasonably well into this model. Two of them (4-551 and 4-492) also appear to have spectral energy distributions consistent (within the large photometric uncertainties) with them being old WDs. This suggests that we may have discovered, through their apparent PMs, a population of ancient WDs that are the local counterparts of the objects responsible for the microlensing events observed towards the LMC.

3 Photographic plate survey

To detect the very nearby counterparts of the population of WD MACHOs tentatively detected in the HDF, we have undertaken [12] complementary wide field photographic plate surveys of very high proper motion ($> 1''$/yr =VHPM) stars. With a survey limit $\sim$ 10 magnitudes brighter than the HDF limit, we need to cover a field one million times larger than the $1.4 \times 10^{-3}\square^\circ$ WFPC2 field to probe the same Halo volume. The expected proper motions can be several $''$/yr, and candidates will be predominantly at the faint limit of the plates, where existing catalogues (cf. LHS catalog, [14]) are heavily incomplete. Faced with the difficulty of reliably identifying VHPM

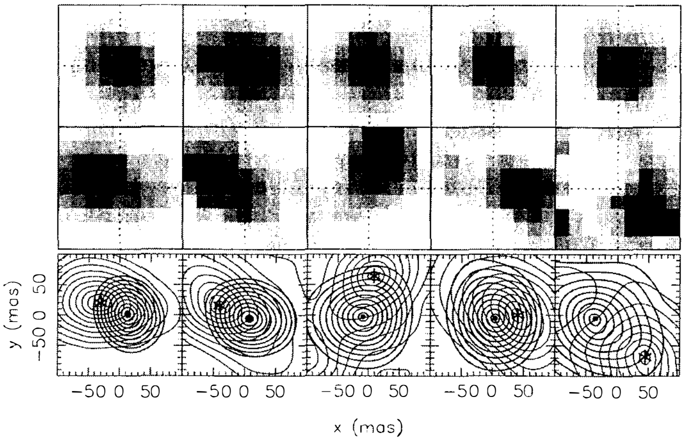

Figure 1: The panels show, from left to right, the five faint HDF point sources with significant PM: 4-551, 2-766, 4-141, 4-492 and 2-455. High resolution images, for the first and second epoch datasets are displayed in the top two rows. The bottom row shows the ($\sim 1\sigma$) likelihood contours of the object centroids obtained from the first epoch data (thick lines) and the second epoch data (thin lines).

stars among thousands of potential candidates, we investigated three independent techniques to cross-check results. Discounting the overlapping regions between adjacent plates, and the area occupied by bright stars and unusable regions of the plates, a total effective area of $\Omega \sim 790\square^\circ$ was explored.

The high proper motion candidate stars were first imaged to confirm the motion, and for the 22 objects passing this test, a further low resolution spectrum, suitable for spectral identification, was obtained. Two very high proper motion WDs were found in the surveys: F351-50, a featureless WD with $B_J = 19.76$, $B_J - R = 1.65$ and $\mu = 2.33''$/yr and LHS 542.

The measured parallax of LHS 542 implies Halo membership. Though the parallax of F351-50 is not yet known, comparison to WD models shows that it must be located at a distance $d > 15$ pc. At this distance its total space velocity with respect to the Sun is $v > 170\,\mathrm{km\,s^{-1}}$, which clearly indicates that it is not a thin or thick disk member. The only remaining alternative is that it is a Halo object. Assuming an upper limit to the space motion of $300\,\mathrm{km\,s^{-1}}$, its distance is constrained to be closer than 26.5 pc (this neglects the radial velocity component). Finally, assuming, for now, a similar absolute magnitude to WD0346+246 places it at a distance of ~ 25 pc. At that distance the expected reflex solar motion for a stationary Halo object is $\mu = 1.95''$/yr at PA 145.2°, in good agreement with the observed motion.

We have only followed up obvious detections up to R = 19. Model predictions (B. Hansen, priv. comm.) for $T > 3500$ K DA WDs are that $M_R < 16.4$, so we are sensitive to a distance modulus of $m - M_0 = 2.7$, that is, a distance of $d = 33$ pc. Lacking any information on individual masses, we assume a reasonable value of $M_\star \sim 1\,M_\odot$ [4]. This leads to a local mass density of $\sim 0.0007\,M_\odot\,\mathrm{pc}^{-3}$, that is, $\sim 10\%$ of the local density ($0.0079\,M_\odot\,\mathrm{pc}^{-3}$) of a "standard" dark matter Halo model. In comparison, the expected mass density of white dwarfs in the stellar spheroid, given the subdwarf star counts, and assuming a standard IMF, is approximately two orders of magnitude lower than this estimate.

4 Conclusions

Though these analyses have revealed the presence of halo WDs, further work is needed to provide a clearer constraint on the halo fraction in such objects. An all-sky survey to R $\sim$ 19 at Galactic latitudes $b > |30|$ (as is feasable to undertake with extant photographic plates), and with completeness similar to our photographic plate work, should find $\sim$ 14 such stars. With a larger sample of objects such as WD0346+246 or F351-50, one may also age-date halo in a way independent of isochrone fits [15]. Furthermore, very deep HST proper motion data towards the Galactic center and anticenter directions will constrain the radial density gradient of this population, thereby checking whether this is a local, perhaps transient, feature, or a massive Galactic structure.

References

[1] Afonso, C. *et al.* , 1999, A&A 344, 63

[2] Alcock, C. *et al.* , 1997, ApJ 486, 697

[3] Alcock, C. *et al.* , 2000, astro-ph/0001272

[4] Chabrier, G., 1999, ApJ 513, 103-106

[5] Fields, B., Freese, K., Graff, D. 1998, New Astronomy 3, 347

[6] Gibson, B. & Mould, J., 1997, ApJ 482, 98-103

[7] Graff, D., Freese, K., Walker, T., Pinsonneault, M. 1999, ApJ 523, 77L

[8] Gould, A., Flynn, C., Bahcall, J. 1998, ApJ 503, 798

[9] Hansen, B., 1998, Nature 394, 860

[10] Hodgkin, S., Oppenheimer, B., Hambly, N., *et al.* Nature 403, 57

[11] Ibata, R., Richer, H., Gilliland, R., Scott, D. 1999, ApJ 524, 9.5L

[12] Ibata, R., Irwin, M., Bienaymé, O., Scholz, R., Guibert, J. 2000, ApJ 532, 41L

[13] Kawaler, S., 1996, ApJ 467, L61-64

[14] Luyten, W. 1979, "LHS catalogue", Minneapolis: University of Minnesota

[15] Richer *et al.* , 1997, ApJ 484, 741

[16] Saumon, D. & Jacobson, S., 1999, ApJ 511, L107-110

EROS 2 PROPER MOTION SURVEY FOR HALO WHITE DWARFS

B. GOLDMAN, for the EROS Collaboration
PCC, Collège de France, 11 place Marcellin Berthelot,
75231 Paris Cedex 05, France

Since 1996 EROS 2 has surveyed $440^{\circ 2}$ at high Galactic latitude to search for high proper motion stars in the Solar neighbourhood. We present here the analysis of $250^{\circ 2}$ for which we have three years of data. No object with halo-like kinematics has been detected. Using a detailed Monte-Carlo simulation of the observations, we calculate our detection efficiency for this kind of object and place constraints on their contribution to various halo models. If 14 Gyr old, the halo cannot be made of more than 18% of hydrogen white dwarfs (95% C.L.).

1 Introduction

Cool white dwarfs (WDs) have become very popular in the recent years, since the MACHO [1] results suggested that they contribute to the halo introduced to explain the Galactic rotation curve. Furthermore, recent atmosphere models [12] taking into account collision induced absorption predict the hydrogen WDs to be bluer than earlier, reducing the previous constraints from colour- and infrared surveys. Such blue cool WDs have recently been discovered [8].

On the other hand, the EROS collaboration [9] lowered its limit on the microlensing optical depth towards the Magellanic Clouds. A large number of population III WDs in the halo would also contradict some of our current ideas: a strange IMF of their progenitors, metal and Helium enrichment of the Galaxy, extragalactic observations of young haloes. Hence the question remains to know what the MACHO lenses are, and to what population the detected cool WDs correspond. Cool WDs will also teach us about the early stages of star formation in the Galaxy.

High proper motion surveys are a way to distinguish them from the more numerous brighter and more distant stars with disk kinematics. We first describe the data we used and the way the high proper motion catalogue was created; then we present the current results of the EROS 2 survey concerning the contribution of cool hydrogen white dwarfs to the halo.

2 Description of the Survey

2.1 The Data

We used the EROS 2 wide field imager, located at La Silla Observatory, Chile. It delivers us $1^{\circ 2}$, $8k \times 4k$ CCD images in two broad band filters, a visible band, between V and R, and an red band close to I. Observations for the proper motion survey are conducted nearly all year round, during dark time, close to the meridian to reduce atmospheric refraction. Exposure time varies between 5 and 10 minutes, with limiting magnitudes of $V \simeq 21.5$ in the visible band and $I \simeq 20.5$ in the red band. The pixel size is 0."6.

Since 1996 we acquired 3,600 images of 442 fields located at high Galactic latitudes, mostly at 22.5h< α < 3.5h and $\delta = -39°, -45°$ (South Galactic Pole fields), and at 10h< α < 14.4h and $\delta = -6°, -12°$ (North Galactic Hemisphere fields). In this paper we use data taken between 1996 and 1999, for 2.50^{o2} for which we have three epochs, separated by one year. The remaining fields will be analyzed when we get a third epoch.

2.2 The Reduction

The flat-fielding and debiasing were performed using the EROS package PEIDA. The astrometric reduction was done by fitting a two dimensional Gaussian on the objects detected by correlation with a Gaussian PSF. The parameters of the fit were used in order to remove non-stellar objects (bad pixels, cosmic rays and the largest galaxies). The images were then geometrically aligned over 11 arcmin chunks, using the bright stars of the field, as galaxies are not numerous enough nor well measured. Then the stars were matched with a search radius corresponding to a maximum proper motion of $6''/yr$, requiring that the fluxes be compatible within 4σ. We produce this way multi-epoch catalogues in two bands.

Errors were described by photon statistics, which dominates for faint stars, in which we expect most of our halo candidates, and by the dispersion of bright star positions, which is due to the optical deformation of the (wide-field, focal reduced) telescope and the proper motion of the stars used to determine our reference frame. Total errors on a single frame range from 30 mas for bright objects, up to 0."15 at the detection limit. The external errors on the proper motion measurements are presented in Fig.1.

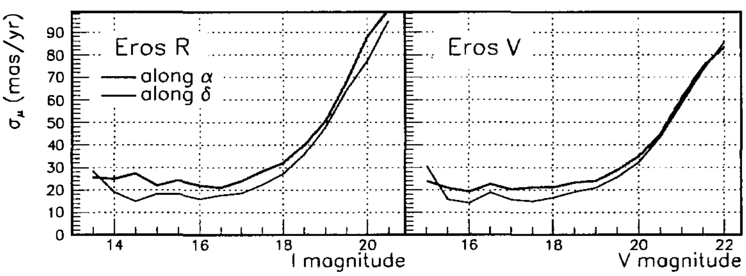

Figure 1: Proper motion dispersion for Eros R and Eros V images, along α (thick lines) and δ (thin lines).

2.3 The Selection Criteria

To eliminate the usual contamination by asteroids, noise detection, remaining cosmic rays and galaxies, we require three detections, among a set of 3 to 8 images, over three years. We then impose that the confidence level of the proper motion fit along α and δ be higher than 0.5%. At this point, depending on the population we want to select, we apply different sets of cuts:

• **slow populations**: objects from the disk are intrinsically slow, with a velocity dispersion of $\sigma \simeq 20 - 50\ km/s$ depending on the age of the stars. At a distance of 100 pc, this translates to a proper motion of $\mu \approx 80\ mas/yr$ which is only a $\sim 2 - \sigma$ detection even for bright stars. This means that no proper motion will be measurable for faint stars over our small time baseline, except for the fastest or closest ones (see 3.1 for an example), and that a cross-selection between the two band catalogues will be needed, to remove noise contamination (bicolour analysis). Thus we require that the proper motion be higher than 60 mas/yr and 3.5σ, and that the visible and red directions of proper motion be within 40°. This selects stars brighter than 18, as fainter stars have too large proper motion errors to be selected.

• **halo**: here we expect proper motions of 1"/yr or more, which makes any detection very significant, even with one single band (monochrome analysis), and intrinsically faint stars of $M_{V(I)} > 16(15)$. Thus to remove the slower, brighter known stars we require that the reduced proper motion (RPM) $H_V = M_V + 5log(V_\perp) - 3.378 = V + 5log(\mu) + 5$, where $V_\perp$ is the transerve velocity in km/s, be higher than 21 in the visible band, and $H_I > 20$ in the red band. Any star with $V > 16$ or $I > 15$ and $V_\perp > 50$km/s will satisfy this cut. Additionally, as a $V = 21$ disk star may have a $3\text{-}\sigma_\mu$ spurious proper motion of 0.4"/yr and a misleading $H_V = 24$, we also require the proper motion be higher than 0.7"/yr, or 200 km/s at 60 pc. This cut removes between 30% ($M_V = 16.5$, co-rotation of 50 km/s) and 10% ($M_V = 18$, no rotation) of detectable halo stars.

3 Results

3.1 Candidates of known Populations

Following the steps described above we select 1,046 objects in the visible band and 1,079 in the red one. Careful examination of these objects reveal that the sample is not free from contamination by spurious detections. Most candidates have a reduced proper motion H_V between 17 and 22. Objects bluer than $V - I \simeq 1.2$ can be interpreted mainly as thin and thick disks white dwarfs, and redder objects as disks red dwarfs. Some candidates with higher reduced proper motion, which may be spheroid objects or nearby, very cool dwarfs have been spectroscopied. DENIS [4] photometry has been checked for the reddest candidates. For example, LHS102B [6] was first detected as a high proper motion star, then associated with LHS102 through their common proper motion [13], and finally confirmed as a L-dwarf by DENIS and spectroscopy.

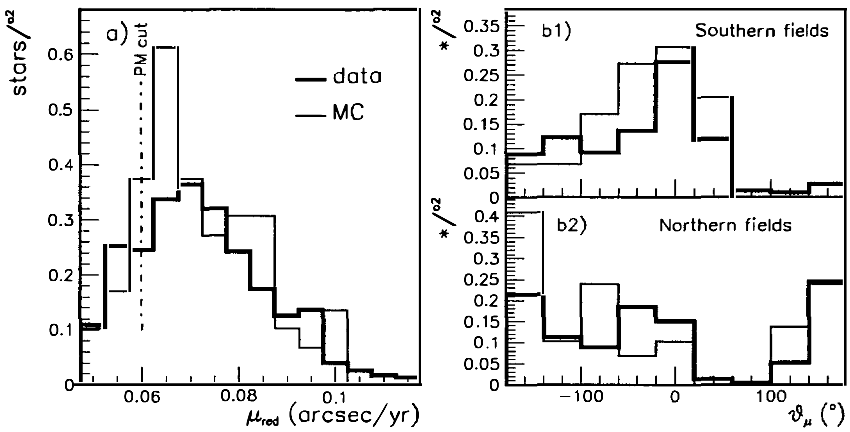

Figure 2: Distribution of detected (thick line) and expected (thin line) bright ($14 < I < 16.6$) bicolour candidates, for the red band. Expectations from a Besançon simulation of the Galaxy, corrected for our detection efficiency. a) Proper motion distribution. b) Proper motion direction distribution in our South Galactic Pole fields (top) and our Northern Galactic Hemisphere fields (bottom).

On a statistical point of view, we might check whether we reproduce well our efficiencies and our errors by comparing the thin and thick disks' and spheroid prediction with our data set. For this we use the Besançon model of the Galaxy [11] to create artificial catalogues of stars in our fields, then simulate the observations for these stars, using the actual distribution of each field (atmospheric conditions, number of exposures,...). We compare star counts, which indicate

Table 1: Expectation and constraints for HWDs of a certain V magnitude, and for different halo ages. Density limit at 95% C.L. For the expectation and mass density figures, we assumed a local density of $7.8\,10^{-3} M_{\odot}/pc^3$, for $0.6M_{\odot}$ HWDs. Figures in the left column are for the red band, in the right band for the visible band.

	V magnitude of HWDs						Halo age (Gyr)				
	16.5		17		17.5		14		15		
explored vol.	2.5	2.9	1.5	1.9	0.5	1.0	0.9	1.3	-	0.3	1000 pc^3
expectation	33.1	37.6	19.2	25.1	6.7	13.3	11.4	17.2	0.7	3.6	WDs
star density	1.2	1.0	2.0	1.6	5.8	2.9	3.4	2.3	-	11	10^{-3} WD/pc^3
mass density	0.7	0.6	1.2	0.9	3.5	1.8	2.0	1.4	-	6.6	$10^{-3} M_{\odot}/pc^3$

compatibility between the data and the Monte-Carlo for bright stars, at the 15% level. For faint objects the stars get dominated by galaxies and detailed comparison is impossible until we get a better classification of our objects. We can then apply to the resulting simulated data the *slow populations* set of cuts to check our sensitivity to *small* proper motions. We observe in Fig.2a that the results agree with the model within 20%. As we lack detailed explanation for the difference, we conservatively lower our sensivity by 20%. We also checked that our proper motion direction distribution, which mainly depends on the Sun own peculiar motion, agrees well with the Besançon distribution (see Fig.2b).

3.2 Constraints on the Halo

As with the known populations simulation, we simulated various kinds of haloes made of old hydrogen white dwarfs, with different HWD ages, masses and kinematics. The luminosity function of HWDs and the colour–magnitude function are those of Chabrier [2] and Saumon & Jacobson [12]. We also indicate our sensitivity to haloes with Dirac-like luminosity functions (see Table 1). The detailed distribution of magnitudes is not crucial as only the stars in the brighter part of the luminosity function ($M_V = 17.2 \pm 0.2$ for a 14 Gyr halo, $M_V \approx 17.8 \pm 0.3$ for 15 Gyr) contribute. Colour is important as a $V - I < 0.5$ WD will be easily missed in the red band, or a $V - I > 1.5$ in the visible, but this effect is compensated in our survey by the independent use of the two filters. Finally the cooling curve evolves with the WD mass; $1.2M_{\odot}$ WDs cool faster than $0.6M_{\odot}$ ones [3]. One should also remember that we measure a local *number* density rather than a mass density. The kinematics used correspond to the usual sets of parameters observed for the spheroid and expected for the halo, with a small rotation $-50 < \omega < 50$ km/s and velocity dispersion of 150–250 km/s. This is not crucial as most of the nearby HWDs in any model will have a proper motion above the 0.7"/yr cut. Conservatively we apply the correction for our sensitivity mentioned above, although it concerns the bicolour search for small proper motions, while we search here for large proper motion in each band independently. An example of a simulation is shown Fig.3a.

We find no halo type candidates in any band. Given our expectations of Table 1, we exclude a local number density higher than $2.3\,10^{-3}$WD/pc^3 of 14 Gyr HWDs at the 95% C.L. The exclusion diagram, as a function of the halo WD M_V magnitude, is shown in Fig.3b.

4 Conclusion

Using the first three years of data for 282 EROS 2 fields, we can place an upper limit of 18% (95% C.L.) to the contribution of white dwarfs of age 14 Gyr or of magnitude $M_V = 17.2$. We are compatible with the EROS microlensing results towards the Magellanic Clouds [9] and the analysis of proper motion observations by Flynn & al [5] and Ibata & al [8]. We exclude a 50% contribution by $M_V \approx 17$ HWDs suggested by Ibata & al [7] or Mendez & al [10], whose blue

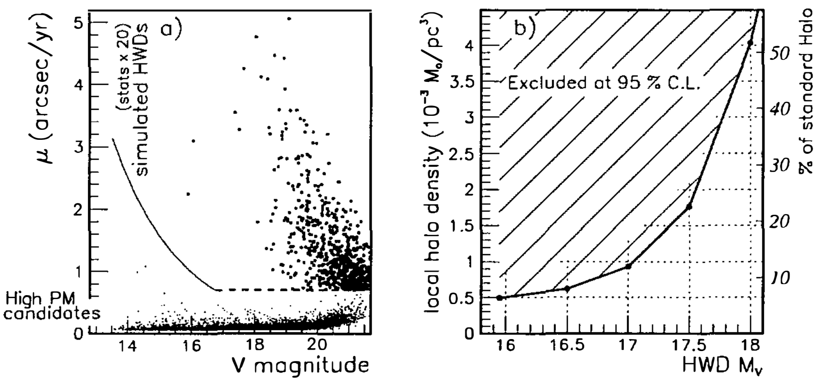

Figure 3: a) Proper motion vs. V for high PM monochrome candidates (dots) and simulated $M_V = 17$, $0.6 M_\odot$ HWDs passing the cuts (statistics ×20, circles), for the visible band. The halo PM cut is indicated by the dashed line. b) Exclusion diagram as a function of the halo WD M_V magnitude, for $0.6 M_\odot$ HWDs.

point-like objects remain to be identified. We do not place constraints on fainter objects, either older or with a pure-helium atmosphere. In the coming months additional data will become available, so that more fields will be analyzed in addition to those presented here.

Note: During the talk in Les Arcs we presented the results of the bicolour halo analysis. Since then we progressed on the more sensitive, monochrome halo analysis, which is presented here.

References

1. C. Alcock *et al*, ApJ **479**, 119 (1997) and astro-ph/0001272.
2. G. Chabrier, ApJ **513**, L103 (1999).
3. G. Chabrier *et al*, accepted by *ApJ*, astro-ph/0006363.
4. X. Delfosse *et al*, A&AS **135**, 41 (1999).
5. Ch. Flynn *et al*, *MNRAS*, astro-ph/9912264 (2000).
6. B. Goldman *et al*, A&A **351**, L5 (1999).
7. R.A. Ibata *et al*, ApJ **524**, L95 (1999).
8. R.A. Ibata *et al*, ApJ **532**, L41 (2000).
9. T. Lasserre *et al*, A&A **355**, L39 (2000).
10. R. A. Méndez and D. Minniti, ApJ **529**, 911 (2000).
11. A. Robin and M. Crézé, A&A **157**, 71 (1986) and http://www.obs-besancon.fr/www/modele/modele.html.
12. D. Saumon and S. B. Jacobson, ApJ **511**, L107 (1999).
13. W.F. van Altena, J.T. Lee, E.D. Hoffleit, *The General Catalogue of Trigonometric Stellar Parallaxes*, Fourth Edition, (Yale University Observatory, 1995).

SEARCH FOR HIGH PROPER MOTION WHITE DWARFS

J.T.A. DE JONG, K.H. KUIJKEN & M.J. NEESER
Kapteyn Astronomical Institute, Postbus 800, 9700 AV Groningen, The Netherlands

Recent results of microlensing surveys, show that 10-20 % of the dark halo mass of the Milky Way consists of compact objects. The masses of these compact objects range from 0.1 to 1 solar mass. New theoretical cooling models for white dwarfs, and the detection of faint blue high proper motion objects, imply that ancient white dwarfs might make up part of this population.
In this pilot project, using data from the C and D patches of the ESO Imaging Survey and data obtained at CTIO, we attempted to find such halo white dwarfs in the solar neighbourhood. With a time baseline of approximately one year between data sets and a limiting I-band magnitude of 23, we can find these high proper motion objects up to distances of 85 parsecs. In the 2.5 deg^2 studied so far we have found three high proper motion candidates.

1 Introduction: dark matter and white dwarfs

It is generally accepted that the Milky Way and most external galaxies contain more mass than observed directly. What makes up this so-called 'dark mass' is, however, not so clear. This mass is often assumed to be distributed in an isothermal halo, which means that dark matter would also be present in the solar neighbourhood. Recent results from galactic microlensing experiments like MACHO [1] indicate that 10 to 20 % of the dark halo mass of the Milky Way may be in compact objects.

Recent number counts of faint blue objects[2] in the Hubble Deep Fields North and South and the detection of faint moving objects[3,4], indicate the presence of a population of faint blueish compact objects in the galaxy. Furthermore, new cooling models for white dwarfs[5,6] show that they are much bluer than was previously believed. The above suggests that the galactic dark halo might, at least partially, consist of very old white dwarfs.

In the project presented here we try to find faint moving objects in the solar neighbourhood, which are likely to be dark halo white dwarfs (see the table on the right). For this purpose we use the C and D patches of the ESO Imaging Survey (EIS) Wide[7] and a smaller survey done with the CTIO 4m telescope. These data serve as a pilot project for a larger survey for which we plan to observe the complete C and D patches of the EIS Wide survey with a larger temporal baseline.

2 Data and Method

The data that are being used for the current project consist of two overlapping sets. The first data set is taken from the C and D patches of the EIS Wide survey[7], which are 6 deg^2 each. These data were obtained between July 1997 and March 1998 in the I-band with individual exposure times of 300 seconds. The second data set was obtained with the 4m telescope at CTIO. This survey covers almost 2 deg^2 of both the EIS C and D patches, making up a total area of nearly 4 deg^2. The CTIO data were taken in the R-band with single pointing exposure times of 2000 seconds. As this second survey was performed in December 1998, we have a time baseline of approximately one year for the high proper motion search.

To find high proper motion objects from the data we use a straightforward method. First, the CTIO data are transformed to the EIS coordinate system. The EIS pixels are smaller than the CTIO pixels, so in this way we do not lose information. Following this, objects are matched within a 2 arcsecond radius. Objects that seem to be offset are selected with a magnitude dependent cutoff. Finally the resulting outliers are visually inspected to filter out close objects, cosmic rays, extended sources, etc. With the time baseline of $\sim$ 1 year we are sensitive to proper motions of 0.5 to 2.0 arcsecond per year.

3 What can we find?

A high proper motion search can be very efficient in finding halo objects because of their large velocities with respect to the solar standard of rest. While the sun follows the galactic rotation, the halo does not. Therefore, halo objects have typical velocities of 200 km/s.

In the event that we find a moving object, how do we know whether it's part of the dark halo? In table 1 we compare the chances of finding objects belonging to the galactic components present in the solar neighbourhood. Our sensitivity to proper motions of 0.5 to 2.0 arcseconds, together with the typical velocities of the objects w.r.t. the sun, gives the distance range where we can find these objects. With these densities we can calculate the average number of objects per square degree. This shows that when we find a moving object, it is most likely part of the dark halo. According to cooling models by Saumon & Jacobsen[6], white dwarfs as cool as 3000 K have $M_I \sim 16$; easily detectable in our survey to distances of 85 pc.

There are, however, some issues that should be mentioned. The two data sets are in different bands (R and I), and have different noise properties because of the different exposure times. Other possible explanations for apparent object motion include close (variable star) binaries, distant supernovae and even Kuiper belt and Oort cloud objects. The motions on the sky of the Kuiper and Oort objects are dominated by parallax, but because our temporal baseline is

Table 1: Calculated estimates of the average number of moving objects one will find for different galactic populations. For these calculations, objects of 0.3 $M_\odot$ are assumed.

Population	v (km/s)	distances (pc)	ρ $(M_\odot pc^{-3})$	objects (deg^{-2})
pop.II halo	200	20-85	5×10^{-5}	**0.001**
thin disk	30	3-13	0.05	**0.03**
thick disk	60	6-25	0.003	**0.01**
dark halo	200	20-85	0.01	**2**

$\sim$ 1 year this possibility can not be excluded with our current data. All of these problems can be solved by doing a third observation run.

4 Results

We have now analyzed 5/8 of the nearly 4 deg^2 of data, and have found three promising candidates for dark halo objects. These are shown in the figures 1 to 3. The first two candidates are located in the C patch of the EIS Wide survey while the third one is in the D patch.

The objects are very faint, which is a further indication that they are not normal stars. Both candidate 1 and 2 have an apparent I-band magnitude of 22. The third candidate is even fainter, around $m_I \sim 23$. It is also striking that the two C patch objects move approximately in the same direction. This direction is consistent with it being due to the galactic rotation of the sun. The same is true for the motion of the D patch candidate.

5 Future

The recently discovered population of faint, moving objects which may be part of the galactic dark halo needs to be studied in detail. For this purpose, a large number of objects is necessary. Therefore, we see the current project as a pilot project for a larger survey. The most efficient way of increasing the chances of finding these objects is to increase the field of view. For the candidates we have so far, further observations need to be done to confirm the proper motions and to get more color information and/or spectra.

References

1. Alcock, C. *et al*, 2000, astro-ph/0001272
2. Mendez, R.A. & Minniti, D., 2000, ApJ, 529, 911
3. Ibata., R.A. *et al*, 1999, ApJ, 524, L95
4. Ibata, R.A. *et al*, 2000, ApJ, 532, L41
5. Hansen, B.M.S., 1999, ApJ, 520, 680
6. Saumon, D. & Jacobsen, S.B., 1999, ApJ, 511, L107
7. Benoist, C. *et al*, 1999, A&A, 346, 58

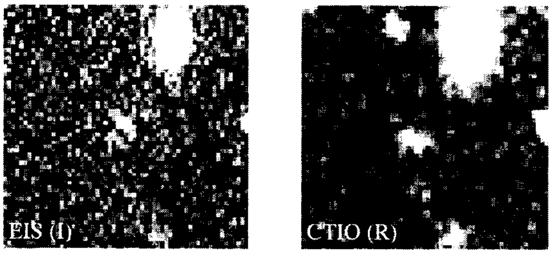

Figure 1: Candidate 1. The two images show the same 16x16 arcsec patch of the sky (located in the EIS Wide C field). On the left is the EIS I-band image, on the right the CTIO 4m R-band image, which was transformed to the EIS coordinate system. The apparent shift of the image is ~ 1 arcsec.

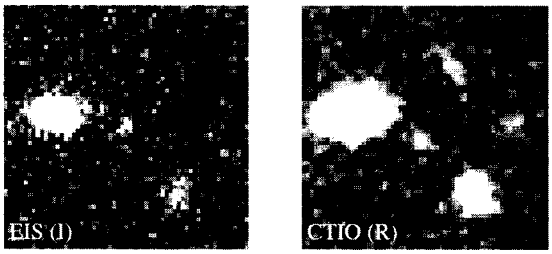

Figure 2: Candidate 2. The shift of this candidate is also ~ 1 arcsec. This candidate is also located in the EIS Wide C patch and seems to be moving approximately in the same direction as candidate 1. This direction is consistent with it being due to the galactic rotation of the sun.

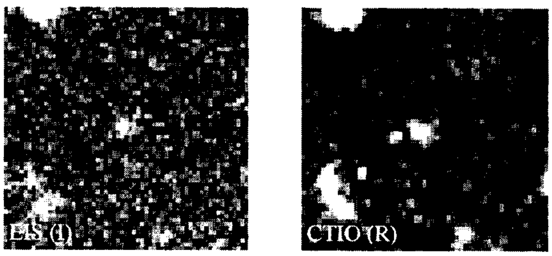

Figure 3: Candidate 3. This candidate has an apparent shift of ~ 0.5 arcsec and is near our brightness and proper motion detection limits. The direction of motion of this object is also consistent with it being due to the galactic rotation of the sun. This candidate is located in the EIS Wide D patch.

MACHOs AND THE CLOUDS OF UNCERTAINTY

Eamonn Kerins
Theoretical Physics, University of Oxford,
1 Keble Road, Oxford OX1 3NP, UK

I review proposals for explaining the current gravitational microlensing results from the EROS and MACHO surveys towards the Magellanic Clouds. Solutions involving massive compact halo objects (MACHOs), both baryonic and non-baryonic, as well as solutions that do not require MACHOs, are discussed. Whilst the existence and nature of MACHOs remains to be established, the prospects for achieving this over the next few years are good.

1 Microlensing and MACHOs — where we now stand

1.1 The EROS *and* MACHO *surveys*

EROS and MACHO [1], have been monitoring millions of stars in the Large and Small Magellanic Clouds (LMC and SMC) on an almost nightly basis since 1992, enabling them to search for MACHOs with masses from around 10^{-4} $M_{\odot}$ up to several Solar masses. EROS also undertook a survey of a smaller number of LMC stars with a sampling of 30 mins, extending its sensitivity down to 10^{-8} $M_{\odot}$. Other experiments are now also targeting the Magellanic Clouds but have yet to publish full results, so in this review we shall concentrate on the EROS and MACHO surveys. Details of these and the other surveys, and of the principles of microlensing, are described elsewhere in these proceedings.

The MACHO experiment has published around fifteen candidates towards the LMC and two candidates towards the SMC. One of the LMC candidates, MACHO LMC-9 [2], appears to be a caustic-crossing event due to a binary lens, as is the SMC candidate, 98-SMC-1 [3]. EROS has three candidate events towards the LMC and two towards the SMC (including 98-SMC-1). Of the two targets, the LMC has been the monitored the most intensively. It is worth noting that there are three strong arguments against the candidate microlensing events being instead some hitherto unknown population of variable stars. Firstly, the impact parameter distributions are consistent with microlensing expectation. Secondly, the positions of the source stars on the

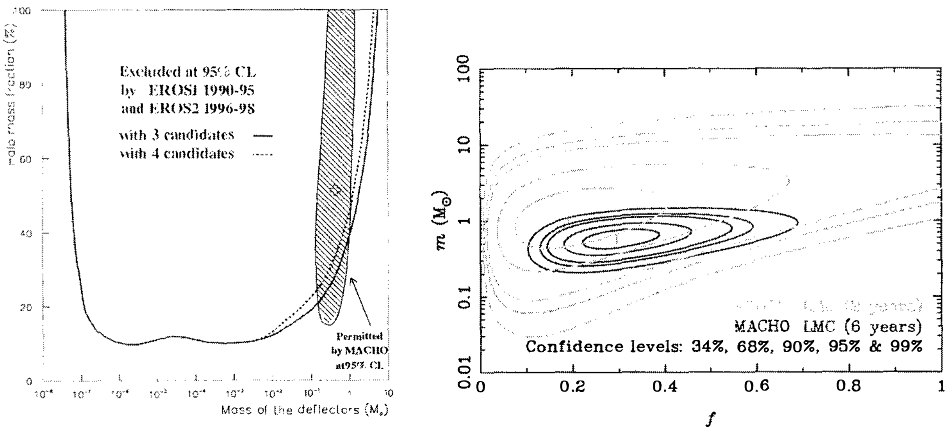

Figure 1: *Left panel*: Upper limits on the halo fraction from the EROS1+2 LMC and SMC experiments, with the MACHO two-year LMC results shown by the shaded region (figure courtesy of EROS). *Right panel*: Likelihood analysis of the MACHO fraction f and mass m from the EROS2 two-year and MACHO six-year LMC datasets, assuming the detected events are due to MACHOs. Both figures are for a "standard" isothermal dark halo.

HR diagram show no obvious clustering. Thirdly, in the case of the microlensing experiments looking towards the Galactic Bulge, the optical depth deduced only from clump giant sources is consistent with that inferred from all the events implying that, at least along this line of sight, contamination levels are small.

1.2 What we've learned so far

Before discussing the different interpretations of the microlensing results we should first reflect upon several conclusions which we are led to from both the EROS and MACHO datasets, and which have important implications for our understanding of Galactic dark matter. They underscore the considerable success of microlensing so far.

It is important to emphasize that the MACHO and EROS LMC/SMC results are statistically consistent with one another, as can be seen in Figure 1. The absence of short-duration events in either survey limits the contribution of low-mass MACHOs[4]. The EROS1+2 LMC and SMC limits in Figure 1 indicate that $f < 0.12$ for MACHOs in the mass range $10^{-6} - 10^{-2}\ M_\odot$. Both EROS and MACHO exclude brown dwarfs as a major constituent of the dark matter and both also agree that MACHOs of around a Solar mass or below do not dominate the halo dark matter budget. If one chooses to interpret the detected events as being due to MACHOs, both EROS and MACHO LMC datasets prefer a MACHO fraction $f \sim 0.2 - 0.3$ and mass $m \sim 0.5 - 1\ M_\odot$. However, the teams themselves have interpreted their results in contrasting fashion, with EROS choosing to place only upper limits on f (as shown in the left panel in Figure 1) and MACHO arguing that its dataset indicates a positive detection of MACHOs (as shown in the right-hand panel). The uncertainty is not whether microlensing has truly been observed, but whether it being caused by MACHOs.

2 MACHO solutions

2.1 Dependency of MACHO mass on halo model

Analyses of the MACHO mass inferred from microlensing data always assume some underlying model for the distribution function of the Galactic halo. The structure of the Galactic halo is

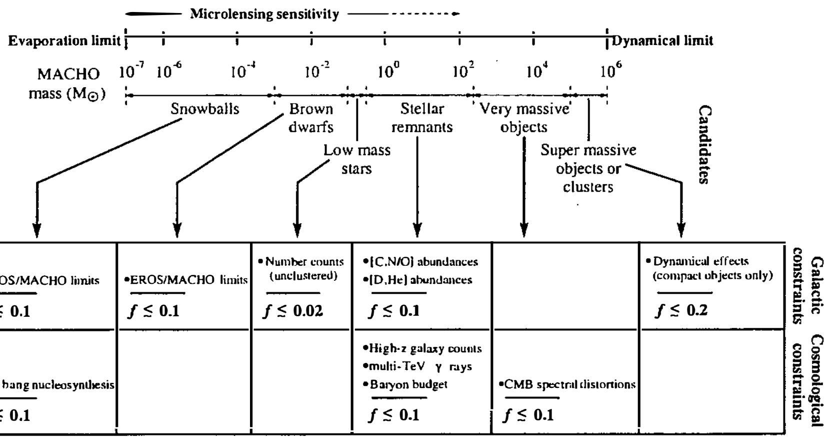

Figure 2: Baryonic MACHO candidates and constraints

very uncertain, so one might expect a large systematic error in MACHO mass determinations. Various studies employing a range of flattened halo models and anisotropic velocity distributions show that the MACHO mass determination is actually rather robust. In particular, brown dwarfs appear to be irreconcilable with current datasets [5]. If the microlensing events are due to MACHOs then their mass is of the order of a Solar mass.

2.2 Baryonic MACHOs

Figure 2 shows the range of baryonic MACHO candidates, as well as a summary of present constraints on them [6]. The microlensing mass sensitivity currently spans about seven of the thirteen orders of magnitude of the candidates, and provides the strongest constraints on snowballs and brown dwarfs. Other constraints involve a wide range of astrophysical arguments but can be loosely classified into those derived from properties of our Galaxy and those derived from cosmological considerations. In order to translate the latter into limits on the halo fraction f for our own Galaxy, one must assume it to be cosmologically representative, which may or may not be the case.

It is interesting to note that the combination of Galactic and cosmological constraints now limits the abundance of all the baryonic MACHO candidates to well below that required to explain the halo dark matter. In fact, even if we populate the halo with a mixture of baryonic candidates, they can provide only just over half of the dark matter if they are to remain consistent with all constraints. However, low-mass stars are the only candidates to be excluded by direct observation. The candidate which is most compatible with the microlensing mass scale is the white dwarf. Ibata et al. have detected a number of faint moving objects in the Hubble Deep Field (HDF) consistent with a population of white dwarfs contributing a significant fraction of the halo dark matter [7]. Subsequently, Ibata et al. obtained spectroscopy of two nearby high proper motion white dwarfs, inferring these to be possibly the nearby counterparts of the HDF objects. The observations clearly lend support to the microlensing results.

These positive findings contrast with the range of constraints in Figure 2. Remnants are constrained by both Galactic and cosmological arguments, which all indicate $f \lesssim 0.1$, barely allowing consistency with the microlensing results [8]. Galactic limits relate to the production of helium and metals, and the depletion of deuterium by the precursor stars. Cosmological limits come from the lack of precursor starlight at high-redshift, the observation that the Universe appears to be optically thin to TeV γ rays out to the redshift of blazar Mkn 501 at $z = 0.034$ (hence the infrared background indicative of the precursor stars is low or not present), and from the fact that too much of the "baryon budget" allowed by Big-Bang nucleosynthesis predictions may still be in gas by $z \sim 1$. All of these arguments can be countered on an individual basis. For example, the recent positive detection of an infrared background [9] casts doubt on our understanding of the intrinsic spectrum of Mkn 501, whilst the latest cosmic microwave background data from BOOMERANG favour a baryon density 50% larger than nucleosynthesis models predict [10]. However, the fact that these diverse constraints are all consistent with each other seriously undermines the white-dwarf hypothesis.

A recently proposed alternative to the white-dwarf solution is the beige dwarf, a kind of "genetically-modified" brown dwarf. Hansen [11] has shown that slow accretion of gas onto a brown dwarf can prevent the core temperature from rising to the point where hydrogen-burning commences. Beige dwarfs can have masses up to 0.3 $M_\odot$ if they continue to accrete at the maximum rate over a Hubble time, so providing compatibility with microlensing data.

2.3 Non-baryonic MACHOs

Though MACHOs are generally assumed to be baryonic there are a few non-baryonic cold dark matter (CDM) candidates, such as primordial black holes (PBHs), which would give rise to microlensing signatures. The fact that microlensing searches now exclude more than half of the dark matter from comprising MACHOs may be both good news and bad for CDM. On the one hand it supports the view that at least half of the dark matter is non-baryonic (though, conceivably, it could also comprise cold clumps of gas). On the other hand it limits the contribution of non-baryonic MACHO candidates as much as it does baryonic dark matter. Furthermore, if the detected microlensing events are, at least in part, due to MACHOs then we need either a combination of baryonic dark matter and CDM or *two* types of CDM: one to provide the MACHOs and one to provide the rest of the dark matter. This constitutes at least an aesthetic constraint: if MACHOs are being detected it may be easier to believe they are baryonic than to believe in two species of CDM.

The PBH scenario also requires fine-tuning. A first-order phase transition at the QCD epoch provides a natural formation mechanism to produce PBHs of about the right mass [12], however the PBH abundance must be finely tuned in order that they do not rapidly dominate the energy density of the early Universe as it expands.

3 Non-MACHO solutions

Do the microlensing results require MACHOs at all? We now examine the arguments for and against a number of alternative solutions.

3.1 Milky Way disk

The microlensing contribution of a standard Milky Way disk is an order of magnitude too small to account for the LMC events. Evans et al. [13] investigated the possibility that the disk may be significantly flared and warped in the direction of the Magellanic Clouds. Whilst such a model could account for the events, a subsequent study ruled out this proposal on the basis of star counts [13]. Gates & Gyuk [14] have advocated the existence of an old, super-thick disk with a scale height of ~ 3 kpc comprising white-dwarf remnants. The model succeeds in evading the constraints on white dwarfs because their total mass is much less than required by halo models. Whilst the model is strictly a very fat disk, it can also be viewed as a strongly dissipated MACHO halo. It is an *ad hoc* solution but, more importantly, a currently viable one.

3.2 Intervening debris

Zhao [15] has considered the effects of stellar "debris" along the line of sight to the Magellanic Clouds, either associated in some way with the Clouds or simply a chance alignment of some disrupted satellite galaxy. The proposal received tentative observational support from Zaritsky & Lin [16], who interpreted an observed vertical HR extension to the LMC red clump population as evidence of a foreground stellar population. Beaulieu & Sackett [17] claimed that such a feature is indicative of stellar evolution rather than a foreground population, whilst Bennett argued that if the structure has a similar star formation history to the LMC its optical depth would be an order of magnitude too small to explain the MACHO results [17]. Gould [18] has presented a series of arguments against intervening populations. If they are unassociated with the Magellanic Clouds then they must have a highly improbable spatial and velocity alignment with the Clouds to have remained undetected. On the other hand, if the debris is associated with the Clouds, Gould argues that its mass function would need to be dominated by sub-stellar objects in order to explain the microlensing timescales. However, it has been suggested recently that such a population may have been observed [19]. Of course, it is possible that the debris is mostly dark, in which case it is essentially a MACHO solution in disguise.

3.3 LMC/SMC self-lensing

The last possibility is that the sources in the Magellanic Clouds themselves are also providing the lenses [20]. Gould [21] has shown that if the LMC can be represented by a thin disk in virial equilibrium then its optical depth would be about an order of magnitude too small to explain the microlensing results. Though this may be too strict an assumption for what is a poorly understood structure, recent self-consistent numerical models yield similar optical depths [22].

The strongest support for the self-lensing scenario may come from the microlensing data. The two binary caustic crossing events, MACHO LMC-9 and 98-SMC-1, provide information on their line-of-sight location. Their caustic-crossing timescales indicate the time taken for the caustic to cross the face of the source and so depends on the size of the star and the projected transverse velocity of the lens. The typical transverse velocity of halo or Galactic disk lenses is of the order of 1000 km s^{-1} or more, where as for lenses in the Clouds it is typically only $\sim 60-80$ km s^{-1}. In the case of 98-SMC-1, the second caustic crossing is well resolved [3] and the projected velocity is determined to be 65–75 km s^{-1}, consistent with it being within the SMC and highly inconsistent with it being a MACHO. The second caustic crossing of MACHO LMC-9 is only partially resolved [2] and the projected velocity is inferred to be only 20 km s^{-1}, which is low even for a lens within the LMC, but certainly excludes a MACHO interpretation. Statistically, the two binary events strongly favour self-lensing over Galactic MACHOs [23]. However, it is possible that the A-type source of event LMC-9 may itself be an equal luminosity binary [2], in which case the timescale is indicative of the binary separation and the projected transverse velocity could be large enough to be consistent with the lens being a MACHO after all.

Finally, the lenses could reside in a dark halo associated with the Clouds, rather than the Milky Way halo [23]. Alves & Nelson [22] have recently argued that the LMC rotation curve does not require a halo, though in any case an LMC halo must count as a MACHO solution.

4 Summary and future prospects

Despite the many successes of microlensing, as yet there is no firm evidence that we are detecting MACHOs. Of the proposed solutions involving MACHOs, halo white dwarfs appear to be all but excluded by a host of constraints, whilst beige dwarfs and primordial black holes, though not constrained, require finely-tuned formation scenarios. As far as non-MACHO solutions are concerned, visible stellar populations do not appear to be able to provide the observed optical depth. Viable models include a dark super-thick disk, mostly dark tidal debris, or dark haloes around the Magellanic Clouds. Each of these solutions requires a major revision in our understanding of the structure of our Galaxy or its satellites, and each is really a MACHO solution in a new form.

In order to resolve the issue what is required is the ability to identify MACHO events from other microlensing events. The Andromeda galaxy presents an attractive possibility. If it is surrounded by a spherical halo of MACHOs the microlensing rate to the far side of its inclined disk should be larger than the rate towards the near side. The detection of such a gradient would provide clear evidence of MACHO rather than stellar lensing. Experiments are now in progress to try to detect this signal [24]. For our own Galaxy, the spatial distribution of the LMC microlensing events, or the velocity or magnitude distributions of the sources [25], may soon provide a conclusive answer. If not, measurements by astrometric satellites such as SIM [26] or GAIA could settle the issue by determining the line-of-sight location of a handful of events.

Acknowledgments

I am grateful to the organisers and the EU TMR programme for partial funding to attend this meeting, and to PPARC for supporting my postdoctoral fellowship.

References

1. T. Lasserre, these proceedings; W. Sutherland, these proceedings.
2. D. Bennett et al, Bucl. Phys. B **51B**, 131 (1996).
3. C. Afonso et al., ApJ **532**, 340 (2000).
4. C. Alcock et al., ApJ **499**, L9 (1998).
5. G. Gyuk, N.W. Evans, E. Gates, ApJ **502**, L29 (1998).
6. B. Carr, ARA&A **32**, 531 (1994).
7. R. Ibata et al., ApJ **524**, 195 (1999); R. Ibata et al., ApJ **532**, L41 (1999).
8. For references and an overview of the constraints see K. Freese, astro-ph/0002058 (2000).
9. V. Gorjian, E. Wright, R. Chary, ApJ **536**, 550 (1999).
10. A. Lange et al., astro-ph/0005004 (2000).
11. B. Hansen, ApJ **517**, L39 (1999).
12. K. Jedamzik, Phys. Rev. D **55**, 5871 (1997).
13. N.W. Evans, G. Gyuk, M. Turner, J. Binney, ApJ **501**, 45 (1998); G. Gyuk, C. Flynn, N.W. Evans, ApJ **521**, 190 (1999).
14. E. Gates, G. Gyuk, astro-ph/9911149 (1999).
15. H. Zhao, MNRAS **294**, 139 (1998).
16. D. Zaritsky, D. Lin, AJ **114**, 2545 (1997).
17. J.-P. Beaulieu, P., Sackett, AJ **116**, 209 (1998); D. Bennett, ApJ **493**, L79 (1998).
18. A. Gould, ApJ **525**, 724 (1999).
19. D. Graff et al., astro-ph/9910360 (1999).
20. K. Sahu, Nat **370**, 275 (1994).
21. A. Gould, ApJ **441**, 77 (1995).
22. D. Alves, C. Nelson, ApJ, in press, astro-ph/0006018 (2000).
23. E. Kerins, N.W. Evans, ApJ **517**, 734 (1999).
24. E. Kerins et al., MNRAS, in press, astro-ph/0002256 (2000); R. Uglesich, these proceedings.
25. H. Zhao, ApJ **526**, 141 (1999); H. Zhao, ApJ **527**, 167 (1999).
26. A. Gould, S. Salim, ApJ **524**, 794 (1999).

A NEW (OLD) COMPONENT OF THE MILKY WAY

E. Gates

Adler Planetarium & Astronomy Museum, Chicago, IL 60605 and Department of Astronomy & Astrophysics, University of Chicago, Chicago, IL 60637

We suggest a new component of the Milky Way that can account for both the optical depth and the event durations implied by microlensing searches targeting the Large Magellanic Cloud. This component, which represents less than 4% of the total dark matter halo mass, consists of mainly old white dwarf stars in a distribution that extends beyond the thin and thick disks, but lies well within the dark matter halo. It is consistent with recent evidence for a significant population of faint white dwarfs detected in a proper motion study of the Hubble Deep Field that cannot be accounted for by stars in the disk or spheroid. Further, it evades all of the current observational constraints that restrict a halo population of white dwarfs.

1 Introduction

The past few years have yielded exciting new data from observational teams searching for evidence of MACHOs (dark compact objects) in the halo of our galaxy, data which have raised many new questions. The microlensing optical depth toward the Large Magellanic Cloud (LMC) obtained by the MACHO collaboration [2], $\tau_{\rm LMC} = (1.2^{+0.4}_{-0.3}) \times 10^{-7}$, is consistent with a significant fraction of the galactic halo ($\sim$ 20%) in the form of MACHOs. The duration of these events also indicates that, under the assumption of a spherical isothermal halo distribution for the MACHOs, the average MACHO mass is $\sim 0.5 M_\odot$ (with large statistical uncertainties). Such masses suggest several candidates for the lenses including faint halo stars, white dwarfs, and black holes. In the standard halo model interpretation, however, white dwarfs appear to be the remaining strong candidate for the lenses.

Recent results from a proper motion study of the Hubble Deep Field (HDF) [15], and from a comparison of the north and south HDF images [18] have added a new piece to the puzzle. These studies provide further evidence that there may be a previously undetected population of old white dwarfs in the galaxy. Using new models for white dwarf cooling [13], the sources detected by Ibata et al. are consistent with 2 to 5 old ($> 12 Gyr$), $0.5 M_\odot$ white dwarfs with kinematics roughly consistent with that expected for halo objects. While earlier searches for the local counterparts did not find any such objects [7], recent surveys have turned up several candidates [14,16]. Overall, these data strengthen the interpretation of the MACHO lenses as white dwarfs in our own galaxy, and thus make alternative scenarios, such as LMC self-lensing, less appealing.

2 White Dwarfs in the Halo?

When considering the possibility that a large fraction (or all) of the galactic halo might be in the form of white dwarfs, it is extremely important to recall the evidence for galactic dark matter, including estimates of the total mass of the Milky Way. A recent analysis of satellite radial and proper motions[20] found a total mass of the Galaxy $M_{TOT} \sim 2 \times 10^{12} M_{\odot}$, in good agreement with other recent estimates[17,21]. Wilkinson and Evans also find that the halo extends to at least 100 kpc, and possibly much further to 150 or 200 kpc. Thus the total mass in a white dwarf population that comprises a significant fraction of the halo would be of order $10^{12} M_{\odot}$, a number which already severely strains the baryon budget of the Universe.

Models which propose such a population must also account for the mass in the progenitor population of stars and in the metal enriched gas produced during the formation of the white dwarfs. Combined with the above mass estimate for the galactic halo, such considerations provide serious challenges for these models.

From a cosmological point of view, we can consider the contribution of the white dwarfs and the progenitor population to the matter density of the Universe. The Milky Way has a mass to light ratio $M/L \sim 100$ or greater[21]. If we assume that this is a typical value for all galaxies, then galaxies contribute $\Omega_g \gtrsim 100/1200h = 0.08h^{-1}$. Comparing this with $\Omega_b h^2 = 0.019 \pm 0.0024$ (95%cl)[3], we find that a 50% white dwarf halo exceeds the baryon budget ($\frac{\Omega_{MACHO}}{\Omega_b} \sim 2h$) even before considering the effects of processing most of the baryons through an early star phase. A 20% white dwarf halo is also difficult to reconcile with the above estimate of Ω_b, since the contributions of the progenitor stars will exceed Ω_b.

There are several other constraints on a halo population of white dwarfs:

- The initial mass function (IMF) of the progenitor stars must be markedly different than the disk IMF.[1]
- The metal enriched gas produced when these stars become white dwarfs will pollute the remaining unprocessed gas, leading to high metallicities predicted for the Galactic disk and the interstellar medium (into which much of this gas must be blown out since the total mass in processed gas is much larger than the mass of the disk)[6,9].
- White dwarfs in the halo would also produce heavy metals via Type Ia supernovae[4].
- Deep galaxy counts limit the fraction of the halo in white dwarfs to less than about 10%, since the brightly burning progenitor stars would be visible[5].
- An all white dwarf halo would rule out the existence of other dark matter in the Universe (for example cold dark matter)[8], opening the door to a host of problems with large scale structure formation.

3 A New Component of the Galaxy

Given the evidence for a previously undetected population of white dwarfs and the severe constraints on a halo population consistent with this evidence we propose a new component of the Galaxy. This new component is essentially a very thick (scale height > 2 kpc) population of (mostly) old white dwarf stars. It is distinct from known galactic populations, both in distribution and age. This "shroud" extends beyond the thin and thick disk populations, but lies well within the halo. While the details of the distribution cannot be determined without significantly more data, the general features of this proposed model can be illustrated with the following example:

Consider an exponential disk with a volume density given by

$$\rho(r,z) = \frac{\Sigma_0}{2h_z} exp((r_0 - r)/r_d) sech^2(z/h_z) \tag{1}$$

where $r_d = 4.0$ kpc is the scale length and $h_z = 2.5$ kpc is the scale height. We assume standard values for the position and circular velocity of the Sun, $r_{\bullet} = 8.0$ kpc and $v_c = 220$ km/s.

We can also consider a spheroid-like distribution for this component. Dynamical estimates for the mass of the spheroid are considerably larger than the luminous mass, although recent studies of the mass function of the spheroid indicate that the known spheroid population is unlikely to be able to account for the microlensing events [10]. Thus a spheroidal distribution would again correspond to a previously undetected component. For such a distribution the total mass is constrained in order not to conflict with the inner rotation curve of the galaxy, which limits LMC optical depths $\tau \lesssim 1.2 \times 10^{-7}$.

The shroud supports approximately half of the local rotation speed, with the remainder coming from the thin disk and dark (non-MACHO) halo. The dark halo in these models has a large core radius (> 7 kpc) and an asymptotic rotation speed of $\approx$ 180 kpc. The total mass in the Galaxy out to 50 kpc is $\approx 4.6 \times 10^{11} M_{\odot}$. For a total mass in the white dwarf extended protodisk of $M_{wd} = 7 \times 10^{10} M_{\odot}$, we find:

- The optical depth toward the LMC generated by this component is $\tau \sim 1 - 1.5 \times 10^{-7}$;
- The lens mass estimates for the current MACHO event durations is $m \sim 0.5 M_{\odot}$, consistent with white dwarf masses;
- We expect to see roughly twice as many white dwarfs in the HDF-South compared to HDF-North, similar to the halo models;
- Simulations of the proper motions for white dwarfs in this model are broadly consistent with the observations of Ibata et al. (1999).

The main feature of this model, however, is that it has a much lower total mass in white dwarfs than halo models. As outlined above, it is consistent with both the MACHO data and the HDF studies for a total mass in white dwarfs of $M_{wd} \lesssim 7 \times 10^{10} M_{\odot}$. Thus constraints on a halo white dwarf population can be evaded, including those which consider the progenitor population and the ejected metal enriched gas. The total mass in this new component represents less than about 4% of a total halo mass of 2×10^{12}. Since essentially all of the current constraints on white dwarf halos which limit the halo mass fraction in white dwarfs do so at only the 10% level, these constraints can be satisfied by our model. This includes the Type Ia supernovae constraints which are dependent on the mass in white dwarfs today, and cannot be evaded by scenarios which involve somehow hiding the metal enriched gas produced by the progenitor stars.

There are several predictions of this model that can eventually allow it to be distinguished from a standard halo white dwarf population. First, the LMC optical depth cannot be much greater than about 1.5×10^{-7}. Second, because the lenses are concentrated closer to the plane of the galaxy, the typical lens-observer distance will be smaller (of order 5 kpc). This in turn implies an increase in the expected number of parallax events [11]. Finally, the ratio of optical depths toward the Small and Large Magellanic Clouds is expected to be of order $\tau_{SMC}/\tau_{LMC} \sim 0.8$, in contrast with $\tau_{SMC}/\tau_{LMC} \sim 1.5$ [19] predicted for a standard halo.

4 Conclusions

We have argued that the microlensing data toward the LMC, combined with observations of white dwarf stars in a proper motion study of the HDF indicate the presence of a new component of the galaxy. This component can be generally described as an extended distribution that extends at least 2 kpc above the galactic plane, but resides well within the dark matter halo. It is consistent with all data and observations of the structure and kinematics of the galaxy, and significantly alleviates the considerable problems with a halo population of white dwarf stars that is consistent with microlensing data. Much work remains to carefully consider the implications of such a component, in particular the formation and evolution of the early population of progenitor stars (and resulting metal enriched gas) that produced this component. However, the significantly lower mass in the progenitor population as compared to that for a halo population of white dwarfs will allow a reasonable fraction of the baryonic mass of the Universe to remain in gas that has not been processed through these very early stars. Moreover, this component may be a more reasonable distribution for the remains of an early starburst population, in which one would expect a more condensed distribution than that of the halo.

Acknowledgments

This work was supported in part by the DOE (at Chicago).

References

1. Adams, F. & Laughlin, G. 1996 ApJ 46, 586
2. Alcock, C., et al. 2000, astro-ph/0001272, submitted to ApJ
3. Burles, S., Nollett, K.M., Truran, J.N. & Turner, M.S. 1999, PRL 82, 4176
4. Canal, R., Isern, J., and Ruiz-Lapuente, P. 1997, ApJL 488, L35
5. Charlot, S. and Silk, J. 1995, ApJ 445, 124
6. Fields, B.D., Matthews, G. & Schramm, D. 1997, ApJ, 483, 625
7. Flynn, C., Sommer-Larsen, J., Fuchs, B., Graff, D., & Salim, S. 2000, astro-ph 9912264
8. Gates, E. & Turner, M.S. 1994, *Phys. Rev. Lett.* 72, 2520
9. Gibson, B.K. & Mould, J.R. 1997, ApJ 482, 98
10. Gould, A., Flynn, C. & Bahcall, J.N. 1998, ApJ 503, 798
11. Gyuk, G. & Gates, E. 1999, Mon. Not. R. Astron. Soc. 304, 281
12. Gyuk, G. & Gates, E. 1998, Mon. Not. R. Astron. Soc., 294, 682
13. Hansen, B. 1999, ApJ 520, 680
14. Hodgkin, S., Oppenheimer, B., Hambly, N., Jameson, R., Smartt, S., & Steele, I. 2000, Nature, 403,57
15. Ibata R., Richer H., Gilliland, R., & Scott, D. 1999, ApJL, 524, 1
16. Ibata, R., Irwin, M., Bienayme, O., Scholz, R., & Guibert, J. 2000, ApJ, 532, L41
17. Kochanek, C. 1996 ApJ, 457, 228
18. Mendez, R.A. & Minniti, D. 1999, ApJ in press; astroph/9908330
19. Sackett, P. & Gould, A. 1993, ApJ, 419, 648
20. Wilkinson & Evans 1999, astro-ph/9906197, MNRAS in press
21. Zaritsky, D., 1998, "The Third Stromlo Symposium", ASP Conf. Series, 165, 34

BINARIES, BLENDING, AND MEASUREMENTS OF THE MICROLENSING OPTICAL DEPTH

Rosanne Di Stefano
Department of Physics and Astronomy, Tufts University, Medford, MA 02155
and
Harvard-Smithsonian Center for Astrophysics, Cambridge, MA 02138

Analysis of binary-lens light curves tells us that (1) a large fraction of all the lenses detectioned to date, perhaps all of them, are binaries; (2) blending is a ubiquitous feature of the microlensing data sets; and (3) the most likely positions of the lenses discovered along directions to the Magellanic Clouds are in the Clouds themselves. Other lessons, possibly including some about the influence of the combination of blending and binarity on measurements of the optical depth, are in store.

1 All of the Lenses May be Binaries

When people think of binary-lens light curves, they tend to focus on those exhibiting the distinctive wall-like structures associated with caustic crossings. Caustic-crossing light curves are, however, only a small fraction of binary-lens light curves. Others binary-lens light curves exhibit significant, but less singular perturbations from point-lens light curves, while the large majority of light curves expected when a binary serves as a lens are difficult to distinguish from point-lens light curves. Figure 1 in Di Stefano & Perna (1997) illustrates the diversity of light curve shapes.

The relative numbers of caustic-crossing, more gently perturbed, and point-lens-like light curves depend on the linear dimensions of the caustic structures. For each lens geometry, as defined by the projected orbital separation of the binary components and their mass ratio, these relative numbers can be determined either through a pictorial examination of the caustic structures, or through a set of scattering experiments. The results of a set of scattering experiments are summarized in Figure 1. Note that, even for the large values of q that maximize the probability of a caustic crossing, there is only 1 caustic-crossing event for every $4.5 - 5$ events. Furthermore, we must take into account the fact that most binary lenses have orbital separations that, when projected onto the lens plane, are either smaller than $0.1\,R_E$ or larger than $3.0\,R_E$. If the combination of such closer and wider binaries accounts for $2/3$ of all binary-lens events, then there should be 14 or more non-caustic-crossing events for every caustic-crossing event. We can observe significantly fewer non-caustic-crossing events per caustic-crossing light curve only if binary lenses with projected separations near R_E are more numerous than other binaries, while there should be more non-caustic-crossing events if the distribution of mass ratios is peaked at values of q smaller than ~ 0.4.

When these simple consequences of the geometry of binary lenss are compared with observations, the result is striking. All of the microlensing monitoring teams that have been active

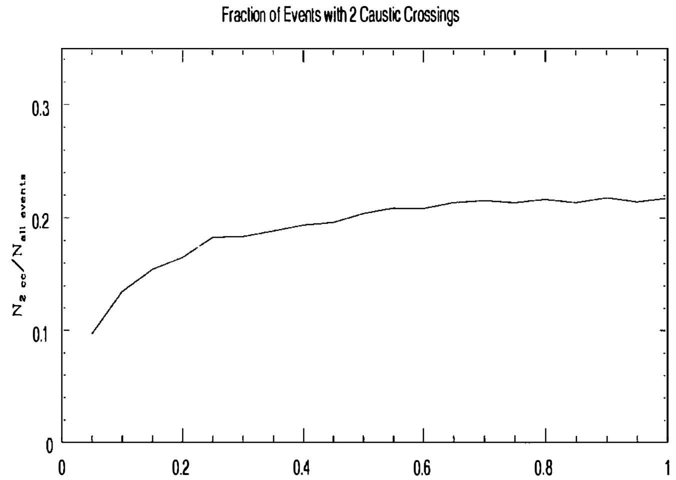

Figure 1: Ratio of the number of events with 2 caustic crossings to all events vs mass ratio, q. We have averaged over values of a ranging from $0.1\,R_E$ to $3.0\,R_E$. An "event" is any deviation from baseline with $A > 1.34$.

for several years have observed caustic-crossing events, and the ratio of caustic-crossing to other events ranges from 1/20 to 1/2. The figure of 1/20 comes from the data set with the largest number of events, the MACHO team's store of some 350 events along directions to the Galactic Bulge (Alcock *et al.* 1999). The OGLE I collaboration and the DUO team, with smaller numbers of events have found the ratio of caustic-crossing to other events to be $\sim 1/12$ (Udalski *et al.* 1994a; Alard, Mao, & Guibert 1995). This is similar to the LMC results published by the MACHO team (Alcock *et al.* 1997a), although the latest results reduce the ratio to between 1/13 and 1/17 (Alcock *et al.* 2000). The ratio of 1/2 comes from the SMC data set. Thus, in each data set, along every line of sight investigated so far, the ratio of the numbers of caustic-crossing events to other events is so high that it is consistent with a lens population composed entirely of binaries. Indeed, the hypothesis that all of the lenses are binaries cannot presently be falsified. If the lenses are primarily located in the Galactic Halo, then we may be on the verge of establishing the intriguing result that MACHOs travel in pairs.

2 Blending is Ubiquitous

At least in some of the microlensing data sets, the number of non-caustic-crossing events may be too small to be consistent with the geometry of the caustic structures. If we are indeed observing too few non-caustic-crossing events, the blending of light from the lensed star with light from other stars located along the same line of sight could be part of the explanation. Indeed, blending decreases the observed peak magnification and shortens the time duration of microlensing events, decreasing the numbers of detectable events. There are two reasons why caustic-crossing light curves are less likely to be missed, even when blending is a significant factor. First, the shape of the distinctive wall-like structures associated with caustic crossings is not changed by blending. Second, the peak magnifications tend to be high; even the minimum occurring between two successive caustic crossings has a magnification greater than 3. Thus, measuring the blending parameters for caustic-crossing events allows us to sample the distribution of blending parameters in a fairly complete way, at least if the fraction, f, of light provided by the lensed star is greater than ~ 0.2; if the fraction is smaller, then blending can reduce the efficiency with which we detect even caustic-crossing events. It is therefore interesting that, among the caustic-crossing events published by the MACHO team, virtually all events exhibit measurable blending, with roughly half of the events events having values of f smaller than 0.3. This preliminary study of blending among the caustic-crossing events makes it clear that blending is playing a large role in the data sets.

3 The Magellanic-Cloud Events May Be Due to Lenses in the Magellanic Clouds.

I have made the case that each caustic-crossing event can essentially carry with it ~ 10 or more other events, most of which are point-lens-like, and that these additional events may comprise the majority of the events discovered so far. Thus, if we could discover the location of the lenses responsible for the caustic-crossing events, we would also know the location of most of the other lenses. In fact, we have been able to determine that the most likely lens location for each of the two caustic-crossing events along directions to the Magellanic Clouds is in the Clouds themselves. (See, e.g., Alcock *et al.* 1997a, Afonso 2000.) This determination depends on being able to use information about the caustic crossing to constrain the value of the transverse velocity, and then comparing the value so derived with the probability distributions of transverse velocities expected for lenses in the Galactic Halo and in the Magellanic Clouds. The discovery and study of a relatively small number of additional caustic-crossing events would provide the simplest route to establish that the majority of the lenses are in the Magellanic Clouds, should that prove to be true, or that a significant fraction of the lenses are Halo objects. Thus, each caustic-crossing event subject to the sort of intensive study accorded 98-SMC-1 (Afonso *et al.* 2000 and references therein) has the potential not only to break the degeneracy in the physical parameters associated with that event, but also to determine the location of a large number of other lenses and to thereby help determine the MACHO halo fraction.

4 A Challenge

Another inescapable element of the binary-lens story is that every caustic-crossing light curve carries with it several non-caustic-crossing light curves that are not point-lens-like. In fact, each caustic-crossing event typically carries with it $\sim 2-4$ non-caustic-crossing events that are significantly perturbed from the point-lens form; half of these additional events are likely to exhibit multiple peaks. This is not what is reported by the observing teams. In fact, only the MACHO team has published some of these more gently perturbed binary-lens light curves, and they have found approximately a third as many of them as caustic-crossing light curves. Where are the majority of the gently perturbed binary-lens light curves?

There is probably no single answer to this question, but there are two possibilities which, in combination, must to explain the discrepancy between the predictions and the published data. One possibility is that they are in the data sets, but have not yet been identified as microlensing events. This is possible because algorithms to identify binary-lens events have not been systematically applied to the data. In addition, because some binary-lens light curves begin to deviate from the point-lens form early in their rise from baseline, some binary-lens events may not get to be subjects of the intensive study that occurs when the monitoring teams call alerts after identifying microlens candidates in real time. (See, e.g., Albrow *et al.* for a description.) A second possibility is that the events have been identified as microlens candidates, but that the characteristics that could distinguish them from point-lens light curves are washed out by blending. Note that both possibilities also apply to binary-source events, which are expected but nevertheless are largely missing from the data sets. The systematic discovery of these gently perturbed binary-lens events poses a challenge to the observing teams.

5 Implications

With many or most events caused by binaries lensing stars whose light is blended with that from other stars, both binarity and blending must be systematically included in the analyses of the microlensing data and in computations of the optical depth. The need to do this is reinforced by the fact that, in the Bulge "control" fields, as well as towards the LMC, the value of the optical depth measured via the microlensing observations is too large to be consistent with predictions based on known stellar populations. Since most of the lenses toward the Bulge are stars, the discrepancy there must be caused by drawing incorrect estimates of the optical depth from the microlensing data when the lenses and sources are not idealized, but are instead drawn form ordinary stellar populations. The combination of blending and binarity is a possible explanation for such misestimates. Furthermore, these effects can influence the data for directions to the Magellanic Clouds as well.

The work described above does *not* imply that measurement of the optical depth due to MACHOs cannot be accomplished. It simply means that the "noise" due to ordinary astronomical effects, blending and binarity in particular, is larger than anticipated. It may therefore be more difficult to discover any real signal due to lensing by MACHOs. Including binarity and blending in the analyses is a necessary step if we are to successfully scout for that elusive signal.

Acknowledgments

This paper summarizes of research described more fully in Di Stefano (1999, 2000a), where more references can be found. The work was supported by NSF under grant AST-9619516. I would like to thank Tim Axelrod, Andy Becker, Wyn Evans, and Eamonn Kerins for discussions.

References

1. M. Albrow *et al.*, ApJ **509**, 687 (1998).
2. C. Afonso *et al.*, ApJ **ApJ**, 340 (2000).
3. C. Alard, S. Mao, & J. Guibert, A&A **300L**, 17 (1995).
4. C. Alcock *et al.*, ApJ **486**, 697 (1997a).
5. C. Alcock *et al.*, ApJ **479**, 119 (1997b).
6. C. Alcock *et al.* 2000, astro-ph/0001272.
7. C. Alcock *et al.* 1999, astro-ph/9907369.
8. N. Bissantz, P. Englmaier, J. Binney, & O. Gerhard, MNRS **289**, 651 (1997).
9. R. Di Stefano, 2000, to appear in ApJ.
10. R. Di Stefano, 1999, astro-ph/9901035.
11. R. Di Stefano& R. Perna., ApJ **488**, 55 (1997).
12. A. Udalski A. et al.ApJ **436L**, 103 (1994a).
13. A. Udalski A. et al.AcA **44**, 165 (1994b).

MICROLENSING BY NON-BARYONIC (NON-COMPACT) OBJECTS

A.F. ZAKHAROV
Institute of Theoretical and Experimental Physics,
B. Cheremushkinskaya, 25, 117259, Moscow, Russia

Microlensing distant stars by non-compact objects such as neutralino stars is considered. Recently Gurevich and Zybin considered the objects as microlenses. Using the non-singular density distribution we analyse microlensing by non-compact objects. We obtain the analytical solutions of the gravitational lens equation and the analytical expression for the amplification factor of the gravitational lens. We show that using the model of microlensing by non-compact objects it is possible to interpret microlensing event candidates having two typical maximums of light curves which are usually interpreted as binary microlenses.

The first results of observations of microlensing which were presented in the papers [1,2,3] have discovered a phenomenon, predicted in the papers [4,5]. The basics of microlensing theory and observational data are given in the reviews [6,7,8,9] and in the book [10]. A matter of the gravitational microlens is unknown till now, although the most widespread hypothesis assumes that they are compact dark objects as white dwarfs. Nevertheless, they could be presented by another objects, in particular, an existence of the dark objects consisting of the supersymmetrical weakly interacting particles (neutralino) has been recently discussed in the papers [11,12]. The authors showed that the stars could be formed on the early stages of the Universe evolution and to be stable during cosmological timescale. Using the singular model distribution microlensing by non-compact lenses were analysed in the papers [13,14,15,16,17].

We approximate the density of distribution mass of a neutralino star in the following form

$$\rho_{NeS}(r) = 2\rho_0 \frac{{r_c}^2}{r^2 + r_c^2}, \tag{1}$$

where r is the current value of a distant from stellar center, ρ_0 is a mass density of a neutralino star for a boundary of a core (or for a distance r_c from a center), r_c is a radius of a core. So we use the nonsingular isothermal sphere model (or the model of an isothermal sphere with a core). The dependence is approximation of the dependence which has been considered in the paper [8], where the authors considered the model of non-compact object with a core. It is clear that the singular (degenerate) dependence is the limiting dependence of (1) for $r_c \to 0$.

So, it is not difficult to obtain surface density mass, according to expression (1)

$$\Sigma(\vec{\xi}) = 4\rho_0 r_c^2 \int_0^{\sqrt{{R_x}^2-\xi^2}} \frac{{a_0}^2}{\xi^2 + h^2 + r_c^2} dh = 4\rho_0 \frac{{r_c}^2}{\sqrt{\xi^2 + r_c^2}} \quad \mathrm{atan} \frac{\sqrt{{R_x}^2 - \xi^2}}{\sqrt{\xi^2 + r_c^2}}.$$

In the case, if $R_0 \gg \xi$, then $\Sigma(\vec{\xi}) \longrightarrow 2\pi\rho_0 \frac{{r_c}^2}{\sqrt{\xi^2 + r_c^2}}$. In that case the lens equation has the following form

$$\vec{\eta} = \frac{D_s}{D_d}\vec{\xi} - D_{ds}\vec{\alpha}_{NeS}(\vec{\xi}), \tag{2}$$

where D_s is a distance from the source to the observer, D_d is a distance from the gravitational lens to the observer, D_{ds} ia a distance from the source to the gravitational lens, vectors $(\vec{\eta}, \vec{\xi})$ define a deflection on the plane of the source and the lens, respectively

$$\vec{\alpha}_{NeS}(\vec{\xi}) = \int_{R^2} d^2\xi' \frac{4G\Sigma(\vec{\xi'})}{c^2} \frac{\vec{\xi} - \vec{\xi'}}{|\vec{\xi} - \vec{\xi'}|^2}. \tag{3}$$

We calculate the microlens mass

$$M_x = 8\pi\rho_0 r_c^2 \int_0^{R_x} \frac{r^2 dr}{r^2 + r_c^2} = 8\pi\rho_0 r_c^2 (R_x - r_c \mathrm{atan}\frac{R_x}{r_c}) \approx 8\pi\rho_0 r_c^2 R_x. \tag{4}$$

We use characteristic value of a radius r_c, corresponding the microlens "mass" $M_x = 8\pi\rho_0 r_c^2 R_x$, thus we obtain lens equation in the dimensionless form. We introduce the dimensionless variables by the following way

$$\vec{x} = \frac{\vec{\xi}}{r_c}, \quad \vec{y} = \frac{\vec{\eta}}{\eta_0}, \quad \eta_0 = r_c \frac{D_s}{D_d}, \tag{5}$$

$$\Sigma_{\mathrm{cr}} = \frac{c^2 D_s}{4\pi G D_d D_{ds}}, \quad k(\vec{x}) = \frac{\Sigma(a_0\vec{x})}{\Sigma_{\mathrm{cr}}}, \quad \vec{\alpha}(\vec{x}) = \frac{1}{\pi}\int_{R^2} d^2x' k(\vec{x'}) \frac{\vec{x} - \vec{x'}}{|\vec{x} - \vec{x'}|^2}.$$

As we supposed that surface density is an axial symmetric function then the equation of the gravitational lens may be written in the scalar form [18,10]

$$y = x - \alpha(x) = x - \frac{m(x)}{x}, \quad m(x) = 2\int_0^x x' dx' k(x').$$

We remind, that we have the following expression for the function $k(x)$

$$k(x) = \frac{k_0}{\sqrt{1+x^2}}, \quad k_0 = \frac{2\pi\rho_0 r_0}{\Sigma_{\mathrm{cr}}} = \frac{2\pi M_x}{r_c R_x} \frac{G}{c^2} \frac{D_d D_{ds}}{D_s} = \frac{\pi}{4 r_c R_x} \frac{4GM_x}{c^2} \frac{D_d D_{ds}}{D_s} = \frac{\pi}{4} \frac{R_E^2}{r_c R_x}.$$

Hence, the lens equation has the following form [10]

$$y = x - D\frac{\sqrt{x^2+1} - 1}{x}, \tag{6}$$

where $D = 2k_0$.

We will show that gravitational lens equation has only one solution if $D < 2$ and have three solutions if $D > 2$ and $y > y_{\mathrm{cr}}$ (we consider gravitational lens equation for $y > 0$), where y_{cr} is a local maximal value of right hand of Eq. (6). It is possible to show that we determine the value x_{cr} which corresponds to y_{cr} using the following expression

$$x_{\mathrm{cr}}^2 = \frac{2D - 1 - \sqrt{4D+1}}{2}, \tag{7}$$

It is easy to see that according to (7) $x_{\mathrm{cr}}^2 > 0$ if and only if $D > 2$ and

$$y_{\mathrm{cr}} = x_{\mathrm{cr}} - D\frac{\sqrt{1 + x_{\mathrm{cr}}^2} - 1}{x_{\mathrm{cr}}}, \tag{8}$$

If we choose $x_{\rm cr} < 0$ then $y_{\rm cr} > 0$. So, if $D \le 2$ then gravitational lens equation has only one solution for $(y > 0)$, if $D > 2$ then gravitational lens equation has one solution (if $y > y_{\rm cr}$), three distinct solutions (if $y < y_{\rm cr}$), one single solution and one double solution (if $y = y_{\rm cr}$).

It is possible to show that gravitational lens equation is equivalent to the following equation

$$x^3 - 2yx^2 - (D^2 - y^2 - 2D)x - 2yD = 0, \tag{9}$$

jointly with the inequality

$$x^2 - yx + D > 0. \tag{10}$$

Thus it is possible to obtain the analytical solutions of gravitational lens equation by the well-known way. We perform $z = x - 2y/3$ and obtain incomplete equation of third degree

$$z^3 + pz + q = 0, \tag{11}$$

where $p = 2D - D^2 - \dfrac{y^2}{3}$ and $q = \dfrac{2y}{3}\left(\dfrac{y^2}{9} - D(D+1)\right)$, so we have the following expression for the discriminant

$$Q = \left(\frac{p}{3}\right)^3 + \left(\frac{q}{2}\right)^2 = \frac{D^2}{27}\left[-y^4 + y^2(2D^2 + 10D - 1) + D(2-D)^3\right]. \tag{12}$$

If $Q \ge 0$ then Eq. (11) has unique real solution (therefore the gravitational lens equation (6) has unique real solution). We use Cardan expression for the solution

$$x = \sqrt[3]{-q/2 + \sqrt{Q}} + \sqrt[3]{-q/2 - \sqrt{Q}} + 2y/3. \tag{13}$$

We suppose the case $D > 2$. If $y > y_{\rm cr}$ then the gravitational lens equation has unique solution. If $Q \ge 0$ then we use the expression (13) for the solution. If $Q < 0$ then we have the following expression

$$x = 2\sqrt{-\frac{p}{3}}\cos\frac{\alpha + 2k\pi}{3} + 2y/3, \quad (k = 0,1,2); \quad \cos\alpha = -\frac{q}{2\sqrt{-(p/3)^3}}, \tag{14}$$

and we select only one solution which corresponds to the inequality (10) which corresponds to $k = 0$ in (14) because if the gravitational lens equation has only one solution then we have a positive solution x for a positive value of impact parameter y therefore there is the inequality $x > y$ which is easy to see from (8). It is possible to check that maximal solution of (9) corresponds to $k = 0$ therefore the solution is the solution of (8).

If $y < y_{\rm cr}$ then the gravitational lens equation has three distinct solutions and we use the Eqs. (14) to obtain the solutions.

We consider now the case $D < 2$. We know that the gravitational lens equation has unique solution for the case. If $Q \ge 0$ then we use the expression (13) for the solution. If $Q < 0$ then we have the following expressions (14) and we select only one solution which corresponds to the inequality (10) which also corresponds to $k = 0$ as in the previous case.

It is known that magnification for gravitational lens solution x_k is defined by the following expression

$$\mu_k = \left|\left(1 - \frac{D(\sqrt{1+x^2} - 1)}{x}\right)\left(1 + D\frac{\sqrt{1+x^2} - 1}{x^2} - D\frac{1}{\sqrt{1+x^2}}\right)\right|, \tag{15}$$

so the total magnification is equal $A_{\rm tot}(y) = \sum \mu_k$, where the summation is taken over all solutions of gravitational lens equation for a fixed value y.

The light curve corresponding to non-compact microlens (for $D = 4$). is shown in paper [20]. It is easy to see that the light curves resemble the light curve for OGLE # 7 event candidate that is usually interpreted by binary lens model [19]. Thus, the light curve for OGLE # 7 event candidate could be interpreted as well as by the non-compact microlens model [20]. More detailed analysis of the non-singular model and its consequences are presented in the paper [20]. Using the singular and non-singular models polarization during microlensing was analysed and degenerate properties of the singular model are discussed in the paper [9].

I appreciate M.V. Sazhin for useful and stimulating discussions of different aspects of microlensing. The work was supported in part by Russian Foundation of Basic Research (grant N 00-02-16108).

References

1. C.Alcock *et al, Nature* **365**, 621 (1993).
2. E. Aubourg *et al., Nature* **365**, 623 (1993).
3. A. Udalski *et al, Astrophys. J.* **426**, L69 (1994).
4. A. V. Byalko, *Astron. Zhurn.* **46**, 998 (1969).
5. B. Paczynski, *Astrophys. J.* **304**, 304 (1986).
6. B. Paczynski, astro-ph/9604011.
7. E. Roulet and S. Mollerach, astro-ph/9603119.
8. A.V. Gurevich, K.P. Zybin K.P. and V.A. Sirota, *Uspekhi Phys. Nauk* **167**, 913 (1997).
9. A.F. Zakharov and M.V. Sazhin, *Uspekhi Phys. Nauk* **168**, 1041 (1998).
10. A.F. Zakharov, *Gravitational Lenses and Microlenses*, (Janus-K, Moscow, 1997).
11. A.V. Gurevich and K.P. Zybin, *Phys. Lett. A* **208**, 276 (1995).
12. A.V. Gurevich, K.P. Zybin and V.A. Sirota, *Phys. Lett. A* **214**, 232 (1995).
13. A.F. Zakharov and M.V. Sazhin, *Journ. Exper. Theor. Phys.* **110**, 1921 (1996).
14. A.F. Zakharov and M.V. Sazhin, *Journ. Exper. Theor. Phys. Lett.* **63**, 894 (1996).
15. A.F. Zakharov and M.V. Sazhin, *Pis'ma v Astron. Zhurn.* **23**, 403 (1997).
16. A.F. Zakharov and M.V. Sazhin, *Phys. Atom. Nucl.* **61**, 1120 (1998).
17. A.F. Zakharov and M.V. Sazhin, *Phys. Atom. Nucl.* **61**, 1126 (1998).
18. P. Schneider, J. Ehlers and E.E. Falco, *Gravitational Lenses*, (Springer, Berlin - Heidelberg - New York, 1992).
19. A. Udalski *et al, Astrophys. J.* **436**, L103 (1994).
20. A.F. Zakharov, *Astron. Reports* **43**, 325 (1999).
21. A.F. Zakharov, *Phys. Lett. A* **250**, 67 (1998).

PROBING THE GALACTIC CENTER BY GRAVITATIONAL LENSING

S. CAPOZZIELLO[(1)], G. IOVANE[(1)], G. LAMBIASE[(1)], D.F. TORRES[(2)]
[(1)]*Dipartimento di Scienze Fisiche "E.R. Caianiello", Università di Salerno Via S. Allende, Baronissi (SA) I-84081, Italy.*
[(2)]*Instituto Argentino de Radioastronomía, C.C.5, 1894 Villa Elisa, Buenos Aires, Argentina.*

The nature of Galactic Center could be probed by lensing experiments capable of testing the spatial and velocity distributions of stars nearby and beyond it. Several hypotheses are possible (e.g. massive neutrino condensation, boson star) which avoid the shortcomings of the supermassive black hole model.

1 Introduction

Several observational campaigns have identified the center of our Galaxy with the supermassive compact dark object Sagittarius A* (Sgr A*) which is an extremely loud radio source [1]. Detailed information comes from dynamics of stars moving in the gravitational field of such a central object. The statistical properties of spatial and kinematical distributions are of particular interest: Using them, it is possible to establish the mass and the size of the object which are $(2.61 \pm 0.76) \times 10^6 M_\odot$ concentrated within a radius of 0.016 pc (about 30 lds) [2]. From this data, it is possible to state that a supermassive compact dark object is present at the Galactic Center and, furthermore, it is revealed by the motion of stars moving within a projected distance of less than 0.01 pc from the radio source Sgr A* at projected velocities in excess of 1000 km/s. Furthermore, a large and coherent counter-rotation, expecially of the early-type stars, is revealed. Observations of stellar winds nearby Sgr A* give a mass accretion rate of $dM/dt = 6 \times 10^{-6} M_\odot yr^{-1}$. Hence, the dark mass must have a density $\sim 10^9 M_\odot pc^{-3}$ or greater and a mass-to-luminosity ratio of at least $100 M_\odot / L_\odot$. The result is that the central dark mass is statistically very significant ($\sim 6 - 8\sigma$) and cannot be removed even if a highly anisotropic stellar velocity dispersion is assumed. As a first conclusion, several authors state that, in the Galactic Center, there is either a single supermassive black hole or a very compact cluster of stellar-size black holes. Due to the above mentioned mass accretion rate, if Sgr A* is a supermassive black hole, its luminosity should be more than $10^{40} erg\, s^{-1}$. On the contrary, observations give a bolometric luminosity of $10^{37} erg\, s^{-1}$. This discrepancy is the so-called "blackness problem" which has led to the notion of a "black hole on starvation" at the Galactic Center. Besides, the most recent observations probe the gravitational potential at a radius larger than 4×10^4 Schwarzschild radii of a black hole of mass $2.6 \times 10^6 M_\odot$ [1] so that the supermassive black hole hypothesis is far from being conclusive. On the other hand, stability criteria rule out the hypothesis of a very compact stellar cluster in Sgr A*. In fact, detailed calculations of evaporation and collision mechanisms give maximal lifetimes of the order of 10^8 years which are much shorter than the estimated age of the Galaxy. Recently, other viable alternative models for the Galactic Center (and the center of several other galaxies) has been proposed. Essentially, the authors wonder if nonbaryonic condensations, given by massive neutrinos (or other fermions as gravitinos), or massive bosons could account for dynamics and size of Sgr A*, without considering the supermassive black hole [3,4,5]. The main ingredient of such proposals is that nonbaryonic matter interacts gravitationally forming a supermassive ball in which the degeneracy pressure of fermions or Heisenberg uncertainty principle for bosons balance their self–gravity. Both mechanisms, also if in a completely different way, prevent from gravitational collapse. Such nonbaryonic condensations could have formed in the early epochs during a first–order gravitational phase transition.

2 Sgr A* as a neutrino star

Various experiments are today running to search for neutrino oscillations. It is very likely that exact predictions for $\nu_\mu - \nu_{tau}$ and $\nu_\mu - \nu_\tau$ oscillations will be soon available. From all this bulk of data, it is possible to infer reasonable values of mass for ν_e, ν_μ, and ν_τ. For our purposes, we are particularly interested in fermions which masses range between 10 and 25 keV/c^2. This choice allows the formation of supermassive degenerate objects[3] (from $10^6 M_\odot$ to $10^9 M_\odot$). with a the large amount of radio emission. The theory of heavy neutrino condensates, bound by gravity, can be easily sketched [3,4] by a Thomas–Fermi model for fermions. We can set the Fermi energy E_F equal to the gravitational potential which binds the system, that is $\frac{\hbar^2 k_F^2(r)}{2m_\nu} - m_\nu \Phi(r) = E_F = -m_\nu \Phi(r_0)$, where $\Phi(r)$ is the gravitational potential, k_F is the Fermi wave number and $\Phi(r_0)$ is a constant chosen to cancel the gravitational potential for vanishing neutrino density. The length r_0 is the estimated size of the condensation. If we take into account a degenerate Fermi gas, we get $k_F(r) = \left(6\pi^2 n_\nu(r)/g_\nu\right)^{1/3}$, where $n_\nu(r)$ is the neutrino number density and we are assuming that it is the same for neutrinos and antineutrinos within the condensation. The number g_ν is the spin degeneracy factor. Immediately we see that the number density is a function of the gravitational potential, i.e. $n_\nu = f(\Phi)$, and the model is specified by it. The gravitational potential will obey a Poisson equation where neutrinos (and antineutrinos) are the source term: $\Delta\Phi = -4\pi G m_\nu n_\nu$. We can assume the spherical symmetry and define the variable $u = r[\Phi(r) - \Phi(r_0)]$ then the Poisson equation reduces to the radial Lané–Emden differential equation

$$\frac{d^2u}{dr^2} = -\left(\frac{4\sqrt{2}m_\nu^4 G g_\nu}{3\pi\hbar^3}\right)\frac{u^{3/2}}{\sqrt{r}}, \tag{1}$$

with polytropic index $n = 3/2$. This equation is equivalent to the Thomas–Fermi differential equation of atomic physics, except for the minus sign that is due to the gravitational attraction of the neutrinos as opposed to the electrostatic repulsion between the electrons. If M_B is the mass of the baryonic star internal to the condensation, the natural boundary conditions are $u(0) = GM_B\,, u(r_0) = 0$. The general solution [3] of (1) has scaling properties and it is able to reproduce the observations. It well fits the observations toward the Galactic Center which estimate a massive object of $M = (2.6 \pm 0.7) \times 10^6 M_\odot$ which dominates the gravitational potential in the inner (≤ 0.5pc) region of the bulge. In summary, a degenerate neutrino star of mass $M = 2.6 \times 10^6 M_\odot$, consisting of neutrinos with masses $m \geq 12.0$ keV/c^2 for $g_\nu = 4$, or $m \geq 14.3$ keV/c^2 for $g_\nu = 2$, does not contradict the observations. Considering a standard accretion disk, the data are in agreement with the model if Sgr A* is a neutrino star with radius $R = 30.3$ ld ($\sim 10^5$ Schwarzschild radii) and mass $M = 2.6 \times 10^6 M_\odot$ with a luminosity $L \sim 10^{37}$erg sec^{-1}. Similar results hold also for the dark object ($M \sim 3 \times 10^9 M_\odot$) inside the center of M87. Assuming the existence of such a neutrino condensate in the Galactic Center, it could act as a spherical lens for the stars behind so that their apparent velocities will be larger than in reality. Comparing this effects with the proper motion of the stars of the cluster near Sgr A*, exact determinations of the physical parameters of the neutrino ball could be possible. In this case, gravitational lensing, always used to investigate baryonic objects, could result useful in order to detect a nonbaryonic compact object. Furthermore, since the astrophysical features of the object in Sgr A* are quite well known [2], accurate observations by lensing could contribute to the exact determination of particle constituents which could be, for example, neutrinos or gravitinos. Our heavy neutrino ball, being massive, extended and transparent, can be actually considered as a magnifying glass for stars moving behind it. If an observer is on Earth and he is looking at the Galactic Center, he should appreciate a difference in the motion of stars since lensed stars and non-lensed stars should have different projected velocity distributions. In other words, depending on the line of sight (toward the ball or outside the ball) it should be possible to correct or not the projected velocities by a gravitational lensing contribution and try to explain the bimodal distribution actually observed [1,2]. Detailed calculations in this sense are given in Capozziello & Iovane 1999 [4] where the spatial and kinematical distributions of the stars nearby the Galactic Center are reproduced by using the neutrino condensate as a thick lens (a sort of magnifying glass).

3 Sgr A* as a boson star

Also a gravitationally–bound boson condensate could explain the supermassive object in Sgr A*. In general, the theory of a boson star can be constructed starting from the Lagrangian density of a massive complex self-gravitating scalar field (taking $\hbar = c = 1$)

$$\mathcal{L} = \frac{1}{2}\sqrt{|\,g\,|}\left[\frac{m_{\rm Pl}^2}{8\pi}R + \partial_\mu\psi^*\partial^\mu\psi - U(|\psi|^2)\right], \tag{2}$$

where R is the scalar of curvature, $|g|$ the modulus of the determinant of the metric $g_{\mu\nu}$, and ψ is a *complex* scalar field with potential U. Since the potential is a function of the squared modulus of the field, we obtain a global $U(1)$ symmetry. This symmetry is related with the conserved number of particles [5]. The form of the potential gives a *mini-boson*, a *boson*, or a *soliton* stars. Conventionally, it is given by $U = m^2|\psi|^2 + \frac{\lambda}{2}|\psi|^4$ where m is the scalar mass and λ a dimensionless coupling constant. Mini-boson stars are spherically symmetric equilibrium configurations with $\lambda = 0$. Boson stars, on the contrary, have a non-null value of λ. Soliton stars are non-topological solutions with a finite mass, confined in a region of space, and non-dispersive. They are given by a potential of the form $U = m^2|\psi|^2\left(1 - \frac{|\psi|^2}{\Phi_0^2}\right)^2$, where Φ_0 is a constant. Let us see, now, which are the parameters of the different scalar objects which may reproduce the features of the central object in our Galaxy. We are looking for a mass of $(2.6 \pm 0.76) \times 10^6 M_\odot$, a radius of the accretion disk of 0.016 pc$\sim$30 light days, and a luminosity of 10^{37} erg s^{-1}. An interesting fact is that, for all the above scalar objects, the radius is always related with the mass in the same way [5]: $M = m_{\rm Pl}^2 R$, where $m_{\rm PL}$ is the Planck mass. In the case of Galactic Center, it is clear that the main parameter is the mass and not the radius. In the scalar star models, from the given central mass, the radius we obtain for the star is comparable to that of the horizon ($R = m_{\rm Pl}^{-2} \times 2.61 \times 10^6 M_\odot = 3.9 \times 10^{11} cm$). In other words, we expect an object which extends about 10 solar radius from the center and which is singularity free. Due to this intrinsic feature, it is impossible to use gravitational lensing as above [4]: There the presence of an "extended" supermassive neutrino condensation in Sgr A* allows to distinguish the stars 'nearby' and 'behind' the object which effectively acts as a thick spherical lens. The star spatial positions and projected kinematics have a bimodal distribution depending on the line of sight (toward the ball or outside the ball). In the boson condensation case, we have a pointlike lens (with respect to an observer on Earth) and, also if the boson star is "transparent" [6], we cannot expect any bimodal distribution of stars behind it. However, due to the extremely large mass of the object, a standard gravitational lens analysis fails, since *strong* lensing effects have to be considered. The observed bimodal distributions in space and velocities [1 2] have to be ascribed to intrinsic, in some sense 'genetic', effects. The question is now for which values of the parameters, we can obtain a scalar object of such a mass. For the case of mini-boson star, we need an extremely light boson $m = 5.08 \times 10^{-17}\text{eV}/\text{c}^2$. This is the only parameter of this model and so it is unequivocally fixed. For boson stars, we get $m[\text{GeV}] = 7.9 \times 10^{-4}(\lambda/4\pi)^{1/4}$. It is possible to fulfill the previous relationship, for instance, with a boson of about 1 MeV and $\lambda = 1$. In the case of a non-topological soliton, we obtain $m[\text{GeV}] = 7.6 \times 10^{12}\text{GeV}^3/(\Phi_0^2[\text{GeV}]^2)$. If the parameter Φ_0 is of the order of boson mass, we need very heavy bosons: $m = 1.2 \times 10^4\text{GeV}/\text{c}^2$. Based only on the constraints imposed by the above mass–radius relationship, we may conclude that: *i*) if the boson mass is comparable to the expected Higgs mass (hundreds of GeV), then the Galactic Center could be a non-topological soliton star; *ii*) an intermediate mass boson could be enough to produce a heavy object in the form of a boson star; *iii*) a mini-boson star needs the existence of an ultra-light boson. If boson stars really exist, they should be the remnants of first-order gravitational phase transitions and their mass should be ruled by the epochs when they decoupled from the cosmological background. The Higgs particle, besides its leading role in inflationary models, should be the best and natural candidate as constituent of a boson condensation, if the phase transition occurred in early epochs. A boson condensate should be considered as a sort of topological defect. In this case, Sgr A* should be a soliton star. If soft phase-transitions took place during cosmological evolution (e.g. soft inflationary events), the leading particles could have been intermediate mass bosons and so our supermassive object should be a genuine boson star. If the phase transitions are very recent, the ultra-light bosons could belong to the Goldstone sector giving rise to mini-boson stars. In literature, we can find several examples of particles capable to fit the issues of boson stars but the ultimate answer is left to the cosmological observations and particle physics experiments.

As it is widely discussed in literature, gravitational lensing observations or very large baseline interferometry (VLBI) could give the "signature" to discriminate among the models of Galactic Center present in literature. For example, the investigation of the large "shadow" of the event horizon of the central object by an observer (we on Earth) should give information on dynamics and intrinsic structures. Interesting proposals and simulations in this sense are given in [8]. Besides, the project ARISE (Advanced Radio Interferometry between Space and Earth) is going to use the technique of Space VLBI to increase our understanding of black holes and their environments, by imaging the extreme physical configurations produced in their proximities by strong gravitational fields [9]. From a theoretical point of view, developments and results in gravitational lensing in very strong field regimes will be of extreme importance [6, 7].

1. A.M. Ghez *et al*, ApJ **509**, 678 (1998).
2. R. Genzel *et al*, ApJ **472**, 153 (1996).
3. N. Bilic *et al*, PPNP **40**, 17 (1998).
4. S. Capozziello and G. Iovane, PLA **259**, 185 (1999).
5. D.F. Torres *et al*, astro-ph/0004064 (2000).
6. M. P. Dąbrowski and F. E. Schunck, astro-ph/9807207 (1999).
7. K. S. Virbhadra and G.F.R. Ellis, astro-ph/9904193 (1999).
8. H. Falcke *et al*, astro-ph/9912263 (1999).
9. J.S. Ulvestad, astro-ph/9901374 (1999).

AGAPE: RESULTS FROM MICROLENSING ON UNRESOLVED STARS

Yann Le Du, on behalf of the AGAPE collaboration.

http://cdfinfo.in2p3.fr/Experiences/AGAPE/

Abstract

I give a review of the aims and actual state of the data analysis of the AGAPE collaboration concerning the observation of microlensing effects on unresolved stars in the M31 galaxy. On the three years of data taken at the TBL in the Pic du Midi from 1994 to 1996, we have detected 9 candidates that satisfy our selection criterias. If we include the data taken in 1998 at the MDM, in Kitt Peak, Arizona, we keep 2 candidates, with 2 more yet to be tested. The best candidate, unique in its short duration of $\sim$ 5 days and large amplification at maximum $m_R = 18$, is called Z1 and was fully described in [Ansari et al., 1999]. We are now ready to apply our analysis tools described in [Le Du, 2000] to the data taken at the Isaac Newton Telescope, in the framework of the POINT-AGAPE collaboration, which provides a much larger statistics, cf. [Kerins et al., 2000].

1 Overview of AGAPE

Our aim is to detect MACHOs in the halo of M31 galaxy lying at 725 kpc by observing microlensing events on unresolved stars. The light curves are constructed on the pixels that make up the data images, a process called "pixel lensing", and we detect the characteristic amplification on light curves through shape analysis.

The original AGAPE observations took place at the Pic du Midi (southern France) with the TBL 2 m telescope, using a 1024 x 1024 pixels CCD camera with 0.3″ per pixel. Our target was a $\sim 20' \times 10'$ regions centered on the bulge of M31, cf. figure 1, divided into 6 fields of observation labelled A to F. We collected images for 3 years, between 1994 and 1996. We have $\sim$ 1 image of each field A to D for $\sim$ 80 nights of observation divided as such : 38% in 1994, 50% in 1995 and 12% in 1996. We focus on red filter images and fields A to D, because these have a better sampling. Before analyzing the images, we made a photometric ($\sim$ 0.3% stability) and geometric ($\sim$ 0.3 pixel precision) alignment of the pictures. We give a detailed description of our procedures in [Ansari et al., 1997] and [Le Du, 2000].

Our pixel lensing analysis method relies on the analysis of the shape of pixel light curves. We have performed Monte-Carlo simulations that show that AGAPE is sensitive to $17 < m_\star < 26$, and that there are $\sim$ 10 stars detectable through lensing per 0.3″ pixel for the bulge, implying $\sim 20 \times 10^6$ potential sources on 4 fields, more than resolved stars followup like EROS or MACHO. The typical parameters that we expect are given in table 1, and are described in figure 2. The underlying physical parameters of a Paczynski lightcurve may be extracted using methods developed by [Baltz & Silk, 1999] and [Gondolo, 1999].

We study 7 x 7 superpixels instead of individual pixels in order to reduce the effect of seeing variations on the lightcurves, but dispersion on light curves is still correlated with seeing variations. So once the lightcurves are built from the pre-processed images, we apply an algorithm to reduce

Table 1: The typical parameters that we expect in AGAPE three years observations.

$t_{1/2}$	$m\,(A_{max} \times \phi_\star)$	Milky Way halo	M31 halo	M31 bulge
$\leq$ 40 days (80%)	~ 20.5	$\sim 20\%$	$\sim 50\%$	$\sim 30\%$

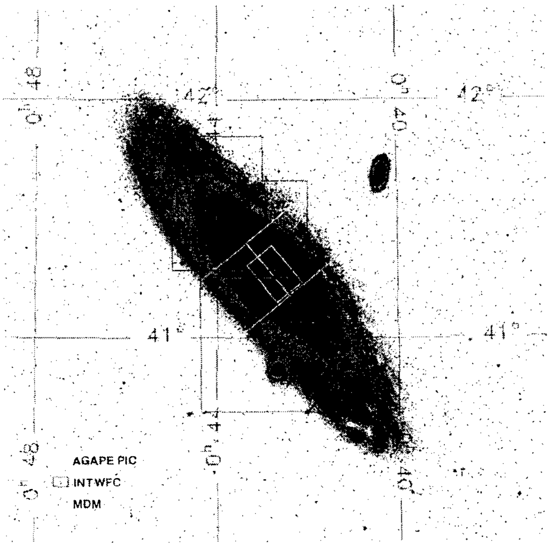

Figure 1: Here, we see the different coverage of the central part of M31 on the TBL (Pic du Midi), MDM and INT telescopes.

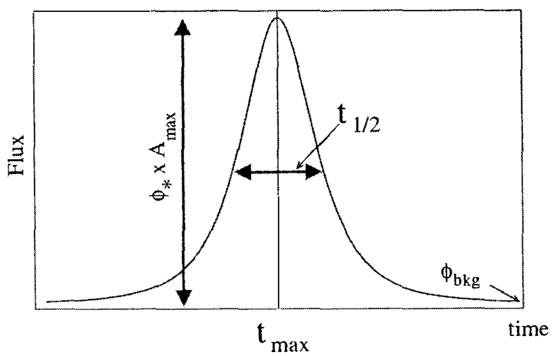

Figure 2: Here is a description of the parameters given in table 1, as they appear on a light curve where a microlensing amplification took place.

Table 2: The selection criterias that we apply to select candidate microlensing events on superpixel lightcurves.

Successive steps for selection of candidate light curves	Result of criteria
I. Detecting significant flux increases in light curves	2165 clusters
II. Finding the most interesting superpixels	2165 light curves
III. Paczyński fit and compatibility test	$\sim -95\%$
IV. Contained events.	$\sim -41\%$
IV. Limits on magnitude (Monte-Carlo simulation)	$\sim -88\%$
Number of candidates selected in 1994-96	**9 events**

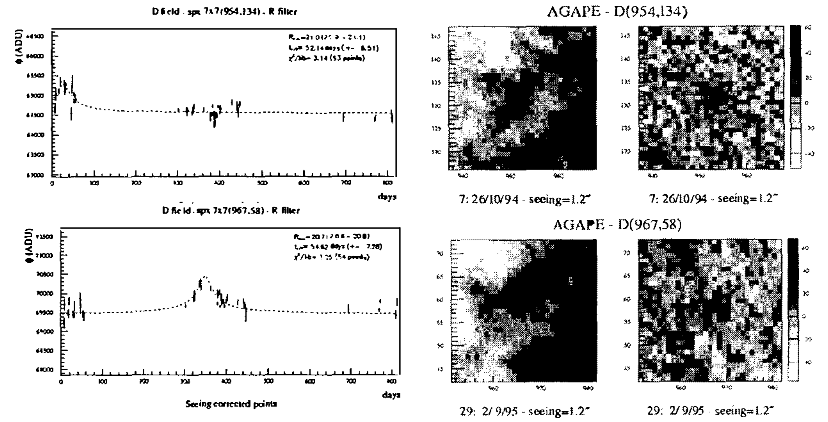

Figure 3: Two of the candidate lightcurves and their image$_{min\ flux}$ followed by image$_{max\ flux}$ $-$ image$_{min\ flux}$.

the dispersion due to seeing variations, as described in detail in [Le Du, 2000]. The idea behind that algorithm is to correct for the flux that leaks outside of the superpixel when the seeing varies.

2 The selection of candidates

We start with $\sim 2.4 \times 10^6$ light curves, and then apply a number of selection criterias listed in table 2. This has led us to select 9 candidates, and we shall see in the next section how the new 1998 data taken on the MDM telescope gave us the possibility to test these candidates by studying the extended lightcurve. As a reference, for 100% MACHO halo, Monte-Carlo simulations predict between 3 and 5 events detected, depending on mass of bulge and disk lens. The sensitivity of our analysis pipeline is displayed in figure 3 where we see two of the candidate lightcurves and the subtraction of the image at maximum and image at minimum : a very weak but significant pattern is visible, just above the noise. The last candidate is called Z1, and its characteristics are very interesting, because it is a very short $t_{1/2} \sim 5$ days and strong $R_{max} \sim 18$ event compared to the 8 first candidates which all lie in the $t_{1/2} \sim 50$ days and $R_{max} \sim 20$. We were able to find some HST archive images on which it was possible to look for the source star of the event, and we reported our study in [Ansari et al., 1999]. AGAPE Z1 is very probably a lensing phenomena : it cannot be a mira (color), bumper (amplitude), nova (light curve shape) or dwarf nova (repetition and rest magnitude), and is possibly a binary event.

Today, AGAPE pursues its research of microlensing events towards M31 with other telescopes :

we started a new collaboration, POINT-AGAPE, that uses the INT (2.5 m Isaac Newton Telescope). Data started in 1999, and Monte-Carlo simulations, cf. [Kerins et. al., 2000], predict ~ 140 events per season (60 nights) for 100% MACHO halo. One of the interesting features is that M31 tilted disk implies a gradient of the number of detected events from the far side to the near side, which traces mass and density. The existing analysis pipeline developed for AGAPE is in the process of being adapted.

We have also made observations on the MDM (1.3 m Kitt Peak, with A. Crotts, A. Gould & R. Uglesich) since 1998 : we have already processed 35 nights of observation, ~ 20 short duration images each night. The final analysis is underway by Italian collaborators in *Napoli* and *Salerno,* and S. Calchi Novati. MDM data overlaps the data from AGAPE Pic du Midi, and by using the same selection criterias as for the TBL data, on the 9 initial candidates, we retain only 4 events, two of which have yet to be tested on MDM data :

9 events on AGAPE Pic du Midi
5 exhibit significant variations on processed MDM data
2 events retained, 2 more to test

The next figure shows the continuation of the lightcurves for the two selected events :

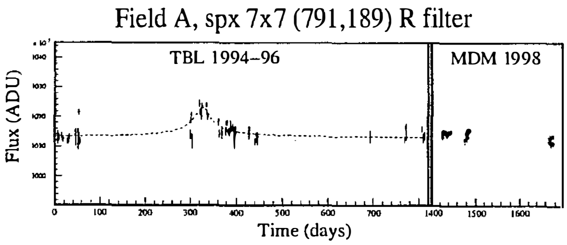

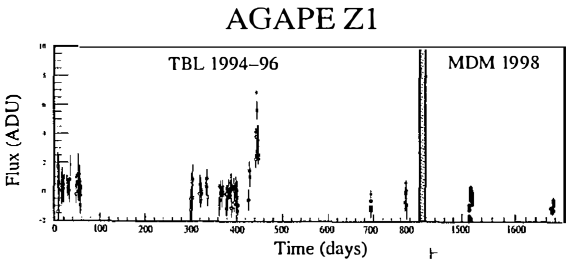

References

[Ansari et al., 1997] Ansari, R., et al, A&A, 324, 843 (1997).

[Ansari et al., 1999] Ansari, R., et. al., 1999, *A&A*, **344**, L49.

[Baltz & Silk, 1999] Baltz, A. E., Silk, J., astro-ph/9901408.

[Gondolo, 1999] Gondolo, P., ApJ, 1999, 455, 44.

[Kerins et al., 2000] Kerins, E., et al., Collaboration POINT-AGAPE, astro-ph/0002256.

[Le Du, 2000] Le Du, Y., PhD thesis, 12^{th} May 2000, Collège de France, ref. PCC-00-T1, download at `http://cdfinfo.in2p3.fr/~ledu/`.

ANALYSIS OF MICROLENSING OBSERVATIONS USING PURELY DIFFERENTIAL METHODS

C. Alard

Institut d'Astrophysique de Paris, 98bis boulevard Arago, 75014 Paris, France.

The detection of hundreds of microlensing events by the microlensing collaborations OGLE (Udalski 2000) and MACHO, (Alcock *et al.* 2000) bears the promise to explore the mass function of the Galactic Bulge region. However, due to the crowding of the fields, a large number of faint unresolved sources contribute to the lensing rates. The contribution of these heavily blended faint sources introduce a large bias in the lensing rates, which is dominant in the brown dwarf regime. To overcome the source confusion and the resulting blending of light, it is essential to introduce new photometric methods which are purely differential. The recent developement of the optimal image subtraction method allows to performs differential photometry, with an accuracy close to the photon noise. By construction the photometry obtained using this method is un-biased, but does not allow to reconstruct the baseline flux of the event. Thus, using this differential photometry will not permit to derive the duration of the events, and the lensing rates. However, it is shown that the statistical information contained in the light curves can be related directly to the mass function. In particular, it is demonstrated that projecting the set of light curves on a basis of function is equivalant to project the mass function on another function. The optimal set of basis functions in the space of the light curves are the principal components of the light curves. It is demonstrated that all the information about the mass function is contained in the projection of the light curves on a small number of principal components.

1 The blending of the sources biases the microlensing experiments.

The stellar fields investigated by the different microlensing experiments towards the Galactic Bulge or the LMC are so dense that for 1 star resolved in the image, there are about 50 unresolved stars in the surrounding. If one of these faint unresolved stars is amplified, it is very likely that due to the extreme crowding conditions the event will be attributed to a brighter star which is well resolved in the image. The consequence of this effect is that the baseline flux of the event will be very over-estimated. Unfortunately fitting a microlensing light curve with the wrong baseline flux results in serious biasing in the determination of the impact parameter and duration of the event. Over-estimating the baseline flux is equivalant to under-estimating the duration, which in turns result in a serious reduction of the mass of the lens. The obvious consequence is that this class of biased events will simulate the presence of a large fraction of brown dwarf, which are of course a pure artefact (Alard 1997, Han 1997). It is clear also that since the effective number of sources of much larger than the supposed number of actual resolved sources, much more amplification of stars will be observed at a given time than expected. This effect will result in a very significant increase of the optical depth. Some numerical simulations shows that it is very difficult to get rid of this bias, since the degeneracy in the fitting of the ligth curve is very high. As shown in Fig. 1, blended and un-blended are very similar.

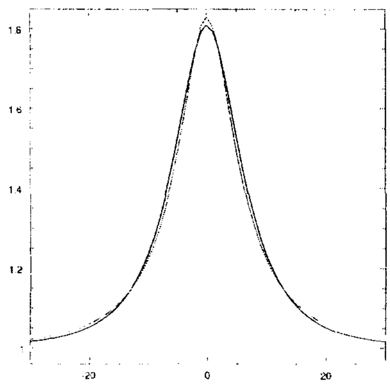

Figure 1: Comparison of light curves with blending (dashed curve) and without blending of the source. By choosing properly the impact parameter and the duration, one can see that un-blended light curve and the blended light curve can be very close.

2 Differential photometry.

One of the possible solution that can be used to cancel the effect of blending is to measure only the variation of light between the images. In this case, whether the source is blended or not, the resulting light curve of the differential variations should be un-biased. One of the basic problem in the comparison of 2 images is that in general they have different seeings, or different PSF's. Theoritically, the seeing between 2 images can be adjusted by convolving one of the image with an appropriate convolution kernel. In principle once the seeing adjustement has been performed, the 2 images can be subtracted with an accuracy good to the photon noise. This method of subtraction after seeing adjustement is usually nicknamed "image subtraction". One interesting problem is to seek for the optimal solution, that will give a minimum residual between the 2 images. This problem is equivalant to finding the best convolution kernel. This issue has been solved by using a least-square approach by Alard & Lupton (1998).

2.1 A short description of the optimal image subtraction method.

If we need to subtract 2 images, I_1 and I_2, assuming I_1 is the best seeing (reference image), we have to match I_1 to I_2. It can be achieved by convolving I_1 with the proper (least-square optimal) kernel solution:

$$\sum_{pixels} [I_1 \otimes Kernel \ - I_2]^2 \quad \text{minimal} \tag{1}$$

Solving Eq. (1) is a full non-linear problem which requires a very large amount of computing time (Kochanski *et al.* 1996). A realistic solution to Eq. (1) need to be much quicker. Such improvement can be done if one notice that the problem can be transformed into a linear least-square problem, provided the kernel is expanded on a basis of functions:

$$Kernel(u,v) = \sum_i a_i B_i(u,v)$$

Then Eq. (1) become:

$$\sum_{pixels}\left[\sum_i a_i I_1 \otimes B_i - I_2\right]^2 \quad \text{minimal}$$

Which is a simple linear least-square problem. For the basis of function a gaussian polynomial expansion has been selected. These functions have a number of interesting properties (see Alard & Lupton 1998 for more details).

$$B_{i,j} = e^{-r^2}\ u^i v^j$$

With: $r = \sqrt{u^2 + v^2}$ To complete the presentation of the basic image subtraction method, we show that differential background variations between the images can also be handled in a linear way. If we expand the background variations using 2 dimensional polynomials, Eq. (1) can be transformed into the final linear expression:

$$\sum_{pixels} + \left[\sum_i a_i\ I_1 \otimes B_i \sum_j b_{k,l}\ x^k y^l - I_2\right]^2 \quad \text{minimal}$$

2.2 spatially variable kernel

Provided the density of objects is large in the image, one can always cut the image into small pieces and make image subtraction in these small areas. In the crowded fields of the microlensing experiments, the Galactic Bulge, or the magellanic clouds, the density of stars is so large that one can make image subtraction in very small area, where the kernel variations are negligible. However in fields with low density of objects (for instance the fields investigated by supernovae surveys), it is not possible to ignore the variations of the kernel across the field. These kernel variations are usually due to the optics of the telescope. A natural solution is to fit these kernel variations by linear expansion of the kernel coefficients:

$$Kernel(x, y, u, v) = \sum_i a_i(x, y)\ B_i(u, v)$$

with:

$$a_{i,j}(x, y) = \sum_i c_i x^i\ d_j y^j$$

Although it is obvious that if the spatial variations are expanded for instance to order 3, the number of coefficients to evaluate by least square will be increased by a factor of 10. Considering that most of the computations are associated with building a square matrix of scalar products between the least-square vectors, the computing time will be increased by a factor close to 100. Such computing requirement cannot be afforded with the current computers. Fortunately, it is possible to speed up the calculations by a considerable factor if we notice that the matrix for the spatially variable kernel can be deduced form the matrix relevant to the constant kernel with a minimum number of operations. The basic idea is that provided the images is divided in small stamps which have about the size of the kernel, inside these stamps the kernel variations can be neglected, and the scalar products are almost identical to the scalar products for constant kernel. Thus the matrix elements of the spatially variable kernel can be decuded from the constant kernel matrix with a minimum number of operations, the fundamental improvement in that the costly scalar products of the vectors need not to be re-calculated each time. In practise, a full solution of the least-square equations with spatially variable kernel does not require more than 20 or 30 % of addtional cost with respect to constant kernel solutions. For more details see Alard (2000a).

2.3 Flux conservation in spatially variable kernels.

In spatially variable kernel, the sum of the kernel which correponds to the flux scaling between the images is not necessary constant. This can be an annoying additional source of noise and it is necessary to remove these degree of freedom from the space of kernel solutions. The most straightforward way to do this is to make a least-square fit with constraints by using Lagrange multipliers. However this methods leads to a set of equations which is costly to solve. A better alternative is to recombine the kernel expansion in order that the constant scaling condition be automatically verified. For instance if we use the following kernel expansion:

$$Kernel(x,y,u,v) = a_0\ B_0(u,v) + \Sigma_{i=1,N}\ a_i(x,y)\ \ [B_i(u,v) - B_0(u,v)]$$

Provided the B_i function are normalized ($\int B(u,v)\ dudv = 1$), it is very easy to see that $\int Kernel(x,y,u,v)\ dudv$ does not depend any more of the position in the image (x,y).

2.4 Examples of application.

Images.

To illustrate the application of the optimal image subtraction method to microlensing data, a small field containing a variable star has been selected (Fig. 2). This field has been extracted from a data set of OGLE II observations of fields in the direction of the Galactic Bulge. The result achieved after convolution and subtraction has a quality that is very close to the theoritical limit as calculated from the Poisson fluctuation (Alard & Lupton 1998).

Photometry.

The photometry of the microlensing events is greatly improved by using the subtracted images. Since all the disturbing effects of blending and crowding of the fields are cancelled in the subtracted images, the photometry is free of systematic biases. The resulting improvement in the fitting of the theoritical lensing curve is of more than a factor of 2 (see Fig. 3). In some case of large blending, the improvement can be as large as a factor of 8, as illustrated in the case of OGLE #5 (see Fig. 4).

3 From the light curves to the mass function.

3.1 Introduction

When analyzing microlensing observations one has to deal with the light curves of a number N of microlensing candidates. We will assume that we have purely differential photometry only, with a baseline flux equal to zero. We emphasize that high quality differential photometry can always be obtained after the events have been detected by classical methods by using the image subtraction method (Alard 1999). These light curves will be represented by the symbol $\mathbf{S_j(t)}$, $(j = 1,..,N)$. Assuming that un-amplified flux of the source is $\mathbf{A}$, the expression of the $\mathbf{S_j(t)}$ as a function of time will be given by the theoretical microlensing amplification formula:

$$S_j(t) = A\left(\frac{u(t)^2+2}{u(t)\ \sqrt{u(t)^2+4}} - 1\right) \tag{2}$$

With:

$$u(t) = \sqrt{u_0^2 + \left(\frac{t}{t_E}\right)^2}$$

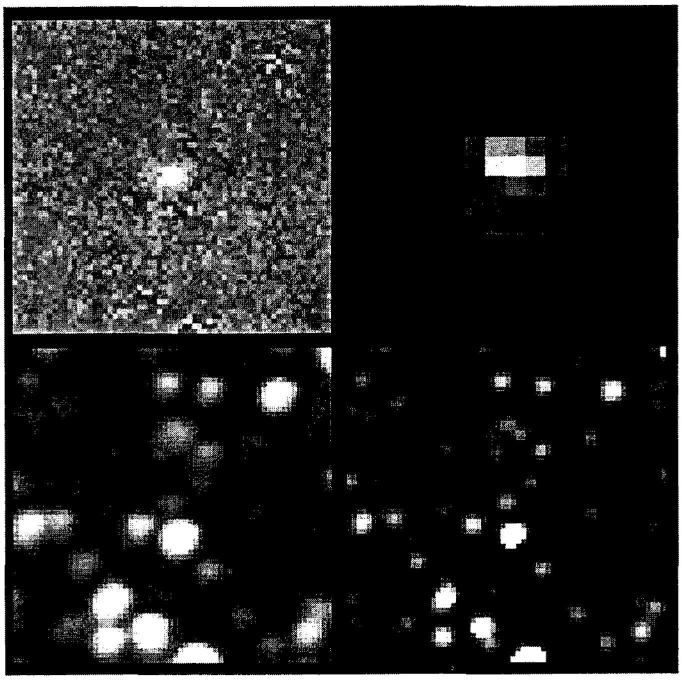

Figure 2: Example of application of the optimal image subtraction method. The image with good seeing (lower right) has been convolved with the best kernel solution (upper right) in order to match the bad seeing image (lower left). The final subtracted image is present in th upper left corner. Note that a variable star is visible near the center of the image.

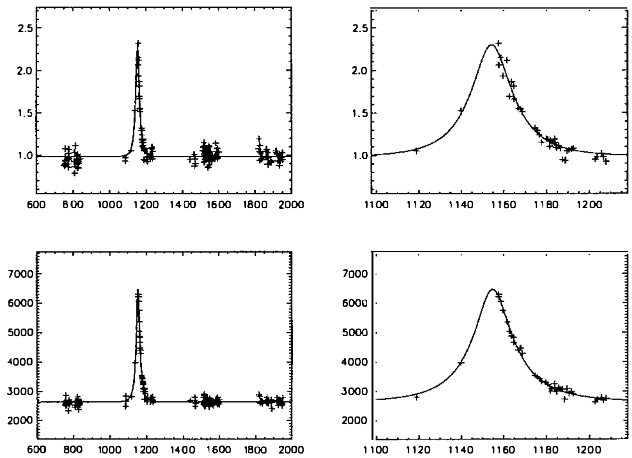

Figure 3: The OGLE I light curves, using DoPHOT (2 upper figures), and using the image subtraction package ISIS. The improvement measured using ISIS with respect to DopHOT is about 2.2. OGLE I is typical of the mean improvement achhived using image subtraction.

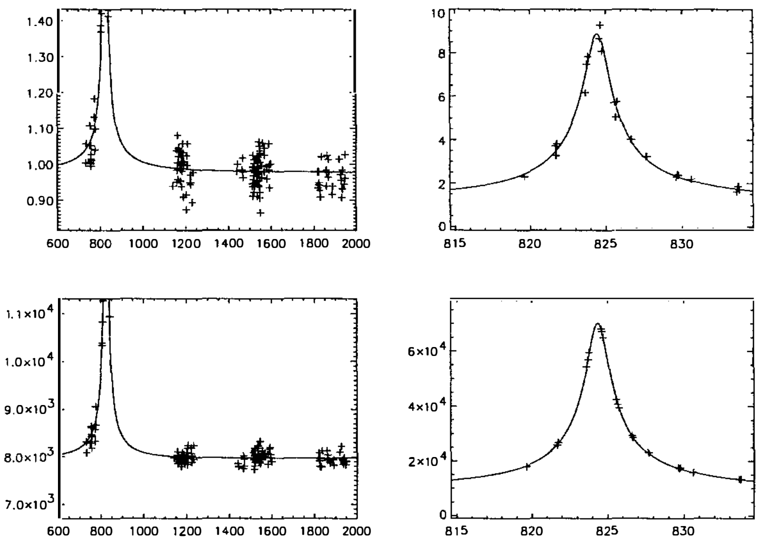

Figure 4: The OGLE I light curves, using DoPHOT (2 upper figures), and using the image subtraction package ISIS. The improvement measured using ISIS with respect to DopHOT is about 8 during the amplification, is about 3 for baseline points.

(we recall that we are working in the assumption that we have at our disposal a differential flux only, with for convenience a baseline flux equal to 0).

The most important issue is of course how do we relate these observations to the microlensing parameters: the impact parameter, $\mathbf{u_0}$, and the time to cross the Einstein ring: $\mathbf{t_E}$. And furthermore how do we relate the microlensing parameters to the mass function itself. The first serious difficulty we encounter is that of course $\mathbf{u_0}, \mathbf{t_E}$, cannot be extracted easily by fitting the light curve due to the extreme blending degeneracy (Alard 1997, Han 1997, Wozniak & Paczynski 1997). Thus our first and most essential step will be to derive a better set of parameters. This set of parameters will have to be non degenerated with respect to blending. The most simple and most natural way to deal with such problem is to express the observations as a linear combination of a small number of vectors. The best way to make such a decomposition is known as principal components analysis, it is equivalent to an eigen value decomposition. Thus all we have to do is to look for the firsts eigen functions, and to calculate the scalar product of the components with our vectors (time series) of observations.

3.2 Statistical distribution of the projections on the principal components.

We consider that most of the information is contained in a number $\mathrm{N_C}$ of principal components of the light curves. To eliminate the baseline flux the light curves are normalized in amplitude. To perform this normalization a microlensing light curve is fitted to the data. The normalized model fitted to the light curve S_i will be called $\tilde{S}_i$. Note that even if the solution is degenrated, all we need is to find a solution that fit the data well. Almost all the information can be extracted from the distribution of the projection of the N_1 time series on the $\mathrm{N_C}$ principal components. The first meaningful quantity concerning the distribution of the a_{ij} is the first order moment of the distribution:

$$\langle a_j \rangle = \sum_i a_{ij}$$

The second interesting quantity is the second order moment of the distribution:

$$\left\langle a_j^2 \right\rangle = \sum_i a_{ij}^2$$

But it is important to notice, that $a_{ij}^2 = [\beta\ (\mathrm{u_0}, \mathrm{t_E})]^2$, can be written as a scalar product of the data with a given function. Since that according to theorem of Fischer-Riesz of linear functional analysis, we can always find a function $F(\mathrm{t})$ such that:

$$a_{ij}^2 = [\beta\ (\mathrm{u_0}, \mathrm{t_E})]^2 = \int \overline{\tilde{S}_i}\ (\mathrm{u_0}, \mathrm{t_E}, \mathrm{t})\ \mathrm{F(t)\ dt} \tag{3}$$

Using the principal components decomposition of $\overline{\tilde{S}_i}$ we can write:

$$a_{ij}^2 \simeq \sum_{j=1}^{\mathrm{N_C}} \left[\int P_j\ \mathrm{(t)\ F(t)\ dt}\right]\ a_{ij}$$

Thus, finally we see that the distribution of the second moment is not more than a linear combination of the the $\mathrm{N_C}$ firsts moments (mean). Thus the mean of the second moment will not bring any additional information with respect to the mean. With a similar reasoning it is possible to show that the same property is true for the N^{th} moment.

Consequently we can conclude that all the information concerning the distribution of the a_{ij} is contained in the mean of these components. No additional information (uncorrelated information) will be found by looking at higher order moments.

3.3 From the principal components to the mass function.

It is possible to re-express the previous definition of $\langle a_j \rangle$ by using the number density $\rho(\mathrm{u_0}, \mathrm{t_E}, \mathrm{M})$ to observe a given amplification of parameters $(\mathrm{u_0}, \mathrm{t_E})$ with a lens of mass M. In such case, the sum can be approximated very closely with an integral expression:

$$\langle a_j \rangle \simeq \int\int\int \rho(\mathrm{u_0}, \mathrm{t_E}, \mathrm{M})\ \mathrm{a_j}\ (\mathrm{u_0}, \mathrm{t_E})\ \mathrm{du_0\ dt_E\ dM}$$

If we define the efficiency function of the experiment, $\Theta\,(\mathrm{u_0}, \mathrm{t_E})$, the lensing rates for 1 solar mass lenses, $\Gamma_0(t)$ and the mass function, $\phi(M)$ the formulae for ρ reads:

$$\rho\,(\mathrm{u_0}, \mathrm{t_E}, \mathrm{M}) = \Gamma_0 \left(\frac{t_E}{\sqrt{M}}\right) \phi(M)\ \Theta\,(\mathrm{u_0}, \mathrm{t_E})$$

Leading to the following expression for $\langle a_j \rangle$:

$$\langle a_j \rangle \simeq \int\int\int \Gamma_0 \left(\frac{t_E}{\sqrt{M}}\right) \phi(M)\ \Theta\,(\mathrm{u_0}, \mathrm{t_E})\ \ a_j\ (\mathrm{u_0}, \mathrm{t_E})\ \mathrm{du_0\ dt_E\ dM}$$

It is easy to re-arrange this integral in the following way:

$$\langle a_j \rangle \simeq \int \psi(M)\phi(M)\ dM$$

With:

$$\psi(M) = \int\int \Gamma_0 \left(\frac{t_E}{\sqrt{M}}\right) \Theta\,(\mathrm{u_0}, \mathrm{t_E})\;\; a_{ij}\;(\mathrm{u_0}, \mathrm{t_E})\;\mathrm{du_0}\;\mathrm{dt_E} \tag{4}$$

Thus we see that basically projecting the microlensing light curve on a basis of function and taking the statistical sum is equivalent to projecting the mass function itself on another function. Consequently, we see that a projection in the space of the observation (the light curve) is directly equivalent to a projection in the space of the mass function. The problem of finding the optimal set of projections for the observations, is solved by using the principal component method. Then all we have to do is to calculate the "image" of these principal components in the space of the mass function.

3.4 Illustration of the method using a Monte-carlo simulation.

To illustrate this method and show how the mass function can be reconstructed, we will use a series of Monte-Carlo simulations. We will simulate microlensing events by selecting the parameters of the events according to the density distribution, $\rho(\mathrm{u_0}, \mathrm{t_E}, \mathrm{M})$. One additional parameter we will have to select is the amplitude of the source. To get random variables which reproduces the distribution ρ we need to decompose the problem. Basically $\rho(\mathrm{u_0}, \mathrm{t_E}, \mathrm{M})$ has 3 parts:

- **The rates,** $\Gamma_M(t_E)$:

$$\Gamma_M(t_E) = \Gamma_0(\frac{t_E}{\sqrt{M}})$$

For Γ_0 we will adopt the analytical expression given in Mao & Paczyński (1996).

The efficiency function, $\Theta\,(\mathrm{u_0}, \mathrm{t_E})$:

For the efficiency we will adopt the following criteria: an event is detected if it has a minimum number (N_m) of data points above a 5 σ threshold. For a given duration t_E this criteria is simply equivalent to put a threshold on the impact parameter u_0. All we have to do is to search for the maximum value u_T of u_0 such that the amplification of at least N_m data points is above 5 σ. If the sampling is even, with a time step δt, it just mean that the amplification must be larger than 5 σ in a window of time around the maxima $\Delta T = N_m\ \delta t$. Provided the maxima is at the origin of the time axis, it will finally result in the condition:

$$S_j\left(\mathrm{u_T}, \mathrm{t_E}, \frac{\Delta \mathrm{T}}{2}\right) > 5\ \sigma \tag{5}$$

The distribution of u_0 itself is uniform, to get et set of u_0 values we will use a random generator which will provide a uniform distribution between 0 and the maximum value for u_0, $u_M(t_E)$. $u_M(t_E)$ corresponds to the impact parameter for the brightest source given by Eq xx. Once we have selected t_E from the distribution $\Gamma_M(t_E)$, we will calculate $u_{0,thresh}$ using Eq xx, if our random u_0 value is above $u_{0,thresh}$, $\Theta\,(\mathrm{u_0}, \mathrm{t_E}) = 0$, otherwise $\Theta\,(\mathrm{u_0}, \mathrm{t_E}) = 1$. To summarize:

$$\Theta\,(\mathrm{u_0}, \mathrm{t_E}) = \begin{cases} 1 & u_0 < u_T \\ \\ 0 & u_0 > u_T \end{cases}$$

The mass function, $\phi(M)$ **:**

In all our simulation we will adopt a pure power law expression for the mass function, with a lower (M_I) and an upper cut-off (M_S).

$$\phi(M) = \begin{cases} M^{-\alpha} & M_I < \mathrm{M} < M_S \\ 0 & \text{otherwise} \end{cases}$$

The amplitude:

we will assume that the the flux of the un-amplified source amplitude distribution is a power law with an exponent of -2 (Zhao, *et al.* 1995), in a given range of amplitude A_{max} and A_{min}. In our simulation, the amplitudes will be generated by Monte-Carlo method, using this power law.

Results.

In this example we will take an amplitude range which is typical for microlensing images towards the Galactic Bulge:

$A_{max} = 10^6$, $A_{min} = 10$

For the mass function we take the following parameters:

$$\phi(M) = \begin{cases} M^{-2} & 0.05 < \mathrm{M} < 10.0 \\ 0 & \text{otherwise} \end{cases}$$

Using these parameters we simulated several series of microlensing light curves. For illustration, we extracted a sample of light curves from one of these simulations, they are presented in Fig. 5. The parameters were adjusted in order that in a simulation the total number of microlensing events simulated be close to 100. Then we proceeded to the principal components decomposition. The orthonormal set of principal components was calculated using a singular value decomposition. The first 4 principal components are presented in Fig. 6.

The functions $\psi(M)$ corresponding to the principal components in the space of the mass function can be computed using Eq. 4. Projecting the data on the principal components is equivalent to projecting the mass function on $\psi(M)$. To illustrate our discussion, an example of $\psi(M)$ functions calculated using the settings of the previous Monte-Carlo simulation are presented in Fig. 7. The functions $\psi(M)$ can be used to reconstruct the mass function, for more details, see Alard (2000b).

References

1. Alard, C., 2000b, astro-ph/0004071
2. Alard, C., 2000a, A&AS, in press
3. Alard, C., 1999, A&A, **343**, 10
4. Alard, C., & Lupton, R. 1998, ApJ, **503**, 325
5. Alard, C., 1997, A&A3, **21**, 424
6. Alcock *et al.*, 2000, astro-ph/0002510
7. Han, C., 1997, ApJ, **484**, 555
8. Udalski, A., 2000, *et al.*, astro-ph/0002418

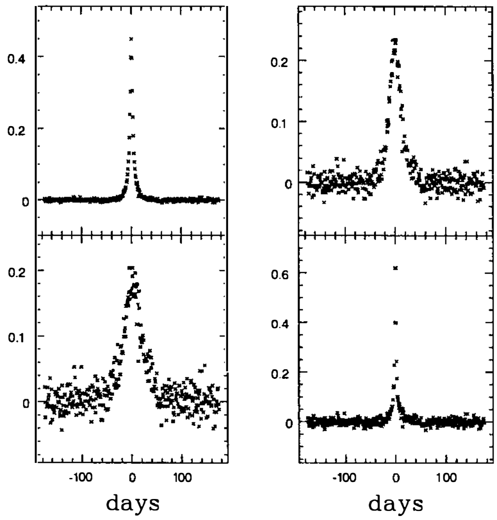

Figure 5: Example of light curves as obtained using the Monte-Carlo simulation procedure described above.

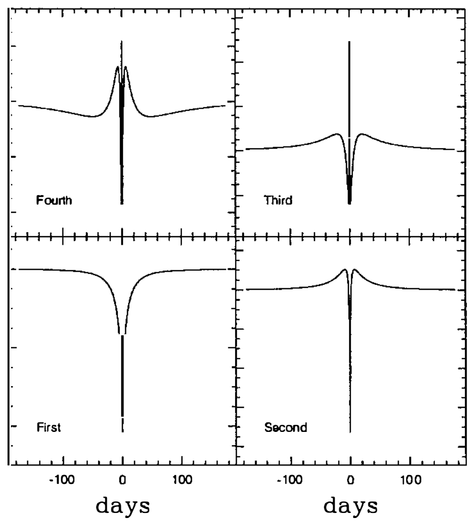

Figure 6: The first 4 principal components corresponding to the simulation presented in Fig. 5.

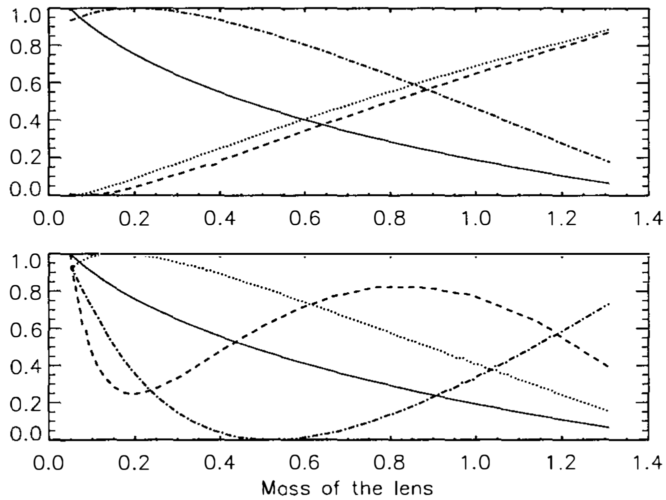

Figure 7: The function $\psi(M)$ which corresponds to the principal components. In the right panel we present the 4 original function, while in the other panel we present an orthonormal linear combination of these 4 functions. (Note that in the right panel the function were scaled to have the same amplitude).

BREAKING THE DEGENERACY OF MICROLENSING TOWARDS THE LMC

HongSheng Zhao
Sterrewacht Leiden, Niels Bohrweg 2, 2333 CA, Leiden, The Netherlands

We propose several observational tests that can break the degeneracy of two main classes of microlensing models to the Large Magellanic Cloud. If the lenses are located in the LMC, then the source stars in the latter (self-lensing) models tend to be at the far side of the LMC, hence should show subtle, measurable differences from random stars in the same field in terms of intrinsic brightness, dust extinction, reddening and polarisation, and radial velocity. No such biases should be detected if they are lensed by (halo) objects well in front of the LMC. The tests require multi-band photometry and spectroscopy in good seeing conditions or with the HST.

1 Introduction

One of the main puzzles of Galactic microlensing surveys is the poorly determined location of the lens population of the events towards the Magellanic Clouds. Currently there are two popular views on the issue: (a) the lenses are located in the halo, hence are likely baryonic dark matter candidates (Alcock et al. 2000, Ibata et al. 2000); (b) both the lenses and sources are part of the Magellanic Clouds, hence are stars orbiting in the potential well of the Clouds (Sahu 1994, Zhao 1998). The amount of star-star lensing is sensitive to assumptions of the structure and equilibrium of the Magellanic Clouds. It can be efficient if the LMC has a significant depth along the line of sight, as non-equilibrium models of, e.g., Zhao & Evans (2000), where a gap or misalignment between the LMC disk and its off-centered bar is suggested. The generic effect of putting the lenses in the LMC is the source star is pushed to the far side of the LMC systematically. Hence such models are falsifiable if we could design observations which are sensitive to the distance of the sources. Several lines of attack have been proposed in Zhao, Graff & Guhathakurta (2000). Here we illustrate the effect of combining these together.

2 Tests

Suppose we have multi-band photometry and spectroscopy of small patches of the sky centered on each microlensing candidate; presently there are 13-17 events towards the LMC. We can then extract radial velocities from the spectra to define the mean motion of stars in each LMC field, and construct CMDs to define the mean isochrone of each field. Then we can then plot a scatter diagram of the offset of each star from the mean isochrone and offset from the mean motion, and overlay the distributions of all fields together. A simulated distribution is shown by small dots in Fig.1, where we assume a dispersion of 30 km/s for the radial velocity, and allow for a dispersion of ± 0.3 magnitude due to photometric error, intrinsic differences, and differential

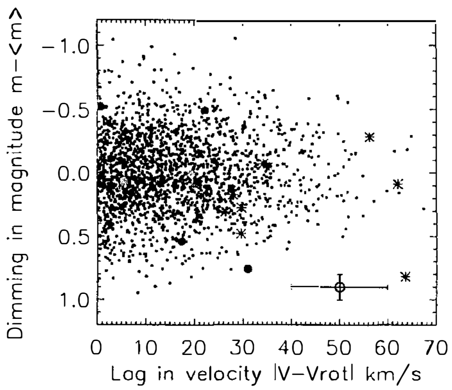

Figure 1: show the systematic biases of the properties of the sources in LMC-LMC lensing events (asteriks) and MACHO-LMC lensing events (filled circles) vs. the average stars in the LMC (small dots). The horizontal axis is the observable velocity of the star (after discounting the mean rotation of the LMC) and the vertical axis is the observable magnitude of the star (after discounting the mean magnitude of stars of the same color). A typical error bar for observations is also drawn. The LMC-LMC events shift to the fainter and redder part of the diagram.

reddening within each field. Extinction is patchy in the LMC on scales of arcmin (Harris et al. 1997). It is important to make field larger enough to build a sensible CMD, but small enough to limit the scatter of differential extinction.

In the macho models, the sources should be drawn randomly from stars in Fig.1, as shown by filled circles. But if the sources are at the far side of the LMC systematically, as models of LMC-LMC lensing predict, then we would expect a higher dispersion of the source stars and a fainter magnitude, shown by the asteriks. The reason for the fainter magnitude is in part because of larger distance modulus (here 0.05^m), and increased extinction (here 0.25^m in V). The stars far away from the mid-plane of the LMC disk will also lag (typically about 30 km/s) behind of average disk stars in terms of rotation around the center of the LMC. Hence they show up as outliers in rotation and in magnitude. Detection of such effects could clean out non-macho lenses on an event-by-event basis, and purify current estimate for the fraction of machos in the halo. For example, the MACHO-LMC-1a is suspected to be a red clump star at the far side of the LMC, which would explain its shift to the red and fainter side of the clump (Zhao, Graff & Guhathakurta 2000).

It has been proposed many times that proper motion and distance of the lens can be constrained in the future by measuring sub-milliarcsec astrometric centroid shift of the image during a bright event. Information can also be obtained photometrically by densely sampling the light curve during a high amplification events. In comparison, the techniques proposed here have the advantage that it is not crucial to schedual the observations during an event. Given a larger southern telescope data can be collected for all past events with any base-line brightness.

Acknowledgments

I thank Rodrigo Ibata for discussions.

References

1. Alcock C. et al. 2000 (astro-ph/0001272)
2. Harris, J., Zaritsky, D. & Thompson, I., 1997, AJ, 114, 1933
3. Ibata, R. 2000, these proceedings.
4. Sahu A. 1994, Nature, 370, 275
5. Wu X.P. 1994, ApJ, 435, 66
6. Zhao H.S. 1998, MNRAS, 294, 139
7. Zhao H.S. 1999, ApJ, 527, 167
8. Zhao H.S. 2000, ApJ, 530, 299
9. Zhao H.S., Graff D., & Guhathakurta P., 2000, ApJ, 532, L37

PERTURBATIVE ANALYSIS IN MULTIPLE AND PLANETARY GRAVITATIONAL LENSING

V. BOZZA
Dipartimento di Scienze Fisiche "E.R. Caianiello", Università di Salerno
Via S. Allende, Baronissi (SA) I-84081, Italy.

The lens equation for a multiple Schwarzschild lens is not exactly solvable in general situations. This is a hard problem for any analytical investigation of this physical system. However, perturbative methods can be successfully employed to gain a deep insight of the mathematical structure of this lens in some interesting cases. Here I present the full derivation of the caustics structure (including cusps, area and duality transformation) for a lens very far from the others, for a system where mutual distances are much smaller than the global Einstein radius and for planetary systems. In this particular case, the situation is very favourable, so that even a completely analytical formula for microlensing light curves can be derived, providing a very useful description of planetary perturbations to the observed luminous flux.

1 Introduction

While the general picture for the binary lens is somewhat well defined at present day, as regards the critical structure, the same cannot be said about general multiple lenses. The attempts to enlighten this kind of lenses have really been very few. This is because of the mathematical complexity of the lens equation.

The critical curves and the caustics of multiple lenses can develop very complicated structures. However there is a great interest in this problem for its applications in particular situations, such as planetary systems [1], rich clusters of galaxies and microlensing of quasars by individual stars in the haloes of the lensing galaxies [2].

In this talk we have presented some works aiming to a systematic investigation of the caustics of multiple lenses whenever they can be referred to well-defined situations to be employed as starting points in perturbative expansions. The three cases where this happens have been pointed by Dominik [3].

Sect. 2 deals with the case of a lensing mass that is very far from the others[4]; in Sect. 3 a system formed by near (with respect to the Einstein radius of the total mass) lenses is studied[4,5]; Sect. 4 considers the case of a multiple planetary system[6].

In the latter case, the situation is such that the lens equation can be perturbatively inverted and analytic microlensing light curves can be drawn.

2 Single lens perturbed by far masses

Let's consider a mass m_1 placed at the origin of the lens plane. The other masses $m_2, ..., m_n$ are at the positions $\mathbf{x}_2, ..., \mathbf{x}_n$. In polar coordinates, we put $\mathbf{x}_i = (\rho_i \cos\varphi_i; \rho_i \sin\varphi_i)$ and the generic coordinate in the lens plane is $\mathbf{x} = (r\cos\vartheta; r\sin\vartheta)$. The hypothesis we start from is that $\rho_i \gg \sqrt{m_j}$ for each i and j. This allows us to expand the Jacobian determinant in series of inverse powers of ρ_i. The zero order solution is simply the Einstein radius $r = \sqrt{m_1}$. We build the general solution as an infinite series in $1/\rho_i$:

$$r = \sqrt{m_1}\,(1 + \varepsilon_1 + \varepsilon_2 + \varepsilon_3 + ...) \tag{1}$$

where $\varepsilon_j \sim 1/\rho_i^j$. Substituting this expression in the equation $\det J = 0$ and expanding again, we can easily solve the equation of critical curves at each order to find the perturbations.

A linear superposition principle is valid at the second and the third order. In the fourth order there are "interaction" terms that make the calculations more difficult.

The second order can be easily recognized as the sum of the Chang–Refsdal expansions for each mass to the first order in the γ_i. Actually, the full second order can be identified with a Chang–Refsdal lens. The third order breaks the symmetry of the caustic and becomes important when the perturbative hypothesis is more forced.

Exploiting the perturbative results just shown, we can find the caustic formed in this case. It suffices to apply the lens equation and expand it again.

Having at our disposal good approximate expressions for the caustics of multiple lenses, an interesting quantity to compute is the area covered by these curves. We can find it for arbitrary multiple lenses at the second order and for a binary lens at the third order.

3 Close multiple lenses

Now we consider a set of n point-like lenses whose mutual distances are small compared to the total Einstein radius of the system. The starting point for our analysis is the Schwarzschild lens we would obtain if the total mass M were concentrated at the barycentre. The separations between the masses modulate the deviations from the Schwarzschild lens and then constitute the perturbative parameters in our expansion.

Besides the main critical curve, which is a slight modification of the Einstein ring of the barycentral lens, some secondary critical curves are present near the centre of mass. They give rise to very small and far caustics which must be treated separately.

3.1 Main critical curve and central caustic

Now we assume that $\rho_i \ll \sqrt{M}$ for each i. We carry the expansion of the Eq. $\det J = 0$ in series of powers of ρ_i.

The zero order terms give the Einstein ring for a point mass M at the origin. Interference terms arise at the second order already and no superposition principle holds.

We can consider an expression analogue to Eq. (1) for the radial coordinate r:

$$r = \sqrt{M}\,(1 + \varepsilon_1 + \varepsilon_2 + ...) \tag{2}$$

where now $\varepsilon_j \sim \rho_i^j$. Substituting in the equation $\det J = 0$ and expanding again, we can solve for the ε_j at each order.

This perturbative expansion is tightly related to the quadrupole lens, which also has a four cusped caustic. The area of the caustic can be calculated as in the former case.

At the second order, the caustic is always symmetric, even if the mass ratio is not 1.

3.2 Secondary caustics

We introduce the complex coordinate in the lens plane $z = x_1 + ix_2$ and the complex source coordinate $y = y_1 + iy_2$. The positions of the masses will be denoted by $z_i = x_{i1} + ix_{i2}$. The eq. $\det J = 0$ is equivalent to

$$\prod_{i=1}^{n} |z - z_i|^4 - \left| \sum_{i=1}^{n} m_i \prod_{j \neq i} (z - z_j)^2 \right|^2 = 0. \tag{3}$$

Searching for z's of the same order of z_i, the lowest order equation is

$$\sum_{i=1}^{n} m_i \prod_{j \neq i} (z - z_j)^2 = 0. \tag{4}$$

The $2n - 2$ solutions of this polynomial equation are the positions of the secondary critical curves.

If the root has multiplicity p, the first non trivial order after the first is $q = \frac{p+2}{p}$. The critical curve is a circle and the caustic has $p + 2$ cusps. The caustic position is of order -1, i.e. the secondary caustics can lie very far from the optical axis of the lens.

Multiple secondary caustics exist only for particular choices of the parameters of the system forming a zero measure set in the parameters space. Multiple caustics are formed when two or more simple triangular caustics meet at the same place. The transitions between simple and multiple caustics can occur by suppression of two cusps through beak–to–beak singularities, or by formation of butterflies.

4 Planetary systems

A particularly interesting case of multiple lensing is that of planetary systems. Here a stellar mass is surrounded by planets having masses much smaller. Their effects can usually be treated as slight perturbations to the main lensing object.

We can distinguish between the central caustic which is generated by the distortion of the star's Einstein ring and the planetary caustics which are the images of the planetary critical curves and can be well approximated by Chang–Refsdal critical curves.

4.1 Central caustic

Consider a star with mass m_1 placed at the origin, surrounded by planets with masses $m_2, ..., m_n$ placed at $\mathbf{x}_2, ..., \mathbf{x}_n$. The planetary hypothesis states that $m_i \ll m_1$ for $i > 1$. So we can expand the Jacobian determinant in powers of m_i. Starting from the Einstein ring of the star $r = \sqrt{m_1}$ as zero order solution, we can find the perturbations leading to a non trivial central caustic.

A superposition principle for the effects of the planets holds on the central caustic.

In many studies of the central caustic of a planetary system, a principle of duality between planets external and internal to the Einstein ring was often claimed[7,3]. This principle can be directly verified on perturbative formulae which are invariant under the transformation

$$\mathbf{x}_i \to \frac{m_1}{|\mathbf{x}_i|^2} \mathbf{x}_i \tag{5}$$

So the conjecture of duality has an effective analytical basis.

4.2 Planetary caustics

The planetary critical curve is always localized in the neighbourhood of the planet and assumes the shape of an elongated ring, when the planet is outside of the star's Einstein ring, or splits into two specular ovals, when the planet is inside.

The zero point of the expansion of these critical curves is then the position $\mathbf{x}_2$ of the planet we are considering. The first non trivial order is $\mathbf{x} - \mathbf{x}_2 \sim \sqrt{m_2}$, since the critical curve of a very far planet is nothing but its Einstein ring with radius $\sqrt{m_2}$.

The lowest order Jacobian is just the Jacobian of the Chang–Refsdal lens. Then the lowest order critical curve is exactly Chang–Refsdal.

The planetary caustic of each planet is not affected, at the first order, by the presence of other planets. It has an area much greater than the central caustic. At the second order a sum containing the effects of the other planets appears. It only represents a displacement of the caustic towards the other planets.

4.3 Planetary microlensing

The lens equation cannot be solved exactly. Anyway, starting from the single lens images of the star, we can calculate the perturbations induced by the planet. By this perturbative inversion of the lens equation, we can compute the magnification of the two main images, which is influenced partly from the displacement of the two images and partly from the direct modification of the Jacobian determinant by the planet.

A third image rises very close to the planet. This image as well can be found by perturbative expansions around the planet position. However, its magnification is negligible with respect to the magnification of the two main images and their perturbations.

Summing up the magnifications of the two images, we can find analytic light curves for planetary microlensing events. Rigorously these curves could not be used in caustic crossing events, since we have not considered the two additional images. Anyway, the contributions of these images is negligible if we also take in account the finite source size.

The availability of analytic expressions for microlensing light curves opens new possibilities in the investigation of the connection between the observed curve and the physical parameters.

Acknowledgments

Work supported by fund ex 60% D.P.R. 382/80.

References

1. B.S. Gaudi, R.M. Naber, M. Richard, P.D. Sackett, ApJ **502**, 33 (1998).
2. R. Kayser, A. Weiß, S. Refsdal, P. Schneider, A&A **214**, 4 (1988).
3. M. Dominik, A&A **349**, 108 (1999).
4. V. Bozza, A&A **355**, 423 (2000).
5. V. Bozza, astro-ph/0002287, in press on A&A.
6. V. Bozza, A&A **348**, 311 (1999).
7. K. Griest, N. Safizadeh, ApJ **500**, 37 (1998).

MICROLENSING OF QUASARS

Joachim Wambsganss
Universität Potsdam, Institut für Physik, Am Neuen Palais 10, 14469 Potsdam
and
Max-Planck-Institut für Gravitationsphysik, Am Mühlenberg 1, 14476 Golm, Germany

There are two possible causes of variability in gravitationally lensed quasars: intrinsic fluctuations of the quasar and "microlensing" by compact objects along the line of sight. If disentangled from each other, microlens-induced variability can be used to study two cosmological issues of great interest, the size and brightness profile of quasars on one hand, and the distribution of compact (dark) matter along the line of sight. Here we present a summary of recent observational evidence for quasar microlensing as well as of theoretical progress in the field. Particular emphasis is given to the questions which microlensing can address regarding the search for dark matter, both in the halos of lensing galaxies and in a cosmologically distributed form. A discussion of desired observations and required theoretical studies is presented as a conclusion/outlook.

1 What is Microlensing of Quasars?

1.1 Mass, length and time scales

The lensing effects on quasars by compact objects in the mass range $10^{-6} \leq m/M_\odot \leq 10^3$ is usually called "quasar microlensing". The microlenses can be ordinary stars, brown dwarfs, planets, black holes, molecular clouds, globular clusters or other compact mass concentrations (as long as their physical size is smaller than the Einstein radius). In most practical cases, the microlenses are part of a galaxy which acts as the main (macro-)lens. However, microlenses could also be located in, say, clusters of galaxies or they could even be imagined "free floating" and filling intergalactic space.

The relevant length scale for microlensing (in the quasar plane) is the Einstein radius of the lens:

$$r_E = \sqrt{\frac{4GM}{c^2}\frac{D_S D_{LS}}{D_L}} \approx 4 \times 10^{16}\sqrt{M/M_\odot}\,\mathrm{cm},$$

where "typical" lens and source redshifts of $z_L \approx 0.5$ and $z_S \approx 2.0$ are assumed for the numerical value on the right hand side (G and c are the gravitational constant and the velocity of light, respectively; M is the mass of the lens, D_L, D_S, and D_{LS} are the angular diameter distances between observer – lens, observer – source, and lens – source, respectively). Quasar microlensing turns out to be an interesting phenomenon, because (at least) the size of the continuum emitting region of quasars is comparable to or smaller than the Einstein radius of stellar mass objects.

This length scale translates into an angular scale of

$$\theta_E = r_E / D_S \approx 10^{-6} \sqrt{M/M_\odot} \ \text{arcsec}.$$

It is obvious that image splittings on such angular scales cannot be observed directly. What makes microlensing observable anyway is the fact that observer, lens(es) and source move relative to each other. Due to this relative motion, the micro-image configuration changes with time, and so does the total magnification, i.e. the sum of the magnifications of all the micro-images. This change in magnification over time can be measured: microlensing is a "dynamical" phenomenon.

There are two time scales involved: the standard lensing time scale t_E is the time it takes the source to cross the Einstein radius of the lens, i.e.

$$t_E = r_E / v_{\perp,\text{eff}} \approx 15 \sqrt{M/M_\odot}\, v_{600}^{-1} \ \text{years},$$

where the same assumptions are made as above, and the effective relative transverse velocity $v_{\perp,\text{eff}}$ is parametrized in units of 600 km/sec: v_{600}. This time scale t_E results in discouragingly large values. However, in practice we can expect fluctations on much shorter time intervals. The reason is that the sharp caustic lines separate regions of low and high magnification. Hence, if a source crosses such a caustic line, we can observe a large change in magnification during the time t_{cross} it takes the source to cross its own diameter R_{source}:

$$t_{cross} = R_{source} / v_{\perp,\text{eff}} \approx 4 R_{15} v_{600}^{-1} \ \text{months}.$$

Here the quasar size R_{15} is parametrized in units of 10^{15}cm.

1.2 Early Promises of Quasar Microlensing

The early papers exploring microlensing made four predictions concerning the potential scientific results. Microlensing should help us to determine: 1) the existence and effects of compact objects between the observer and the source, 2) the size of quasars, 3) the two-dimensional brightness profile of quasars, 4) the mass (and mass distribution) of lensing objects. In Section 3 the observational results to date will be discussed in some detail. It can be stated here that 1) has been achieved. Some limits on the size of quasars have been obtained, so 2) is partly fulfilled. We are still (far) away from solving promise 3), and concerning point 4) it is fair to say that the observational results are consistent with certain (conservative) mass ranges.

1.3 Quasar Microlensing versus "Local Group" Microlensing

In most cases of quasar microlensing, the surface mass density (or optical depth) is of order unity. In contrast to that, the "local group" microlensing deals with very low optical depths, where the action is due to single lenses or physical binaries. Since there are interesting similarities as well differences between these two kinds of microlensing, in Table 1 a few quantities relevant to microlensing are compared to each other for the two regimes.

Table 1: A few lensing properties for the two regimes of microlensing are compared to each other: local group microlensing and quasar microlensing.

Lensing galaxy:	Milky Way	Lens in Q0957+561
distance to Macho known?	no	yes
velocity of Macho known?	no	(no)
mass?	???	???
optical depth?	$\approx 10^{-6}$	≈ 1
Einstein angle (1 $M_\odot$)?	$\approx$ 1 milliarcsec	$\approx$ 1 microarcsec
time scale?	hours to years	weeks to decades
event?	individual/simple	coherent/complicated
default light curve?	smooth	sharp caustic crossing
when/who proposed?	Paczyński 1986	Gott 1981
first detection?	EROS/MACHO/OGLE 1993	Irwin et al. 1989

2 Theoretical Work on Quasar Microlensing

For a multiply imaged quasar, the surface mass density (or "optical depth") at the position of an image is of order unity. If this matter is made of compact objects in the range described above, microlensing is expected to be going on basically "all the time", due to the relative motion of source, lens(es) and observer. In addition, this means that the lens action is due to a coherent effect of many microlenses, because the action of two or more point lenses whose projected positions is of order their Einstein radii combines in a very non-linear way (cf. Wambsganss 1998).

The lens action of more than two point lenses cannot be easily treated analytically any more. Hence numerical techniques were developed in order to simulate the gravitational lens effect of many compact objects. Paczyński (1986) had used a method to look for the extrema in the time delay surface. Kayser, Refsdal, Stabell (1986), Schneider & Weiss (1987) and Wambsganss (1990) had developed and applied an inverse ray-shooting technique that produced a two-dimensional magnification distribution in the source plane. An alternative technique was developed by Witt (1993) and Lewis et al. (1993); they solved the lens equation along a linear source track. All the recent theoretical work on microlensing is based on either of these techniques.

Recently, Fluke & Webster (1999) explored analytically caustic crossing events for a quasar. Lewis et al. (1998) showed that spectroscopic monitoring of multiple quasars can be used to probe the broad line regions. Wyithe et al. (2000a, 2000b) investigated and found limits on the quasar size and on the mass function in Q2237+0305.

Agol & Krolik (1999) and Mineshige & Yonehara (1999) developed techniques to recover the one-dimensional brightness profile of a quasar, based on the earlier work by Grieger et al. (1988, 1991). Agol & Krolik showed that frequent monitoring of a caustic crossing event in many wave bands (they used of order 40 simulated data points in eleven filters over the whole electromagnetic range), one can recover a map of the frequency-dependent brightness distribution of a quasar. Yonehara (1999) in a similar approach explored the effect of microlensing on two different accretion disk models. In another paper, Yonehara et al. (1998) showed that monitoring a microlensing event in the X-ray regime can reveal structure of the quasar accretion disk as small as AU-size.

3 Observational Evidence for Quasar Microlensing

Fluctuations in the brightness of a quasar can have two causes: they can be intrinsic to the quasar, or they can be microlens-induced. For a single quasar image, the difference is hard to tell. However, once there are two or more gravitationally lensed (macro-)images of a quasar, we have a relatively good handle to distinguish the two possible causes of variability: any fluctuations due to intrinsic variability of the quasar show up in all the quasar images, after a certain time delay. (This argument could even be turned around: the measured time delays in multiple quasars are the ultimate proof of the intrinsic variability of quasars.) So once a time delay is measured in a multiply-imaged quasar system, one can shift the lightcurves of the different quasar images relative to each other by the time delay, correct for the different (macro-)magnification, and subtract them from each other. All remaining incoherent fluctuations in the "difference lightcurve" can be contributed to microlensing. In a few quadruple lens systems we can detect microlensing even without measuring the time delay: in some cases the image arrangement is so symmetrical around the lens that any possible lens model predicts very short time delays (of order days or shorter), so that fluctuations in individual images that last longer than a day or so and are not followed by corresponding fluctuations in the other images, can be safely attributed to microlensing. This is in fact the case of the quadruple system Q2237+0305.

3.1 The Einstein Cross: Quadruple Quasar Q2237+0305

In 1989 the first evidence for cosmological microlensing was found by Irwin et al. (1989) in the quadruple quasar Q2237+0305: one of the components showed fluctuations. In the mean time, Q2237+0305 has been monitored by many groups (Corrigan et al. 1991; Østensen et al. 1996; Lewis et al. 1998). The most recent (and most exciting) results (Wozniak et al. 2000) show that all four images vary dramatically, going up and down like a rollercoaster in the last three years: $\Delta m_A \approx 0.6$ mag, $\Delta m_B \approx 0.4$ mag, $\Delta m_C \approx 1.3$ mag (and rising?), $\Delta m_D \approx 0.6$ mag.

3.2 The Double Quasar Q0957+561

The microlensing results for the double quasar Q0957+561 are not as exciting. In the first few years there appears to be an almost linear change in the (time-shifted) brightness ratio between the two images ($\Delta m_{AB} \approx 0.25$ mag over 5 years). But since about 1991, this ratio stayed more or less "constant" within about 0.05 mag, so not much microlensing was going on in this system recently (Schild 1996; Pelt et al. 1998; Schmidt & Wambsganss 1998). The possibility for some small amplitude rapid microlensing (cf. Colley & Schild 2000) cannot be excluded; however, one needs a very well determined time delay and very accurate photometry, in order to confirm it.

With numerical simulations and limits obtained from data of three years of Apache Point monitoring data of Q0957+561, and based on the Schmidt & Wambsganss (1998) analysis, Wambsganss et al. (2000) extend the limits on the masses of "Machos" in the (halo of the) lensing galaxy in 0957+561: the small "difference" between the time-shifted and magnitude-corrected lightcurves of images A and B excludes a halo of the lensing galaxy made of compact objects with masses of $10^{-7}M_{\odot} - 10^{-2}M_{\odot}$.

3.3 Other multiple quasars/radio microlensing?

A number of other multiple quasar systems are being monitored more or less regularly. For some of them microlensing has been suggested (e.g. H1413+117, Østensen et al. 1997; or B0218+357, Jackson et al. 2000). In particular the possiblity for "radio"-microlensing appears very interesting (B1600+434, Koopmans & de Bruyn 2000), because this is unexpected, due to the presumably larger source size of the radio emission region. The possibility of relativistic motion of radio jets may make up for this "disadvantage".

4 Unconventional Microlensing of Quasar Microlensing

4.1 Microlensing in individual quasars?

There were a number of papers interpreting the variability of individual quasars as microlensing (e.g., Hawkins & Taylor 1997, Hawkins 1998). Although this is an exciting possibility and it could help us detect a population of cosmologically distributed lenses, it is not entirely clear at this point whether the observed fluctuations can be really attributed to microlensing. After all, quasars are intrinsically variable, and the expected microlensing in single quasars must me smaller than in multiply imaged ones, due to the lower surface mass density. More studies are necessary to clarify this issue.

4.2 "Astrometric Microlensing": Centroid shifts

An interesting aspect of microlensing was explored by Lewis & Ibata (1998). They looked at centroid shifts of quasar images due to microlensing. At each caustic crossing, a new very bright image pair emerges or disappears, giving rise to sudden changes in the "center of light" positions. The amplitude could be of order 100 microarcseconds or larger, which should be observable with the SIM satellite (Space Interferometry Mission), to be launched in June 2006.

5 Quasar Microlensing: Now and Forever?

Monitoring observations of various multiple quasar systems in the last decade have clearly established that the phenomenon of microlensing exists. There are uncorrelated variations in multiple quasar systems with amplitudes of more than a magnitude and time scales of weeks to months to years. However, in order to get closer to a really quantitative understanding, much better monitoring programs need to be performed.

On the theoretical side, there are two important questions: what do the lightcurves tell us about the lensing objects, and what can we learn about the size and structure of the quasar. As response to the first question, the numerical simulations are able to give a qualitative understanding of the measured lightcurves (detections and non-detections), in general consistent with "conservative" assumptions about the object masses and velocities. But due to the large number of parameters (quasar size, masses of lensing objects, transverse velocity) and due to the large variety of lightcurve shapes, no satisfactory quantitative explanation or even prediction could be achieved. So far mostly "limits" on certain parameters have been obtained. The prospects of getting much better lightcurves of multiple quasars, as shown by the OGLE collaboration, should be motivation enough to explore this direction in much more quantitative detail.

The question of the structure of quasars deserves more attention. Here gravitational lensing is in the unique situation to be able to explore an astrophysical field that is unattainable by any other means. Hence more effort should be put into attacking this problem. This involves much more ambitious observing programs, with the goal to monitor caustic crossing events in many filters over the whole electromagnetic spectrum, and to further develop numerical techniques to obtain useful values for the quasar size and profile from unevenly sampled data in (not enough) different filters.

References

1. Agol, E., Krolik, J.: 1999, *ApJ* **524**, 49,
2. Colley, W., Schild, R.: 1999, *AAS* **195**, 4801
3. Corrigan, R.T., Irwin, M.J., Arnaud, J., Fahlman, G.G., Fletcher, J.M. et al.: 1991, *AJ* **102**, 34
4. Fluke, C.J., Webster, R.L.: 1999, *MNRAS* **302**, 68
5. Gott, J.R.: 1981, *ApJ* **243**, 140,
6. Grieger, B., Kayser, R., Refsdal, S.: 1988, *A&A* **194**, 54
7. Grieger, B., Kayser, R., Schramm, T.: 1991, *A&A* **252**, 508
8. Hawkins, M.R.S.: 1998, *A&A* **340**, L23
9. Hawkins, M.R.S., Taylor, A.N.: 1997, *ApJ* **482**, L5
10. Irwin, M.J., Webster, R.L., Hewett, P.C., Corrigan, R.T., Jedrzejewski, R.I.: 1989, *AJ* **98**, 1989
11. Jackson, N., Xanthopoulos, E., Browne, I. W. A.: 2000, *MNRAS* **311**, 389
12. Kayser, R., Refsdal, S., Stabell, R.: 1986, *A&A* **166**, 36
13. Koopmans, L. V. E., de Bruyn, A. G: 2000 *A&A* **358**, 793
14. Lewis, G.F., Miralda-Escudé, J., Richardson, D.C., Wambsganss, J.: 1993, *MNRAS* **261**, 647,
15. Lewis, G.F., Irwin, M.J., Hewett, P.C., Foltz, C.B.: 1998, *MNRAS* **295**, 573
16. Lewis, G.F., Ibata, R.A..: 1998, *ApJ* **501**, 478
17. Mineshige, S., Yonehara, A.: 1999, *PASJ* **51**, 497
18. Østensen, R., Refsdal, S., Stabell, R., Teuber, J. et al.: 1996, *A&A* **309**, 59
19. Østensen, R., Remy, M., Lindblad, P.O., Refsdal, S., Stabell, R. et al.: 1997, *A&AS* **126**, 393
20. Paczyński, B.: 1986, *ApJ* **301**, 503
21. Pelt, J., Schild, R., Refsdal, S., Stabell, R.: 1998, *A&A* **336**, 829
22. Schild, R.: 1996, *ApJ* **464**, 125
23. Schneider, P., Weiss, A.: 1987, *A&A* **171**, 49
24. Schmidt R., Wambsganss, J.: 1998, *A&A* **335**, 379
25. Wambsganss, J.: 1998, *Living Reviews in Relativity* **1**, No.12, (accessible via `http://www.livingreviews.org/Articles/Volume1/1998-12wamb/`)
26. Wambsganss, J., 1990, PhD thesis, also MPA report 550
27. Wambsganss, J., Schmidt R., Turner, E.L., Kundić, T., et al. 2000, (in preparation)
28. Witt, H.J.: 1993, *ApJ* **403**, 530
29. Woźniak, P. R. , Alard, C., Udalski, A. , Szymański, M., Kubiak, M., Pietrzyński, G., Żebruń, K.: 2000 *ApJ* **529**, 88
30. Wyithe, J.S.B., Webster, R.L., Turner, E.L.: 2000a, *MNRAS* **315**, 51
31. Wyithe, J.S.B, Webster, R.L., Turner, E.L., Mortlock, D.J.: 2000b, *MNRAS* **315**, 62
32. Yonehara, A., Mineshige, S., Manmoto, T., Fukue, J., Umemura, M., Turner, E. L.: 1998, *ApJ* **501**, L41
33. Yonehara, A.: 1999, *ApJ* **519**, L31

MICROLENSING IN Q2237+0305

J. Stuart Wyithe[1,2]
[1] *School of Physics, University of Melbourne, Parkville, Vic, 3052, Australia*
[2] *Princeton University Observatory, Peyton Hall, Princeton, NJ 08544, USA*

Q2237+0305 offers a unique opportunity to use spectrophotometric observations of microlensed high magnification events to examine the central engine of a quasar. The high quality of recent OGLE monitoring, in addition to the lengthening overall monitoring history for Q2237+0305 have allowed probabilities for the parameters of microlens mass, galactic transverse velocity and continuum source size to be determined. We discuss interpretations of features of the OGLE light-curves using the estimate for each parameter. The combination of optical and IR flux ratios provides a constraint on the extent of the mid-IR emission region.

1 Introduction

The QSO 2237+0305, sometimes known as Huchra's lens or the Einstein Cross (Huchra et al. 1985), is perhaps the most remarkable gravitational lens yet discovered. It comprises a foreground barred Sb galaxy (z=0.0394) whose nucleus is surrounded by four images of a radio-faint QSO (z=1.695). Broad band monitoring has shown that significant microlensing events occur. Since the optical depth to microlensing is of order unity at each of the image positions (eg. Kent & Falco 1988), the magnification effects on the source can be considered as a network of caustics moving across the source plane. Strong variation in a particular image results from the source either crossing a caustic or passing close to a cusp. Q2237+0305 is an ideal microlensing laboratory due to the relative closeness of the lensing galaxy and the nearly on-axis alignment. The time delay between the four quasar images is therefore less than a day, and the time-scale for events is typically 30-50 days. Analysis of light-curves for Q2237+0305 has yielded strong limits on the existence of low mass objects (eg. Wyithe, Webster & Turner 2000). In addition, analysis of caustic crossing events for Q2237+0305 hold the promise of a mapping of the intensity profile of the inner regions of the quasar central engine (eg. Agol & Krolic 1999).

Although Q2237+0305 has been monitored since its discovery, data collected by the OGLE collaboration over the last 3 years (Wozniak et al. (2000); see also http://www.astro.princeton .edu/~ogle/ogle2/huchra.html) has for the first time obtained data of sufficient coverage to clearly demonstrate smooth independent flux variation between the images. We provide interpretations for several features in the image A and C light-curves, and discuss their implications for future microlensing. The OGLE data adds to approximately 10 years of previously obtained, but less densely sampled photometry (eg. Corrigan et al. (1990) and Østensen et al. (1996)).

Table 1: Table of probabilities for model light-curve features corresponding to those in the 1999 image C event.

Event type	$P(\Delta t < 2wk)$	$P(\dot{M}_{mx} < 2)$	$P(M_{hgt} < .5)$	$P(\Delta M_{mn} < 0)$	$P(\Delta M_{mn} < 0)$
Cusp	0.11	0.83	0.55	0.50	0.95
$+ve$ caustic	0.07	0.01	0.02	0.02	0.38
$-ve$ caustic	0.05	0.04	0.13	0.98	0.99

2 Analysis of the OGLE Light-Curve

We apply simple statistics describing event heights and light-curve derivatives a postiori to specific features in the published light-curves. We use the results to interpret features found in monitoring data. In particular we discuss whether the large scale variation in image C (1999) was due to the source having crossed a caustic or moved outside of a cusp.

2.1 Statistics of the 1999 light-curve peak in image C

The image C light-curve shows a remarkable resolved peak described by $\sim$ 35 points on separate days spanning $\sim$ 7 months. By December 1999 the image C light-curve had dropped to a level similar to the end of the 1998 observing season. The peak is quite symmetric having reached a height $M_{hgt} \sim 0.5$ magnitudes above the 1998 level. The maximum derivative reached both before and after the event peak was $\dot{M}_{mx} \sim 2$ mags/year. Images B and D remained fairly constant during this period suggesting constant intrinsic luminosity. The event properties are discussed in relation to model calculations of the probability for their values for cusp events, and caustic crossings with appearing ($+ve$) and disappearing ($-ve$) critical images. The results are summarised in Tab. 1.

We find that a $\dot{M}_{mx}$ of $\sim$ 2 magnitudes per year is inconsistent at $> 99\%$ level with the event having been a $+ve$ caustic crossing. In addition, we find that a $-ve$ caustic crossing is excluded at the 95% level. A cusp cannot be excluded on the basis of the maximum derivative (though it is higher than expected). If the light-curve minimum preceding the 1999 image C event is assumed to have been at the level of the 1998 season then the height of the peak maximum above the previous local minimum is $M_{hgt} \sim 0.5$ magnitudes. $\Delta M_{hgt} \sim 0.5$ magnitudes is typical if the event is due to a cusp, and is ruled out at the 98% level if the event is $+ve$ caustic crossing. If the event is a $-ve$ caustic crossing the results are inconclusive.

Wyithe, Webster, Turner & Agol 2000 describes a general function to determine how long one should wait (Δt_e) for a HME following a hypothetical observed light-curve derivative. On the 19th of June 1999 monitoring showed image C rising at a rate of 1.21-1.78 mags/year. The light-curve peaked on $\sim$ 1 July, about 2-weeks after the aforementioned derivative. This is surprisingly early for all types of events. At the 90% – 95% level, caustic crossing events are excluded.

Constraints on the event type of the OGLE image C HME are placed by both the maximum derivative observed prior to the event peak, and the height of the peak above the previous minima. $+ve$ caustic crossings are excluded by both these measurements (even when potential systematic errors in source size are assumed). In addition, $-ve$ caustic crossings are excluded by the measured maximum derivative. The cusp interpretation is consistent with both measurements. Based on the above evidence we therefore conclude that the event observed for image C was probably a cusp event rather than a caustic crossing.

At the time of writing the image C light-curve was still in decline, but appeared to be decelerating ($+ve$ second derivative). If the light-curve flattens out at a level approximately equal to that of the 1998 season ($\Delta M_{mn} \sim 0$), then the $-ve$ caustic crossing interpretation will

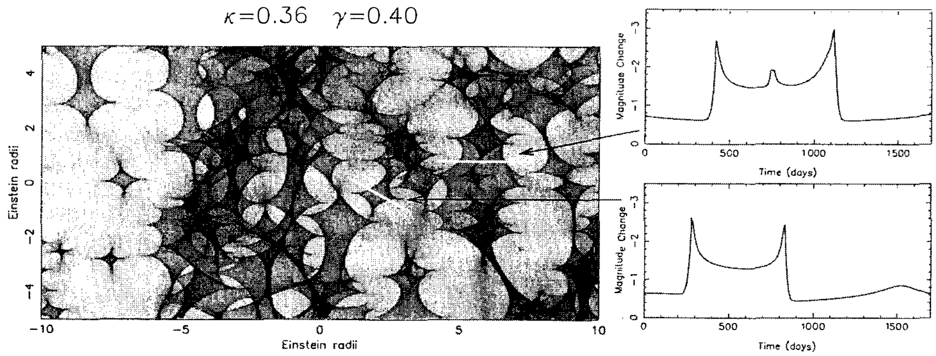

Figure 1: Examples of double-horned profile (top right) and double horned profile with an additional cusp event (lower right). Corresponding source tracks are overlayed on a magnification pattern.

be ruled out at the 95% level. Assuming that the previous light-curve minimum occurred during 1998, the $+ve$ caustic crossing interpretation is already ruled out at $> 95\%$.

Monitoring shows a $\Delta M_{mn} \sim 0.8$ magnitude rise between the 1997 image C minimum and the 1998 level, suggesting an event in between those observing seasons. We assume that the intrinsic source luminosity was approximately constant over this period, which is supported both by the facts that image A changed by < 0.2 magnitudes and that the other images show opposite trends. We find that ΔM_{mn} is consistent with a $+ve$ caustic crossing having occurred between the 1997 and 1998 observing seasons, but rules out $-ve$ caustic crossings ($\sim$ 99%) and cusp events ($\sim$ 95%). We therefore infer that a $+ve$ caustic crossing was missed between the 1997 and 1998 observing seasons.

2.2 The next image C HME

Now we assume that there was a $+ve$ caustic crossing between the 1997 and 1998 observing seasons, and investigate when we should next see a caustic crossing in image C. Due to the typical diamond formation of fold caustics, the case of a $+ve$ followed by a $-ve$ caustic crossing is common. Similarly, inspection of model light-curves shows that cusp events follow $-ve$ caustic crossings as the source moves past the cusp associated with that caustic (this feature is seen in the double horned profile that is characteristic of the Chang-Refsdal lens). However we have inferred that the OGLE image C light-curve shows a $+ve$ caustic crossing followed by a cusp event. Such a combination is much less common and is due to the source moving past a cusp formed from two fold caustics other than the one responsible for the $+ve$ caustic crossing HME. However, it too can be found in model light-curves. Examples of the two scenarios are shown in Fig. 1. One way of analysing the separation between the cusp event peak and the next caustic crossing is to calculate the ratio of the time between the cusp event peak and last caustic crossing and the time between the cusp event peak and next caustic crossing. The typical ratio is 1 and we expect it to be between $\sim \frac{1}{4}$ and ~ 4, yielding a most likely arrival time for the next event of $\sim$ 500 days, and an upper limit of $\sim$ 2000 days ($\sim$ 90%).

2.3 The next image A HME

The OGLE data also shows image A brightening over the 1999 season, with the most rapid variations occurring in the latter observations. On the 30th of October 1999 monitoring showed a rise in image A, of 1.41-1.88 mags/year (we used observations on the 20th of October, 30th of October and 9th of November). Having observed a derivative in the quoted range means that a $+ve$ caustic crossing is very unlikely, and a $-ve$ caustic crossing is the most likely option. Unfortunately, these results predict that an event will occur in image A between the 1999 and 2000 observing seasons. If the impending event is assumed to be a $-ve$ caustic crossing, with a previous minimum occurring during the 1998 season, then we predict that the image A light-curve should have a subsequent minimum at a level $\sim 1-1.5$ magnitudes fainter than the November 1999 level.

2.4 Combining IR and Optical observations

Observations in September 1999 show an image B:A I-band flux ratio of ~ 0.3. However, at the same epoch, mid-IR observations (Agol et al. 2000) yield an image B:A K-band flux ratio of $\sim 1.1 \pm 0.1$. This dramatic colour difference between images A and B is interpreted as being due to microlensing of the optical continuum emission region (which is smaller than the microlens Einstein radius), while the larger IR emission region more closely reflects the true magnification ratio. Modelling shows that given the optical flux ratio, the IR emitting region should be $\sim 100-1000$ times larger than the I-band emission region to produce the observed K-band flux ratio. This indicates that the infrared emission is produced by hot dust rather than non-thermal synchrotron emission (Agol et al. 2000).

3 acknowledgements

The author would like to thank Ed Turner, Rachel Webster, Eric Agol and Przemyslaw Wozniak for many useful discussions. This work was supported by NSF grant AST98-02802. JSBW acknowledges the support of an Australian Postgraduate Award.

1. Agol, E., Krolik, J., 1999, Ap. J., 524, 49
2. Agol, E., Jones, B., Blaes, O., 2000 ApJ submitted
3. Corrigan et.al, 1991, Astron. J., 102, 34
4. Huchra, J., Gorenstein, M., Horine, E., Kent, S., Perley, R., Shapiro, I. I., Smith, G., 1985, Astron. J., 90, 691
5. Kent, S. M., Falco, E. E., 1988, Astron. J., 96, 1570
6. Østensen, R. et al. 1996, Astron. Astrophys., 309, 59
7. Wozniak, P. R., Alard, C., Udalski, A., Szmanski, M., Kubiak, M, Pietrzynski, G., Zebrun, K., 2000a, Ap. J., 529, 88
8. Wyithe, J. S. B, Webster, R. L., Turner, E. L., 1999, MNRAS, 309, 261
9. Wyithe, J. S. B, Webster, R. L., Turner, E. L., 2000, MNRAS 315, 51
10. Wyithe, J. S. B, Webster, R. L., Turner, E. L., D. J. Mortlock, 2000, MNRAS, 315, 62
11. Wyithe, J. S. B, Webster, R. L., Turner, E. L., Agol, E., 2000, accepted, astro-ph/0001306

RADIO-MICROLENSING IN B1600+434: PROBING MACHOs AT HIGH-REDSHIFTS

L.V.E. Koopmans[1,2,3], A.G. de Bruyn[4,1], J. Wambsganss[5,6], C.D. Fassnacht[7],R.D. Blandford[3]
[1]*Kapteyn Astronomical Institute, P.O.Box 800, NL-9700 AV Groningen, The Netherlands*
[2]*Jodrell Bank Observatory, Lower Withington, Macclesfield, Cheshire SK11 9DL, UK*
[3]*Caltech, Mail Code 130-33, Pasadena CA 91125, USA*
[4]*NFRA-ASTRON, P.O.Box 2, NL-7990 AA Dwingeloo, The Netherlands*
[5]*University of Potsdam, Institute for Physics, Am Neuen Palais 10, 14469 Potsdam, Germany*
[6]*MPI für Gravitationsphysik, "Albert-Einstein-Institut", Am Mühlenberg 1, 14476 Golm, Germany*
[7]*NRAO, P.O.Box 0, Socorro, NM 87801, USA*

We shortly review the evidence for the detection of *radio-microlensing* in the CLASS gravitational lens system B1600+434. We then present some of the latest results from our multi-frequency monitoring campaign and compare these observations with preliminary results from new Extreme-Scattering-Event (ESE) and radio-microlensing simulations.

1 Introduction

There is growing evidence that the lensed images of the CLASS[a] gravitational lens system B1600+434 (Jackson et al. 1995; Jaunsen & Hjorth 1997; Koopmans, de Bruyn & Jackson 1998) show strong non-intrinsic (i.e. 'external') flux-density variations, when observed at radio wavelengths (Koopmans et al. 2000a). A detailed analysis of 8.5–GHz lightcurves of B1600+434 obtained during a 1998 VLA monitoring campaign showed that these external flux-density variations are most likely caused by μas-scale relativistic subcomponents in the lensed source, which are being microlensed by massive compact objects in the dark-matter halo around the lensing galaxy at z=0.41 (Koopmans & de Bruyn 2000). The most likely alternative explanation, i.e. Galactic scintillation, was shown to implausible, based on a number of arguments (see Koopmans & de Bruyn 2000; Koopmans et al. 2000b). An optical monitoring campaign with the Nordic Optical Telescope (NOT) in 1998-1999 has shown evidence for the presence of optical microlensing in B1600+434 (Burud et al. 2000) as well, although it is not yet clear which of two lensed images (or both) undergo microlensing.

In Sect.2 we present some of the latest results from our 1999-2000 multi-frequency VLA observations of B1600+434. In Sect.3.1, we focus on a second alternative explanation (besides scintillation) for the external radio variability, i.e. Extreme Scattering Events (ESE). In Sect.3.2, we report on some very preliminary results from new *radio-microlensing* simulations for B1600+434. In Sect.4, we summarize our results.

2 Multi-Frequency VLA Observations of B1600+434

In 1999 a new VLA monitoring campaign of B1600+434 in A- and B-array was started at 1.4, 5 and 8.5 GHz (e.g. Koopmans et al. 2000b). We chose to observe over a wide frequency range, because it enables us to disentangle different sources of external variability, such as microlensing and scintillation (Koopmans & de Bruyn 2000). Here, we will *only* report on some preliminary results of the 5–GHz observations. The light curves of the the lensed images of B1600+434 are shown in Fig.1.

The 5–GHz lightcurve of image A, which predominantly passes through the dark-matter halo of the edge-on spiral lens galaxy, shows strong external variations, continuing the behavior

[a]Cosmic Lens All Sky Survey

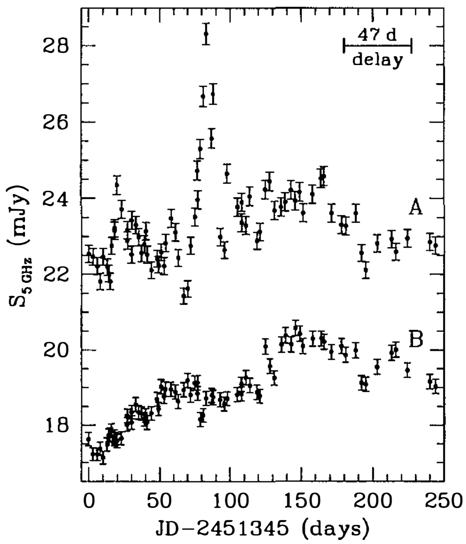

Figure 1: Preliminary results (at 5 GHz) from the 1999/2000 VLA monitoring campaign of B1600+434. The upper light curve (image A) passes through the dark-matter halo of the edge-on spiral lens galaxy. Note several strong (up to 30%) events in the upper lightcurve and the complete absence of these events in the lower light curve (image B) after the time delay of ~47 days.

already seen in the 1998 VLA 8.5–GHz lightcurves (Koopmans & de Bruyn 2000). In 1998 and again in 1999-2000, the lightcurve of image B shows much less short-term variability during the monitoring campaign. In this proceeding we will *only* focus on the strongest 5-GHz event that starts around day 67 (Fig.1). A ~30% increase in the flux-density is seen with a maximum around day 83. After that an almost similar decrease in flux-density is observed, reaching a minimum around day 96. This comparatively well-sampled ~1–month event is *not* detected in the other lensed image after the time delay of about 47 days (Koopmans et al. 2000a; see also Burud et al. 2000) and must therefore be of external origin. The VLA 8.5-GHz lightcurve of image A simultaneously shows the same external event with almost comparable amplitude. At 1.4 GHz the event is not detected.

3 Observations versus Simulations

3.1 Extreme Scattering Events: Can they explain what we see in B1600+434?

ESEs are strong non-intrinsic variations in the lightcurves of compact extra-galactic radio sources and pulsars, first discovered by Fiedler et al. (1987). ESEs can typically be characterized by a strong decrease (up to 50% in some cases) in the source flux-density at low frequencies (~2 GHz) during a period of several weeks to months (e.g. Fiedler et al. 1994). In most ESEs almost no variations are seen at higher frequencies (~8 GHz), with the exception of 0954+658 (Fiedler et al. 1987, 1994). The most plausible explanation of these events is that a plasma cloud with high electron density moves across the line-of-sight to the source, causing strong refractive (de)focusing (Romani, Blandford & Cordes 1987) and/or stochastic broadening (Fiedler et al. 1987, 1994), resulting in observable flux-density variations.

We have have examined the strongest event seen at 5 GHz (Fig.1) in terms of the refractive (de)focusing model. The stochastic-broadening model — which can be understood in terms of a source convolution with a space-varying kernel (Fiedler et al. 1994) — has great difficulties in explaining 'caustic-type' *increases* in flux-density, which have been observed in for example 0954+658. We therefore use the simple refractive (de)focusing model model from Clegg, Fey

& Lazio (1998), who describe the plasma cloud as a Gaussian over- or underdensity. We have examined other models as well, but the precise details of the model do not alter the main conclusions. In Fig.2a, we have shown the results from one of the models that gives a fairly good representation of the observed event seen in Fig.1. The model gives a similar event at 8.5 GHz and almost no variations at 1.4 GHz, as has been observed. However, at 5 GHz the model requires a negative lens strength $\alpha \approx -0.2$, where $\alpha = 3.6\lambda^2 \Delta N_0 D\, a^{-2}$, λ is the radio-wavelength in cm, ΔN_0 is the central electron surface-density contrast of the cloud in units of cm^{-3} pc, D is the cloud distance in kpc (for a source at infinity) and a is the cloud size in units of AU (see Clegg et al. 1998 for more details). For the model in Fig.2a, we require a source size at 5 GHz equal to $\beta \approx 1.0$ times the cloud size. We assume that the source size grows linearly with λ. Changing α and/or β only slighty from these values quickly results in a very poor comparison with the lightcurves of at least one of the frequencies. No solutions for positive α have been found, independent of the precise model for the electron surface density. The result is therefore quite robust. However, because $\alpha < 0$, one immediately notices that $\Delta N_0 < 0$. In other words, one requires a considerable electron *underdensity* of the 'cloud' (i.e. 'bubble') compared to its immediate surroundings. Filling in some typical numbers of genuine ESEs ($D \approx 0.5$ kpc, $a \approx 1$ AU; e.g. Fiedler et al. 1994) and taking λ=6 cm, we find $\Delta N_0 = -3 \cdot 10^{-3}$ cm^{-3} pc. If we assume the 'bubble' is spherical, the central electron underdensity is $\Delta n_0 \approx -10^3$ cm^{-3}, which is a more than 10^3 times the typical electron density in the Galactic ISM. Consequently, the surrounding of this 'bubble' must have a similar electron *overdensity*. If the electron temperature inside the 'bubble' is about $T_e = 10^4$ K, it would collapse within about 2 weeks. This time scale is smaller than the event duration of $\sim$1 month. Reducing a by a factor of say 10 would still require $\Delta n_0 \approx -10^2$ cm^{-3}, but more seriously it reduces the collapse time to only several days.

All in all, it appears unlikely that the observed event (Fig.1) can be a genuine ESE. It (i) does not resemble any other ESE (see Fiedler et al. 1994), (ii) requires a severely localized electron *underdensity* and consequently a similar electron overdensity around it, and (iii) it is difficult to see how such a 'bubble' could be generated and remain stable for a considerable period of time (i.e. several weeks).

3.2 Radio Microlensing

In Koopmans & de Bruyn (2000), the VLA 8.5-GHz light curves were compared with microlensing simulations. Because of the absence of a distinct isolated microlensing events in the lightcurves, several assumptions had to be made in deriving properties of the compact objects in the halo and the source structure. The strong events in the 1999/2000 VLA light curves (Fig.1) allows us to improve this analysis and do a comparable study as for Q0957+561 (e.g. Schmidt & Wambsganss 1998; Refsdal et al. 2000). We have generated microlensing magnification patterns on grids of 4096×4096 pixels, having sidelengths of 409.6 Einstein radii. We generate a number of magnification patterns, taking κ=γ=0.2 for the image (A) passing through the dark-matter halo (e.g. Koopmans et al. 1998), for different fractions of the surface density composed of compact objects (f_c=10%, 30% and 100%) and different sizes for the relativistic subcomponents. We then simulate $\sim 10^5$ lightcurves for a range of relativistic-subcomponent velocities and for each combination of f_c and source size. The analysis of these lightcurve and the comparison with the observations is still work in progress. A not uncommon example of one of the light curves, however, is shown in Fig.2b for f_c=30% and a component size of 0.5 Einstein radius. For a subcomponent containing 10% of the total source flux-density, this event would correspond to a $\sim$30% event in the light curve of image A, comparable to the event in Fig.1.

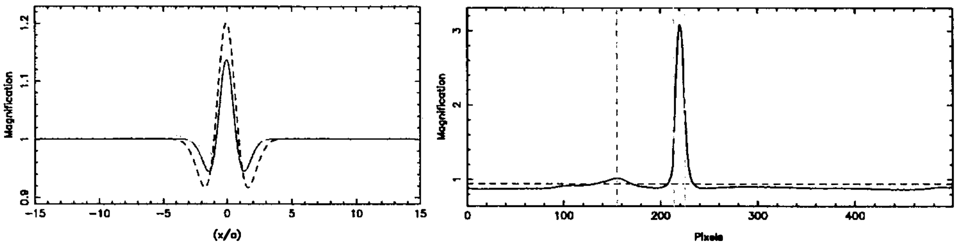

Figure 2: **Left:** ESE simulation of the strongest 'external' event shown in Fig.1. The light curves are for 8.5 GHz (solid), 5 GHz (dash) and 1.4 GHz (dot-dash). **Right:** A microlensing simulation. The horizontal dashed line gives the average of the light curve. The two close vertical dashed lines indicate the FWHM of the strongest event. The other vertical dashed line indicates the second strongest event. See Sections 3.1–2 for more details about these models.

4 Conclusions

We find that ESEs can only explain the strongest non-intrisic 5-GHz variation in lensed image A of B1600+434 (Fig.1), if the Galactic ionized ISM contains ~1–AU sized regions that have electron densities differing by $\Delta n_0 \approx -1000$ cm^{-3} from their immediate surrounding. Not only have these type of flux-density variations never been seen before in (unlensed) radio sources, but the hypothesised plasma structures responsible are unlikely to be stable for longer than several weeks. We are currently investigating even more 'exotic' plasma models. Preliminary microlensing simulations show that the flux-density variations as seen in B1600+434 *can* occur quite regularly *if* the lensed source contains relativistic sub-components with a size similar to the Einstein radius of the compact objects, even if the surface density of massive compact objects in the lens galaxy is much lower than the critical surface density. More complete data, ESE and microlensing analyses will be given in several forthcoming papers.

References

1. Burud, et al. 2000, astro-ph/0007136
2. Clegg, Fey & Lazio, 1998, ApJ 496, 253
3. Fiedler, Dennison, Johnston & Hewish, 1987, Nature 326, 675
4. Fiedler, Dennison, Johnston, Waltman, & Simon, 1994, ApJ 430, 581
5. Jackson et al. 1995, MNRAS 274, L25
6. Jaunsen & Hjorth, 1997, A&A 317, L39
7. Koopmans, de Bruyn, & Jackson, 1998, MNRAS 295, 534
8. Koopmans, de Bruyn, Xanthopoulos, & Fassnacht, 2000a, ApJ 356, 391
9. Koopmans, de Bruyn, Wambsganss, Fassnacht, 2000b, astro-ph/0004285
10. Koopmans & de Bruyn, 2000, A&A 358, 793
11. Refsdal, Stabell, Pelt, Schild, 2000, astro-ph/0005371
12. Romani, Blandford & Cordes, 1987, Nature 328, 324
13. Schmidt & Wambsganss, 1998, A&A 335, 379

CONSTRAINTS ON THE GRAVITATIONAL FORCE ON PHOTONS FROM MICROLENSING

J-F.Glicenstein
DAPNIA/SPP,CEA Saclay, F-91191 Gif-sur-Yvette, France

Abstract

Gravitational microlensing observations are used to study the radial dependence of the gravitational force acting on photons. The Newton inverse square law is shown to be valid at a few % level at a distance scale of a few AU. Constraints on possible non-Newtonian terms are derived.

1 Introduction

The gravitational force on photons is known from studies of the deflection of light by the Sun at the scale of a few AU (where 1 AU = $1.496\ 10^8$km is the Astronomical Unit) and by gravitational lensing observations on larger (galactic) scales [1]. The deflection of light by the Sun has been shown to be consistent with the inverse square law [2].

Gravitational microlensing is sensitive to gravitational interactions at a scale of a few to a few tens of AU. Hence it would fill a small part of the gap between the solar system scale (where Newton's law is known to be accurate at the 10^{-9} level [3]) and the galactic scale. The purpose of this paper is to address the following question : can we learn something on the gravitational interaction of photons from microlensing experiments?

2 The gravitational lens equation

2.1 Angular position of images

The usual lensing geometry is shown on figure 1. A source star located at S is lensed by a massive

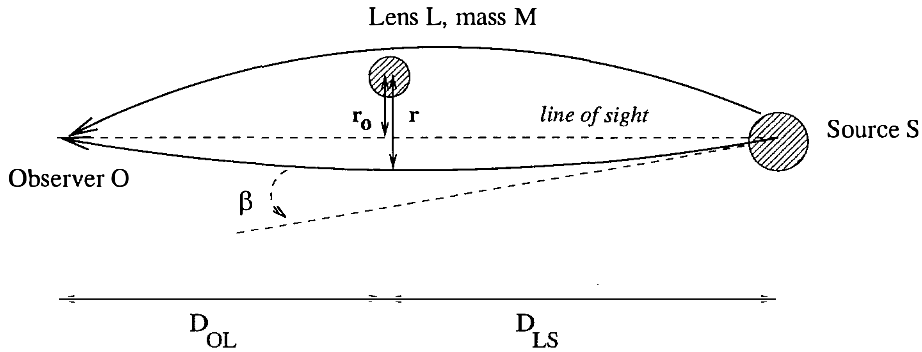

Figure 1: An observer located at O receives photons from a source star at S. The source star is lensed by a lens star at L. The distance between the observer and the lens is D_{OL}, the distance between the lens and the source is D_{LS}. The lens plane is normal to the line of sight OS.

lens star (mass M) at L and observed at O. The Schwarzschild radius r_S and the Einstein radius r_E are defined by:

$$r_E = \sqrt{\frac{4GMD_{LS}D_{OL}}{c^2 D_{OS}}} \tag{1}$$

$$D_{OS} = D_{OL} + D_{LS} \tag{2}$$

The image positions r are given by the normalized lens equation:

$$r - r_o = \alpha(r) \tag{3}$$

where r_o is the projected position of the source in the plane perpendicular to the line of sight containing the lens, and α is related to the deflection angle β by:

$$\alpha = \frac{D_{LS}D_{OL}}{D_{OS}}\beta \tag{4}$$

2.2 The deflection angle

In the weak field approximation, the deflection angle is related to the gravitational potential Φ by

$$\beta = -2\int_S^O \partial_\perp \Phi dz \tag{5}$$

where z is a coordinate along the source-observer axis. For a Schwarzschild lens, one finds

$$\alpha(r) = \frac{r_E^2}{r}(1 + O(\frac{r_S}{r})) \tag{6}$$

Since deviations from the inverse square law are not expected to be large, the class of lenses for which

$$\alpha(r) = \frac{r_E^2}{r}(1 + f(r)) \quad f(r) \ll 1 \tag{7}$$

(quasi-Schwarzschild (QS) lenses), is especially important.

2.3 Models of deviations from the inverse square law

Three models for a deviation from the inverse square law and the motivations for such models are investigated in reference [4]. Here, we consider only two of these models. The first model has a power law gravitational potential given by:

$$\Phi \propto r^{-\delta} \tag{8}$$

This model is empirical and convenient for lensing analysis, since the deflection angle is also found to follow a power law with index $-\delta$. When $\delta \sim 1$, this model is equivalent to a QS lens with

$$f(r) = (1 - \delta)\ln r \tag{9}$$

The other model is obtained by simply adding an extra $1/r^2$ term to the ordinary $1/r$ deflection.

$$\beta \propto \frac{1}{r}(1 + \epsilon' \frac{r_E}{r}) \tag{10}$$

The extra $1/r^2$ term might be important for some exotic lenses such as lenses with scalar charges[5].

3 Solution of the lens equation

For a Schwarzschild lens, equation (3) is readily solved. Two images r_+ and r_- are found. The image r_+ tends to r_o at large r_o, while $|r_-| \leq r_E$. However, these images are not detected individually in microlensing observations. Instead, the experiments take advantage of the apparent magnification of the flux of the lensed source.

The magnification factor is given by:

$$A(r_o) = \left|\frac{r_+}{r_o}\frac{dr_+}{dr_o}\right| + \left|\frac{r_-}{r_o}\frac{dr_-}{dr_o}\right| \tag{11}$$

It is assumed here that the lens equation (3) has only 2 solutions by analogy with Schwarzschild lenses. For an arbitrary gravitational potential, it has been be shown in [4] that the solutions $r_\pm$ of the lens equation (3) generalize for arbitrary $\alpha(r)$ to:

$$r_+ = r_o + \sum_{n=1}^{\infty} \frac{1}{n!}\frac{d^{n-1}}{dr_o^{n-1}}(\alpha(r_o))^n \tag{12}$$

$$r_- = -\alpha^{-1}(r_o) + \sum_{n=1}^{\infty} \frac{(-1)^{n+1}}{n!}\frac{d^{n-1}}{dr_o^{n-1}}\left(\frac{d\alpha^{-1}(r_o)}{dr_o}(\alpha^{-1}(r_o))^n\right) \tag{13}$$

$$= \sum_{n=1}^{\infty} \frac{(-1)^n}{n!}\frac{d^{n-1}}{dr_o^{n-1}}(\alpha^{-1}(r_o))^n \tag{14}$$

It is clear that these expressions have a restricted validity range in r_o. In the worst case (that of Schwarzschild lenses), the expansions converge for $r_o \geq 2r_E$.

Simple first order expressions can be obtained for QS lenses.

$$r_+ = r_o + \frac{r_E^2}{r_o}(1 + f(r_o)) - \frac{r_E^4}{r_o^3}(1 + 2f(r_o) - r_o\frac{df}{dr}) \tag{15}$$

$$r_- = -\frac{r_E^2}{r_o}(1 + f(\frac{r_E^2}{r_o})) \tag{16}$$

It is now straightforward to calculate the magnification factor for a QS lens, keeping only the lowest order terms in f and r_E^2/r^2. It has a simple expression:

$$A(r_o) = 1 + \frac{r_E^2}{r_o}\frac{df}{dr} + 2\frac{r_E^4}{r_o^4} \tag{17}$$

In the large r_o limit, the magnification is obtained by summing the magnification of a Schwarzschild lens (f=0) and an additional term. In this limit, a pure Schwarzschild lens has a magnification which is only second order in $r_E^2/r_\bullet^2$. The non-Newtonian term of the magnification (17) is first order both in f and r_E^2/r_o^2, and can become dominant at large enough r_o. It is basically this circumstance which allows one to look for deviations from the inverse square law.

4 Constraints on the gravitational force from a microlensing event

A good candidate to give constraints on possible deviations from Newton's law is the event 1999-BUL-44, which is a microlensing alert [6] of the OGLE collaboration. The I band light curve of the alert has been released on the Web [a]. The contribution of non-Newtonian terms can be obtained by using an extension of equation (17). Only low magnification data points ($< 5\%$) are used in this analysis.

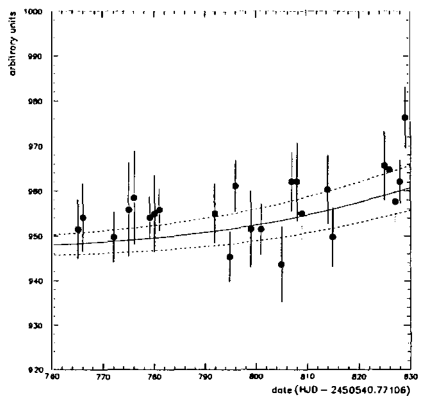

Figure 2: Microlensing observations of OGLE 1999-BUL-44. The solid line shows the fit to a pure Schwarzschild lens. The dotted lines show the expected magnification when the gravitational potential is $1/r^{1\pm.066}$.

The fit of the power law model (9) is illustrated on figure 2. It gives

$$\delta - 1 = -0.006 \pm 0.066 \tag{18}$$

The gravitational potential is found to be Newtonian at the 7% level.

The fit to the parameter of model (10) gives

$$\epsilon' = -0.008 \pm 0.05 \tag{19}$$

The maximum contribution of an extra $\epsilon' r_E^2/r^2$ in the gravitational potential is thus

$$\epsilon' \leq 5\ 10^{-2} (68\ \%\ \mathrm{CL}) \tag{20}$$

Further constraints from another gravitational model, a Yukawa potential, are derived in reference [4].

1. A.Dar, Nuclear Physics B (Proc.Suppl.),**28A**,321 (1992)
2. C.Riveros and H. Vucetich, Phys.Rev.D **34**,321 (1986)
3. E.G Adelberger,B.R. Heckel, C.W. Stubbs and W.F Rogers, Ann.Rev.Nucl.Part.Sci., **41**, 269 (1991)
4. J-F Glicenstein, DAPNIA/SPP-00-02 (2000), submitted to Phys. Rev. D
5. K.S Virbhadra, D. Narasimha and S.M.Chitre,Astron. & Astrop. **337**,1 (1998) S.Liebes, Phys.Rev. **133B**, 835 (1964)
6. A.Udalski,M. Szymański,J. Kałużny ,M. Kubiak, M. Mateo, W. Krzemiński, and B.Paczyński ,Acta Astron. **44**, 227 (1994)

[a]The Web address of OGLE alerts is http://www.astrouw.edu.pl/ ogle/ogle2/ews/ews.html

GRAVITATIONAL LENSING BY GALAXIES, GROUPS AND CLUSTERS

GRAVITATIONAL LENSING AND CLUSTER OF GALAXIES

Jean-Paul KNEIB
Laboratoire d'Astrophysique, Observatoire Midi-Pyrénées
14 avenue E.-Belin, F-31400 Toulouse, France

Multiple images, giant arcs, Einstein cross, fold, cusp, lip, caustics, critical lines, sources, mapping, time delay, arclets, weak shear, magnification bias, depletion, ellipticities, polarization, smearing, convergence, kernel, mass reconstruction, sub-structure, dark halos, natural telescope, amplification, distant galaxies, faintest sources ...

This is a non exhaustive list of favorite terms used when using gravitational lensing in clusters of galaxies. I will introduce here lensing in clusters as a useful tool in modern *observational* cosmology. I will give a summary of what we are learning in terms of cluster *mass distribution* in the strong and weak regime, and what information we will gain in terms of the cluster physics. I will underline the benefit of using cluster-lenses as *natural telescopes* to probe the distant Universe.

1 Introduction

Cluster of galaxies are the largest and most massive bounded structures in the Universe. Due to their important mass density they locally deformed the Space-Time. Therefore, the wave front of the light coming from any distant galaxy (or more generally any emitting light source) passing through a galaxy cluster will be distorted. Moreover, for the most massive clusters the mass density in the core is sufficiently high to break the wave front into pieces hence producing multiple images of distant galaxies, which usually form these extraordinary gravitational giant

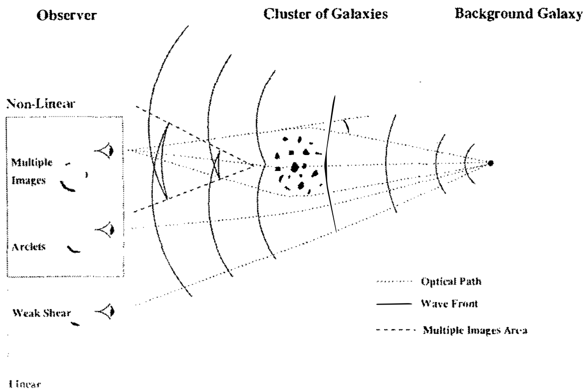

Figure 1: Gravitational lensing in clusters: A simple representation of how gravitational images are formed.

arcs (the *strong lensing* domain). Distant galaxies will thus appeared distorted and magnified, we usually call them arclets because of their noticeable elongated shape tangentially aligned toward the cluster center. Note however that their shape is a combination of the intrinsic shape and the distortion induced by the cluster, thus a lensed galaxy can appear round if its intrinsic orientation is perpendicular to the shear direction. If the alignment between the observer, the cluster and distant galaxies is less perfect the distortion induced by the cluster will be less important and can not be recognize immediately – statistical method are required – (we entering the *weak regime* domain). Indeed in this region, the shape of the galaxies are dominated by their intrinsic ellipticity or worse contaminated by the distortion of the camera and/or the point spread function (PSF) of the image.

In the thin lens approximation (which usually holds for cluster-lenses *e.g* Schneider, Ehlers & Falco, 1992), the deflection of light between the position of the source $\vec{\theta}_S$ and the position of the image $\vec{\theta}_I$ is given by the lensing mapping equation:

$$\vec{\theta}_S = \vec{\theta}_I - \frac{2\mathcal{D}}{c^2}\vec{\nabla}\phi_N^{2D}(\vec{\theta}_I) = \vec{\theta}_I - \vec{\nabla}\varphi(\vec{\theta}_I) \tag{1}$$

where $\mathcal{D} = D_{LS}/D_{OS}$ is the angular distance ratio between the Lens and the Source and the Observer and the Source [this ratio therefore depends on the redshift of the cluster z_L and the background source z_S, as well as - but only weakly - on the cosmological parameter Ω_m and Ω_λ], and ϕ_N^{2D} is the Newtonian projected gravitational potential, and φ the lensing potential. This transformation is thus a mapping from Source plane to Image plane, and the Hessian of this transformation relates a source element of the Image to the Source plane:

$$\frac{d\vec{\theta}_S}{d\vec{\theta}_I} = \mathcal{H} = \mathcal{A}^{-1} = \begin{pmatrix} 1-\partial_{xx}\varphi & -\partial_{xy}\varphi \\ -\partial_{xy}\varphi & 1-\partial_{yy}\varphi \end{pmatrix} = \begin{pmatrix} 1-\kappa-\gamma_1 & -\gamma_2 \\ -\gamma_2 & 1-\kappa+\gamma_1 \end{pmatrix} \tag{2}$$

where we have defined the convergence $\kappa = \Sigma/2\Sigma_{crit}$, the shear $\vec{\gamma} = (\gamma_1, \gamma_2)$ and the magnification matrix $\mathcal{A}$. This matrix also governs the shape transformation from the Source to the Image plane.

Thus, cluster lenses can be used in 2 ways: *i)* Firstly by understanding and modeling the gravitational optics of this system: by probing the **total mass** distribution of the cluster – which explains the observed image configuration and distortions –, by constraining the **distance** of the lensed galaxies – the more distant the more distorted they are –, to put constraints on the cosmological parameters - although this is a second order effect –. *ii)* Secondly as a *Natural telescope*: galaxies seen through massive cluster cores are amplified by the gravitational lensing effect making them easier to study in details; the faintest sources – which would otherwise remain unknown – can be detected/identified as the sensitivity of instruments is boosted by the gravitational amplification.

2 Cluster Lens Properties

2.1 Strong Lensing

Massive clusters can produce multiple images, this will happen when the surface mass density of the cluster reach or is larger than the *critical density* $\Sigma_{crit} = \frac{c^2}{4G}\frac{D_{OS}D_{OL}}{D_{LS}}$. The configuration of multiple images tells us about the structure of the mass distribution. A cluster with one dominant clump of mass will produce *fold* or *cusp* arcs, radial arcs (*e.g* MS2137.3-2353: Fort et al 1992, Mellier et al 1993; AC114: Natarajan et al 1998; A383: Smith et al 2000); a bimodal cluster can produce straight arcs (*e.g* Cl2236-04: Kneib et al 1994a), triplets (A370: Kneib et al 1993, Bezecourt et al 1999) or even triangular image; a very complex structure with lots of massive halos in the core can produce multiple image system with seven or more images of the same source (*e.g* Cl2244-04, A2218).

A particular useful and popular mass estimate in the strong lensing regime is the mass within the Einstein radius R_E: $M(< R_E) = \pi\Sigma_{crit}\theta_E^2$; R_E is the location of the critical line for a circular mass distribution, usually approximated by the arc radius R_{arc}. It is a very handy expression – independent of the mass profile for a circular mass symmetry –, but one should be careful in using it: either because the arc used to derive the mass as a unknown redshift, or the arc is a single image and thus does not trace the Einstein radius (for a singular isothermal sphere model, a single image can not be closer to twice the Einstein radius or it will have a counter image!), or the mass distribution is very complex with a lot of sub-structure. In conclusion, **this estimator does generally overestimate the mass.**

The only route to accurately constrain the mass in cluster cores is to use multiple images with preferably a spectroscopic redshift to absolutely calibrate the mass. As the problem is generally degenerate –*in the sense that there is not a single mass distribution but a family of model that is fitting the observables* –, one should used physically motivated representation of the mass distribution and adjust it in order to best reproduce the different family of multiple images (*e.g* Kneib et al 1996). As the position of the images are known to great accuracy and are usually located in different places of the cluster cores a simple mass model with one clump can usually not reproduce the image configuration. The lens model needs to include the cluster galaxies to match up the image configuration and positions. As there is not an infinite number of multiple images and thus number of constraints, it is important to limit the number of free parameters of the model and keep it physically motivated – as in the end – we are interested to derive physical properties of the cluster. Alternative method, using non-parametric description have been explored (*e.g.* Abdelsalam et al 1999), but usually lack the resolution of a parametric form due to the large dynamical range of the mass density expected in a cluster core - but clearly this is an interesting approach than should explored further.

The strong lensing mass modeling technique is an iterative method, in the sense that once a multiple images is securely identified, other multiple images systems can be discovered using morphological or color criteria as well as the predictions from the lens model. The lens model can then predict redshift for these multiple systems (Kneib et al 1993, Natarajan et al 1998) as well as for the arclets (Kneib et al 1994b, 1996): on the basis that on average a distant galaxy is randomly orientated, and its ellipticity follow a relatively peaked ellipticity distribution. These prediction can then be tested/verified (*e.g.* Ebbels et al 1998) and an improved mass model can be derived integrating the new constraints.

The ultimate step of strong lensing modeling is to constrain the cosmological parameters. This can be undertaken, when in a cluster core, a sufficient number of multiple images (> 3) are identified and for which spectroscopic information can be measured (see Golse et al this conference).

2.2 Weak Lensing

In the weak lensing regime the game is different: we measure the *mean* ellipticity and/or the *mean* number density of faint galaxies, and we want to relate these statistics to the mean surface mass density κ of the cluster. There are two issues in doing that:

• one for a *theorist*: What is the best method to reconstruct the mass distribution κ (as a mass map or a radial mass profile) from the 'shear field' $\vec{\gamma}$ and/or the magnification bias?

• one for an *observer*: How best determined the 'true' ellipticity of a faint galaxy which is smeared by a PSF barely smaller than the object (when using ground-based images) that is not circular (camera distortion, tracking errors ...) and not stable in time? How best estimate the variation in the number density of faint galaxies due to the lensing effect, taking into account the crowding effect due to the cluster and the intrinsic fluctuations in the distribution of galaxies?

Various approaches have been proposed to solve these two problems, and we can distinguish two families of methods: **direct** and **inverse** methods.

For the theorist issue, the direct approaches are: *i)* the Kaiser & Squires (93) method (an integral method, that express κ as the convolution of $\vec{\gamma}$ by a kernel) and subsequent refinements (*e.g.* Seitz et al. 1995, 1996); *ii)* the local inversion method (Kaiser, 1995, Schneider, 1995, Lombardi & Bertin 1998) integrates the gradient of $\vec{\gamma}$ within the boundary of the observed field to then derive κ. The inverse approach works on κ or the lensing potential φ and uses maximum likelihood (Bartelman et al 1996, Schneider et al 2000) or maximum entropy method (Bridle et al 1998) to determine the most likely mass distribution (as a 2D mass map or a 1D mass profile) that reproduce the shear field $\vec{\gamma}$ and/or the variation in the faint galaxy number densities. These inverse methods are of great interest as they allow: to quantify the errors in the resultant mass maps or mass estimates (Bridle et al 1999), as well as to introduce external constraints (such as strong lensing, or X-ray).

For the observer, before any data handling, the first priority is to choose the telescope that will minimize the source of noise in the determination of the ellipticity of faint galaxies. Although the *Hubble Space Telescope* (*HST*) has the best characteristics in terms of the PSF, it has a very limited field of view not really appropriate to probe the large scale distribution of a cluster (note this is of course less of a problem when looking at high redshift clusters). What is really needed is a wide field imager and excellent seeing conditions!
Then, we can use a direct approach using for example the Kaiser, Squires and Broadhurst (1995) method [KSB implemented in the *imcat* software], or any other improvement of it (Luppino & Kaiser 1998, Rhodes et al 2000, Kaiser 2000): that relates the true ellipticity to the observed ellipticity correcting it from the smearing of an elliptical PSF (using the second moments of the galaxy and the PSF).
The inverse approach use maximum likelihood method to find the source galaxy shape that when convolved by the local PSF reproduce best the observed galaxy (*e.g.* Kuijken, 2000). Again the inverse approach has the advantage to give directly an uncertainty in the parameter recovery. The weak-shear mass reconstruction techniques have been applied to wide-field camera data (UH8k, CFH12k, ESO-WFI, CTIO-MegaCam) and impressive results have started to be published on a high redshift super-cluster (Kaiser et al 1998) and on low ($z < 0.1$) redshift clusters (Joffre et al 2000). For high ($z > 0.5$) redshift clusters large aperture telescope (*e.g.* Clowe et al 2000) or *HST* (Hoekstra et al 2000) are probably more adequate.

2.3 Cluster Galaxies Halos

We know that galaxies are massive and that their stellar content does only represent a small part of their total mass. Although the existence of a dark halo has been obvious very early for disk galaxies with the study of their flat velocity curve out to large radius (*e.g.* van Albada et al 1985), the existence of a dark halo has been accepted for ellipticals relatively recently (*e.g.* Kochanek 1995, Rix et al 1997). These studies found that the stellar content dominates the central part of the galaxies, but at distance larger than the effective radius the dark halo dominates the total mass.

Galaxy lensing effect were first detected in clusters by Kassiola et al (1992) who notes that lengths of the triple arc in Cl0024+1654 can only be explained if the galaxies near the B image were massive enough. Detailed treatment of the galaxy contribution to the cluster mass became important with the refurbishment of the *HST* as first shown by Kneib et al 1996 – who concluded that galaxies (and their dark halos) in cluster cores contributes by about 10% of the total mass. The theory of what is usually called galaxy-galaxy lensing in clusters was first discussed in details by Natarajan & Kneib 1997, and application to data followed shortly (Natarajan et al 1998 and Geiger & Schneider 1998). A recent analysis of this effect in various cluster-lenses at various redshift seems to indicate an increase of the cluster ellipticals dark halo size with redshift (Natarajan et al 2000). These new developments are very interesting, as for the first time they offer a powerful tool to relate the total mass of cluster galaxies to their morphological aspects. This tool will probably help us in better understanding the strong morphological evolution seen in cluster galaxies. The standard direct *weak shear* methods generally miss the small scale fluctuations (typically the galaxy halo scales) because of the *averaging* of the galaxy ellipticities. Thus dedicated methods are necessary to probe this effect in the weak shear method. The only easy route is to use an inverse approach which will examine the galaxies **individually**.

2.4 Lensing and other Estimators

Gravitational lensing allow to measure the *total* mass distribution of clusters – and this without making any assumption on the cluster physical state. Other estimators always require some assumption when trying to relate the observables to the *total* mass. Generally these assumptions looks reasonable but may suffer strong bias due to the unknown physical state of the cluster. By providing the *total* mass, lensing does constitute a **key** tool to understand cluster physics. Probably then, the best way is to first derive the total lensing mass using lensing, and then from other observations derive physical properties of the cluster like: dynamical parameters for the galaxy velocities (Natarajan & Kneib 1996), the temperature profile of the X-ray gas (Pierre et al 1996), the baryon fraction or the equilibrium status of the cluster – however lensing mass estimates have also their limitations (in particular line of sight projection effects).

The alternative way is to compare the different estimators directly. As an example, X-ray mass estimates generally differ sensibly from the strong/weak lensing estimates - however not always. The differences can be explained for different reasons depending on the cluster studied (*e.g.* Miralda & Babul 1995): *i)* projection effects: 2 clusters can be aligned on the line of sight and boost the lensing mass; *ii)* simple X-ray modeling: for example multiphase gas distribution are necessary in cooling flow clusters (*e.g* Allen, Fabian & Kneib 1996); *iii)* non-thermal effect can modify the central mass estimates; *iv)* the cluster just suffer a major merger event and the dynamical state of the gas can not be considered as in thermal equilibrium.

The canonical lensing clusters Abell 370 and Cl0024+1654 are two examples were the X-ray mass and lensing mass do not agree. For Abell 370, the disagreement is directly visible on the ROSAT/HRI X-ray surface brightness map that only peaks on the Southern cD galaxy, despite the lensing mass model requires a bimodal structure with equivalent mass around the 2 cDs – this difference, may however disappear when better X-ray observations (with *Chandra* and *XMM-Newton*) are made of this cluster. For Cl0024+1654, the X-ray emission is weak compared to the large Einstein ring observed. A recent redshift survey of $\sim$300 cluster galaxies (Czoske et al 2000) does however unveils some of the mystery. The redshift histogramme show a complex structure with a main relaxed structure compatible with the X-ray emission and a foreground structure along the line of sight that boost the lensing strength of this cluster.

Recently, Sunyaev-Zeldovich (SZ) effect has been routinely measured on the most X-ray luminous clusters (*e.g.* Carlstrom et al 2000). As SZ is probing the intra-cluster gas in a different way than X-ray observations, it is important to use SZ as a complementary approach to the lensing, X-ray and galaxies velocities estimators as a detailed study will teach us a lot on the cluster physics. Attempts of combining these different informations were presented during this Conference.

Ideally, one wants to looks at the mass properties of clusters as a function of time to derive their evolution. But to do that we need well defined samples of clusters, studied in an homogenous way. However, precise and systematic comparison is still relatively rare in the literature, as they usually rely on published data, either on the X-ray or on the lensing part, and thus do no tackle a well defined sample, nor do they address carefully the limits and bias of the two different approaches. This is however currently changing rapidly, as a number of dedicated surveys based on well defined cluster catalogue (Ebeling et al 1996, 2000) are in progress (*e.g.* Czoske et al, this conference).

2.5 Dark lenses?

It has been known for a while that some of the multiple image quasars can only be modeled if an important external shear contribution was added to the main lens contribution (Keeton et al 1997). In other cases the image separation between the multiple quasars is so large that large M/L for the main lensing galaxy are required. Thus, the existence of so-called *dark clusters* has been discussed. Recent deep inspection of these systems, followed by optical spectroscopy seems to reveal that *dark clusters* are not so dark after all (Benitez et al 1999, Kneib et al 2000, Soucail et al 2000). A systematic deep survey of those multiple quasar systems where either a too high M/L ratio or a large external shear is required would be useful to understand whether *dark or not so dark* lump of matter are affecting the lensing of the quasars.

In this respect the detection of a dark lump of matter near the cluster Abell 1942 by Erben et al (2000) is very puzzling. Either it is an extremely rare (?) cosmic conspiracy in the distribution of the faint galaxy ellipticities or what is detected is really a massive dark concentration of mass which true nature should be understood.

3 Cluster Lenses as Nature Telescopes

The most massive clusters can be used as efficient *Natural Telescope.* The key feature of these systems is that any distant object seen through the clusters is amplified (and distorted). This amplification can easily exceed a factor of > 2–$3\times$ for the central 4 sq. arcmin of the lens and will be still higher than $> 1.4\times$ over a 20 sq. arcmin field of view for the most massive clusters. The amplification provides a magnified view of a correspondingly smaller region of the source plane – so the 4 sq. arcmin region seen through the core of a cluster lens will actually translate to a < 2 sq. arcmin patch of the background sky. Thus a lens provides a more sensitive, but also more restricted, view of the high redshift sky. These effects, the amplification and the reduction in the available area, compensate each other for a source population with a count slope, $\alpha = 1$, where $N(> S) \propto S^{-\alpha}$ (or equivalently for a count slope $\gamma = 0.4$, where $N(m) \propto 10^{\gamma m}$). However, the sources we identify in the lens field will be on average intrinsically $\sim 2\times$ fainter than those identified in an equivalent blank field.

Depending on the waveband used, we will either see, more, or less, sources than in blank field regions. As a first example, in the sub-mm waveband α is indeed very close to unity at the faintest flux (Blain et al. 1999) and so we expect to detect equivalent numbers of sources in lensed fields as in a blank field in the *same* exposure time (see also Ivison, this conference). In the optical and Near-Infra red (NIR), the slope γ is about 0.3 at the faintest flux, thus we expect less sources than in blank field. Finally, in the Mid-Infra red (MIR), the slope α is ~ 1.5 at the faintest flux (Metcalfe et al 1999) and we detect more sources than in the blank fields. A particular, the faintest MIR sources were detected in the deep ISOCAM pointing of Abell 2390 (Altieri et al 1999).

The cluster-lens technique therefore allows you to reach below the sensitivity limit of normal observations. To successfully employ this lens technique we need to be able to correct the observations for the amplification by the cluster using a detailed mass model of the lens constructed from *HST* imaging is necessary (see section 2.1).

This technique has three major advantages: *i)* the image resolution in the source plane is effectively finer leading: to a fainter confusion limit for the sub-mm maps and MIR observations, and to smaller resolution elements in optical/NIR allowing to better identify the morphological aspects of these faint sources; *ii)* cluster-lenses are some of the best studied regions of the extragalactic sky – thus deep multi-wavelength observations are generally available making the identification of distant galaxy much easier; *iii)* in the case of rare events where the amplification is larger than 10, detailed physical observation of the distant lensed galaxy can be made on morphological aspects (Pelló et al 1999, Soucail et al 1999) or on spectroscopical aspects (Pettini et al 2000).

Similar lensing techniques are starting to be used to search for high-redshift supernovae [SN] (*e.g.* Sullivan et al 2000) or to detect Lyman-α emitters (Ellis et al 2000, in prep). In the case of a detection of a SN in a multiple image, if we are able to measure a time delay, it will give a unique way to precisely constrain the *Hubble* parameter H_0.

4 Future and Prospects

Since the discovery of giant arcs and arclets in the end of the 80's gravitational lensing applications in cluster of galaxies have grown considerably.

• We are now able to reconstruct the mass distribution in clusters in great details from the galaxy scale to the virial radius. The lensing mass estimate will be usefully compared to other mass estimators to provide critical information on the cluster physics (from the largest cluster scale to the galaxy scale) on well defined cluster samples.

• Wide field survey of *mass selected* cluster using lensing techniques will allow to make direct comparison to analytic/numerical models of the Universe and thus better understand the growth of structure and the large scale distribution of mass. It will also confirm or otherwise the existence of dark lump of mass.

• Multiple images in cluster cores are about to measure directly the cosmological parameters through an optical geometrical test of the curvature of the Universe, although more spectroscopic and mass modeling are needed, it is a very clean way to tackle this problem.

• Likewise, time dependant phenomenom like Supernovae or AGN fluctuations if observed behind well-known lensing clusters, may prove to be a very accurate way to probe the H_0, as it has been initiated using multiple quasars.

• Finally, massive clusters will always be the *unique place* to look at to boost telescope and instrument sensitivities to push ahead the discoveries to the faintest detection level.

Acknowledgments

I acknowledge support from the LENSNET network as well as from INSU/CNRS. I thanks all my collaborators for the fruitful work we are conducting to better understand our Universe using lensing as a powerful tool. I specially thanks Yannick Mellier who chaired the organization of this wonderful meeting and who first with Bernard Fort taught me about lensing in clusters.

References

1. Allen, S., et al, 1996, *Mon. Not. Roy. Astr. Soc.* , 279, 615
2. Altieri, B., et al 1999, *Astron. Astroph.* , 343, L65
3. Bartelman, M., et al., 1996, *Astroph. Journ.* , 446, L115
4. Bezecourt, J., et al., 1999, *Astron. Astroph.* , 347, 21
5. Blain, A., et al 1999, *Astroph. Journ.* , 512, L87
6. Bridle, S., et al 1998, *Mon. Not. Roy. Astr. Soc.* 299, 895
7. Benitez, N., et al 1999, *Astroph. Journ.* , 527, 31
8. Carlstrom, J., et al 2000, *Physica Scripta*, volume T, 85, 148-155
9. Clowe, D., et al 2000, *Astroph. Journ.* , 539, 540

10. Czoske, O., et al 2000, *Astron. Astroph.* in prep
11. Ebeling, H., et al 1996, *Mon. Not. Roy. Astr. Soc.* 281, 799
12. Ebeling, H., et al 2000, *Astroph. Journ.* submitted (astro-ph/0009101)
13. Ebbels, T., et al 1998, *Mon. Not. Roy. Astr. Soc.* , 295, 75
14. Erben, T., et al 2000, *Astron. Astroph.* , 355, 23
15. Fort, B., et al 1992, *Astroph. Journ.* , 399, L125
16. Hoekstra, H., et al 2000, *Astroph. Journ.* , 532, 88
17. Geiger, B., Schneider, P., 1998, *Mon. Not. Roy. Astr. Soc.* , 295, 497
18. Geiger, B., Schneider, P., 1999, *Mon. Not. Roy. Astr. Soc.* , 302, 118
19. Joffre, M., et al 2000 *Astroph. Journ.* , 534, L131
20. Kaiser, N., & Squires, G., 1993 *Astroph. Journ.* , 404, 441
21. Kaiser, N., 1995 *Astroph. Journ.* , 439, L1
22. Kaiser, N., et al 1995 *Astroph. Journ.* , 449, 460
23. Kaiser, N., et al 2000 *Astroph. Journ.* , submitted (astro-ph/9809268)
24. Kaiser, N., 2000 *Astroph. Journ.* , 537, 555
25. Keeton, C. et al, 1997 *Astroph. Journ.* , 482, 604
26. Kneib, J.-P. et al, 1993, *Astron. Astroph.* , 273, 367
27. Kneib, J.-P. et al, 1994a, *Astron. Astroph.* , 290, L25
28. Kneib, J.-P. et al, 1994b, *Astron. Astroph.* , 286, 701
29. Kneib, J.-P. et al, 1996, *Astroph. Journ.* , 471, 643
30. Kneib, J.-P. et al, 2000 *Astroph. Journ.* in press (astro-ph/0006106)
31. Kochanek, C. et al, 1995 *Astroph. Journ.* , 445, 549
32. Kassiola, A. et al, 1992 *Astroph. Journ.* , 400, 41
33. Kuijken, K., 1999 *Astron. Astroph.* , 352, 355
34. Lombardi, M. & Bertin, G., 1998, *Astron. Astroph.* 348, L38
35. Mellier, Y., et al, 1993, *Astroph. Journ.* , 407, 33
36. Metcalfe, L. et al, 1999 In "The Universe as seen by ISO", 1999, eds.: P.Cox, M.F.Kessler, ESA Publication Division, ESTEC, Noordwijk, NL
37. Miralda-Escudé, J., & Babul, A., 1995, *Astroph. Journ.* , 449, 18
38. Natarajan, P., Kneib, J.-P. 1996, *Mon. Not. Roy. Astr. Soc.* , 283, 1021
39. Natarajan, P., Kneib, J.-P. 1997, *Mon. Not. Roy. Astr. Soc.* 287, 833
40. Natarajan, P., et al, 1998, *Astroph. Journ.* , 499, 600
41. Natarajan, P., et al, 2000, *Astroph. Journ.* , in preparation
42. Pelló, R., et al, 1999, *Astron. Astroph.* , 346, 359
43. Pettini, M., et al, 2000, *Astroph. Journ.* , 528, 96
44. Rix, H.W., et al 1997, *Astroph. Journ.* , 448, 702
45. Rhodes, J., et al 2000, *Astroph. Journ.* , 536, 79
46. Schneider, P., et al, 1992, "Gravitational Lensing' A&A library series.
47. Schneider, P., 1995, *Mon. Not. Roy. Astr. Soc.* , 302, 639
48. Seitz, C., & Schneider, P., 1995, *Astron. Astroph.* , 297, 287
49. Seitz, S., & Schneider, P., 1996, *Astron. Astroph.* , 305, 383
50. Smail, I., et al 1998, *Astroph. Journ.* , 507, L21
51. Smith, G., et al 2000, *Astroph. Journ.* , submitted, (astro-ph/0008315)
52. Sullivan, M., et al 2000, *Mon. Not. Roy. Astr. Soc.* , accepted, (astro-ph/0007228)
53. Soucail, G., et al 2000, *Astron. Astroph.* , submitted, (astro-ph/0006382)
54. van Albada, T.S., et al, 1985, *Astroph. Journ.* , 295, 305

MAXIMUM ENTROPY WEAK LENSING MASS RECONSTRUCTION

S. BRIDLE
Cavendish Astrophysics, Cavendish Laboratory, Madingley Road, Cambridge, England

We demonstrate that the maximum-entropy method for gravitational lens reconstruction presented in Bridle et al. (1998) may be applied even when only shear (and no magnification) information is present. We contrast these results with those from reconstruction using magnification information alone. We also demonstrate that the method can easily handle irregularly shaped observing fields.

In an earlier paper (Bridle et al. 1998, hereafter BHLS) we presented a maximum-entropy method for reconstructing the projected mass distribution from both shear and magnification data. We find the most probable mass density distribution given the data and the entropic prior. The probability of a given mass distribution is $\propto \exp\left(-\chi^2 + \alpha S\right)$ where χ^2 is from the difference between the observations and the predictions and αS is the maximum entropy prior. In contrast to comparable methods, we optimise the projected mass density distribution itself, rather than reconstructing the two-dimensional Newtonian potential and then converting this into the mass distribution. This seems to us to be a more elegant and only slightly more computationally expensive method. As a result, we are then able to use the shape of the probability function in order to estimate the errors on our reconstruction. In addition, the method allows reconstruction outside the observed field, which makes fuller use of the shear information. In this paper we demonstrate the way in which this method may be extended to the cases where no shear information is available, or where no magnification data are available, and illustrate the effect on the resulting reconstructions. We also highlight the flexibility of the method in analysing observations of irregularly-shaped patches of sky. More details about this work and further investigations may be found in Bridle et al. 2000 (hereafter BHSL).

The lensing mass distribution we use for the simulations is plotted in Fig. 1 and and consists of two clusters each with a truncated King profile. The ellipticities and magnifications expected from this mass distribution are calculated at each point on the same grid of pixels used for the mass distribution. For convenience we consider as input data the inverse magnification rather

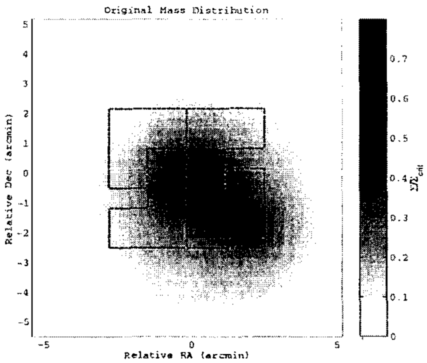

Figure 1: Original mass distribution used for the simulations. The dashed lines contain the regions of sky for which simulated observations are made.

than the magnification. We then add random noise to each shear and magnification data point. We then only use observations from a finite patch of sky which is made up of the two regions enclosed by the dotted lines in Fig. 1: four HST WFPC2 pointings which do not fit together perfectly. For comparison with the equivalent values found in the reconstructions, the total mass inside the observing boxes would be $5.41 \times 10^{14} M_{\odot}$ if the cluster were at $z = 0.4$ and the background galaxies at $z = \infty$.

The result of reconstructing from both shear and magnification data is shown in Fig. 2 (a). As detailed in BHLS, we estimate the marginalised errors on each pixel using the curvature matrix of the logarithm of the probability function evaluated at the best-fit mass distribution. The errors on the reconstruction calculated from the curvature matrix (see details in BHLS) are plotted in Fig. 2 (b). This reconstruction demonstrates clearly the ability of the method to cope with irregularly-shaped data fields. Assuming the lens geometry described in BHSL, the total mass in the observing area in the reconstruction is $5.15 \times 10^{14} M_{\odot}$, and the rms mass within the observing area on the error estimates map is $0.16 \times 10^{14} M_{\odot}$. Thus not only has the shape of the mass distribution been well reproduced, but also the total mass in the observed field is well reproduced and the error estimate gives a good indication of the uncertainty in this quantity. Two cross sections through the reconstruction are shown in the left hand column of Fig. 3. The original mass distribution is shown by the solid line and the reconstructed values by the crosses. The error bars are those found from the curvature matrix. The edges of the observation field are the dotted lines. The errors can be seen to be a reasonable indication of the differences between the original and reconstructed mass distributions within the observed area and a short distance beyond.

The result of reconstructing from magnification data alone is shown in Fig. 2 (c), with errors as shown in Fig. 2 (d). This clearly illustrates the fact that the magnification data gives very little information about the mass outside the observed field. The cross sections plotted in the middle panel of Fig. 3 show that the reconstruction inside the observed field is reasonable. In addition, the total mass in the observing box, $5.15 \pm 0.25 \times 10^{14} M_{\odot}$ may be compared with that of the true mass distribution, and seen to be in agreement.

The result of reconstructing from shear data alone is shown in Fig. 2 (e), with errors shown in Fig. 2 (f). The most striking point to note is that this reconstruction is not very much worse than that using both shear *and* magnification data (Fig. 2 (a)). Although on closer inspection it is clear that this reconstruction is a little more noisy. The total mass inside the observed field in this reconstruction is $3.22 \times 10^{14} M_{\odot}$ and the sum of the rms errors in this field $0.28 \times 10^{14} M_{\odot}$. This compares with $5.41 \times 10^{14} M_{\odot}$ for the original mass distribution. So despite the mass sheet

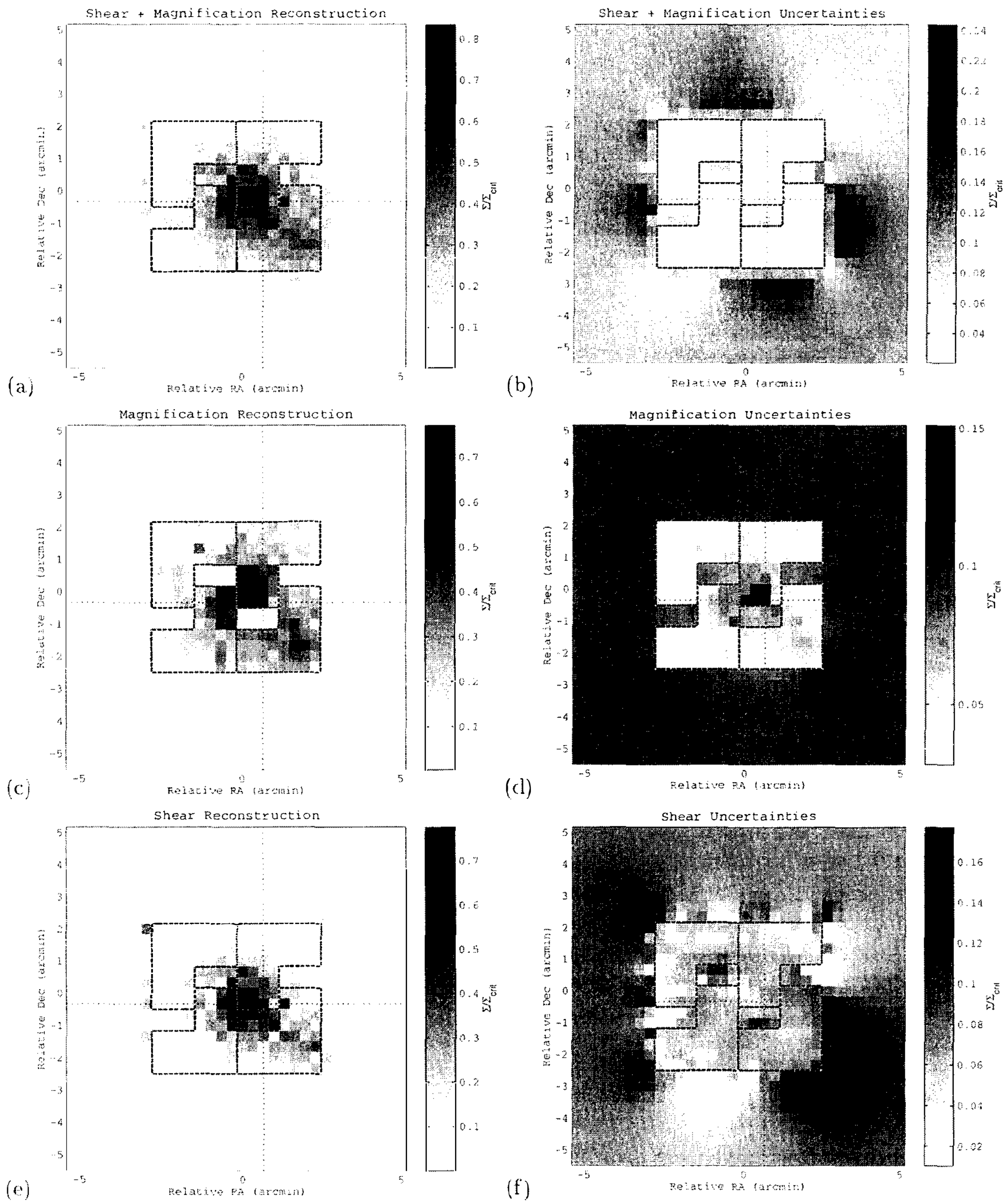

Figure 2: (a) Mass distribution reconstructed using shear and magnification information. (b) Errors on the mass distribution reconstructed using shear and magnification information. The dotted lines show the lines along which the cross sections are taken. (c) Mass distribution reconstructed using only magnification information. (d) Errors on the mass distribution reconstructed using only magnification information. The dotted lines show the lines along which the cross sections are taken. (e) Mass distribution reconstructed using only shear information. (f) Errors on the mass distribution reconstructed using only shear information. The dotted lines show the lines along which the cross sections are taken.

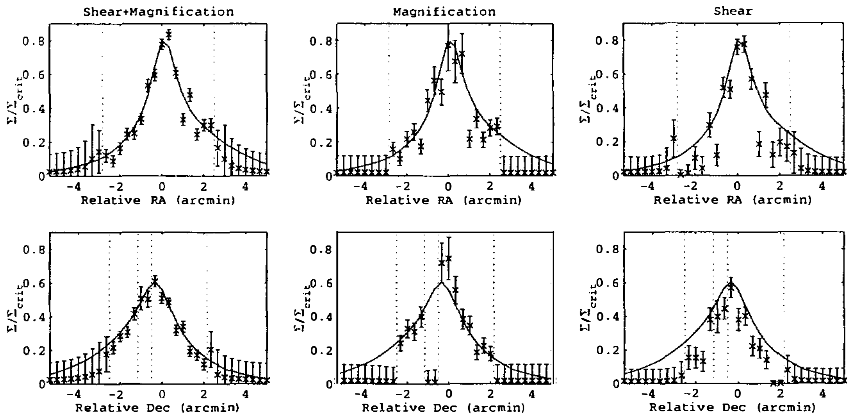

Figure 3: Cross sections through the mass reconstructions shown in Fig. 2.

degeneracy, 60 ± 5 per cent of the mass has been detected. Qualitatively this is because the shears provide information about the spatial variations in the mass, and the prior constrains the mass to be positive. It is also significant that because we take into account the errors on the shears, and regularize with a prior, we do not over fit to the noise, and only find mass where there is sufficient evidence in the data.

Conclusions

In investigating how well the BHLS maximum entropy method is capable of deducing the matter distribution of typical massive galaxy clusters at $z \approx 0.4$ from typical shear data, from magnification data and from both, we have demonstrated the following:

- Shear data alone provide a useful estimate of the mass of clusters: in simulations with realistic signal to noise and field of view, the algorithm detects 60 per cent of the mass of the cluster despite the mass degeneracy.
- Our reconstruction method can easily handle irregularly shaped and disjoint observing regions.
- Because shear information is a non-local function of the mass, small gaps in observations can be bridged successfully when shear information is used in the reconstruction.
- We are also successful at reconstructing mass distributions from simulated magnification data alone.

Acknowledgements

This work was done in collaboration with Mike Hobson, Richard Saunders and Anthony Lasenby. I acknowledge the receipt of a PPARC studentship.

References

1. Bridle, S. L., Hobson, M. P., Lasenby, A. N., Saunders, R., 1998, MNRAS, 299, 895
2. Bridle, S. L., Hobson, M. P., Saunders, R., Lasenby, A. N., 2000 in preparation

INFRARED OBSERVATIONS OF A DEPLETION OF DISTANT GALAXIES BEHIND ABELL 2219 WITH CIRSI

Meghan E. Gray[1], Richard S. Ellis[1], Alexandre Refregier[1], Jocelyn Bézecourt[2], Richard G. McMahon[1]
Martin G. Beckett[(1,3)], Craig D. Mackay[1], and Michael D. Hoenig[1]
1. Institute of Astronomy, Madingley Road, Cambridge, CB3 0HA, UK
2. Kapteyn Institute, Postbus 800, 9700 AV Groningen, The Netherlands
3. Observatories of the Carnegie Institution of Washington, 813 Santa Barbara Street, Pasadena, CA 91101, USA

We present the first detection of a gravitational depletion signal at near-infrared wavelengths, based on deep panoramic images of the cluster Abell 2219 (z=0.22) taken with the Cambridge Infrared Survey Instrument (CIRSI) at the prime focus of the 4.2m William Herschel Telescope. Infrared studies of gravitational depletion offer a number of advantages over similar techniques applied at optical wavelengths, and can provide reliable total masses for intermediate redshift clusters. Using the maximum likelihood technique developed by Schneider, King & Erben (2000), we detect the gravitational depletion at the 3σ confidence level. By modeling the mass distribution as a singular isothermal sphere and ignoring the uncertainty in the unlensed number counts, we find an Einstein radius of $\theta_{\rm E} \simeq 13.7^{+3.9}_{-4.2}$ arcsec (66% confidence limit). This corresponds to a projected velocity dispersion of $\sigma_v \sim 800$ km s^{-1}, in agreement with constraints from strongly-lensed features. We investigate the uncertainties arising from the observed fluctuations in the unlensed number counts, and show that clustering is the dominant source of error. We extend the maximum likelihood method to include the effect of incompleteness, and discuss the prospects of further systematic studies of lensing in the near-infrared band.

1 Depletion in the Infrared

A gravitational lens will change the observed surface number density of background galaxies according to $n(<m) = n_0(<m)\mu^{2.5\alpha-1}$, where μ is the magnification of the lens, n_0 and n are the unlensed and observed surface number densities, and $\alpha = d\log n/dm$ is the logarithmic slope of the number counts. The net effect depends on the value of α: for $\alpha > 0.4$ the observed surface number density will increase, while for $\alpha < 0.4$ a depletion is measured.[1] Such methods have previously been applied at optical wavelengths to the massive cluster Abell 1689.[2]

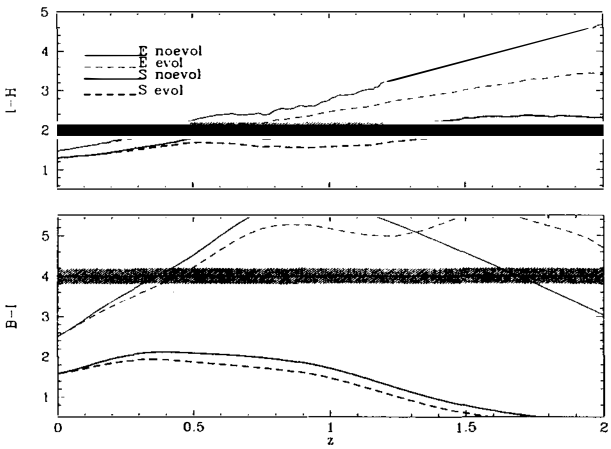

Figure 1: Dependence of optical-infrared and optical-optical colour on redshift for early- and late-type galaxies derived from the GISSEL96 spectrophotometric codes (Bruzual & Charlot, in prep) with and without evolution. The shaded area shows a range of colour when taking into account typical photometric errors of ±0.2 for the measurement of a typical early-type cluster sequence at intermediate redshift. Clearly the addition of the infrared magnitude reduces the dependence of colour on spectral type and allows for a more efficient selection of a background population.

Here we are concerned with extending the depletion method to near-infrared wavelengths, and we illustrate the possible advantages via an initial application to the rich cluster Abell 2219. A number of factors enter when considering the merits of undertaking depletion studies at near-infrared wavelengths. Foremost, we can expect the counts to flatten considerably at cosmologically-significant depths for any passband longward of 1μm. Our lensing study will be undertaken using the H-band filter, where recent counts at H show a sub-critical slope [3] with $\alpha = 0.31 \pm 0.02$ for $20 < H < 24.5$.

Secondly, in terms of colour-selection, the degeneracy between redshift and spectral class likewise improves dramatically when infrared magnitudes are added. Fig. 1 illustrates a typical measurement of the $I-H$ and $B-I$ colour of a cluster early-type sequence at intermediate redshift. For the optical-optical colour we see that the single measurement is not enough to break the degeneracy between colour and redshift: an object bluer than the cluster sequence may be a low redshift elliptical or a late-type galaxy at any redshift. But when the optical-infrared colour is considered, the sensitivity to spectral type is greatly reduced, and we see that the bluer and redder galaxies map more clearly onto foreground and background populations. This leads to a much cleaner and efficient method of eliminating likely cluster members than relying on optical colours alone: we retain both the flat slope and sufficient numbers required for measurement of the depletion effect.

2 Observations

The Cambridge Infrared Survey Instrument (CIRSI [4]) is a wide-field infrared imager consisting of a mosaic of four 1K × 1K Rockwell Hawaii HgCdTe detectors. The H-band CIRSI observations of the rich cluster Abell 2219 were made at the prime focus of the 4.2-m William Herschel Telescope (WHT). Each CIRSI detector has a field of view of 5.5 × 5.5 arcmin separated by a gap of approximately one chip width. The field configuration was chosen to optimally overlap with existing B- and I-band EEV CCD data. Two adjacent CIRSI pointings were arranged to provide two contiguous strips of approximately 5 × 20 arcmin each, one of which overlaps the two-pointing 16 × 16 arcmin EEV field. Thus multicolour data was available in the central cluster region and in two adjacent offset fields, and a catalogue of object positions and colours was created using SExtractor 2.0.

We remove likely cluster members according to the tight early-type locus $I-H$ vs H colour-magnitude diagram. We can divide the remaining population of field galaxies into 'red' (background) and 'blue' (foreground) field populations. We show elsewhere [5] that for the purposes of our depletion measurements it is not necessary to have a complete catalogue, so long as the incompleteness function responsible for the observed fall-off from the intrinsic power-law distribution is the same for the offset fields as for the lensed fields, and so we adopt a magnitude limit of $H < 24$. When the area obscured by the cluster galaxies is considered, a clear radial depletion of background galaxies is seen.

3 Maximum Likelihood Techniques

To investigate the magnitude and significance of this possible depletion, we adopted a maximum likelihood approach based on that developed by Schneider, King & Erben.[6] In this formulation, which avoids the loss of information induced by the radial binning, the log-likelihood equation takes the form:

$$l = -n_0 \int d^2\theta [\mu(\theta)]^{2.5\alpha-1} + (2.5\alpha - 1) \sum_{i=1}^{N} \ln \mu(\theta_i), \tag{1}$$

where n_0 is the unlensed number density of background galaxies (arcmin^{-2}), μ is the magnification, θ_i is the position vector of the ith galaxy in the field with respect to the cluster centre, N is the total number of galaxies observed, and α is the intrinsic logarithmic slope of the number counts. The first term in the log-likelihood function addresses the probability of finding N galaxies in the field of view given the lens model $\mu(\theta)$ and the population parameters α and n_0, while the second term concerns the probability of finding each galaxy i at position θ_i. By maximizing l we find the most likely parameter(s) for a given lens model.

We model the cluster according to a singular isothermal sphere (SIS) parametrized with the Einstein radius, $\theta_{\rm E}$: $\mu_{\rm SIS}(\theta) = |1 - \theta_{\rm E}/\theta|^{-1}$. The filled circles in Fig. 2 show the resulting log-likelihood curve. The peak of the likelihood function is reached at $\hat{\theta}_{\rm E} = 13.7$ arcsec, which is consistent with the location of the red giant arc located 13 arcsec from the cluster centre. Simulations to recover an input Einstein radius reveal the 95% confidence limit spans the range $6.8 < \hat{\theta}_E < 26.5$ arcsec. Assuming a median redshift of $z = 1.3$ we translate this result for a SIS into a velocity dispersion of $\sigma_v = 814^{+112}_{-139}$ km s^{-1} (66% confidence level). Our SIS model is in good agreement with previous strong lensing results which show $\sigma_v \sim 930$ km s^{-1} using strong lensing constraints.[7]

We perform a test of the depletion by applying the same maximum-likelihood test on one of the offset fields. Using the same colour selection criteria to define a population of red objects we find no evidence for any depletion effect. Furthermore, we also test the population of 'foreground' galaxies (those with colours bluer than the cluster sequence) in the cluster field, and again find as expected no evidence for depletion. The log-likelihood functions for these two samples, both peaking at $\theta_E = 0$ arcsec, are also shown as open symbols in Fig. 2.

4 Effect of uncertainty in number counts and future prospects

Schneider, King & Erben[6] demonstrate that, to first order, most of the magnification information is provided by the unlensed number density n_0. Without adequate knowledge of this normal-

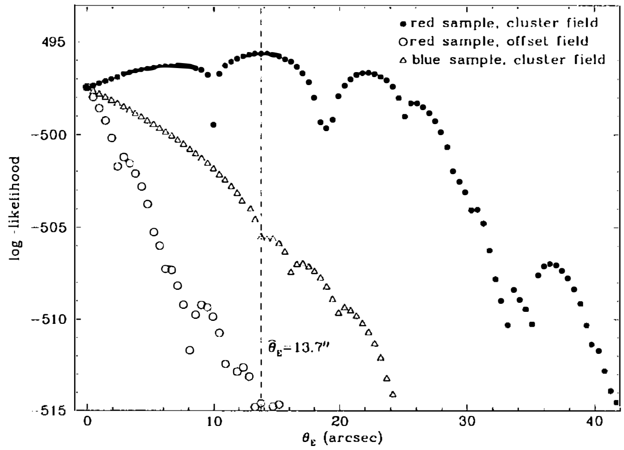

Figure 2: Maximum likelihood analysis for depletion of the red background galaxy sample (solid circles). The model corresponding to the peak is a SIS parametrized by the Einstein radius $\hat{\theta}_E = 13.7$ arcsec. By contrast, the same analysis for the red galaxy sample in one of the offset fields (open circles) peaks at $\hat{\theta}_E = 0$ arcsec and shows no evidence of depletion, as does the sample of blue (foreground) galaxies in the cluster field (open triangles). The curves have been vertically shifted to the same zeropoint for clarity.

ization, the mass-sheet degeneracy cannot be broken. Prior knowledge of the uncertainty in n_0 can be included in the maximum-likelihood analysis. Using the full H-band dataset, we derive a fractional error of 8.6% on the normalisation of the background number density (consistent with clustering on these scales). When this error is incorporated into the maximum-likelihood analysis the error bars become too large to make a precise statement about the magnitude of the lensing (although our previous measurement is not ruled out). This demonstrates the crucial importance of the background density n_0 for an accurate depletion analysis.

The depletion method is an elegant and relatively simple way to derive mass estimates of clusters of galaxies. Deeper IR surveys will provide more accurate knowledge of clustering on arcmin scales, allowing us to better understand the degree to which the method is affected. Future studies with wide-field optical-IR data (e.g. with the VISTA telescope) covering a wide wavelength range could provide more accurately selected background populations via photometric redshifts and allow us to add another sample of independent mass profiles to be compared with those derived from velocity dispersions, X-ray measurements, and strong and weak lensing. The problem posed by the uncertainty in the background number counts can be overcome by selecting similar clusters (e.g. by their X-ray temperatures) and stacking the depletion signal to obtain an average cluster mass profile: a feasible project for future IR survey telescopes.

References

1. Broadhurst T., Taylor A., Peacock J., 1995, ApJ, 438, 49
2. Taylor, A., et al., 1998, ApJ, 501, 539
3. Yan L., et al., 1998, ApJ, 503, L19
4. Beckett M., et al., 1998, Proc. SPIE, 3354, 431
5. Gray M.E., et al., 2000, MNRAS (in press); astro-ph/0004161
6. Schneider P., King L., Erben T., 2000, A&A, 353, 41
7. Smail I., et al., 1995, MNRAS, 277,1

A COMBINED HST/CFH12k/XMM SURVEY OF X-RAY LUMINOUS CLUSTERS OF GALAXIES AT $z \sim 0.2$

OLIVER CZOSKE[1], JEAN-PAUL KNEIB[1], IAN SMAIL[2], GRAHAM P. SMITH[2], HARALD EBELING[3]

[1]*Laboratoire d'Astrophysique, Observatoire Midi-Pyrénées, 14 av. Ed. Belin, 31400 Toulouse, France*

[2]*Department of Physics, University of Durham, South Road, Durham DH1 3LE, UK*

[3]*Institute for Astronomy, University of Hawai'i, 2680 Woodlawn Drive, Honolulu, HI96822, USA*

We describe a project to study a sample of X-ray luminous clusters of galaxies at redshift $z \sim 0.2$ at several scales (with HST/WFPC2 and CFHT/CFH12k) and wavebands (optical and X-ray). The main aims of the project are (i) to determine the mass profiles of the clusters on scales ranging from $\sim 10\,h^{-1}$ kpc to $\gtrsim 1.5\,h^{-1}$ Mpc using weak and strong lensing, thereby testing theoretical predictions of a "universal mass profile", and (ii) to calibrate the $M_{\rm total}$—$T_{\rm X}$ relation in view of future application in the study of the evolution of the cluster mass function at higher redshift.

1 Introduction

Current models describe the formation and evolution of large-scale structure in the Universe in a hierarchical, "bottom-up", way. Since clusters of galaxies are the most massive gravitationally bound objects found in the Universe at the present time, their evolution is observable at low redshift, $z \lesssim 1$. Clusters of galaxies are therefore powerful probes for testing cosmological scenarios and determining cosmological parameters.

Two theoretical predictions are of particular interest. The first one concerns the evolution of the cluster mass function with redshift, which can be described using linear theory. As shown by Eke et al. [1], in a low matter density universe ($\Omega_{\rm M} \sim 0.3$) we expect to see about 30 times as many clusters out to $z = 1$ as in a high matter density universe ($\Omega_{\rm M} = 1$), using the current cluster abundance to normalize the density fluctuation power spectrum.

A second theoretical prediction concerns the internal structure of clusters. Numerical simulations suggest that dark matter haloes over a wide range of masses can be accurately described by a universal mass profile [2]. In the context of numerical simulations this is a very robust prediction, as the profile works over a wide range of masses, radii and cosmological parameters.

Other groups, however, find different behaviour of the mass distribution in their simulations, notably in the centres of haloes[3].

The obserational tool of choice for investigating cluster mass profiles is gravitational lensing, which in principle permits to access the mass distribution directly (albeit a weighted sum of all the mass between the observer and the source plane).

Even given the large upcoming CCD mosaic cameras (such as MEGACAM), large-area cluster searches (necessary for testing predictions concerning the evolution of the cluster mass functio) using their weak lensing signature will be difficult at best. More practical will be cluster searches from X-ray all-sky surveys. The temperature T_X of the hot intracluster gas is directly related to the depth of the gravitational potential of the cluster if the gas is in hydrostatic equilibrium. In that case the cluster mass function can be transformed into a temperature function which retains the large separation between high- and low-Ω_M universes [1]. However, current observations indicate that the M_{total}—T_X relation differs from simple theoretical predictions, possibly related to pre-heating of the gas[4]. Also the impact of substructure in the mass and gas distribution within clusters on the scatter around the M_{total}—T_X relation has yet to be studied in a systematic way. It is therefore imperative to calibrate the shape of and the scatter around the M_{total}—T_X relation observationally on a well-defined sample of clusters of galaxies before using it to test cosmological predictions.

Our project aims at studying a sample of massive galaxies at redshift $z \sim 0.2$ using HST and CFH12k observations in order to constrain mass profiles on length scales between $\sim 10h^{-1}$ kpc out to $\gtrsim 1.5h^{-1}$ Mpc and to relate the lensing masses to X-ray observables (notably T_X) from observations with XMM-Newton.

2 Sample selection

Our sample is drawn from the XBACs catalogue [6], a flux-limited catalogue of Abell clusters detected in the ROSAT All-Sky Survey. We apply limits in redshift space of $0.18 < z < 0.26$ in order to have an approxiomately luminosity-limited sample. It has been shown that X-ray luminosity is correlated with cluster mass and therefore, given the difficulty of measuring X-ray temperatures with current instruments, a luminosity-limited sample is the best approximation to a mass-limited sample. The redshift range has been chosen to maximize the lensing efficiency for a background galaxy population at $\langle z \rangle = 0.8$ [5]. Applying further limits in declination (for accessibility from CFHT), galactic latitude (to minimize contamination by stars) and hydrogen column density N_H leads to a sample of 14 clusters (listed in table 1), 8 of which will be observed by HST under PI Kneib and 6 of which are available in the HST archive. Figure 1 shows that our sample covers the corresponding region in the XBACs catalogue well.

3 Observations

To date (June 2000) five clusters have been observed with HST, three more are scheduled for observation before the end of 2000; six cluster observations are available in the HST archive. The observations are done with the WFPC2 through the F702W filter, three orbits are allocated for each cluster. The excellent spatial resolution of these images allows precise modelling of the mass distribution in the cluster centres ($\lesssim 100\,h^{-1}$ kpc) due to their strong lensing effects. For most of the clusters in our sample no giant arcs were known previous to these observations. Therefore, they will constitute a valuable sample for investigating the probablity of formation of giant arcs which depends strongly on the cosmological parameters, in particular Ω_Λ [7].

On larger scales, observations with the CFH12k camera on CFHT will be used to determine mass profiles out to $1.5\ldots2h^{-1}$ Mpc using the systematic distortion of the background galaxies due to weak lensing by the cluster potential. CFH12k observations were finished in June 2000.

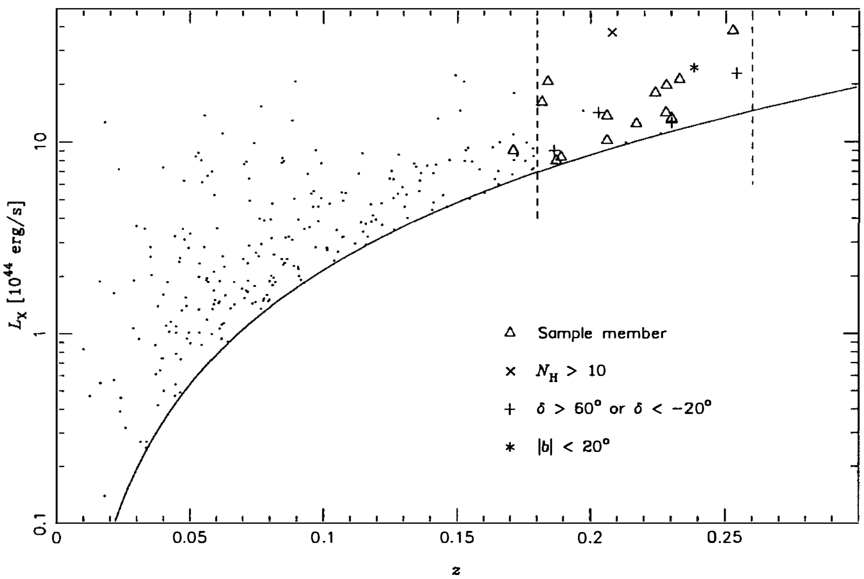

Figure 1: Location of our sample within the XBACs catalogue. Cosmological parameters used are $h = 0.5$, $\Omega_M = 1$ and $\Omega_\Lambda = 0$. A 2218 falls outside the specified redshift range but will be observed in the same manner as the other clusters.

During three observing runs (7 nights) 11 clusters were observed in three bands (B, R, I), typically reaching a limiting magnitude of 25 in R. Photometry in three filters allows robust discrimination between cluster members and background galaxies.

Seven of our eight core sample clusters have been allocated XMM time in category B under PI Kneib, with integration times between 20 and 30 ksec. All the other clusters will be observed by XMM under different PIs. The observations will be done with the EPIC camera with a field of view of 3.8 Mpc at $z = 0.2$; images will allow study of the morphology of the X–ray surface brightness and detection of significant substructure, spectra will permit precise measurement of X–ray temperatures and temperature profiles.

These core observations will be supplemented by spectroscopy of giant arcs and cluster galaxies, as well as miscellaneous observations in different wave bands, notably in the near infrared in order to permit determination of photometric redshifts in the central cluster regions.

4 Conclusions

At the time of writing (June 2000), most of the optical observations have been finished and are currently being reduced. A first paper describing and modelling several arcs and multiple image systems in Abell 383 is in preparation. Previously unknown arcs have already been found in Abell 68, 383, 773, 963 and 1835. X–ray observations will begin after the end of the XMM calibration phase and should be finished by mid– to end–2001. Further projects studying similar cluster samples at redshifts ~ 0.1 and ~ 0.4 are in preparation.

Table 1: Physical data for our sample. Note that the temperatures given are *estimated*[6]. The first eight clusters are observed with HST under PI Kneib, observations of the remaining six clusters are available in the HST archive.

	z	$L_X[10^{44}\,\mathrm{erg/s}]$	T_X [keV]
Abell 68	0.1889	8.36	7.7
Abell 209	0.2060	13.75	9.6
Abell 267	0.2300	13.32	9.4
Abell 383	0.1871	8.03	7.5
Abell 773	0.2170	12.52	9.2
Abell 963	0.2060	10.23	8.4
Abell 1763	0.2279	14.23	9.7
Abell 1835	0.2528	38.34	15.1
Abell 1689	0.1840	20.74	10.8
Abell 2218	0.1710	8.99	6.7
Abell 2219	0.2281	19.80	11.2
Abell 2261	0.2240	18.06	10.8
Abell 2390	0.2329	21.25	11.6
Abell 665	0.1818	16.22	8.3

Acknowledgements

This work has been supported by the French-UK programme "Alliance" under contract No. 00161XM.
OC acknowledges financial support by the European Commission under contract No. ER-BFM-BI-CT97-2471.

References

1. Eke, V. R., Cole, S., Frenk, C. S. 1996, *Mon. Not. Roy. Astr. Soc.* **282**, 263
2. Navarro, J. F., Frenk, C. S., White, S. D. M. 1997, *Astroph. Journ.* **490**, 493
3. Moore, B., Governato, F., Quinn, T., Stadel, J., Lake, G. 1998, *Astroph. Journ.* **499**, L5
4. Bower, R. G. 1998, *Mon. Not. Roy. Astr. Soc.* **288**, 355
5. Natarajan, P., Kneib, J.-P. 1997, *Mon. Not. Roy. Astr. Soc.* **287**, 833
6. Ebeling, H., Voges, W., Böhringer, H., Edge, A. C., Huchra, J. P., Briel, U. G. 1996, *Mon. Not. Roy. Astr. Soc.* **281**, 799
7. Bartelmann, M., Huss, A., Colberg, J. M., Jenkins, A., Pearce, F. R. 1998, *Astron. Astroph.* **330**, 1

CLUSTER MASS PROFILES FROM WEAK LENSING: CONSTRAINTS FROM SHEAR AND MAGNIFICATION INFORMATION

L.J. King
Max Planck Institut für Astrophysik, Karl Schwarzschild Str 1, Garching bei München, Germany. [a]

In the weak lensing regime, a cluster acting as a gravitational lens changes the shapes (shear effect) and number density (magnification effect) of the faint background galaxy population. In Schneider, King & Erben (2000) maximum likelihood techniques were developed, to compare how the shear, magnification and combined information constrain a cluster's mass profile. Before, single slope power-law models were considered. This work has been extended and here these techniques are applied to the NFW profile. In general, the shear information provides a better means to constrain this profile. Using ensemble-averaged log-likelihood functions is a very powerful way to assess and predict the uncertainties of cluster model parameters obtained from weak lensing data.

1 Introduction & Motivation

In Schneider, King & Erben (2000) [hereafter SKE] we compared how parameterised lens models can be constrained by their weak gravitational lensing signatures.

The basis of the magnification method is that magnification bias causes a depletion in the number counts of faint background galaxies near the centre of a cluster (Broadhurst et al 1995). The local cumulative number counts above a flux limit S, $n(\theta;S)$, are related to the unlensed number counts through

$$n(\theta;S) = \frac{1}{\mu} n_0 \left(\frac{S}{\mu}\right), \tag{1}$$

where μ is the magnification. If the number counts of the background sources locally follow a power law of the form $n_0 \propto S^{-\beta}$ then

$$n(\theta) = n_0 \mu^{\beta-1}. \tag{2}$$

If the intrinsic number counts are flatter than 1, then the lensed counts are reduced with respect to the unlensed counts.

The basis of the shear method is as follows: The tidal gravitational field of a lens causes a distortion of the ellipticities of background galaxies (note that we define $|\epsilon| = (1-r)/(1+r)$

[a] current address: IAEF Universität Bonn, Auf dem Hugel 71, Bonn, Germany.

where r is the axis ratio of elliptical isophotes). The image (ϵ_l) and source (ϵ_s) ellipticity of a background galaxy is related through

$$\epsilon_l = \frac{\epsilon_s + g}{1 + g^* \epsilon_s}, \tag{3}$$

where g is the complex reduced shear, and is given by

$$g = \frac{\gamma}{1 - \kappa}, \tag{4}$$

γ being the complex shear and κ the dimensionless surface mass density. The ellipticity probability distribution after lensing can be obtained for the unlensed distribution through

$$p_{\epsilon_l}(\epsilon_l|g) = p_{\epsilon_s}(\epsilon_s(\epsilon_l|g)) \frac{(|g|^2 - 1)^2}{|g^* \epsilon_l - 1|^4}. \tag{5}$$

The shear method has its grounding in the equivalence of the expectation value of the ellipticity of lensed galaxies $\langle \epsilon_l \rangle$ to that of the complex reduced shear g.

A signal-to-noise estimate for the detection of a shear signal compared to a magnification signal suggests that the shear method is considerably superior. However, in SKE one finding was that the magnification information complements the shear information if the former has accurate calibration.

In order to investigate the relative merits of the shear and magnification information in the constraint of cluster profiles, a maximum likelihood approach, using both analytic and numerical techniques, is adopted. As in SKE, the validity of the analytic approach can be assessed with numerical simulations.

2 Likelihood Functions

In the likelihood treatment, it is assumed that a cluster is observed in an aperture with inner radius $\theta_{\rm in}$ and outer radius $\theta_{\rm out}$. There are N_μ images above a certain flux limit, and N_γ images for which an ellipticity can be measured. The sources of noise are: (i) poisson noise on the number of galaxies observed and (ii) that the intrinsic probability distribution for their ellipticities has a dispersion (in this work $\sigma_{\epsilon_s} = 0.2$). The cluster itself is described by a parametric model, parameters π_i. **What are the best-fitting parameters are for a particular observation?** Likelihood (or log-likelihood) functions for the magnification and shear methods enable us to obtain the probability for model parameters, given the observables – hence the best-fitting parameters are obtained. Further, ensemble-averaged log-likelihood functions allow one to estimate the dispersion of the parameters obtained during a single realisation. Thus they also provide a powerful means to predict the effectiveness of the shear and magnification information in constraining cluster parameters for various observing conditions and aperture sizes.

For the magnification method, the information used is that there are N_μ galaxy images at positions $\vec{\theta}_i$; the likelihood function to be maximised is

$$\mathcal{L}_\mu = P(N_\mu; \langle N_\mu \rangle) \prod_{i=1}^{N_\mu} \frac{[\mu(\vec{\theta}_i)]^{\beta-1}}{\int \mathrm{d}^2\theta \, [\mu(\vec{\theta})]^{\beta-1}}, \tag{6}$$

where $P(N_\mu; \langle N_\mu \rangle)$ accounts for the poisson noise.

For the shear method the observables are galaxies at positions $\vec{\vartheta}_i$ having ellipticities $\epsilon_{l,i}$; the likelihood function is

$$\mathcal{L}_\gamma = \prod_{i=1}^{N_\gamma} p_{\epsilon_l}(\epsilon_{l,i}|g(\vec{\vartheta}_i)). \tag{7}$$

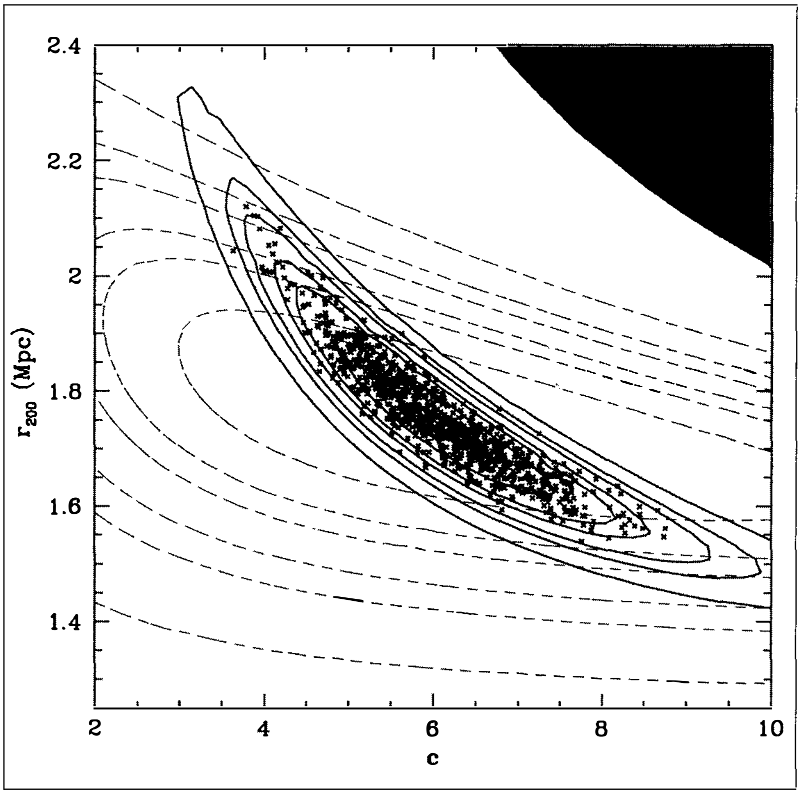

Figure 1: The solid lines are contours of constant $\langle \ell_\gamma \rangle$ and the dashed contours correspond to $\langle \ell_\mu \rangle$. Contours are drawn for $2\Delta\ell = \{2.30, 4.61, 6.17, 9.21, 11.8, 18.4\}$, within which one expects that 68.3%, 90%, 95.4%, 99%, 99.73% and 99.99% respectively, of parameter estimates from realizations will be enclosed. The crosses correspond to the best-fit parameters recovered by applying the shear likelihood analysis to 1000 simulated data sets. The study is limited to the weak lensing regime and lens models with parameters in the upper right corner are excluded.

In this case, to proceed analytically and derive the ensemble-averaged log-likelihood function, one has to make approximations. The reader is referred to SKE for further details, and for the ensemble-averaged log-likelihood functions for both methods.

3 Lens and Source Models

The cosmological parameters adopted are: $H_0 = 65\text{kms}^{-1}\text{Mpc}^{-1}$, $\Omega_{\rm M} = 1.0$ and $\Omega_\Lambda = 0.0$. Only the weak lensing regime is considered, with the lens at redshift $z_l = 0.2$ and the background galaxy population at $z_s = 1.0$. These galaxies have a Gaussian intrinsic ellipticity distribution, and the slope of their number counts $\beta = 0.5$. The number density of background galaxies for which an ellipticity can be measured is $n_\gamma = 30/\text{arcmin}^2$ and the number density used for the magnification method is $n_\mu = 120/\text{arcmin}^2$.

3.1 The NFW profile

The NFW profile (Navarro, Frenk & White 1995;1996) is a good description of the radial density of haloes formed in cosmological simulations of hierarchical clustering. It can be parameterised with a virial radius r_{200}, and a concentration parameter c, which are related through a scale radius $r_s = r_{200}/c$. Inside r_{200}, the mass density of the halo equals $200\rho_c$, where $\rho_c = \frac{3H^2(z)}{8\pi G}$ is the critical density of the Universe at the redshift of the halo and $H(z)$ is the Hubble parameter at the redshift of the halo. The characteristic overdensity of the halo, δ_c, is related to c through:

$$\delta_c = \frac{200}{c} \frac{c^3}{\ln(1+c) + (c/1+c)}. \tag{8}$$

Then the density profile is:

$$\rho(r) = \frac{\delta_c \rho_c}{(r/r_s)(1+(r/r_s))^2}, \tag{9}$$

which is shallower than isothermal near the halo centre and steeper than isothermal near the virial radius. Expressions for the lensing properties of the profile can be found in Bartelmann (1996) for example.

The model under consideration here has $c = 6.0$ and $r_{200} = 1.75$Mpc; this corresponds to a rich galaxy cluster, with virial mass $M_{200} \sim 10^{15} M_\odot$, and Einstein radius $\theta_{\rm E} \sim 0\overset{\prime}{.}2$.

4 Some Results

An NFW lens model with true parameters π_t : $c = 6.0$, $r_{200} = 1.75$Mpc was used to generate catalogs of lensed galaxies and to derive the ensemble-averaged log-likelihood contours. The inner and outer radii of the annulus are $\theta_{\rm in} = 0\overset{\prime}{.}6$, $\theta_{\rm out} = 4\overset{\prime}{.}0$. In Fig.1 the best fit parameters recovered by applying the shear likelihood analysis to 1000 synthetic catalogs are superimposed on the analytic ensemble-averaged log-likelihood contours. The magnification ensemble-averaged log-likelihood contours are also shown. Recalling that the analysis is restricted to the weak lensing regime (outside the Einstein radius), the region in the upper right corner is excluded since it corresponds to combinations of r_{200} and c where the Einstein radius falls inside the aperture. Note that the spatial scatter of the points in the $c - r_{200}$ plane is consistent with the ensemble-averaged log-likelihood contours for the shear method. The contours for the shear information are tighter than those for the magnification information. Elsewhere it will be shown that if the outer radius of the aperture is increased further, then the shear contours tighten considerably more than those of the magnification. This demonstrates the power of using shear data from wide field imaging studies of lensing clusters.

Acknowledgements

This work was supported by the TMR Network "Gravitational Lensing: New Constraints on Cosmology and the Distribution of Dark Matter" of the EC under contract No. ERBFMRX-CT97-0172.

References

1. P. Schneider, L.J. King and T. Erben, *A&A* **353**, 41 (2000)
2. T.J. Broadhurst, A.N. Taylor and J.A. Peacock, *ApJ* **438**, 49 (1995)
3. J.F. Navarro, C.S. Frenk and S.D.M. White, *MNRAS* **275**, 720 (1995)
4. J.F. Navarro, C.S. Frenk and S.D.M. White, *ApJ* **462**, 563 (1996)
5. M.S. Bartelmann, *A&A* **313**, 697 (1996)

CLUSTER GALAXIES: CONTRIBUTION TO THE ARC STATISTICS

M. MENEGHETTI[1,2], M. BOLZONELLA[3], M. BARTELMANN[2],
L. MOSCARDINI[1] AND G. TORMEN[1]

[1]*Dipartimento di Astronomia, Università di Padova, vicolo dell'Osservatorio 5, I-35122 Padova, Italy*
[2]*Max Planck Institut für Astrophysik, P.O. Box 1523, D-85740 Garching, Germany*
[3]*Istituto di Fisica Cosmica G.P.S. Occhialini, via Bassini 15, I-20133 Milano, Italy*

We present the results of a set of numerical simulations aiming at evaluating the effects of cluster galaxies on the arc statistics. At this goal we use nine different galaxy clusters obtained from N-body simulations. We mimic the presence of a population of galaxies inside each cluster, trying to reproduce the observed luminosity function and the spatial distribution. We compare the statistical distributions of the properties of the gravitational arcs produced by our clusters with and without galaxies. We find that the cluster galaxies do not introduce perturbations strong enough to significantly change the number of arcs and the distributions of the properties of long arcs.

1 Introduction

The statistics of arcs is a potentially very sensitive probe for the cosmological matter density parameter Ω_0 and for Ω_Λ. Theoretical studies showed that more arcs can be expected in a universe with low density and small cosmological constant. In fact, low density makes clusters form earlier, and a low cosmological constant makes them more compact individually. Previous analyses (e.g. Bartelmann et al. 1998) neglected the granularity of the gravitational cluster potentials due to the presence of galaxies which can be considered using numerical simulations.

2 The cluster sample

The simulated clusters used as lenses in the present analysis are presented in Tormen et al. [6]. The sample is formed by the nine most massive clusters obtained in a cosmological simulation of an Einstein-de Sitter universe, evolved using a P3M code. The original box-size is $L = 150$ Mpc (a Hubble constant of 50 km s^{-1} Mpc^{-1} is used). The initial conditions have a scale-free power spectrum $P(k) \propto k^{-1}$, very close to the behaviour of the standard CDM model on the scales relevant for cluster formation. The normalization is chosen to roughly match the observed local abundance of clusters [8] and corresponds to $\sigma_8 = 0.63$, where σ_8 is the r.m.s. matter density fluctuation in spheres of radius $r = 8h^{-1}$ Mpc. Each cluster was obtained using a tree/SPH code adopting a re-simulation technique [6], which allows a much higher spatial and mass resolution. The masses of these clusters are in the range $5 \times 10^{14} \div 3 \times 10^{15} M_\odot$.

3 Lensing properties of the clusters

We centred each cluster in a cube of side 6 Mpc, where we placed a regular grid of $N_g = 128^3$ cells. For each of them we extracted three different surface-density fields Σ, by projecting the 3-D density field ρ (obtained by *Triangular Shape Cloud* method) along the three cartesian axes. This produces three lens planes, which we consider as independent cluster models for the purpose of this study. This made possible to perform 27 different lensing simulations starting from our sample of 9 clusters. We fix the redshifts of the lens and of the source planes equal to $z_L = 0.4$ and $z_S = 2$ respectively, leading to a value of the critical density for our clusters of $\Sigma_{cr} \simeq 1.975 \times 10^{15} M_\odot/\mathrm{Mpc}^2$. We shot a bundle of 1024×1024 rays across the central fourth of the lens plane, where most of the cluster mass is projected. In fact, our goal is to study the strong lensing properties of the clusters. The deflection angle α of each ray is computed by summing the contribution from all the cells of the grid on which Σ is defined. Finally, solving the lens equation, the arrival positions of the rays on the source plane are calculated. Once the deflection angles are known, all the lensing properties of the cluster can be easily evaluated.

4 Simulating the galaxy distribution inside the cluster

To simulate a population of galaxy lenses inside the cluster, in such a way that their observational properties are well reproduced, we start from the luminosity function of the Coma cluster, whose mass is similar to that or our simulated clusters. This luminosity function has been recently derived in the V-band by Lobo et al. [2]. In the magnitude range $13.5 < V \leq 21.0$ (corresponding to the absolute magnitude range $-22.24 < M_V \leq -14.74$) it is well described by the combination of a steep Schechter function and of a Gaussian function.

Using Monte Carlo methods, we generate a sample of galaxies with luminosities distributed in a way close to the Coma cluster galaxies. To convert the luminosity to masses, we take the average relation $\langle M/L \rangle = 3.2(M_\odot/L_\odot)$ (see [8,7]). In this procedure the total number of galaxies to place into each simulated cluster is determined by imposing a baryonic fraction equal to that estimated by White et al. [8] for the Coma cluster ($M_b/M_{tot} \simeq 0.009$, where M_b is the baryonic mass in galaxies and M_{tot} the total mass within the Abell radius). Moreover, to consider the presence of a dark matter halo around each galaxy, we obtain the total (virial) masses M_{vir} by multiplying the baryonic masses previously obtained by the factor f_b^{-1}, where f_b represents the average baryonic fraction inside single galaxies. As this quantity is not well known observationally, we take a fiducial value f_b ($\sim 5\%$), close to the value predicted by the standard model of primordial nucleosynthesis. To place galaxies inside the cluster in a realistic way, we made the assumptions that the galaxy number density should follow the total density field and that the most massive galaxies should be placed at the centre of the cluster or in other large subclumps.

The galaxies are modelled as spheres with a NFW density profile [5], truncated at a cut-off radius, where the galaxy density falls below the local cluster density. In fact, for lensing analysis we are interested only to the galaxy mass which emerges from the mean local density of the cluster. Galaxies placed close to the cluster centre have a smaller radius because the cluster density is higher there, so only a small part of the galaxy profile can emerge. The

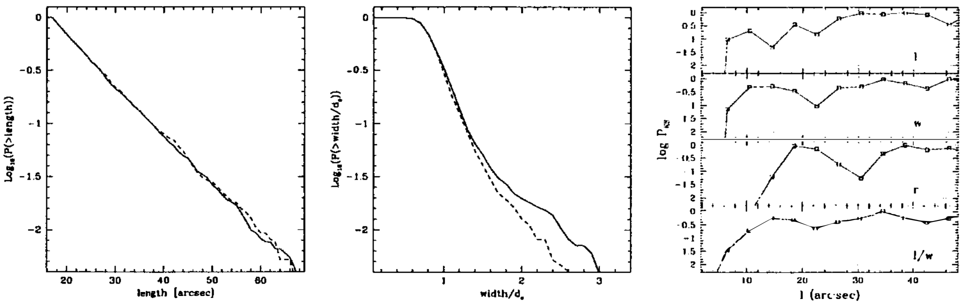

Figure 1: Cumulative distributions of arc lengths (left panel) and widths (central panel) for arcs longer than 16″. Results for DM and GAL simulations are shown by solid and dashed lines, respectively. Right panel: the behaviour of the probability P_{KS} (as computed in a Kolmogorov-Smirnov test) that the arc property distributions in data sets obtained from the simulations DM and GAL can be drawn from the same parent distribution. Subsamples of arcs with a given length $l \pm 2''$ are considered. The subpanels refer to different properties: length l, width w, curvature radius r and length-to-width l/w from top to bottom.

galaxy contribution to the deflection angles can be analytically computed and summed to the contribution from the remaining dark matter in the cluster.

5 Properties of arcs and results

We use our clusters to lens a large number of elliptical sources (with axial ratios randomly drawn in the interval [0.5,1] and area equal to that of a circle of diameter 2″) on the source plane. Following the method introduced by Miralda-Escudé [4] and developed by Bartelmann & Weiss [1], we find and classify the images of all these sources, measuring their lengths l, widths w, curvature radii r and length to width ratios l/w. We then perform a statistical analysis of the distributions of the arc properties (more details are presented in [3]).

The results obtained from the first set of 27 simulations using the original simulated clusters (i.e. without galaxies inside, hereafter "DM" simulations) are compared to those obtained after the introduction of the galaxies in the lens clusters (hereafter "GAL" simulations).

The total number of arcs in the DM and GAL simulations is quite similar: 447112 and 448927 respectively. The majority of these arcs are quite short. Considering only giant arcs with $l > 16''$ the sample reduces to 1823 and 1721 arcs for DM and GAL simulations. In Figure 1 we show the cumulative distributions of lengths and widths for arcs longer than 16″. The distributions of arc length do not seem to be sensitive to the inclusion of the galaxies in the clusters. We found a similar result also for the distributions of arc curvature radii. On the other hand, the distributions of arc widths show some differences between simulations DM and GAL. Such differences are partially found also between the distributions of arc length to width ratios.

Considering arcs with a given length $l \pm 2''$, we perform the Kolmogorov-Smirnov test to evaluate the significance of the differences between the distributions of the arc properties. The significance level obtained from the test as a function of l_{min} is also shown in Figure 1 for all the considered arc properties. Concerning arc widths, the probability that the data sets obtained from simulations DM and GAL are drawn from the same distribution becomes slightly lower for arcs with $l < 22''$. On the other hand, the differences between the other property distributions become significant only when very short arcs are included in the sample.

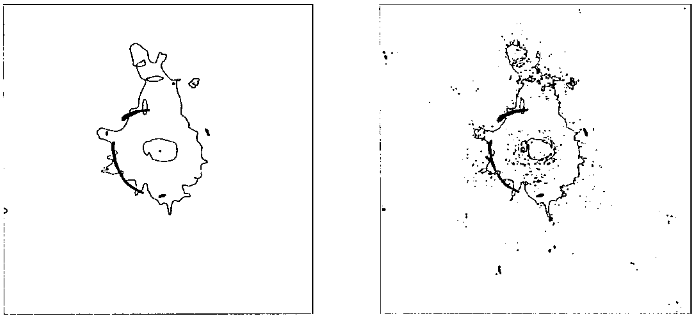

Figure 2: Example of arc perturbed and splitted by cluster galaxies. The left panel refers to the DM simulation, while the right one shows the image of the same source in the corresponding GAL simulation. We show also critical curves, which tend to be wiggled when the galaxies are present.

6 Conclusions

We expected these effects by cluster galaxies: *a)* they tend to increase the cluster cross section for strong lensing by wiggling the cluster critical curves, increasing their length; *b)* because of the larger curvature of the critical lines, they can perturb arcs, splitting them; *c)* the local steepening of the density profile near cluster galaxies tends to make arcs thinner.

The results of the KS test indicate that, concerning the arc lengths, curvature radii and length to width ratios, the effect of cluster galaxies on arc statistics is negligible if very short arcs are excluded. This means that the first two effects previously mentioned are almost exactly counter-acting and that the splitting of some arcs is partially compensated for the increased strong lensing ability of the clusters (Figure 2). The results show also that, as expected, the galaxies tend to make arcs thinner. This effect becomes evident for arcs shorter than $22''$.

The longest arcs, which form in the central regions of the clusters, where most of the mass is concentrated, are not sensitive to cluster galaxies. We think that this is due to the fact that in these dense regions only a small fraction of the total galaxy mass emerges from the underlying dark matter distribution.

References

1. Bartelmann M. & Weiss A., 1994, A&A, 297, 1
2. Lobo C., Biviano A., Durret F., Gerbal D., Le Fevre O., Mazure A. & Slezak E., 1997, A&A, 317, 385
3. Meneghetti M., Bolzonella M., Bartelmann M., Moscardini L. & Tormen G., MNRAS, 314, 338
4. Miralda-Escudé J., 1993, ApJ, 403, 497
5. Navarro J.F., Frenk C.S.& White S.D.M., 1997, Ap.J, 490, 493
6. Tormen G., Bouchet F.R., White S.D.M., 1997, MNRAS, 286, 865
7. Van der Marel R.P., 1991, MNRAS, 273, 710
8. White S.D.M., Navarro J.F., Evrard A.E., Frenk C.S., 1993, Nat, 366, 429

A MULTIWAVELENGTH STUDY OF THE CLUSTER OF GALAXIES CL0016

F.J. CASTANDER[1], G.P. HOLDER[2], D. CLOWE[3], J.E. CARLSTROM[2], M. SCHIRMER[3], E.D. REESE[2], J.-P. KNEIB[1]
[1]*Observatoire Midi-Pyrénées, 14 Av Edouard Belin, 31400 Toulouse, France*
[2]*Department of Astronomy & Astrophysics, University of Chicago, 5640 S Ellis Ave, Chicago IL 60637, USA*
[3]*Max-Planck Institut-für-Astrophysik, 85740 Garching, Germany*

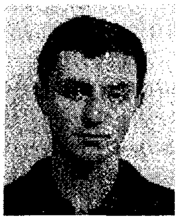

We combine observations in the optical, radio and X-rays of the cluster of galaxies CL0016 to constrain its gravitational potential. These observations include deep Keck imaging in the optical; BIMA and OVRO interferometric observations at cm wavelengths and ROSAT PSPC and HRI X-ray imaging. Each observation provides different information about the cluster: the distortions of background galaxies depend on the cluster projected potential; the Sunyaev-Zeldovich decrement, on the integrated pressure and the X-ray emission, on the square of the projected gas density (if isothermal).
We use a maximum likelihood analysis to combine these data to derive the cluster potential. We discuss different approaches to construct the likelihood functions, the different assumptions required and the current status of the project.

1 Introduction

Clusters of galaxies are valuable tools to study cosmology. For example, their abundance evolution is very sensitive to the underlying matter content of the universe. However, cluster of galaxies are a mixture of dark matter, hot gas and galaxies whose detailed structure and composition are still not fully understood. In order to carry out precision cosmology with clusters we need to understand the physical processes taking place in them and their influence into their internal structure and evolution.

Observationally clusters can be studied from different point of view and wavelengths. For instance, in the optical one can count galaxies to select clusters and assign richnesses and colour properties. Spectroscopy can measure redshifts, velocity dispersions and the properties of the galaxy members. In X-rays one can measure the surface brightness and temperature. Deep imaging can allow us to measure the gravitational distortions of background galaxies. Radio observations can detect the decrement at long wavelengths in the temperature of the cosmic microwave background (CMB).

Given the different physical processes probed by those measurements, a combination of them can help us understand the physical processes taking place in them. Here, we present a method to combine several observation at different wavelengths which we apply to the cluster of galaxies CL0016.

2 The cluster of galaxies: CL0016+16

CL0016+16 was originally discovered by Richard Kron searching photographic plates. Koo (1981) measured a richness twice as large as that of the Coma cluster in the first optical study published. A decade later, Dressler & Gunn (1992) measured a cluster redshift of $z = 0.5455$ and a velocity dispersion of $\sigma = 1324$ km/s with 30 cluster galaxy members. The CNOC group (e.g., Carlberg et al 1996) measured the redshifts of 47 extra cluster members obtaining $z = 0.5481$ and $\sigma = 1243$ km/s. They computed a mass-to-light ratio of $M/L = 260\ h^{-1}$.

In X-rays, the EMSS measured an X-ray luminosity of $L_x = 14.6 \times 10^{44} h_{50}^{-2}$ erg/s for this cluster (Gioia et al 1990). Several authors (Neumann & Böhringer 1997; Hughes & Birkinshaw 1998; Reese et al 2000) have analysed the ROSAT PSPC and HRI observations of this cluster, fitting a standard beta model profile (2), obtaining values of $\beta = 0.75$-0.80 and $r_c = 40$-$45''$. Furuzawa et al (1998) and Hughes & Birkinshaw (1998) have analysed the ASCA observations measuring a cluster temperature of $T_x \sim 8$ KeV.

Clowe et al (2000) obtained deep Keck images of this cluster which they use to reconstruct its projected mass distribution. In particular, they fit the cluster mass profile to an isothermal sphere and to a NFW profile. Both fits are statistically acceptable, the NFW being slightly better. The isothermal fit gives a velocity dispersion of ~ 800 km/s, lower than that found by the CNOC group.

Carlstrom et al (2000) observed CL0016 at the OVRO and BIMA observatories using radio interferometric techniques at cm wavelengths. Reese et al (2000) used these data in conjuction with the ROSAT X-ray data to measure the Hubble constant.

3 Methodology

We have chosen to combine the lensing, X-ray and SZ data mentioned above using a maximum likelihood method. The main idea is to constrain the cluster potential constructing a likelihood function which is the product of the likelihoods of the different observations, that is,

$$\mathcal{L}(\phi) = \mathcal{L}_{lensing}(\phi) * \mathcal{L}_{x-rays}(\phi) * \mathcal{L}_{SZ}(\phi) \tag{1}$$

and maximize that function. This formulation allows us to attack the problem for each observation separately.

Deep optical images measure the ellipticities, magnitudes and sizes of background galaxies. The reduced shear, g, can be computed from the background galaxies ellipticities. In fact, it is the expected value of the ellipticities in the weak lensing regime. The reduced shear can also be directly obtained from the second derivatives of the projected potential. Several authors have developed methods to formulate likelihood functions (or similar) for weak lensing observations. Bartelmann et al (1996) evaluate a χ^2 function comparing the reduce shear coming from observations and from the cluster potential in a grid. Seitz et al (1998) developed an entropy regularized likelihood similar to the previous method but using the ellipticities of all the background galaxies without a grid and including a regularization term. Briddle et al

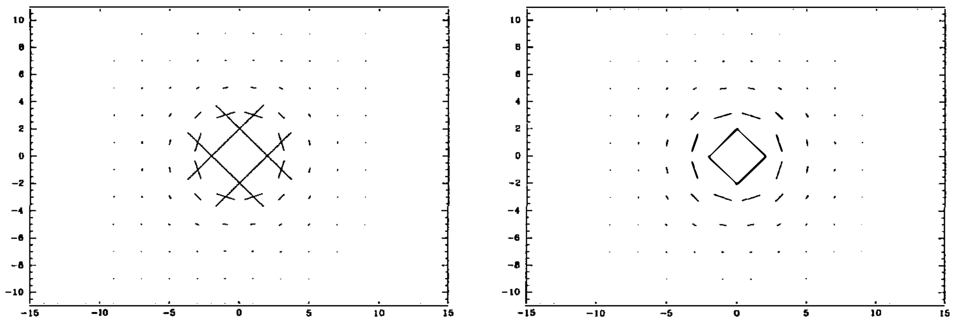

Figure 1: Reduced shear of a simulated cluster potential. Left: original potential. Right: parametric reconstruction of the potential. The inner values differ because the g values are computed in the original potential (left) at the center of the grid where the potential is nearly critical, while the g values obtained from the simulation (right) come from averaging ellipticities within the grid cell where, in general, distortions are smaller than near the critical line.

(1998) developed a maximum entropy method, similar to the previous one, but using a Bayesian formulation.

X-rays observations measure the surface brightness (and the temperature of the intracluster gas if enough spectral resolution is available) of the X-ray emission. The gas density can be inferred from the surface brightness and the temperature. If hydrostatic equilibrium is assumed then one can obtain the cluster potential. Hughes & Birkinshaw (1998) computed a likelihood function for X-ray observations taking into account the Poissonian nature of the X-ray data.

Radio observations of the SZ effect measure the temperature decrement (at long wavelengths) of the CMB due to the hot intracluster medium. This decrement is proportional to the integrated pressure along the line of sight. Knowing the temperature, one can obtain the gas density, and assuming hydrostatic equilibrium one can get the cluster potential. The radio data available were obtained using interferometric techniques, in which one measures intensities in the u-v plane. Reese et al (2000) constructed a likelihood function which is computed in the Fourier Plane where observations are obtained.

4 Current status

We have started developing the code to compute the total likelihood function and maximize it. In our prescription the likelihood function is naturally separated into individual likelihoods coming from the different observations. Each of these is implemented as a different module.

For the weak lensing module we have implemented parametric and non-parametric methods. We have carried out simulations to check the accuracy of the cluster potential reconstruction. For example, figure 1 shows the discrepancies that could arise near the critical lines in reconstructions using a grid. In general, this grid reconstruction method tends to underestimate the value of the potential at the cluster center (see also Bartelmann et al 1996).

Figure 2 shows the non-parametric reconstruction of the projected potential of cluster CL0016. The reconstructed potential is remarkably smooth. This is expected as no obvious strong lensing features are observed in this cluster in HST images.

We have also implemented the X-ray and SZ modules. The code is very similar to that of Reese et al (2000) and our results are almost indistinguishable from theirs, when fitting isothermal beta models.

We have started combining the different likelihoods. As a starting point we have chosen to

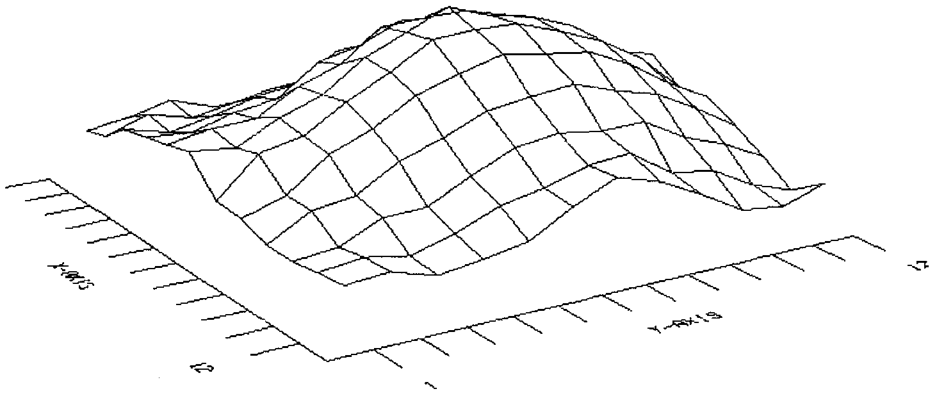

Figure 2: Non-parametric reconstruction of the CL0016 cluster projected potential using weak lensing data.

use the parametric spherically symmetric beta model, where the gas density profile is given by

$$n(r) = n_0 \left(1 + \left(\frac{r}{r_c}\right)^2\right)^{-\frac{3}{2}\beta}. \qquad (2)$$

The X-ray data and SZ data are fitted to the X-ray surface brightness and temperature decrement (for their expressions see for example Reese et al 2000). Assuming isothermal hydrostatic equilibrium one can then differentiate the logarithm of the gas density and integrate to get the potential. One can then integrate along the line of sight to obtain the projected potential to use for the lensing module. Preliminary results indicate that the SZ data is the least constraining data set and that the X-ray and SZ data are consistent in describing the same gas distribution. However, the shallow potential inferred from the lensing data (under the assumptions made) requires a shallower gas distribution than that observed in X-rays and SZ.

This project is still a work in progress. We expect to finish a detailed study of the beta model parameterization and then move on to other models (parametric, non-parametric, triaxial,...) and a larger cluster sample that will help us understand better the physical processes in clusters.

Acknowledgments

FJC acknowledges financial support from the TMR network of the European Commission under contract No: ERBFMRX-CT98-0172.

References

1. Bartelmann, M. et al, ApJ **464**, L115 (1996).
2. Briddle, S.L. et al, MNRAS **299**, 895 (1998).
3. Carlberg, R. G. et al, ApJ **462**, 32 (1996).
4. Carlstrom, J. et al, PhST **85**, 148 (2000).
5. Clowe, D., Luppino, G., Kaiser, N. & Gioia, I., ApJ , submitted (astro-ph/0001356).
6. Dressler, A. & Gunn, J.E., ApJS **78**, 1 (1992).
7. Furuzawa, A. et al, ApJ **504**, 35 (1998).
8. Gioia, I. et al, ApJS **72**, 567 (1990).
9. Hughes, J.P. & Birkinshaw, M., ApJ **501**, 1 (1998).
10. Koo, D., ApJ **251**, L75 (1981).
11. Neumann, D. & Böringher, H., A&A **289**, 123 (1997).
12. Reese, E.D. et al, ApJ **533**, 38 (2000).
13. Seitz, S. et al, A&A **337**, 325 (1998).

CLUSTER DEPROJECTION WITH MULITPLE DATA SETS: FIRST APPLICATIONS TO SIMULATIONS

Katrin Reblinsky and Matthias Bartelmann
Max-Planck-Institut für Astrophysik, P.O. 1317, D-85741 Garching, Germany

We introduce a new, parameter-free cluster deprojection algorithm for recovering the structure of clusters of galaxies along the line-of-sight. The algorithm is based on the Richardson-Lucy (RL) algorithm and combines multiple sets of observable data from clusters of galaxies, namely the lensing potential ψ, the X-ray surface brightness S_x and the Sunyaev-Zel'dovich temperature decrement ΔT_{SZ}, to extract the 3-dimensional gravitational potential ϕ. Using gas-dynamical simulations, the quality of the reconstructions is demonstrated. The results are shown to be stable and reliable.

1 Richardson-Lucy deprojection algorithm

Resolving the line-of-sight structure of clusters of galaxies is a fundamental problem in astronomy. It is a so-called inverse problem which can be formulated as an integral equation,

$$\psi(x) = \int \phi(\zeta) P(x|\zeta) \mathrm{d}\zeta, \tag{1}$$

where $\phi(\zeta)$ is the function of interest, $\psi(x)$ the function accessible through measurement, and the integral kernel $P(x|\zeta)$ is normalized and non-negative.

With the help of Bayes' theorem for conditional probabilities an iterative algorithm can be derived (Lucy [1 2], Richardson [3]),

$$\psi_n(x) = \int \phi_n(\zeta) P(x|\zeta) \mathrm{d}\zeta, \qquad \phi_{n+1}(\zeta) = \int \frac{\psi(x)}{\psi_n(x)} P(x|\zeta) \mathrm{d}x, \tag{2}$$

which approximates $\phi(\zeta)$. Here $\phi_n(\zeta)$ is the n-th estimate of the function of interest, ϕ, and $\psi_n(x)$ is the n-th estimate of the measured data, ψ, as obtained from ϕ_n. Assuming axial symmetry for the cluster, the kernel $P(x|\zeta)$ becomes (Binney et al.[4])

$$P(x,y|R,Z) = \frac{\delta\left[(\frac{y}{\cos i} - Z\tan i)^2 - (R^2 - x^2)\right]}{\pi\cos i}. \tag{3}$$

Here i is the inclination angle with respect to the line-of-sight.

2 Observables sensitive to the line-of-sight

The line-of-sight (los) structure of clusters of galaxies can be described in terms of the gravitational potential ϕ. Typical observables which are sensitive to the los comprise the lensing potential ψ, the X-ray surface brightness S_x, and the Sunyaev-Zel'dovich temperature decrement ΔT_{SZ}. Choosing a suitable model (Reblinsky & Bartelmann [5]) all three observables can be related to the 3-dimensional potential ϕ:

$$\psi(x,y) \propto \int_{-\infty}^{\infty} \phi(R,Z)\mathrm{d}z, \tag{4}$$

$$S_x(x,y) \propto \int_{-\infty}^{\infty} \sqrt{T}\exp\left[-2\phi'(R,Z)\right]\mathrm{d}z, \tag{5}$$

$$\Delta T_{SZ}(x,y) \propto \int_{-\infty}^{\infty} T\exp\left[-\phi'(R,Z)\right]\mathrm{d}z. \tag{6}$$

For the X-ray case and the SZ-effect an isothermal gas distribution is assumed. The inclination angle i and the temperature T are input parameters.

The Richardson-Lucy algorithm can be applied to reconstruct the function of interest, namely the gravitational potential ϕ from the functions accessible through measurement, in this case ψ, S_x, and ΔT_{SZ}. Exploiting the different dependences of ψ, S_x, and ΔT_{SZ} on ϕ, the result of the reconstruction can be optimized.

3 Multiple data Richardson-Lucy algorithm

Now we are in a position to propose the multiple-data Richardson-Lucy (MDRL) deprojection-algorithm. The combination of multiple data sets can be achieved in three separate steps: In a first step we compute the three line-of-sight integrals of the observables leading to iterated input data ψ_n, $S_{x,n}$, and $\Delta T_{SZ,n}$. In the second step we define the integrals

$$F_n^i = \int f_n^i(x,y)P(x,y|R,Z)\mathrm{d}x\mathrm{d}y, \tag{7}$$

where the f_n^i's are defined as $f_n^1 = \frac{\psi}{\psi_n}$, $f_n^2 = \frac{S_x}{S_{x,n}}$, and $f_n^3 = \frac{\Delta T_{SZ}}{\Delta T_{SZ,n}}$. In the last step of the MDRL-algorithm, the results of the integrations (7) are combined after each iteration step as

$$\phi_{n+1} = \phi_n\left[\alpha F_n^1 + \beta\left(1 - \frac{1}{2}\ln F_n^2\right) + \gamma\left(1 - \ln F_n^3\right)\right]. \tag{8}$$

α, β, and γ are weighting factors with $\alpha+\beta+\gamma = 1$, which can be used to determine the relative weight put on the respective input data. In this way, it is possible to recover the case of a single set of input data.

4 Deprojection of cluster images from gas-dynamical simulations

In this section we present reconstructions obtained from gas-dynamical simulations. For this purpose, mock observational data are constructed from the simulations which are then used as input data for the MDRL-algorithm and compared to the true, original potential obtained

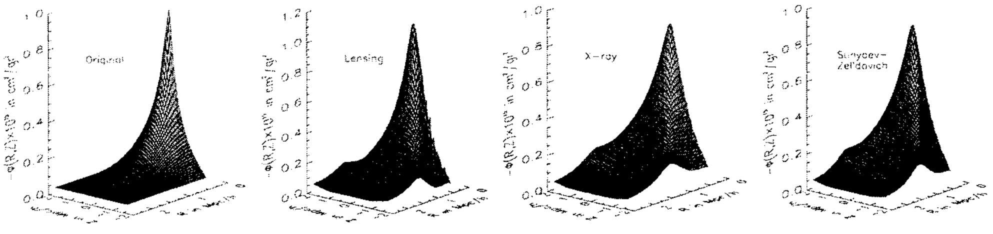

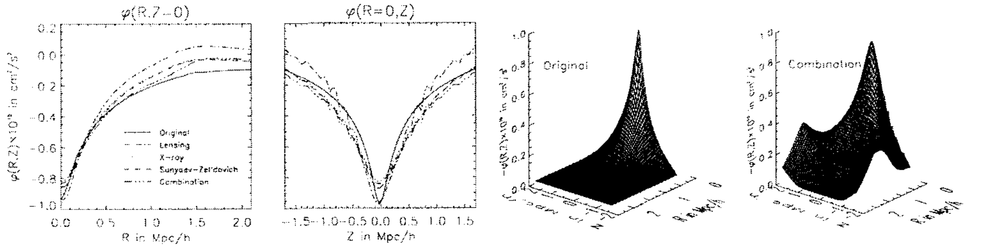

Figure 2: Result of the reconstruction obtained by combining all data sets shown in Fig. 7, each with a weighting of 1/3. The two left-most plots show two different cuts through the resulting potential comparing the original potential with the results for the single data sets from Fig. 8. The two right-most plots compare the original potential reconstructed with the combined data sets as surface plots.

directly from the simulations (Reblinsky & Bartelmann [6]). In the following we choose the assumed inclination angle of the cluster's symmetry axis with respect to the line-of-sight as $i = 30°$ and stop the algorithm after 8 iterations.

In Fig. 1 we compare the true, original gravitational potential ϕ to the results of the reconstructions using the lensing potential ψ, the X-ray surface brightness S_x, and the SZ temperature decrement ΔT_{SZ}, respectively, alone as input data for the MDRL-algorithm. In this way the amount of information already present in a single data set can be assessed. From Fig. 1 we can conclude that all three types of input data give qualitatively very similar results and thus each set contains information about the main features of the gravitational potential ϕ.

Fig. 2 displays the results obtained by combining all three types of input data, where the weight factors are chosen to be $\alpha = \beta = \gamma = 1/3$. In the two left-most plots two cuts through the multiple data set reconstructions are compared to the original potential and to the results of the single data set reconstructions, respectively. These cuts show the improvement of the combined reconstruction over the single data set reconstructions. The surface plot of the combined reconstruction demonstrates that the MDRL-algorithm is able to recover all important features of the potential.

In order to assess the quality of the reconstructions in a more quantitative way, it is instructive to look at the relative errors between the original gravitational potential, $\phi_{\rm orig}$, and the reconstructed one, $\phi_{\rm rec}$, which is computed as $|\phi_{\rm orig} - \phi_{\rm rec}|/|\phi_{\rm orig}|$ and displayed in Fig. 3. For all four reconstructions we see that the deviation over large parts of the potential is less than 5 %. For the lensing reconstruction we note that the zone with an error margin of less than 5 % is relatively wide, especially in the Z-direction. The X-ray and the SZ-case both show

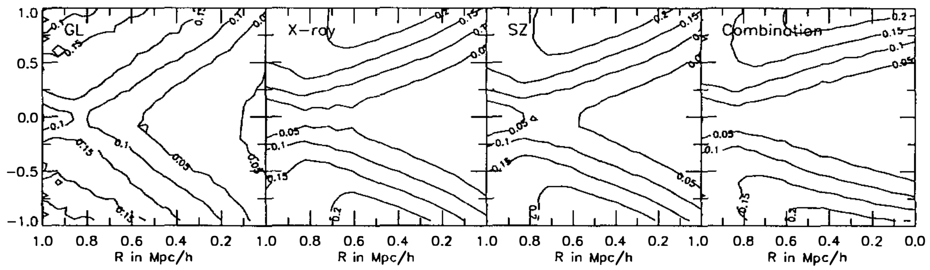

Figure 3: The relative error between the original gravitational potential $\phi(R, Z)$ and the reconstructed potential computed as $|\phi_{\rm orig} - \phi_{\rm rec}|/|\phi_{\rm orig}|$. The central part of the potential is displayed: $R \in (0, 1.0)h^{-1}$ Mpc and $Z \in (-1.0, 1.0)h^{-1}$ Mpc. From left to right: lensing data only, X-ray data only, Sunyaev–Zel'dovich data only, combination of all three data types. Contours mark deviations of $(0.05, 0.1, 0.15, 0.2)$.

excellent reconstructions in the central part of the cluster $((R, Z) < 0.5h^{-1}$ Mpc), but the quality towards the outer parts of the reconstruction degrades faster than in the lensing case. This reflects the theoretical expectation that the data from the X-ray and the SZ case have their main contributions coming from the cluster center.

5 Conclusion and outlook

In this paper we demonstrated that the recovery of the structure of clusters of galaxies along the line-of-sight is feasible. To achieve this goal we have proposed a deprojection algorithm based on the Richardson-Lucy algorithm. Even though already a single set of input data does contain important information about the overall shape of the gravitational potential ϕ, the combination of multiple input data – lensing data, X-ray data and SZ-data were explicitly considered – leads to a further improvement.

With the advent of an ever increasing number of clusters of galaxies, which have superb data sets including lensing, X-ray and SZ images, the MDRL-algorithm tested here with simulated data will be a valuable tool to determine the line-of-sight structure of clusters of galaxies.

Acknowledgments

This work was supported by the TMR Network "Gravitational Lensing: New Constraints on Cosmology and the Distribution of Dark Matter" of the EC under Contract No. ERBFMRX-CT97-0172 and the "Sonderforschungsbereich 375-95" für Astroteilchenphysik der Deutschen Forschungsgemeinschaft.

References

1. L.B. Lucy, AJ 79, 745 (1974)
2. L.B. Lucy, A&A 289, 983 (1994)
3. W. Richardson, J. Opt. Soc. Am. 62, 55 (1972)
4. J.J. Binney, R.L. Davies, G.D. Illingworth, ApJ 361, 78 (1990)
5. K. Reblinsky and M. Bartelmann in *Gravitational Lenses: Recent Progress and Future Goals*, 1999,ed. T.G. Brainerd and C.S. Kochanek
6. K. Reblinsky and M. Bartelmann, in preparation

DETECTION OF A DARK MATTER CONCENTRATION NEAR THE CLUSTER ABELL 1942 WITH WEAK GRAVITATIONAL LENSING

T. Erben[1], L. Van Waerbeke[2], F. J. Castander[3], P. Schneider[1,4], Y. Mellier[5,6]

[1] *Max Planck Institut für Astrophysik, Karl-Schwarzschild-Str. 1, Postfach 1317, D-85741 Garching, Germany.*

[2] *Canadian Institut for Theoretical Astrophysics, 60 St Georges Str., Toronto, M5S 3H8 Ontario, Canada.*

[3] *OMP, 14 Av. Edouard Belin, 31400 Toulouse, France*

[4] *IAEF, Universität Bonn, Auf dem Hügel 71, D-53121 Bonn, Germany*

[5] *Institut d'Astrophysique de Paris. 98 bis, boulevard Arago. 75014 Paris, France.*

[6] *Observatoire del Paris. DEMIRM. 61, avenue de l'Observatoire. 75014 Paris, France.*

A weak-lensing analysis of a wide-field V-band image centered on the cluster Abell 1942 has uncovered the presence of a mass concentration projected ~ 7 arcminutes South of the cluster center. From an additional wide-field image, taken two years later with a different camera in the I-band, the presence of this mass concentration is confirmed. A statistical analysis, using the aperture mass technique, shows that the probability of finding such a mass concentration from a random alignment of background galaxies is 10^{-6} and 4×10^{-4} for the V- and I-band image, respectively. No obvious strong concentration of bright galaxies is seen at the position of the mass concentration. The analysis of archival ROSAT-HRI data show the presence of a weak extended X-ray source about $1'$ displaced from the lensing centre.

1 Finding matter concentrations with weak gravitational lensing

A massive foreground object causes a coherent distortion on the image ellipticities of faint galaxies in its background. This signature of weak gravitational lensing has up to now mostly been used to study the mass distributions of known galaxy clusters (see e.g. Hoekstra et al. 1998[2]).

This argument can be reverted and the lens effect can be used to search for new, unknown massive objects. Assuming that galaxy ellipticities are intrinsically randomly distributed, a significant coherent alignment of galaxy images around an arbitrary point $\boldsymbol{\vartheta}$ directly indicates a large amount of mass around this position. An automatic weak-lensing cluster finder has been developed by Schneider [4], introducing the so-called $M_{\rm ap}$ statistics, a filtered integral over the two-dimensional surface mass density κ

$$M_{\rm ap}(\boldsymbol{\vartheta}) = \int_{|\boldsymbol{\vartheta}'|\le\theta} {\rm d}^2\vartheta' \; \kappa(\boldsymbol{\vartheta}+\boldsymbol{\vartheta}')\, U(|\boldsymbol{\vartheta}'|). \tag{1}$$

With $\int_0^\theta {\rm d}\theta \; \theta\, U(\theta) = 0$ this integral can directly be converted to a filtered integral over the tangential shear $\gamma_{\rm t}$

$$M_{\rm ap}(\boldsymbol{\vartheta}) = \int_{|\boldsymbol{\vartheta}'|\le\theta} {\rm d}^2\vartheta' \; \gamma_{\rm t}(\boldsymbol{\vartheta}';\boldsymbol{\vartheta})\, Q(|\boldsymbol{\vartheta}'|). \tag{2}$$

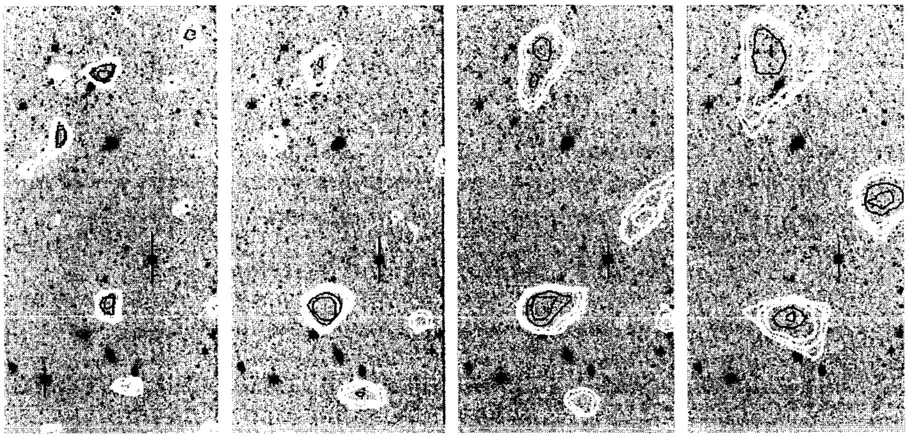

Figure 1: The four panels show the significance of the M_{ap} maps of the UH8K field. We chose $N_{rand} = 5000$, the black contours mark areas with $\nu = 1, 10, 30/5000$ and the white contours $\nu = 100, 180, 260/5000$. The filter scales are 80″ (upper left panel), 120″ (upper right panel), 160″ (lower left panel) and 200″ (lower right panel). For the larger scales the cluster components and the dark clump are detected with a very high significance.

This integral can easily be estimated by a sum over image ellipticities at discrete positions. An estimate for the significance of a measurement of M_{ap} can be obtained by randomising the galaxy orientations and comparing the value of M_{ap} from the randomised catalogs with the original measurement. Repeating this process N_{rand} times, the fraction ν of randomizations where M_{ap} is larger than the original meaurement gives the probability to find the measured value from a random distribution of galaxies, i.e. in the absence of a massive object.

2 The detection of our dark clump

The application of the M_{ap} statistics to a high-quality wide field V-band image around the cluster Abell 1942 showed a significant alignment of galaxy ellipticities around a position $\approx 7'$ South of the cluster. The significance is as high as around Abell 1942 itself. No obvious overdensity of bright foreground galaxies is associated with the gravitational lens signature. Unfortunately, the centre of our dark matter candidate was close to the border of the data field. On an I-band image from the UH8K mosaic camera, observed two years after the V-band data, our candidate lies in the centre of one of the chips. The application of the M_{ap} statistics to these data confirmed the existence of the dark clump, and the errorlevels ν are shown in Fig. 1.

3 Properties of the dark clump

For our dark matter candidate we find the following physical properties:

- The probability to find the observed alignment of galaxies in a random distribution is $\nu \approx 1 \times 10^{-6}$ for the V-band and $\nu \approx 4.2 \times 10^{-4}$ for the I-band data.

- The lens signal does not come from a few background galaxies only or from galaxies at a particular separation from the clump centre. See Fig. 2.

- If the signal comes from an object at a well defined redshift, the clump is probably at a redshift $z \leq 1$. This conclusion originates from the comparison of the magnitude distri-

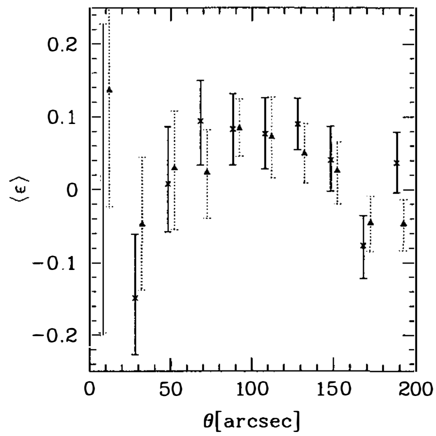

Figure 2: Mean tangential image ellipticity in independent bins of width 20″ around the dark clump, crosses (triangles) show the mean, solid (dashed) error bars the 80% error interval obtained from bootstrapping, using the MOCAM (Chip 3) data. For better display, the points and error bars are slightly shifted in the θ direction.

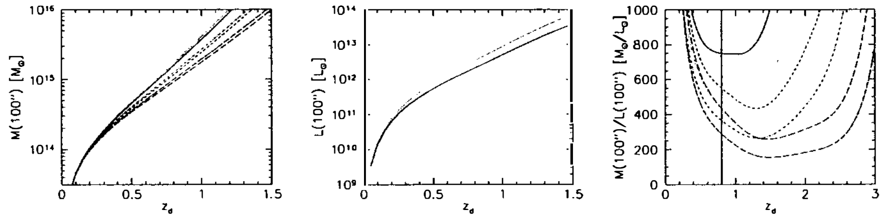

Figure 3: Estimate of the lensing mass (left panel), an upper bound for the luminosity of the lens (middle panel), and a lower limit on the mass-to-light ratio (right panel), as a function of assumed lens redshift z_d. All estimates are for an aperture size of 100″. The solid, short dashed and long dashed curves show the M/L ratio in an EdS universe for $\langle z_s \rangle = 0.8$, $\langle z_s \rangle = 0.9$ and $\langle z_s \rangle = 1.0$. The dotted, dot-short dashed and dot-long dashed curves show the same in an $\Omega = 0.3$, $\Lambda = 0.7$ universe. We have assumed a redshift distribution $\propto z^2 \exp[-(z/z_0)^{3/2}]$ for the source galaxies; hence $\langle z_s \rangle \approx 1.5 z_0$. A value of $\gamma(100'') = 0.06$ was assumed - see Fig.2

bution of the galaxies we used for the analysis with a magnitude-redshift relation from simulated redshift distributions (Lilly et al. 1995[3]).

- Assuming a singular isothermal sphere for the mass distribution we estimate the mass of our clump to be $M \geq 1 \times 10^{14} M_\odot$. Also estimates for the light and hence the mass-to-light ratio of the object were obtained. We arrive at $M/L \geq 500$. More details are given in Fig. 3.

- An archival ROSAT/HRI image of Abell 1942 shows, in addition to the emission of the cluster, a 3.2σ detection of a source about 1′ away from the clump centre. It is unclear whether this weak X-ray emission is connected with our dark clump or whether it is associated with a slight galaxy overdensity and hence a galaxy group seen at the position of the X-ray emission.

4 Conclusions

Using weak gravitational lensing techniques, we have found a strong lens signature $7'$ South of the cluster Abell 1942. The signal is highly significant in two high-quality data sets that were taken in two different years, with two different instruments and in two different optical bands. This makes it highly unlikely that our discovery originates from systematics like uncorrected PSF effects. Concerning the nature of our clump, no firm conclusion can be drawn at this moment. The lack of strong X-ray emission rules out a normal cluster. Already approved infrared observations, and Chandra X-ray data that we applied for, may reveal the nature of our discovery. But whatever the interpretation at this point, one must bear in mind that weak lensing opens up a new channel for the detection of massive halos in the Universe, so that one should perhaps not be surprised to find a new class of objects, or members of a class of objects with unusual properties. The potential consequences of the existence of such highly underluminous objects may be far reaching: if, besides the known optical and X-ray luminous clusters, a population of far less luminous dark matter halos exist, the normalization of the power spectrum may need to be revised, and the estimate of the mean mass density of the Universe from its luminosity density and an average mass-to-light ratio may change.

Acknowledgments

This work was supported by the TMR Network "Gravitational Lensing: New Constraints on Cosmology and the Distribution of Dark Matter" of the EC under contract No. ERBFMRX-CT97-0172, the "Sonderforschungsbereich 375-95 für Astro–Teilchenphysik" der Deutschen Forschungsgemeinschaft, and a PROCOPE grant No. 9723878 by the DAAD and the A.P.A.P.E.

References

1. T. Erben, L. Van Waerbeke, Y. Mellier, P. Schneider, J. C. Cuillandre, F. J. Castander and M. Dantel-Fort *Astronomy and Astrophysics* **355**, 23 (2000).
2. H. Hoekstra, M. Franx, K. Kuijken and G. Squires *Astrophysical Journal* **504**, 636 (1998).
3. S. J. Lilly, L. Tresse, F. Hammer, D. Crampton, O. Lefevre *Astrophysical Journal* **455**, 108 (1955).
4. P. Schneider *MNRAS* **283**, 837 (1996).

WEAK LENSING AND LARGE-SCALE STRUCTURES

WEAK LENSING STUDY OF LOW MASS GALAXY GROUPS: IMPLICATIONS FOR Ω_m

H. Hoekstra[1], M. Franx[2], K. Kuijken[1], R.G. Carlberg[3], & H.K.C. Yee[3]

[1] *Kapteyn Astronomical Institute, P.O. Box 800, 9700 AV, Groningen, The Netherlands*
[2] *Leiden Observatory, P.O. Box 9513, 2300 RA, Leiden, The Netherlands*
[3] *Department of Astronomy, University of Toronto, Toronto, Ontario M5S 3H8, Canada*

We report on the first measurement of the average mass and mass-to-light ratio of galaxy groups by analysing the weak lensing signal induced by these systems. The groups, which have velocity dispersions of 50-400 km/s, have been selected from the Canadian Network for Observational Cosmology Field Galaxy Redshift Survey (CNOC2). This survey allows the identification of a large number of groups with redshifts ranging from $z = 0.12 - 0.55$. For our analysis we use a sample of 50 groups which are selected on the basis of a careful dynamical analysis of group candidates. We detect a signal at the 99% confidence limit. The best fit singular isothermal sphere model yields an Einstein radius $r_E = 0\farcs72 \pm 0\farcs29$. This corresponds to a velocity dispersion of $\langle\sigma^2\rangle^{1/2} = 274^{+48}_{-59}$ km/s, which is in good agreement with the dynamical estimate. Under the assumption that the light traces the mass, we find an average mass-to-light ratio of $191 \pm 81\ h\mathrm{M}_\odot/\mathrm{L}_{B\odot}$ in the restframe B band. Unlike dynamical estimates, this result is insensitive to problems associated with determining group membership. We use the observed mass-to-light ratio to estimate the matter density of the universe, for which we find $\Omega_m = 0.19 \pm 0.10$ ($\Omega_\Lambda = 0$), in good agreement with other recent estimates. For a closed universe ($\Omega_m + \Omega_\Lambda = 1$), we obtain $\Omega_m = 0.13 \pm 0.07$.

1 Introduction

Galaxy groups, like the Local Group, are common structures in the universe. Altough they are numerous, groups are difficult to identify because the contrast with the smooth background of galaxies is quite low, and their galaxy properties are similar to that of the field. To date most systems have been studied using the results of large redshift surveys (e.g., Turner & Gott 1976; Ramella, Geller, & Huchra 1989; Huchra, Geller, & Corwin 1995) or X-ray observations (Mulchaey et al. 1996). The X-ray emission from groups provides a good diagnostic to examine whether the selected groups are bound systems, and not chance projections (e.g., Zabludoff & Mulchaey 1997). However, selecting groups on the basis on their X-ray emission might lead to a selection of more massive, or more evolved systems.

Measuring the amount of matter locked up in these typical systems is important, but a measurement of the average mass-to-light ratio of galaxy groups may be even more important (e.g., Gott & Turner 1977). This is because it provides a good measure of the mass-to-light ratio of the field, i.e., the universe as a whole. Subsequently, this result can be used to obtain an estimate for the matter density Ω_m (Oort 1958; Gott & Turner 1977), similar to what has been done for rich clusters of galaxies (e.g., Carlberg et al. 1997; Carlberg et al. 1999).

However, measuring the mass or mass-to-light ratio of groups selected from redshift surveys is difficult. Nolthenius & White (1987) showed that the dynamical masses inferred from such surveys depend on the survey parameters, the group selection procedure, and the way galaxies cluster. Consequently, an independent measure of the group mass is needed. In this letter we study galaxy groups by their weak lensing effect on the shapes of the images of the faint background sources.

The amplitude of the weak lensing signal is proportional to the mass of the lens, and as a result the expected signal from an individual galaxy group is very low. To circumvent this problem we study the properties of the ensemble averaged group by stacking the signals of many groups at intermediate redshifts, where the lensing signal is maximal.

Galaxy groups identified in the Canadian Network for Observational Cosmology Field Galaxy Redshift Survey (CNOC2) (Lin et al. 1999; Yee et al. 2000; Carlberg et al. 2000) are ideal for a weak lensing study of their mass distribution: the survey provides a large sample of groups at intermediate redshifts, which can be imaged efficiently by wide field imaging.

2 Observations and analysis

The CNOC2 survey targeted four widely separated patches on the sky to study the dynamics of galaxy clustering at intermediate redshifts. Redshifts of approximately 6200 galaxies down to $R_C = 21.5$ have been measured, resulting in a large sample of galaxies at intermediate redshifts ($z = 0.12 - 0.55$). A detailed description of the survey and the catalogues is given in Yee et al. (2000). We have observed the central parts of the two patches 1447+09 and 2148-05 using the 4.2m William Herschel Telescope at La Palma. To cover the central regions of the patches, a mosaic of 6 pointings was observed, resulting in a field of view of 31 by 23 arcminutes, with a typical total integration time per pointing of 1 hour in R, and seeing ranging form $0\overset{''}{.}6$ to $1\overset{''}{.}0$.

Our object analysis is based on the procedure developed by Kaiser, Squires, & Broadhurst (1995) and Luppino & Kaiser (1997), with a number of modifications which are described in Hoekstra et al. (1998) and Hoekstra et al. (2000). The weak lensing analysis uses galaxies with $22 < R < 26$ as background sources. This results in a sample of 31615 galaxies for the 1447 field, and 25982 sources for the 2148 field. These catalogs contain some faint group members, but we find that the contamination of the lensing signal by these galaxies is negligible.

3 Galaxy Groups

Finding galaxy groups in a redshift survey such as CNOC2 is a difficult problem. The crucial step is to determine the group membership, which is complicated by velocity space interlopers. This makes a reliable dynamical mass estimate difficult. The weak lensing mass estimate is more robust against contamination by interlopers, as it relies only on the position of the overdensity. Lensing in itself does not provide information as to whether the studied structures are gravitationally bound galaxy groups. For our analysis we use the groups presented by Carlberg et al. (2000). The detailed selection scheme is described in detail by Carlberg et al. (2000), but here we will mention briefly the important steps:

1 Pick a cosmology for the analysis (H_0 = 100 km/s/Mpc, $\Omega_m = 0.2$, and $\Omega_\Lambda = 0$). We note here that the resulting sample of groups does not change significantly if a different cosmology is used.

2 Set the sample's redshift and absolute luminosity limits (k-corrected and evolution-compensated, of $M_R^{ke} = -18.5$ mag, no initial redshift limits).

3 Pick a maximum projected radius r_p (we use $0.25h^{-1}$ Mpc) and velocity range (which corresponds to $5h^{-1}$ Mpc) and use these to define the local density relative to a smooth

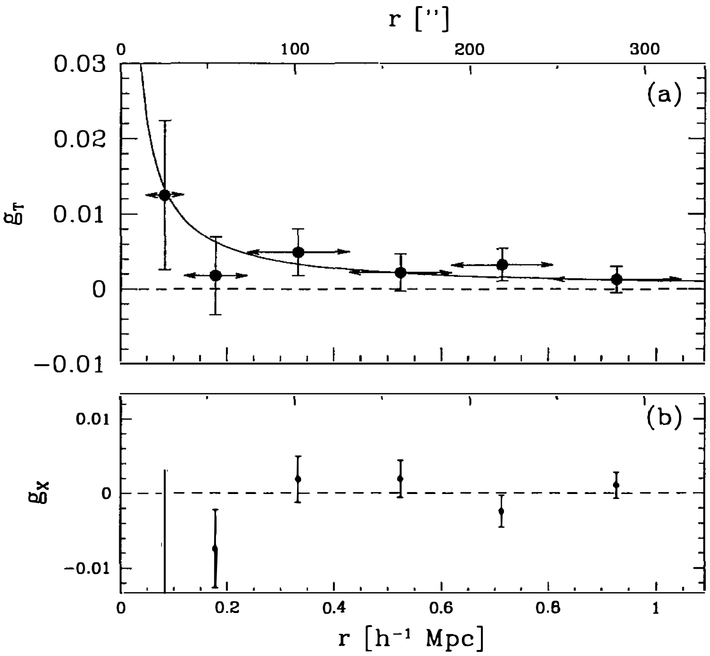

Figure 1: (a) The ensemble averaged tangential distortion as a function of radius around the 50 galaxy groups from Carlberg et al. (2000). The amplitude of the signal corresponds to that of the 'average' group at the median group redshift $z = 0.33$. The profile of the best fit singular isothermal sphere model (to the solid points), which has a velocity dispersion of 274^{+48}_{-59} km/s, is indicated by the solid line. (b) The signal when the phase of the distortion is increased by $\pi/2$: no signal should be present if the signal in (a) is due to lensing.

$n(z)$. If the search radii initially give less than three neighbors, then multiply the smoothing lengths by 1.5 and repeat it for this galaxy.

4 Select the highest density ungrouped galaxy and begin a new group.

5 Add to the group all galaxies having density greater than the mean field density within the fixed maximum projected radius and velocity separation.

6 Determine the weighted mean x, y, z and σ_1. Based on σ_1, estimate the corresponding r_{200}, and trim galaxies beyond, or add galaxies within, $r_p = 1.5r_{200}$ and $\Delta v = 3\sigma_1$. Repeat step 6 four more times, requiring that the last two iterations have an identical result.

7 Finally, drop galaxy singles and pairs from the catalogue.

The resulting sample consists of 50 groups which are within the fields we have observed. The average redshift of the groups is $z = 0.33$, and they have velocity dispersions ranging from $50 - 400$ km/s. Approximately one quarter of the galaxies are assigned to a group. The redshift information is crucial because the contrast of the groups with the field is low: the average group corresponds to a 1.2σ overdensity in number counts.

4 Mass and mass-to-light of galaxy groups

We stack the average distortion as a function of radius of the groups, taking into account the fact that the various groups are at different redshifts. The azimuthally averaged tangential distortion as a function of radius around the 50 groups is presented in Figure 1a. The amplitude of the signal corresponds to that of the 'average' group at a redshift of $z = 0.33$. The signal is significant at the 99% confidence level. We tested the robustness of the signal in various ways, and conclude that the observed signal is due to weak lensing by galaxy groups.

The best fit singular isothermal sphere model ($\kappa(r) = r_E/2r$) to the ensemble averaged distortion from the sample of 50 galaxy groups from Carlberg et al. (2000) yields an Einstein radius of $r_E = 0''.72 \pm 0''.29$.

The next step is to relate the Einstein radius to an estimate of the velocity dispersion. To do so we use photometric redshift distributions inferred from the Hubble Deep Fields (Fernández-Soto, Lanzetta, & Yahil 1999; Chen et al. 1998), which generally work well as has been demonstrated by Hoekstra et al. (2000) The strength of the lensing signal as a function of source redshift is characterized by β, which is defined as $\beta = \max[0, D_{ls}/D_s]$, where D_{ls} and D_s are the angular diameter distances between the lens and the source, and the observer and the source. For each group-galaxy pair we compute the corresponding value of β based on the R band magnitude of the source and the redshift of the group.

We find $\langle\beta\rangle = 0.39$, which results in an ensemble averaged group velocity dispersion of $\langle\sigma^2\rangle^{1/2} = 274^{+48}_{-59}$ km/s ($\Omega_m = 0.2$, and $\Omega_\Lambda = 0$) for the sample of groups from Carlberg et al. (2000). For $\Omega_m = 0.2$ and $\Omega_\Lambda = 0.8$ it changes to $\langle\sigma^2\rangle^{1/2} = 258^{+45}_{-56}$ km/s. These results are in good agreement with the average velocity dispersion of 230 km/s from the velocities of the group members.

Under the assumption that the light traces the mass, we derive the expected tangential distortion as a function of radius. To measure the mass-to-light ratio, we scale the resulting tangential distortion to match the observed signal. In Figure 2a the resulting profile (solid line) is shown. The ratio of the computed and observed signal is presented in Figure 2b, and is consistent with a constant mass-to-light ratio with radius for which we find a value of 191 ± 81 $h\mathrm{M}_\odot/\mathrm{L}_{\mathrm{B}\odot}$ in the restframe B band.

This measurement of the mass-to-light ratio has not been corrected for luminosity evolution. If the luminosity evolution scales with redshift as $L_B \propto (1 + z)$ (e.g., Lin et al. 1999), we obtain a value of 254 ± 108 $h\mathrm{M}_\odot/\mathrm{L}_{\mathrm{B}\odot}$, corrected to $z = 0$. Carlberg et al. (1997) measured the mass-to-light ratio of a sample of 16 rich clusters, for which they found an average value of $M/L_r = 237 \pm 41 \mathrm{M}_\odot/\mathrm{L}_{r\odot}$. Their result in the B-band corresponds to 438 ± 76 $h\mathrm{M}_\odot/\mathrm{L}_{\mathrm{B}\odot}$ (where we also corrected for luminosity evolution to $z = 0$). Thus the average group mass-to-light ratio in the B band is lower than the value typically found for rich clusters.

Lensing is sensitive to all matter along the line of sight. To examine the contribution of the remaining galaxies we redid the calculation of the light profile, using all galaxies with redshifts. In this case the average mass-to-light ratio is found to be 183 ± 78 $h\mathrm{M}_\odot/\mathrm{L}_{\mathrm{B}\odot}$, in excellent agreement with our measurement from group members only. An important consequence of this exercise is that the weak lensing estimate of the mass-to-light ratio is insensitive to the determination of group membership, unlike the dynamical estimators.

5 Estimate of Ω_m

A well known method to estimate the matter density of the universe was proposed by Oort (1958): Ω_m is the product of the universe's mass-to-light ratio and its luminosity density. Carlberg et al. (1997) used the observed mass-to-light ratios of a sample of rich clusters to estimate Ω_m, for which they found a value of $\Omega_m = 0.19 \pm 0.06$.

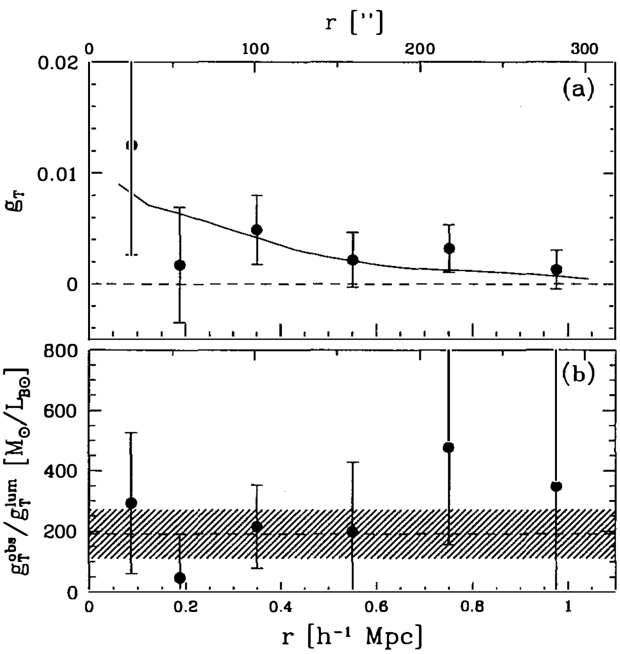

Figure 2: (a) Plot of the average tangential distortion as a function of radius from the ensemble of 50 galaxy groups from the CNOC2 survey. The solid line is the expected tangential distortion (scaled by the mass-to-light ratio to fit the observations) derived from the average radial light profile, under the assumption that the mass-to-light ratio is constant with radius. (b) The ratio of the observed distortion and the derived distortion from the light (taking $M/L_B = 1$ in solar units). The shaded region indicates the one σ region around the average of the points. The observations are consistent with a constant mass-to-light ratio of 191 ± 81 $h\mathrm{M}_\odot/\mathrm{L}_{B\bullet}$.

The galaxy properties of rich clusters are quite different from that of the field, and a large correction is needed to relate the cluster mass-to-light ratio to the mass-to-light ratio of the universe. However, we found a small difference between the average restframe colours of group galaxies and the field, which is caused by a small difference in stellar populations. We make a small correction for this effect, and find that the B band mass-to-light ratio of the field is lower by a factor 1.15 compared to the value found for the groups.

We combine our estimate of the mass-to-light ratio with the results from Lin et al. (1999), which are based on the same data. Convolving the redshift distribution of the groups with their redshift dependent luminosity density yields $j = (3.2 \pm 0.6) \times 10^8 h\mathrm{L}_{B\odot}\mathrm{Mpc}^{-3}$ (assuming $\Omega_m = 0.2$ and $\Omega_\Lambda = 0$). We obtain $\Omega_m = 0.19 \pm 0.10$ for an $\Omega_\Lambda = 0$ cosmology. Our estimate for Ω_m decreases to a value of $\Omega_m = 0.13 \pm 0.05$ for $\Omega_\Lambda = 0.87$.

Our results on Ω_m agree well with the result from Carlberg et al. (1997), and combined constraints from high redshift supernovae (e.g., Perlmutter et al. 1999) and CMB measurements (e.g., Efstathiou et al. 1999, De Bernardis et al. 2000)

Some caveats should be noted as well. We have assumed that the light traces the mass. If the dark matter is more extended than the light our estimate for Ω_m should be interpreted as a lower limit. In particular, if a large fraction of the mass is distributed uniformly through the universe, it cannot be detected by our analysis, as the weak lensing analysis is only sensitive to mass contrasts. Also the correction for the colour difference between group members and the field is somewhat uncertain.

The results presented here are based one quarter of the sample of groups found by Carlberg et al. (2000). Observations of the remaining groups would approximately double the accuracy of the measurements, which is important to test main assumption made in our analysis: does the light trace the mass?

Acknowledgments

The WHT observations for this project have been supported financially by the European Commission through the TMR program 'Access to large-scale facilities', awarded to the Instituto de Astrofisica de Canarias. The conference visit was supported by the TMR Network 'Gravitational Lensing: New Constraints on Cosmology and the Distribution of Dark Matter' of the EC.

1. Carlberg, R.G., Yee, H.K.C., & Ellingson, E. 1997, ApJ, 478, 462
2. Carlberg, R.G., Yee, H.K.C., Morris, S.L., Lin, H., Ellingson, E. Patton, D., Sawicki, M., & Shepherd, C.W. 1999, ApJ, 516, 552
3. Carlberg, R.G. et al. 2000, in preparation
4. Chen, H.-W., Fernández-Soto, A., Lanzetta, K.M., Pascarelle, S.M., Puetter, R.C., Yahata, N., & Yahil, A., preprint, astro-ph/9812339
5. De Bernardis, P., et al. 2000, Nature, 404, 955
6. Efstathiou, G., Bridle, S.L., Lasenby, A.N., Hobson, M.P., & Ellis, R.S. 1999, MNRAS, 303, 47
7. Fernández-Soto, A., Lanzetta, K.M., & Yahil, A. 1999, ApJ, 513, 34
8. Gott, J.R. III, & Turner, E.L. 1977, ApJ, 213, 309
9. Hoekstra, H., Franx, M., Kuijken, K., & Squires, G. 1998, ApJ, 504, 636
10. Hoekstra, H., Franx, M., Kuijken, K. 2000, ApJ, 532, 88
11. Huchra, J.P., Geller, M.J., & Corwin, H.G. 1995, ApJS, 99, 391
12. Kaiser, N., Squires, G., & Broadhurst, T. 1995, ApJ, 449, 460
13. Lin, H., Yee, H.K.C., Carlberg, R.G., Morris, S.L., Sawicky, M., Patton, D.R., Wirth, G., & Shepherd, C.W. 1999, ApJ, 518, 533
14. Luppino, G.A., Kaiser, N. 1997, ApJ, 475, 20
15. Mulchaey, J.S., Davis, D.S., Mushotzky, R.F., & Burstein, D. 1996, 456, 80
16. Nolthenius, R., & White, S.D.M. 1987, MNRAS, 235, 505
17. Oort, J.H. 1958, in La Structure et L'évolution de L'Universe, Onzième Conseil de Physique, ed. R. Stoops (Solvay: Bruxelles), 163
18. Perlmutter, S., Aldering, G., Goldhaber, G., Knop, R.A., Nugent, P., et al. 1999, ApJ, 517, 565
19. Ramella, M., Geller, M.J., & Huchra, J. 1989, ApJ, 344, 57
20. Turner, E.L., & Gott, J.R. III 1976, ApJS, 32, 409
21. Yee, H.K.C., Ellingson, E., & Carlberg, R.G. 1996, ApJ, 102, 269
22. Yee, H.K.C. et al. 2000, ApJS, accepted, astro-ph/0004026
23. Zabludoff, A.I., & Mulchaey, J.S. 1998, ApJ, 496, 39

WEAK WEAK LENSING: HOW ACCURATELY CAN SMALL SHEARS BE MEASURED?

K. KUIJKEN
Kapteyn Instituut, PO Box 800, 9700 AV Groningen, The Netherlands

Now that weak lensing signals on the order of a percent are actively being searched for (cosmic shear, galaxy-galaxy lensing, large radii in clusters...) it is important to investigate how accurately weak shears can be determined. Many systematic effects are present, and need to be understood. I show that the Kaiser et al. technique can leave residual systematic errors at the percent level (through imperfect PSF anisotropy correction), and present an alternative technique which is able to recover shears a factor of ten weaker.

1 Introduction

Weak lensing has evolved in the last ten years into a quantitative tool in cosmology. The goal is no longer to demonstrate a convincing detection of the effect, but to make real measurements of the shear, and turn these into real measurements of the projected mass density in a given direction.

An important aspect of this quantitative work is to control systematic effects. While it is now relatively straightforward to demonstrate convincingly a coherent alignment of galaxy distortions around a massive foreground cluster, for example, it is much harder to quantify the amount of this shear in the presence of seeing, camera distortions, or uncertain redshift distributions of the source galaxies. As an example, Fig 1 shows the weak shear field around the $z \sim 0.83$ cluster MS1054-03 from a 6-exposure WFPC2 mosaic[5]. In order to come to this shear field, many of the effects to be discussed in the following section had to be quantified and corrected for.

Nevertheless, this is an example of a rather strong lensing effect, shears around 10%. The field is also evolving in the direction of working with weaker and weaker gravitational shears. Ground-based cameras now have wider fields which allow the outskirts of clusters to be observed efficiently. For a singular isothermal sphere model the shear falls with radius as r^{-1}, and it is now routinely possible to reach the region of clusters where the shear should be around 1%. While formally signal-to-noise is a very weak function of radius (the shear drops outwards, but the number of available background galaxies whose shapes may be averaged to yield a shear estimate increases with radius), systematic effects become a serious concern. Also lower-mass clusters and groups, much more representative of the universe than the massive X-ray clusters, are now within reach (Hoekstra et al 2000).

In clusters there is at least the independent sanity check of making sure that the shear is aligned roughly with the observed cluster. Lately, though, a lot of effort has gone into the search

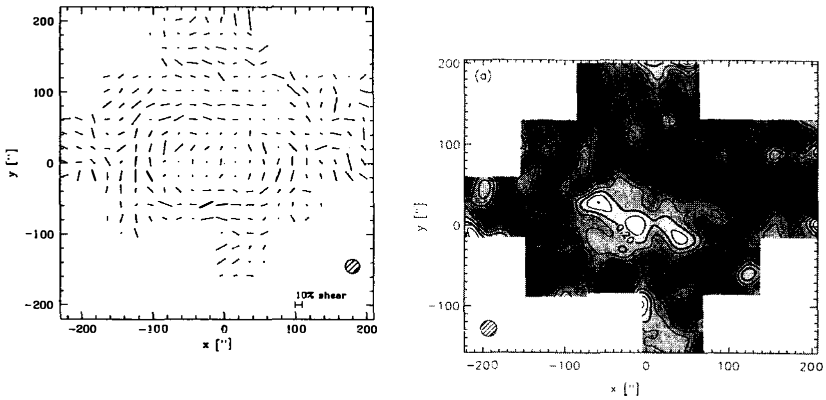

Figure 1: Weak Lensing shear field (top), and mass map (right) of the $z = 0.83$ cluster MS1054-03 by Hoekstra et al (2000).

for cosmic shear, which is the lensing effect caused by large-scale structure[14,1,15,9]). Here the measurement is rather similar to the early cosmic background radiation anisotropy experiments, and constitutes the search for an excess variance. The effect is also on the level of a percent shear or less, but its geometry is a priory unclear.

Also galaxy-galaxy lensing is now being carried out with enormous numbers of lens-source pairs, and formal averaging statistics allow shears of well below a percent to be measured (see Fisher, this conference). As in galaxy-galaxy lensing the lens and source are rather close together on the sky, any large-scale systematic distortion cancels out to first order, making it a little less susceptible to residual systematics.

2 Systematic errors

The image of a distant galaxy that we record on a CCD is a

- charge-transferred,
- pixellated,
- camera-distorted,
- atmospherically blurred,
- gravitationally lensed,
- random-shape,
- randomly-oriented

galaxy. We can only extract the lensing information if we can control all these other effects, either by avoiding them, or by measuring and correcting for their effects.

Fortunately the sky contains a number of calibrators, stars in the field. These are for our purposes point-like, and so measure the smearing effects of atmosphere and optics simultaneously with the galaxies. Galaxy orientations on the sky are random as far as we know. CCD effects can be calibrated by observing at different orientations with respect to the pixel grid, or by using totally different cameras altogether. The distortion of the camera can be calibrated with astrometric standard fields, or by comparing offset exposures.

In principle, therefore, it looks as if the required information exists to disentangle the effects of gravitational lensing from the other ones. Assuming for the moment that this has been done, this means that for each background galaxy an estimate for the distortion can be obtained.

The distortions g_i, (i = 1, 2) are equivalent to the axis ratio and major axis orientation observed when an intrinsically round source is lensed. g is related to the distortion matrix

$$\begin{pmatrix} 1-\kappa-\gamma_1 & -\gamma_2 \\ -\gamma_2 & 1-\kappa+\gamma_1 \end{pmatrix} \tag{1}$$

through $g_i = \gamma_i/(1-\kappa)$. Here γ is the gravitational shear, and κ the convergence. The latter is a measure of the surface mass density in the lens plane, and is the goal of weak lensing.

There are several complications in converting the observed distortions into a projected mass density.

- *PSF.* The Point Spread Function affects galaxy images in various ways. If the PSF is anisotropic, it will imprint this anisotropy onto the observed image. On the other hand, since it has a finite width it will tend to increase the size of faint images. As the PSF acts as a convolution, galaxies of different size are affected by PSF in different degrees.

- *Camera Shear.* The camera maps the sky onto the focal plane, but often does not do this without introducing some distortion. It is easy to show that such a distortion produces shear, and that this acts as a simple additive effect onto the observed gravitational shear.

- *(1-κ).* The measured distortion is a combination of γ and κ. To derive the shear it is therefore necessary to have an estimate of the convergence. This is a fundamental limitation of weak lensing, and is known as the mass-sheet degeneracy[12]. Usually one assumes that the mass distribution at the outer edges of the field follows some simple model (zero, singular isothermal, ...), or one leaves the uncertain κ zeropoint in the result[6].

- *Redshift Distribution.* The deflection angle in lensing depends on the relative distances between observer, source and lens. As the source distances are usually unknown, or only known statistically, the lensing angles, and hence the shears, need to be corrected to infinite source redshift. This correction factor is usually referred to as the β factor:

  $$\gamma(\text{observed}) = \beta\gamma(\text{infinite source distance}), \tag{2}$$

  where β is the ratio of lens to source distance. The effect is most important for distant cluster work, or for situations where lenses and sources are distributed similarly down the line of sight as in cosmic shear measurements. Source galaxies used for lensing are usually so faint that they are beyond the reach of spectroscopic redshift surveys, so models or photometric redshift studies need to be used. The analysis performed for MS1054 (fig. 1) relied on the HDF redshift distributions[3,2]. A discrepancy of around 10%, which may well be a form of cosmic variance, exists between the two Deep Fields.

- *β spread.* Even once the mean redshift of the sources is determined, a second-order effect exists which depends on the width of the distribution of β. This is because the distortion is not linear in κ, and so the observed distortion is

  $$g(\text{observed}) = \frac{\gamma(\text{observed})}{1-\kappa(\text{observed})} = \frac{\beta\gamma}{1-\beta\kappa} = \beta\gamma + \beta^2\kappa\gamma + O(\kappa^2) \tag{3}$$

  which, when averaged over source galaxies with different redshift requires knowledge of $\overline{\beta^2}$, and hence of the variance of the β-distribution[5,13].

Most of these effects are important when it comes to properly calibrating the strength of a detected distortion pattern, and turning it into a real mass.

The correction for PSF effects is technically the most difficult of these steps. The most extensively used method is the KSB[8] method, which can be considered the current 'industry standard.' Of the many weak lensing results that have been obtained to date[11], most have employed this technique.

3 Tests of the KSB method

The KSB method uses a combination of centered second image moments as its shape statistic. This is a logical choice: these moments measure the orientation and elongation of an ellipse, which is a reasonable first approximation to galaxy images. KSB worked out how these image moments, and the shape statistics derived from them, behave under various distorting effects. The result is a formalism for deriving 'polarizabilities', matrices which express the response of the image polarization

$$(e_1, e_2) \equiv \left(\frac{I_{xx} - I_{yy}}{I_{xx} + I_{yy}}, \frac{2I_{xy}}{I_{xx} + I_{yy}} \right) \tag{4}$$

to gravitational shear, and to PSF smearing. KSB show how these polarizabilities can themselves be written as combinations of higher-order image moments. The image moments I_{ij} of the galaxy image intentity $f(x, y)$ are computed with a circular weight function $W(r)$, to prevent poisson noise from dominating the measurements:

$$I_{ij} = \int dx dy f(x, y) W(r). \tag{5}$$

In particular, the effect on (e_1, e_2) of a distant galaxy under smearing by an anisotropic PSF is given by

$$\delta e_\alpha = P^{\rm sm}_{\alpha\beta} p_\beta \tag{6}$$

where p is the PSF anisotropy, $(I_{xx} - I_{yy}, 2I_{xy})$, this time constructed from unweighted second moments.

This formalism works very well, but not perfectly. An example is shown in figure 2, which is the average of two normalized gaussians, of (x, y)-variance $(1.1, 1)$ and $(3.9, 4)$ respectively. The total variances in x and y of this PSF are the same, i.e. its anisotropy p is zero. No matter what the polarizability of a source, therefore, the KSB formulae would predict no effect on the polarization of a source after convolution with this PSF. However, as figure 2 shows, this is not correct, because of the radial weight function used in the computation of the polarizations. Errors of the order of a percent in the image polarization can result.

A set of simulations illustrating such systematic effects is shown in fig. 3. A more extensive discussion is given in Kuijken (1999)[10].

The residual systematics are not fundamental: the PSF is known perfectly, so all required information is there. It is instead a consequence of a mathematical assumption made by KSB (that the PSF can be written as a convolution of a very compact anisotropic kernel with a more extended, round function) to enable the polarizabilities to be constructed.

4 An alternative algorithm: Constant Ellipticity Objects

Alternative algorithms have been developed, but none are in as wide a use as KSB. One class is based on reconvolving the data with a circularizing kernel[15,7]. This is a rather direct way to reduce PSF effects, but creates correlated noise and, unavoidably, somewhat degrades the data.

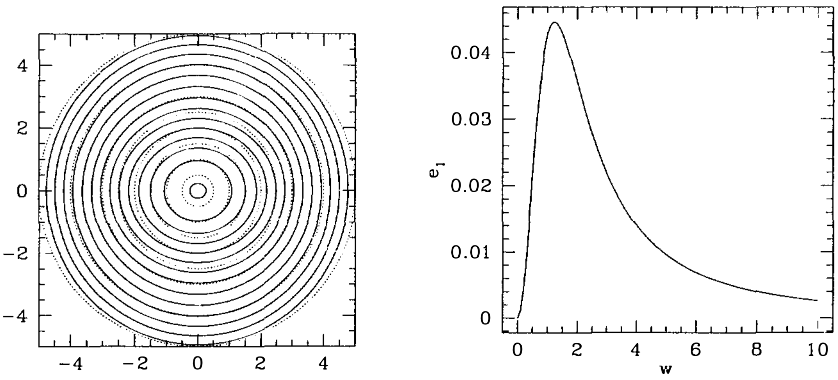

Figure 2: Left: An example of a PSF which is isotropic in its second moments, but not intrinsically. Right: the polarization of this PSF when it is measured with different gaussian weight functions (1-σ radius w).

An alternative algorithm[10] does not rely on modelling the second moments, but instead is a direct fit of the sources to a sheared, instrinsically circular source, convolved with the PSF. As a sheared circular source has ellipticity which is constant with radius, the algorithm has been dubbed Constant Ellipticity Objects (CEO).

An exhaustive discussion will not be given here, as the details may be found in the original paper. The essence of the results are as follows:

- When the sources are instrinsically round, the algorithm recovers the shears from noise-free images, even for very anisotropic PSF's which the KSB technique does not correct to better than a percent.

- When Poisson noise is added to simulated images, the best-fit shears are unbiased, and the scatter is very similar to the KSB method. (This shows that the KSB method, even though it only uses a few moments of each image, is close to optimal in the amount of information it uses from the images).

- When the algorithm is applied to sources which are not intrinsically round, but which are made to look like disk/bulge systems seen at various orientations and inclinations, the ensemble average of the individual shear estimates is within a few tenths of a percent of the correct value. I.e., even though the individual galaxies are fit with a model which is not correct (they are not intrinsically round) the errors made average out (see Fig 4).

5 Consistency Checks

However shears are measured, it is important to be able to perform consistency checks on the results. Below are listed a set of tests that can be performed.

- Transform corrected galaxy polarizations $e_1 \rightarrow e_2$; $e_2 \rightarrow -e_1$. Surface mass density should now be consistent with zero.
- There should be no correlations between γ and e^*, the polarization of the stars used in the correction for PSF effects.
- Results should be independent of wavelength observed in, or instrument.

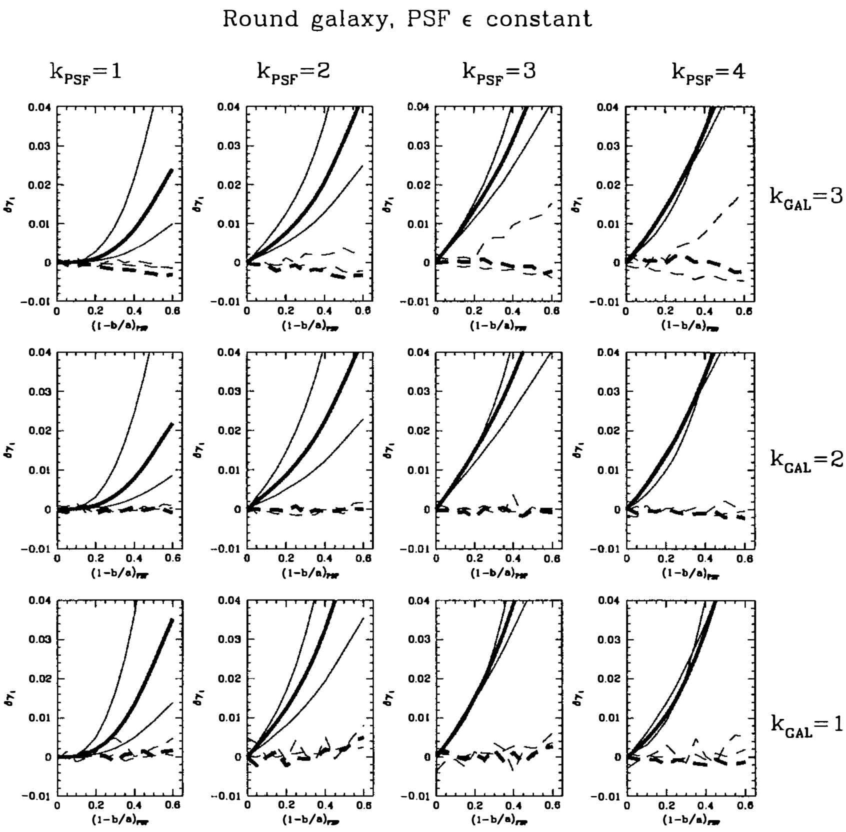

Figure 3: Simulations of the extent to which the KSB (solid lines) and CEO (ashed lines) algorithms corrects an input PSF anisotropy. Double-gaussian PSF's of axis ratio b/a were convolved with round double-gaussian 'galaxies', and analysed with both algorithms. k is the ratio of the dispersions of the two gaussian components: $k=2$ is roughly exponential, $k=3$ is roughly de vaucouleurs. No lensing was simulated here, so the derived shears should be zero. Several percent residuals remain for the most non-gaussian PSF's.

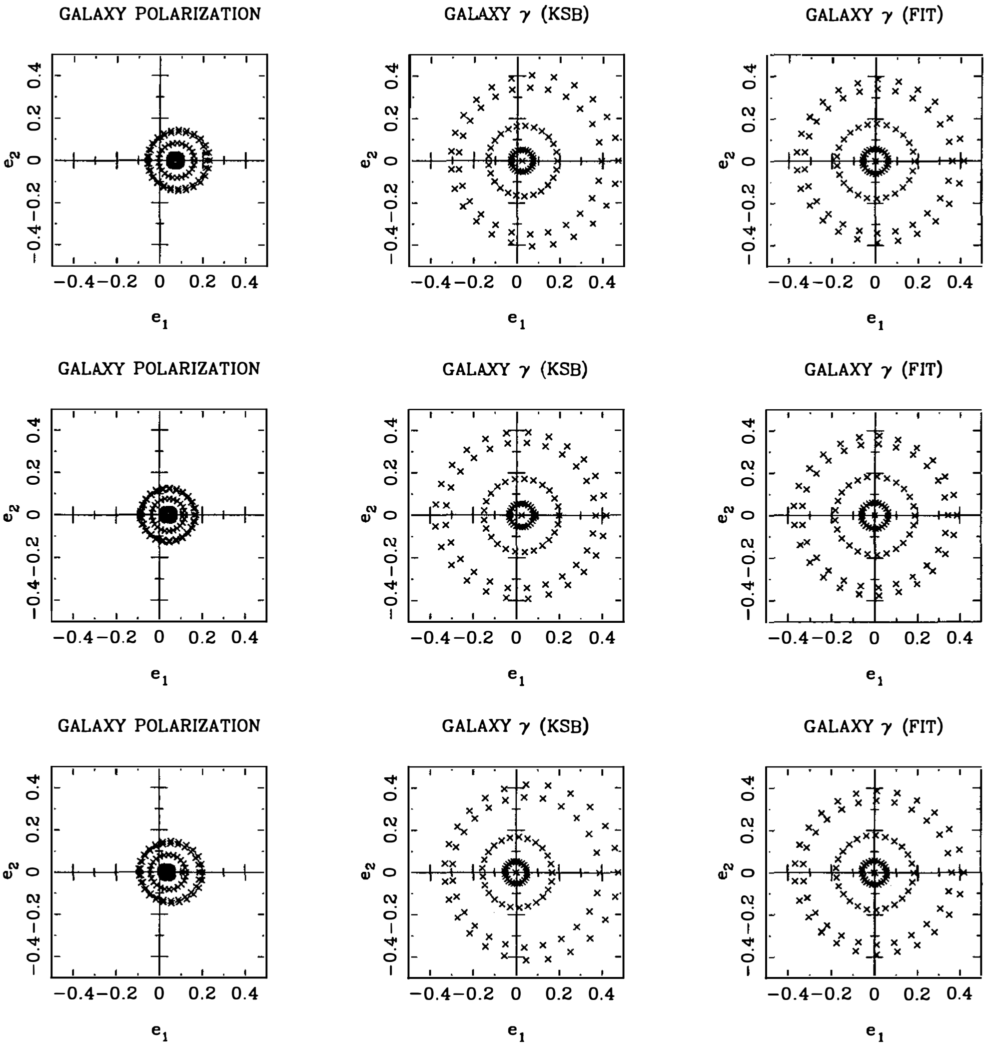

Figure 4: Various galaxy models, of different elongations and orientations, convolved with anisotropic PSFs and then analysed with the CEO and KSB algorithms. Left column: raw polarizations. Middle column: shear deduced from the KSB formalism. Right column: shear deduced from the CEO method. The different rows correspond to different radial ellipticity profiles of the PSF.

- Shear fields should not rotate with the instrument or detectors.
- Smear image data with a typical PSF, and re-analyse these images. Results may be a little noisier, but should be consistent with original result. [this tests algorithm, not data]
- Vary the weight function radius in KSB
- Track the signal as a function of source size. Smaller sources are more sensitive to PSF

6 Summary

Weak lensing work is moving into the regime of very weak signals. Lensing by large-scale structure, the outskirts of clusters, and low-mass galaxy groups and individual galaxies are all being targetted. Particularly the first results being reported elsewhere at this conference on the detection of lensing by large-scale structure are very exciting.

Measuring these very weak distortions is a tricky business, because many other effects need to be characterized and corrected for. I have described a new algorithm, which performs very well on test data, which is able to reduce systematic uncertainties associated with the correction for PSF anisotropy considerably. Applications on real data are in progress.

Acknowledgments

This work, and this conference visit, was supported by the TMR Network "Gravitational Lensing: New Constraints on Cosmology and the Distribution of Dark Matter" of the EC under contract No. ERBFMRX-CT97-0172.

References

[1] Bacon, D., Refregier, A., and ELlis, R. 2000, MNRAS, in press (astro-ph/0003008)
[2] Chen, H.-W., et al. 1998, preprint (astro-ph/9812339)
[3] Fernández-Soto, A., Lanzetta, K. M. and Yahil, A. 1999, ApJ, 513, 34
[4] Hoekstra, H., Franx, M., Kuijken, K. and Squires, G. 1998, ApJ, 504, 636
[5] Hoekstra, H., Franx, M. and Kuijken, K. 2000, ApJ, 532, 88
[6] Kaiser, N. 1995, ApJl, 439, L1
[7] Kaiser, N. 2000, ApJ, 537, 555
[8] Kaiser, N., Squires, G. and Broadhurst, T. 1995, ApJ, 449, 460
[9] Kaiser, N., Wilson, G. and Luppino, G.A., ApJL, submitted (astro-ph/0003338)
[10] Kuijken, K. 1999, A&A, 352, 355
[11] Mellier, Y. 1999, ARAA, 37, 127
[12] Schneider, P., Ehlers, J. ;. and Falco, E. E. 1992, Gravitational Lenses. Springer-Verlag:Berlin
[13] Seitz, C. and Schneider, P. 1997, A&A, 318, 687
[14] Van Waerbeke, L. and 12 colleagues 2000, A&A, 358, 30
[15] Wittman, D.M., Tyson, J.A., Kirkman, D., Dell'Antonio, I. and Bernstein, G. 2000, Nature, in press (astro-ph/0003014)

COSMIC SHEAR WITH THE CFHT

L. VAN WAERBEKE[1,2], Y. MELLIER[2,3], T. ERBEN[4], J.C. CUILLANDRE[5], F. BERNARDEAU[6], R. MAOLI[2,3], E. BERTIN[2,3], H.J. Mc CRACKEN[7], O. LE FEVRE[7], B. FORT[2], M. DANTEL-FORT[3], B. JAIN[8], P. SCHNEIDER[4]

[1] *Canadian Institut for Theoretical Astrophysics, 60 St Georges Str., Toronto, M5S 3H8 Ontario, Canada.*

[2] *Institut d'Astrophysique de Paris. 98 bis, boulevard Arago. 75014 Paris, France.*

[3] *Observatoire de Paris. DEMIRM. 61, avenue de l'Observatoire. 75014 Paris, France.*

[4] *Max Planck Institut fur Astrophysiks, Karl-Schwarzschild-Str. 1, Postfach 1523, D-85740 Garching, Germany.*

[5] *Canada-France-Hawaii-Telescope, PO Box 1597, Kamuela, Hawaii 96743, USA*

[6] *Service de Physique Théorique. C.E. de Saclay. 91191 Gif sur Yvette Cedex, France.*

[7] *Laboratoire d'Astronomie Spatiale, 13376 Marseille Cedex 12, France*

[8] *Dept. of Physics, Johns Hopkins University, Baltimore, MD 21218, USA*

We present preliminary results of our cosmic shear survey currently in progress at the Canada-France-Hawaii Telescope (CFHT). We analysed 1.7 sq. degrees of high quality data (seeing below 1 arcsec), out of which we were able to measure a significant correlation of galaxy shape-orientation over several arcmin scale. We present measurements of the variance of the shear $\langle\gamma^2\rangle$ and of the correlation functions $\langle e_r(\theta)e_r(0)\rangle$, $\langle e_t(\theta)e_t(0)\rangle$, and we show that the signal is consistent with gravitational lensing by large scale structures predictions. The level of residual systematics after Point Spread Function correction is discussed and shown to be small compared to our measured signal. We outline several possible future evolutions of our work by using additional data of our lensing survey now extended to 9 sq. degrees.

1 Introduction

Since the pioneering works by [3,12,19,29], gravitational lensing by large scale structure has been recognized as a potential powerful probe of the mass distribution in the Universe at scales from 1 arcmin to several degrees. The effect we are looking for consists of a small stretching of distant galaxies by the foreground matter, with an amplitude of 1-5 percents of distortion. Since the induced distortion is very small compared to the intrinsic ellipticities of the galaxies (~ 0.3), it can be observed only statistically by measuring the averaged orientation and elongation of several galaxies. Unfortunately telescope imaging defects (like optical distortion, tracking errors, etc...) induce also a significant coherent elongation of the galaxies, very similar to the gravitational lensing effect we wish to measure. Therefore the most challenging part of the analysis is the correction of the intrinsic telescope defects (which makes the Point Spread Function anisotropic) down to a level smaller than the expected lensing signal. This problem prevented the detection of the lensing effect in the earlier searches [20,24,28]. Recently a significant measurement of the galaxy alignment was found thanks to the improvement of the image quality [23], but the analyzed fields were small, and yet it was not clear what sort of mass distribution was responsible for the lensing effect.

Table 1: List of the fields. Most of the exposures were taken in the I band at CFHT. The total area is 1.7 deg^2, and the 8 fields are uncorrelated.

Target	Name	Camera	Used area	Filter	Exp. time	Period	seeing
F14P1	F1	CFH12K	764 arcmin^2	V	5400 sec.	May 1999	0.9"
F14P2	F2	CFH12K	764 arcmin^2	V	5400 sec.	May 1999	0.9"
F14P3	F3	CFH12K	764 arcmin^2	V	5400 sec.	May 1999	0.9"
CFDF-03	F4	UH8K	669 arcmin^2	I	17000 sec.	Dec. 1996	0.75"
SA57	F5	UH8K	669 arcmin^2	I	12000 sec.	May 1998	0.75"
A1942	F6	UH8K	573 arcmin^2	I	10800 sec.	May 1998	0.75"
F02P1	F7	CFH12K	1050 arcmin^2	I	9360 sec.	Nov. 1999	0.8"
F02P4	F8	CFH12K	1050 arcmin^2	I	7200 sec.	Nov. 1999	0.9"

The fundamental importance of a clean PSF correction pushed many groups to design specific methods of image analysis [4,13,14,16,21,27]. During the preparation of our cosmic shear program, we tested intensively the Kaiser, Squires and Broadhurst (KSB) correction scheme on highly realistic simulations [7]. We found that the KSB method can easily reach the 1% accuracy PSF correction even for severely deteriorated PSF's as we obtain in real observations. A 1% accuracy might be not sufficient to measure the gravitational lensing effect at the degree scale, but at the arcmin scale the gravitational lensing signal is enhanced by the non-linear evolution of the large-scale-structures [9], and the variance of the shear $\langle\kappa^2\rangle$ can be as high as $3-5\%$. We are therefore confident that the present day technology is enough to detect the cosmic shear effect, even if significant improvements remain to be done to fully exploit the scientific case.

Four independent groups almost simultaneously reported a significant detection [1,15,26,30] and a new detection is coming with VLT data [17,18]. Here, we present our own detection [26], and discuss different aspects of the PSF correction and of the statistical measurement. Next we compare the measurements with the predictions and discuss their consistency. We show how our cosmic shear program will hopefully improve the situation very shortly: we outline the new measurements and the new tests of PSF correction we plan to do next.

2 From the data set to the galaxy catalogues

Table 1 show the list of the fields used in our cosmic shear detection. Despite the relatively large differences in the filter and the exposure time, the mean redshift depth is approximately 1 according to the deepest spectroscopic surveys done so far [5], with a dispersion probably very large (~ 1). It is impossible to give a more accurate determination of redshifts as we do not have enough colors for this. A complete scientific interpretation of our signal would require the missing redshift information, but in the early stages of the work we were more interested in a *detection* of the cosmic shear effect rather than its scientific exploitation. As discussed in the last Section, the scientific analysis requires some crucial issues to be addressed first.

The total field covers about 6300 arcmin^2 and has a number density of galaxies of about $n_g \simeq 30$ gal/arcmin^2. However, after a proper weighting of the galaxies their effective number density is about half (details are in the original paper [26]). Our procedure of shape measurement using IMCAT[a] is described in details elsewhere [7,18,26] so it is unnecessary to give it here, therefore we assume that we have already a catalogue of PSF corrected ellipticities for the galaxies.

[a] See Nick Kaiser's home page at http://www.ifa.hawaii.edu/~kaiser/.

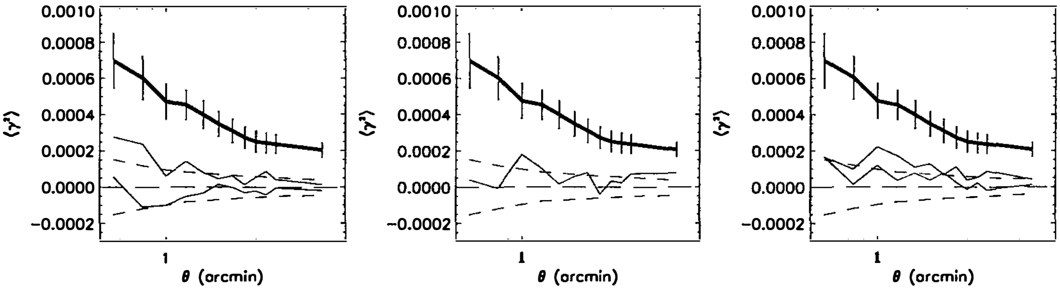

Figure 1: The thick solid line show the measured $\langle\gamma^2\rangle$, and the error bars are calculated using randomized ellipticity orientations. The dashed lines show the $\pm 1\sigma$ levels. From left to right: (a) the thin solid lines are $\langle\gamma^2\rangle$ measured in bins of N galaxies, where the galaxies are chosen with respect to the star ellipticity strength e_1 and e_2. The number of galaxies is then converted into a fictive *scale* which is used to make the plot. (b) The N galaxies are chosen with respect to the optical distortion amplitude. (c) The N galaxies are chosen with respect to the CCD lines and columns.

3 From the galaxy catalogues to the cosmological parameters

3.1 What is the relevant information?

The easiest quantities to measure for the detection of the cosmic shear effect are the variance of the shear $\langle\gamma^2\rangle$ and the ellipticity correlation functions. For a simplified cosmological model (zero cosmological constant, power law power spectrum with slope n and normalization σ_8, and a single redshift plane z_s), we can show that [9]:

$$\langle\gamma^2\rangle^{1/2} \simeq 0.01\sigma_8\Omega_0^{0.75}z_s^{0.75}\left(\frac{\theta}{\text{arcmin}}\right)^{\left(\frac{n+2}{2}\right)}, \tag{1}$$

where Ω_0 is the density of the Universe and θ the measurement scale in arcmin. There are similar relations for the correlation functions, but we can define several types of correlation functions. Here we are interested in $\langle e_t(\theta)e_t(0)\rangle$, $\langle e_r(\theta)e_r(0)\rangle$ and $\langle e_t(\theta)e_r(0)\rangle$, where e_t and e_r are the tangential and the radial component of the shear respectively:

$$\begin{aligned} e_t &= -\gamma_1\cos(2\theta_{gal}) - \gamma_2\sin(2\theta_{gal}) \\ e_r &= -\gamma_2\cos(2\theta_{gal}) + \gamma_1\sin(2\theta_{gal}), \end{aligned} \tag{2}$$

where γ_i are the Cartesian components of the shear and θ_{gal} is the position angle of the pair of galaxies. The correlation functions mentioned above have a particular interest because of the specific signatures induced from weak lensing by large scale structures [19]: from the scalar nature of the gravity we can show that $\langle e_t(\theta)e_r(0)\rangle$ should vanish, that $\langle e_t(\theta)e_t(0)\rangle$ is positive and $\langle e_r(\theta)e_r(0)\rangle$ should become negative for a finite range of scale.

3.2 Measurements and amplitude of the residual systematics

We assumed that we already have a catalogue of galaxy ellipticities $\mathbf{e}$ corrected from the PSF anisotropy. We call σ_ϵ the ellipticity dispersion. From a set of N galaxies at positions $\boldsymbol{\theta}_k$ with ellipticities $e_\alpha(\boldsymbol{\theta}_k)$ we can built an estimate of the variance of the shear at the position $\boldsymbol{\theta}_i$

$$E[\gamma^2(\boldsymbol{\theta}_i)] = \sum_{\alpha=1,2}\left(\frac{1}{N}\sum_{k=1}^{N}e_\alpha(\boldsymbol{\theta}_k)\right)^2, \tag{3}$$

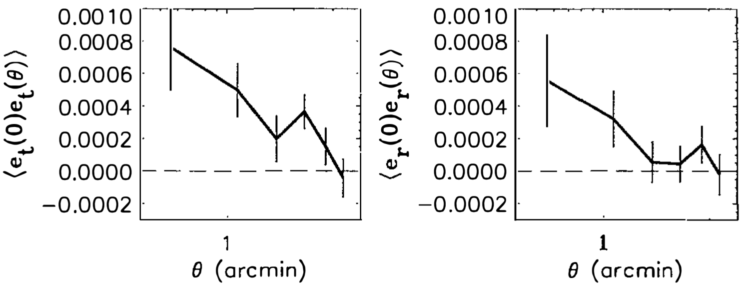

Figure 2: Measured ellipticity correlation functions $\langle e_t(\theta)e_t(0)\rangle$ (left) and $\langle e_r(\theta)e_r(0)\rangle$ (right) .

whose the ensemble average is $\langle E[\gamma^2(\theta_i)]\rangle = \sigma_\epsilon^2/N + \langle\gamma^2\rangle$. The term σ_ϵ^2/N can be removed either by measuring it on randomized catalogues, or by choosing and unbiased estimate equal to Eq.(3) without the diagonal elements.

An estimate of the correlation function $E[e_i(0)e_j(r)]$ (where i and j are either t and/or r) is built by summing $e_i(0)e_j(r)$ for all the possible pairs of galaxies separated by a distance r

Figure 1 shows the measured variance of the shear in our survey. The signal (thick line) exhibits the characteristic power law scale dependence as predicted from Eq.(1), and the amplitude of the signal has the correct order of magnitude. However, as we shall see in the next Section, the cosmic variance and the error bars are too large to put tight constraints on the cosmology.

We have shown in our original paper[26] that the corrected ellipticity of the galaxies are uncorrelated with the ellipticity of the stars, which demonstrates the low level of residual systematics present in the catalogues[b]. We have reproduced in Figure 1 (thin solid lines) the variance of the shear measured when the galaxies are picked up according to the local star ellipticity instead of taking the galaxies falling into a given smoothing window. Each estimate of the shear variance is done using Eq.(3), where the N galaxies have in common a similar PSF anisotropy amplitude on the data. It is then easy to convert N to a *scale* θ, since the number density of galaxies is roughly constant. The resulting shear variance is shown as the thin solid lines on Figure 1 for three cases of possible source of residual systematics (see caption for details). It shows that any residual systematic cannot be due to star ellipticity, optical distortion and CCD frame alignment.

A robust test of the gravitational lensing origin of the signal is to measure the correlation function as indicated above. Figure 2 shows the two relevant correlation functions $\langle e_t(r)e_t(0)\rangle$ and $\langle e_r(r)e_r(0)\rangle$. The third one, not shown here, $\langle e_t(r)e_r(0)\rangle$ is zero as we expect from the scalar origin of the gravitational field. This results from the fact that systematics are almost non-existent in the galaxy catalogue, which is a strong supports for the cosmic origin of our signal. However the survey size is still too small to have a low noise measurement of these quantities, and to extract the useful cosmological information. Instead, we shall see this detection as a success showing the feasibility of the cosmic shear searches.

3.3 Cosmological constraints

Although it is hard to calculate the cosmic variance of the measured quantities at small scale, we can use ray tracing numerical simulations in order to compare our measurement with some

[b]However we found a constant bias of $\langle e_1\rangle \simeq -0.01$ for all the galaxies which we corrected for. The source of the bias is still unclear.

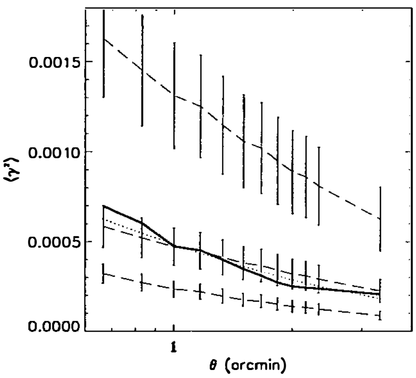

Figure 3: The thick solid line is drawn from Figure 2 without the measurement error bars. The dashed lines show the prediction of $\langle\gamma^2\rangle$ from ray-tracing simulations and the cosmic variance obtained from several realizations. From top to bottom: $(\Omega_0, \sigma_8) = (1., 1.)$; $(0.3, 0.85)$; $(0.3, 0.6)$. The source redshift is 1 and the power spectrum CDM-type.

realistic scenario. Such numerical simulations are available [10] and provide several realizations for a set of cosmological models, thus allowing a first analysis of the cosmic variance. Figure 3 is a comparison of our shear variance measurement (thick solid line) with three different models: $(\Omega_0, \sigma_8) = (1., 1.)$; $(0.3, 0.85)$; $(0.3, 0.6)$ from top to bottom (see the caption for details). The error bars show the cosmic variance measured out of several realizations for each model. Although we can only marginally reject the two extreme models, this figure shows that the data are already in favor of cluster normalized models, as suggested by the simplified analytical estimate Eq.(1).

4 Future prospects

The aim of the above Section was to present a condensed view of our recent cosmic shear detection with the first stream of data obtained at CFHT. All the relevant technical details can be found elsewhere [7,26]; here we emphasized the control of the systematics to a reasonable level and that the signal is consistent with the gravitational lensing predictions, although we are not yet in good position to put tight constraints on the cosmology. However, we now have 9 sq. degres in I (instead of 2), ready for scientific analysis, of comparable image quality of the data discussed here, and the numerical simulations [10,25] indicate that this is enough to make a very significant measurement of various lensing statistics.

It is worthwhile to ask what can be done next. The next step is the confirmation of the cosmological nature of the signal over many different aspects. There are two areas with significant room for improvement:

1-Beating the systematics: following the same strategy in our cosmic shear paper, we can search for systematics by binning the data in various ways. With 9 sq. degrees we can bin the data in a much refined way than we did before. We can study the alignment of the galaxies with the stars in bins of magnitude, size or other parameter. We can also split the survey into smaller parts and analyze independently the different parts.

2-Search for specific gravitational lensing signatures: this was done with the correlation function, but we can do much more with 9 sq. degrees. Of course the signal-to-noise of the correlation function will be much better, and we can study its shape as a function of size and magnitude of the galaxies. The variance of the shear measured with another filter than top-hat will be possible: for instance the Map statistic [22,25] is known to have a specific angular dependence if induced by gravitational lensing. With a 9 sq. degrees survey we can also measure the skewness of the convergence [10,25], which is a direct probe of the cosmological parameters [2,9]. Such measure would require accurate mass reconstruction in non-trivial topologies (non-straight edges and holes in the field), and preliminary studies show that such reconstructions give stable and unbiased mass maps. Peak statistics [11] is also accessible with a good signal-to-noise with such a survey size. Measurement of the shear power spectrum will be done in order to check that the power is distributed over the different scales like what weak lensing theory predicts (and do not dominate at one specific scale for instance).

It has recently been suggested that galaxies might have an intrinsic ellipticity correlation [6,8]. Although this could also be tested using specific lensing statistics (yet to be developed), we can completely get rid of the effect by measuring the correlation between different source redshift planes. Since our full survey will be 16 sq. degrees in four colors, we hope to have the luxury to work with many different redshift planes (using photometric redshifts) and to extract without ambiguity the cosmic shear information *and* the intrinsic correlations.

Acknowledgments

We are very gratefull to the organisers for this interesting and lively meeting. We are particulary gratefull to Dmitri Pogosyan who was forced to attend all the talks and succeeded brillantly in the hard task to make a non-conventional and accurate summary talk. This work was supported by the TMR Network "Gravitational Lensing: New Constraints on Cosmology and the Distribution of Dark Matter" of the EC under contract No. ERBFMRX-CT97-0172. We thank the TERAPIX data center for providing infinite computing resources for the reduction of the CFH12K and UH8K data.

References

1. Bacon, D., Refregier, A., Ellis, R., 2000, astro-ph/0003008.
2. Bernardeau, F., Van Waerbeke, L., Mellier, Y., 1997, A&A, 322, 1.
3. Blandford R., Saust, A., Brainerd, T., Villumsen, J., 1991, MNRAS, 251, 600.
4. Bonnet, H., Mellier Y., 1995, A&A, 303, 331.
5. Cohen, J. G., Hogg, D., W., Blandford, R., Cowie, L., Hu, E. , Songaila, A., Shopbell, P., Richberg, K., 1999, astro-ph/9912048.
6. Croft, R., Metzler, C., 2000, astro-ph/0005384.
7. Erben, T., Van Waerbeke, L., Bertin, E., et al., 2000, A& A, astro-ph/0007021.
8. Heavens, A., Refregier, A., Heymans, C., 2000, astro-ph/0005269.
9. Jain, B., Seljak, U., 1997, ApJ, 484, 560.
10. Jain, B., Seljak, U., White, S., 2000, ApJ, 530, 547.
11. Jain, B., Van Waerbeke, L., 2000, ApJL, 530, L1.
12. Kaiser, N., 1992, ApJ, 388, 272.
13. Kaiser, N., 2000, ApJ, 537, 555.
14. Kaiser, N., Squires, G., Broadhurst, T., 1995, ApJ, 449, 460.
15. Kaiser, N., Wilson, G., Luppino, 2000, astro-ph/0003338.
16. Kuijken, K., 1999, A&A, 352, 355.
17. Maoli, R., et al., 2000, *in preparation.*
18. Maoli, R., et al., these proceedings.
19. Miralda-Escude, J., 1991, ApJ, 380, 1.
20. Mould, J., Blandford, R., Villumsen, J., et al., 1994, MNRAS, 271, 31.
21. Rhodes, J., Refregier, A., Groth, E., 2000, ApJ, 536, 79.
22. Schneider, P., Van Waerbeke, L., Jain, B., Kruse, K., 1998, MNRAS, 296, 873.

23. Schneider, P., Van Waerbeke, L., Mellier, Y., et al., 1998, A& A, 333, 767.
24. Valdes, F., Jarvis, J.F., Tyson, J.A., 1984, ApJ, 271, 431.
25. Van Waerbeke, L., Bernardeau, F., Mellier, Y., 1999, A&A, 342, 15.
26. Van Waerbeke, L., Mellier, Y., Erben, T., et al., 2000, A& A, 358, 30.
27. Van Waerbeke, L., Mellier, Y., Schneider, et al., 1997, A&A, 317, 303.
28. Villumsen, J., 1995, astro-ph/9507007.
29. Villumsen, J., 1996, MNRAS, 281, 369.
30. Wittman, D., Tyson, J.A., Kirkman, D., et al., 2000, Nature, 405, 143.

DETECTION OF COSMIC SHEAR WITH THE WILLIAM HERSCHEL TELESCOPE

D. J. BACON, A. R. REFREGIER & R. S. ELLIS
Institute of Astronomy, Madingley Road, Cambridge, CB3 0HA, England

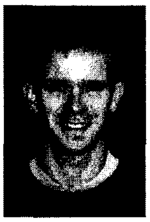

Gravitational lensing by large-scale structure induces weak coherent alignments in the shapes of background galaxies. Here we present evidence for the detection of this 'cosmic shear' at the 3.4σ significance level with the William Herschel Telescope. Analysis and removal of notable systematic effects, such as shear induced by telescope optics and smearing by tracking and seeing, are conducted in order to recover the physical weak shear signal. Positive results for shear recovery on realistic simulated data are presented, enhancing confidence in the measurement method. The detection of cosmic shear is statistically characterised, and its cosmological significance is discussed.

1 Introduction

Understanding the large-scale distribution of matter in the universe continues to be a major issue in modern cosmology. Weak gravitational lensing promises to be a particularly effective method for determining properties of large-scale structure, since it provides direct information concerning the total mass distribution, independently of its state and nature.

The images of distant field galaxies obtained at a telescope are slightly coherently distorted, due to weak lensing by large-scale structure. With extensive measurements of this shear on various scales, one would obtain a direct measure of the power spectrum of density fluctuations along the line of sight.

However, the first stage in such a programme is the detection of the cosmic shear signal; this itself is a challenge, because the rms shear amplitude is small - a few percent on arcminute scales. Recently four papers describing the detection of this effect have been released (Wittman et al 2000, van Waerbeke et al 2000, Bacon et al 2000, Kaiser et al 2000), presenting mutually consistent results with careful analysis of systematic effects.

Here we overview the detection of cosmic shear obtained with the 4.2m William Herschel Telescope, fully discussed in Bacon, Refregier & Ellis (2000). The current paper describes the survey strategy, and discusses how the data are analysed to overcome convincingly the contribution of systematic effects to the shear. Simulations used to check our methodology are explained, and the cosmological implications of our results are discussed.

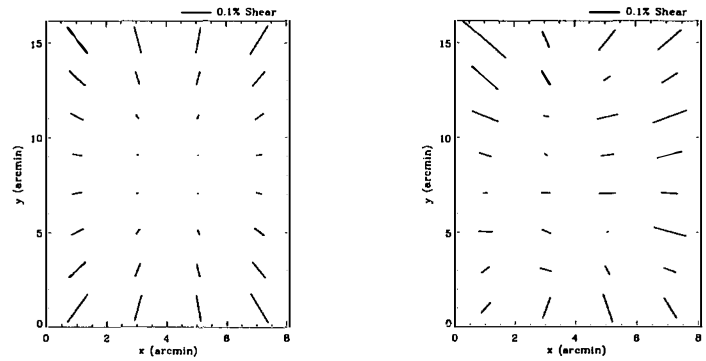

Figure 1: Expected (left) and measured (right) instrumental shear pattern for the WHT Prime Focus. The expected pattern was derived from the distortion model given in the WHT Prime Focus manual (Carter & Bridges 1995). The observed pattern was measured using 3 astrometric frames in one of our fields.

2 Observations

The goal of our survey is to obtain a homogeneous sample of deep fields, chosen to be on random lines of sight separated by $> 5°$ in order to sample independent structures. The galactic latitude of the fields was tuned to afford $\simeq$ 200 stars within the field of view, necessary to correct for anisotropic PSF systematics.

We carried out deep R-band imaging on 14 such fields with the Prime Focus camera on the WHT. This has an 8'×16' field of view and pixel size 0.237". The fields were exposed for one hour in R; median seeing was 0.81", having excluded exposures with seeing > 1.2". We reach a magnitude depth of $R_{\rm median} = 25.2$, with $R_{\rm median}$ of 23.4 for our selected sample, $z_{\rm median} \simeq 0.8$, and a number density $N = 14.3$ arcmin^{-2}.

3 Analysis of Systematic Effects

The aim of our analysis is to remove carefully systematic effects from the galaxies' measured ellipticities, leading to unbiased measures of the small ($\simeq$1%) mean shear components for each field. We wish to measure the mean shear in 8'×8' cells, for increased shear signal and to allow cross-correlation tests.

We used the Kaiser, Squires & Broadhurst (1995) method (KSB) implemented by Kaiser's `imcat` software for object detection and shape measurement. A detection signal-to-noise $\nu > 15$ limit was imposed on our usable galaxy catalogue to remove correction systematics found at low signal-to-noise level.

The shear induced by telescope optics must be dealt with; by calculating the telescope distortion using objects' relative positions in several dithers, we show that this is negligible (shear due to telescope < 0.003 everywhere; see figure 1).

Next, the PSF anisotropy from e.g. tracking errors must be removed (see figure 2). Before correction this effect induces an rms stellar ellipticity $e = 0.07$, but after subtracting a fitted 2-dimensional cubic to stellar ellipticities, the residual stellar rms is a mere $e = 1.4 \times 10^{-3}$. We correct the galaxy ellipticities following Luppino & Kaiser (1997), using the stellar fit model and responsivities to smear measured for the galaxies.

Finally, galaxies are corrected for isotropic smear, i.e. the fact that smaller galaxies' shapes have been more affected by seeing-induced circularisation. Again we follow Luppino & Kaiser's (1997) method; this results in estimates for the mean shear components in each 8'×8' cell.

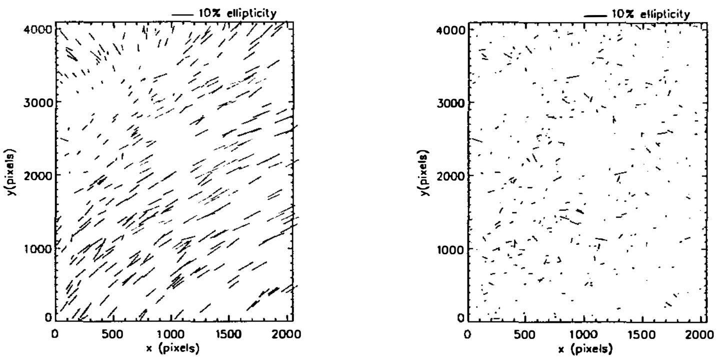

Figure 2: Left: Stellar ellipticity distribution before correction for observed field (CIRSI2). Mean value observed $\bar{e}^* \simeq 0.07$. Right: Residual stellar ellipticity after correction. The residual mean ellipticity is $\bar{e}^{res} \simeq 2.6 \times 10^{-3}$.

4 Shear Measurements on Simulated Data

In order to check our correction of systematics, and to calibrate KSB-measured shear to real shear, we constructed simulated WHT fields on which to carry out the above shear analysis (Bacon et al 2000, in preparation); one can apply a chosen shear to a field, and test its recovery by our algorithm. By creating a joint probability model of the magnitude - number density - ellipticity - radius distribution of galaxies in Ebbels' (1998) HST Groth Strip survey catalogue, we were able to draw out statistically similar simulated catalogues for shearing and analysis.

The catalogues were visualised with IRAF artdata; telescope-specific pixelisation, throughput, anisotropic PSF, poisson and readout noise were added. A null set of 20 simulated fields without shear were created, together with a further 30 fields with an rms shear of 1.5%. The KSB analysis described above was carried out on each field.

5 Results

We shall now compare the detection results for the simulated and real data. The left-hand panel of figure 3 shows the mean shear components found for our 1.5% rms shear simulations (30 cells). The inner circle represents the variance that would be expected from noise alone; one can see that there is an excess variance $\sigma^2_{\rm lens}$, which turns out to be significant; $\sigma^2_{\rm lens} = (0.013)^2 \pm (0.006)^2$, to be compared with our input $\sigma^2_{\rm lens} = (0.015)^2$. The fact that the method has detected the simulated signal with the correct amplitude is encouraging.

The middle panel of figure 3 shows the mean shear components for 20 simulations with no shear added. Note that here the variance is accounted for by noise alone; as expected, there is no excess variance.

The shear results for our observed fields are shown in the right-hand panel of figure 3. Again we see an excess variance; with a thorough statistical analysis we find this to be significant, with $\sigma^2_{\rm lens} = (0.016)^2 \pm (0.008)^2 \pm (0.005)^2$, the errors being due to noise and uncertainty on any remaining systematics respectively. This corresponds to a 3.4σ detection of cosmic shear.

By comparing our $\sigma^2_{\rm lens} = (0.016)^2 \pm (0.012)^2$ (error now includes cosmic variance) with that expected for popular cosmological models, we find that COBE-normalised SCDM is ruled out at 3σ level, whereas cluster-normalised τ-, Λ-, and OCDM are highly consistent with the data.

Our results also afford us a measure of σ_8 for a given cosmological model. For instance, for ΛCDM with $\Omega_m = 0.3$, we obtain $\sigma_8 = 1.47 \pm 0.51$, consistent with cluster abundance determinations, $\sigma_8 = 1.13 \pm 0.19$ (Viana & Liddle 1996).

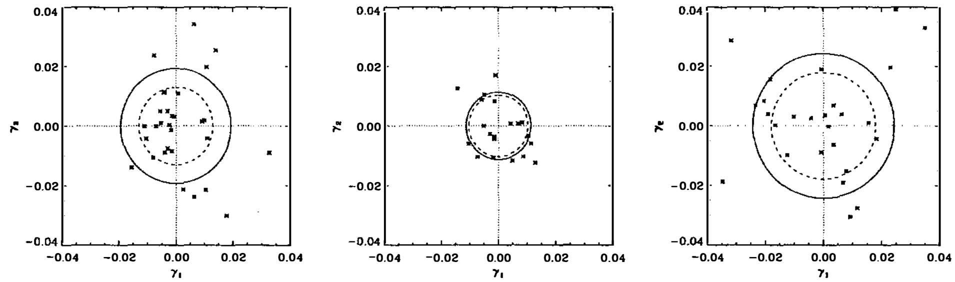

Figure 3: Mean γ_1 and γ_2 for: (left) 30 simulated cells with rms 1.5% shear; (centre) 20 simulated null cells; (right) 26 observed cells. The dashed circle shows the noise rms, the solid circle shows the total rms. In the null case, the total rms is consistent with noise alone; in the other cases the excess shear variance is significant.

With increased numbers of fields in the future, cosmic shear variance measurements will afford very precise estimates of σ_8, while skewness measurements of the distortion field will provide an independent estimate of Ω_m.

6 Conclusion

Evidence for the detection of shear arising from large-scale structure has been presented based on an analysis of 14 fields obtained at the William Herschel Telescope. Particular attention has been paid to questions of systematic correction and testing of measurement method by simulations. Prospects are now bright for measuring with greater accuracy the amplitude of the cosmic shear signal. The key uncertainties to overcome are noise and cosmic variance, i.e. more independent lines of sight will lead to a better estimate of the shear amplitude. Future cosmic shear surveys will consequently provide powerful constraints on cosmological parameters.

Acknowledgments

Particular thanks go to Nick Kaiser for providing the Imcat software, and to Douglas Clowe for valuable discussions as to its use. We also thank Roger Blandford, Chris Benn, Andrew Firth, Mike Irwin, Konrad Kuijken, Peter Schneider, Andrew Liddle, Yannick Mellier, Roberto Maoli and Jason Rhodes for useful discussions. Max Pettini kindly provided us with one of the WHT fields. This work was performed within the European TMR lensing network.

References

1. Bacon D., Refregier A., Ellis R., 2000, preprint astro-ph/0003008
2. Bacon D., Refregier A., Clowe D., Ellis R., 2000, in preparation
3. Carter D., Bridges T., 1995, WHT Prime Focus and Auxiliary Port Imaging Manual
4. Ebbels T., 1998, Ph.D. thesis, University of Cambridge
5. Kaiser N., Squires G., Broadhurst T., 1995, ApJ, 449, 460
6. Kaiser N., Wilson G., Luppino A., 2000, preprint astro-ph/0003338
7. van Waerbeke L. et al, 2000, to appear in A&A, preprint astro-ph/0002500
8. Viana P., Liddle A., 1996, MNRAS, 281, 323
9. Wittman D. et al, 2000, Nature, 405, 143

COSMIC SHEAR WITH THE VLT

R. MAOLI[1,2], Y. MELLIER[2], L. VAN WAERBEKE[2,3], P. SCHNEIDER[4,5], B. JAIN[6], T. ERBEN[5], F. BERNARDEAU[7], B. FORT[2]

[1] *Dipartimento di Fisica, Università di "Roma La Sapienza", Italy*

[2] *Institut d'Astrophysique de Paris, France*

[3] *Canadian Institute for Theoretical Astrophysics, Toronto, Canada*

[4] *Institut für Astrophysik und Extraterrestrische Forschung, Bonn, Germany*

[5] *Max Planck Institut für Astrophysik, Garching, Germany*

[6] *Department of Physics, Johns Hopkins University, Baltimore, USA*

[7] *Service de Physique Théorique, C.E. de Saclay, France*

We report on the detection of cosmic shear on angular scales of 1.3-6.5 arcmin using 45 independent empty fields observed with the Very Large Telescope (VLT). This result confirms previous measurements obtained with the CFH Telescope at the same angular scales. We present the data analysis and the first preliminary results.

1 Introduction

The large scale structures of the Universe induce gravitational distortion of the shape of the background galaxies which can be observed on CCD images as a correlated ellipticity distribution of the lensed sources (the cosmic shear). The analysis of cosmic shear permits to extract information on the geometry of space (Ω and λ) as well as on the power spectrum of the (dark) matter density perturbations responsible for the distortion. Therefore, it directly compares observations with cosmological models, without regards on the light distribution.

In contrast to weak lensing analysis of clusters of galaxies, measuring cosmic shear is still a challenge. It has a very small amplitude (≈ 5 times lower than in clusters) and demands deep images of a large portion of the sky obtained with high precision instruments. Up to now, this task was beyond the reach of the available technology. Although a first detection in a blank sky region was reported two years ago[1], it is only recently that four different groups have succeeded in observing cosmic shear[2,3,4,5].

The critical issues regarding the reliability of the cosmic shear measurement are the three sources of noise:

- intrinsic noise
- systematics
- cosmic variance

Minimizing the first one is important to get a significant detection; understanding and controlling the second one is important to be sure that the signal is induced by cosmic shear; then minimizing the third one is important to compare the signal with cosmological scenarios.

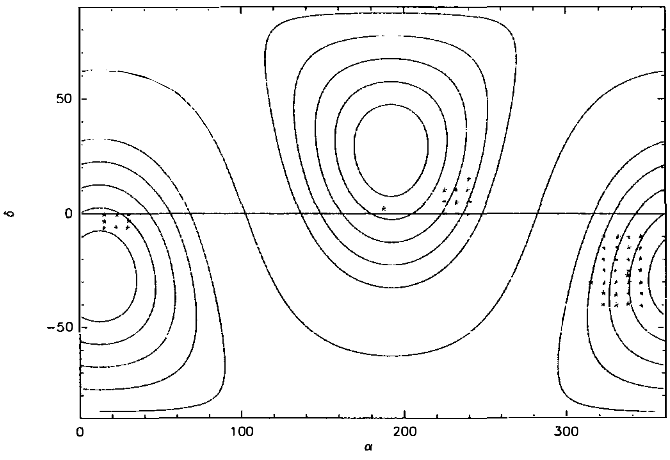

Figure 1: Distribution on the sky of the 50 VLT fields. Continuous lines are for galactic latitudes $b = 0, \pm 30, \pm 40, \pm 50, \pm 60, \pm 70$. Contrary to what it can seem to a first look, they are not on a regular grid.

By using jointly these detections it is possible to rule out some scenarios. However, the cosmic variance is still too large to distinguish among the more common models of the Universe. A significant improvement implies the observation of many independent fields. The Cambridge group[3] used nearly statistical independent areas of the sky, but has only 13 fields. The other experiments cover a larger area but sample compact regions with few independent fields. In this case the amplitude of the cosmic variance is estimated by running numerical simulations for each current cosmological models. In any case, the cosmic variance is greater than in the case of observation of completely statistical independent fields. The alternative is to observe many independent fields in order to infer the cosmic variance from the fluctuations of the shear observed from field-to-field. This is the strategy we developed with the VLT/FORS1 survey. In the following, we describe the analysis of cosmic shear in 50 FORS1 fields. This is a preliminary study which does not include an extensive investigation of systematics. Nevertheless, the signal is strong and highly significant, so we are confident in the results shown in this proceeding.

2 Observational strategy analysis of VLT/FORS1 data

All the data were obtained in the I band with the FORS1 instrument, a 2048x2048 pixel CCD with a $6.8'$ field of view, mounted at the Cassegrain focus of the VLT-UT1.

In figure 1 we plot the sky distribution of the 50 VLT fields. Their main characteristics are:
- at least 5 degrees of separation, to be statistically independent;
- absence of bright stars ($m_B > 14$), to avoid diffraction spikes and light scattering;
- intermediate galactic latitudes ($30° \leq b \leq 70°$), to have enough stars for the PSF correction;
- two fields in common with the HST/STIS project and two with the WHT project, to allow for cross checking of the results.

Observations were made between May and September 1999 using the service mode available at ESO. This observing strategy is particularly well suited for cosmic shear surveys, ensuring a seeing always lower than 0.8" and taking advantage from the possibility to spread the targets over a very large part of the sky.

Each field was observed for 36 minutes with 6 individual exposures per field distributed over

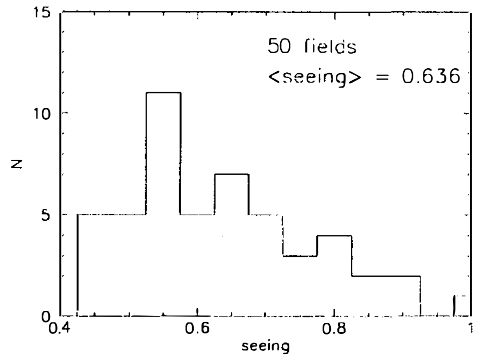

Figure 2: Histogram of the seeing for the 50 final coadded fields.

a circle of 10″ of radius. The median seeing for all the fields is 0.64″ (see figure 2) and the limiting magnitude is $I_{AB} \sim 24.5 - 25$.

Each image was overscan corrected, bias subtracted and flatfielded with a superflat computed with the exposures of the same night. No fringe correction was necessary. The FORS1 images get through a four port readout, so we treated separately the image subsets coming from the four quadrants of the CCD. Then we normalized the gain of the different subsets to obtain an image with an homogeneous background. Finally, we aligned the six individual exposures to produce the final coadded image. An example is given in figure 3.

At this stage, the images are ready for weak lensing analysis. The incoming light, crossing the atmosphere and getting through the optical system of the telescope, undergoes a smearing and a circularization. If we define the ellipticity of the source as

$$\mathbf{e} = \left(\frac{I_{11} - I_{22}}{Tr(I)}; \frac{2I_{12}}{Tr(I)}\right) \quad \text{with} \quad I_{ij} = \int \mathrm{d}^2\theta\, W(\theta)\, \theta_i \theta_j\, f(\theta), \tag{1}$$

the observed ellipticity can be expressed by the KSB formalism [6, 7, 8],

$$\mathbf{e}^{obs} = \mathbf{e}^{source} + P_\gamma \gamma + P^{sm}\mathbf{p} \tag{2}$$

where $\mathbf{e}^{source}$ is the intrinsic ellipticity of the source, P^{sm} is the smear polarizability tensor associated with the effects produced by the anisotropic part of the point spread function (PSF from now on) and $\mathbf{p}$ is connected to the anisotropic kernel $g(\boldsymbol{\theta})$ of the PSF through the two equations:

$$\mathbf{p} = (q_{11} - q_{22}; 2q_{12}); \quad q_{lm} = \int \mathrm{d}^2\theta\, \theta_l \theta_m\, g(\boldsymbol{\theta}). \tag{3}$$

The vector $\mathbf{p}$ can be computed from the stellar ellipticity $\mathbf{e}^\star$

$$p_\alpha = \frac{e^\star_\alpha}{P^{sm}_{\alpha\alpha}}. \tag{4}$$

The quantity P_γ is the preseeing shear polarizability tensor, that takes into account both the effect of the gravitational shear and the circularization effect of the isotropic part of the PSF. It is given by the equation

$$P^\gamma = P^{sh} - \frac{P^{sh}_\star}{P^{sm}_\star} P^{sm} \tag{5}$$

where P^{sh} is the shear polarizability tensor and the subscript "$\star$" refers to the quantity computed for stars.

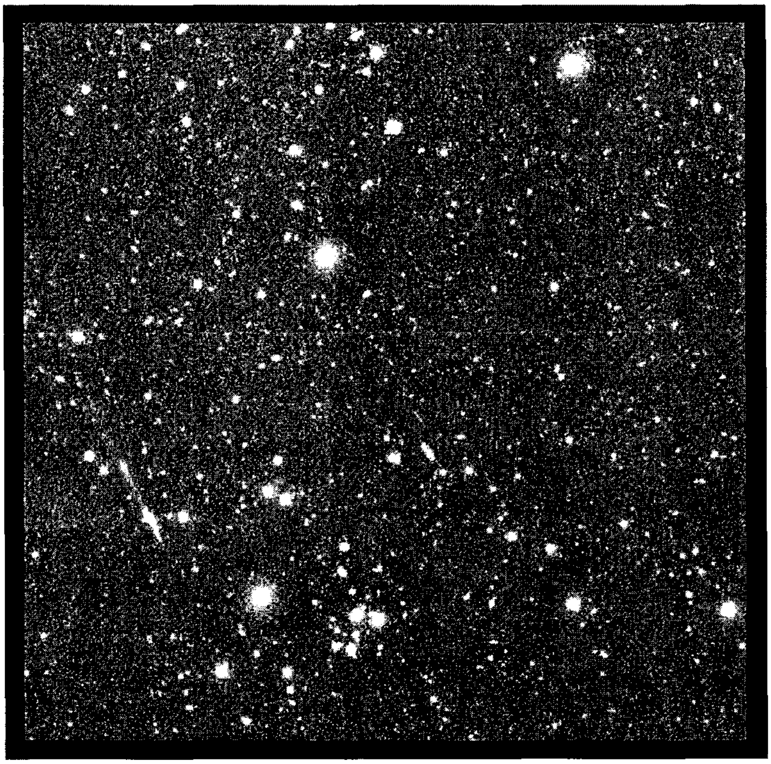

Figure 3: Final coadded image of a VLT field. In this case the seeing is 0.53″, the source density is 35.3 sources/arcmin^2, with a $6.5' \times 6.5'$ field and with 67 not saturated stars.

Assuming that there is no preferred direction for the intrinsic ellipticity of the sources, the cosmic shear at a given angular scale is

$$\gamma = \langle P_\gamma \rangle^{-1} \cdot \left\langle \mathbf{e}^{obs} - P^{sm}\mathbf{p} \right\rangle \tag{6}$$

where the average is computed over a given angular scale.

Two main tasks can be identified in shear computation:

- separation between stars and galaxies and selection of stars to compute the PSF correction for the galaxies;

- selection of galaxies for which the ellipticity can be computed with a small error.

Practically, this is translated in the following steps (for details, see[2]).

a) *Masking of images:* we remove all the boundaries of the four quadrants of the CCD. this includes the external boundaries and the central cross delineating the four quadrants. We remove also all sources too close to bright sources that can deform them, satellite traces and in general all those sources whose shape is difficult to compute correctly. About 12% of objects are removed in this way.

b) *Stars selection:* as usual, we use a radius vs magnitude plot to select not saturated stars. A low cut in the magnitude or an high cut in the radius would result in selecting small galaxies instead of stars therefore producing lower quality PSF corrections.

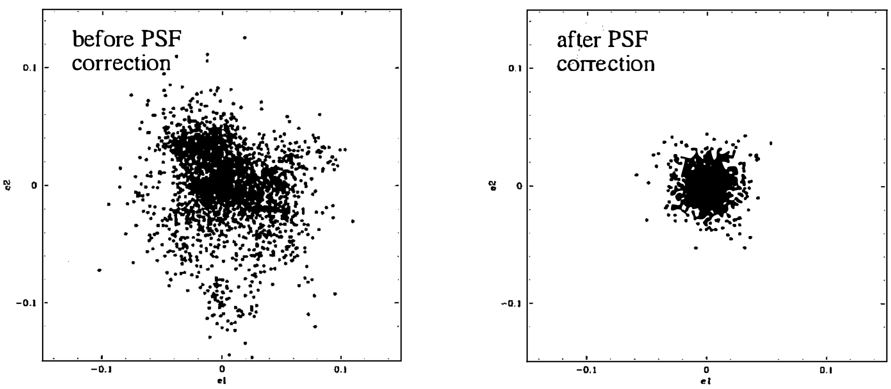

Figure 4: Star ellipticities before (at right) and after (at left) the PSF correction, for all the 45 selected VLT fields. A good PSF correction implies a zero mean value for e_1 and e_2 with small symmetric fluctuations.

c) *Fit of the stellar polarizability tensors:* using stars, we compute $p_\alpha = \frac{e^\star_\alpha}{P^{sm}_{\alpha\alpha}}$ and $\frac{P^{sh}_\star}{P^{sm}_\star}$ in all the image, fitting with a third order polynomial.
d) P^γ *computation:* using the stellar fits, we compute Eq. 5 for all the sources. P^γ is a very noisy matrix with huge fluctuations. For a given source, we then compute P^γ making an average among its values for the 30 nearest neighbors (see van Waerbeke *et al.*, 2000).
e) *Source selection:* we select sources with stellar class (given by SExtractor) < 0.9, with radius $>$ stellar radius and with separation > 10 pixels.

In figure 4 we plot the star ellipticities for all VLT fields before and after the PSF correction. Five fields had a poor PSF correction and were eliminated.

At the end we have 45 fields with in average 60 stars/field (a minimum of 20 and a maximum of 120); we have roughly 58700 sources for 1900 arcmin^2 that is $\sim$ 31 sources/arcmin^2 and 1300 sources/field.

3 Results and conclusion

For each final corrected image, we computed the variance of the shear, $\langle\gamma^2\rangle$, at different angular scales, where the angular scale is given by the angular dimension of the top-hat window function. Then we made an average of $\langle\gamma^2\rangle$ over the 45 fields.

In this way we can associate an error to the value of $\langle\gamma^2\rangle$ at a given scale. It is important to stress that with 45 fields this also includes the cosmic variance.

In figure 5 we plot our results together with those of the other cosmic shear measurement projects. Note the remarkable agreement between the VLT and the CFHT results, although they were obtained with different observational strategies. This is the best guarantee that cosmic shear measurement is not associated with any local systematic effect.

Different theoretical models are also plotted in the figure. This plot rules out COBE-normalized standard CDM, which show the important potential of cosmic shear for cosmology. However, the errors are still too large to give precise predictions on the value of cosmological parameters Ω_0 and Λ and the shape of the power spectrum of primordial density fluctuations. Only a larger amount of data together with a complete control of the systematics will allow to reach this important goal.

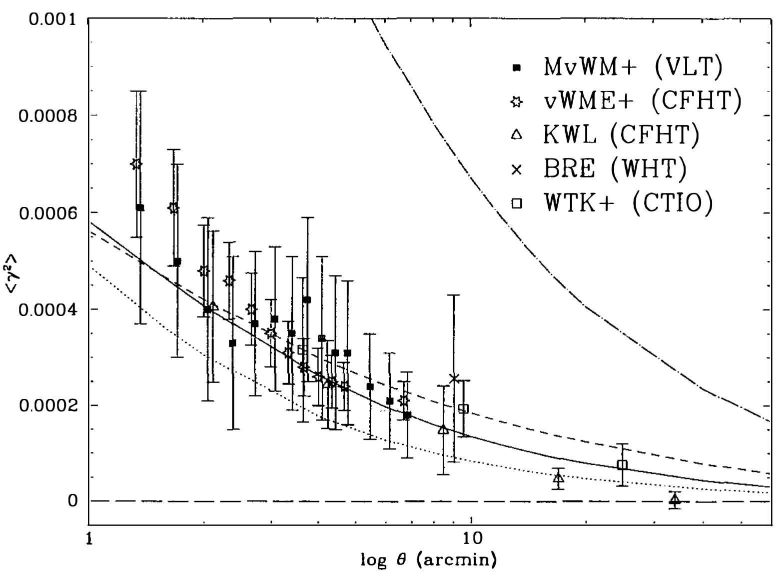

Figure 5: Summary of cosmic shear measurements. This work is referred as MvWM+. Some predictions of current models are also plotted, assuming sources $z_0 = 1$. The solid line corresponds to λCDM, with $\Omega_m = 0.3$, $\lambda = 0.7$, $\Gamma = 0.21$; the dot-dashed line corresponds to COBE-normalized SCDM; the dashed line corresponds to cluster-normalized SCDM and the dotted line corresponds to cluster-normalized Open CDM with $\Omega_m = 0.3$.

Acknowledgments

We thank the ESO service observing team at the VLT for performing the observations. We thank V. Charmandaris (Dr IRAF), D. Bacon and A. Refregier for helpful discussions. This work was supported by the TMR Network "Gravitational Lensing: New Constraints on Cosmology and the Distribution of Dark Matter" of the EC under contract No. ERBFMRX-CT97-0172.

References

1. P. Schneider *et al*, *Astr. & Astrophys.* **333**, 767 (1998).
2. L. van Waerbeke *et al*, *Astr. & Astrophys.* **358**, 30 (2000).
3. D. Bacon, A. Refregier & R. Ellis, *MNRAS submitted*, astro-ph/0003008.
4. D. Wittman *et al*, *Nature* **405**, 143 (2000).
5. N. Kaiser, G. Wilson & G. Luppino, *Astrophys. J. submitted*, astro-ph/0003338.
6. N. Kaiser, G. Squires & T. Broadhurst, *Astrophys. J.* **449**, 460 (1995).
7. G. Luppino & N. Kaiser, *Astrophys. J.* **475**, 20L (1997).
8. H. Hoekstra *et al*, *Astrophys. J.* **504**, 636 (1998).

STATISTICAL PROPERTIES OF THE CONVERGENCE DUE TO WEAK GRAVITATIONAL LENSING BY NON-LINEAR STRUCTURES

P. VALAGEAS
Service de Physique Théorique, CEA Saclay, 91191 Gif-sur-Yvette, France

Density fluctuations in the matter distribution lead to distortions of the images of distant galaxies through weak gravitational lensing effects. This provides an efficient probe of the cosmological parameters and of the density field. In this study, we investigate the statistical properties of the convergence due to weak gravitational lensing by non-linear structures (i.e. we consider small angular windows $\theta \leq 2'$). We present a method to obtain *an estimate of the full p.d.f. of the convergence* κ. We show that our predictions agree very well with the results of N-body simulations for the convergence. Hence this gives a very powerful tool to constrain scenarios of structure formation.

1 Probability distribution of the convergence

1.1 Density field

In order to obtain the properties of the weak gravitational lensing effects we need a detailed description of the density field which gives rise to these distortions. Hence we briefly recall here the formalism we use to characterize the density fluctuations. It is convenient to express the probability distribution of the density contrast $\delta = (\rho - \overline{\rho})/\overline{\rho}$ at scale R and redshift z (here $\overline{\rho}(z)$ is the mean universe density) in terms of the many-body correlation functions $\xi_p(\mathbf{r}_1, ..., \mathbf{r}_p)$. Thus we define the quantities ($p \geq 2$):

$$S_p = \frac{\overline{\xi}_p}{\overline{\xi}_2^{\,p-1}} = \frac{\langle \delta_R^p \rangle_c}{\langle \delta_R^2 \rangle^{\,p-1}} \quad \text{with} \quad \overline{\xi}_p = \int_V \frac{d^3r_1 ... d^3r_p}{V^p} \; \xi_p(\mathbf{r}_1, ..., \mathbf{r}_p) \tag{1}$$

where $V = 4\pi/3R^3$ is the volume of a spherical sphere of radius R and $\langle \delta_R^p \rangle_c$ are the cumulants of the density contrast δ at scale R. Next we introduce the generating function

$$\overline{\varphi}(y) = \sum_{p=2}^{\infty} \frac{(-1)^{p-1}}{p!} \, S_p \, y^p. \tag{2}$$

Then, one can show [1] that the probability distribution of the density contrast δ within spheres of size R is:

$$P(\delta) = \int_{-i\infty}^{+i\infty} \frac{dy}{2\pi i \overline{\xi}} \, e^{[\delta y - \overline{\varphi}(y)]/\overline{\xi}} \tag{3}$$

where we note $\overline{\xi}_2$ as $\overline{\xi}$. The interest of the generating function $\overline{\varphi}(y)$ is that in the highly non-linear regime, where the stable-clustering ansatz [2] provides a good description of the density field, it is independent of time. Then, in order to get the properties of the non-linear density field we only need the evolution of the two-point correlation function ξ_2, or of the power-spectrum $P(k)$, which is given by the fits obtained from numerical simulations [3]. This *scaling property* has been checked in details against numerical simulations for various power-spectra and it also characterizes the mass functions of collapsed objects as well as underdense regions [4].

1.2 Convergence κ

The gravitational lensing effects produced by density fluctuations along the trajectory of a photon lead to an apparent displacement of the source and to a distortion of the image. In particular, one can show [5] that the convergence κ is given for small values of $|\kappa|$ by:

$$\kappa = \frac{3}{2}\,\Omega_m \int_0^{\chi_s} d\chi\; w(\chi,\chi_s)\,\delta(\chi) \quad \text{with} \quad w(\chi,\chi_s) = \frac{H_0^2}{c^2}\,\frac{\mathcal{D}(\chi)\mathcal{D}(\chi_s-\chi)}{\mathcal{D}(\chi_s)}\,(1+z) \tag{4}$$

where χ is the radial comoving coordinate (and χ_s corresponds to the redshift z_s of the source) while $\mathcal{D}$ is the angular distance. In order to obtain the p.d.f. $P(\kappa)$ we simply need to derive the cumulants $\langle\kappa^p\rangle_c$. This will provide the parameters $S_{\kappa,p}$, similar to Eq. 1, and the generating function $\tilde{\varphi}_\kappa(y)$, similar to Eq. 2. From Eq. 4 we can write the cumulants $\langle\kappa^p\rangle_c$ in terms of the cumulants $\langle\delta^p\rangle_c$ of the density field and using Eq. 1 we can express these quantities in terms of the coefficients S_p. Next, the resummation of these cumulants $\langle\kappa^p\rangle_c$ as in Eq. 2 can be written in terms of the generating function $\tilde{\varphi}(y)$ which characterizes the underlying density field. This procedure is described in details in Valageas [6]. It is convenient to introduce first a "normalized" convergence $\hat{\kappa}$ by:

$$\hat{\kappa} = \frac{\kappa}{|\kappa_{\rm min}|} \quad \text{with} \quad \kappa_{\rm min}(z_s) = -\frac{3\Omega_m}{2}F_s(\chi_s) \quad \text{and} \quad F_s(\chi_s) = \int_0^{\chi_s} d\chi\; w(\chi,\chi_s) \tag{5}$$

where $\kappa_{\rm min}(z_s)$ is the minimum value of the convergence for a source located at redshift z_s as seen from Eq. 4 (since $\delta \geq -1$). Then, we obtain the simple expressions:

$$\tilde{\varphi}_{\hat{\kappa}}(y) = \int_0^{\chi_s} d\chi\, \frac{\xi_{\hat{\kappa}}}{I_\kappa}\, \tilde{\varphi}\left(y\frac{w}{F_s}\frac{I_\kappa}{\xi_{\hat{\kappa}}}\right) \;,\quad P(\hat{\kappa}) = \int_{-i\infty}^{+i\infty} \frac{dy}{2\pi i \xi_{\hat{\kappa}}}\, e^{[\hat{\kappa}y - \tilde{\varphi}_{\hat{\kappa}}(y)]/\xi_{\hat{\kappa}}} \quad \text{and} \quad P(\kappa) = \frac{P(\hat{\kappa})}{|\kappa_{\rm min}|} \tag{6}$$

for the p.d.f. $P(\hat{\kappa})$ and $P(\kappa)$ of the convergence smoothed over the top-hat angular window of radius θ. In Eq. 6 we defined:

$$I_\kappa(z) = \pi \int_0^\infty \frac{dk}{k}\,\frac{\Delta^2(k)}{k}\,W^2(\mathcal{D}k\theta) \quad \text{with} \quad \Delta^2(k) = 4\pi k^3 P(k) \quad \text{and} \quad \xi_{\hat{\kappa}} = \int d\chi \left(\frac{w}{F_s}\right)^2 I_\kappa, \tag{7}$$

where $W(\mathcal{D}k\theta) = \frac{2}{\mathcal{D}k\theta}\,J_1(\mathcal{D}k\theta)$ is the window function which corresponds to an angular top-hat of radius θ. Thus, Eq. 6 shows that the generating function $\tilde{\varphi}_{\hat{\kappa}}(y)$ is directly related to its counterpart $\tilde{\varphi}(y)$ which is relevant for the 3-dimensional density field smoothed within spherical cells. In fact, a simple approximation is to use:

$$\tilde{\varphi}_{\hat{\kappa}}(y) \simeq \tilde{\varphi}(y) \quad \text{which implies} \quad S_{\hat{\kappa},p} \simeq |\kappa_{\rm min}|^{2-p}\, S_p. \tag{8}$$

This means that to a good approximation the p.d.f. $P(\kappa)$ is obtained from $P(\delta)$ through a mere rescaling.

2 Numerical results

In this section we present the numerical results we obtain from the formalism described above, for the cases of a critical density universe, with $H_0 = 50$ km/s/Mpc and $\sigma_8 = 0.6$, and a low-density flat universe with $\Omega_m = 0.3$, $\Omega_\Lambda = 0.7$, $H_0 = 70$ km/s/Mpc, $\sigma_8 = 0.9$ and $\Gamma = 0.21$. See Valageas [6] for a more detailed description.

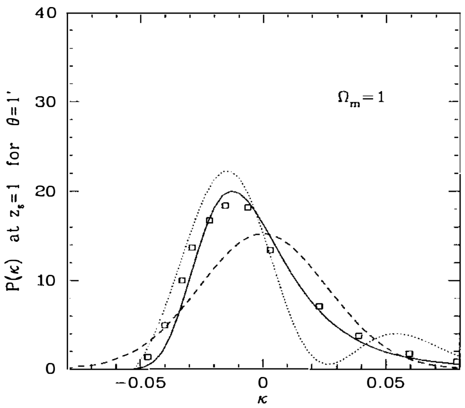

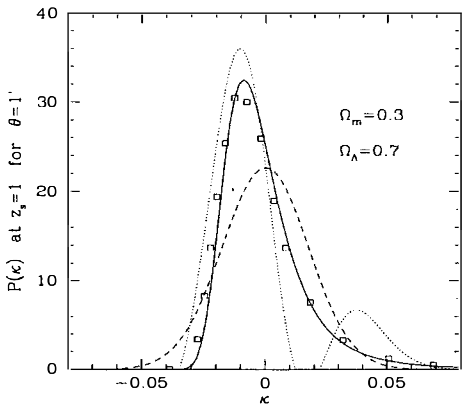

Figure 1: The *p.d.f.* $P(\kappa)$ of the convergence κ for a source at redshift $z_s = 1$ for the angular window $\theta = 1'$. The solid lines show our prediction. The dashed lines show the gaussian which has the same variance $\langle\kappa^2\rangle$. The dotted lines correspond to the Edgeworth approximation obtained from the skewness. The squares show the results of numerical simulations.

We compare in Fig.1 our predictions for the p.d.f. $P(\kappa)$ with the results of numerical simulations [7]. We can see that *our predictions* (solid lines) *agree very well with the numerical results* (open squares). This good agreement means that even if our approximation for the high-order cumulants $\langle\kappa^p\rangle_c$ is not very accurate the p.d.f. we obtain can still be a very good approximation to the actual $P(\kappa)$. Note also that Fig.1 shows that the generating function $\tilde{\varphi}(y)$ does not strongly depend on the cosmological parameters $(\Omega_m, \Omega_\Lambda)$.

We also display in Fig.1 the gaussian (dashed line) which would have the same variance $\langle\kappa^2\rangle$ as our prediction. This shows that $P(\kappa)$ cannot be approximated by a gaussian. In particular, one can clearly see the asymmetry of $P(\kappa)$, with a maximum at a small negative value of κ and an extended tail at large positive κ. Of course, this is due to the features of the p.d.f. of the density contrast itself. Indeed, on small non-linear scales most of the volume is made up of very low density regions ("voids") which explains why $P(\kappa)$ peaks at a negative value of κ (corresponding to negative density contrasts along the line of sight, see (4)). On the other hand, overdense collapsed matter condensations show an exponential tail at large densities which translates into the large-κ tail of $P(\kappa)$. When a p.d.f. shows a small departure from a gaussian it is customary to consider the asymptotic Edgeworth expansion [8]. We display in Fig.1 this expansion up to the first order in $\xi_{\hat{\kappa}}$ (which only involves the skewness). We see that it captures the shift of the maximum of $P(\kappa)$ towards negative κ. However it fails for large κ where a spurious oscillation appears. Thus, even to obtain the shape of $P(\kappa)$ within a 1-sigma interval one needs the complete set of the coefficients S_p.

3 Conclusion

Thus, the method described in this study allows one to express the moments of the convergence in terms of the moments of the density field at all orders, working in real-space. Then, one can sum up the series of the cumulants and to write the full p.d.f. $P(\kappa)$ of the convergence in terms of the p.d.f. $P(\delta_R)$ of the density contrast on comoving scales $x \sim 0.1$ Mpc (for angular windows $\theta \leq 2'$). This provides an explicit link between two properties of the density field: the counts-in-cells statistics and the convergence of weak gravitational lensing distortions. Our results apply to the case of a broad redshift distribution of the sources as well as to the case where all sources are located at the same redshift.

We showed that we obtain a good agreement with the results of numerical simulations. Hence, using the relations between the properties of the density field and the gravitational lensing effects we have described above, one could constrain the cosmological scenario of structure formation from observations. Our results can also be extended to other measures of weak gravitational lensing, like the shear or the aperture mass[9].

However, we must note that we did not take into account several effects which might distort the p.d.f. $P(\kappa)$ we obtained: non-linear coupling between deflecting lenses along the line of sight, higher-order terms beyond the Born approximation, coupling between the sources and the lenses. Although we can expect these effects to be rather small it would be interesting to investigate in details these processes.

References

1. Balian R., Schaeffer R., A&A **220**, 1 (1989).
2. Peebles P.J.E. in *The large scale structure of the universe*, Princeton University Press, 1980.
3. Peacock J.A., Dodds S.J., MNRAS **280**, L19 (1996).
4. Valageas P., Lacey C., Schaeffer R., MNRAS **311**, 234 (2000).
5. Bernardeau F., van Waerbeke L., Mellier Y., A&A **322**, 1 (1997).
6. Valageas P., A&A **356**, 771 (2000).
7. Jain B., Seljak U., White S., ApJ **530**, 547 (2000).
8. Bernardeau F., Kofman L., ApJ **443**, 479 (1995).
9. Bernardeau F., Valageas P., submitted to A&A, astro-ph 0006270.

NUMERICAL STUDY OF THE COSMIC SHEAR

T. HAMANA[1], S. COLOMBI[1,2], and Y. MELLIER[1,3]

[1] *Institut d'Astrophysique de Paris, CNRS, 98bis Boulevard Arago, 75014 PARIS, FRANCE*

[2] *NIC (Numerical Investigations in Cosmology) Group, CNRS*

[3] *Observatoire de Paris, DEMIRM, 61 avenue de l'Observatoire, 75014 PARIS, FRANCE*

We study the cosmic shear statistics using the ray-tracing simulation combined with a set of very large N-body simulations. In this contribution, we first describe our method. Then we show some results, especially, focusing on effects of the deflection of light rays and the lens-lens coupling which are neglected in computing the theoretical predictions of the cosmic shear statistics.

1 Introduction

The cosmic shear statistics have been known as a powerful tool for probing the large-scale structure formation as well as the cosmological model[1]. Recently, four independent groups have reported estimations of cosmic shear variance[2,3,4,5]. Although the current estimations were done with relatively small fields which limit its accuracy, on going wide field cosmic shear surveys will provide a precious measurement of the cosmic shear variance as well as higher order statistics such like the skewness of the lensing convergence.

Since the pioneering work by Gunn[6], there has been a great progress in the theoretical study of the cosmic shear statistics[7]. The analytical formulae for computing the theoretical prediction of the cosmic shear statistics are based on the perturbation theory of the cosmic density field combined with the nonlinear clustering ansatz. The accuracy and limitations of the theoretical predictions should be tested against numerical simulations[8,9].

In this contribution, we summarize, briefly, the methods and selected results of our research project on the numerical study of the cosmic shear, details are presented in[10,11]. The project aims (1) to test the analytical predictions against the numerical simulation (2) to examine the higher order statistics of the cosmic shear (3) to simulate the observation to examine the possible effects caused by, e.g., the source clustering.

Table 1: Parameters in Three Cluster normalized CDM Models

	Ω_m	Ω_Λ	σ_8	h
SCDM	1.0	0.0	0.6	0.5
OCDM	0.3	0.0	0.85	0.7
ΛCDM	0.3	0.7	0.9	0.7

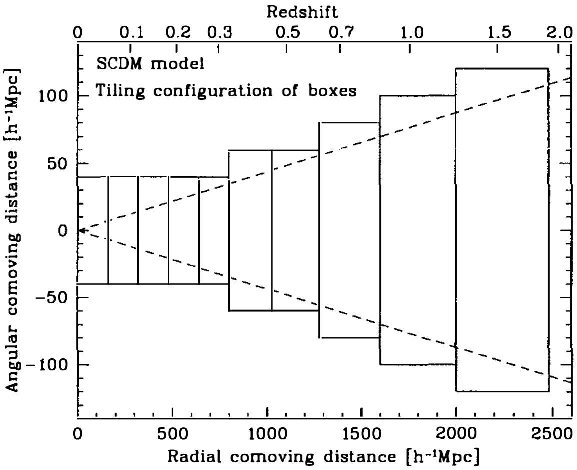

Figure 1: Tiling configuration of simulation boxes. Dashed lines shows the angular comoving distance of ±2.5 degrees.

2 Models and methods

We consider three cluster normalized cold dark matter (CDM) models, parameters in the models are summarized in Table 1. N-body simulations were performed with a vectorized particle-mesh code. They use $256^2 \times 512$ particles and the same number of force mesh in a periodic rectangular comoving box and use light-cone output [10,12]. In order to generate the density field from $z = 0$ to $z \sim 2$, we performed 10, 11 and 12 independent simulations for SCDM, OCDM and ΛCDM model, respectively. We adopted the *tiling* configuration of the boxes[9], i.e., the box size of each realization is chosen so that we have a field of view of 5 x .5 square degrees (see Figure 1).

Light rays are traced through the simulations adopting the multiple-lens plane algorithm[13], the lens planes are located at intervals of $80h^{-1}$. Rays are initially traced backward from the observer point on a 512^2 grid. We computed positions of rays on each lens plane and the lensing magnification matrix, M_{ij}, for each ray. The lensing convergence, shear and net rotation are expressed by $\kappa = (M_{11}+M_{22})/2, \gamma = (M_{11}-M_{22})/2+i(M_{12}+M_{21})/2$, and $\omega = (M_{12}-M_{21})/2$, respectively. We performed 40-set of the ray tracing simulations for each model by randomly shifting the simulation boxes using periodic boundary condition. The error bars shown in Figures 3 and 4 represent the standard deviation among 40 realizations.

Figure 2 shows the convergence field of the source redshift of $z_s = 1$ from one of SCDM model realizations. The filed is 5-degree on a side and contains 512^2 lines of sight. The angular resolution is limited by the spatial resolution of N-body simulation. We found that the effective resolution is about 2 arcmin for the source redshift of $z_s = 1$ and is slightly better (worse) for the higher (lower) redshift.

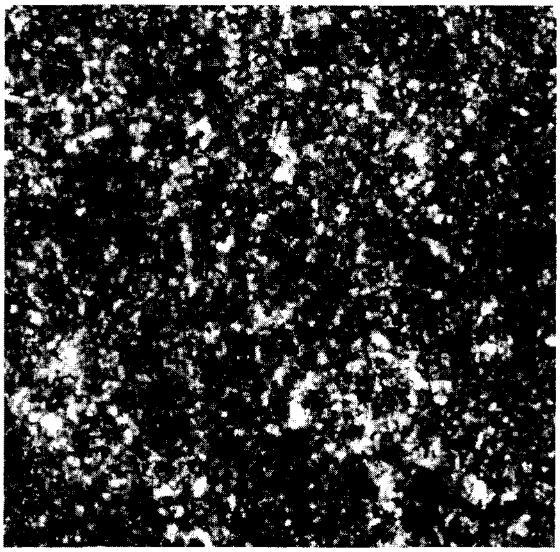

Figure 2: The lensing convergence, κ, field of the source redshift of $z_s = 1$ in SCDM model. The filed is 5-degree on a side.

3 Results and discussion

Figure 3 shows the root-mean-square of the top-hat filtered lensing convergence measured from the ray-tracing simulation compared with the nonlinear prediction. The dumping on smaller scales simply reflects the resolution of the simulation while that on larger scales reflects the finite field effect. One may find the very good agreement between the measurements and the nonlinear predictions.

In order to examine the effects of the deflections of the light rays and the lens-lens coupling[14] which are neglected in computation of the theoretical predictions, we also performed the ray-tracing simulation without including those two. The results are compared with those of the *full* ray-tracing simulations. It is found that the difference in the variance of the lensing convergence (and of shear) between *full* and *approximated* ray-tracing is very small, $|\Delta RMS/RMD| < 0.01$. Therefore the the deflections of the light rays and the lens-lens coupling has no significant effect on the variance.

The skewness parameter S_3 defined by $S_3 = \langle\kappa^3\rangle/\langle\kappa^2\rangle^2$ is known as a powerful probe of density parameter, Ω_m[14], though, it is difficult to make a precious prediction of its value. Figure 4 shows S_3 measured from the ray-tracing simulations compared with the prediction based on the quasi-linear theory of density perturbation. It is clearly shown in Figure 4 that the nonlinearity of the evolution of density field is very important even at the scale $\theta \sim 10$ arcmin. The lower panel of Figure 4 shows the difference in S_3 between measured from *full* and *approximated* ray-tracing. We found that the difference is not significant, $|\Delta S_3/S_3| < 0.05$ for three cosmological models. The theoretical predictions of the skewness parameter with taking the nonlinear clustering into account is made by authors[11,15], those predictions are compared with our numerical results[16].

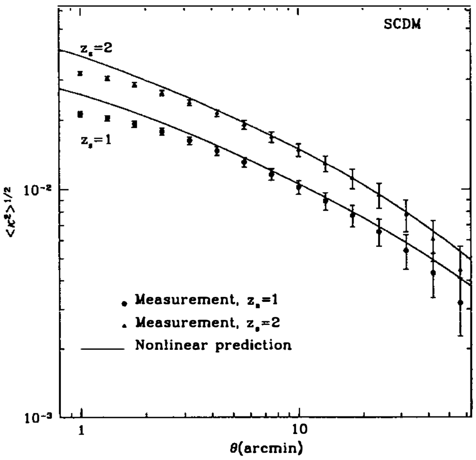

Figure 3: Root-mean-square of the lensing convergence field filtered by the top-hat window function as a function of the filter scale.

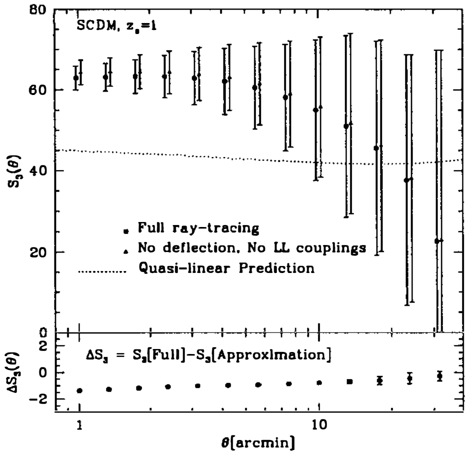

Figure 4: *Top panel*: The skewness parameter S_3 as a function of the filter scale of top-hat window. *Bottom panel*: The difference in S_3 between measured from κ field of *full* ray-tracing and that of *approximated* ray-tracing.

Acknowledgments

We would like to thank L. van Waerbeke, F. Bernardeau and A. Thion for many discussions. This research was supported in part by the Direction de la Recherche du Ministère Français de la Recherche. The computational means (CRAY-98) to do the N-body simulations were made available to us thanks to the scientific council of the Institut du Développement et des Ressources en Informatique Scientifique (IDRIS) Numerical computation in this work was partly carried out at the the TERAPIX data center. TH would like to thank Moriond organization for financial supports.

References

1. Y. Mellier, ARAA, **37**, 127 (2000).
2. L. van Waerbeke et al., A&A, **358**, 30 (2000).
3. D. Bacon, A. Refregier and R. Ellis, MNRAS submitted (astro-ph/0003008), (2000).
4. D. N. Wittman et al., Nature, **405**, 143 (2000).
5. N. Kaiser, G. Wilson and G. A. Luppino, ApJ submitted (astro-ph/0003338), (2000).
6. J. E. Gunn, ApJ, **150**, 737 (1967).
7. M. Bartelmann and P. Schneider, submitted to Physics Report (astro-ph/9912508), (2000)
8. B. Jain, U. Seljak and S. White, ApJ, **530**, 547 (2000).
9. M. White and W. Hu, ApJ, **537**, 1 (2000).
10. T. Hamana, S. Colombi and Y. Mellier, in preparation, (2000).
11. L. van Waerbeke et al., in preparation (2000).
12. T. Hamana, S. Colombi and Y. Suto, A&A submitted (2000).
13. P. Schneider, J. Ehlers, & C. C. Falco, *Gravitational Lenses* (Springer, Berlin, 1992).
14. F. Bernardeau, L. van Waerbeke and Y. Mellier, A&A, **323**, 1 (1997).
15. L. Hui, ApJ, **519**, L9 (1999).

A NUMERICAL STUDY OF COSMIC SHEAR STATISTICS

A. Thion[1], Y. Mellier[1,2], F. Bernardeau[3], E. Bertin[1,2], T. Erben[4], L. van Waerbeke[5]
[1] *Institut d'Astrophysique de Paris, 98 bis bvd Arago 75014 Paris, France*
[2] *DEMIRM, Observatoire de Paris, 61 avenue de l'Observatoire 75014 Paris, France*
[3] *SPhT, CEA/Saclay, F-91191 Gif-sur-Yvette cedex, France*
[4] *Max-Planck-Institut für Astrophysik, Karl-Schwarzschild-Str. 1, 85741 Garching, Germany*
[5] *CITA, 60 St. George Street, Toronto M5S 3H8, Canada*

Abstract

We explore the stability of the variance and skewness of the cosmic gravitational convergence field, using two different approaches: first we simulate a whole MEGACAM survey (100 sq. degrees). The reconstructed mass map, obtained from a shear map recovered by the usual method via a maximum likelihood method, shows that the actual state-of-the-art data analysis methods can accurately measure weak-lensing statistics at angular scales ranging from 2.5' to 25'. We looked also at the influence of a varying signal-to-noise ratio over the shear map (due to local variations of source density) on the mass reconstruction, by means of Monte-Carlo simulation. The detectable effect at small scales can easily be corrected-for in most of the relevant cases. These results enhance the confidence in the capability of future large surveys to measure accurately cosmologically interesting quantities.

1 Introduction

The cosmic shear effect has recently been detected (see Bacon et al. 2000, Wittman et al. 2000, Kaiser et al. 2000, van Waerbeke et al. 2000 and these proceedings) and the shear variance has been measured in a range of scales from 30" to 10'. However, theoretical investigation of lensing statistics (Bernardeau et al 1997) show that the measurement of the third order moment of the convergence κ is necessary to break the degeneracy between Ω_m and σ_8 (for symmetry reasons, the third order moment of the shear is null). This implies to proceed to a full reconstruction of the convergence map.
Knowing that the skewness of the convergence field is a statistic much more difficult to measure than the variance, this raises a few questions: (1) do the measurement errors preserve the correlation between cells? (2) How the measurement errors of the shear propagate into the convergence reconstruction? (3) How to correctly estimate the noise due to the intrinsic ellipticity of galaxies in an observational context? (4) How clustering of the galaxies (leading to a spatially varying S/N ratio) affects this reconstruction?
The points 1) and 2) have been adressed by van Waerbeke et al. (1999), considering only the noise coming from intrinsic ellipticity. We tried a different approach: we performed two kinds of simulations to partly address all those problems.

2 The simulated lensing survey

We performed the simulation of a large (100 deg^2) compact survey whose characteristics are similar to those of the future MEGACAM dedicated survey at CFHT. The simulation is generated in 6 steps:
First we have created the synthetic catalog of the whole survey (in an open CDM Universe), using the *SkyStuff* [a] program. We then modified the relevant galaxy parameters (axis ratio, luminosity, etc.) accordingly to 2-dimensional simulations of dark matter with an angular resolution of 2.5' (see van Waerbeke et al (1999) for details). We generated in this manner numerous sub-catalogs (40×40) and used the *SkyMaker* [a] software to create the synthetic images of the galaxies lensed by this 2D simulation. These images have been analyzed with *IMCAT* [b], and we used SExtractor to clean the catalogs of spurious detections (and to select

[a] SkyStuff and SkyMaker are freely available at ftp://ftp.iap.fr/pub/from_users/bertin
[b] see http://www.ifa.hawaii.edu/faculty/kaiser/

Table 1: Characteristics of the simulated survey: the catalog is obtained from a Schechter function and a PDE prescription, and designed to reproduce observations. The images are simulation of CCD frames taken at CFHT.

Size	100 sq. degrees
Catalog initial density	≈ 31 galaxies/arcmin^2
Density of detected objects	≈ 22 galaxies/arcmin^2
Catalog features	$m_{gals} \in [17, 24.5]$, LMC ext. law
Image pixel size	0.2"
Seeing FWHM	0.7"
PSF anisotropy	0.05" rms/axis (tracking)
Sky SB, read-out noise	20 mag/arcsec^2 (I Band), 5e$^-$/ADU
Object selection	FLAG = 0, $\lvert e_{1,2}\rvert \leq 1$
Stars	$m_* \in [10, 21.5]$, 60 usables/image

the objets with uncorrupted photometry as indicated by the FLAG keyword). The measured shear was then used to reconstruct the κ map.
The characteristics of the survey are listed in table 1. As we have only 2-dimensional dark matter simulations for a 10×10 degrees map, all sources in a given area are affected the same way, regardless of their redshift. Considering the wide variety of shear values and galaxy parameters, this should not weaken our conclusions. The shear is estimated by the quantities $\frac{\langle e_1\rangle}{\langle P^\gamma_{11}\rangle}$ and $\frac{\langle e_2\rangle}{\langle P^\gamma_{22}\rangle}$, where the P^γ's are components of the shear susceptibility tensor and $\langle\rangle$ means a *spatial* average.
To correct for the noise coming from intrinsic ellipticity, we have simply calculated $\frac{\langle e_1^2\rangle}{\langle P^{\gamma^2}_{11}\rangle}$.
Since the theoretical noise is defined from the complex ellipticity,

$$\epsilon = \frac{a-b}{a+b} e^{i2\theta} \tag{1}$$

which is not equal to the KSB-defined ellipticity (which is itself filtered by Gaussians windows, etc.) it is interesting to get such a simple estimator. Nevertheless, this estimation is in very good agreement with the noise one can measure directly on the power spectrum of $|\gamma|$, indicating that we obtain a white noise. We applied the results of Bernardeau et al (1997) to correct for the cosmic variance, using a 'sample size' equal to 6 times our largest scale of measure, i.e. 2.5 degree. The variance and skewness of κ that we obtain as a function of the filtering scale are shown in fig 1.

Although the simulated images still have a quality superior of those of real data (e.g. no strong PSF anisotropy - we still performed the anisotropy correction -, no big diffraction spikes, no bad columns, no strong gradients), the accuracy of those measures shows that current measurement techniques, applied to high-quality data, are reliable enough to allow a good determination of large-scale lensing statistics.

3 Varying the S/N ratio on the shear map

In the weak lensing approximation one usually estimates the shear inside a window by the mean of the galaxies' ellipticities inside the window, i.e.

$$\tilde{\gamma}_\alpha = \gamma_\alpha + \frac{\sum_1^N \epsilon_\alpha}{N} \tag{2}$$

So one considers the variance of the estimator

$$\langle\tilde{\gamma}^2\rangle_{\epsilon,N} \simeq \langle\gamma^2\rangle + \frac{\sigma_\epsilon^2}{\bar{n}} \tag{3}$$

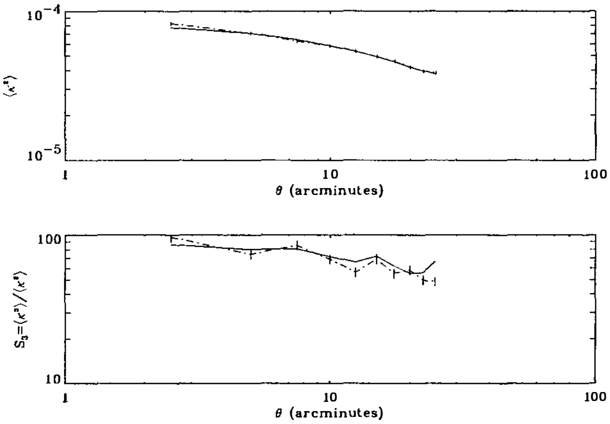

Figure 1: Variance and skewness of the convergence field measured from the simulated survey (dash-dotted lines) compared to the theoretical values (solid lines). The "error" bars are the minimal errors calculated by van Waerbeke et al (1999).

where $\bar{n}$ is the mean number of objects per window and $\langle\rangle_{\epsilon,N}$ means averaging on the ellipticity distribution and the spatial distribution of tracers. It is then clear that the signal-to-noise ratio of the shear depends on the local density of tracers, leading to local noise variation. To investigate this effect, we performed a simulation of a 25 $\deg^2$ survey, again with 2-dimensional shear maps; the positions of tracers were drawn either from a random (Poisson) distribution, or as the result of a random-walk process, of which third and fourth moment are independant of scale, while the angular autocorrelation function of the galaxies has an amplitude roughly one order of magnitude higher than that of faint blue galaxies (~ 0.15 at 1', see e.g. Brainerd & Smail (1998)). We used 60 realizations of the dark matter maps, and for each of them we have distributed intrinsically elliptical tracers ($\sigma_{|\epsilon|} \approx 0.2$), distributed in the two differents manners, and we studied 3 different densities (10, 30 and 200 objects/arcmin^2).

The results on the variance for $\bar{n} = 30$ galaxies/arcmin^2 are show in fig. 2.; an excess of power at small scales is visible in the case of clustering of galaxies. Note however that in this set of simulations galaxy positions are uncorrelated with dark matter distribution (Bernardeau 1998). Although this is not presented on a plot, we checked that the effect on the skewness is only due to the alteration of the variance. To correct for the effect, one has to realize the simple fact that the noise correction must not be done by means of eq. (3), but instead that

$$\langle\tilde{\gamma}^2\rangle_{\epsilon,N} \simeq \langle\gamma^2\rangle + \sigma_\epsilon^2 \times \langle\frac{1}{N}\rangle \tag{4}$$

where $\langle\frac{1}{N}\rangle$ is filtered at the scale of interest. For strongly correlated, low-density samples, the $\langle\frac{1}{N}\rangle$ statistic can significantly differ from $\frac{1}{\bar{n}}$. We can see on fig. 2. that this suffices to solve the problem. Such a correction is not as accurate in the $\bar{n} = 10$ galaxies/arcmin^2 case, but this should not constitute a problem in an observational context as the current surveys have galaxies samples with larger density and correlation length.

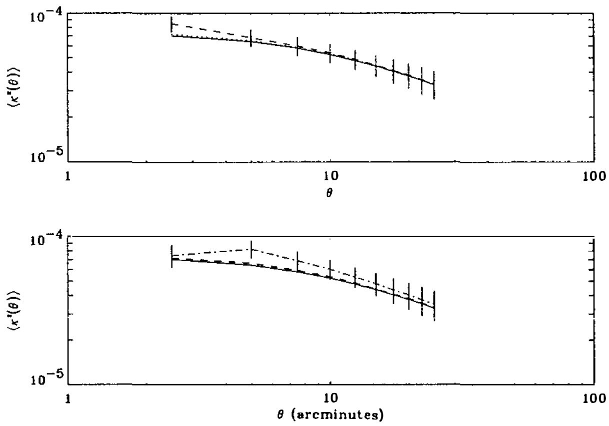

Figure 2: The variance of the convergence field for a 25 sq degrees survey. *Top panel* : the tracers density is 30 objects/arcmin^2 and a the ellipticity noise correction made by $\frac{\sigma_\epsilon^2}{\bar{n}}$. The solid line is the theoretical value, the dotted line is the value obtained for a poisson distribution of tracers, the dashed-line is obtained when the tracers positions are drawn from a random-walk. *Bottom panel* : the dashed line is the variance of the random-walk case, with noise corrected as $\sigma_\epsilon^2 \times < \frac{1}{N} >$. The dash-dotted line is the same case with a tracer density of 10 objects/arcmin^2. For clarity only error bars of the 'problematic' cases are shown.

4 Conclusion

In the framework of future wide field surveys (e.g. the MEGACAM lensing survey), it is essential to verify the stability of the statistics of the density field through the measurement process. We checked this stability in two ways: first we performed a detailed simulation of a large (100 deg^2), compact survey and analyzed the obtained images, and we succeeded to extract the cosmological signal. Secondly, we investigated the effect of rapidly varying S/N ratio on the convergence reconstruction via realizations of a random-walk process; the effect introduces spurious variance at small scales but can easily be corrected for in most relevant cases. This work therefore enhances our confidence on the capability of future wide surveys to accurately measure cosmic shear statistics.

Acknowledgments

This work was supported by the TMR Network "Gravitational Lensing: New Constraints on Cosmology and the Distribution of Dark Matter" of the EC under contract No. ERBFMRX-CT97-0172. A. T. is grateful to the MAGIQUE center (IAP) for providing storage and computational facilities. The authors would also like to thank the organizers of the Rencontres de Moriond.

References

1. Bacon, D. J., Réfrégier, A., Ellis, R. S., *MNRAS* , (2000), submitted
2. Bartelmann, M., Narayan, R., Seitz, S., Schneider, P., *ApJ* **464**, L115-L118 (1996)
3. Bartelmann, M., Schneider, P., astro-ph/9912508, submitted to Elsevier Preprint
4. Bernardeau, F., *A&A* **338**, 375:382 (1998)
5. Bernardeau, F., van Waerbeke, L., Mellier, Y., *A&A* **322**, 1:18 (1997)
6. Bertin, E., Arnouts., S., *A&AS* **117**, 393-404 (1996)
7. Hoekstra, H., Franx, M., Kuijken, K., Squires, G., *ApJ* **504**, 636 (1998)
8. Brainerd, T. G., Smail, I., *ApJ* **494**, L137B (1998)
9. Kaiser, N, Squires, G. & Broadhurst, T., *ApJ* **449**, 460 (95)
10. Kaiser, N., Wilson, G., Luppino, G., astro-ph/0003338, *ApJ Letters* , (2000), submitted

11. Luppino, G. A., Kaiser, N., *ApJ* **475**, 20 (1997)
12. Mellier, Y., *ARAA* **37**, 127:189 (1999)
13. van Waerbeke, L., Bernardeau, F., Mellier, Y., *A&A* **342**, 15:33 (1999)
14. van Waerbeke, L. *et al.*, *A&A* , (2000), in press
15. Wittman, D. M. *et al.*, *Nature* **405**, 143-148 (2000)

FOREGROUND-BACKGROUND GALAXY CORRELATIONS IN THE HUBBLE DEEP FIELDS

D. HERRANZ[1], N. BENITEZ[2] & J.L. SANZ[1]

(1) IFCA (CSIC-UC), Avda. los Castros s/n, 39005 Santander, Spain

(2) Astronomy Department, UC Berkeley, 601 Campbell Hall, Berkeley, CA, U.S.A.

A change in the density of distant galaxies is expected around foreground galaxies due to gravitational lensing. The Hubble Deep Field North and the Hubble Deep Field South provide us with the deepest sample of galaxies up to now available and therefore with a good test field for this magnification bias effect. We have used Bayesian Photometric Redshifts (BPZ) to separate clearly distinct foreground and background populations in different slices of redshift. The BPZ technique minimizes the possibility of contamination between background and foreground populations. We have studied the distribution of $I_{814} < 27$ background galaxies around foreground galaxies. For low redshift foreground galaxies ($z_f < 0.6$) in the HDF-N we detect with 99% c.l. a negative correlation consistent with the slope of the background number counts and gravitational lensing. The results in the HDF-S are not conclusive due to the lower number of spectroscopic redshifts available. Finally, we use the measured correlations together with autocorrelation function models of the foreground galaxies taken from the literature to estimate Ω/b. The number of galaxies we have is too small to constraint well this quantity.

1 Introduction

The Hubble Deep Field North (Williams *et al.* 1996) and the Hubble Deep Field South (Williams *et al.* 1999) provide us with the deepest sample of galaxies up to now available. Here we study the magnification bias induced by foreground galaxies in the background sources. As it is known, dark matter fluctuations act as gravitational lenses. Galaxy formation takes form preferably in overdense regions (under the biasing hypothesis), so galaxies are tracers of the underlying dark matter fluctuations. Therefore, a correlation appears between foreground and background galaxies. In the weak lensing regime, $w_{fb} = b(\alpha_b - 1)C_{\mu\delta}$, where b is the bias factor and $C_{\mu\delta}$ is the correlation between the magnification and the matter fluctuations. The quantity α_b is related to the slope of the cumulative number counts of galaxies with magnitude lower than m through $\alpha_b = 2.5\frac{dlog(N<m)}{dm}$. Finally, $C_{\mu\delta}$ can be calculated in terms of the power spectrum of matter fluctuations and the cosmological parameters (Sanz *et al.* 1997) and is related to the foreground autocorrelation w_{ff}. Then it is possible to calculate w_{fb} in any case, although it can be very complicated. Assuming that the foreground and background galaxies are concentrated at the effective distances λ_f and λ_b, it can be proven (Benítez & Sanz 1999) that

$$\frac{w_{fb}}{w_{ff}} \simeq Q(z_f, z_b)\Omega b^{-1}(\alpha_b - 1)\Delta z_f \tag{1}$$

In this equation Δz_f is the width of the p.d.f. of the foreground galaxies (e.g. the FWHM for a Gaussian distribution). $Q(z_f, z_b)$ is a geometrical factor which depends only on the Cosmology and it has some desirable properties: for $z_f < 1$ and $z_b > 1$, it changes very slowly with z_b and almost linearly with z_f. Most important, it is approximately independent on Ω. Then the dependence in Ω in eq. (1) is linear and w_{fb}/w_{ff} can be used to estimate Ωb^{-1}.

Given a sample of galaxies, if we can clearly separate foreground and background subsamples in such a way that they are not physically connected, the cross-correlation between the subsamples will be due to gravitational lensing. If the thin screen approximation is valid, the correlation can be used to constrain the value of Ωb^{-1}.

2 Data, Photometric Redshifts and Correlation Estimation

The data we use are the well known Hubble Deep Field North and South images. Both HDF-N and HDF-S are believed to be *typical fields* and therefore any conclusion drawn from them should lead to constraints applicable to the whole sky. The photometry is taken from the literature and includes the optical HDF bands F300W, F450W, F606W and F814W as well as infrared J, H and K filters (Fernández-Soto *et al.* 1999). During the final field selection we excluded the region occupied by the Planetary Camera images and divided each of HDF-N and HDF-S fields in three square regions of 1800x1800 pixel^2, covering an angular area of 72x72 arcsec^2 each. The resulting regions correspond to the inner parts of the Wide Field Camera and contains 291, 325 and 349 galaxies inside the HDF-N regions and 330, 344 and 383 inside the HDF-S ones.

To separate foreground and background subsamples, we need to know the redshift of each galaxy. There are only few dozens of spectroscopic redshifts measured in the HDF-N galaxies, and very few in the HDF-S, so we need the best available photometric redshift technique. Bayesian Photometric Redshift (BPZ) technique (Benítez 2000) allows the inclusion of all valuable information, e.g. the redshift distribution of the galaxy type mix, and therefore prevents color/redshift degeneracies. Moreover, it provides a useful way of quantifying the accuracy of redshift estimation. There is an excellent agreement between the HDF-N spectroscopic redshifts and the estimated photometric redshifts, with no significant biases, and the rms error is $\Delta z/(1 + z_{spec}) = 0.08$ up to $z < 6$.

There are several estimators of the 2-point correlation function commonly used in Cosmology. The most straightforward and extensively used are based in the count of pairs of points distributed in bins of angular separation. For a detailed review on the different estimators and its properties, see Pons-Bordería *et al.* (1999). Among these estimators, we tested the most commonly used and finally chose a symmetrized form of the Landy & Szalay estimator (Landy & Szalay 1993):

$$\hat{w} = 1 + \frac{BF(r)}{RR(r)} \times \frac{N_{RR}}{N_{BF}} - \frac{BR(r)}{RR(r)} \times \frac{N_{RR}}{N_{BR}} - \frac{FR(r)}{RR(r)} \times \frac{N_{RR}}{N_{FR}} \tag{2}$$

where the notation XY denotes the number pairs composed by a galaxy of a sample X and the other galaxy from the sample Y. The samples considered are foreground galaxies (F), background ones (B) and synthetic, uniformly distributed random sample (R). This random sample has to be big enough to cover all the area under study and for this particular case a number of 10^5 random points (in each square field) is needed.

To obtain error bars we compute the correlation function estimators for 500 simulated samples with the same number of galaxies as the original one generated by bootstrap resampling. The variance in the estimates gives a measure of the uncertainty in w. The bootstrap technique in correlation analysis is well-established and its performance is proven to be optimal.

3 Results

The BPZ technique provides us with a solid method to estimate and control uncertainties. This has been used to construct reliable confidence intervals for each galaxy redshift. Let us define the intervals in redshift that delimitate the foreground and background subsamples, and let us include in those subsamples only the galaxies whose 99% confidence interval do not intersect with the redshift limits. Doing this, we can be pretty sure of severely reducing the contamination effects. The drawback is that only the galaxies satisfying a certain requirement can be considered: we loose a big number of galaxies. This problem can not be avoided and it is inherent to the usage of photometric redshifts.

In the final election of the intervals we have to bear in mind also several other factors. First, $Q(z_f, z_b)$ must be almost constant along the background interval. The width Δz_f has to be small. To have a measurable effect $(\alpha_b - 1)$ must depart form 0. This point is particularly tricky in the HDF: $(\alpha_b - 1)$ is always close to 0 and the difference is very small for $1.0 < z_b < 1.5$ (to ensure completeness we only consider background galaxies with magnitude $I_{814} < 27.0$). Finally, there should be enough number of galaxies in each redshift interval to estimate both the cross-correlation function and the autocorrelation functions. Using our criteria, is impossible to satisfy both requirements *at the same time*: if we choose a foreground interval big enough to calculate w_{ff} with statistical significance, the background interval has few galaxies and the number of pairs background-foreground is not enough to estimate w_{fb} properly, and vice versa. We choose to make a estimation as good as possible of w_{fb} and take w_{ff} from the literature.

HDF-N results: The cross-correlation function w_{fb} is shown in Figure 1 for the intervals $0 < z_f < 0.6$, $z_b > 0.65$. For this case, the slope α_b is 0.66 ± 0.06 and therefore we expect a negative correlation (the autocorrelation function of the foreground galaxies is positive). We fit the points to a model $\hat{w}(r) = A_{fb}r^{-\gamma} - C$, where C is a integral constraint which is calculated numerically and for this particular geometry its value is about 10^{-3} times the value of the amplitude A_{fb}. The slope γ is fixed to a value 0.8. The fit gives $A_{fb} = -0.32 \pm 0.18$ (at $1''$). If we don't use the last point of the graphic, which does not fit very well to the model, we obtain a similar value of $A_{fb} = -0.38 \pm 0.18$. A simple Spearman's correlation test gives a 99% confidence level for the detection. From the literature we obtain the amplitude of the foreground-foreground autocorrelation function $A_{ff} = 1.07 \pm 0.57$ (Arnouts *et al* 1999). The foreground distribution has a width of $\Delta z_f \simeq 0.3$ and the background slope is $(\alpha_b - 1) \simeq -0.34 \pm 0.06$. Using eq. (1) we obtain $\frac{\Omega}{b} \simeq 4.2 \pm 3.3$.

Other intervals of redshift are not so favorable for cross-correlation analysis. For example, it would be desirable to use the overdensity region $0.4 < z < 1.2$ as our foreground interval, hoping that the stronger w_{ff} would give a clearer detection of w_{fb}. Unfortunately, background galaxies behind that region have $\alpha_b = 0.95 \pm 0.07$, very close to the critical value of 1. No significant correlation is expected and none was found.

HDF-S results: The lack of spectroscopic redshifts in the HDF-S advise against the construction of foreground subsamples using the photometric redshift confidence intervals. Any reasonably thin foreground slice will contain only a handful of galaxies, and if we widen the redshift interval the thin screen approximation is not valid any more. To illustrate this, let us consider the foreground interval $0.0 < z_f < 0.6$. In that interval, and considering the confidence intervals in photometric redshifts, we find 62 galaxies in the HDF-N, 41 of them having spectroscopic redshifts. If we look to the HDF-S, we find 27 galaxies and only one of them has a spectroscopic redshift. The difference is even greater if we consider the number of foreground-background that can be formed in both fields: 23560 in the HDF-N versus 7155 in the HDF-S. This severely limits the significance of HDF-S based results. There was not found any coherent correlation signal in the different redshift slices tested by the authors.

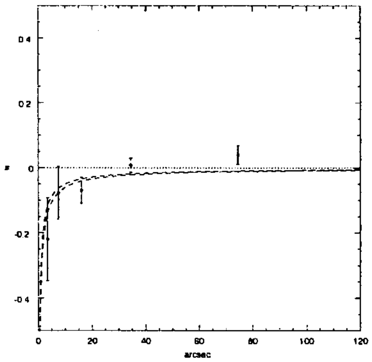

Figure 1: Foreground-background correlation in the HDF-N for the case $0 < z_f < 0.6$, $0.65 < z_b$. The lower dashed line corresponds to the fit discarding the last point of the figure.

4 Conclusions

We have detected a cross-correlation due to gravitational lensing effect with a 99% confidence level in the Hubble Deep Field North. In the Hubble Deep Field South we don't have enough statistic to reach any conclusion. Using HDF-N data, we constrained $\frac{\Omega}{b} \simeq 4.2 \pm 3.3$. This a quite large value, as there is strong evidence of the true values of the parameters is near $\Omega \simeq 0.3$ and $b \sim 1$. The result is qualitatively consistent with magnification bias but quantitatively is bigger than expected. This kind of result is not new in cross-correlation analysis history. QSO-galaxy correlation results tend towards larger effects of lensing than predicted by theory (see Benítez *et al.* 2000 and references therein for a short review on observations and the different hypothesis that could explain them). In the HDF-S the results are too noisy to extract any meaningful conclusion from them. The main reason is the absence of spectroscopic redshifts, so we conclude that the presence of spectroscopic redshifts is vital to this kind of study.

References

1. Arnouts, S., Cristiani, S., Moscardini, L., Matarrese, S., Lucchin, F., Fontana, A. & Giallongo, E., 1999 MNRAS, 310, 540
2. Benítez, N., 2000, ApJ, 536, 571
3. Benítez, N. & Sanz, J.L., 1999, ApJ, 525L, 1
4. Benítez, N., Sanz, J.L. & Martínez-González, E., 2000, submitted to MNRAS
5. Fernández-Soto, A., Lanzetta, K. M., & Yahil, A., 1999, ApJ, 513, 34
6. Pons-Bordería, M. J., Martínez, V. J., Stoyan, D., Stoyan, H. & Saar, E., 1999, ApJ, in press
7. Sanz, J.L., Martínez-González, E. & Benítez, N., 1997, MNRAS, 291, 418
8. Williams, R. *et al.*, 1996, AJ, 112, 1335-1389
9. Williams, R. *et al.*, 1999, AJ, in press

GRAVITATIONAL LENSING EFFECT ON TWO-POINT CORRELATION FUNCTION OF HOTSPOTS IN THE CMB MAPS

Masahiro Takada, Eiichiro Komatsu and Toshifumi Futamase
Astronomical Institute, Graduate School of Science, Tohoku University, Sendai 980-8578, Japan

We investigate the weak gravitational lensing effect on the two-point correlation function of local maxima (*hotspots*) in the cosmic microwave background (CMB) maps, which is caused by the gravitational field due to the intervening large-scale structure. The lensing signatures to the hotspots correlation function can efficiently probe the mass fluctuations with relatively large wavelength modes around $\lambda \approx 50h^{-1}$ Mpc. Using the numerical experiments, we quantitatively show that the lensing signatures can provide robust constraints on the normalization of matter power spectrum for the flat universe with and without the vacuum energy density, provided that we use realistic maps with 65% sky coverage expected from *Planck Surveyor*.

1 Introduction

The recent high precision balloon-borne experiments, BOOMERANG[1] and MAXIMA[2], revealed that the measured angular power spectrum of the cosmic microwave background (CMB) is in good agreement with that predicted by standard inflation paradigm. The inflationary scenarios also predict that the primordial temperature fluctuations are Gaussian and, in this case, statistical properties of any primary CMB field can be exactly predicted based on the Gaussian random theory [3,4]. It has been recently shown that the two-point correlation function of local maxima (*hotspots*) in the CMB maps, $\xi_{\rm pk-pk}(\theta)$, has more oscillatory features than the shape of the conventionally used two-point correlation of temperature fluctuations field itself [5]. This physically means that the pairs of hotspots are distributed with some characteristic angular separations on the last scattering surface. We then found that the weak lensing fairly smooths out the oscillatory shape of $\xi_{\rm pk-pk}(\theta)$ as a result of the redistribution in the observed maps of the intrinsic pairs of hotspots separated with those characteristic angles [6]. In particular, the lensing signatures to the depression feature of $\xi_{\rm pk-pk}(\theta)$ around large angular scales ($\theta \approx 70'$) are pronounced, and therefore it can be a efficient probe of the mass fluctuations with the large wavelength modes such as $\lambda \approx 50h^{-1}$Mpc.

2 Lensing effects on the two-point correlation function of hotspots

To derive the lensed two-point correlation function of hotspots, we consider the number density fluctuations field of hotspots defined by $\delta n_{\rm pk}(\boldsymbol{\theta}) \equiv (n_{\rm pk}(\boldsymbol{\theta}) - \bar{n}_{\rm pk})/\bar{n}_{\rm pk}$, where $n_{\rm pk}(\boldsymbol{\theta})$ and $\bar{n}_{\rm pk}$ are the number density field and the average density of hotspots. Since the CMB photons are randomly deflected by the gravitational field due to the intervening large-scale structure during their propagations, the lensed number density fluctuation field $\delta n^{\rm GL}_{\rm pk}(\boldsymbol{\theta})$ observed at a certain angular direction $\boldsymbol{\theta}$ is the intrinsic filed $\delta n_{\mathrm{pk}}(\boldsymbol{\theta}+\delta\boldsymbol{\theta})$ emitted from the another direction $\boldsymbol{\theta}+\delta\boldsymbol{\theta}$ on the last scattering surface, where $\delta\boldsymbol{\theta}$ is the lensing deflection angle field. Since the weak lensing effect can be measured only in a statistical sense, we focus our investigations on the lensing effects on the two-point correlation function of hotspots. We can easily derive the lensed (observed) two-point correlation function of hotspots[6,7] in the similar way as the method developed by Seljak [8];

$$\xi^{\mathrm{GL}}_{\mathrm{pk-pk}}(\theta)=\left\langle \delta n^{\mathrm{GL}}_{\mathrm{pk}}(\boldsymbol{\theta}_1)\delta n^{\mathrm{GL}}_{\mathrm{pk}}(\boldsymbol{\theta}_2)\right\rangle_{|\boldsymbol{\theta}_1-\boldsymbol{\theta}_2|=\theta}\approx\frac{1}{(2\pi\theta)\sigma_{\mathrm{GL}}(\theta)}\int d\theta'\theta'\xi_{\mathrm{pk-pk}}(\theta')K(\theta,\theta') \qquad (1)$$

where the kernel $K(\theta,\theta')$ is given by $(1/\sigma^2_{\mathrm{GL}}(\theta))\exp[-(\theta^2+\theta'^2)/(2\sigma^2_{\mathrm{GL}}(\theta))]I_0[\theta\theta'/\sigma^2_{\mathrm{GL}}(\theta)]$ and $I_0(x)$ is the modified zeroth-order Bessel function. The important quantity $\sigma_{\mathrm{GL}}(\theta)$ is the dispersion of lensing deflection angle field, which depends on the projected matter power spectrum[6,7,8]. The unlensed $\xi_{\mathrm{pk-pk}}(\theta)$ can be exactly computed based on the Gaussian random theory once the angular power spectrum C_l is given [5]. Especially, the equation (1) shows that the lensing signature ($\delta\xi_{\mathrm{pk-pk}}(\theta)=\xi^{\mathrm{GL}}_{\mathrm{pk-pk}}(\theta)-\xi_{\mathrm{pk-pk}}(\theta)$) at a certain angle θ is a measure of the lensing dispersion $\sigma_{\mathrm{GL}}(\theta)$ at the same scale. However, since the more fundamental quantity is the three-dimensional mass fluctuations field $\delta(\boldsymbol{x})$, we need to carefully investigate the projection effect how scale mass fluctuations and how redshift structures produce dominant contributions to $\sigma_{\mathrm{GL}}(\theta)$ in order to constrain the cosmological parameters from $\delta\xi_{\mathrm{pk-pk}}(\theta)$.

3 Dependence of the lensing signatures on the normalization of matter power spectrum

To perform quantitative predictions, we specify the cosmological models. Here we consider two background models with $\Omega_{\mathrm{m}0}=1, h=0.5$ (SCDM) and $\Omega_{\mathrm{m}0}=0.3, \Omega_{\lambda 0}=0.7, h=0.7$ (LCDM), where $\Omega_{\mathrm{m}0}$ and $\Omega_{\lambda 0}$ are the energy densities of the non-relativistic matter and the vacuum and h is a Hubble parameter in units of $H_0=100h$km s^{-1} Mpc^{-1}. As for the matter power spectrum, we employed BBKS transfer function. The free parameter of our model is only the normalization of matter power spectrum, which is conventionally expressed in terms of the rms mass fluctuations of a sphere of $8h^{-1}$Mpc, i.e., σ_8. The dependences of σ_8 on the lensing effect on $\xi_{\mathrm{pk-pk}}(\theta)$ are demonstrated by sets of $\sigma_8=0.5,1.0,1.5$ in SCDM and $\sigma_8=1.0,1.5,2.0$ in LCDM, respectively.

Furthermore, in order to quantitatively investigate the detectability of the lensing signatures to $\xi_{\mathrm{pk-pk}}(\theta)$ for the future sensitive satellite mission *Planck Surveyor*, we correctly estimate the effect of the cosmic variance on measurements of $\xi_{\mathrm{pk-pk}}(\theta)$ by using a lot of realizations of the numerically simulated CMB maps with and without the lensing effect. Then we also take into account the observational errors associated with the beam smearing of a telescope and the detector noise. Here we adopted specifications of the 217GHz channel on Planck; the beam size is $\theta_{\mathrm{fwhm}}=5.5'$ and the noise level per FWHM pixel is $\sigma_{\mathrm{noise}}(=\delta T_{\mathrm{noise}}/T_{\mathrm{CMB}})=4.3\times10^{-6}$. It is straightforward to include those experimental effects into the theoretical predications of $\xi_{\mathrm{pk-pk}}(\theta)$ as well as the numerical simulations of the lensed and unlensed CMB maps (see [7] in detail).

Figure 1 shows an example of the numerical results of the lensed two-point correlation function of hotspots of height above the threshold $\nu=1(\Delta_{\mathrm{pk}}=\sqrt{\langle\Delta^2\rangle})$ in SCDM and LCDM expected from Planck, respectively. Here we assumed $\sigma_8=1.5$ in both models. For comparison, the solid and dashed curves show the theoretical predictions of the lensed and unlensed $\xi_{\mathrm{pk-pk}}(\theta)$, respectively. The error bar in each bin is calculated by scaling the variance of the estimates obtained from a lot of realizations of simulated CMB maps by the factor corresponding to 65% sky coverage[7]. The figure clearly shows that the weak lensing fairly smooths out the oscillatory shape of the intrinsic $\xi_{\mathrm{pk-pk}}(\theta)$ and the theoretical predictions are in good agreement with

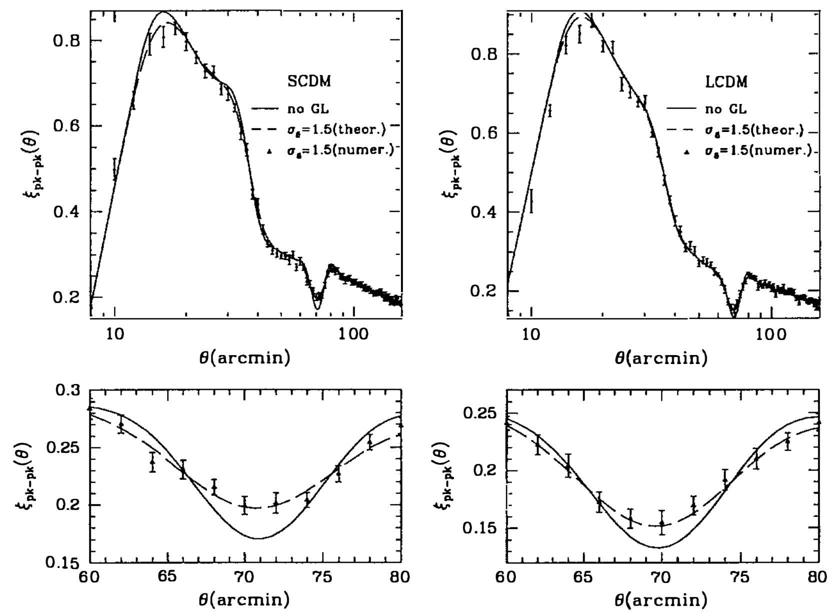

Figure 1: An example of the numerical experiments of the lensed two-point correlation of hotspots of height above the threshold $\nu = 1$ expected from the Planck in SCDM and LCDM with $\sigma_8 = 1.5$, respectively. The solid and dashed curves show the theoretical predictions of unlensed and lensed $\xi_{\rm pk-pk}(\theta)$. The error in each bin is calculated from a lot of realizations of the simulation CMB maps and is caused by the cosmic variance and the experimental effects of the beam smearing and the detector noise. The bottom panels show the results around the depression scale ($\approx 70'$) in each model.

the numerical results. Especially, we wish to emphasize that the lensing causes the pronounced smoothing at large angular scales ($\approx 70'$) where $\xi_{\rm pk-pk}(\theta)$ has the depression feature (see bottom panels). We have confirmed that the direct observable quantity $\sigma_{\rm GL}(\theta)$ at the depression scale is sensitive to the matter fluctuations with large wavelength modes such as $\lambda = 50h^{-1}$Mpc and the structures in the redshift range of $1 < z < 3$ [7]. Therefore, the lensing signatures can efficiently provide robust constraints on amplitudes of such large scale mass fluctuations independently of those provided by the survey of galaxies clustering and the primary CMB anisotropies alone.

Since the free parameter of our model is only σ_8, we thus present the sensitivity of the lensing signatures $\delta\xi_{\rm pk-pk}(\theta)$ to σ_8 for simplicity. In Table 1 we summarize the results obtained for the determinations of σ_8 with a best fit and the error associated with this determinations. The error is calculated from the numerical experiments and represents the variance of the best fit values of σ_8 among a lot of sets of the numerical experiments. The best fit is then obtained mainly from the simulation data around the depression scale. The table shows that the accuracy of σ_8 determinations is more significant for the larger values of input σ_8 in each cosmological model. Furthermore, if comparing both results of SCDM and LCDM with $\sigma_8 = 1.5$, it is clear that robuster constraints can be obtained in SCDM than in LCDM, more generally for background models with larger $\Omega_{\rm m0}$. The lensing effect on $\xi_{\rm pk-pk}(\theta)$ can thus provide constraints on σ_8-$\Omega_{\rm m0}$ plane in a general case. To break the degeneracy between σ_8 and $\Omega_{\rm m0}$ determinations, we need to detect the scale dependence of the lensing signatures $\delta\xi_{\rm pk-pk}(\theta)$. For example, we require the detection of $\delta\xi_{\rm pk-pk}(\theta)$ at $\theta \approx 20'$, but this seems to be difficult because the shape of $\xi_{\rm pk-pk}(\theta)$ at $\theta < 20'$ is also sensitive to the effects of the beam smearing and the detector noise [7].

Table 1: Summary of best fit values of σ_8 determinations from the lensing signatures to $\xi_{\rm pk-pk}(\theta)$ using the numerical experiments for the expected Planck survey in SCDM and LCDM models. We here assumed 65% sky coverage, and the 1σ error in each determination is the variance of the best fit values of σ_8 among a lot of sets of the numerical experiments.

input values of σ_8	SCDM ($\Omega_{\rm m0}=1, h=0.5$)	LCDM ($\Omega_{\rm m0}=0.3, \Omega_{\lambda 0}=0.7, h=0.7$)
0	0.30 ± 0.31	0.32 ± 0.30
0.5	0.47 ± 0.24	-
1.0	1.03 ± 0.13	0.93 ± 0.23
1.5	1.52 ± 0.12	1.49 ± 0.17
2.0	-	1.97 ± 0.16

4 Conclusion

We showed that the weak lensing effect on the two-point correlation function of hotspots can be a powerful probe of cosmological parameters associated with the matter power spectrum. In particular, the lensing signatures are sensitive to the mass fluctuations with large wavelength modes ($\sim 50h^{-1}$Mpc). Since such fluctuations are now in the linear regime and their evolution history is well understood in the context of the gravitational instability in an expanding universe, we therefore expect that the projection effect is not a serious problem and the constraints provided from the lensing signatures to $\xi_{\rm pk-pk}(\theta)$ will be precise. The weak lensing can be a *direct* probe of mapping the inhomogeneous distribution of dark matter, and indeed it has been recently shown that the measurements of cosmic shear [9] can successfully constrain the mass fluctuations at angular scales of $2' < \theta < 10'$. Therefore, by combining those independent methods of using the weak lensing, we hope that the shape of matter power spectrum could be *observationally* reconstructed in near future.

Acknowledgments

M.T. thanks the Hayakawa Fund of the Astronomical Society of Japan for a helpful support of traveling expenses to attend this Meeting.

References

1. P. de Bernardis, et al. Nature **404** (2000) 955; A. E. Lange, et al. astro-ph/0005004.
2. S. Henany, et al. astro-ph/0005123; A. Balbi et al. astro-ph/0005124.
3. J. M. Bardeen, J. R. Bond, N. Kaiser & A. S. Szalay ApJ **304** (1986), 15 (BBKS).
4. J. R. Bond & G. P. Efstathiou MNRAS **226** (1987) 655.
5. A. F. Heavens & R. K. Sheth MNRAS **310** (1999) 1062.
6. M. Takada, T. Futamase & E. Komatsu ApJ **533** (2000) L83.
7. M. Takada & T. Futamase, submitted to ApJ (2000).
8. U. Seljak ApJ **463** (1996) 1.
9. L. Van Waerbeke, et al. Astronomy and Astrophysics, **358** (2000) 30.

CROSS-CORRELATIONS OF CMB AND WEAK LENSING SURVEYS

K. BENABED[†], F. BERNARDEAU[†], L. VAN WAERBEKE[‡]
[†] *SPhT, C.E. De Saclay, 91191 Gif-Sur-Yvette, France*
[‡] *CITA, 60 St George Str., Toronto M5S 3H8 Ontario, Canada*

Abstract

We propose two methods to measure weak lensing effects in CMB data. Both rely on the fact that the weak lensing effect on a source plane at redshift one is significantly correlated with the same effect at redshift 1100, allowing us to cross correlate CMB data with weak lensing surveys. We study the efficiency of the cross correlation, the signal-to-noise of the two methods and for the most promising one, its sensitivity to the cosmological parameters.

1 Introduction

The study of weak lensing effects on the CMB offers a unique probe of the mass distribution up to very high redshifts. However, this effect is only a small correction to the CMB anisotropies and the methods previously proposed to extract lens contribution out of the CMB data suffer in general from low signal-to-noise ratios [1]. We present here two alternate approaches that use external data to enhance the detection of the lens effects. Observing that there is a significant correlation between lens effects for source planes at $z = 1$ and $z = 1100$, we point out that CMB patterns should exhibit significant correlations with weak lensing surveys [2]. The first method we propose exploits this idea by comparing the relative orientation of the CMB ellipticities and the galaxy field . The second one takes advantage of the geometrical properties of the small scale CMB polarization expected to hold in inflation theory.

2 Weak lensing at $z = 1$ and $z = 1100$

A photon coming from redshifts 1100 share one about third[a] of its line of sight with one emerging from $z = 1$. Therefore a significant fraction of the gravitational potentials that can alter the

[a] in EdS universe.

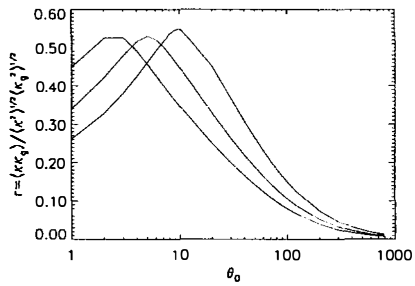

Figure 1: Correlation coefficient r for Λ CDM model. θ_0 is the smoothing angle for $\kappa_{\rm gal}$. The three curves correspond to a beam size of 2.5′, 5′ an 10′ for $\kappa_{\rm cmb}$. The stronger correlations are obtained when both beam match.

light paths acts on both photons.It is thus natural to expect that the gravitational deviations applied on both light rays are fairly correlated. An estimation of this correlation is given by r, the cross-correlation coefficient, defined by

$$r \equiv \frac{\langle \kappa_{\rm cmb}\,\kappa_{\rm gal}\rangle}{\sqrt{\langle \kappa^2_{\rm cmb}\rangle \langle \kappa^2_{\rm gal}\rangle}}. \tag{1}$$

We have introduced here $\kappa_{\rm cmb}$ the convergence field at $z = z_{\rm cmb} = 1100$ and $\kappa_{\rm gal}$ the one at $z = 1$. In a crude model (EdS, $n = -1.5$ power law spectrum for the density fluctuation) this ratio can be easily computed and gives a 42% correlation between the two convergence fields.

In practice, the two κ fields that appear in (1) will be extracted from different experiments so that they will be smoothed with possibly different filtering scales. This effect changes the value of the cross-correlation coefficient. Fig.1 presents results for r in a CDM [b] model, taking into account the difference in beam sizes and a realistic spread of the galactic source plane. The ratio is found to be maximal when both filtering scales match, and can be higher than 50%.

The high amplitude of r betrays a significant cross-correlations between the lens effect on the CMB and on the galaxy surveys.

3 Relative orientations of background galaxies and CMB ellipticities

The gravitational lenses deviate the photon paths. This effect distorts the observed images of the galaxies as well as the observed CMB temperature anisotropies. As a result, the galaxies observed orientations are align toward the shear field. In the same way, the structures of the CMB maps will be stretched along the direction of the gravitational lenses. The value of the r coefficient computed before predict that the two shear field are significantly aligned. Hence, the structures of the CMB temperature anisotropies and the galaxies orientations should be very comparable.

We will use the local ellipticity of the CMB temperature field as a tracer of the local orientation of CMB structures

$$\mathbf{e} = \left(\frac{\partial_x^2\delta_T - \partial_y^2\delta_T}{\partial_x^2\delta_T + \partial_y^2\delta_T}; \frac{2\partial_{xy}\delta_T}{\partial_x^2\delta_T + \partial_y^2\delta_T}\right). \tag{2}$$

Remembering that the gravitational lenses affects CMB by changing the apparent position of the structures, we can write $\hat{\delta}_T(\boldsymbol{\theta}) = \delta_T(\boldsymbol{\theta} + \boldsymbol{\xi})$, where $\hat{\delta}_T$ is the observed (lensed) temperature field

[b] non-linear evolution of the power spectrum is taken into account

and $\boldsymbol{\xi}$ the lens induced displacement [3]. Then, at first order, and neglecting the shear gradients (which will not contribute in our analysis) it is straightforward to obtain the ellipticity of the lensed CMB temperature field, as a function of the primordial ellipticity and the shear field:

$$\hat{\mathbf{e}} \simeq \mathbf{e} + 4(\boldsymbol{\gamma}\cdot\mathbf{e})\mathbf{e} - \boldsymbol{\gamma}. \tag{3}$$

In the inflation theory, the primordial CMB temperature anisotropies are expected to be Gaussian. In this framework, the ellipticity distribution is very specific and has been calculated in [4]

$$p(e)\mathrm{d}e = p(e_1, e_2)e\mathrm{d}e = \frac{8\epsilon}{(1+8e^2)^{3/2}}\mathrm{d}e. \tag{4}$$

From this point, we can compute the distribution of the lensed ellipticity using our first order eq. (3)

$$P(\hat{\mathbf{e}}|\boldsymbol{\gamma}) \simeq \frac{8e}{(1+8e^2)^{3/2}}\left(1 - 36\frac{\hat{\mathbf{e}}\cdot\boldsymbol{\gamma}}{(1+8\hat{e}^2)}\right). \tag{5}$$

This last equation describes the statistical alignment of the lensed CMB field toward the shear field. We have now all the tools needed to estimate the properties of the relative orientations of the CMB structures and the local shear field. Let define θ_g the angle between the ellipticity and the shear field at $z=1$; $\cos(\theta_g) \equiv \hat{\mathbf{e}}\cdot\boldsymbol{\gamma}_g/\hat{e}\gamma_g$. If the CMB is not lensed (i.e. its ellipticities are not aligned to the shear field) the distribution of θ_g is flat. On the contrary, if the CMB is affected by lenses, θ_g will have prefered values around 0 and 2π.[c] Using eq. (5) and assuming that at the smoothing scale of CMB data the lens effects at $z=1$ and $z=1100$ can be described by a joint Gaussian distribution, we can compute the distribution of the angle θ_g and the mean value of $\cos(\theta_g)$

$$\mathcal{P}(\theta_g)\mathrm{d}\theta_g = \frac{\mathrm{d}\theta_g}{2\pi}\left(1 + 3\sqrt{\frac{\pi}{2}}\frac{\langle\kappa\kappa_g\rangle}{\langle\kappa_g^2\rangle^{1/2}}\cos(\theta_g)\right) \qquad \langle\cos(\theta_g)\rangle = \frac{3}{2}\sqrt{\frac{\pi}{2}}\frac{\langle\kappa\kappa_g\rangle}{\langle\kappa_g^2\rangle^{1/2}}. \tag{6}$$

The distribution of θ_g presents a departure from the flat distribution. This modulation is proportional to the ratio $\langle\kappa\kappa_g\rangle/\langle\kappa_g^2\rangle^{1/2}$ which is a measure of the cross-correlation between the lensing effect at the redshift of the galaxies and the lensing effect on the CMB. The mean value of $\cos(\theta_g)$ show the same feature. Instead of being null (unlensed case) it is now proportional to the same ratio; its measure will then be a direct detection of the cross-correlation of the weak lensing effects at different redshifts. In paper [5] we presents this computation in details as well as an estimation of $\langle\cos(\theta_g)\rangle$ and its signal to noise ; at a smoothing scale of $5'$ we have $\langle\cos(\theta_g)\rangle = 0.06$ and a signal to noise around 5 for survey sizes of 900 deg^2. Figure 2 summarizes these results.

4 Lens effects on CMB polarization

The signal to noise ratio of the measure of the alignment of the CMB temperature anisotropies along the local shear is large enough for a detection of this effect. However building a survey large enough for a precise determination of $\cos(\theta_g)$ is quite demanding. To increase the signal to noise of a cross-correlation between CMB and the weak lensing survey, it is natural to extend this investigation to the CMB polarization.

The CMB photons are polarized by Thomson scattering on the quadrupolar anisotropies at recombinaison. The CMB polarization field, just like any vectorial field, can be described in terms of a scalar field E (also called the *electric polarization*) and a pseudo-scalar one B (*magnetic polarization*), which describe the non local geometrical properties of the CMB polarization.

[c] note here that due to its definition, θ_g is twice the physical angle; therefore, $\theta_g = \pi$ when the structures in CMB and the shear field are perpendicular to each other.

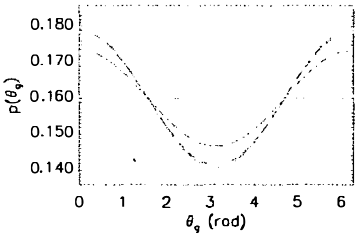

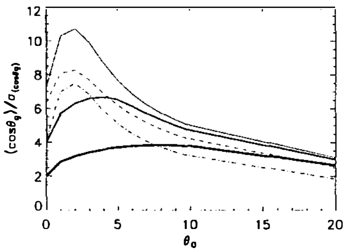

Figure 2: Left figure show the distribution function of θ_g. The solid line is the uniform distribution (for the unlensed case). The dot-dashed line is for $\Omega_M = 0.3$, $\Lambda = 0$, $\sigma_8 = 1$, the triple dot-dashed line for $\Omega_M = 0.3$, $\Lambda = 0.7$, $\sigma_8 = 1$ and the dashed line for $\Omega_M = 1$, $\Lambda = 0$, $\sigma_8 = 0.6$. Right figure is the signal-to-noise ratio of $\langle\cos(\theta_g)\rangle$ as a function of the convergence smoothing scale θ_0. The CMB and the galaxy surveys have both a size of 900 deg^2. The cosmological models are standard-CDM (dashed line), open-CDM (dotted line) and Λ-CDM (solid lines). The beam size is always $2.5'$ except for the thick line (Λ-CDM, $5'$ beam) and the double thick line (Λ-CDM, $10'$ beam).

Accounting for these properties, the primordial E polarization is induced by scalar and tensorial perturbations whereas the primordial B part can only be generated by tensors. Inflation theory predict that the tensorial perturbations (namely the gravitational waves) will have a very low contribution at small scales which then will be dominated by scalar modes [8]. It has been shown that the lensing effects redistribute the power between the two components of the polarization [9]. Therefore, the small scale B polarization is expected to be dominated by lensing effects. We will take advantage of this effect to build cross-correlations between the CMB polarization and galaxy surveys with a high signal-to-noise.

Just like in previous section, the lensing effect on the local polarization vector reduces to a displacement [7] $\hat{\mathbf{P}}(\theta) = \mathbf{P}(\theta + \boldsymbol{\xi})$. This mechanism alters the geometrical properties of the polarization field, that is to say, changes the proportion of the E and B components. In the weak lensing regime where distortions are small, we obtain, at leading order:

$$\Delta\hat{B} = -2\epsilon_{ij}\left(\gamma^i\Delta\hat{P}^j + \gamma^i_{,k}\hat{P}^{j,k}\right). \tag{7}$$

The ϵ_{ij} (the totally antisymmetric tensor) accounts for the geometrical properties of the B field. It comes in front of two shear-polarization mixing terms. One which we will call the Δ-term couples the shear with second derivative of the polarization field. The other one, hereafter the ∇-term, mixes gradient of the shear and polarization.

As a consequence, the B field directly reflects the properties of the shear maps. Fig. 3 shows a comparison of relation (7) with the exact lensing effect. The agreement is excellent.

With the help of eq.(7), one can try to recover lensing information out of B polarization. Unfortunately, a direct inversion is not possible since it leads to a huge degeneracy in the resulting shear maps[6]. Here again, we will try instead to cross-correlate the B polarization with quantities built upon weak lensing surveys data. Looking at eq. (7), the most simple idea is to construct *guess* B-fields, b_Δ and b_∇, with local shear instead of the CMB one and to correlate them with our polarization data,

$$b_\Delta \equiv \epsilon_{ij}\gamma^i_{\rm gal}\Delta\hat{P}^j, \quad b_\nabla \equiv \epsilon_{ij}\partial_k\gamma^i_{\rm gal}\partial_k\hat{P}^j. \tag{8}$$

Then, the amplitude of the cross-correlation between ΔB and b_Δ can easily be estimated. At leading order, we have

$$\left\langle\Delta\hat{B}\,b_\Delta(\vec{\alpha})\right\rangle = -\left\langle\Delta E^2\right\rangle\langle\kappa\kappa_{\rm gal}\rangle, \quad \left\langle\Delta\hat{B}\,b_\nabla(\vec{\alpha})\right\rangle = -\frac{1}{2}\left\langle(\vec{\nabla}E)^2\right\rangle\left\langle\vec{\nabla}\kappa\cdot\vec{\nabla}\kappa_{\rm gal}\right\rangle. \tag{9}$$

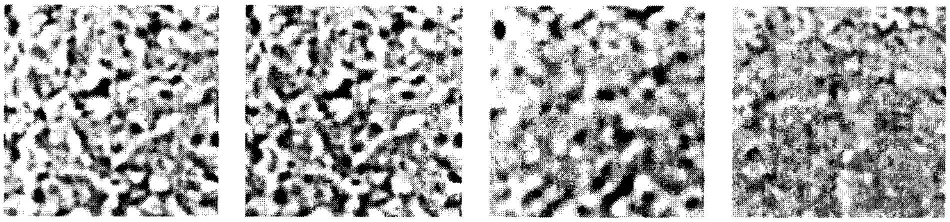

Figure 3: Numerical simulation results for 4.4 square degree maps. Right panel is the result of an exact simulation of a B field. Middle left is the result of the first order approximation. The two right panels are the b_Δ and b_∇ maps. The convergence fields used here have a cross-correlation coefficient of 0.48. The cross-correlation coefficient between the guess maps and one of the real maps are respectively 0.37 and 0.16.

Table 1: Values of the cosmic variance of $\mathcal{X}_\natural$. The survey size is 100 deg^2. We used the results of ray-tracing simulation from [10]. From this estimations, we can expect a cosmic variance for $\mathcal{X}_\natural$ of less than 10% for realistic scenarii.

	$CosVar\,(\mathcal{X}_\Delta)$		$CosVar\,(\mathcal{X}_\nabla)$	
	$\Omega_0=0.3$	$\Omega_0=1$	$\Omega_0=0.3$	$\Omega_0=1$
$\theta=5'$, $\theta_{\rm gal}=2.5'$	6.4%	4.8%	6.0%	4.7%
$\theta=5'$, $\theta_{\rm gal}=5'$	6.6%	4.8%	5.0%	4.2%
$\theta=10'$, $\theta_{\rm gal}=5'$	8.7%	6.7%	9.5%	7.6%

Note that these results remain valid even when filtering effects are included (see [6] for complete calculation).

Fig. 3 shows a numerical illustration of this cross-correlation. The similarities between the left and the right maps are not striking. Yet, under close examination one can recognize individual patterns shared between the maps. Moreover, computation of correlation coefficient gives significant overlapping up to 40%.

Using this results, we define two quantities insensitive to the normalization of CMB and σ_8 and to filtering effects, which probe the cross-correlation between two lensing planes:

$$\mathcal{X}_\Delta \equiv \frac{\left\langle \Delta\hat{B}\, b_\Delta(\vec{\alpha})\right\rangle}{\left\langle \Delta\hat{E}^2\right\rangle \left\langle \kappa_{\rm gal}^2\right\rangle} = -\frac{\langle \kappa\kappa_{\rm gal}\rangle}{\left\langle \kappa_{\rm gal}^2\right\rangle}, \quad \mathcal{X}_\nabla \equiv \frac{\left\langle \Delta\hat{B}\, b_\nabla(\vec{\alpha})\right\rangle}{\left\langle (\vec{\nabla}\hat{E})^2\right\rangle \left\langle (\vec{\nabla}\kappa_{\rm gal})^2\right\rangle} = -\frac{1}{2}\frac{\left\langle \vec{\nabla}\kappa\cdot\vec{\nabla}\kappa_{\rm gal}\right\rangle}{\left\langle \vec{\nabla}\kappa_{\rm gal}^2\right\rangle} \tag{10}$$

Previous methods to probe weak lensing in CMB anisotropies [1] ran into low signal-to-noise problems. This is not surprising since lens effect which is not dominant can be masked by statistical deviations of the primary CMB signal, thus reducing the accuracy of lens detection. Since B polarization only emerges in presence of lensing, this last effect should be avoided. Indeed, we showed in [6] that the noise on the detection of $\mathcal{X}_\Delta$ is dominated by the cosmic variance. It can be can be simply estimated in terms of the cosmic variances of the polarization field and of the shear field,

$$CosVar(\mathcal{X}_\Delta)^2 = CosVar\left(\left\langle \Delta E^2\right\rangle\right)^2 + \left(\frac{1+r^2}{2\,r^2}\right) CosVar\left(\left\langle \kappa^2\right\rangle\right)^2. \tag{11}$$

The same kind of equation holds for $\mathcal{X}_\nabla$. This expression leads to values for the cosmic variance of $\mathcal{X}_\Delta$ of less than 8% for realistic 100 square degree surveys (see table 1).

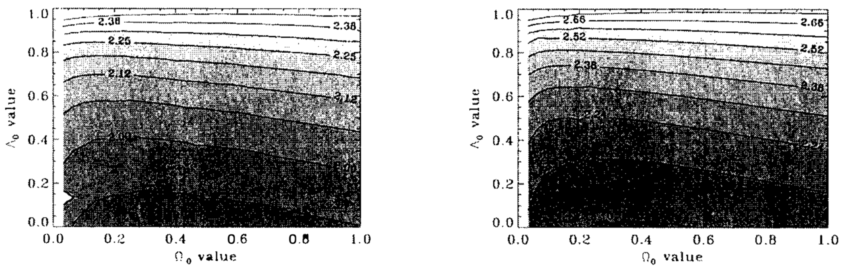

Figure 4: $\mathcal{X}_\Delta$ (left figure) and $\mathcal{X}_\nabla$ for a CDM model. The filtering beam is 2 arc minutes for all fields.

5 Conclusion - Sensitivity to the cosmic parameters

Cross correlating the CMB data with weak lensing surveys is a promising topic. It allows for comparison of the lensing effects on different source redshift, for example by measuring the coefficient r. As it is sensitive to different redshifts, It could provide new probes of the geometrical properties of the universe.

We showed here two simple ways of performing correlations between CMB and weak lensing. The first method is based on the comparison of the relative orientation of the CMB temperature anisotropies and of the shape of galaxies. The second, directly compares the lensing effect in the B component of the CMB polarization to the weak lensing surveys. This last method seems very promising. Its intrinsic cosmic variance is predicted to be very low. Beside, it would provide good unbiased cosmic parameter tracers. Fig. 4 shows the behavior of $\mathcal{X}_\natural$ in the (Ω_0, Λ) plane which indeed exhibit a fair sensitivity to the vacuum energy density.

Acknowledgments

We thank B. Jain, U. Seljak and S. White for the use of their ray-tracing simulations. KB and FB thank CITA for hospitality and LvW is thankful to SPhT Saclay for hospitality. We are all grateful to the TERAPIX data center located at IAP for providing us computing facilities.

References

1. F. Bernardeau, A&A **324** (1997) 15 ; M. Zaldarriaga, astro-ph/9910498 ; F. Bernardeau, A&A **338** (1998) 767 ; U. Seljak, M. Zaldarriaga, Phys.Rev.Lett. **82** (1999) 2636; M. Zaldarriaga, U. Seljak, Phys.Rev. D; J. Guzik, U. Seljak & M. Zaldarriaga, astro-ph/9912505; M. Takada, E. Komatsu, T. Futamase ApJ **533** (2000), L83.
2. Y. Mellier, ARAA **37** (1999) 127.
3. A. Blanchard, J. Schneider A&A **184** (1987) 1 ; U. Seljak ApJ **463** (1996) 1 .
4. Bond, J.R., and Efstathiou, G, 1987, MNRAS, 266, 655
5. L. Van Waerbeke, F. Bernardeau & K. Benabed, to appear in ApJ, astro-ph/9910366.
6. K. Benabed, F. Bernardeau & L. van Waerbeke, astro-ph/0003038.
7. V. Faraoni, Astron.Astrophys. **272** (1993) 385.
8. U. Seljak, ApJ **482** (1997) 6; W. Hu & M. White, New Astronomy **2** (1997) 323.
9. M. Zaldarriaga, U. Seljak, Phys.Rev. **D58** (1998) 023003 ; K. Benabed & F. Bernardeau, Phys. Rev. D 61, 123510 (2000); W. Hu, astro-ph/0001303.
10. B. Jain, U. Seljak, S. White, ApJ **530** (2000) 547.

COSMIC STRINGS LENS PHENOMENOLOGY REVISITED

Francis BERNARDEAU[1] & Jean-Philippe UZAN[2]
[1] *Service de Physique Théorique, CE de Saclay*
F-91191 Gif-sur-Yvette Cedex, France
[2] *Laboratoire de Physique Théorique, UMR-8627 du CNRS, université Paris XI,*
F-91405 Orsay Cedex, France

We present investigations of lens phenomenological properties of cosmic strings for deep galaxy surveys. General results that have obtained for lineic energy distribution are presented first. We stress that generically the local convergence always vanishes in presence of strings although there might be some significant distortions. We then propose a simplified model of strings, we call "Poisson strings", for which exhaustive investigations can be done either numerically or analytically.

1 Motivations

At a time when the observational data seem to converge towards models of structure formation with scalar adiabatic initial fluctuations obeying Gaussian statistics [1], it is probably worth recalling that cosmic strings, and more generally tolopological defects, form under very general circumstances. Therefore, although they may not be the main seeds of the large-scale structure of the universe or of the CMB anisotropies, relics of such objects due to early time phase transitions may still exist. With the advance of a new generation of telescopes and large field CCD cameras we think it is worth to keep in mind what could be their observational effects.

In this presentation we are thus interested in the observational signature of cosmic strings on background galaxies. Future large-scale surveys that are in preparation for weak lensing observations and that are going to cover a fair fraction of the sky with unprecedented image quality are a natural playground for elaborating detection strategies of such strings.

2 General lens properties of strings

2.1 Uniform straight strings

The case of uniform straight string (with Goto-Nambu equation of state) has been exhaustively described in the literature [2]. In this case the metric is actually flat around the string. The only effect of the string is to induce a "missing angle" so that space is conical around the string. As a result galaxies that are behind the string may exhibit double images. The pair separation of these images is directly proportional to the lineic energy density of string μ_0. For strings that formed at the Grand Unification scale, that would corresponds to image separation of a few

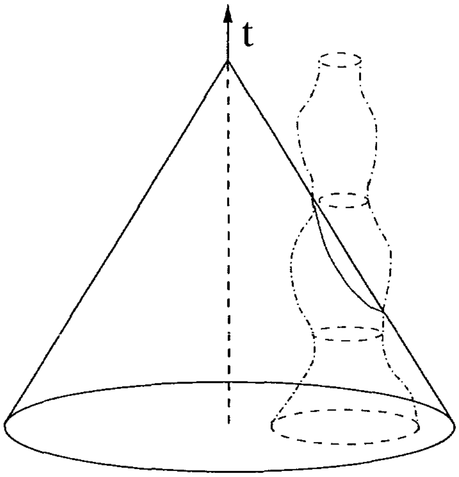

Figure 1: Schematic view of the source term for the lens effect of a string. It corresponds to the intersection of the loop world-sheet and the past light cone of the observer.

arcsecs. Optical investigations, for that respect, seem the most appropriate way of detecting such strings.

However, the idea strings induce series of image pairs is however coming from a simplified description of the string energy properties. Simple numerical experiments[3] done with numerical simulations of string networks suggest that this is too naive a view and that the lens phenomenology of strings is much more complex.

2.2 General string effects

In general the displacement field induced by strings is not uniform, and thus significant deformation effects of background galaxies can be induced. One can show that, under very general hypothesis (with respect to the string equation of state and geometry), there exists a potential from which the elements of the deformation matrix derive[5]. It can formally be written in terms of the angular positions (x, y),

$$\varphi(x,y) = 4\,G\,\frac{D_{\rm LS}}{D_{\rm OS}}\int {\rm d}s\;\mu[x_{\rm str.}(s), y_{\rm str.}(s)]\;\log\left([x - x_{\rm str.}(s)]^2 + [y - y_{\rm str.}(s)]^2\right)^{1/2} \tag{1}$$

where $(x_{\rm str.}(s), y_{\rm str.}(s))$ are the angular string coordinates for the angular curvilinear position s, $\mu(x_{\rm str.}(s), y_{\rm str.}(s))$ is the "projected energy density" at those positions, G is the Newton constant and $D_{\rm LS}/D_{\rm OS}$ is the ratio of the angular distance between the string and the source-plane to the one between the observer and the source plane in the thin lens approximation. The projected energy density is located on the intersection between the string world-sheet and the past light cone of the observer (e.g. Fig. 1). Its amplitude is given by a combination of the projected T_{00}, T_{0z} and T_{zz} components of the stress-energy tensor of the string if the line-of-sight is along the z direction. The displacement field is given by,

$$\xi_i = -\partial_i\varphi(x,y), \tag{2}$$

and the elements of the deformation matrix can be written as,

$$\gamma_1 \;=\; \left(\partial_x^2 - \partial_y^2\right)\;\varphi(x,y), \tag{3}$$

$$\gamma_2 \;=\; 2\,\partial_x\partial_y\;\varphi(x,y), \tag{4}$$

the local convergence being zero except on the string itself. This result holds despite the fact that not only scalar fluctuations are contributing to the lens effects, but also vector and tensor modes [5].

3 A simplified model: the Poisson strings

In order to have analytical insights into the string lens phenomelogy, realistic moels for string shape and energy should incorpate complex features: the string are very far from being straight lines with uniform energy distribution. We choose[4] to describe the energy fluctuation in a simple manner, assuming that the string follows a straight line, but with local energy fluctuations. This fluctuations are assumed to account for the various changes of shape, density of the strings, to possible non-standard equation of states, or to the existence of currents along the string. We therefore assume the string to be straight along the y direction, and the local projected lineic energy density $\mu(s)$ *to be a random field.* To specify our model we still need to explicit the statistical properties of the μ field. Its average value obviously does not vanish and is given by

$$\langle\mu(s)\rangle = \mu_0 \equiv \frac{\xi_0}{4\pi G\, D_{LS}/D_{OS}}, \tag{5}$$

where ξ_0 is the typical angular displacement induced by the string ($2\xi_0$ would be the pair separation if the string were uniform).

With the lack of any well understanding of the string microscopic physics, we simply assume the coherence length of μ to be much smaller than the other distances intervening in the problem. In this case the 2-point correlation function of μ can be written,

$$\langle\mu(s_1)\mu(s_2)\rangle = s_0\,\mu_0^2\,\delta_{\mathrm{Dirac}}(s_1 - s_2). \tag{6}$$

An important consequence of this assumption is that, at finite distance from the string, the deformation matrix elements are sourced by an infinite amount of independent portions of the string. They thus obey Gaussian statistics. The lens properties of the string are thus entirely determined by (6), independently of what could be the one-point probability distribution function of μ.

Elementary phenomenology of "Poisson string"

On Fig. 2 we depict an example of numerical implementation of such a cosmic string, showing various features associated with this lens system. The grey levels show the variation of amplification given by the determinant of amplification matrix. Along the brightest areas the amplification is infinite; these locations form the critical lines. This is where the most dramatic lens effects could be detected: giant arcs, merging of images... Note that such lines simply do not exist for strings with uniform density! The critical lines are made mainly of two long lines running along the string without crossing it.

It is worth noting that we are here generically in a regime of 3 images in the vicinity of the string (except in rare cases where it can be 5) instead of 2 as for a strictly uniform string. The dashed lines show the locations of the counter images of the critical lines. It delimits the region, in the image plane, within which multiple images can be found. It can be noted however that the amplification rapidly decreases in the vicinity of the string, so that central images (i.e. the ones situated in between the two infinite critical lines) are expected to be strongly de-amplified, except when they are close to one of the critical lines.

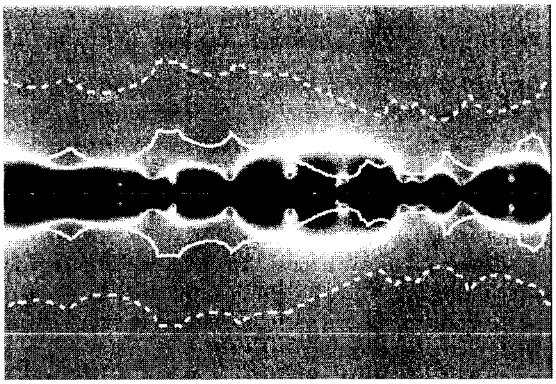

Figure 2: Numerical experiment showing the amplification map, i.e. det($\mathcal{A}$), of a "Poisson string". The brightest pixels correspond to infinite magnification: they form the critical lines. The darkest pixels correspond to a magnification close to zero. The solid lines correspond to the caustics, positions of the critical lines in the source plane. The external dashed lines are the counter images of the critical lines.

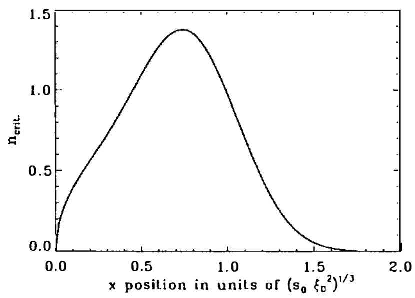

Figure 3: Shape of the function $\overline{n}_{\rm crit.}(x)$.

3.1 Statistical properties

The necessary conciseness of these notes does not allow to present a detailed presentation of the statistical properties of such a system. The simplicity of the model allows however the computation of a lot of general properties, from the position of the critical lines, to the total length of the caustics [4].

In Fig. 3 we present for instance the number density of intersection points of the critical lines with any horizontal axis. From this one can infer for instance the average number of intersection points (on one side of string):

$$\overline{n} = \int_0^{+\infty} \mathrm{d}x\, n_{\text{crit.}}(x) = \frac{2}{\sqrt{3}} \approx 1.155. \tag{7}$$

The number of intersection points being an odd number, it means that the critical line crosses one horizontal line more than once in at most 7% of the cases. It supports the fact that we are dominated by the two long critical lines located on each side of the string. In rare cases, however, inner critical lines can give rise to complex multiple image systems.

The typical distance of the critical lines to the string can also be computed. It is given by

$$d_{\text{crit.}} = \frac{\int_0^{+\infty} \mathrm{d}x\, x\, \overline{n}_{\text{crit.}}(x)}{\int_0^{+\infty} \mathrm{d}x\, \overline{n}_{\text{crit.}}(x)} \approx 0.70\, (s_0\, \xi_0^2)^{1/3} \tag{8}$$

whereas the scatter of this distance is about

$$\Delta d_{\text{crit.}} = 0.31\, (s_0 \xi_0^2)^{1/3}. \tag{9}$$

The total length of the critical lines (per unit string length) turns out to be also calculable. Remarkably one finds

$$L_{\text{crit.}} = \frac{4}{\sqrt{3}} \mathbf{E}\left(\frac{3}{4}\right) L \approx 2.80\, L, \tag{10}$$

where $\mathbf{E}$ is the complete elliptic integral, *independently* of the parameter of the model. In particular it does not depend on the dimensionless ratio s_0/ξ_0, nor on the position of the source plane! And because this result is finite, it also proves that the closed critical lines have a finite total length despite the fact that they are in infinite number.

4 Observational prospects

In Fig. 4 we present a simulated image of background galaxies deformed by a straight Poisson string (the case of a Poisson string loop is depicted on the cover). On these images pairs can be clearly identified, although distances and orientations fluctuate from pair to pair contrary to the standard picture. One can also notice numerous small images that appear along the string. The presence of these images are due to the fluctuating small scale structures of the string. They are associated with an infinite number of critical lines (and caustics) near the string. In high resolution images, that might be the most effective way of detecting strings.

This investigation provides a new description of the phenomenological properties of lens physics for cosmic strings. The model we present is based on general results which state that the lens effects of string are those obtained from lineic energy density. The model we propose should capture most of the generic properties expected in such a case. Although we have obviously not demonstrated the validity of the description we adopted, its resemblance with previous numerical results obtained with simulated string networks [3] makes us think that this model could serve as a guideline for detection strategies in future large angular surveys.

Figure 4: Example of a deformed image by a Poisson string. The field corresponds to an external region of cluster A2218 (taken by the Hubble Space Telescope). If such a field was put at $z = 1$, then an intercepting string along the line-of-sight would produce multiple images as observed on this picture (the typical pair separation is about 5 arcsec) if resolution can reach 0.1 arcsec.

Acknowledgments

We would like to thank Y. Mellier and P. Peter for fruitful discussions on this subject, and T. Vachaspati for his encouragements.

References

1. A. E. Lange et al., astro-ph/0005004 and references therein
2. A. Vilenkin and P. Shellard, *Cosmic strings and other topological defects*, Cambridge University Press, Cambridge (1994)
3. A. De Laix, L. M. Krauss and T. Vachaspati, astro-ph/9702033
4. F. Bernardeau and J.-P. Uzan, astro-ph/0004102
5. J.-P. Uzan and F. Bernardeau, astro-ph/0004105

QUASARS AND H_0, LENSING AND HIGH-Z GALAXIES

PHOTOMETRIC REDSHIFTS AND GRAVITATIONAL TELESCOPES

R. PELLO[1], M. BOLZONELLA[2,1], J.F. LE BORGNE[1], J.P. KNEIB[1], B. FORT[3], Y. MELLIER[3], M. DANTEL[4], L. CAMPUSANO[5], R.S. ELLIS[6], I. SMAIL[7], I. TIJERA[8]

[1] *LAT, Observatoire Midi-Pyrénées, UMR5572, 14 Av. Edouard-Bélin, 31400 Toulouse, France*

[2] *Istituto di Fisica Cosmica "G. Occhialini", via Bassini 15, I-20133 Milano, Italy*

[3] *Institut d'Astrophysique de Paris, 98 bis boulevard Arago, 75014 Paris, France*

[4] *Observatoire de Paris, DEMIRM, 61 Av. de l'Observatoire, 75014 Paris, France*

[5] *Observatorio Cerro Calán, Dept. de Astronomía, U. de Chile, Casilla 36-D, Santiago, Chile*

[6] *Astronomy 105-24, Caltech, Pasadena CA 91125, USA*

[7] *Department of Physics, University of Durham, South Road, Durham DH1 3LE, England*

[8] *Departament d'Astronomia i Meteorologia, U. de Barcelona, Diagonal 648, 08028 Barcelona, Spain*

We review the use of photometric redshifts in the particular context of Gravitational Telescopes. We discuss on the possible application of such a technique to the study of both the faint population of distant sources and the properties of cluster lenses. Photometric reshifts could be used to derive the redshift distribution and properties of a very faint subsample of high-z lensed galaxies, otherwise out of reach. Concerning the mass distribution in lensing clusters, photometric reshifts are strongly needed to scale the mass in weak lensing analysis, and to characterize the lensing structure.

1 Introduction

Photometric redshifts (hereafter z_{phot}s) are a promising technique in deep universe studies. The interest for this technique has recently increased with the development of large field and deep field surveys, in particular the HDF. The relatively high number of objects accessible to photometry allows to enlarge the spectroscopic sample towards the faintest magnitudes. For this reason, z_{phot}s are also important when using lensing clusters as Gravitational Telescopes (GTs), for the study of both the background sources and the lenses.

One of the most widely used z_{phot} techniques is the SED fitting procedure. The observed photometric spectral energy distributions (SEDs) are compared to those obtained from a set of template spectra, using the same photometric system. The method is based on the detection of strong spectral features, and it has been largely applied on HDF studies [19 17 13 25 12 8 2 11]. The examples presented in this paper have been produced using our public code called *hyperz*, which adopts a standard SED fitting method, but most results should be completely general when using other z_{phot} tools. *hyperz* is presented in a recent paper by Bolzonella et al. (2000)[6], and it is available on the web at `http://webast.ast.obs-mip.fr/hyperz`. When applying *hyperz* to the spectroscopic samples available on the HDF, the uncertainties are typically $\delta z/(1+z) \sim 0.1$, and this value gives an idea of the expected accuracy of z_{phot}s for the purposes of this paper.

2 Photometric redshifts and background sources

The idea is to take benefit from the amplification factor in GTs to study the properties of the distant background population of lensed galaxies. The typical amplification ranges between 1 to 3 magnitudes in the cluster core. In principle, GTs are useful to build-up and study an independent sample of high-z galaxies, which complements the large samples obtained in standard field surveys. The advantage is that this sample is less biased in luminosity than the field.

2.1 Redshift distribution of faint galaxies

One of the main goals of the GT is to determine the z distribution of a very faint subsample of high-z lensed galaxies, invisible otherwise, and this can be achieved using z_{phot}s. In order to prevent the biases towards or against a particular type of galaxy or redshift domain, z_{phot} shall be computed from broad-band photometry using a large wavelength interval, from B (U when possible) to K. This allows also to reduce the errors on z_{phot} (see Bolzonella et al. 2000 for a detailed discussion).

We have obtained the (photometric) N(z) distribution of arclets in several well known clusters (A2390, A370, Cl2244-02, AC114,...). Figure 1 displays a recent example, the z_{phot} distribution for different source samples in MS1008-1224[3], corresponding to different limits in magnitude. In this case, z_{phot}s were computed from VLT BVRI (FORS) and JK' (ISAAC) public data obtained during the Science Verification phase. The sample includes 559 sources located on the central 2.5 arcminute field of ISAAC, excluding obvious cluster members. The typical number of high-z sources found in the inner 1' radius region of the cluster is $\sim$ 30 to 50 at $1 \leq z \leq 7$, for a photometric survey performed with the HST and different 4m class telescopes. Clusters with well constrained mass distributions enable to recover precisely the $N(z_{phot})$ distribution of lensed galaxies, by correcting the relative impact parameter on each redshift bin.

2.2 Optimization of spectroscopic redshift surveys

An interesting issue for z_{phot} when using GTs for the spectroscopic study of faint amplified sources is the optimization of the survey, that is selecting the best spectral domain in the visible or near-IR bands. This means in practice to produce a criterion based in z_{phot} to discriminate between objects showing strong spectral features in the optical and in the near-IR.

An additional benefit of z_{phot} is that this technique efficiently contributes to the identification of objects with ambiguous spectral features, such as single emission lines. An example of this is given in a recent paper by Campusano et al. (in preparation, see also Le Borgne et al., this conference).

2.3 Identification and study of very high-z sources

The signal/noise ratio in spectra of amplified sources and the detection fluxes are improved beyond the limits of conventional techniques, whatever the wavelength used for this exercise. An example is the ultra-deep MIR survey of A2390[1], and the SCUBA cluster lens survey[2,4,5].

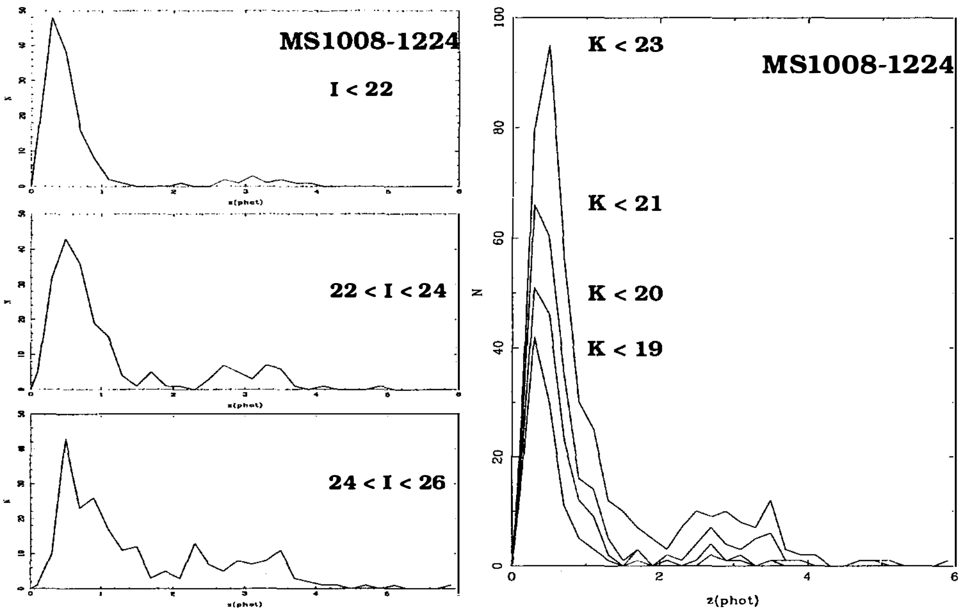

Figure 1: Photometric redshift distribution of 559 gravitationally amplified sources in the core of MS1008-1224. z_{phot}s were obtained from BVRIJK' photometry. Different limits in magnitude are considered in I (left) and K' (right) bands.

Number of $z \gtrsim 4$ lensed galaxies have been found recently, and these findings strongly encourage our approach[26, 9, 10, 22]. Cluster lenses are the natural way to search for primeval galaxies, in order to constraint the scenarios of galaxy formation.

High-z lensed sources could be selected close to the appropriate critical lines, and identified using z_{phot} criteria. z_{phot}s are computed from broad-band photometry on a large wavelength interval, from B (U when possible) to K.

Whatever the z_{phot} method used, a crucial test is the comparison between the photometric and the spectroscopic redshifts obtained on a restricted subsample of objects. Thanks to the magnification factor, cluster lenses could be used to enlarge the training sample towards the faintest magnitudes.

2.4 Combining photometric and lensing redshifts

Lensing inversion and z_{phot} techniques produce independent probability distributions for the redshift of amplified sources. Therefore, the combination of both methods provides an alternative way to determine the redshift distribution of the faintest high-z sources. Figure 2 displays the results for 4 sources in A2390, with z_{phot} computed from BgVrRiIJK' photometry[22]. When comparing the z_{phot} and lensing redshift (z_{lens}) values for a subsample of 98 arclets in the core of A2390, all selected according to morphological criteria (minimum elongation and right orientation are requested), we find that about 60% of the sample have $|z_{phot} - z_{lens}| \leq 0.25$. The discrepancy mostly corresponds to sources with $z_{phot} \gtrsim 2$, but it must be noticed that the lensing inversion technique is characterized by a trend against the identification of high-z images, whereas z_{phot} does not show this trend. This behaviour is expected as a result of the relative low sensitivity to z of the inversion method for high-z values. Thus, in general, the z_{phot} determination is more accurate than the z_{lens}. Nevertheless, the combination of both distributions is

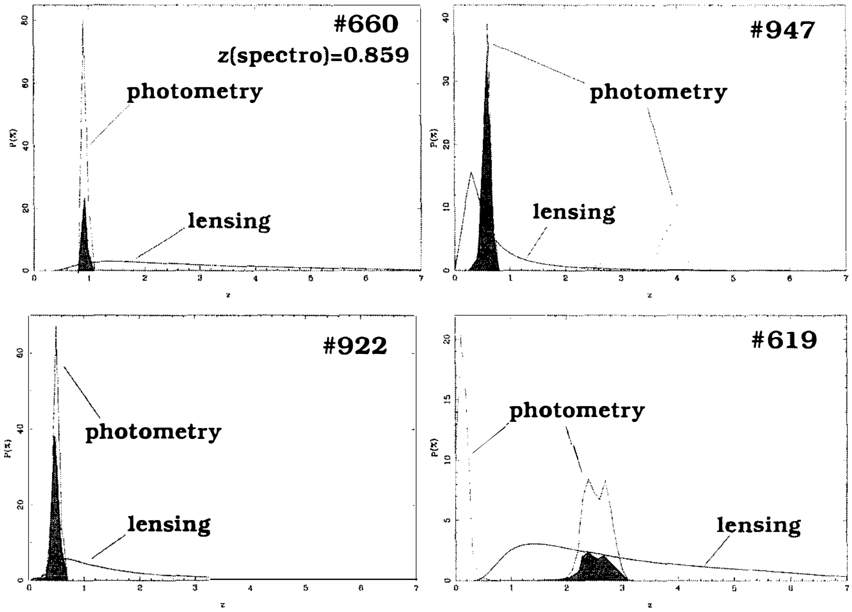

Figure 2: Combined z_{phot} and lensing inversion probability distributions for the redshift of 4 different sources in A2390, representing the typical cases found in this field. Shaded regions correspond to the final composite probability. For most objects, such as #660 and #922, z_{phot} gives a more accurate redshift value compared to z_{lens}, except in the cases with a degenerate z_{phot} solution (#947 and #619)

particularly useful when a degenerate solution appears using z_{phot}, as shown in Figure 2.

3 Photometric redshifts and cluster lenses

3.1 Identification of multiple images

Cluster lenses are useful only when their mass distribution is highly constrained by multiple images, revealed by HST and multicolor photometry. The z_{phot} technique is useful to identify objects with similar SEDs within the errors, thus compatible with a multiple image configuration. z_{phot}s can be used advantageously when data span a large wavelength range, and particularly if near-IR photometry is available, because this allows to obtain accurate z_{phot} in the sensitive region of $0.8 \leq z \leq 2$.

3.2 Scaling the mass in weak lensing analysis

z_{phot}s are particularly useful when deriving the mass from weak shear analysis: they are used to eliminate cluster and foreground galaxies from the analysis, and to scale the lensing distance modulus in order to compute the mass from the gravitational convergence. The average convergence $\kappa \equiv \Sigma/\Sigma_{cr}$, which corresponds to the ratio between the surface mass density and the critical value for lensing, may be obtained as a function of the radial distance θ using different methods (see Mellier 1999[18] for a review). The mass within an aperture θ is given by

$$M(<\theta) = \kappa(<\theta)\ \Sigma_{cr} \cdot \pi\,(\theta D_{ol})^2 = \kappa\,(<\theta)\ \theta^2\,\frac{c^2}{4G}\left\langle\frac{D_{ls}}{D_{os}D_{ol}}\right\rangle^{-1} \tag{1}$$

where D_{ij} are the angular size distances between the cluster (l), the observer (o) and the source (s), and $\kappa(<\theta)$ is the averaged convergence within the radius θ. Using the $N(z_{phot})$ computed through a suitable filter set, the mean value of $\left\langle \frac{D_{ls}}{D_{os}D_{ol}} \right\rangle$ can be computed, thus leading to a fair estimate of the mass. This method has been recently applied to the lensing clusters MS1008-1224[3] and A2219[4] (see also Abdel Salam and Gray, this conference). Because of the small projected surface across the redshift space, the effective surface which is "seen" through a cluster lens is relatively small, thus producing a strong variance from field to field. Obtaining the $N(z_{phot})$ distribution for each cluster could help to improve the mass determination. Nevertheless, the distortion on the $N(z_{phot})$ distribution itself depends on the mass distribution (sect. 2.1). An iterative process is needed to reduce the error bar on the mass, which is $\sim 30\%$ without this second order correction[3].

3.3 Identification and Characterization of lensing structures

z_{phot}s are useful to improve the detection of clusters in wide-field surveys, and to identify the visible counterpart of complex lenses. It has been shown that including such a z_{phot} technique in an automated identification algorithm allows to improve significantly the detection levels for clusters[21], whatever the algorithm used[16 20 14]. In general, the S/N is improved by a factor of 3 to 6 up to $z \sim 1$, depending on the redshift and magnitude limits. The detection efficiency in the $0.8 \leq z \leq 2.2$ region is improved only when using a z_{phot} selection based on optical *and* near-IR filters. These comments also apply to multiple, complex and/or dark lenses, where z_{phot}s allow to identify the main lensing structures. Examples of composite lenses recently identified by z_{phot} are MS1008-1224[3], where a secondary lens exists at $z \sim 0.9$, and the multiple-quasar fields Q2345+007[23] and the Cloverleaf[15].

Cluster members could be also selected using z_{phot} criteria. The present version of *hyperz* is also able to display the probability of each object to be at a fixed redshift. This is useful when looking for clusters of galaxies at a given (or guessed) redshift. In this way, the number density and luminosity density distributions of cluster galaxies can be computed, and M/L ratios could be estimated.

4 Conclusions and Perspectives

Concerning the lensing clusters, z_{phot}s appear as an essential tool for mass calibration in weak shear studies (see the recent papers on MS1008 [3] and A2219 [4]). z_{phot}s allow to improve the identification of the "visible" counterpart of lensing structures, to determine their redshifts and to measure M/L ratios of clusters, groups, etc.

z_{phot}s allow to optimize the spectroscopic surveys of faint lensed sources (visible versus near-IR domains), and to identify ambiguous spectral features (emission lines). Before the recent VLT survey on AC114 (Le Borgne et al. this conference), all spectroscopically confirmed lensed sources were "bright" ($M_B \lesssim -21$). Because a redshift accuracy of $\delta z \sim 0.1(1+z)$ is enough for most applications, z_{phot}s allow to go further in magnitude when deriving the statistical properties of faint sources. Besides, combining z_{phot} and lensing inversion techniques provides with an alternative way to determine the redshift distribution of sources. A future development should be the study of the systematics and biases introduced by GTs when they are used to access the distant population of faint sources. The typical uncertainty in the amplification factor is $\Delta m \sim 0.3$ magnitudes, a value which is similar to model uncertainties when deriving intrinsic luminosities and SFRs of background sources with relatively well constrained SED ($\sim 30\%$ accuracy). Only well known lenses are actually useful as GTs.

Conversely, lensing clusters could be considered as a tool to calibrate z_{phot}s beyond the reach of standard spectroscopy, up to the faintest limits in magnitude, thus allowing to extend the training set for z_{phot}s. The sample of lensing clusters available has to be enlarged, in order to obtain a weakely biased image of the averaged properties of sources along different lines-of-sight. In order to sample a statistically significant field at $z \geq 2$ in the strong amplification domain (close to the corresponding caustic lines), we need to study about 10 different and well-known cluster lenses. The Ultra-Deep Photometric Survey of cluster lenses and the subsequent spectroscopic follow up of sources constitute a well defined program for 10m ground-based telescopes and the future NGST.

Acknowledgments

This work was supported by the TMR *Lensnet* ERBFMRXCT97 - 0172 (http : // www.ast.cam. ac.uk /IoA/lensnet), the ECOS SUD Program, the French *Centre National de la Recherche Scientifique*, and the French *Programme National de Cosmologie* (PNC).

References

1. Altieri, B., et al. A & A 343, L65 (1999).
2. Arnouts, S., Cristiani, S., Moscardini, L., Matarrese, S., Lucchin, F., Fontana, A., Giallongo, E., MNRAS 310, 540 (1999)
3. Athreya R., Mellier Y., Van Waerbeke L., Fort B., Pelló R., Dantel-Fort M., A & A submitted, astro-ph/9909518 (2000).
4. Bézecourt J., Hoekstra H., Gray M. E. , AbdelSalam H. M. , Kuijken K. , Ellis R. S., A & A submitted, astro-ph/0001513 (2000).
5. Blain, A. W., Kneib, J.-P., Ivison, R. J., Smail, I., ApJ 512, L87 (1999)
6. Bolzonella, M., Miralles, J.M., Pelló, R., A & A *submitted*, astro-ph/0003380, (2000).
7. Ebbels, T.M.D., et al., MNRAS 295, 75 (1998).
8. Fernández-Soto, A., Lanzetta, K.M., Yahil, A., ApJ 513, 34 (1999)
9. Franx, M., et al., ApJ 486, 75 (1997)
10. Frye, B., Broadhurst T., ApJ 499, 115 (1998)
11. Furusawa, H., Shimasaku, K., Doi, M., Okamura, S., ApJ in press, astro-ph/9912447, (2000)
12. Giallongo, E., D'Odorico,, S., Fontana, A., Cristiani, S., Egami, E., Hu, E., McMahon, R.G., AJ 115, 2169 (1998)
13. Gwyn, S.D.J., Hartwick F.D.A., ApJ 468, L77 (1997)
14. Kawasaki W., Shimasaku K., Doi M., Okamura S., A&AS 130, 567 (1998)
15. Kneib, J.-P., Alloin, D., Pelló, R., A & A 339, 65 (1998).
16. Kepner J., Fan X., Bahcall N., Gunn J., Lupton R., ApJ 517, 78 (1999)
17. Lanzetta, K.M., Yahil, A., Fernández-Soto, A., Nature 381, 759 (1996)
18. Mellier, Y., ARA & A 37, 127 (1999)
19. Mobasher, B., Rowan-Robinson, M., Georgakakis, A., Eaton, N., MNRAS 282, L7 (1996)
20. Olsen L.F., et al., A&A 345, 363 (1999)
21. Pelló, R., Leborgne, J.F., Miralles, J.M., Bruzual, G., Proceedings of the 14th IAP Meeting "Wide Field Surveys in Cosmology" (1998).
22. Pelló, R. et al., A & A 346, 359, (1999).
23. Pelló, R., Miralles, J. M., Le Borgne, et al., A & A 314, 73 (1996).
24. Smail, I., Ivison, R. J., Blain, A. W., Kneib, J.-P., AAS 192, 4813 (1998).
25. Sawicki, M.J., Lin, H., Yee, H.K.C., AJ 113, 1 (1997)
26. Trager, S. C., Faber, S. M., Dressler, A., Oemler, A. Jr., ApJ 485, 92 (1997).

STUDY OF THE DEPLETION EFFECT IN THE CLUSTER MS1008-1224

C. MAYEN, G. SOUCAIL
Observatoire Midi-Pyrénées, Laboratoire d'Astrophysique, UMR 5572, 14 Avenue E. Belin, 31400 Toulouse, France

We present a detailed study of the depletion effect (the radial manifestation of the magnification bias) in the cluster MS1008-1224. Following our results concerning the simulations of depletion curves (see Mayen and Soucail, 2000 [7] for a complete description of the code), we propose to constrain the mass profile of the cluster and the main characteristics of its potential (orientation and ellipticity). This application is based solely on deep photometry of the field and does not require the measurement of the shape parameters of the faint background galaxies.

1 Introduction

When the logarithmic slope of the galaxy counts is lower than 0.4 (this is the case in all filters at large magnitude), the magnification bias due to a gravitational lens makes the number density of objects decrease, and consequently, the radial distribution shows a typical depletion curve. This effect results from the competition between the gravitational magnification that increases the detection of individual objects and the deviation of light beam that spatially magnifies the observed area and thus decreases the apparent number density of sources. Since a few years, several tentative analysis have been proposed to determine cluster mass distribution (Broadhurst et al., 1995 [2]; Taylor et al., 1998 [9]), the redshift distribution of sources and to bring constraints on cosmological parameters (Fort et al., 1997 [4]).

Here, we propose to use depletion curves in order to constrain the mass profile of MS1008-1224 and some characteristics of its potential (orientation and ellipticity) by combining results of simulations of depletion curves obtained with different lens models (Mayen and Soucail, 2000 [7]) and high quality multicolor images of MS1008-1224 obtained with FORS and ISAAC during the science verification phase of the VLT-ANTU (UT1) at Cerro Paranal. It is a very rich galaxy cluster, located at $z = 0.3062$ (Lewis et al., 1999 [6]), slightly extended in X-rays, with a galaxy distribution quite circular, surrounding a North-South elongated core. There is a second clump of galaxies to the North. Some gravitationally lensed arcs to the North and the East of the field have been reported by Le Fèvre et al., 1994 [5] as well as by Athreya et al., 2000 [1] who also detected a high redshift cluster lensed by MS1008-1224 in the South-West part of the field using photometric redshifts.

In practice, we used only the FORS data which extend to a larger distance and are more suited for our study. Background sources were selected by removing the elliptical galaxies sequence in a color-magnitude diagram ($R - I$ *vs* R), essentially valid at relatively bright magnitudes. This statistical correction is not fully reliable as it does not eliminate bluer cluster members or foreground sources.

Our counts may also present an overdensity of objects in the inner part of the cluster ($r < 20''$) due to the non-correction of the surface of cluster elliptical galaxies we have removed. This effect is more sensitive in the inner part of the cluster where these galaxies are dominant. But as it is not in the most interesting region of the depletion area, we did not try to improve the measures there.

In addition, due to the presence of two 11 magnitude stars in the northern part of the FORS field, two occulting masks were put to avoid excessive bleeding and scattered light. We took into account this partial occultation of the observed surface for the radial counts above a distance of 130". This may possibly induce some additional errors in the last two points of the curves, which are probably underestimated, because of the difficulty to estimate the surface of the masks and some edge effects at the limit of the field.

2 Depletion curves and mass density profile

The first step would be to locate the cluster center. Its position is rather difficult to estimate directly from the distribution of the number density of background sources, although in principle one should be able to identify it as the barycenter of the points with the lower density around the cluster. We did not attempt to fit it and preferred to fix it 15" North of the cD, following both the X-ray center position (Lewis et al., 1999 [6]) or the weak lensing center (Athreya et al., 2000) [1].

The radial counts were performed in a range of 3 magnitudes up to the completeness magnitude in the B, V, R and I bands and up to a radial distance of 210" from the center, which covers the entire FORS field. The depletion was clearly detected in the four bands (see Mayen and Soucail, 2000 [7] and Figure 1). The count step was fixed to 30 pixels (6") in the innermost 80" and for the rest of the field we adopted a count step of 60 pixels (12") in order to reduce the statistical error bars. These values are a good balance between statistical errors in each bin which increase for small steps and a reasonable spatial resolution in the radial curve, limited by the bin size.

We fitted the observed depletion curve in the I band with three mass models (Figure 1), namely a singular isothermal sphere (SIS), a power-law density and a Navarro, Frenk & White [8] (NFW) profiles. For each model, a χ^2 minimization was introduced to derive the best fit and their related parameters (Table 1). The absolute normalization of the mass profiles results from the count model in empty field we have used (which fix the redshift distribution of the background sources before magnification by the gravitational lens). The curve was fitted after removing some clear deviant points : the last two points probably poorly corrected from edge effects, and those associated to the overdensity seen at $r \simeq 80''$. This bump is easily identifiable in the V, R and I curves, and can be partly explained by the presence of a background cluster lensed by MS1008-1224 and identified by Athreya et al., 2000 [1]. Nevertheless, even if we remove from our data all the lower right quadrant of the field where this structure is located, the bump is still there although significantly reduced. This suggests that it may be more extended behind the cluster center than initially suspected.

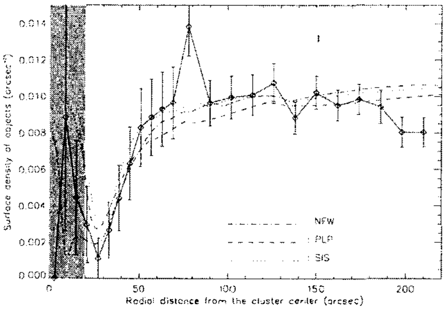

Figure 1: Depletion curve measured in MS1008-1224 in the I band. The best fit by the three models described in text are given. Error bars correspond to Poisson statistical noise. In the shaded area, the signal cannot be constrained observationally (decrease in the observed area, obscuration by the brightest cluster galaxies ...).

Table 1: Results of the fit of the model parameters. The errors are given at the 99.9 % confidence level.

Model	Parameter	reduced χ^2
SIS	$\sigma = 1200\pm^{200}_{175}$ km s^{-1}	0.49
PLP	$\rho_E = 2.4 \pm^{1.3}_{0.6} \times 10^{15}$ M$_\odot$/Mpc^3	0.62
PLP	$\alpha = 1.88\pm^{0.27}_{0.25}$	0.65
NFW	$r_{200} = 3.2\pm^{0.7}_{0.6}$ Mpc	0.44
NFW	$c = 8.9\pm^{6.7}_{4.0}$	0.45

- The velocity dispersion derived from the SIS model ($\sigma_{\rm fit} = 1200\pm^{200}_{175}$ km s^{-1}) is in good agreement with the value measured by Carlberg et al., 1996[3] ($\sigma_{\rm obs} = 1054 \pm 107$ km s^{-1}) but is more discordant with the value of 900 km s^{-1} inferred from the shear analysis of Athreya et al., 2000[1].

- The slope of the potential fit with a power-law density profile is close to an isothermal one ($\alpha = 1.88\pm^{0.27}_{0.25}$), although slightly shallower.

- For a NFW profile, we find a virial radius ($r_{200} = 3.2h_{50}^{-1}$ Mpc) and a concentration parameter ($c = 8.9$) quite in good agreement with those of Athreya et al., 2000[1] derived from weak lensing measures.

- The comparison between the 3 fits favors a NFW profile as the best fit of our depletion curve (Table 1), also in agreement with the shear results for this cluster.

It is important to note that the mass profiles inferred from the depletion analysis are in good agreement with the shear masses (Figure 2). Thus, the masses found by using two independent lensing mass estimates are consistent whatever the radial distance from the cluster center. The discrepancy with X-ray mass still remains, although it is slightly reduced at large distance from the center. This encouraging result allows to consider the use of the depletion as a secure alternative solution against the other lensing mass estimates when the quality of the data is not sufficient to allow the use of the usual ones.

The study of the shape of the depletion area, which can be easily related to the ellipticity and the orientation of the mass distribution, has also allowed us to constrain these parameters with a good accuracy for MS1008-1224 (see Mayen and Soucail, 2000[7]).

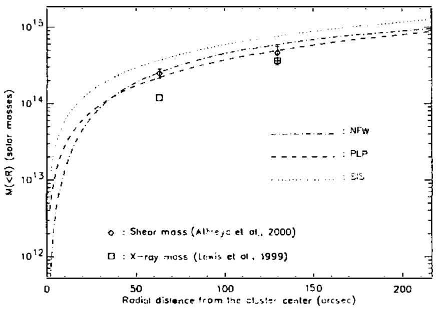

Figure 2: Mass profiles of MS1008-1224 inferred from the depletion analysis. X-ray and shear masses are also shown. The agreement between the two lensing mass estimates is very good.

3 Conclusion and outlook

The study of the depletion effect in the cluster MS1008-1224 with very deep and high quality VLT images has allowed us to constrain the mass profile up to a reasonable distance from the center and to constrain the ellipticity and the orientation of the mass distribution with a good accuracy. The results found are consistent with those inferred from other lensing techniques. Thus, the depletion reveals itself as a secure technique. The next step to explore is the influence of the clustering of background sources and the interest of wide field imaging : The normalization of the field number counts for the magnification bias can also be estimated outside the cluster, in exactly the same observing conditions (filter, magnitude limit, seeing, ...), giving an absolute calibration of the depletion effect. A more prospective point which still requires to be studied in details is the reconstruction of two-dimensional mass maps of clusters from the depletion signal only.

Acknowledgments

We wish to thank the European TMR Programme *Gravitational Lensing : New Constraints on Cosmology and The Distribution of Dark Matter* for its financial support.

References

1. Athreya, R., Mellier, Y., Van Waerbeke, L., Fort, B., Pelló, R., Dantel-Fort, M., 2000, submitted to A&A, astro-ph/9909518
2. Broadhurst, T. J., Taylor, A. N., Peacock, J. A., 1995, ApJ, 438, 49
3. Carlberg, R. G., Yee, H. K. C., Ellingson, E., Abraham, R., Gravel, P., Morris, S., Pritchet, C. J., 1996, ApJ, 462, 32
4. Fort, B., Mellier, Y., Dantel-Fort, M., 1997, A&A, 321, 353
5. Le Fèvre, O., Hammer, F., Angonin, M. C., Gioia, I. M., Luppino, G. A., 1994, ApJ, 422, L5
6. Lewis, A. D., Ellingson, E., Morris, S. L., Carlberg, R. G., 1999, ApJ, 517, 587
7. Mayen, C., Soucail, G., 2000, submitted to A&A, astro-ph/0003332
8. Navarro, J. F., Frenk, C. S., White, S. D. M., 1996, ApJ, 462, 563
9. Taylor, A. N., Dye, S., Broadhurst, T. J., Benítez, N., Van Kampen, E., 1998, ApJ, 501, 539

SPECTROSCOPIC FOLLOW UP OF ARCLETS IN AC114 WITH THE VLT

J.F. LE BORGNE[1], L. CAMPUSANO[2], R. PELLO[1], J.P.KNEIB[1], R. ELLIS[3], B. FORT[4], Y. MELLIER[4], I. SMAIL[5]

[1] *Laboratoire d'Astrophysique, OMP, Toulouse, France*

[2] *Observatorio Cerro Calán, Dept. de Astronomía, U. de Chile, Santiago, Chile*

[3] *Caltech, Passadena, USA*

[4] *Institut d'Astrophysique de Paris, France*

[5] *Pysics Dept.,Durham University, Durham, UK*

We present here the first results on the VLT/FORS-1 spectroscopic survey of amplified sources and multiple images in the lensing clusters AC114 and Cl0054. Background sources were selected in the cluster core, close to the critical lines, using photometric redshifts combined with lensing inversion criteria. Spectroscopic results are given, together with a brief summary of the properties of some of these high-z galaxies.

1 Introduction

To study distant galaxies properties, we can either observe *blank fields* or use clusters of galaxies as natural telescopes. Cluster lenses allow to study in greater details the same population seen in blank field surveys and to probe intrinsically fainter galaxies that can otherwise not be studied. Of particular interest is to define a new sample of high-z galaxies in the cluster cores where the amplification is the highest (typically 1 to 3 magnitudes). For these galaxies, the signal to noise ratio in the spectra and the detection fluxes are improved beyond the limits of conventional techniques.

Such lensing techniques have been succesfully applied in various wavebands from UV to Submm. To get rid of the cluster galaxies, the selection criteria of the distant galaxy candidates are based on a combination of photometric redshits and lensing inversion methods (Kneib et al. 1996; Ebbels et al. 1998, Pelló et al 1999a,b). In our study, photometric redshifts are computed from broad-band photometry on a large wavelength interval. This allows to reduce errors on the redshift determination, and reduces the biases towards or against a particular type of object or redshift domain. Furthermore, it helps to optimize the instrument choice for the spectroscopic follow-up (visible vs. near-IR). Photometric redshifts were computed through a standard minimization procedure, using the public code *hyperz* (Bolzonella et al. 2000). This procedure uses a template library of spectra derived from the new Bruzual & Charlot evolutionary code (GISSEL98, Bruzual & Charlot 1993).

We report here the results obtained using the VLT/FORS instrument in the cluster-lenses AC114 (z=0.312). More details will be given in a forthcoming paper (Campusano et al., 2000)

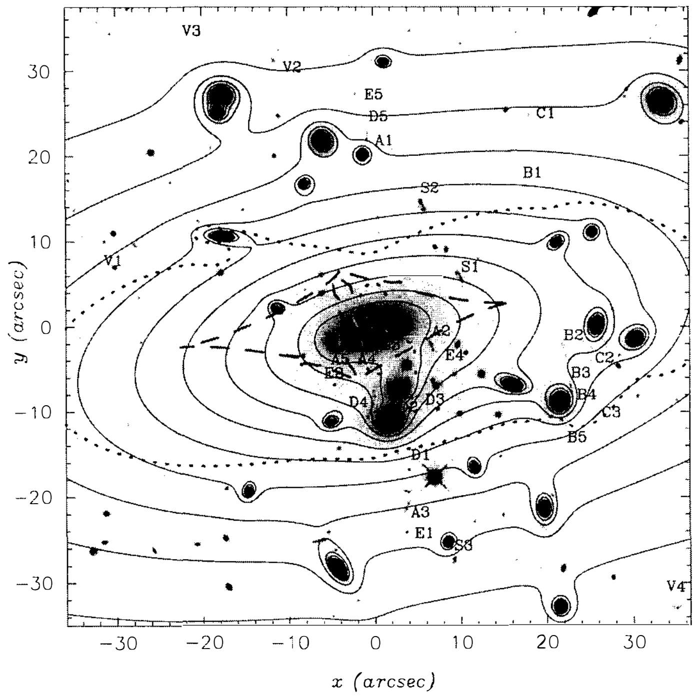

Figure 1: HST/WFPC2 image (F702W) of AC114 cluster core with the identified high redshift galaxies and multiple images. The thin contour lines represent the total mass distribution as modelled by Natarajan et al. (1998). The critical line (dotted lines) and the caustic lines (dashed lines) are shown for $z = 3.35$.

2 Observations and data reduction

The spectra were obtained with the multi-objet spectroscopy mode of FORS1 at the UT1 of VLT on 1999 October 5. The grism used was G300V, with a wavelength coverage between ~4000Å and ~8600Å, and a wavelength resolution of $R = 500$ for the 1" slit width used. 3 masks were cut for AC114, with total exposure times of 2h15, 1h30 and 1h10 respectively. Spectra of the spectrophotometric standard star Feige 110 were obtained for spectrophotometric calibration. The data reduction was done with standard *IRAF* packages. From the 3 masks, 61 spectra of objects were extracted and calibrated, some of them being on several masks. Among these 61 objects, 30 are cluster galaxies, 20 are background galaxies and 11 are foreground objects.

3 Redshifts of amplified sources

The photometric selection in the cluster core was done using the available data set, which includes deep F702W/WFPC2 HST image, J and K images obtained with SOFI at NTT and older U (ESO-NTT) and V (Danish 1.5m telescope at ESO). In the present case, the lack of deep B images prevents a selection in terms of pure photometric redshift criteria, in such a way that the weight of the lens inversion method has been used advantageously in the selection. The size of the CCD images being different from one to another, the photometric selection could only be done effectively on the central HST field of ~ 80"×80". This field is also ideal for lens inversion thanks to the high resolution of HST images (Kneib et al. 1996). As a consequence, all the objects selected for spectroscopic follow up in the HST field, using both photometry and

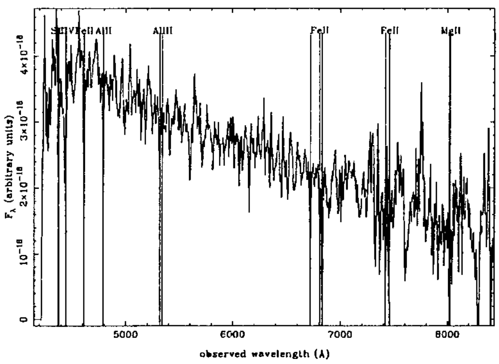

Figure 3: Spectrum of object S2 which confirm the identification of Smail et al 1995. Note the blue excess in that galaxy.

lens inversion, are high-z candidates, and they were found to have redshifts between $\sim$ 1 and 3.5. Our selection method was therefore 100% efficient to identify high redshift galaxies in the cluster core. Figure 1 displays the HST image of the central region of AC114 in F702W, together with the identification of the background sources. Table 1 summarizes the information about the redshifts and photometry for these objects. Magnitudes are computed within arbitrary apertures, adapted to the shape of each object, and fixed for all the filters. The idea is to keep the same physical region in the different filters when computing colors. Even though photometric redshifts are highly uncertain in this case, because of the lack of deep B photometry, we give the values found for comparison, with the corresponding 1σ error bars. In all cases the photometric estimate is fully compatible with the spectroscopic redshift within the errors.

We have computed the absolute M_B magnitudes for these amplified sources through a direct scaling of the observed SED, taking into account the spectroscopic z, and using the best-fit templates from the Bruzual & Charlot code (Bruzual & Charlot 1993) to derive the k-corrections. The values, corrected for amplification, given in Table 1, are computed using an estimated value of the amplification obtained through the Natarayan et al. (1998) model. These results, ranging from $M_B \sim -18$ to -20, show that these objects are substantially fainter than the corresponding ones in the present conventional studies.

3.1 The multiple image S at z=1.867

The previous determination of the redshift by Smail et al. (1995) is confirmed by the present results. Figure 3 displays the high S/N spectrum as well as the line identification. This line identification is not complete, more work has to be done.

3.2 The multiple image system E at z=3.347

The spectrum of this compact source shows a strong Ly_α in emission, in good agreement with the photometric estimate. From the morphologic point of view, it is compact on the WFPC images with a faint extension towards the NW direction. Because of its location in the cluster core, it is found to be a multiple-image showing a clear 5 image lensing configuration. The other 4 images are also identified on Figure 1. Given its morphology and the width of the emission line, this galaxy might be a seyfert 2.

References

1. Bolzonella, M., Miralles, J.M., Pelló, R., 2000, A & A submitted.

Table 1: Characteristics of some background sources studied in the core of AC114. When available, the identifications are given according to Natarayan et al. 1998. M_B have been corrected for magnification. Error bars in photometric redshifts correspond to 1σ.

Id.	z (spectro)	z (photometric)	Δz	R	M_B	M_B (corrected)
A1-A2	1.605	1.00/1.69	0.68-1.91	23.51	-21.89	∼-20.
B2-B3	1.66:	1.58	1.20-1.92	24.01	-22.74	∼-20.
C3	2.84:	2.56	2.44-2.84	22.50:	-22.50	-20.0
E1	3.34695	3.15	2.46-3.43	24.18	-21.79	-20.4
S2	1.86710	2.25	1.66-2.57	21.90	-22.57	-20.5
V2	1.2143	1.53	1.19-1.75	23.22	-20.80	-20.2
V3	2.08	2.29	0.95-2.74	24.36	-22.36	-21.7
V4	2.90	2.71	2.18-2.80	23.15	-22.93	-22.3

2. Bruzual, G., Charlot, S. 1993, ApJ 405, 538
3. Campusano et al., 2000, in preparation.
4. Ebbels, T.M.D., Ellis R.S., Kneib J.P., Le Borgne J.F., Pelló R., Smail I., Sanahuja B., 1998, MNRAS 295, 75
5. Kneib, J.-P., Ellis R.S., Smail I., Couch, W.J., Sharples, R., 1996, ApJ 471, 643
6. Natarajan, P., Kneib, J.p., Smail, I., Ellis, R.S., 1998, ApJ 499, 600
7. Pelló, R., J.-P. Kneib, J.-F. Le Borgne, J. Bezecourt, T. M. Ebbels, I. Tijera, G. Bruzual, J. M. Miralles, I. Smail, G. Soucail, T. J. Bridges 1999a, A&A 346, 359, astro-ph/9810390
8. Pelló, R., Kneib, J.-P., Bolzanella, M., Miralles, J.-M, 2000, Conference Proceedings of the "Photometric Redshifts and High Redshift Galaxies", April 28-30, 1999b, Pasadena, astro-ph/9907054.
9. Smail, I., Couch, W.J., Ellis, R.S., Sharples, R.M., 1995, ApJ 440, 501.

SHEDDING LIGHT ON THE DARK SIDE OF GALAXY FORMATION: SUBMILLIMETRE SURVEYS THROUGH LENSING CLUSTERS

ROB IVISON [a]
Dept of Physics & Astronomy, University College London, Gower Street, London WC1E 6BT, UK

Most new sub-mm/mm surveys, both deep and shallow, are being targeted at rich cluster fields. I explain why, comparing surveys that have exploited weak lensing by massive foreground clusters with those done in blank fields.

1 Historical perspective

Sub-mm/mm surveys have revolutionised our understanding of star formation in the early Universe[10] through the discovery of a vast population of very luminous galaxies,[39,3,28,19,6] clarifying the relative importance of obscured and unobscured emission. Many are extremely red[17,41,31] (a factor $\geq$100 in flux between 1 and 2 μm) and most are optically invisible, $BVRI > 26$, even to the *Hubble Space Telescope*[28,40] (*HST*).

The impact of sub-mm/mm surveys has been due to the commissioning of revolutionary bolometer cameras such as SCUBA[26] on the James Clerk Maxwell Telescope and MAMBO[33] at the Institut de Radioastronomie Millimétrique and the sensitivity of those devices to heavily extinguished galaxies[8] – to *'the optically dark side of galaxy formation'*.[25] SCUBA, in particular, has made a huge impact in cosmology through its ability to measure the bolometric output of $1 < z < 5$ dust-enshrouded galaxies (albeit with a resolution of only 14″) whose energy distributions peak in the sub-mm band.

The foundations of sub-mm/mm cosmology are already in place, only a few years after the commissioning of SCUBA, and the community is moving rapidly to build on them, developing new telescopes and instrumentation (e.g. the Atacama Large Millimeter Array in Chile, the Large Millimeter Telescope in Mexico, and the next-generation of ground-based bolometer cameras, SCUBA-2 and BOLOCAM).

[a] This work is being undertaken with Andrew Blain, James Dunlop, Thomas Grève, Jean-Paul Kneib, Kirsten Knudsen, John Peacock, Ian Smail and Paul van der Werf.

Table 1: Published and ongoing sub-mm/mm surveys and their claimed areas and rms sensitivities.

Survey name	Wavelength[d]/ FWHM of beam	Area /arcmin^2	Depth (rms) /mJy beam^{-1}
Completed:			
SCUBA lens survey[39]	850μm/14$''$[b]	36[b]	1.7[b]
Hawaii survey fields[4]	850μm/14$''$	104[e]	2.7[e]
HDF[28] (UK sub-mm survey consortium)	850μm/14$''$	5.6	0.5
Hawaii HFF radio-selected survey[5]	850μm/14$''$	31	2
Canada-UK deep sub-mm survey[19] (CUDSS)	850μm/20$''$[a]	92	1.2
Dutch lens survey[43]	850μm/14$''$[b]	50[b]	$\sim$2[b,f]
Canada HFF survey[13]	850μm/17$''$	121	$\sim$3
Canada lens survey[16]	850μm/14$''$[b]	42[b]	$\sim$2[b]
MAMBO survey[7]	1250μm/10$''$	450[c]	0.5[c]
Ongoing:			
8mJy survey (UK sub-mm survey consortium)	850μm/14$''$	240	2.7
High-z signpost survey[31]	850μm/14$''$	78	1
UK shallow lens survey	850μm/14$''$[b]	45[b]	2.5[b]
A370/A2218 SCUBA lens surveys	850μm/14$''$[b]	11[b]	0.5[b]
A2218 MAMBO lens survey	1250μm/10$''$[b]	20[b]	0.3[b]

[a] Effective FWHM is 20$''$ after convolving with beam to achieve depth of 1.2 mJy beam^{-1} rms.
[b] Divide values by $\sim$2.5 to calculate the effective source-plane area/depth/resolution.
[c] Equivalent to $\sim$1.2 mJy beam^{-1} rms at 850 μm for $z \sim 2.5$.
[d] Note that 450-μm source counts have also been reported[12].
[e] Sub-area of 7.7 arcmin^2 to 0.8 mJy beam^{-1} rms.
[f] Two/two/four fields to 1.5/2/3mJy beam^{-1} rms.

2 Sub-mm/mm surveys and the nature of sub-mm galaxies

The first generation of sub-mm/mm surveys, completed and ongoing, are listed in Table 1.

It is apparent that conventional blank fields have soaked up most of the time spent on cosmology surveys. Areas and rms depths range from the UKSSC 8-mJy survey's 200 arcmin^2/2.7 mJy beam^{-1} to the UKSSC HDF[28] survey's 5.6 arcmin^2/0.5 mJy beam^{-1}, and MAMBO has now completed its first deep 1250-μm survey[7] (450 arcmin^2/0.5 mJy beam^{-1}, FWHM 10$''$).

These blank-field surveys have been tremendously successful, determining the 850-μm source counts above 2 mJy and thereby resolving directly up to about half of the *COBE* background at 850 μm. The deepest map, of the HDF[28], has also yielded a statistical detection of the sub-mm emission from Lyman-break galaxies[37].

After initial uncertainty, there is now a growing consensus amongst the sub-mm/mm community that the sources uncovered by SCUBA (and now MAMBO) are massive, intensely star-forming galaxies at $\bar{z} \sim 3$ (possibly slightly closer[35]), resembling ultraluminous *IRAS* galaxies in some respects, usually with only a tiny fraction (<1%) of their luminosity released in the rest-frame UV[38] (c.f.[1,34]) so that many qualify as 'extremely red objects'[17,41,31] (EROs, $R - K \gtrsim 6$).

The road to this consensus has been paved by painstaking efforts to determine the nature of individual galaxies, largely through a process of trial and error, slowly determining the most efficient techniques for identifying near-IR or optical counterparts, investigating basic properties and, in pitifully few cases, measuring redshifts[29,30].

To date, deep imaging in the radio and near-IR bands[41,42] have been far and away the most effective techniques, pinpointing counterparts (see Figures 1 and 2 and their captions) and facilitating spectroscopic follow up. This has culminated in several CO detections that suggest molecular gas masses consistent with the formation of elliptical galaxies.[21,22,32]

Radio flux measurements or limits at 1.4 GHz have also provided a plausible redshift distribution[42] based on new photometric techniques[14,15]. Other techniques – mm interferometry, for example[18,6,24] – have been less successful at elucidating what we know of the SCUBA galaxy population, but clearly hold promise for the future[23], particularly for very bright sources ($\gtrsim$8 mJy at 850 μm) found in the field, through cluster lenses or near luminous radio galaxies[31]. There are hopes that broad-band spectral devices may be able to determine spectroscopic redshifts using CO transitions, regardless of the availability of plausible optical/IR counterparts, though the technical challenges are immense.

The current samples of sub-mm/mm galaxies contain a small but significant fraction of active galactic nuclei (AGN), though deep, hard-X-ray imaging[20,27,36] has so far failed to uncover the large, heavily obscured AGN population that some had suspected from the earliest follow-up work[29] and from theoretical arguments[2].

3 The problem of confusion – lifting and separating with a lens

Had the galaxies discovered in sub-mm surveys been only fractionally fainter or less numerous, a second, more sensitive generation of bolometer cameras would have been required to discover them. Early surveys[39,3,28,19] would collectively have uncovered only a couple of sources – the first, an obvious AGN[29] (SMM J02399−0136) and the second,[28] a puzzle with no optical or near-IR counterpart (HDF850.1). Who can say what conclusions might have been reached and how future surveys, e.g. with *FIRST*, may have suffered?

We have been fortunate, then, that first-generation bolometer arrays were sufficiently sensitive to enable rapid progress in sub-mm cosmology. We have been less fortunate regarding source confusion: few would have predicted that SCUBA would reach its effective confusion limit[9] within a few months of being commissioned. The deepest direct counts[28] are already at the confusion limit, suggesting that further progress in constraining the intensity of the sub-mm background and the nature of the faint sub-mm population requires an innovative approach.

To probe below the confusion limit using the existing sub-mm/mm cameras requires the use of the natural magnifying glasses that provide the raison d'être for this conference: gravitational lenses. Massive clusters provide a magnified (although distorted) image of a small region of the background sky; thus both the effective resolution and sensitivity of the survey are increased, as measured on the background sky. This enables surveys to probe faint flux densities without suffering confusion, albeit at the price of a distorted view.

With an accurate cluster mass model, the distortion can be corrected. The first lens survey[39,10] illustrated the advantages of this approach for the counts.[11] About 100% of the *COBE* 850-μm background was resolved down to 0.5 mJy. Follow-up observations,[21,29,22,41,23,30,42] also benefitted from achromatic gravitational amplification: not only was the effective depth of the sub-mm maps increased, but the counterparts at all other wavelengths were similarly amplified. This allows useful follow-up observations to be obtained in several hours or tens of hours using the current generation of telescopes and instrumentation: it is no coincidence that of the $\sim$100 known sub-mm galaxies, only a handful have reliable spectroscopic redshifts and *all* of these were discovered through cluster lenses.

Another advantage of using clusters is that extraordinarily deep images – X-ray, optical, IR and radio – exist or are scheduled for these fields. The HDF is the only blank field that is equally blessed. Abell 851, 1835 and 2218 (and many other cluster fields) have superb *HST* images and near-IR data; Abell 370, 851 and 2125 have 1.4-GHz maps with <10-μJy beam^{-1} noise levels.

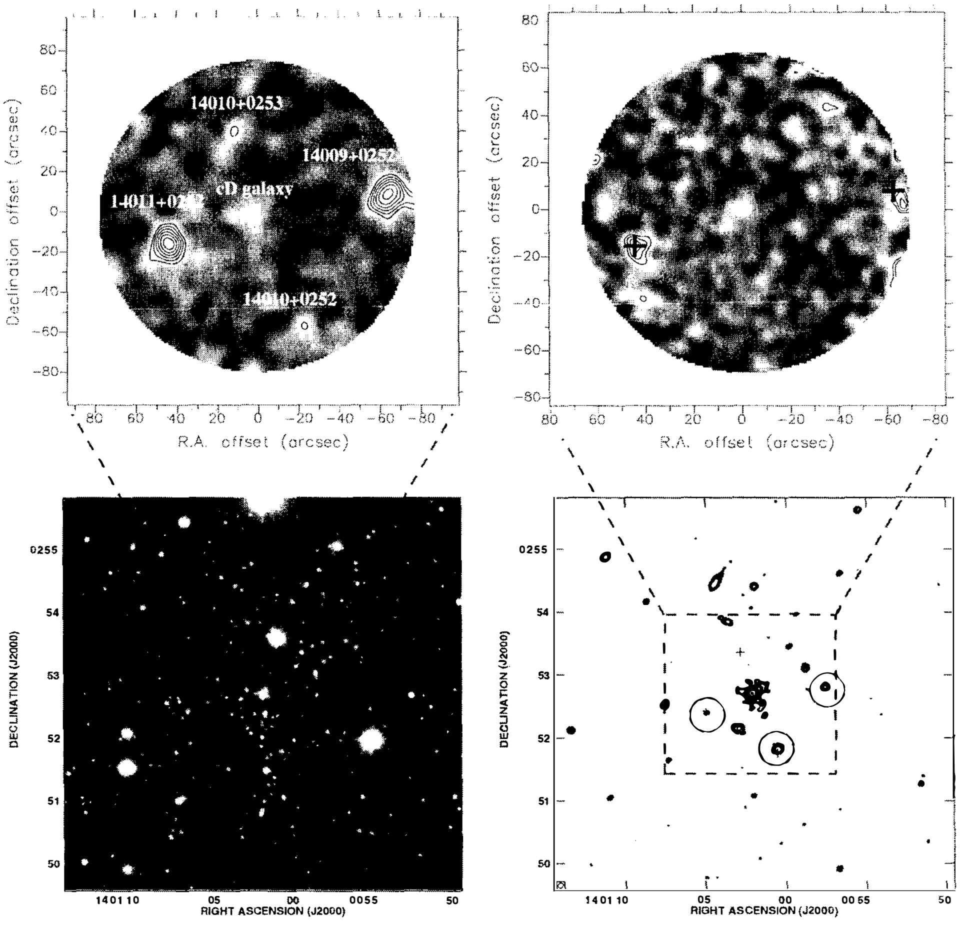

Figure 1: An illustration of the detection and further investigation of sub-mm galaxies in the Abell 1835 cluster field[30]. *Top left*: 850-μm map (field diameter $\sim 150''$); *top right*: 450-μm map. Sources are labelled on the 850-μm image. Below these are a true-colour *UBI* image (*lower left*) and a 1.4-GHz map from the VLA (*lower right*), both $\sim 370''$ across. The sub-mm sources are easily detected in the very deep radio map (red circles), with far better positional accuracy than afforded by SCUBA. Twenty other radio sources seen in the VLA image can be used to co-align the radio/optical (or radio/near-IR) coordinate frames, yielding counterpart positions accurate to $0.1''$. Note that the radio image shown here represents only 6% of the VLA's primary beam area at 1.4 GHz.

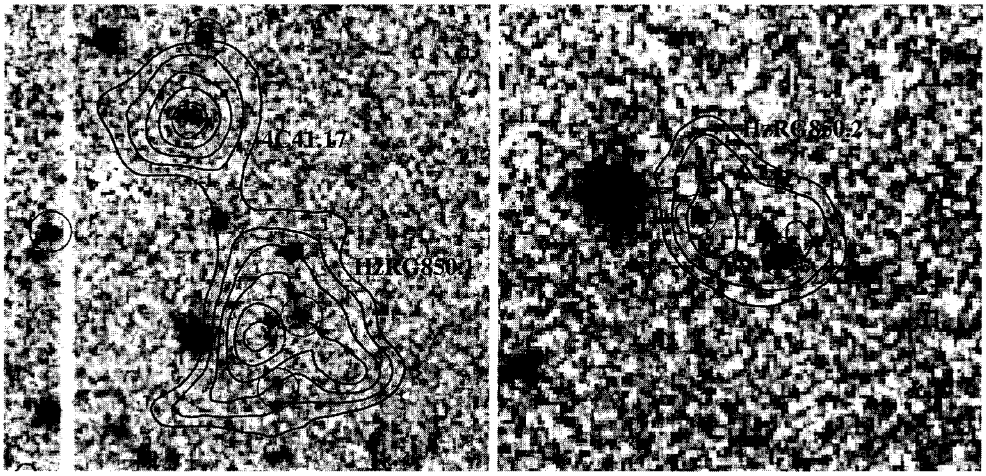

Figure 2: K-band images of regions around the $z = 3.8$ radio galaxy, 4C 41.17, where there is an order-of-magnitude over-density of sub-mm sources[31]. 850-μm data are shown as contours. Red circles (solid lines) denote EROs ($R - K \gtrsim 6$). Two EROs are probably associated with the blended sub-mm galaxy, HzRG850.2. For the other sub-mm galaxies (HzRG850.1, 4C 41.17), green circles (dashed lines) denote the likeliest counterparts (faint and red, in the case of HzRG850.1, though a bona fide ERO could also be responsible for the sub-mm emission).

4 Future plans and concluding remarks

Following on from the success of the earliest sub-mm cluster survey[39,10], groups in the UK, Holland and Hawaii are currently undertaking more surveys with SCUBA and MAMBO that exploit cluster lenses. The latest of these will combine a long integration (equal to that obtained on the HDF) with amplification by the cores of amongst the most massive, well-constrained cluster lenses known, A 370 and A 2218.

At modest amplifications ($A \sim 2$–5), it should be possible to detect the optically-identified arclet population; probing fainter, it is likely that a new, largely unexplored class of lensed feature may appear: multiply-imaged pairs, recognised in the first *HST* cluster images.

These appear in the optical/near-IR as symmetric images with typical separations of 5–10″ (i.e. within a single SCUBA or MAMBO beam) and can be simply and successfully modelled as highly magnified images ($A \sim 10$–100) of very faint, compact sources which lie close to a critical line. In a well-constrained lens such as A 2218, their location in the cluster, combined with the positions and separation of any radio/IR/optical counterparts, can give the source redshift and amplification to high precision. The area of the source plane in which pairs are formed can also be estimated from the lens models, allowing their rate of occurence to be converted into an estimate of the surface density of extremely faint (tens of μJy) sub-mm/mm background sources, with the bonus of crude redshift information.

Using the superb recent *HST* imaging of A 2218, at least 4 highly magnified pairs have been identified (from a source population with a comparable surface density to that expected for the very faint sub-mm/mm population, $\sim$10 arcmin^{-2}) suggesting that the cluster amplification cross-section is high and that the chance of finding such systems is good. Failure to detect any of these highly magnified sources using SCUBA and MAMBO would indicate convergence of the source counts and can be used to impose strong limits on the surface density of very faint sources and the total intensity in resolved sources in the sub-mm background.

Acknowledgments

I acknowledge a PPARC Advanced Fellowship and support from the Training and Mobility of Researchers Programme.

References

1. Adelberger K.L., Steidel C.C., 2000, ApJ, submitted (astro-ph/0001126)
2. Almaini O., Lawrence A., Boyle B.J., 1999, MNRAS, 305, L59
3. Barger A.J. et al., 1998, Nature, 394, 248
4. Barger A.J. et al., 1999, ApJ, 518, L5
5. Barger A.J. et al., 2000, AJ, 119, 2092
6. Bertoldi F. et al., 2000, A&A, submitted (astro-ph/0006094)
7. Bertoldi F. et al., 2001, in preparation
8. Blain A.W., Longair M.S., 1993, MNRAS, 264, 509
9. Blain A.W., Ivison R.J., Smail I., 1998, MNRAS, 296, L29
10. Blain A.W. et al., 1999, MNRAS, 302, 632
11. Blain A.W. et al., 1999, ApJ, 512, L87
12. Blain A.W. et al., 2000, ASP Conf. Series 193, 246 (astro-ph/9908024)
13. Borys C. et al., 2001, ApJ, in preparation
14. Carilli C.L., Yun M.S., 1999, ApJ, 513, L13
15. Carilli C.L., Yun M.S., 2000, ApJ, 530, 618
16. Chapman S.C. et al., 2001, ApJ, in preparation
17. Dey A. et al., 1999, ApJ, 519, 610
18. Downes D. et al., 1999, A&A, 347, 809
19. Eales S.A. et al., 1999, ApJ, 515, 518
20. Fabian A.C. et al., 2000, MNRAS, 315, L8
21. Frayer D.T. et al., 1998, ApJ, 506, L7
22. Frayer D.T. et al., 1999, ApJ, 514, L13
23. Frayer D.T. et al., 2000, AJ, in press (astro-ph/0005239)
24. Gear W.K.P. et al., 2001, MNRAS, in press (astro-ph/0007054)
25. Guiderdoni B. et al., 1997, Nature, 390, 257
26. Holland W.S. et al., 1999, MNRAS, 303, 659
27. Hornschemeier A.E. et al., 2000, ApJ, in press (astro-ph/0004260)
28. Hughes D.H. et al., 1998, Nature, 394, 241
29. Ivison R.J. et al., 1998, MNRAS, 298, 583
30. Ivison R.J. et al., 2000, MNRAS, 315, 209
31. Ivison R.J. et al., 2000, ApJ, in press (astro-ph/0005234)
32. Kneib J.-P. et al., 2000, A&A, in preparation
33. Kreysa E. et al., 1999, SPIE 3357, 319
34. Lawrence A., 2000, MNRAS, submitted
35. Lilly S.J. et al., 1999, ApJ, 518, 641
36. Mushotzky R.F. et al., 2000, Nature, 404, 459
37. Peacock J.A. et al., 2000, MNRAS, in press (astro-ph/9912231)
38. Sanders D.B., 2000 (astro-ph/9910028)
39. Smail I., Ivison R.J., Blain A.W., 1997, ApJ, 490, L5
40. Smail I. et al., 1998, ApJ, 507, L21
41. Smail I. et al., 1999, MNRAS, 308, 1061
42. Smail I. et al., 2000, ApJ, 528, 612
43. van der Werf P. et al., 2000, A&A, in preparation

PROSPECTS FOR THE LENSING OF SUPERNOVAE

R. BENTON METCALF
Institute of Astronomy, Cambridge
Madingley Road
Cambridge CB3 0HA, England

Observations of high redshift type Ia supernovae (SNe) will enable us to probe the structure of galaxy halos and the composition of dark matter. The future prospects for this field are briefly discussed here. First the ability of SN observations to differentiate between dark matter made of macroscopic compact objects and dark matter made of microscopic particles is reviewed. Then a new method for probing the structure of galaxy halos and galaxy cluster halos is described. This method utilizes the correlations between foreground galaxy light and supernova brightnesses to substantially decrease possible systematic errors. This technique may be particularly useful for measuring the size of dark matter halos, a measurement to which the galaxy-galaxy lensing is not well suited, and the level of substructure in galaxy halos, a problematic prediction of the cold dark matter model. The required observations of hundreds of SNe at $z \sim 1$ are already being proposed for the purposes of cosmological parameter estimation.

1 Introduction

There are still many outstanding problems in the fields of structure formation and dark matter which gravitational lensing has not yet been able to address. Outside of the visible extent of galaxies not a great deal is known about the distribution of dark matter (DM) on scales smaller than galaxy clusters. Galaxy–galaxy lensing has put some constraints on the mass of galaxy halos, but their size scale and the degree to which they are smooth mass distributions or collections of subclumps are not well determined.[1,2,3,4,5] Even the concept of galaxy halos, with a single galaxy within each of them and well defined sizes, may not be correct. Nor is it clear how the observable properties of galaxies relate to the DM distribution around them. Recently dark matter simulations have revealed several problems with the cold dark matter (CDM) model. One of these is that CDM predicts a large amount of small scale structure within halos which is unaccounted for in the observed distribution of light.[6] In addition, the composition of DM

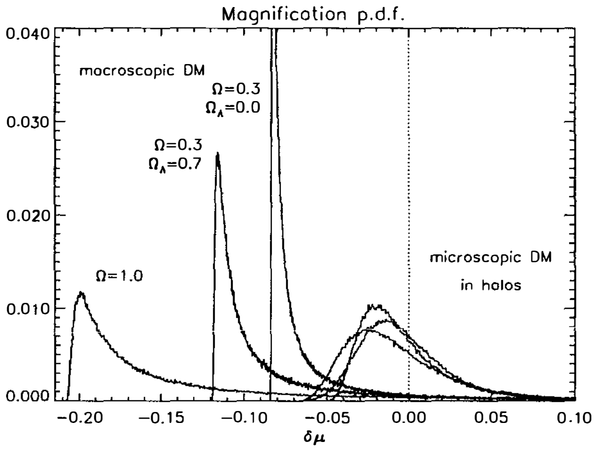

Figure 1: These are the magnification probability distributions for point sources in several models. The three distributions peaking on the left are for DM composed entirely of macroscopic compact objects. The background cosmologies are listed. The more centrally concentrated distributions on the right are for microscopic DM concentrated into galaxy halos. These distributions are functions of both the background cosmology and the halo model. Changing the halo model makes relatively little difference if the fraction of mass in halos is kept fixed.

is still a mystery: it could be large compact objects like black holes or it could be microscopic particles like WIMPS. Even with primordial nucleosynthesis bounds roughly half the baryons are in some form that has yet to be directly detected – conceivably in condensed objects. I will describe here how the gravitational lensing of type Ia SNe can help to answer some of these questions. Lack of space dictates that this only be an outline and that the reader be referred to more detailed papers.

High redshift type Ia SNe have recently been used by two collaborations to measure cosmological parameters.[7,8] These measurements and the proposed application of Ia's to gravitational lensing are made possible by the discovery of a tight correlation between the light curve shapes and peak luminosities of these SNe.[9,10] The measured standard deviation of corrected peak luminosities in local SNe is now $\lesssim 0.12$ mag. The successes of these collaborations have inspired plans for more aggressive, larger searches for high redshift SNe in the near future. The volume and quality of data is likely to increase dramatically. Besides constraining Ω_m and Ω_Λ these data, amongst other things, would be ideal for gravitational lensing studies.

In the next section I will discuss how SNe can be used to determine if dark matter is composed of macroscopic compact objects. In section 3 the case of DM composed of microscopic particles is taken up.

2 Lensing by macroscopic compact objects

Some magnification probability distributions for a point source at $z = 1$ are plotted in figure 1. The means of all these distributions are zero which corresponds to the usual Friedman-Robertson-Walker (FRW) luminosity distance. When DM is made entirely of macroscopic compact objects the distribution peaks well below the mean making most SNe under-luminous. The peak of the distribution is just slightly brighter than the solution corresponding to the empty beam or Dyer–Roeder luminosity distance[11]. This is the formal solution of Sachs optical scalar equations[12] for a beam that passes through only empty space (no Ricci focusing) and has no

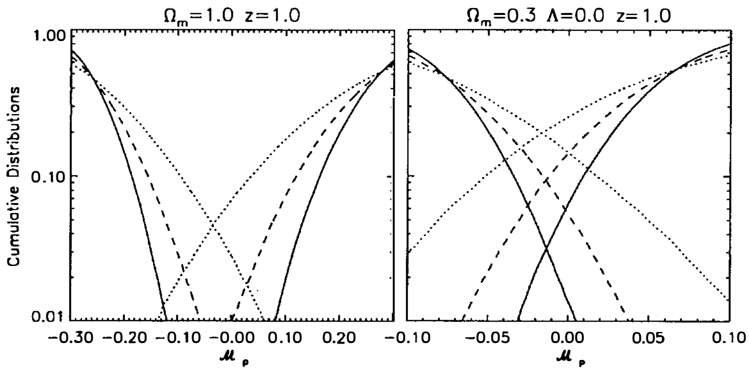

Figure 2: The cumulative distributions of $\mathcal{M}_p$ for different models and different numbers of observed SNe. The dotted curves are for 21 observed SNe, the dashed for 51 and the solid for 101. The pairs of like curves represent the cases of macroscopic and microscopic DM. The distributions for the cases of macroscopic DM rise to the right while if DM is microscopic $\mathcal{M}_p$ is expected to be smaller. The overlap of these distributions is small signifying that DM candidates could be distinguished using this statistic. For a flat cosmological model the constraints are stronger than for the $\Lambda = 0$ model with the same Ω_m. The variance in SN luminosities is $\sigma_{sn} = 0.16$ mag.

shear on it. The long, high magnification tail to these distributions correspond to rare cases where a DM object is very close to the line of sight. At $z < 2$ it is unlikely that multiple lens lie so close to the line of sight that their lensing effects become nonlinearly coupled which significantly simplifies calculations.

The distributions for microscopic DM shown in figure 1 assume that the DM is clustered into halos surrounding galaxies. The exact form of the clustering is not important for this section. These distributions are significantly more centrally concentrated about the FRW solution. With macroscopic DM the magnification is dominated by Ricci focusing – the isotropic expansion or contraction of the image caused by matter within the beam – while in the macroscopic case (with true point sources) it is entirely due to shear caused by matter outside of the beam. This is the essential difference between the two cases and why they can be differentiated using SNe observations.

To differentiate between DM candidates we construct the statistic

$$\mathcal{M}_p \equiv \frac{1}{N_{sn}} \ln \left[\frac{P\left(\{\delta\mu\}|\text{ macro DM,noise}\right)}{P\left(\{\delta\mu\}|\text{ micro DM,noise}\right)} \right]. \tag{1}$$

where the P's are the probability of getting the N_{sn} observed SN magnifications given that DM is of the specified type and given the expected noise. $\mathcal{M}_p$ is close to normally distributed for a modest number of SNe. Some distributions are plotted in figure 2. If DM is microscopic, $\mathcal{M}_p$ is expected to be small while if DM is macroscopic it will be large. Figure 2 shows that with 100 SNe at $z \sim 1$ one is unlikely to confuse the two cases.

This technique works for DM objects with masses $\gtrsim 10^{-3}\ M_\odot$. For smaller masses it is probable that the expanding SN photosphere will make the magnification time dependent which is an interesting subject in itself. For more details on differentiating DM candidates see Metcalf & Silk.[13]

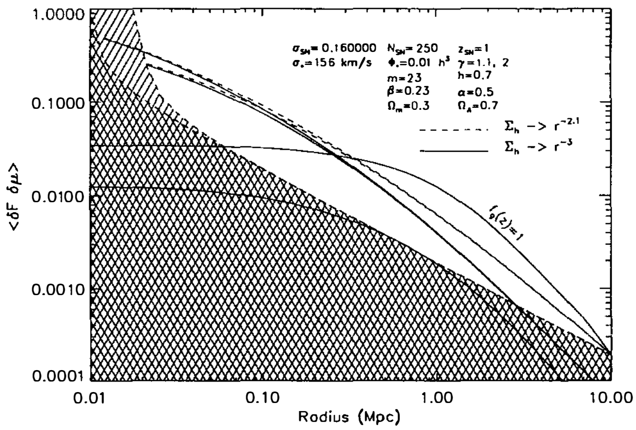

Figure 3: The expected correlation between foreground light and SN luminosity. There are two contributions plotted separately here. The first contribution is from *galactic halos* which are presumed to surround every galaxy and have properties which are related to the observed properties of their resident galaxy. In addition there is a contribution from *extragalactic halos* or galaxy clusters which contain multiple galactic halos and additional matter within them. The total correlation is the sum of the two components. The galactic halo curves are the steeper ones starting in the upper left corner. Two different models which differ in the logarithmic slope of the surface density at large galactic radii are shown. At small galactic radii the galactic halos approach the form of singular isothermal spheres. For each model two inner cutoffs are considered – $R_{min} = 10, 20$ kpc. To avoid obscuration all SNe within R_{min} of any galaxy are excluded. The two curves that flatten out on the left are the contributions from extragalactic halos in the CDM model. These halos have Navarro, Frenk and White profiles. The one marked $f_g(z) = 1$ represents the case where only SNe behind $M > 10^{14}$ $M_\odot$ clusters are selected. The crisscrossed region represents the noise contributed by uncertainties in SN peak luminosities ($\sigma_{sn} = 0.16$ mag) and shot noise in the foreground galaxy counts for the case of 250 observed SNe. The signal to noise ratio at $R = 200$ kpc is $\simeq 4\sqrt{N_{sn}/250}$. The limiting magnitude of foreground galaxies is $m = 23$.

3 Correlations between light and magnification

When the DM is made of microscopic particles it can be treated as a transparent, massive fluid clumped into structures that are much larger than the beam size. Because of lensing the variance of SN brightnesses will increase with redshift[14] which introduces noise into the cosmological parameter estimates. The increases in variance is not the best way of detecting the lensing however. Using the correlation between foreground light and SN brightness reduces possible systematic errors associated with the evolution of the SN population and makes the measurement more directly sensitive to the mass and size scale of dark matter halos.

Lets define the weighted foreground flux for each SN as

$$\mathcal{F} = \sum_{y_i < R} w(z_i, z_s) f_i \tag{2}$$

where f_i the observed flux from the ith galaxy and y_i is its distance (angular or proper) from the line of sight to the SN. The weight function depends on the galaxy and SN redshifts. Figure 3 shows the expected correlation of $\mathcal{F}$ with SN brightness, $\langle \delta\mathcal{F}\delta b\rangle$, for a SN at $z_s = 1$. This quantity is proportional to the average surface density within distance R of a galaxy.

By measuring this correlation the size scale of galactic halos could be constrained significantly better than with galaxy–galaxy lensing using a much larger data set. This is a result of the magnification being a steeper function of galactic radius than shear when the density profile is steeper than isothermal. In addition, by selecting or searching for SNe behind galaxy clusters the structure of clusters and the smaller halos within them can be probed. The tidal truncation of galactic halos could be investigated. Higher order correlations can also be used to look for substructure in galaxy halos. This subject is treated more thoroughly in a complete paper by the author.[15]

4 Discussion

The number of high redshift SNe required for the studies proposed here are well within the projected numbers for future SN searches – the VISTA telescope is expected to find hundreds at $z \gtrsim 1$.[a] and the proposed SNAPSAT satellite could find thousands up to $z \simeq 1.7$.[b] The errors assumed in this paper are quite conservative compared to those expected for satellite observations. The future looks bright for this new field in gravitational lensing.

Acknowledgments

Many thanks to all the friends that made this such an enjoyable conference. Thanks also to J. Silk for all his help while some of this work was being done.

References

1. P. Fischer *et al*, preprint, astro-ph/9912119 (1999)
2. M.J. Hudson *et al*, *ApJ* **503**, 531 (1998)
3. T.G. Brainerd *et al*, *ApJ* **466**, 623 (1996)
4. R.E. Griffiths *et al*, *MNRAS* **282**, 1159 (1996)
5. J.A. Tyson *et al*, *ApJ* **281**, L59 (1984)
6. B. Moore *et al*, *ApJ* **524**, L19 (1999)
7. S. Perlmutter *et al*, *ApJ* **517**, 565 (1997)
8. A.G. Riess *et al*, *ApJ* **116**, 1009 (1998)
9. M. Hamuy *et al*, *AJ* **112**, 2408 (1996)
10. A.G. Riess *et al*, *ApJ* **473**, 88 (1996)
11. C.C. Dyer and R.C. Roeder *ApJ* **189**, 167 (1974)
12. R.K. Sachs, *Proc.Roy.Soc.London A* **264**, 309 (1961)
13. R.B. Metcalf and J. Silk, *ApJ* **519**, L1 (1999)
14. R.B. Metcalf, *MNRAS* **519**, L1 (1999)
15. R.B. Metcalf, preprint, submitted to *MNRAS* (2000)

[a] home page: http://www-star.qmw.ac.uk/~jpe/vista/
[b] home page: http://snap.lbl.gov/proposal/

A GRAVITATIONAL LENS SURVEY WITH THE *PLANCK SURVEYOR*

Andrew W. Blain
Institute of Astronomy, Madingley Road, Cambridge, CB3 0HA, UK

The *Planck Surveyor* cosmic microwave background (CMB) imaging mission will make very sensitive maps of the whole sky at microwave, millimetre (mm) and sub-mm wavelengths. The steep source counts expected in the highest frequency *Planck* bands are likely to be associated with a strong magnification bias, and so the fraction of galaxies magnified by a factor of two or more could be greater than 10%. In this paper, previous predictions of the significance of the *Planck* survey for studies of lensing statistics are updated, to reflect our expanded knowledge of the properties of high-redshift dusty galaxies, obtained from far-infrared and sub-mm surveys. A catalogue of probably about 10^4 galaxies, but perhaps as many as 10^5 or as few as 10^3, is expected to be generated from the final *Planck* all-sky maps. Of order 1000 galaxies, a better determined number, might reasonably be expected to be strongly lensed. Co-ordinated sub-mm and far-infrared follow-up observations made using the SPIRE and PACS instruments aboard the ESA cornerstone mission *FIRST* – *Planck*'s travelling companion to its L2 orbit – and the ground-based ALMA interferometer array will provide accurate positions and very valuable information about the spectral energy distributions (SEDs), redshifts and astrophysical properties of the galaxies in the *Planck* catalogue. ALMA and radio images will also reveal their morphology, and the characteristic arc and multiple image structures produced by gravitational lensing. Studies of these bright sub-mm-selected galaxies will allow new insight into the process of galaxy formation and evolution.

1 Introduction

The *Planck Surveyor* CMB imaging satellite[1] will provide a mm/sub-mm-wave map of the whole sky with a resolution of about 5 arcmin down to a detection limit of order 100 mJy at wavelengths of 350, 550 and 850 μm. These wavelengths are expected to be close to the peak of the redshifted thermal dust emission spectrum of distant galaxies. The effect of redshifting the dust spectrum peak into these observing bands is to provide access to the distant Universe, with little contamination from bright low-redshift galaxies. This remarkable, helpful K-correction is confirmed observationally to be effective in the sub-mm waveband, and is an almost unique feature of the waveband, although a similar effect may be at work in the hard X-ray surveys now being carried out. A priori, the counts of sub-mm galaxies at the faintest depths probed by *Planck* are expected to be very steep, an expectation which seems to be confirmed by the results of recent ground-based sub-mm-wave surveys.[5]

Very steep sub-mm counts generate a strong positive magnification bias,[2,3] and thus boost the fraction of lensed galaxies in a flux-limited sample. This enhancement to the surface density of lensed galaxies will hopefully be exploited in the *Planck* survey to allow a very large catalogue of mainly unknown strongly lensed galaxies to be compiled.

2 Sensitivity and confusion noise in a *Planck* survey

The expected sensitivities of the *Planck*-HFI instrument in its three highest frequency channels, in which the largest number of distant dusty galaxies and lenses will be detected,[3] are listed in Table 1, along with the predicted levels of source confusion noise.

It is important to understand the significance of source confusion noise introduced into the *Planck* images due to the varying number and flux densities of unresolved dusty galaxies in the observing beam. At 5 arcmin across, the *Planck* beam is very much larger than the mean separation of L^* galaxies, and also about 4 times greater in area than the 5-arcmin^2 field of view of the SCUBA camera at the JCMT, from which most observational information about the sub-mm source population has thus far been derived.

In Fig. 1 the results of many independent simulations of sampling a random unclustered distribution of sources on the sky with the observing beam in the relevant *Planck*-HFI channels are compared with the estimates of instrumental noise. Confusion noise due to Galactic cirrus predicted by *IRAS*-based studies,[11] and of simple estimates based on the surface density of galaxies,[6,4] are compared in Table 1. All these calculations of the confusion signal due to extragalactic sources are made assuming a model for the underlying surface density of sources on the sky that is at the top end of the range of possible values, the predictions are therefore likely to be conservatively high, and thus pessimistic for making reliable detections. Extragalactic confusion noise is expected to dominate both the instrumental and Galactic noise in these bands.

In Fig. 1, the results of the simulations are enveloped by solid curves, which represent log-normal distributions providing good representations of the results. The value of σ in the log-normal distribution $(\exp -[\ln x - \bar{x}]^2/2\sigma^2)$ at all three frequencies is close to 0.2.

Unfortunately, the actual level of confusion noise that will be contributed to the *Planck* image depends on the uncertain surface density of galaxies that are brighter than those selected in existing sub-mm surveys (several tens of mJy at 850 μm/350 GHz). The results of future wider-field ground-based sub-mm surveys, and experience gained from the results of long-duration balloon-borne mm- and sub-mm-wave CMB experiments, including the existing BOOMERanG data and forthcoming data from TOPHAT will be useful in this respect. Recent simulations of extraction algorithms,[14] in which the surface density of galaxies is assumed to be a factor of 2-3 times lower than that assumed here,[24] suggest that 350-GHz point sources with flux densities greater than of order 75 mJy could be extracted from the *Planck* all-sky map.

3 Expected source density and numbers of detections

The two very different counts of unlensed galaxies shown in Fig. 2 should provide an envelope to the maximum range of possible values of the sub-mm counts at flux densities at which galaxies will be detected using *Planck*. The two underlying models[8,9] predict very different bright sub-mm counts, but are both consistent with the observed far-infrared and sub-mm-wave counts and background radiation intensity, and with what little is currently known about the redshift distribution of sub-mm-selected galaxies. Our knowledge of the population will continue to improve until the launch of *Planck*. Some of the facilities that will contribute to this knowledge are listed elsewhere.[4]

Current observational limits to the population of sub-mm galaxies are reasonably well determined at flux densities less than about 10 mJy at 350 GHz from the results of several independent surveys: the surface density of galaxies brighter than 4 mJy at 850 μm/350 GHz is about 2000 deg^{-2}. These surveys have mainly been carried out using the SCUBA camera at the JCMT, but results are also now coming in from the MAMBO 1.25-mm bolometer array camera at the IRAM 30-m telescope.[10] These are flux densities considerably fainter than *Planck* will probe, and so far, these instruments have mapped only very small regions of sky (several

Table 1:
Some approximate parameters describing the likely properties of a *Planck* all-sky survey that are relevant to the detection and study of dusty galaxies. The estimated final sensitivity of the *Planck* survey[1] $\sigma_{\rm sens}$, and three estimates of confusion values are listed: that expected from Galactic cirrus[11] in regions with a 100-μm surface brightness $B_0 = 1\,{\rm MJy\,sr^{-1}}$, $\sigma_{\rm cirrus}$, a simple estimate of the value expected due to external galaxies – the flux density at which the surface density of galaxies exceeds 1 beam^{-1},[6,4] – $\sigma_{\rm beam}$, and the width of the distributions shown in Fig. 1, between which 65% of the results of the simulations lie, $\sigma_{\rm sim}$. Note that the confusion noise predicted by the simulations is log-normal and not Gaussian.

ν/GHz	$\sigma_{\rm sens}$/mJy	$\sigma_{\rm beam}$/mJy	$\sigma_{\rm cirrus}$/mJy	$\sigma_{\rm sim}$/mJy
353	16	10	1.3	40
545	19	30	9	60
857	26	63	55	170

hundred square arcminutes). The counts of objects brighter than about 10 mJy has been only weakly constrained.

Information is also available about the counts at the very brightest flux densities, based on the results of a targeted SCUBA survey of low-redshift galaxies selected from the *IRAS* catalogue.[12] This survey was used to define a luminosity function of local *IRAS* galaxies in the sub-mm, which can be used to impose a lower limit to the bright counts at flux densities brighter than the detection limit in the all-sky *Planck* survey: this lower limit is about 10 sources on the sky brighter than 1 Jy at 850 μm/350 GHz.

The probability of lensing by foreground galaxies out to the high redshifts, at which a significant fraction of the sources detected in the *Planck* survey are expected to lie, is reasonably well-known, certainly to within a factor of a few. Specific predictions of this probability, tailored to observations in the sub-mm waveband, are discussed elsewhere.[3,7] The predicted density of lenses on the sky should also be quite well determined at the flux densities that will be probed by *Planck*. This is because the intrinsic flux densities of these objects, after correcting for the effect of lensing, are likely to be of order 10 mJy. At this flux density the surface density of galaxies is reasonably well constrained by SCUBA observations.[4] Predicted numbers of lensed objects[7] are shown by the dot-dashed lines in Fig. 2.

A significant potential uncertainty remains in these results, however, because the maximum magnification that can be produced by a lens is limitted by the size of the source, being smaller for larger sources. In these calculations, we have assumed that background high-redshift sources are less than about 10 kpc in size, so that a maximum magnification of several tens can be produced. This assumption is supported by high-resolution interferometric observations of the size of the continuum emitting region in low-redshift ultraluminous galaxies, which is found to be much smaller – several 100 pc across.[22] However, there are indications that at least some very luminous dusty high-redshift galaxies display CO and dust emission on scales greater than 10 kpc.[19,13] Unfortunately, sub-arcsecond resolution images are required in order to measure the sizes of high-redshift dusty galaxies smaller than 10 kpc, and the necessary interferometric observations are difficult and time-consuming. Hence, as we do not yet know the size distribution of these distant ultraluminous galaxies, we cannot be certain that their sizes are typically small enough for large lensing magnifications to be possible. Despite this caveat, individual examples of high-redshift sub-mm objects lensed by foreground galaxies with magnifications of several tens are known,[20,17,16] and so it is likely that *Planck* will be able to detect a significant number.

Based on an extrapolation of the log-normal distribution of pixel values predicted by the conservative simulations of confusion noise shown in Fig. 1, it is possible to predict the number

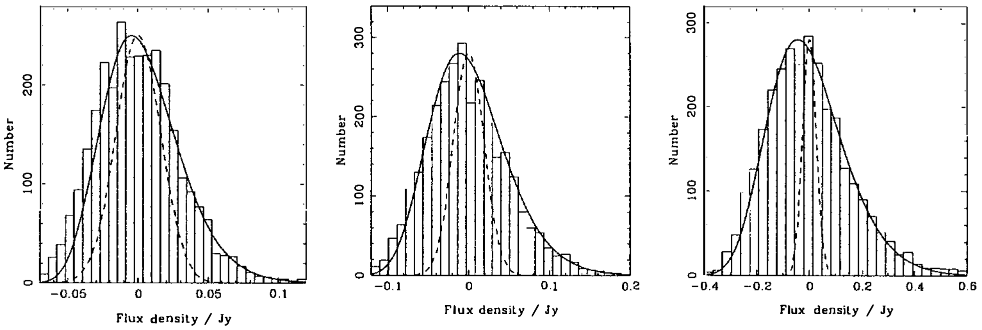

Figure 1:
Results of simulations of confusion noise expected in the 5-arcmin beam of the *Planck*-HFI instrument at frequencies of 353 GHz (left), 545 GHz (middle) and 857 GHz (right). The histograms show the results of 3000 different simulation realisations of the predicted galaxy distribution[8] sampled in in the *Planck* beam, with Gaussian instrumental noise added. The solid curves show analytical log-normal distributions that adequately describe the envelopes of the simulation results. The dashed curves show the expected Gaussian instrumental noise in the *Planck* 14-month survey (16, 19 and 26 mJy beam^{-1} respectively). At frequencies lower than 353 GHz instrumental noise is expected to dominate confusion noise, a trend which can be seen developing from frequency to frequency above. The flux scale has been shifted to give a zero net background. At 353 GHz Galactic foreground confusion noise is not included, as this source of noise is not expected to be more significant than the instrumental noise in regions of low Galactic emission.

of pixels that are likely to exceed a certain flux density due to the effects of confusion over the all-sky *Planck* survey. This expected count of spurious detections, which is shown by the dotted lines in Fig. 2, can then be compared with the expected count of lensed and unlensed galaxies. Reliable detections should be possible if these counts lie safely above the dotted lines at any flux density. Hence, it is likely that lensed galaxies brighter than about 250, 500 and 1500 mJy at 353, 545 and 857 GHz respectively could be detected using *Planck*, even in this pessimistic model of the confusion noise. At these limits, of order 100 lensed sources are expected over the whole sky. If the counts of bright unlensed sources are less than assumed here,[14] then the confusion noise will be reduced, and a greater number will be detected. The counts shown in Fig. 2 allow these different scenarios to be investigated directly. It is important to note that much better estimates of confusion noise will be available well in advance of the launch of *Planck*.

The emission from both lensed and unlensed distant galaxies will pass unattenuated through the Galactic plane in the *Planck* bands; however, the ability to distinguish them against a bright and structured Galactic foreground is likely to be limited. The level of Galactic confusion (see Table 1) depends on the Galactic background intensity B_0 as $B_0^{1.5}$.[11] The results suggest that the sensitivity of the *Planck* survey can only be exploited fully to find extragalactic sources in regions of the sky where the 100-μm surface brightness from the Milky Way is less than about 5 MJy sr^{-1}, a condition which is satisfied over most of the sky.[21]

4 Follow-up observations

From the *Planck* all-sky images alone, point sources will be detectable, but no information will be available about their morphology, including whether or not they display arc and multiple image geometries characteristic of lensing. For this diagnosis, sub-arcsecond mm/sub-mm images using the high-resolution extremely-sensitive interferometer array ALMA,[5] or very deep radio images

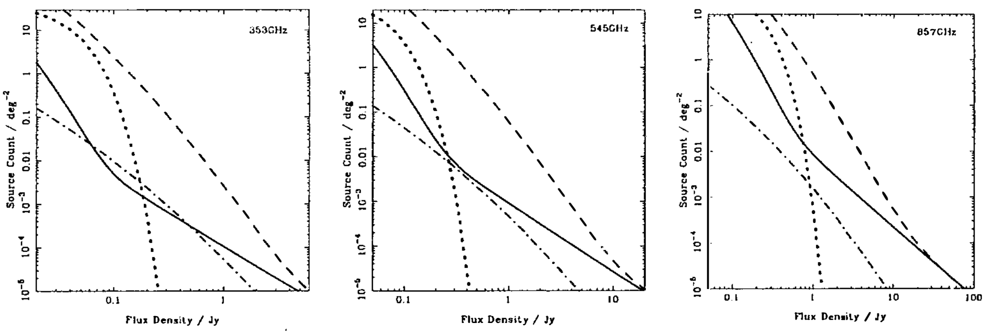

Figure 2:
Examples of counts of galaxies that will be probed in the *Planck* survey. The solid line shows the count of galaxies expected in a model of hierarchical merging galaxies.[9] The dashed line shows the count of galaxies expected in a model of luminosity evolution based on the *IRAS* luminosity function.[8] The dot-dashed line shows the expected count of lensed galaxies, derived in the second model.[7] The dotted line shows the surface density of pixels expected to exceed each flux density due to the effects of source confusion, derived by extrapolating the confusion noise distributions shown by the solid curves in Fig. 1. These correspond to the second source population, and are thus likely to be a conservative, pessimistic estimate of the true confusion noise. To obtain reliable, unconfused detections, the counts of sources being sought must lie above the dotted curves in each figure.

using the VLA will be required. Accurate positions for *Planck* sources will first be required: these could be obtained using either ALMA or the 3.5-m ESA cornerstone *FIRST* telescope.[3] Note that it is very unlikely for the foreground lens galaxy to be bright in the sub-mm waveband,[3] as this would require the foreground lens itself to be a very luminous infrared galaxy, and the space density of such sources is rather low. Hence, only the lensed images will be detected at bright flux levels in an ALMA continuum image, free from the blending and masking effects of emission from the foreground lens. Since the first discussion of a *Planck* lens survey,[2] the specifications of ALMA have been significantly refined.[26] At sub-mm flux densities of order 100 mJy, ALMA will be able to detect galaxies in integrations lasting much less than a second, and to make high-quality images in only several minutes. ALMA will make it easy to confirm lensing features and obtaining good quality images of the galaxies detected in a *Planck* survey.

The form of the mid-infrared SED of the galaxies detected using *Planck* can be determined using the SPIRE and PACS instruments aboard *FIRST*, allowing the redshift/dust temperature of the detected galaxies to be determined. Direct spectroscopic redshifts for the lensed galaxies should come quite easily from molecular emission line data taken using ALMA or from observations of features in the redshifted mid-infrared spectrum taken using *FIRST*-PACS.[18] Redshifts for the lensing galaxies should be readily obtained from the frequencies of CO absorption lines imposed on the bright dust continuum emission of the magnified background galaxies due to the interstellar medium in the foreground lens, a technique which has already been developed and demonstrated using existing mm-wave interferometers.[25]

Other relevant information can be provided by the FIRST radio survey at the VLA, which covers over 5000 deg^2 to a depth of about 1 mJy at 1.4 GHz. The high-resolution radio images from FIRST should detect a significant fraction of the *Planck* detected galaxies with sub-mm flux densities of several hundred mJy, based on our current knowledge of the SEDs of confirmed high-redshift SCUBA galaxies. For example, the 25-mJy 850-μm sub-mm source SMM J02399−0136 has a 1.4-GHz flux of 520 μJy.[15] The brighter cousins of these objects in the *Planck* survey might typically appear at the faintest levels in the FIRST/VLA survey. The 25-mJy 60-μm all-sky image from the *IRIS/ASTRO-F* satellite[23] will also be useful for detecting *Planck* sources.

5 Summary

The *Planck Surveyor* CMB imaging mission should detect many thousands of high redshift dusty galaxies, a significant fraction of which are expected to be gravitationally lensed. In order to make more detailed predictions it will be necessary to better quantify the abundance of sub-mm-selected galaxies with flux densities of order 100 mJy. By combining the *Planck* results with observations made using *FIRST* and ALMA a large catalogue of lenses should be identified, providing a unique sample of objects for further study. The properties of the individual galaxies in the catalogue will be useful for obtaining information about both the geometry of the Universe and the evolution of distant dusty galaxies.

Acknowledgements

The author, Raymond and Beverly Sackler Foundation Research Fellow, gratefully acknowledges generous support from the Foundation as part of their Deep Sky Initiative Programme at the IoA. Attendance at the meeting was made possible by the European Union TMR programme, which supports European research in gravitational lensing via contract number ERBFMRXCT98-0172 (Lensnet). This work was carried out within the Cambridge Planck Analysis Centre (CPAC), supported by PPARC. I thank Vicki Barnard, Dave Frayer, Ben Metcalf, Daniel Mortlock and members of the *FIRST-Planck* extragalactic science team for useful discussions and Kate Quirk for comments on the manuscript.

References

1. M. Bersanelli *et al*, SCI(96)3, (ESA, Paris, 1996).
2. A.W. Blain, MNRAS **283**, 1340 (1996).
3. A.W. Blain, MNRAS **297**, 511 (1998).
4. A.W. Blain, in *Photometric Redshifts*, ed. R. Weymann *et al*, (ASP, San Francisco, 2000).
5. A.W. Blain, in *Science with ALMA*, ed. A. Wootten, (ASP, San Francisco, 2000).
6. A.W. Blain, R.J. Ivison and I. Smail, MNRAS **296**, L29 (1998).
7. A.W. Blain, O. Möller and A.H. Maller, MNRAS **303**, 423 (1999).
8. A.W. Blain, I. Smail, R.J. Ivison and J.-P. Kneib, MNRAS **302**, 632 (1999).
9. A.W. Blain, A. Jameson, I. Smail, M.S. Longair *et al*, MNRAS **309**, 715 (1999).
10. C.L. Carilli *et al*, conference proceeding (astro-ph/9907436).
11. F.X. Désert, F. Boulanger and J.L. Puget, A&A **237**, 215 (1990).
12. L. Dunne *et al*, MNRAS **315**, 115 (2000).
13. D.T. Frayer, I. Smail, R.J. Ivison *et al*, ApJ **in press**, astro-ph/0005239 (2000).
14. M.P. Hobson *et al*, MNRAS **306**, 232 (1999).
15. R.J. Ivison, I. Smail, J.F. Le Borgne, A.W. Blain *et al*, MNRAS **298**, 583 (1998).
16. J.-P. Kneib, D. Alloin, Y. Mellier *et al*, A&A **329**, 827 (1998).
17. G.F. Lewis, S.C. Chapman, R.A. Ibata *et al*, ApJ **505**, L1 (1998).
18. D. Lutz *et al*, ApJ **505**, L103 (1998).
19. P.P Papadopoulos, H.J.A. Röttgering, P.P. van der Werf *et al*, ApJ **528**, 626 (2000).
20. M. Rowan-Robinson *et al*, Nature **351**, 719 (1991).
21. D.J. Schlegel, D.P. Finkbeiner and M. Davis, ApJ **500**, 525 (1998).
22. P.M. Solomon, D. Downes, S.J.E. Radford and J.W. Barrett, ApJ **478**, 144 (1997).
23. T.T. Takeuchi *et al*, PASP **111**, 288 (1999).

24. L. Toffolatti *et al*, MNRAS **297**, 117 (1998).
25. T. Wiklind and F. Combes, Nature **379**, 139 (1996).
26. A. Wootten ed. *Science with ALMA* (ASP, San Francisco, 2000).

GALAXY-GALAXY LENSING PREDICTIONS FROM THE SEMI-ANALYTIC GALAXY FORMATION MODELS

J.GUZIK[†], U.SELJAK[‡]
[†]*Astronomical Observatory, Jagiellonian University, Orla 171, 30-244 Kraków, Poland*
[‡]*Department of Physics, Jadwin Hall, Princeton University, Princeton, NJ 08544, USA*

We use semi-analytic galaxy formation models in combination with the high resolution N-body simulations to make predictions for galaxy-galaxy and magnification bias measurements. We show that the amplitude of the lensing signal depends strongly on the luminosity of the sample (luminosity bias) and on the color of the sample. Dark matter halo parameters cannot be directly inferred from the galaxy-galaxy lensing because halos of different mass dominate at different scales of the correlation. A more detailed modelling is needed to interpret the results of the Sloan Digital Sky Survey and other observations. We also compute the correlation coefficient between galaxies and dark matter and show it approaches unity on scales above 1 h^{-1} Mpc. This means that galaxy-galaxy lensing or magnification bias in combination with galaxy correlations can be used to extract bias and dark matter power spectrum on large scales.

1 Introduction

Understanding the dark matter distribution in the Universe over the whole range of spatial scale, from galactic (a few kpc) to large scale structure (hundreds of Mpc) is one of the fundamental goals of current cosmological investigations. One serious obstacle to this comes from the fact that one can directly observe only luminous content of the Universe. The dark matter distribution can only be studied indirectly, for example via its gravitational influence on nearby structures (dynamical effects) or propagation of light (gravitational lensing). The latter method, through the galaxy-galaxy lensing effect, seems to be a promising tool for measuring galaxy-dark matter correlations on scales from several kpc up to a Mpc. In our work we assume a cosmological model and galaxy formation model to make predictions for galaxy-galaxy lensing in the observationally interesting range. We restrict ourselves to the flat, cosmological constant dominated model with $\Omega_m = 0.3$, $\Omega_\Lambda = 0.7$ and $H_0 = 70$ km s^{-1}Mpc^{-1}.

2 Galaxy-galaxy lensing

We use N-body simulations performed by GIF collaboration in a 141 h^{-1}Mpc box to trace the dark matter distribution and the semi-analytic galaxy formation models to identify galaxies in the dark matter haloes [1]. Carrying out the spectral analysis of the dark matter and galaxy distributions allows us to obtain the power spectra and correlation functions for the dark matter, galaxies and their cross-correlation [2]. We are especially interested in the cross-correlation function which measures the average dark matter distribution around the galaxies.

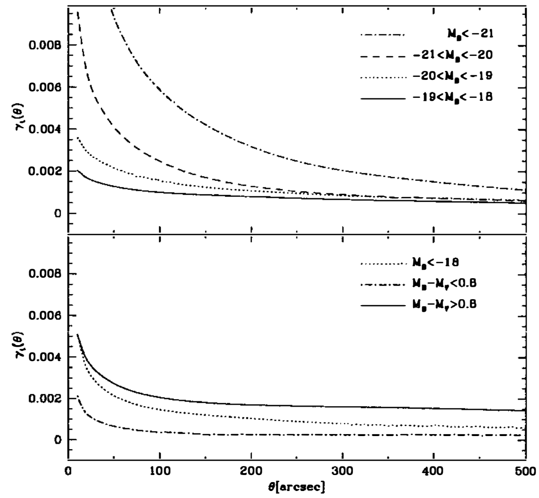

Figure 1: Mean tangential shear as a function of angular distance from the lens galaxy.

Applying the cross-correlation analysis to the galaxy-galaxy lensing studies allows us to perform a comparison with the present measurements of the effect[3] and make predictions for achievable galaxy-galaxy lensing signal from future observations. In galaxy-galaxy lensing one measures the tangential deformations of images of distant galaxies relative to the lens galaxy. The relation between the mean projected matter density expressed in terms of the mean convergence $\overline{\kappa}(\theta)$ inside a given circular aperture of radius θ and the mean tangential shear along the aperture boundary $\langle\gamma_t(\theta)\rangle$ is given by the expression[4]: $2\langle\gamma_t(\theta)\rangle = -d\,\overline{\kappa}(\theta)/d\ln\theta$. The mean convergence associated with a given galaxy type is expressed by the respective cross-correlation function. For simplicity we model lens and source galaxies as being at fixed redshifts $z_l = 0.16$ and $z_s = 0.32$, which corresponds to the mean values of galaxy redshift distributions measured by the SDSS team[3], but we also performed the analysis including galaxy redshift distribution[2]. In Fig.1 we show the mean tangential shear as a function of angular distance from the lens galaxy of a given type. For cosmological model considered here the angular separation of 100 arcsec corresponds to the physical distance about 0.22 h^{-1}Mpc in the lens plane.

As shown in the upper panel of the Fig.1 the shear depends strongly on the galaxy luminosity, reflecting the fact that more luminous galaxies reside in more massive haloes. These results are consistent with the predictions of the Tully-Fisher relation. The slope of the shear steepens with increasing luminosity and depends on the scale considered. The shear profile is not well fitted by power-law halo profiles $\rho \propto r^{-\alpha}$. Our results are in rough agreement with the SDSS measurements[3], as galaxies with luminosities $L > L_\star$ ($L_\star \approx -20.3$) which are brighter than $m_B \approx 19$ for assumed lens redshift corresponding to the SDSS sample of lens galaxies. We note however that the predictions are very sensitive to detailed galaxy formation modelling, so we expect galaxy-galaxy lensing to be one of the most powerful discriminators of such models.

In the lower panel of the Fig.1 we present the shear for red, blue and all galaxies with the luminosity cut $M_B < -18$ imposed. The red galaxies sample ("ellipticals") seems to be more promising in galaxy-galaxy lensing detection as they give a few times stronger signal than the blue sample ("spirals") for the whole range of angular scales. Large value of the shear in the case of red sample for scales of order several hundred kpc does not mean that haloes of particular

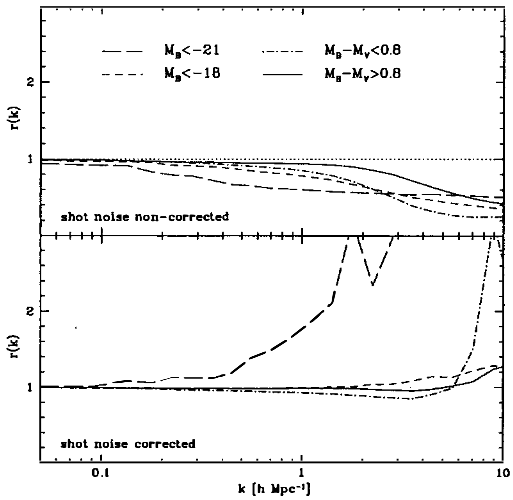

Figure 2: The correlation coefficient as a function of wavevector and galaxy sample.

galaxies extend to such large distances. Instead it argues that the red galaxies are more likely to be found in groups and clusters. The galaxy-galaxy lensing studies could be helpful in searches for galaxy groups and proving physical connections between the galaxies involved in apparent groups. On the other hand blue galaxies are more suitable for investigations of dark matter halo properties because they are mostly placed in the field and their shear profile reflects more the real profile of the dark matter haloes.

3 Cross-correlation coefficient

The cross-correlation analysis may be applied in studying the biasing between luminous and dark matter distributions. Not to confine to the simplest, linear bias relation we may account for the cross-correlation coefficient defined as $r^2(k) = P^2_{\rm g,dm}(k)/(P_{\rm g,g}(k)P_{\rm dm,dm}(k))$, where $P_{\rm dm,dm}(k)$, $P_{\rm g,g}(k)$ and $P_{\rm g,dm}(k)$ are power spectra for dark matter, galaxies and the cross-power spectrum respectively. The linear bias gives $r(k) = 1$. In Fig.2 we show the correlation coefficient as a function of scale for a few galaxy samples. In the upper panel we show $r(k)$ without shot noise correction in which case $r(k) < 1$ as expected. With the shot noise subtraction $r(k)$ is shown in the lower panel of Fig.2. This can be larger than unity on small scales because of shot noise subtraction. For large scales $r(k) \approx 1$ which allows one to extract the bias and the dark matter power spectrum from the galaxy and cross-power spectra. Thus galaxy-galaxy lensing which allows us to measure the galaxy-dark matter correlations should become a useful tool in determining the bias. The correlation coefficient is dependent on the abundance of galaxies in haloes, which is seen when one considers red and blue samples, especially on small scales of order hundreds of kpc. Blue galaxies, which are often the only galaxy in the halo, show stronger scale dependence of $r(k)$ than red ones, which are usually members of groups and clusters and roughly trace the dark matter distribution in the haloes. Large values of $r(k)$ for small scales occur because in the haloes with only one galaxy the cross-correlation is strongly enhanced with respect to the dark matter correlation. These results are supported by analytical treatment[5].

4 Summary

We have performed cross-correlation analysis of dark matter and galaxy distributions using N-body simulations coupled with the semi-analytic galaxy formation models. We have shown its importance in interpreting the observations of the galaxy-galaxy lensing effect. The cross-correlation function contains information not only on galaxy halo profiles but also on the halo mass function and galaxy abundance in haloes. Because of contributions from different mass haloes and clustering of galaxies the galaxy-galaxy lensing signal cannot be interpreted simply as a measure of the mean galaxy halo profile. The prospects can be improved if one selects galaxies by colour or clusters by richness. Moreover, cross-correlations together with the galaxy correlations can become a useful method to extract the bias parameter and the dark matter power spectrum on large scales, where the cross-correlation coefficient is approximately unity independently of the galaxy sample taken into considerations. The upcoming surveys such as SDSS or 2dF should be able to extract information on the dark matter-galaxy correlations via the galaxy-galaxy lensing with high precision, making them an important tool in galaxy haloes investigations.

Acknowledgments

We thank Guinevere Kauffmann and Antonaldo Diaferio for providing results of GIF N-body simulations and semi-analytic simulations and for help with H them. J.G. thanks Phil Fischer for encouraging discussions during the conference. J.G. was supported by KBN grants 2P03D00618 and 2P03D01417. U.S. acknowledges the support of NASA grant NAG5-8084.

References

1. G.Kauffmann, J.M.Colberg, A.Diaferio & S.D.M.White, *MNRAS* **303**, 188 (1999)
2. J.Guzik and U.Seljak, to be submitted (2000)
3. P.Fischer, et al., astro-ph/9912119 (2000)
4. G.Squires and N.Kaiser, *ApJ* **473**, 65 (1996)
5. U.Seljak, astro-ph/0001493 (2000)

A SPECTROSCOPIC SURVEY FOR STRONG GALAXY–GALAXY LENSES

J.P. WILLIS[1,2], P.C. HEWETT[1], S.J. WARREN[3], G.F. LEWIS[4]

1. Institute of Astronomy, Madingley Road, Cambridge CB3 0HA, UK.

2. Departamento de Astronomía y Astrofísica, P. Universidad Católica, Avenida Vicuña Mackenna 4860, Casilla 306, Santiago 22, Chile. (present address)

3. Blackett Laboratory, Imperial College of Science Technology and Medicine, Prince Consort Road, London SW7 2BZ, UK.

4. Anglo-Australian Observatory, P.O. Box 296, Epping, NSW 1710, Australia.

We present a spectroscopic survey for strong galaxy–galaxy lenses. Exploiting optimal sight-lines to massive, bulge-dominated galaxies at redshifts $z \sim 0.4$ with wide-field, multifibre spectroscopy, we anticipate the detection of 10–20 lensed Lyman-α emitting galaxies at redshifts $z \gtrsim 3$ from a sample of 2000 deflectors. Initial spectroscopic observations are described and the prospects for constraining the emission-line luminosity function of the Lyman-α emitting population are outlined.

1 Introduction

Despite considerable advances over the past two decades in the study of individual gravitational lens systems, the assembly of large, uniformly-selected samples of systems multiply imaged by individual galaxies has proved extremely hard. Searches for individual examples of strong lensing have relied on the examination of a sample of objects, such as quasars or flat-spectrum radio-sources, where a large fraction of the sample lie at high redshift. Thus, towards each object there is a significant path-length over which an intervening deflector may interpose itself close to the line-of-sight. The lens search proceeds through the identification of sources whose morphology, multiple images or extended arcs for example, is consistent with the effects of lensing. Further imaging, at different wavelengths, and spectroscopy is then necessary to establish the source as a bona-fide lens and to obtain redshifts for the source and the deflecting galaxy. In practice, obtaining the redshifts is very difficult, particularly for radio-selected objects, and in the compilation of Kochanek et al (1999: *http://cfa-www.harvard.edu/castles*) only 19 of the 45 lensed systems possess both deflector and source redshifts.

An alternative search strategy is to examine optimal lines-of-sight by identifying a population of very effective deflectors, where it is known that any source lying behind the deflector will be significantly lensed, and then to examine the spectra of the deflectors for evidence of lensed background sources. Miralda-Escudé and Lehár [1] pointed out that provided the surface density of faint, small, galaxies at high redshift is large, significant numbers of galaxy–galaxy lenses should exist. Subsequent observational developments have shown that the surface density of high-redshift, star-forming objects is indeed large[2,3]. Provided a suitable sample of deflectors can be identified the optimal line-of-sight search strategy offers significant advantages, including i) high efficiency, the probability a lens will be seen along a line-of-sight is significant, ii) the deflector and source redshifts may be readily acquired, allowing the full lensing geometry to be defined, iii) the small, but extended, star-forming objects lead to resolved gravitational lenses, not unlike the radio-rings arising from morphologically extended radio emission, which provide much greater constraints on the deflector masses than the more familiar two- or four-image lenses of unresolved quasars.

Using APM measures of United Kingdom Schmidt Telescope B_JRI plates it is possible to identify the ideal population of deflectors - massive, bulge-dominated, galaxies at redshift $z \sim 0.4$, essentially half-way between ourselves and any high redshift source. Specifically, locating the population of relatively bright, $m_R \leq 20$, red, $B_J - R \geq 2.2$, galaxies with redshifts $0.25 \leq z \leq 0.6$ is straightforward [4]. The galaxy population has a surface density of $\sim 50\,\mathrm{deg}^{-2}$ and associated with each galaxy there is an area of sky, $\sim 1\,\mathrm{arcsec}^2$, in which any distant source will be multiply imaged, with an associated increase in brightness of a factor $\gtrsim$10. These early-type galaxies represent essentially optimal lines-of-sight to search for examples of strong lensing.

The presence of a lens is revealed by the detection of an anomalous emission line in the spectrum of one of the target distant early-type galaxies, so obtaining spectra of a large sample of the deflector galaxies represents the first stage in the lens survey. Examination of intermediate-resolution optical spectra of an initial sample of 160 colour-selected early-type galaxies revealed the presence of an emission line at 5589Å in a galaxy with redshift $z = 0.485$. Follow-up spectroscopy [5] and imaging [6] have confirmed the B0047–2808 system as an optical Einstein ring with the source, a star-forming galaxy at $z = 3.595$, the first confirmed example of a normal galaxy lensing another normal galaxy and a demonstration of the viability of the optimal line-of-sight survey strategy.

2 Spectroscopic observations and candidate selection

With an efficient method for acquiring spectra along many optimal lines-of-sight there is the prospect of obtaining a large sample, $\sim$ 20 objects, of spatially resolved gravitationally lensed systems. The low-surface density of the galaxies on the sky means the Anglo-Australian Telescope's 2dF multifibre instrument, with a $3\,\mathrm{deg}^2$ field, is ideally suited to the initial spectroscopy. In September 1998 we obtained spectra of $\sim$ 500 early-type galaxies over two nights using the 2dF facility. Total exposure times of $\sim$ 8000 s produce galaxy spectra for which the completeness of redshift measurement is 95% and in which anomalous emission lines of fluxes $\sim 5 \times 10^{-17}$ erg $\mathrm{s}^{-1}\mathrm{cm}^{-2}$ may be reliably detected i.e. fluxes comparable to those seen in high-redshift galaxy samples [3] can be reached. The unlensed fluxes are a factor $\sim$ 10 fainter. Example spectra of galaxies from 2dF are shown in Figure 1.

Candidate gravitational lenses are identified by applying an automated emission-line detection algorithm to the early-type galaxy spectra. The identification software matches a template early-type galaxy SED (derived from the mean of the sample) to each early-type galaxy spectrum via a wavelength-dependent transformation. The transformation is derived from the median smoothed ratio of the two spectra. Subtraction of the transformed template from the individual galaxy spectra removes large scale ($\lambda \gtrsim 100$Å) continuum variations while retaining small-scale differences such as narrow ($\lambda < 50$Å) emission lines. Such emission features may then be identified using standard matched filter techniques [7]. The effectiveness of the emission-line detection routine is demonstrated by the identification of [OII]3727 emission in 20% of the early-type galaxy sample (104/485 galaxies). Four anomalous emission lines, consistent with gravitationally-lensed Lyman-α emission, have also been identified utilising this technique. Candidate lenses must be confirmed via a second observation of the emission-line prior to follow-up observations to obtain the source redshift, via observation of a second emission feature [5], and the morphology of the lensed emission [6].

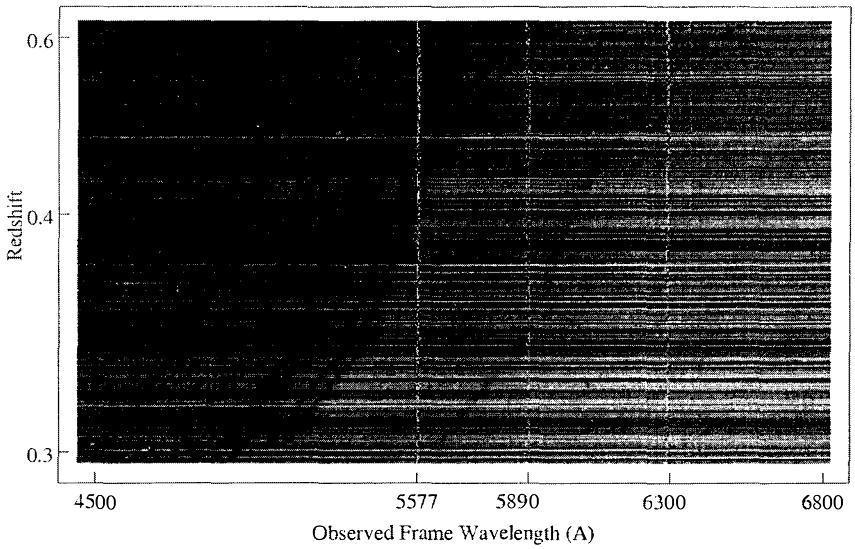

Figure 1: Observed-frame spectra of 485 distant early-type galaxies, redshifts $0.3 \leq z \leq 0.6$, arranged by increasing redshift. A number of prominent night-sky features are visible as vertical lines while features present in the galaxies, such as Calcium H+K and the G-band move to longer wavelength with increasing redshift.

3 Constraining the luminosity function of high-redshift Lyman-α emitting galaxies using gravitational lensing

A spectroscopic survey for gravitational lenses, employing a quantitative detection algorithm and a well-defined sample of deflectors, permits a unique experiment to probe the luminosity function of high-redshift Lyman-α emitting galaxies - to fainter flux limits than currently achievable.

The line-of-sight to each deflector may be considered as magnifying a region of the distant source plane. The total source plane magnification as a function of deflector-source impact parameter is calculated for the deflector sample using a ray-tracing algorithm, incorporating variations in deflector (e.g. central velocity dispersion and redshift) and source (e.g. surface brightness morphology and redshift) properties. To reproduce the effects of atmospheric seeing, lensed images are convolved with a Gaussian kernel of FWHM = $1''\!.5$, while to reproduce the 2dF observations, the lens model considers the total flux received from a $1''$ radius optical fibre centred on each deflector.

The sample of deflectors presents a magnified view of the distant source population, characterised by a Lyman-α emission-line luminosity function. The probability of detecting a lensed emission line of given observed frame properties (i.e. flux, wavelength and FWHM) drawn from this population is calculated via a 'monte-carlo' procedure whereby a grid of simulated emission lines of specified properties are superimposed onto observed early-type spectra, to be processed using the automated line detection algorithm.

Combining the magnification profiles generated by the deflector sample with an assumed Lyman-α emission-line luminosity function describing the source population, produces the number distribution of detected lenses as a function of Lyman-α luminosity (Figure 2). The number-luminosity diagram of identified lenses generated by a spectroscopic sample of 2000 early-type galaxies, considering two competing luminosity function models, clearly demonstrates the potential of the survey technique to probe the characteristics of the faint Lyman-α emitting galaxy population.

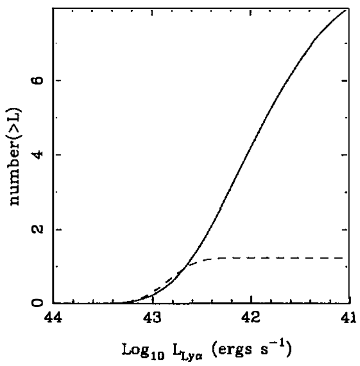

Figure 2: Cumulative number distribution of gravitational lenses versus intrinsic Lyman–α emission luminosity identified within a projected sample of 2000 early-type galaxy spectra. Two model luminosity functions are considered; a Schechter function described by the parameters $L^* = 1 \times 10^{43}$ h^2 ergs s^{-1}, $\alpha = -1.6$, $\phi^* = 1 \times 10^{-3}$ h^3 Mpc^{-3} $(\log L)^{-1}$ (solid line) and a Gaussian function of equal L^* and ϕ^* with a width parameter $\sigma = 0.25 \log L$ (dashed line). The model was realised using a cosmological model specified by the parameters $\Omega = 0.3$, $\Lambda = 0.7$.

4 Conclusions

We have presented the strategy and initial observations for a spectroscopic survey for strong galaxy–galaxy lenses. The optimal line–of–sight strategy offers a powerful probe of the faint, Lyman–α emitting, galaxy population and of the dark matter profiles of massive early–type galaxies at cosmological distances. Application of the deflector–based survey strategy to other galaxy samples is underway [8] and we hope to compile a much larger sample of systems using additional 2dF observations.

Acknowledgments

J. Willis acknowledges the support of a PPARC research studentship during the completion of this work and the generous financial support of the IoA, Cambridge and the European TMR network in order to attend the conference.

References

1. J. Miralda–Escudé and J. Lehár, MNRAS **259**, 31 (1992)
2. C.C. Steidel, M. Giavalisco, M. Pettini, M. Dickinson, K. Adelberger, ApJ **462**, L17 (1996)
3. E.M. Hu, L.L. Cowie and R.G. MacMahon, ApJ **502**, 99 (1998)
4. S.J. Warren, P.C. Hewett, G.F. Lewis, P. Møller, A. Iovino and P.A. Shaver in *ASP Conf. Series 51: Observational Cosmology*, eds. G. Chincarini, A. Iovino, T. Maccacaro and D. Maccagini (San Francisco 1993).
5. S.J. Warren, A. Iovino, P.C. Hewett and P.A. Shaver, MNRAS **299**, 1215 (1998).
6. S.J. Warren, G.F. Lewis, P.C. Hewett, P. Møller, P. Shaver and A. Iovino, A&A **343**, 35 (1999).
7. W.K. Pratt in *Digital Image Processing* (Wiley 1978).
8. P.B. Hall, H.K.C. Yee, H. Lin, S.L. Morris, M.D. Gladders, R.G. Carlberg, D.R. Patton, M. Sawicki, C.W. Shepherd, G.D. Wirth, 2000, *astro-ph/0006434*.

THE CURRENT STATUS OF CLASS

P. HELBIG (for the CLASS collaboration)
Rijksuniversiteit Groningen, Kapteyn Instituut, Postbus 800,
NL-9700 AV Groningen, The Netherlands

I give a brief overview of the current status of some aspects of the Cosmic Lens All-Sky Survey, CLASS.

1 Who and What?

CLASS, the Cosmic Lens All-Sky Survey, is a collaboration between groups at the Jodrell Bank Observatory (UK), ASTRON (NL), the Kapteyn Astronomical Institute at the University of Groningen (NL), Caltech (USA), the University of Pennsylvania (USA) and NRAO (USA). It is a survey for flat-spectrum radio sources ($\alpha \geq -0.5$ for $S_f \sim f^\alpha$ between L-band (Condon et al.[1] (NVSS)) and C-band (Gregory et al.[2] (GB6))) with the selection criteria $0 \leq \delta \leq 75°$ (due to the area covered by GB6), $|b| > 10°$ and $S_{\mathrm{C-band}} > 30\,\mathrm{mJy}$: 11685 objects. The objects thus selected were then observed with the VLA in A-configuration at X-band. CLASS has many goals, many of which are lens-related (measuring λ_0 and Ω_0 with lensing statistics and H_0 with time delays, studying the properties of lensing galaxies). (The definition of CLASS has evolved, mainly due to improvements in the input catalogues used. The above definition is the current, final one. However, objects were observed which are not part of the currently definied 'statistically complete CLASS' and, if they happened to be lens systems, were of course followed up.)

2 Why and How?

Radio surveys can be particularly good gravitational-lens surveys, for a number of reasons:

- Using interferometry, the beam size is much smaller than the image separation.
- Flat-spectrum objects are compact (i.e. (almost) point sources), allowing typical lensing morphologies to be recognised easily.

- Somewhat related to the previous point, the lensing probability depends on the cross section determined by the lens population; for extended sources, the source geometry partially determines what is recognised as a lens system.
- Most sources are quasars at high redshift, which leads to a high lensing rate.
- Since flat-spectrum objects are compact, they can be variable on relatively short timescales, which aids in determining time delays.
- There is no bias from lens galaxies due to extinction by the lens or comparable brightness of source and lens, as can be the case with optical surveys.
- High-resolution followup is possible with interferometers such as MERLIN, the VLBA, VLBI....

But there is one disadvantage:

- Additional work is required to get redshifts.

From our own CLASS VLA observations (i.e. A-configuration at X-band), objects with multiple compact (< 170 mas) are marked as lens candidates if the separation is between 300 mas and 6 arcsec, the flux ratio <10:1 and the total flux at X-band in the compact components is >20 mJy. These constraints are chosen so that sufficient followup is possible for all such candidates. Candidates are then observed at progressively higher resolution, first at C-band with MERLIN (50 mas resolution) and then, if necessary, the VLBA (3 mas resolution) and finally if needed with VLBI, at additional frequencies if needed. About 80% of the candidates are rejected after the MERLIN 'filter' due to different surface brightnesses in the components (gravitational lensing, of course, conserves surface brightness). Other reasons for rejection include obvious non-lens structure (such as a core-jet morphology) and different spectral indices or polarisation. It is interesting to note that, with one possible exception, every candidate which has passed these tests and thus been deemed to be a lens system on the basis of radio data alone has yielded a lens galaxy when observed optically (usually with HST). Since the source and lens redshifts are needed for various purposes, these are also checked to be consistent with lensing ($z_l < z_s$, the same z_s for all components of the source), though in practice no candidates which have passed the above-mentioned tests have been ruled out on this basis.

Table 1 shows the current CLASS and JVAS lens systems. It should be noted that missing redshifts are mostly from relatively new systems (though in the case of B1938+666, a redshift might could have been measured if UKIRT were able look this far north). It thus appears to be a realistic goal to have the survey complete with respect to both source and lens redshifts within the next several months. Note also the relatively narrow range of image separations, which is definitively *not* due to any sort of bias or incompleteness but reflects a real fact about the universe (more precisely, the mass spectrum of lens galaxies).

3 λ_0 and Ω_0 from Lensing Statistics

We have done an analysis of JVAS (essentially the brightest 2308 sources in CLASS). Lensing statistics, at least in the interesting part of parameter space, essentially measures $\lambda_0 - \Omega_0$. As discussed in Helbig[3], we obtain

$$-2.69 < \lambda_0 - \Omega_0 < +0.68 \tag{1}$$

at 95% confidence; for a flat universe, this corresponds to

$$-0.85 < \lambda_0 - \Omega_0 < +0.84 \tag{2}$$

Table 1: The JVAS and CLASS gravitational lenses

Survey	Name	# images	$\Delta\theta''$	z_l	z_s	lens galaxy
			confirmed lenses			
CLASS	B0128+437	4	0.542	?	?	?
JVAS	B0218+357	2 + ring	0.334	0.6847	0.96	spiral
JVAS	MG0414+054	4	2.09	0.9584	2.639	elliptical
CLASS	B0712+472	4	1.27	0.406	1.34	spiral
CLASS	B0739+366	2	0.540	?	?	?
JVAS	B1030+074	2	1.56	0.599	1.535	spiral
CLASS	B1127+385	2	0.701	?	?	?
CLASS	B1152+119	2	1.56	0.439	1.019	?
CLASS	B1359+154	4	1.65	?	3.212	?
JVAS	B1422+231	4	1.28	0.337	3.62	?
CLASS	B1555+375	4	0.43	?	?	?
CLASS	B1600+434	2	1.39	0.414	1.589	spiral
CLASS	B1608+656	4	2.08	0.63	1.39	spiral
CLASS	B1933+507	4 + 4 + 2	1.17	0.755	2.62	?
JVAS	B1938+666	4 + 2	0.93	0.878	?	?
CLASS	B2045+265	4	1.86	0.867	1.28	?
CLASS	B2319+051	2	1.365	0.624	?	?
			puzzling probable lenses			
JVAS	B2114+022	2 or 4	2.57	0.32 & 0.59	?	?

It should be noted that the probability distribution in the λ_0-Ω_0 plane is not Gaussian; in particular, the above numbers were obtained from 'real contours' (cf. Helbig[4] and references therein) and not by plotting contours at some fraction of the peak likelihood, and of course they depend on the region of parameter space examined as long as there is a non-negligible likelihood outside of it. These caveats should be kept in mind when comparing these constraints to others in the literature.

Of course, not only an analysis of CLASS but a better analysis of CLASS is in the works. However, first the survey and lens followup have to be finished and the S-z plane of the parent population (i.e. non-lenses in the survey and objects 'amplified in' to the survey by lensing) must be determined. This information is needed in two quite distinct contexts, even though they are really two sides of the same coin:

- The number–flux-density relation at the redshifts of the sources in the lens systems is needed for the calculation of the amplification bias.
- The flux-density–dependent redshift distribution is needed as a proxy for the redshifts of the non-lenses in the survey.

Even without this information, however, there is the interesting possibility of using CLASS for the lens-redshift test; see Helbig[5] for discussion.

4 H_0 from Time Delays

Since all observables in a gravitational lens system are dimensionless except for the time delay between the images, this can be used to scale the model of the system and thus, if the redshifts are known, measure H_0 (with a higher-order dependency on λ_0 and Ω_0). A radio survey offers the advantages that microlensing is less of a worry and that the sources are 'pre-selected' to be variable (due to their flat-spectrum nature, as mentioned above). The angular separation probed by CLASS corresponds to galaxy-mass lenses and thus time delays of weeks, which is convenient. To date, there are 6 measured gravitational-lens time delays, 3 from CLASS, of which 5 agree quite well (see, e.g., Koopmans & Fassnacht[6] for discussion). In principle, as first pointed out by Refsdal[7], one can use time delays from several systems to measure λ_0 and Ω_0. Although it is too early to make a definitive statement, it is interesting to note that the derived values for H_0 agree better if currently favoured values for λ_0 and Ω_0 are assumed. To quote a number for posterity, $H_0 = 68$. More CLASS systems are being monitored, so statistics should improve in the future.

5 Dark Lenses?

As mentioned above, there is only one possible lens system which has passed all the radio tests but in which no lens galaxy has been detected, and could thus be a 'dark lens' (cf. Jackson et al.[8] and references therein). However, statistical arguments favour the alternative explanation of this system, B0827+525, being the first binary radio-loud QSO. On the other hand, the case is not clear-cut. If the latter explanation is true, it will have the smallest separation of all known QSO pairs. On the other hand, if it is a lens system, it will have the largest separation of all CLASS lenses. See Koopmans et al.[9] for further discussion.

6 Wide-Separation Lenses

Although CLASS originally examined the range between 300 mas and 6 arcsec, this has been extended up to an arc-minute in two new surveys. First, CLASS has been extended to search up to 15arcsec in a manner identical to the original survey, made possible by the increase in computing power since CLASS began. Second, a new survey, the Arc-Minute Radio Cluster-Lens Search (ARCS), has looked for lensing of extended sources on the 15 to 60 arcsec scale (due to the longer time delays, many of the arguments used to rule out candidates at smaller separation will not work at larger separation and the number of chance coincidences on the sky of course increases with the separation, so a different strategy is called for). To date, *no* lens systems have been found in this range of angular separation, though one candidate remains. More details can be found in Phillips et al.[10].

Acknowledgments

It is a pleasure to thank the rest of the CLASS collaboration for input.

References

1. J.J. Condon et al., AJ **115**, 1693 (1998)
2. P.C. Gregory et al.,ApJS **103**, 427 (1996)
3. P. Helbig et al., A&A **136**, 297 (1999)
4. P. Helbig A&A **350**, 1 (1999)
5. P. Helbig, these proceedings
6. L.V.E. Koopmans & C.D. Fassnacht, ApJ **527**, 513 (1999)
7. S. Refsdal, MNRAS **132**, 101 (1966)
8. N. Jackson et al., A&A **334**, L33 (1998)
9. L. Koopmans et al., A&A, in press
10. P. Phillips et al., MNRAS, submitted

TIME DELAYS

T. WIKLIND
Onsala Space Observatory, SE-43992 Onsala, Sweden

The present status of measured time delays in gravitational lens systems and the analysis methods are presented. The use of molecular absorption lines to derive the time delay in PKS1830-211 is discussed. Finally, an assesment is made of how accurate the Hubble parameter H_0 can derived and where the major uncertainties remains.

1 Background

Until just a few years ago, there was only one gravitational lens where observers had attempted to derive the differential time delay. Today this situation is rapidly changing, with time delays for 7 lenses published and with several in the process of being observed.

The idea of using the differential time delay between two or more images of a lensed background source to determine the value of the Hubble parameter, $H_\bullet$, was around for more than 15 years before the first gravitational lens, Q0957+561, was discovered (Refsdal 1964; Walsh et al. 1979). Q0957+561 turned out to be variable and the first attempts to measure the time delay started almost immediately. Several different methods were used, from radio interferometry (including VLBI) to optical photometry (for list of early attempts, see Haarsma et al. 1997). The results quickly divided themselves into a 'high-value' and a 'low-value' group, where the high value corresponded to $\Delta t \approx 540 \pm 10$ days and the low value to $\Delta t \approx 410 \pm 20$ days. These discrepant results emerged because the two lens components do not vary in the same way. This is most likely due to microlensing in the intervening galaxy, but also because derivation of the time delay is intrinsically difficult. In principle, it is a classical problem, the correlation of two unevenly sampled time series, but with the added complexity that the two time series are not sampled simultaneously.

In order to use the differential time delay for cosmography, it is necessary to have a well determined gravitational potential of the lensing galaxy, as well as the redshifts of both the lens and the background source. With these ingredients, the time delay effectively measures the distance between the two points for which the arrival time difference has been determined. With the known angular separation on the sky, one obtains the angular size distance, independent on any other cosmological distance measurement. This is of course a function of the Hubble parameter H_0, but also Ω_0 and Ω_Λ, the density parameters for matter and a cosmological constant. Hence, a time delay measurement, with a well constrained potential, defines a surface in a multiparameter space (H_0, Ω_0, Ω_Λ). Measurement of differential time delays from several gravitational lenses, at different redshift combinations of the lens and the source, can in principle be used to solve simultaneously for all the parameters. This is presently not feasible due to uncertainties in the lens potentials.

Table 1: Time delay measurements as of March 2000

Name	z_d	z_s		Δt days	$\sigma_{\Delta t}/\Delta t$	Method	Ref.
B0218+357	0.68	0.96		$10.5^{+0.4}_{-0.4}$	4%	Radio (polarimetry)	Biggs et al. 1999
Q0957+561	0.36	1.41		409^{+23}_{-23}	6%	Radio	Pelt et. al. 1994
				423^{+6}_{-6}	1%	Optical	Pelt et. al. 1996
				417^{+3}_{-3}	1%	Optical	Kundic et al. 1997
				425^{+17}_{-17}	4%	Optical	Pijpers 1997
				397^{+20}_{-20}	5%	Radio	Haarsma et. al. 1997
				409^{+30}_{-30}	7%	Radio	Haarsma et. al. 1999
HE1104-1805	0.7?	2.32		$267^{?}_{?}$	—	Spectrophotometry	Wisotzki et al. 1998
PG1115+080	0.31	1.72	CB	$23.7^{+3.4}_{-3.4}$	14%	Optical	Schechter et al. 1997
			A1A2	$9.4^{?}_{?}$	—		
			CB	$25.0^{+3.3}_{-3.8}$	14%	Optical	Barkana 1997
B1600+434	0.42	1.59		47^{+12}_{-9}	23%	Radio	Koopmans et al. 2000
B1608+656	0.63	1.39	BA	26^{+5}_{-5}	19%	Radio	Fassnacht et al. 1999
			BC	34^{+5}_{-5}	15%		
			BD	73^{+5}_{-5}	7%		
PKS1830-211	0.89	2.51		44^{+9}_{-9}	20%	Radio	van Ommen et al. 1995
				26^{+4}_{-5}	17%	Radio	Lovell et. al. 1998
				28^{+4}_{-4}	14%	Millimetric	Wiklind et al. 2000

2 Present status

At the time of writing, time delays have been derived for 7 gravitational lenses, summarized in Table 1. Data for one additional lens (B1422+231) is discussed in these proceedings (Narashima). Some of the values are still rather uncertain, as can be seen from the $\sigma_{\Delta t}/\Delta t$ values in Table 1. The best ones correspond to fractional errors of only a few percent, while some values do not even have estimates of the uncertainties. Typical uncertainties, at the ~90% confidence limit, is 10-20%. The lens with the best estimated time delay is Q0957+561, where time series extending over more than 20 years exist.

Of the seven lenses listed in Table 1, four have been observed at radio wavelengths (including the millimeter band), two in optical bands and one (Q0957+561) at both radio and optical wavelengths. This dominance of radio observations is due to large gravitational lens surveys like CLASS, which have been more successful than optical surveys in finding new lenses. Moreover, the CLASS survey is biased towards flat spectrum radio sources, likely to be beamed towards us and therefore more variable than less beamed sources.

The redshift for the lens in HE1104-1805 remains undetermined and this source can not be used for cosmographic purposes - yet. It also has one of the most uncertain time delays. The remaining six sources have all been used to get estimates of H_0 (see below).

Interestingly, three of the six sources were reasonably good time delay measurements exists, are late type galaxies. This is seen either through morphology (B1600+434) or through detection of molecular gas (B0218+357 and PKS1830-211). It remains to be seen whether this implies that the potentials used for the lens modelling should be modified.

There are still a number of gravitational lens systems detected in the CLASS survey which can be used to derive differential time delays, but for which data do not exist at the moment: B1933+503, where Biggs et al. (2000) found little variability during a monitoring campaign in 1998, and B1030+074, which is presently being monitored (Xanthopoulos et al. 2000).

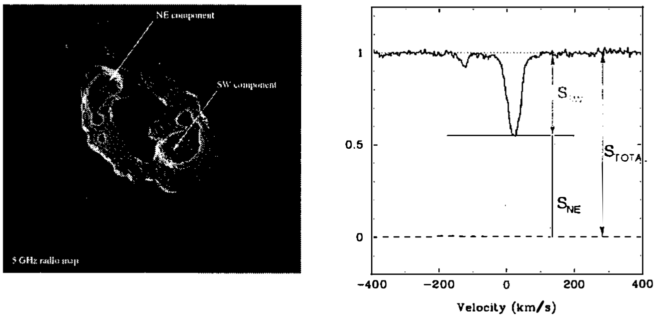

Figure 1: *Left:* A 5 GHz image of PKS1830-211 (courtesy A. Patnaik). The cores, which are the only parts contributing to the continuum at millimeter wavelengths are marked. *Right:* The HCO^+(2-1) spectra at $z = 0.89$ observed with the SEST. The line is saturated and only covers the SW component.

3 Methods

The controversy regarding the time delay for Q0957+561 underlined the difficulties associated with deriving a Δt value from an unevenly sampled time series. It also motivated several groups to design analysis methods appropriate for this type of data.

Apart from correlating unevenly sampled time series, gravitational lenses provide the extra complication that the series are effectively sampled at different times. There are three ways to attack this type of problem: (1) interpolate unobserved data points and use conventional correlation techniques, (2) bin observations to get uniformely spaced data (using uneven window funtions) and use conventional correlation techniques, or (3) use what you have and try to correlate as best as possible. The last method has been developed by Pelt et al. (1994; 1996) with the special goal of analysing the time delay for Q0957+561. It is a nonparametric method which is essentially a cross-correlation, but where the correlation is done with the nearest neighbouring data point (in time). This method has become known as the 'Pelt Dispersion Method'. An elaborate method for optimizing the interpolation between data points has been developed by Press et a.l. (1992a,b), again with the goal of deriving the time delay of Q0957+561. Edelson & Krolik (1988) developed a discret cross-correlation method, aimed for analysis of reverberation mapping of AGNs, which can be used for gravitational lens time delays. The method optimizes the binning (rather than the interpolation) and requires a fairly well sampled data set to retain sufficiently good temporal resolution. In the literature one can find several other techniques that has been developed for gravitational lenses (cf. Pijpers 1998; Barkana 1997, 1999).

Since almost all of these methods have been developed with analysis of the time delay of Q0957+561 in mind, it is fortunate that the controversy arised for this particular source.

4 Using molecular absorption lines: PKS1830-211

A new method for monitoring the fluxes from gravitational lens systems has originated with the detection of molecular line absorption in intervening galaxies (cf. Wiklind & Combes 1995, 1996). The centralized distribution of molecular gas implies that whenever absorption is detected, the background continuum source has an impact parameter of a few kpc or less. This is an ideal situation for strong lensing.

A total of four molecular absorption line systems has been detected, with redshifts in the range z =0.25-0.89. Two of these occur in lensing galaxies: B0218+357 (z_d = 0.68) and

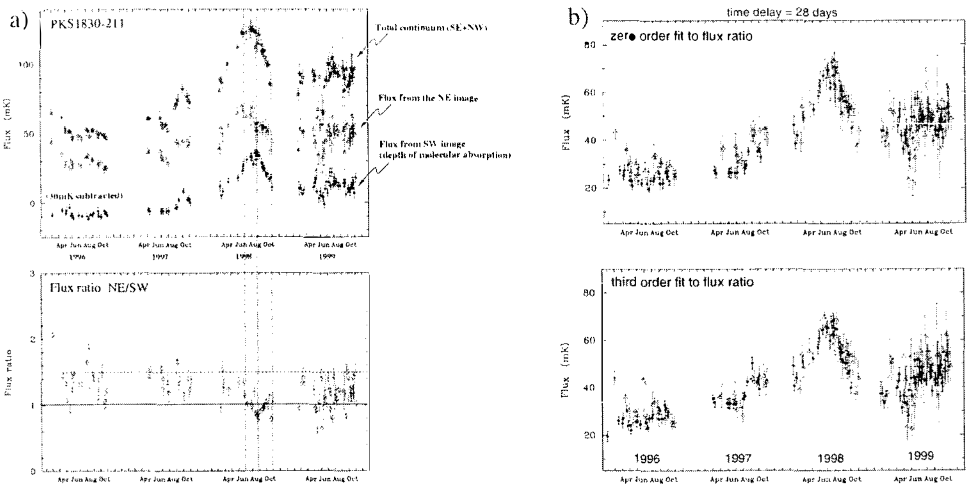

Figure 2: Monitoring of PKS1830-211. **a)** The top panel shows the data obtained over 4 years. The bottom panel shows the flux ratio of the NE and SW components. A clear signature of the time delay between the NE and SW images can be seen during the peak of the outburst in 1998. **b)** The fluxes from the NE (gray) and SW (blue/black) components. The SW component has been shifted by $\Delta t = -28$ days. In the upper panel the components are shown for a constant magnification ratio ($\mu = 1.3$), while the lower panel shows the result when a third order polynomial has been fitted to the magnification ratio when solving for Δt. The latter case represents a much better solution.

PKS1830-211 ($z_d = 0.89$). In both cases, the absorbing molecular gas obscures one of two images. Several different molecular transitions have been observed and some of them are strongly saturated. This is seen through the detection of isotopic species, for instance HCO^+ and the isotopic variants $H^{13}CO^+$ and $HC^{18}O^+$. While the continuum flux at frequencies off an absorption line gives the sum of the fluxes from the images, the depth of a saturated absorption line gives the flux from the obscured image. This can be used to monitor the individual fluxes without actually resolving them. For instance, in PKS1830-211 the separation between the images (see Fig. 1) is $\sim 1''$, but the fluxes of the individual images can be obtained with a telescope with an angular resolution of $\sim 50''$.

Fig. 1 shows PKS1830-211 at radio wavelengths (courtesy A. Patnaik), showing two images with a core+jet morphology. The jet has a steep spectral index and at millimeter wavelengths only the inner cores contribute to the observed continuum. The strong absorption occurs towards the SW component (Wiklind & Combes 1998). Due to heavy Galactic extinction the system can only be detected at wavelengths longer than a few microns. The saturated HCO^+(2-1) transition occuring at $z = 0.89$ towards PKS1830-211, also shown in Fig. 1, has been monitored with the SEST 15m telescope at La Silla since April 1996 (Wiklind & Combes 2000). During this time the total flux has varied by a factor $\sim$2.5 (Fig. 2a). During an outburst in 1998, we detected a clear signal of time delay, which can be seen in the flux ratio of the NE and SW components in Fig. 2a. Analysis of the complete dataset using several different methods, gives a time delay $\Delta t = 28^{+4}_{-4}$ days, with the NE component leading. The results of Lovell et al. (1998), based on low frequency interferometric techniques and model subtraction of the jet components, gives a time delay of $\Delta t = 24^{+5}_{-4}$ days. These two measurements have completely different sets of possible systematic errors and the good agreement gives additional confidence to the results. Using the lens model of Nair et al. (1993), our time delay corresponds to $H_0 = 59^{+9}_{-11}$ km s^{-1} Mpc^{-1}.

The best fit for the molecular data is given by $\Delta t = 28$ days. However, solving for a constant magnification ratio, gives a time dependent offset between the rectified fluxes from the NE and

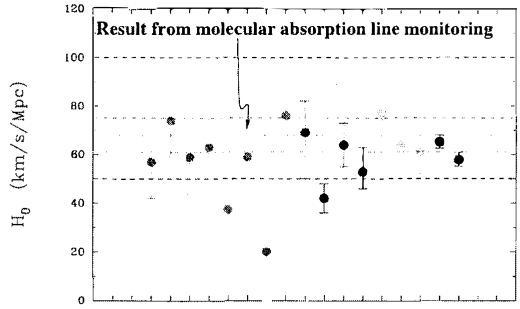

Figure 3: Derived values of H_0 using time delays. The values are taken from the literature and various types of lens potentials have been used in the modelling, from parametrized models to nonparametric ones. Green/gray points represent results based on radio data, blue/black point optical data and light blue/grey Q0957+561 (combined radio and optical). Although the dispersion is large, ~80% of the values are within the uncertainty quoted in the HST Key Project on the Extragalactic Distance Scale, as marked by dot-dashed lines. The two black points to the right represent H_0 values derived from NGC4258; one using water masers and the other using cepheids.

SW components (Fig. 2b). This suggests that a long term variation of the magnification ratio is taking place. A better fit can be achieved by letting the flux ratio vary as a third order polynomia (Fig. 2b). The time scale for this variation is 1-2 years. The size of the background source at millimeter wavelengths is unknown, but likely to be of the order 10^{17}-10^{18} cm. Although this is large for microlensing events, this remains a possible explanation for the long term variation. A further complication here is that the background source could exhibit superluminal motion and it is not only the foreground screen that has a transverse velocity. We hope to follow this source in order to follow up on the behaviour of the magnification ratio.

5 Prospects for deriving H_0

Various estimates of the Hubble parameter using time delays, taken from the literature, are shown in Fig. 3. The dispersion of values is quite large. Differential time delay measures the angular size distance, with H_0, Ω_0 and Ω_Λ as parameters. The strongest dependence, however, is on the Hubble parameter and it is common to set $\Omega_0 = 1$ and $\Omega_\Lambda = 0$ and quote a value for H_0. This has been done for the values shown in Fig. 3 and some of the dispersion could be caused by parameter having intrinsic values different from the assumed ones. However, the strongest cause for the dispersion comes from the different types of lens models used. The number of H_0 values presented in Fig. 3 is almost three times the number of lenses with known time delay. Some values of H_0, derived for the same lens system with the same Δt, gives results which are inconsistent with each other. This shows that the main uncertainty remains in the lens modelling. Nevertheless, in this 'pessimistic' view, 80% of the H_0 values are consistent within the uncertainty quoted in The HST Key Project on the Extragalactic Distance Scale (Mould et al. 2000). A much smaller dispersion of H_0 values, based on time delay measurements, can be achieved by using the same type of lens models for all sources (cf. Koopmans & Fassnacht 1999). However, possible systematic errors could be introduced in this manner.

Acknowledgments

We (Françoise Combes and I) thank the SEST Team for expert help in doing the monitoring of PKS1830-211 during a long time period.

References

1. Barkana R., et al., ApJ **520**, 479 (1999)
2. Barkana R., ApJ **489**, 21 (1997)
3. Biggs A.D., Xanthopoulos E., Browne I.W.A., Koopmans L.V.E., Fassnacht C.D., MNRAS , in press (2000) astro-ph/0004290
4. Biggs A.D., et al., MNRAS **304**, 349 (1999)
5. Edelson R. A., Krolik, J. H., ApJ **333**, 646 (1988)
6. Fassnacht C.D., et al., ApJ **527**, 498 (1999)
7. Haarsma D.B., Hewitt J.N., Lehar J., Burke B.F., ApJ **510**, 64 (1999)
8. Haarsma D.B., Hewitt J.N., Lehar J., Burke B.F., ApJ **479**, 102 (1997)
9. Koopmans L.V.E. & de Bruyn A.G., A&A **358**, 793 (2000)
10. Koopmans L.V.E., de Bruyn A.G., Xanthopoulos E., Fassnacht C.D., A&A **356**, 391 (2000)
11. Koopmans L.V.E. & Fassnacht C.D., ApJ **527**, 513 (1999)
12. Kundic T., et al., ApJ **482**, 631 (1997)
13. Lovell J.E.J., et al., ApJ **508**, L51 (1998)
14. Mould J.R., et al., ApJ **529**, 786 (2000)
15. Nair S., Narasimha D., Rao A.P., ApJ **407**, 46 (1993)
16. Pelt J., Kayser R., Refsdal S., Schramm T., A&A **305**, 97 (1996)
17. Pelt J., Hoff W., Kayser R., Refsdal S., Schramm T., A&A **286**, 775 (1994)
18. Pijpers F.P., Ap&SS **261**, 337 (1998)
19. Press W.H., Rybicki G.B., Hewitt J.N., ApJ **385**, 404 (1992a)
20. Press W.H., Rybicki G.B., Hewitt J.N., ApJ **385**, 416 (1992b)
21. Refsdal S., MNRAS **128**, 370 (1964)
22. Schechter P., et al., ApJ **475**, L85 (1997)
23. van Ommen T.D., Jones D.L., Preston R.A., Jauncey D.L., ApJ **444**, 561 (1995)
24. Walsh D., Carswell R.F., Weymann R.J., Nature **279**, 381 (1979)
25. Wiklind T., Combes F., 2000, in *Gravitational Lensing: Recent Progress and Future Goals*, Boston University July 1999, eds. T.G. Brainerd, C.S. Kochanek, astro-ph/9909314
26. Wiklind T., Combes F., ApJ **500**, 129 (1998)
27. Wiklind T., Combes F., Nature **379**, 139 (1996)
28. Wiklind T., Combes F., A&A **299**, 382 (1995)
29. Wisotzki L., Wucknitz O., Lopez S., Sorensen A.N., A&A **339**, L73 (1998)
30. Xanthopoulos E., et al., 2000, in *Gravitational Lensing: Recent Progress and Future Goals*, Boston University July 1999, eds. T.G. Brainerd, C.S. Kochanek, astro-ph/9909460

TIME DELAY IN GRAVITATIONAL LENS SYSTEMS AND HUBBLE CONSTANT

D. NARASIMHA
Tata Institute of Fundamental Research,
Homi Bhabha Road, Mumbai 400 005, India

The time delay between the multiple images in gravitational lens systems is affected by large scale mass distribution in the lens, even though it might not have observable effects on the macro images. Inhomogeneity at very small scale will not directly affect the time delay but will influence the models of mass distribution in the lens galaxy. How this degeneracy can be eliminated is described. A method to determine time delay based on smoothed cubic splines is explained. The value of the Hubble Constant, inferred from the time delay in 5 well-constrained lens systems is 58 ± 8 km s^{-1} Mpc^{-1} for a Friedmann Universe at closure density and 67 ± 9 km s^{-1} Mpc^{-1} for a Flat Universe with cosmological constant contributing 0.7 of the closure density.

1 Introduction

Gravitational lensing is caused when the beam of photons from a background source is bent and distorted due to the gravitational pull of an intervenous massive object like a galaxy or galaxy-cluster. In the strong lens systems, multiple images of the background source can appear, the maximum separation between them being an indication of the mass of the lens and the effective distance to the system,

$$D_{eff} = \frac{D_{lens} D_{source}}{D_{LS}} \tag{1}$$

where the distances in the right side are respectively angular diameter distances from the lens and source to the observer and from the source to the lens. Intrinsic variability in the source will appear in the images at different times. This time interval is called the *time delay.* It is caused by the different path length of photons forming the multiple images as well as the difference in the gravitational potential along the path. The time delay is proportional to the Effective Distance to the lens system as well as the image configuration. Hence, if the geometry of the lens configuration is determined from the observed image features or the Lens characteristics, D_{eff} can be determined from the time delay.

1.1 Problems in getting the Distance Estimate from Time-delay:

Time delay depends on the gravitational potential integrated along the photon path, while separation between the images on its gradient and magnification, on the second derivatives of the potential. Our failure to determine the gradients of the potential everywhere results in degeneracies in the estimation of the potential. Specifically, multiple components of the lens affect the image separation and time delay differently. A small scale inhomogeneity like a microlens does not change the time delay directly, but the magnification of the images is modified, affecting the lens models. Also, the microlens light curve acts as a noise to the intrinsic variability of the source, leading to faulty values of the time delay.

A large scale mass distribution in the lens increases the image separation though the relative magnifications are not noticeably altered. Consequently, a nearly constant mass sheet having surface mass density $\kappa\times$ the *critical density for strong lens* reduces time delay to a fraction $1-\kappa$.

The effects of the multiple lens components can, in principle, be modeled with extra observations. For instance,
Asymmetry of microlens light curve is directly dependent on the *shear of the macrolens*[3,13] $\frac{\gamma}{1-\kappa}$.
Accurate monitor of the images can be used to have an independent estimate of the shear.
The rotation curve of a spiral lens galaxy like PKS1830-211 or B0218+357 was used to directly estimate the mass distribution in the inner parts of the lens[2,6]. To some extent, this could eliminate the mass degeneracy caused by observations restricted to a single plane.

Equally important is accurate measurement of the time delay. Experience has shown that the time delay estimated from the observations is invariably susceptible to noises. Here we outline a method to alleviate the problem to a good extent, if the intrinsic variability of the source is restricted to a narrow band.

2 Estimation of Time delay using Smoothed Cubic Splines

Conventional methods to cross correlate the fluxes from the images to determine the time delay has not been very successful when the noise at the time period of expected time delay is non-negligible, even though the overall signal to noise ratio of the data could be very good. This was apparent in the case of $0957+561$ where time delay was around 417 days while some of the microlens events had similar duration. This problem is severe for $1422+231$ due to the low amplitude of variability in radio.

Our method is based on identifying single component of the intrinsic variability and using this component to cross correlate between the images. The smoothed cubic spline is used for the identification of the feature. We do not use any specific form for the variability, but in view of its application for many similar systems we shall illustrate and explain the general method through an ideal example where the term phase difference is easily understood.

Let the smooth component of flux obtained from the observed sample is represented by a function of the form,

$$f_\nu(t) = f_o + A sin\left[\omega\left(t-t'\right)+\phi\right] \tag{2}$$

Here f_o is the steady flux, ω is the frequency of intrinsic variability of the signal of interest and the crucial term required for computation of the time delay is the observed phase factor ϕ for the different images.

If the external noises were absent and the sampling were sufficiently good, let the flux be

$$F_\nu(t) = F_o + \Lambda sin\left[\omega_o\left(t-t'\right)+\phi_o\right] \tag{3}$$

We assume that Λ, ω_o and ϕ_o are close to the observed sample values A, ω and ϕ respectively. Then, a Taylor expnasion for the sample values about the population mean is valid. carrying a χ_{square} minimisation we can obtain four linear relations for the four unknowns. If the observations span one cycle of variability or duration much larger than the time scale of variability, the mean values for terms like $\sin(\omega t+\phi)$, $\cos(\omega t+\phi)$ summed over the observed epochs will tend to zero. Consequently, we can select a value of t' close to the mean epoch of the observation such that the computed sample values of A, ω, f_ν and ϕ will be stochastically independent. The variance of ϕ can, then, be approximated by

$$V(\phi) = 2/\sum \frac{\left(f_{\nu,i} - f_\nu^b ar\right)^2}{\sigma_i^2} \tag{4}$$

The time delay between the images can be estimated from the cross-correlation between the variable part of the flux obtained from the smoothed cubic spline. The cross correlation will have the form

$$\Re = cos\left(\omega\tau + \phi_1 - \phi_2\right), \tag{5}$$

where τ is the assumed time delay between the images. The phase factors ϕ_1 and ϕ_2 refer to the variable component of the smoothed cubic spline fit to the observed flux in the images 1 and 2. If the smoothed flux has exactly same form in the images, the correlation will have a peak value of unity, but in practice it will be less when the smoothing is done independently. In view of the form of the expression for $\Re$, the error in the computed time delay is the time interval over which the correlation, R, drops by half the estimated variance of the phase ϕ of the smoothed fit to the flux.

When is this method superior to direct estimation of the time delay? If the smoothed cubic spline can isolate a single component of the intrinsic flux variability apart from the constant flux from the images, and any contribution due to microlens is filtered from the smooth function, then the signal in the correlation will improve compared to the noise by a factor of (n-4), where n is the number of epochs of observation and the number 4 is based on the minimum number of data points required for the computations of the smoothed spline.

This method was applied to the lens B1422+231, using the data kindly given by A.R. Patnaik, taken at 15 GHz using VLA in 1994. The intrinsic variability of the source at 5% at a time scale of 216 days could be extracted from the data and the time delay was estimated to be 7.6 ± 2.5 days between A and C, 8.2 ± 2 days between B and C and 1.5 ± 1.4 days between A and B. The high error is because the interval between observations varied between 2 and 11 days.

3 Estimation of Hubble Constant

We have constructed models of mass distribution in the lens for five well–constrained systems having time delay meausrements as well as considerable amount of multiwavelength data. The estimation of the effective distance for these systems based on time–delay[5] is given in Table 1. Unfortunately each system has one or other problem and hence the values cannot be taken as robust. Hopefully, better monitoring for more accurate time delay and observations like the one carried by Chengalur *et al.*[2] would constrain the value of Hubble constant.

For Q0957+561, VLA and VLBI observations are available for the two images only and hence the partition of mass distribution between the lens galaxy and the cluster remains uncertain. However, we used the position and magnitude of 40 galaxies in the lens cluster around the images[10]. For PG1115+080, the magnification ratio between the images, determined from the available HST archival data indicate that the source is very close to a cusp caustic. This, along with the separation between the merging–like images and their Ly_α flux ratios provide some constraints on the lens mass distribution. However, if the cluster associated with the lens were stronger, our estimation of the effective distance could be a lower bound. But the major problem with the system is the observed ratio between the time delays: The reported value for τ_{C-A}/τ_{A-C} of 0.8[11] rules out any conventional models. For the system PKS1830-211, the multiband VLA and VLBI structures associated with the ring–like feature was used to determine the mass distribution[4]. The core radius as well as orientation of its minor axis estimated from

Table 1: Estimates of Hubble constant (H_o) from time delay in some of the well-constrained gravitational lenses for two combinations of the parameters Ω and Λ (given in brackets).

System	Redshift (z_S,z_L)	Time delay (days)	D_{eff} (Mpc)	H_o for two (0.2, 0)	Cosmologies (0.3, 0.7)	Reference Model
0957+561	(1.4, 0.36)	423±3 [12]	1870	57±10	66±11	10
1115+080	(1.72, 0.31)	$25^{+3.3}_{-3.8}$ [11]	1550	56±?	64±?	7
1830-211	(0.89, 2.5)	28 [14]	3550	62±9	74±11	4
0218+357	(0.68, 0.95)	11.7±0.9 [1]	9900	45±9	53±10	9
1422+231	(0.33, 3.62)	7.6±2.4	860	70±30	77±33	8

the models match very well with the rotation curve derived from the radio spectroscopy[2]. But the value of the time delay between the images continues to be uncertain. For B0218+357, extraction of the multiple images of blobs from the observed ring continues to be uncertain due to the smallness of the scale of the ring and the faintness of the ring. There is no good test to determine the relative importance of the bulge to disk of the lens galaxy. Since the lens is nearly face on[6], the rotation curve is of not much help either. For B1422+231, the time delay between the weak image D and the other images is still not available and hence the effective distance cannot be reliably estimated.

4 Summary

Time delay in gravitational lens systems has still not provided firm results on the cosmological parameters, because of error in the observed time delay as well as insufficient constraints on the large and small scale mass distribution associated with the lens galaxy. However, the five well-constrained lens systems do provide consistent value for the cosmological distance scale.

Acknowledgments

I am grateful to CEFIPRA for support through the Indo-French Project 1410-2.

References

1. A.D. Biggs *et al.*, MNRAS **304**, 349 (1999).
2. J. Chegalur, A.G. de Bruyn, D. Narasimha, Astr. Astrophys. **343**, L79 (1999).
3. S.M. Chitre, D. Narasimha, in *Gravitation and Relativity: At the turn of the Millennium*, GR15, ed. N. Dadhich, J.V. Narlikar, (IUCAA, 1998, p1)
4. S. Nair, D. Narasimha, A.P. Rao, Astrophys. J **407**, 46 (1993).
5. D. Narasimha, Pramana **53**, 921 (1999).
6. D. Narasimha, Pramana **53**, 1039 (1999).
7. D. Narasimha, S.M. Chitre, in *Gravitational Lenses*, eds, R. Kayser, T. Schramm and L. Nieser (1991) p128.
8. D. Narasimha, A.R. Patnaik, in *Gravitational Lenses in the Universe*, eds. J. Surdej *et al*, (1993) p295.
9. D. Narasimha, A.R. Patnaik, R. Porcas, (in preparation)
10. D. Narasimha, K. Subramanian, S.M. Chitre, Mon. Not. Roy. Astr. Soc. **210**, 79 (1984).
11. P.L. Schecter *et al.*, Ap.JL **475**, L85 (1997).
12. R. Schild, D.J. Thomson, AJ **113**, 130 (1997).
13. K. Subramanian, S.M. Chitre, D. Narasimha, Astrophys. J. **289**, 37 (1985)
14. T. Wilkind, (in this conference).

NEAR-IR SPECTROSCOPY OF THE DOUBLE QUASAR HE 110-1805

C. Lidman[1], F. Courbin, G. Meylan, J.-P. Kneib and P. Magain
[1]*European Southern Observatory, P. O. 19001 Santiago 19, Chile*
email: clidman@eso.org

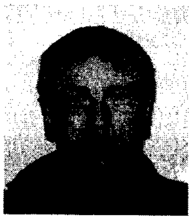

A new technique to spatial deconvolve spectra is applied to near-IR NTT/SOFI (0.95-2.50μ) spectra of the lensed, radio-quite quasar HE 1104-1805 to obtain the spectra of the lens and the two lensed images of the quasar. Although we were unsuccessful at determining the redshift of the lens, we did obtain a high quality spectrum of the quasar. The spectra show no evidence of differential reddening at the redshift of the lens nor at the redshift of the source. Additionally, the difference between the spectrum of the brightest component and that of a scaled version of the faintest component is a featureless continuum. Broad and narrow emission lines, including the FeII features, are subtracted perfectly. Finally, the slope of the continuum in the brightest image is steeper than the continuum in the faintest image and supports the finding by Wisotzki *et al.*[10] that the continuum emitting region of the brightest image is microlensed.

1 Introduction

HE 1104-1805 consists of 2 lensed images (separated by ~3.15 arc-seconds) of a radio-quiet quasar (RQQ) at z=2.32 (Wisotzki *et al.*[10]). From spectrophotometric monitoring, Wisotzki *et al.*[11] derive a time-delay of $\Delta t = 0.73$ years. HE 1104-1805 can therefore be used to constrain the Hubble constant, provided a redshift can be measure for the lensing galaxy. We describe here an unsuccessful attempt to measure the redshift from near-IR spectroscopy. As a by product of the observations, a high quality near-IR spectrum of a RQQ at relatively high redshift was obtained.

2 Observations and Reductions

The data were taken with the red and blue grisms of SOFI, a 1 to 2.5 μ imaging spectrograph on the ESO NTT. With the 1 arc-second slit, the spectral resolution is around 600 for both grisms. The slit was aligned with the two images of the quasar, and, as is standard practice in

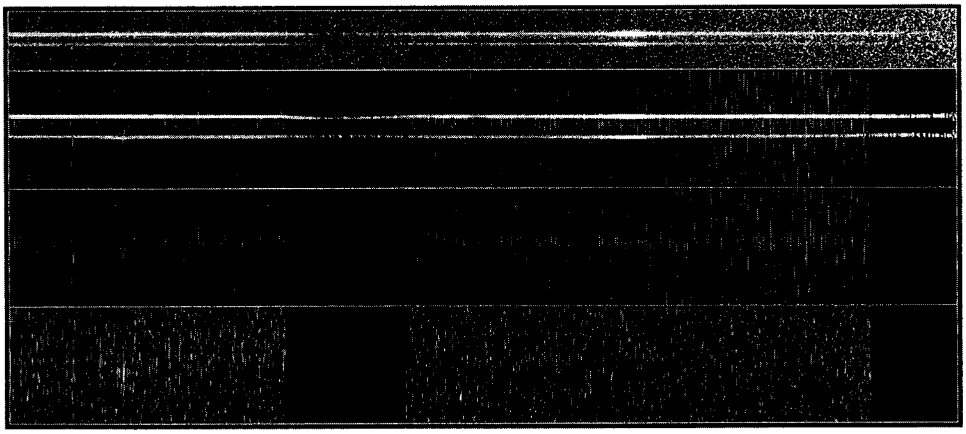

Figure 1: Two dimensional 1.5-2.5 μ spectra of HE 1104-1805. From top to bottom, the 2-D combined near-IR spectrum (seeing $\sim$ 0.6 arcseconds, pixel size $\sim$ 0.14 arcseconds), its deconvolved version (resolution of 0.14 arcseconds, pixel size $\sim$ 0.07 arcseconds), the deconvolved spectrum of the lens alone, and the residual map.

the near-IR, the object was observed at two positions along the slit. The night sky emission features are effectively removed by subtracting the resulting spectra from eachother.

In order to extract separately the spectrum of the lensing galaxy and the spectra of the two quasar images, we deconvolved the 2-D spectra with the method outlined by Courbin *et al.* [3]. The quality of the deconvolution is checked by examining the residual map, which should be flat with a mean value of 1. The different products of the deconvolution are shown in figure 1.

All extracted 1-D spectra were then divided by that of a bright star and then multiplied by a blackbody curve with a temperature that is appropriate for the spectral type of the star.

3 The lens spectrum

The spectrum of the lens does not lead to a redshift measurement. However, the broadband colours suggest a significant break in the spectrum between the R, I and J bands. We have used the photometric redshift code "hyperz" (Bolzonella *et al.* [2]) to estimate a photometric redshift for the lens. The best fitting redshift is $z = 1$ with a 1-sigma range of $0.8 < z < 1.2$. This is slightly higher than the redshifts estimated from the position of the lens on the fundamental plane ($z = 0.77 \pm 0.07$; Kochanek *et al.* [5]) and the time delay (z=0.79; Wisotzki *et al.* [11]).

4 The source spectrum

Following Wisotzki *et al.* [10], we subtracted a scaled version of the fainter component from the brighter one, that is $f_\lambda(A) - A * f_\lambda(B)$. The scale is set so that the Balmer lines vanish. We find that we require $A = 2.9 \pm 0.1$ for the red spectrum and $A = 3.0 \pm 0.1$ for the blue spectrum. Wisotzki *et al.* [10], and Smette *et al.* [7] used A=2.8, which may reflect systematic differences in the way the object was observed or the data reduced rather than anything real.

The difference spectrum and the spectrum of the brighter component are plotted in figure 2. Here we plot the difference spectrum as the thin dotted line, and a smoothed version of this as the thick continuous line. Regions of high atmospheric absorption are set to zero. The Balmer lines: H-alpha, H-beta, and H-gamma, the [OIII] doublet and several broad FeII features

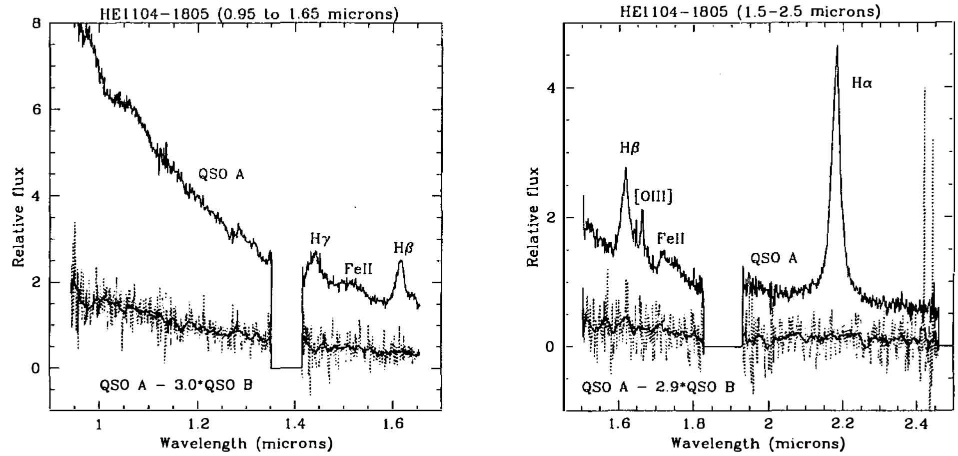

Figure 2: Difference spectrum of the two quasar images for the blue grism (left) and red grism (right).

(Francis *et al.*[4]) are visible in the spectrum of the brighter quasar. The difference spectrum is featureless. Not only are the broad Hydrogen features removed from the spectra, but the broad Fe features and the [OIII] doublet are removed as well. The residual near the strong H-alpha line is less than 1%. As noted by Wisotzki *et al.*[10] there appears to be excess continuum in the brighter component.

The Balmer decrement is around 4 for both components, and this is well within the range expected for unreddened quasars (Baker *et al.*[1]). Thus, there is no evidence for absolute reddening. However, the limits we can set on this are weak as the range of values for the Balmer decrement in quasars is rather broad.

The limits for differential reddening are considerably stronger. The ratio of the emission lines in the brighter and fainter components is 2.9 ± 0.1. The error brackets the measured variation of this ratio over time (six years of observation) and over wavelength. This ratio is remarkably constant over a large wavelength range, from CIV at 1549 Å to $H\alpha$, and we can used it to place an upper bound on the amount of differential extinction between the two components. If we assume that the lens is at $z = 1$ and if we use the standard galactic extinction law, then the differential extinction between the two components is $\Delta E(B - V) < 0.01$ magnitudes.

5 Is microlensing detected in HE 1104-1805?

The continuum is thought to be produced by an accretion disk and is of the order of 10^{14} to 3×10^{15} cms. The Einstein ring is $\sim 3.0 \times 10^{16}$ cms for $H_0 = 60$ and a one solar mass object. Thus, given that there is a suitable alignment, microlensing of the continuum is possible.

The likelihood of microlensing then depends on the density of micro-lenses. If we model the mass distribution of the lensing galaxy as an Single Isothermal Sphere (SIS), one can show that the optical depth, κ, is of order 0.5 for both components. If the mass consists of compact objects (stars, etc.) then microlensing of either component is likely.

The typical timescale between two consecutive microlensing events depends on the transverse velocity of the source and the velocity dispersion of the microlenses. The velocity dispersion for the lensing galaxy is very high (using a SIS, one derives $\sigma \approx 400$kms/s) and it is probably larger than the transverse velocity. Dividing this velocity directly the into diameter of the Einstein ring, one derives a time scale of 3 years. This is quite long; however, it has been shown that stellar proper motions produce a higher microlensing rate than the one produced by a bulk velocity of the same magnitude (Wambsganss and Kurdic[9], Wyithe *et al.*[12]). Furthermore, the typical duration of a microlensing event is the time for the continuum emitting region (10^{15}cm) to cross a Caustic with velocity $\sigma \approx 400$kms/s. This is of the order of a few months and much shorter that the time between consecutive microlensing events.

Thus microlensing is a natural explanation for the relative hardness between the two components.

Conversely, the BLR does not appear to be affected by microlensing. From 1993 to 1999, the ratio of the broad lines between the two components, 2.9 ± 0.1 (Wisotzki *et al.*[11] and this paper), has varied little. The lines of the BLR in the IR spectra presented here subtract very cleanly, better than 1% of the original line flux. Naively, one may then expect that any substructure in the BLR needs to be considerably larger than the Einstein ring (3×10^{16} cms). However, a more secure estimate requires some modeling of how microlensing in this particular lens can affect the profile of lines from the BLR (e.g., Schneider and Wambsganss[6]).

6 Summary

We have obtained $1-2.5\mu$ spectra of the gravitational lens HE 1104-1805. Although we were not successful in measuring a precise redshift for the lens, the lens is probably an early type galaxy with a plausible redshift of $0.8 < z < 1.2$.

We find that the continuum in the A component is harder than the continuum in the B component. The most probable explanation is that the A component is microlensed by compact objects in the lens galaxy.

We find that the ratio of the emission lines between the two components is 2.9 ± 0.1. The constancy of this ratio over a large wavelength range limits the differential extinction between the two components to $\Delta E(B-V) < 0.01$ magnitudes.

We find that broad emission lines can be removed very well by subtracting a scaled version of the spectrum of component B from that of component A. It may be possible to use this near perfect subtraction to limit models of the BLR. This possibility should be investigated further.

References

1. Baker, A. C., Carswell, R. F., Bailey, J. A., Espey, B. R., Smith, M. G. Ward, M. J., 1994, MNRAS, 270, 575.
2. Bolzonella, M, Miralles, J. M., Pellò, R, 2000, astro-ph/0003380.
3. Courbin, F., Magain, P., Kirkove, M., Sohy, S. 1999, ApJ, 529, 1136.
4. Francis, P. J., Hewett, P. C., Foltz, C. B. Chaffee, F. H., Weynmann, R. J., Morris, S. L., 1991, ApJ, 373 465.
5. Kochanek, C. S, Falco, E., Impey, C. D., Lehar, J. Rix, H.-W., Keeton, C. R. Munoz, J. A., Peng, C. Y. 2000, ApJ, In Press.
6. Schneider, P and Wambsganss, J., 1990, A&A, 237, 42
7. Smette, A., Robertson, J. G., Shaver, P. A., Reimers, D., Wisotzki, L., Köhler, T., 1995, A&AS, 113, 199.
8. Wambsganss, J., Paczynski, B., Schneider, P., 1990. ApJ, 235, L33.
9. Wambsganss, J., Kundic, T., 1995, ApJ 450, 19
10. Wisotzki, L., Koehler, T., Kayser, R., Reimers, D., 1993, A&A 358, L15
11. Wisotzki, L., Wucknitz, O., Lopez, S., Sørensen, A, 1998, A&A 339, L73
12. Wyithe, J. S. B., Webster, R., Turner, E. 2000, MNRAS, 312, 843.

THE LENS-REDSHIFT TEST REVISITED

P. HELBIG
Rijksuniversiteit Groningen, Kapteyn Instituut, Postbus 800, NL-9700 AV Groningen, The Netherlands

Kochanek[1] suggested that the redshifts of gravitational lens galaxies rule out a large cosmological constant. This result was questioned by Helbig & Kayser[2], who pointed out that selection effects related to the brightness of the lens can bias the results of this test against a high λ_0 value; however, we did not claim that the observations *favoured* a high λ_0 value, merely that current observational data were not sufficient to say either way, using the test as proposed by Kochanek[1] but corrected for selection effects. Kochanek[3] pointed out that an additional observable, namely, the fraction of measured lens redshifts, provides additional information which restores the sensitivity of the test to the cosmological model, at least somewhat. Here, I consider three aspects. First, I discuss the appropriateness of the correction to the test proposed by Kochanek (1996a). Second, I briefly mention the slightly different statistical methods which have been used in connection with this test. Third, I discuss what results can be obtained today now that more and better-defined observations are available.

1 Introduction

The optical depth for gravitational lensing depends on the cosmological model, the Faber-Jackson and Tully-Fisher relations, lens-galaxy type (or the morphological mix), the luminosity function of lens galaxies and the S-z relation of the source population (e.g. Kochanek[1], Helbig & Kayser[2]). There is an obvious problem with simply measuring the integrated optical depth, i.e. the number of lens systems (according to some useful definition): There is a degeneracy between various parameters such that quite different combinations can result in the same number of lenses. While it is possible to break this degeneracy somewhat, this requires a careful survey and cannot be done with a sample of lenses 'from the literature'. Kochanek[1] pointed out that one could use the *shape* of the optical-depth function $\mathrm{d}\tau/\mathrm{d}z$ as a probe of the cosmological model. The advantage of this approach is that it does not depend on the overall normalisation, as counting the number of lenses obviously does. Also, it is quite sensitive to the cosmological model, with the dependence on the cosmological model of a) the combination of angular size distances and b) the volume element, both of which appear in $\mathrm{d}\tau/\mathrm{d}z$, reinforcing one another. In other words, the redshifts of lens galaxies can be used as a probe of the cosmological model which is relatively little affected by our ignorance of other factors which determine the total optical depth.

2 History

Kochanek[1] used a sample of 4 gravitational lens systems from the literature (estimating the lens redshift from absorption lines if unknown) and found that the Einstein-de Sitter model was 5–10 times more likely than a flat model dominated by a cosmological constant. Helbig & Kayser[2] pointed out that this is potentially subject to a strong bias: It could be that most known lens redshifts are low not because we live in a universe in which this is more probable, but since we could not have measured them if they were higher. To correct for this effect, we suggested comparing the shape of $\mathrm{d}\tau/\mathrm{d}z$ not over the whole range $[0,z_{\mathrm{s}}]$ (in practice, the value of this function is negligible before z_{s} is reached), but rather only out to that redshift where a lens redshift could have been measured, assuming some realistic limiting magnitude (at this redshift, $\mathrm{d}\tau/\mathrm{d}z$ usually still has a non-negligible value) and found that no interesting constraints could be obtained from then-current data (using 6 systems, all with measured, not estimated, lens redshifts), even if many more such systems were found, and that this conclusion did not depend on the precise value assumed for the limiting magnitude.

Kochanek[3] then pointed out that one can use an additional observable to restore cosmological sensitivity to the lens-redshift test: the fraction of lens systems with measured redshifts. If a strong bias were present such that only low lens redshifts could be measured, then there should be many lens systems with unmeasured redshifts. While true, this misses the point of Helbig & Kayser[2]: Our claim was not that the observations supported a large value of the cosmological constant (nor the opposite), but rather that the conclusion of Kochanek[1] did not follow from the sample used (or our sample) since the lens-brightness bias had not been taken into account. Also, the correction proposed in Kochanek[1] assumes that unknown lens redshifts are unknown only because they are faint; in practice, there can be many other reasons why some lens redshifts have not yet been measured (e.g. the maximum declination accessible from UKIRT).

Various different statistical measures have been used to compare the observed and predicted lens-redshift distributions. Here, I only consider the maximum-likelihood method (e.g. Kochanek[3]), which I consider to be most appropriate. However, results from using the binning method of Helbig & Kayser[2] or a Kolmogorov-Smirnov test (Helbig, unpublished) give qualitatively similar results.

3 Using CLASS

The whole issue of unknown lens redshifts and their possible causes can be avoided if one has a sample which is complete with respect to lens redshifts. CLASS (e.g. Helbig[4]) is close to this goal, and the JVAS subset of CLASS (more exactly, the JVAS lens systems in CLASS which are also part of the statistically complete lens-survey sample; see Helbig[4] for more details) is actually complete. While only consisting of four systems, this is the same number used in Kochanek[1], so the time is ripe to revisit this topic. (The last JVAS lens redshift was obtained by Kochanek & Tonry[5].)

Figure 1 shows the likelihood as a function of λ_0 and Ω_0 for the sample from Kochanek[1] while Fig. 2 shows the same for the JVAS lens systems B0218+357, MG0414+054, B1030+074 and B1422+231. It is obvious that the Kochanek[1] sample indicates that the Einstein-de Sitter model is more likely than a flat model dominated by a cosmological constant. The JVAS sample tells a different story. Probably, part of the difference, in particular, the low probability of models

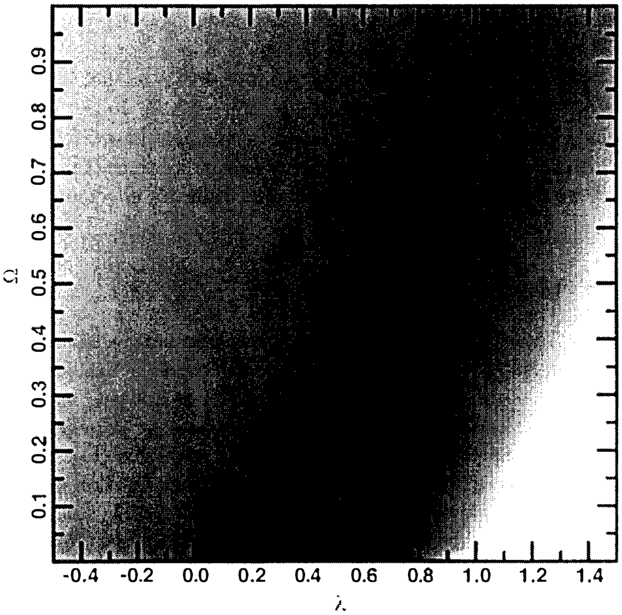

Figure 1: Likelihood as a function of λ_0 and Ω_0 using the Kochanek sample; darker means higher likelihood.

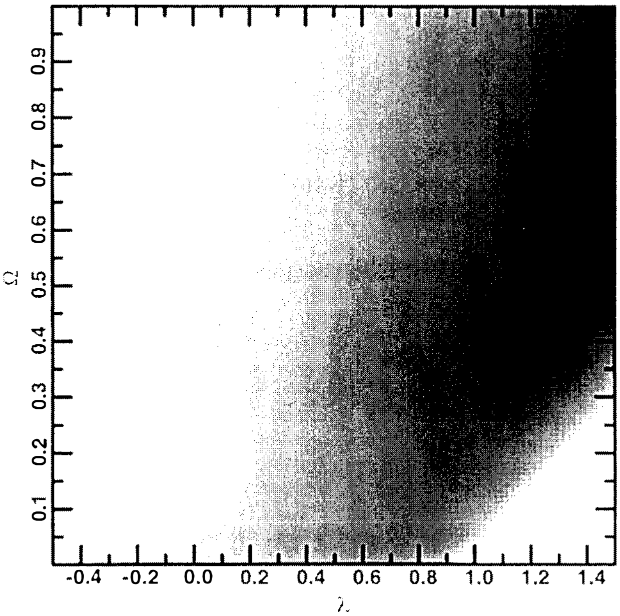

Figure 2: Likelihood as a function of λ_0 and Ω_0 using the JVAS sample; darker means higher likelihood.

near the white area to the lower right (which corresponds to no-big-bang models and is excluded *a priori*) can be explained by the bias noted in Helbig & Kayser[2], while part can be explained by small-number statistics. This will be explored in more detail in Helbig & Rusin[6]. (It should be noted that the results for the Kochanek[1] sample presented here do not correspond exactly to those in Kochanek[1] since there (as in Helbig & Kayser[2]), the now-known-to-be-erroneous $(3/2)^{\frac{1}{2}}$ factor for elliptical galaxies was used. Including this factor increases the relative likelihood of the Einstein-de Sitter model for the Kochanek[1] sample while its effect on the JVAS sample is less pronounced.)

4 Conclusions and Future Prospects

It is obvious that the conclusion of Kochanek[1] was premature: using a better-defined and in particular bias-free (since complete) sample, the lens-redshift test does not disfavour cosmological-constant dominated models, although the significance of this is not yet clear. Since the publication of Kochanek[1], of course, the cosmological constant has become popular again and, although more detailed lens-statistics analyses are not incompatible with this (e.g. Helbig[7]), it is not yet clear whether systematic effects, such as our lack of sufficient information about the S-z plane of the source population (e.g. Kochanek[8]), make current estimates of λ_0 from the analysis of lens surveys unreliable. It is at least interesting that the lens-redshift test does not seem to favour an Einstein-de Sitter universe over a model (flat or not) dominated by a cosmological constant. When the much larger CLASS sample is complete with respect to lens redshifts, the time will be ripe to revisit this topic once again.

Acknowledgments

It is a pleasure to thank David Rusin for useful discussions and the CLASS team for providing the numbers to work with.

References

1. C.S. Kochanek, ApJ **384**, 1 (1992)
2. P. Helbig & R. Kayser, A&A **308**, 359 (1996)
3. C.S. Kochanek, ApJ **466**, 638 (1996)
4. P. Helbig, these proceedings
5. J.L. Tonry & C.S. Kochanek, AJ **117**, 2034 (1999)
6. P. Helbig & D. Rusin, in preparation
7. P. Helbig A&A **350**, 1 (1999)
8. C.S. Kochanek, ApJ **473**, 595 (1996)

THE STATISTICS OF WIDE-SEPARATION LENSES

D.J. MORTLOCK[1,2,3]

[1] *Astrophysics Group, Cavendish Laboratory, Madingley Road, Cambridge CB3 0HE, U.K.*
[2] *Institute of Astronomy, Madingley Road, Cambridge CB3 0HA, U.K.*
[3] *Department of Physics, The University of Melbourne, Parkville, Victoria 3052, Australia*

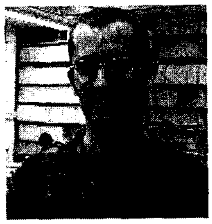

The probability that high-redshift sources are gravitationally-lensed with large image separations (*i.e.*, greater than can be produced by galactic deflectors) is determined by the cosmological population of group- and cluster-sized halos. Thus the observed frequency of wide-separation lensed quasars can be used to constrain not only the halo distribution, but also a number of cosmological parameters. A calculation of the optical depth due to collapsed, isothermal halos is a useful guide to the lens statistics, and illustrates that the number of wide-separation lenses is a sensitive probe of the mean density of the universe and the present day density variance whilst being nearly independent of the cosmological constant.

1 Introduction

Gravitational lensing is a direct probe of the geometry of the universe, and so observations of lensing place constraints on both the distribution of mass and the underlying cosmological model. A large variety of lensing experiments are possible: weak shear surveys; searches for microlensing by compact objects; observations of giant arcs in clusters; measurement of Shapiro delay in binary pulsars; surveys for multiply-imaged qusasrs; and so on. The focus here is on the statistics of wide-separation lensed quasars (which are produced by group- and cluster-mass objects). Using a simple model of the halo population (Section 2), the optical depth to multiple imaging and the expected distribution of image separations can be calculated (Section 3). The results obtained are independent of the source population, which then implies that a more sophisticated analysis is required to constrain model parameters from the observed frequency wide-separation lenses [1, 2].

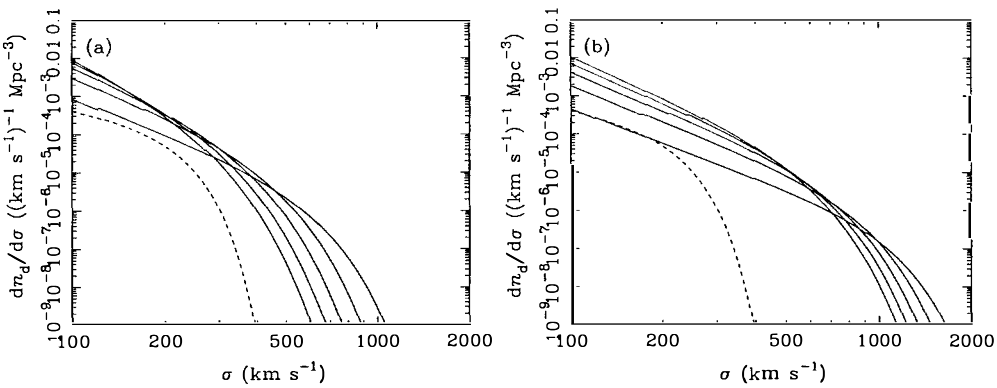

Figure 1: The evolution of the halo population in Press-Schechter theory. A standard CDM model (with $\Omega_{m_0} = 1$ and $\Omega_{\Lambda_0} = 0$) is assumed, with $\Delta_8 = 0.5$ in (a) and $\Delta_8 = 1.0$ in (b). For each model the five solid lines show the population at redshifts of 0, 1, 2, 3 and 4; the number of high-mass halos decreases with redshift (or, equivalently, increases with time). The dashed lines show the local galaxy population, assuming standard magnitude-velocity dispersion relationships.

2 Deflector population

The population of cluster-sized halos is well approximated by the Press-Schechter[3] mass function, which depends on the cosmological model[a] and the matter power spectrum. An approximate cold dark matter (CDM) power spectrum [4] with a spectral slope of $n = 1$ is assumed, and only the normalisation is allowed to vary. The scale of the density fluctuations are normalised to match Δ_8, the present day variance in spheres of 8 Mpc radius, and so is linked to a (co-moving) scale, rather than a mass. The clusters themselves are modelled as singular isothermal spheres, which are characterised by their line-of-sight velocity dispersion, σ, rather than their mass, M. General arguments imply that $M \propto \sigma^3$, but this conversion is somewhat ambiguous, and is an important source of systematic error in the calculation of lensing cross-sections. The resultant halo population (Fig. 1) is most stronly dependent on Δ_8, and can be made consistent with galaxy counts if the Press-Schecter form is assumed only for $\sigma > 200$ km s^{-1}.

3 Lensing optical depth

Given the population of deflectors and a lens model, it is reasonably straightforward to calculate the optical depth, $\tau(z_s)$, to multiple imaging[5,1]. Whilst τ is too crude an estimate of the lensing probability to meaningfully constrain model parameters, it is useful in an illustrative sense, particularly if the source-dependent aspects of the full probability (*e.g.*, the magnification bias) can be factored out of the integral over the deflector population. This is the case for the isothermal sphere, and, in addition, the image separation, $\Delta\theta$, is completely determined by z_d, z_s and σ, and so image separation cut-offs (*i.e.*, $\Delta\theta_{\rm min}$ and $\Delta\theta_{\rm max}$) can be included in τ. Thus the optical depth can be thought of as the fraction of the sphere at redshift z_s inside the Einstein radius (θ_E) of any cluster for which $\Delta\theta_{\rm min} \leq 2\theta_E \leq \Delta\theta_{\rm max}$. Choosing $\Delta\theta_{\rm min} \simeq 3$ arcsec removes the galactic lenses from the calculation (their population being poorly approximated by the naive Press-Schechter form); the value $\Delta\theta_{\rm max}$ is determined by the breadth of the companion search.

[a]This is specified by the present day normalised matter density, Ω_{m_0}, the similarly normalised cosmological constant, Ω_{Λ_0}, and Hubble's constant (although its value is unimportant in this calculation).

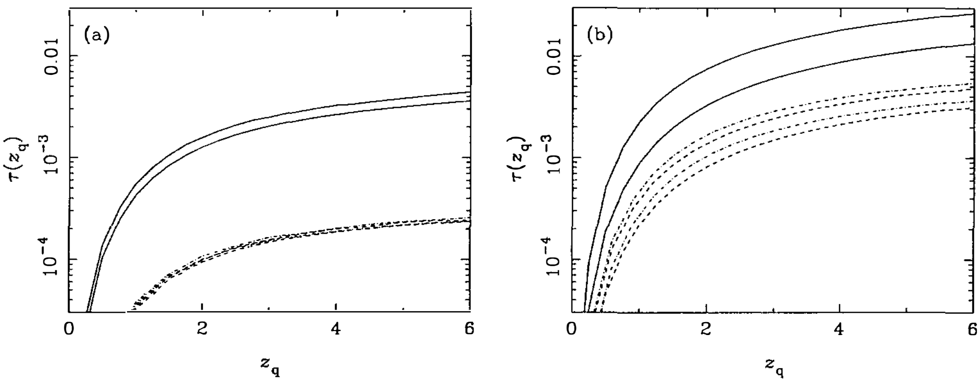

Figure 2: The gravitational lensing optical depth due to a cosmological population of isothermal halos as a function of source redshift. Results are shown for several cosmological models: $\Omega_{m_0} = 1$ and $\Omega_{\Lambda_0} = 0$ (solid lines); $\Omega_{m_0} = 0.3$ and $\Omega_{\Lambda_0} = 0$ (dashed lines); and $\Omega_{m_0} = 0.3$ and $\Omega_{\Lambda_0} = 0.7$ (dot-dashed lines), with $\Delta_8 = 0.5$ in (a) and $\Delta_8 = 1.0$ in (b). The effects of image separation cut-offs are also illustrated: in each case the lower lines are for $\Delta\theta_{\rm min} = 3$ arcsec and $\Delta\theta_{\rm max} = 10$ arcsec and the upper lines are for $\Delta\theta_{\rm min} = 3$ arcsec and and $\Delta\theta_{\rm max} = \infty$.

The optical depth is shown as a function of source redshift in Fig. 2. The standard increase of τ with z_s is apparent, and comparing Fig. 2 (a) and (b) shows the expected dependence on Δ_8. More interesting is the variation with cosmological model and $\Delta\theta_{\rm max}$. The optical depth to lensing by galaxies is primarily dependent on the cosmological constant as the differential volume element is so much larger in high-Ω_{Λ_0} models. This effect is present here, but it is not dominant, for two reasons. Firstly, clusters form earlier in low-density cosmologies – most large-scale structure formed before $z \simeq \Omega_{m_0}^{-1} - 1$ (if $\Omega_{\Lambda_0} = 0$) or, more recently, before $z \simeq \Omega_{m_0}^{-1/3} - 1$ (in flat models)[6]. Thus the lensing probability is greater if Ω_{m_0} is small, there being more high-redshift collapsed deflectors along a given line-of-sight. For a fixed Ω_{m_0}, however, increasing the cosmological constant reduces the number of halos with $\Omega_{m_0}^{-1/3} - 1 < z_d < \Omega_{m_0}^{-1} - 1$, somewhat offsetting the usual increase of τ with Ω_{Λ_0}. Secondly, the mass of a cluster that has collapsed from a given co-moving scale (*e.g.*, 8 Mpc) is proportional to Ω_{m_0}. For the isothermal sphere model the lensing cross-section scales as $\sigma^4 \propto M^{4/3} \propto \Omega_{m_0}^{4/3}$. It is because of this strong dependence that standard CDM models with $\Omega_{m_0} = 1$ are so inconsistent with the low number of wide separation lenses[2,1,7].

The expected distribution of image separations can be estimated by computing $d\tau/d\Delta\theta$, which is illustrated in Fig. 3. As shown, these distributions are normalised to unity, but the vertical scaling can be estimated from the known wide-separation pairs[7]. The immediate implication of this is that the fall-off with increasing $\Delta\theta$ is far too shallow to be consistent with the complete absence of any (confirmed) lenses with $\Delta\theta > 10$ arcsec[1]. One inference that could be drawn is that the mass profiles of clusters are shallower than isothermal[8], but it is difficult to reconcile such models (including the Navarro, Frenk & White[9] profile) with observations of arcs and arclets[10].

4 Conclusions

The statistics of wide-separation lenses are a useful cosmological probe. The lensing probability is sensitive to the geometry of the universe, and the population of collapsed halos at intermediate redshifts whilst being independent of the complexities of galaxy formation. As large-scale structure is dependent on the linear growth of perturbations (and also because the mass in a co-

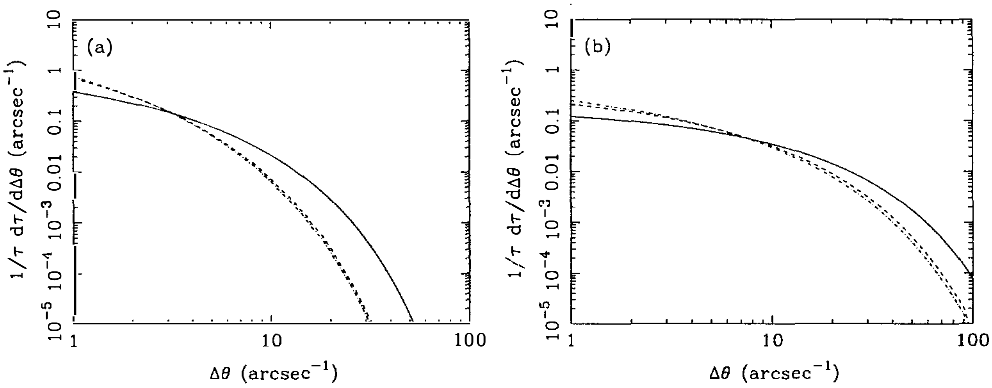

Figure 3: The normalised distribution of image separations produced by a cosmological population of isothermal halos, for a source at $z_q = 3$. Results are shown for several cosmological models: $\Omega_{m_0} = 1$ and $\Omega_{\Lambda_0} = 0$ (solid lines); $\Omega_{m_0} = 0.3$ and $\Omega_{\Lambda_0} = 0$ (dashed lines); and $\Omega_{m_0} = 0.3$ and $\Omega_{\Lambda_0} = 0.7$ (dot-dashed lines), with $\Delta_8 = 0.5$ in (a) and $\Delta_8 = 1.0$ in (b).

moving sphere of a given size is proportional to the density parameter) the likelihood of lensing is most sensitive to Ω_{m_0} and Δ_8. The Large Bright Quasar Survey [11] is devoid of wide-separation lenses [12, 13] which implies that $\Omega_{m_0} < 0.3$ (assuming $\Delta_8 > 0.4$) or that $\Delta_8 < 0.6$ (assuming $\Omega_{m_0} < 0.1$) with 99 per cent confidence [2]. In the future such analyses could be extended to the 2 degree Field quasar survey [14] (with $\sim 3 \times 10^4$ quasars) and the Sloan Digital Sky Survey [15] (which will contain $\sim 10^5$ sources). These samples will be large enough to constrain Ω_{m_0} and Δ_8 to within several per cent from the number of wide-separation lenses alone.

Acknowledgments

Much of this research was done whilst supported by an Australian Postgraduate Award.

References

1. C.S. Kochanek, ApJ **453**, 545 (1995).
2. D.J. Mortlock and R.L. Webster, MNRAS in press (2000).
3. W.H. Press and P. Schechter, ApJ **185**, 397 (1974).
4. G. Efstathiou, J.R. Bond and S.D.M. White, MNRAS **258**, 1P (1992).
5. E.L. Turner, J.P. Ostriker and J.R. Gott, ApJ **284**, 1 (1984).
6. S.M. Carroll, W.H. Press and E.L. Turner, ARA&A **30**, 499 (1992).
7. R. Narayan, S.D.M. White, MNRAS **231**, 97P (1988).
8. P. Madau and C. Porciani, ApJ **532**, 679 (2000).
9. J.A. Navarro, C.S. Frenk and S.D.M. White, ApJ **490**, 493 (1997).
10. L.L.R. Williams, J.F. Navarro, M. Bartelmann, ApJ **527**, 535 (1999).
11. P.C. Hewett, C.B. Foltz and F.H., Chaffee, AJ **109**, 1498 (1995).
12. P.C. Hewett, C.B. Foltz, M.E. Harding and G.F. Lewis, AJ **115**, 383 (1998).
13. D.J. Mortlock, R.L. Webster and P.J. Francis, MNRAS **309**, 836 (1999).
14. B.J. Boyle, S.M. Croom, R.J. Smith, T. Shanks T., L. Miller and N.S. Loaring, Phil. Trans. Royal Ast. Soc. A **357**, 185 (1999).
15. A.S. Szalay in *Large Scale Structure: Tracks and Traces*, eds. V. Miiller, S. Gottlöber and J.P. Mücket (World Scientific, Singapore, 1998), p. 97

WEAK LENSING AND COSMOLOGY

M. Lombardi & G. Bertin
Scuola Normale Superiore, P.zza dei Cavalieri 7, I-56126 Pisa, Italy

A method is described to constrain the geometry of the universe from weak lensing observations, provided that the redshifts of the source galaxies are measured. The quantitative limits and merits of the method are discussed by means of a set of simulations in relation to interval estimation for homogeneous Friedmann-Lemaître models. The constraints turn out to be significant when thousands of source galaxies are used.

1 Introduction

It has long been recognized (see Tyson *et al.* 1984) that the gravitational field of a cluster acts on the images of distant galaxies by changing their orientation so that their major axes tend to become perpendicular to the direction of the center of the cluster. In turn (see Kaiser & Squires 1993) the mean ellipticity of the galaxy images can be used to measure the shear of the lens, a quantity related to the two-dimensional mass distribution.

In the lens reconstruction process, information on the ratio of the distances from the observer to the source galaxies and from the lens to the galaxies is used. For intermediate redshift clusters, one has to take into account the different redshifts of the background galaxies. The result of the gravitational lensing *depends* on the geometry of the universe. Seitz & Schneider (1997) have shown that it is possible to reconstruct the mass distribution of the lens provided that both the probability distribution of galaxy redshifts and the geometry of the universe are known (i.e., the values of Ω and Ω_Λ in the standard Friedmann-Lemaître cosmology).

In recent years the technique to obtain photometric redshifts (Baum 1962) has been greatly improved and tested (Lanzetta *et al.* 1996). This suggests that in a not far future we might use photometric redshift information for galaxies lensed by a cluster.

Here we show how we can determine both the lens mass distribution and the geometry of the universe if the redshifts of the source galaxies are known. At this stage the study proposed here may be seen as a "thought experiment" because of the very high number of redshifts that are found to be required in order to constrain the geometry significantly. We will show below that the galaxies that one should observe can hardly be found behind a single cluster at the magnitudes currently attainable. However, it is possible to combine data from different clusters. Combining the study of 5–10 clusters would lead to statistically meaningful constraints. With such a device, the application of the present method might even become feasible in a not too far future.

2 Method

In this section, for simplicity, we describe the method in the weak lensing approximation (the general case is considered in Lombardi & Bertin 1999).

A lens at redshift z_d acts with different strength on sources at different redshifts. In the weak lensing limit, using a suitable definition for the ellipticity of galaxies, we have (see Seitz & Schneider 1997)

$$\epsilon^s = \epsilon - \gamma(\vec{\theta})w(z) \ , \tag{1}$$

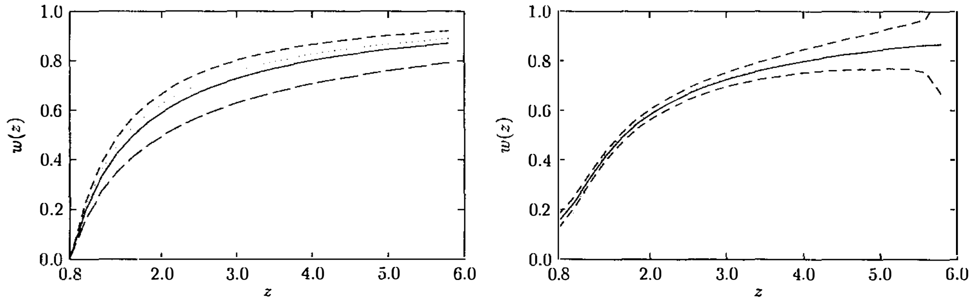

Figure 1: Left: The weight function for a lens at $z_d = 0.8$ in four different universes. From the top to the bottom: $\Omega = 0.3$, $\Omega_\Lambda = 0$ (dashed); $\Omega = 0.3$, $\Omega_\Lambda = 0.7$ (dotted); $\Omega = 1$, $\Omega_\Lambda = 0$ (solid); $\Omega = 1$, $\Omega_\Lambda = 1$ (long dashed). Right: The expected mean and error on the weight function for an Einstein-de Sitter universe. The solid line shows $\langle w \rangle(z)$, the dashed lines the expected errors and the dotted line the true $w_0(z)$. The errors are calculated for $N = 10\,000$ galaxies; errors for different values of N can be obtained by recalling that the error scales as $\sqrt{N}$.

where ϵ^s and ϵ are, respectively, the source (unlensed) and the observed ellipticities of a galaxy at redshift z observed at the angular position $\vec{\theta}$, $\gamma(\vec{\theta})$ is the lens shear, and $w(z)$ is the *cosmological weight function*. As shown in Fig. 1, the cosmological weight function depends on the cosmological model used.

The method we have developed allows us to jointly determine the shear $\gamma(\vec{\theta})$ of a lens (and thus its mass distribution), and the cosmological weight function $w(z)$. Then, given this function, constraints on the cosmological parameters Ω and Ω_Λ can be obtained. The method is based on the assumption that source galaxies have random orientation (isotropy hypothesis), so that the mean source ellipticity vanishes $\langle \epsilon^s \rangle = 0$. Then, taking suitable averages of Eq. (1), we can obtain $\gamma(\vec{\theta})$ and $w(z)$ independently. Note that we can obtain γ and w only up to a multiplicative constant ("global scaling invariance," described in Lombardi & Bertin 1999), and thus the cosmological parameters must be obtained from the sole *shape* of $w(z)$. The method can be summarized in the following points:

1. A guess on the cosmological model is made initially, and the associated cosmological weight function $w(z)$ is evaluated (see Lombardi & Bertin 1999).

2. The lens shear is then obtained from the equation

$$\hat{\gamma}(\vec{\theta}) = -\frac{\sum_{n=1}^{N} W(\vec{\theta}, \vec{\theta}^{(n)}) \hat{w}(z^{(n)}) \epsilon^{(n)}}{\sum_{n=1}^{N} W(\vec{\theta}, \vec{\theta}^{(n)}) \left[\hat{w}(z^{(n)})\right]^2} . \tag{2}$$

   In this equation, $W(\vec{\theta}, \vec{\theta}')$ is the "spatial weight," a function that is used to average the ellipticities of (angularly) close galaxies. The particular form of Eq. (2) ensures an optimal shear determination. Note that we need to know both the ellipticities $\{\epsilon^{(n)}\}$ and the redshifts $\{z^{(n)}\}$ of the source galaxies.

3. Using the lens shear $\hat{\gamma}(\vec{\theta})$, the cosmological weight function is re-evaluated as

$$\hat{w}(z) = -\frac{\sum_{n=1}^{N} W_z(z, z^{(n)}) \Re\left[\hat{\gamma}(\vec{\theta}^{(n)}) \epsilon^{(n)*}\right]}{\sum_{n=1}^{N} W_z(z, z^{(n)}) \left|\hat{\gamma}(\vec{\theta}^{(n)})\right|^2} . \tag{3}$$

   Here $W_z(z, z')$ is the "redshift weight," a function that plays a role similar to $W(\vec{\theta}, \vec{\theta}')$ for the redshift space.

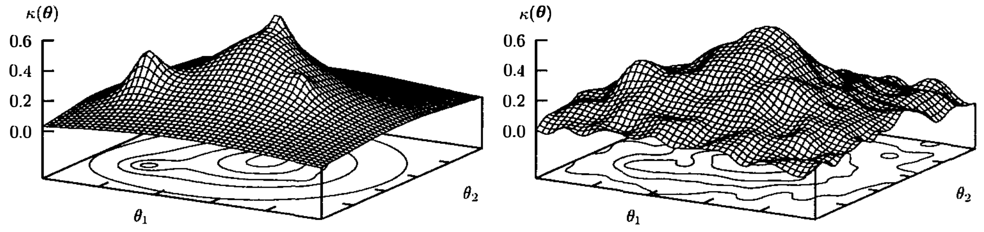

Figure 2: The original (left) and reconstructed (right) dimensionless mass density. The number of galaxies used is $N = 20\,000$; the assumed cosmological model is Einstein-de Sitter. The cluster occupies a square with side of $5'$, which corresponds approximately to $1.23\,h^{-1}$ Mpc.

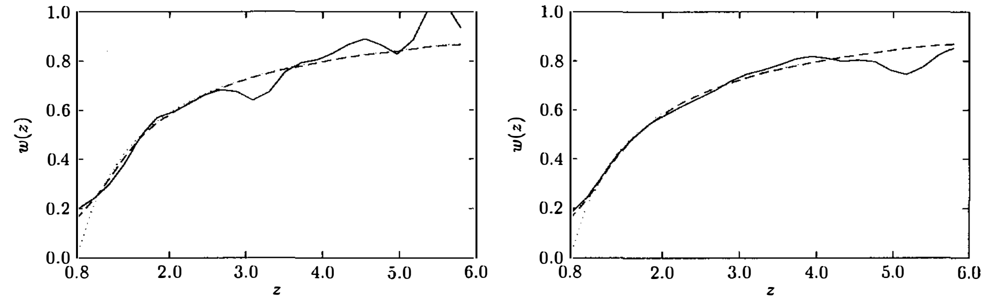

Figure 3: The reconstructed weight function in an Einstein-de Sitter universe ($\Omega = 1$, $\Omega_\Lambda = 0$). The dotted line represent the true weight function $w_0(z)$; the dashed line is the expected mean value $\langle w \rangle(z)$; the solid line is the measured $\hat{w}(z)$. The three figures have been obtained with $N = 20000$ (left) and $N = 50\,000$ (right) source galaxies.

4. Equations (2) and (3) are iterated until a stable solution $\{\hat{\gamma}(\vec{\theta}), \hat{w}(z)\}$ is found.

5. Finally, the cosmological parameters Ω and Ω_Λ are obtained from a fit of $\hat{w}(z)$. If we wish, the shear map $\hat{\gamma}$ can also be used to evaluate the mass map of the lens.

3 Simulations

Simulations have been carried out using a *single* cluster at redshift $z_d = 0.8$ with mass distribution shown in Fig. 2. The cluster has been modeled as a non-singular isothermal sphere with some substructure; in an Einstein-de Sitter universe with Hubble constant $H_0 = 50$ km s^{-1} Mpc^{-1}, the cluster mass within a 1 Mpc aperture would be approximately $2 \times 10^{15}\,M_\odot$. Two examples of reconstructed weight functions are shown in Fig. 3: note that the large number of galaxies used allows for a good determination of $w(z)$, especially at intermediate redshifts, where the density of source galaxies is large. Finally, Fig. 4 shows three typical examples of confidence level regions obtained using the method described here. It should be noted that the constraints obtained are significant only if a rather large number of source galaxies is used. In particular, simulations show that about 10 000–20 000 galaxies are necessary in a field of $5' \times 5'$, corresponding to a density of 400–800 galaxies arcmin^{-2}. This number is beyond the density that can be currently obtained. For example, recent deep HST observations of the cluster MS1054 (which has redshift and mass similar to the cluster considered here) are characterized by a density of nearly 200 galaxies arcmin^{-2} (Hoekstra *et al.* 2000), while VLT observations of MS1008 reach about 100 galaxies arcmin^{-2} (Lombardi *et al.* 2000). Estimates for NGST suggest that this

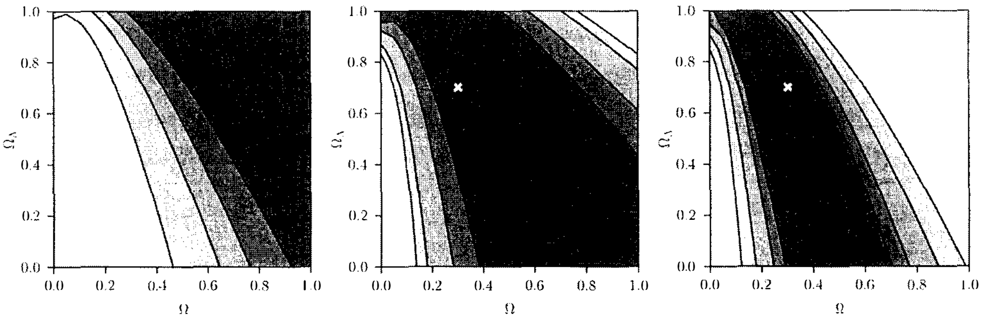

Figure 4: The confidence regions corresponding to CL = 68%, CL = 80%, CL = 90% and CL = 95%. The true values of the cosmological parameters, $\Omega = 0.3$ and $\Omega_\Lambda = 0.7$, are shown as a white cross. The galaxies used are $N = 10\,000$ (left), $N = 20\,000$ (middle), and $N = 50\,000$ (right).

telescope should reach a density of more than 1 000 galaxies arcmin^{-2}. We thus conclude that the method outlined in this paper should be of interest in the NGST era. It is also likely that, with some refinements, the method can already be applied in the near future, when the ACS will be available. In particular, data from several clusters should be combined in order to set stronger cosmological constraints.

4 Conclusions

We have described a method, based on weak lensing and redshift observations, to reconstruct the lens mass distribution and to obtain, at the same time, information on the geometry of the universe. Simulations have shown that the method is viable when the number density of source galaxies is sufficiently high, but not yet available. With some refinements we expect that this method will be applicable to ACS data.

References

1. Baum W.A., 1962, IAU Symp. 15, "Problems of extra-galactic research," ed. McVittie G.C., 390
2. Hoekstra H., Franx M., Kuijken K., 2000, ApJ 532, 88
3. Kaiser N., Squires G., 1993, ApJ 404, 441
4. Lanzetta K.M., Yahil A., Fernández-Soto A., 1996, Nature 381, 759
5. Lombardi M., Bertin, G., 1999, A&A 342, 337
6. Lombardi M., Rosati P., Nonino M., Girardi M., Borgani S., Squires G., 2000, submitted
7. Seitz C., Schneider P., 1997, A&A 318, 687
8. Stiavelli M., Stockman P., Burg R., 1997, ST-ECF Newsletter 24, 4
9. Tyson J.A., Valdes F., Jarvis J.F., Mills A.P., 1984, ApJ 281, L59

CONSTRAINING $(\Omega_m, \Omega_\lambda)$ FROM STRONG LENSING

G. GOLSE, J.-P. KNEIB and G. SOUCAIL
Laboratoire d'Astrophysique, UMR 5572, Observatoire Midi-Pyrénées
14 avenue E.-Belin, F-31400 Toulouse, France

The knowledge of the redshift of multiple images in cluster-lenses allows to determine precisely the total projected mass within the Einstein radius. The observation of various multiple images in a same cluster is opening new possibilities to constrain the curvature of the universe. Indeed, although the influence of Ω_m and Ω_λ on the images formation is of the second order, observations of many multiple images at different redshifts formed by a regular cluster-lens should allow to constrain very accurately the mass distribution of the cluster and to start to be sensitive to the cosmological parameters entering the diameter angular distances. We present, analytical expressions and numerical simulations that allow us to compute the expected error bars on the cosmological parameters provided an HST/WFPC2 resolution image and spectroscopic redshifts for the multiple images. Numerical tests on simulated data confirm the rather small uncertainties we could obtain this way for the two popular cosmological world models: $\Omega_m = 0.3 \pm 0.24$, $\Omega_\lambda = 0.7 \pm 0.5$ or $\Omega_m = 1. \pm 0.33$, $\Omega_\lambda = 0. \pm 1.2$.

1 Introduction

Recent works on constraining the cosmological parameters using the CMB and the high redshift supernovae seem to converge to a "standard cosmological model" favouring a flat universe with $\Omega_m \sim 0.3$ and $\Omega_\lambda \sim 0.7$: White[7]. However these results are still uncertain and depend on some physical assumptions, so the flat $\Omega_m = 1$ model is still possible (Le Dour *et al.*[3]). It is therefore important to explore other independent techniques to constrain these cosmological parameters.

In cluster gravitational lensing, the existence of multiple images – with known redshifts – given by the same source allows to calibrate in an absolute way the total cluster mass deduced from the lens model. The great improvement in the mass modeling of cluster-lenses that includes the cluster galaxies halos (Kneib *et al.*[2], Natarajan & Kneib[6]) leads to the hope that clusters can also be used to constrain the geometry of the Universe, through the ratio of angular size distances, which only depends on the redshifts of the lens and the sources, and on the cosmological parameters. The observations of cluster-lenses containing large number of multiple images lead Link & Pierce [4] (hereafter LP98) to investigate this expectation. They considered a simple cluster potential and on-axis sources, so that images appear as Einstein rings. The ratio of such rings is then independent of the cluster potential and depends only on Ω_m and Ω_λ, assuming known redshifts for the sources. According to them, this would allow marginal discrimination between extreme cosmological cases. But real gravitational lens systems are more complex concerning not only the potential but also off-axis positions of sources. They conclude that this method is ill-suited for application to real systems.

We have re-analyzed this problem building up on the modeling technique developed by us. As demonstrated below, we reach a rather different conclusion showing that it is possible to constrain Ω_m and Ω_λ using the positions of multiple images at different redshifts and some physically motivated lens models.

2 Influence of Ω_m and Ω_λ on the images formation

2.1 Angular size distances ratio term

In the lens equation: $\theta_S = \theta_I - \dfrac{D_{LS}}{D_{OS}} \nabla\varphi_N^{2D}(\theta_I)$, the dependence on Ω_m and Ω_λ is solely contained in the term $F = D_{OL}D_{LS}/D_{OS}$. For a given lens plane, $F(z_s)$ increases rapidly up to a certain redshift and then stalls, with significant differences for various values of the cosmological parameters (see Fig. 1). Thus in order to constrain the actual shape of $F(z_s)$ several families of multiple images are needed, ideally with their redshifts regularly distributed in $F(z_s)$ to maximize the range in the F variation.

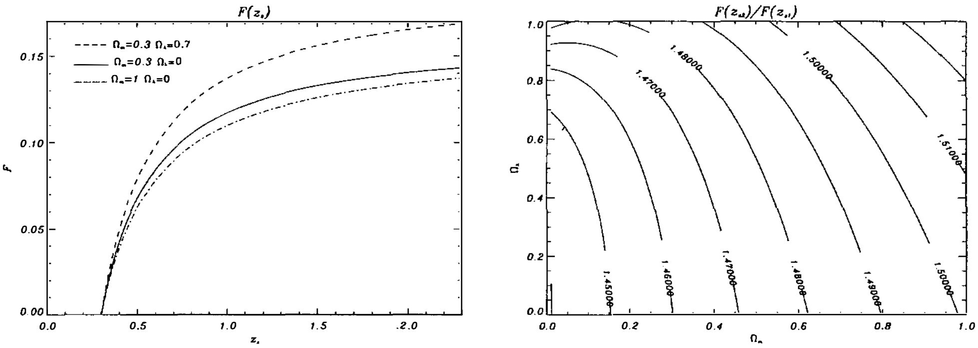

Figure 1: Left. $F(z_s)$ for $z_l = 0.3$ and various cosmological models. Right. $F(z_{s2})/F(z_{s1})$ as a function of Ω_m and Ω_λ for $z_l = 0.3$, $z_{s1} = 0.7$ and $z_{s2} = 2$.

If we consider fixed redshifts for both the lens and the sources, at least 2 multiple images are needed to derive cosmological constraints. In that case F has only an influence on the modulus of $\theta_I - \theta_S$. So taking the ratio of two different F terms provides the intrinsic dependence on cosmological scenarios, independently of H_0. A typical configuration leads to the Fig. 1 plot. The discrepancy between the different cosmological parameters is not very large, less than 3% between an EdS model and a flat low matter density one. The figure also illustrates the expected degeneracy of the method, also confirmed by weak lensing analyzes, with a continuous distribution of background sources (*e.g.* Lombardi & Bertin [5]).

2.2 Relative influence of the different parameters

We now look at the relative influence of the different parameters, including the lens parameters, to derive expected error bars on Ω_m and Ω_λ. To model the potential we choose the mass density distribution proposed by Hjorth & Kneib[1], characterized by a core radius, a, and a cut-off radius $s \gg a$. We can then get the expression of the deviation angle modulus $D_{\theta_I} = \parallel \theta_I - \theta_S \parallel$.

For 2 families of multiple images, the relevant quantity becomes the ratio of 2 deviation angles for 2 images θ_{I1} and θ_{I2} belonging to 2 different families at redshifts z_{s1} and z_{s2}. Let's define $R_{\theta_{I1},\theta_{I2}} = \frac{D_{\theta_{I1}}}{D_{\theta_{I2}}}$. With several families, the problem is highly constrained because a single potential must reproduce the whole set of images. In practice we calculate $\frac{dR_{\theta_{I1},\theta_{I2}}}{R_{\theta_{I1},\theta_{I2}}}$ versus the different parameters it depends on. For a typical configuration: $z_l = 0.3$, $z_{s1} = 0.7$, $z_{s2} = 2$, $\frac{\theta_{I2}}{\theta_{I1}} = 2$, $\frac{\theta_s}{\theta_a} = 10$ ($\theta_a = a/D_{OL}, \theta_s = s/D_{OL}$) and we assume $\Omega_m = 0.3$ and $\Omega_\lambda = 0.7$. We then obtain the following orders of magnitudes for the different contributions :

$$\frac{dR_{\theta_{I1},\theta_{I2}}}{R_{\theta_{I1},\theta_{I2}}} = 0.57\frac{dz_l}{z_l} + 0.74\frac{dz_{s1}}{z_{s1}} + 0.17\frac{dz_{s2}}{z_{s2}} + 0.4\left(\frac{d\theta_{I1}}{\theta_{I1}} - \frac{d\theta_{I2}}{\theta_{I2}}\right) - 0.1\frac{d\theta_a}{\theta_a} - 0.06\frac{d\theta_s}{\theta_s} - 0.015\frac{d\Omega_m}{\Omega_m} + 0.02\frac{d\Omega_\lambda}{\Omega_\lambda} \quad (1)$$

As expected, even with 2 families of multiple images the influence of the cosmological parameters is of the second order. The precise value of the redshifts is quite fundamental, therefore a spectroscopic determination ($dz = 0.001$) is essential. The position of the (flux-weighted) centers of the images are also important. With HST observations we assume $d\theta_I = 0.1''$.

So even if the problem is less dependent on the core and cut-off radii, they will represent the main sources of error. Taking $d\theta_a/\theta_a = d\theta_s/\theta_s = 20$ %, we then derive the errors $d\Omega_m$ and $d\Omega_\lambda$ from the above relation in these two cosmological scenarios :

$\Omega_m = 0.3 \pm 0.24$ $\quad\Omega_\lambda = 0.7 \pm 0.5$ $\quad$ or $\quad \Omega_m = 1 \pm 0.33$ $\quad \Omega_\lambda = 0 \pm 1.2$

As confirmed by the Fig. 1 degeneracy plot, the method is more sensitive to matter density than to the cosmological constant.

3 Constraint on $(\Omega_m, \Omega_\lambda)$ from strong lensing

3.1 Method and algorithm for numerical simulations

We consider basically the potential introduced in section 2.2. After considering the lens equation, fixing arbitrary values (Ω_m^0,Ω_λ^0) and a cluster lens redshift z_l, our code can determine the images of a source galaxy at a redshift z_s. Then taking as single observables these sets of images as well as the different redshifts, we can recover some parameters (the more important ones being σ_0, θ_a or θ_s) of the potential we left free for each point of a grid (Ω_m,Ω_λ). The likelihood of the result is obtained via a χ^2-minimization, where the χ^2 is computed in the source plane.

3.2 Numerical simulations in a typical configuration

To recover the parameters of the potential (ie σ_0, θ_a, θ_s and adjusted lens parameters), we generated 3 families of images with regularly distributed source redshifts.

For starting values $(\Omega_m^0, \Omega_\lambda^0) = (0.3, 0.7)$ we obtained the Fig. 2 confidence levels. The method puts forward a good constraint, better on Ω_m than on Ω_λ, and the degeneracy is the expected one (Fig. 1). Concerning the free parameters, we also recovered in a rather good way the potential, the variations being $\Delta\sigma_0 \sim 150$ km/s, $\Delta\theta_a \sim 3''$ and $\Delta\theta_s \sim 20''$.

This is an "ideal" case, of course, because we tried to recover the same type of potential we used to generate the images, the morphology of the cluster being quite regular and the redshift

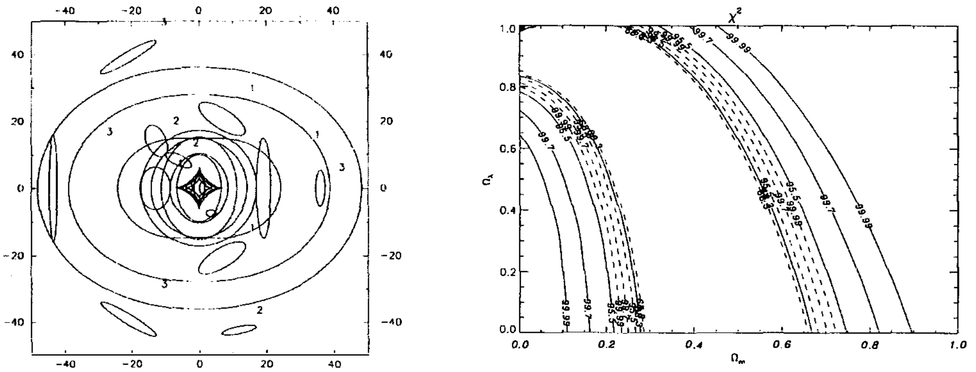

Figure 2: Left. Generation of images by a z_l = 0.3 cluster with σ_0 = 1400 km/s, θ_a = 13.54" and θ_s = 145.8". Close to their respective critic lines, we see 3 families of images at z_{s1} = 0.6, z_{s2} = 1 and z_{s3} = 2. Right. Solid lines : $\chi^2(\Omega_m, \Omega_\lambda)$ confidence levels obtained for this configuration. Generating arbitrary values: $(\Omega_m^0, \Omega_\lambda^0) = (0.3, 0.7)$. Dashed lines: $\chi^2(\Omega_m, \Omega_\lambda)$ confidence levels obtained considering 10 clusters in this same configuration.

range of the sources being wide enough to check each part of the F curve. Such simple approach can be applied to regular clusters like MS2137-23, which shows at least 3 families of multiple images including a radial one. But the spectroscopic redshifts are still missing for the moment.

4 Conclusions & prospects

Following the work of LP98, we discussed a method to obtain informations on the cosmological parameters Ω_m and Ω_λ while reconstructing the lens gravitational potential of clusters with multiple image systems at different redshifts.

This technique gives degenerate constraints, Ω_m and Ω_λ being negatively correlated, with a better constraint of the matter density. With a single cluster in a typical lensing configuration we can expect the following error bars : $\Omega_m = 0.3 \pm 0.24$, $\Omega_\lambda = 0.7 \pm 0.5$. To perform that, several general conditions must be fulfilled: a cluster with a rather regular morphology, "numerous" systems of multiple images, a good spatial resolution (HST) and spectroscopic precision for the different redshifts that should be also regularly distributed, from z_l to high values – this requires deep spectroscopy on 8-10m class telescopes due to the faintness of the multiple images.

Combining the study of about 10 different clusters would tighten the error bars and lead to meaningful constraints. The dashed line confidence levels in the Fig. 2 are the result of a numerical simulation made with 10 *identical* clusters. We are encouraged by more and more known observations including systems with multiple sources and we plan to apply in a first time this technique to clusters like MS2137-23, MS0440+02, A370, AC114 and A1689.

References

1. J. Hjorth and J.-P. Kneib, submitted to *ApJ* (1999).
2. J.-P. Kneib, R. Ellis, I. Smail, W. Couch & R. Sharples, *ApJ* **471**, 643 (1996).
3. M. Le Dour, M. Douspis, J. Bartlett & A. Blanchard, astro-ph/0004282, submitted to *A&A* (2000).
4. R. Link and M. Pierce, *ApJ* **502**, 63 (1998).
5. M. Lombardi and G. Bertin, *A&A* **342**, 337 (1998).
6. P. Nararajan & J.-P. Kneib,*MNRAS* **287**, 833 (1997).
7. M. White, *ApJ* **506**, 495 (1998).

List of Participants

ABDEL SALAM Hanadi
Kaptein Institute
Rijksuniversiteit Groningen
P.O. Box 800
9700 AV Groningen
The Netherlands
hanadi@astro.rug.nl

ALARD Christophe
Institut d'Astrophysique de Paris
CNRS
98bis boulevard Arago
75014 Paris France
alard@iap.fr

ALCALDE MORALES David
Inst. Astrofisica de Canarias
C/Via Lactea s/n
38200 La Laguna
Spain
dalcalde@ll.iac.es

BACON David
Institute of Astronomy
University of Cambridge
Madingley Road
CB3 0HA Cambridge
U.K.
djb@ast.cam.ac.uk

BARRENA DELGADO Rafael
Inst. Astrofisica de Canarias
C/Via Lactea s/n
38200 La Laguna
Spain
rbarrena@ll.iac.es

BELOKOUROV Vassili
Sternberg Astronomical Institute Universitetskii pr. 13
119899 Moscow
Russia
belokuro@sai.msu.su

BENABED Karim
CEA
Service de Physique Théorique
L'Orme des Merisiers
bâtiment 709
91191 Gif-sur-Yvette Cedex
France
benabed@cea.fr

BENNETT David
University of Notre Dame
Physics Department
IN 46556 Notre Dame
U.S.A.
bennett@bustard.phys.nd.edu

BERGSTRÖM Lars
Stockholm University
Department of Physics
Box 6730
11385 Stockholm
Sweden
lbe@physto.se

BERNARDEAU Francis
CEA
Service de Physique Théorique
L'Orme des Merisiers
bâtiment 709
91191 Gif-sur-Yvette Cedex
France
fbernard@spht.saclay.cea.fr

BLAIN Andrew
Institute of Astronomy
University of Cambridge
Madingley Road
CB3 0HA Cambridge
U.K.
awb@ast.cam.ac.uk

BOND Ian
University of Auckland
Department of Physics
Auckland
New Zealand
bondi@scitec.auckland.ac.nz

BOZZA Valerio
Universita' di Salerno
Dipartimento di Scienze Fisiche "E.R. Caianiello"
Via S. Allende
84081 Baronissi (SA)
Italy
valboz@sa.infn.it

BRACCO Christian
IUFM
Département de Physique
89 avenue George V
06046 Nice Cedex 1
France
cbracco@unice.fr

BRIDLE Sarah
MRAO
Cavendish Laboratory
Madingley Road
CB3 0HA Cambridge
U.K.
s.bridle@mrao.cam.ac.uk

CAPOZZIELO Salvatore
Universita' di Salerno
Dipartimento di Scienze Fisiche "E.R. Caianiello"
Via S. Allende
84081 Baronissi (SA)
Italy
capozziello@sa.infn.it

CASERTANO Stefano
STScI
3700 San Martin Drive
MD 21218 Baltimore
U.S.A.
stefano@stsci.edu

CASTANDER Francisco Javier
Observatoire Midi-Pyrénées
14 avenue Edouard Belin
31400 Toulouse
France
fjc@ast.obs-mip.fr

CELNIKIER Ludwik
Observatoire de Meudon
5 place Jules Janssen
92195 Meudon
France
Ludwik.Celnikier@obspm.fr

CLOWE Douglas
MPI für Astrophysik
Postfach 1523
85748 Garching
Germany
clowe@mpa-garching.mpg.de

CZOSKE Oliver
Observatoire Midi-Pyrénées
Laboratoire d'Astrophysique
UMR 5572
14 avenue Edouard Belin
31400 Toulouse
France
oczoske@ast.obs-mip.fr

DE JONG Jelte
Kaptein Institute
Rijksuniversiteit Groningen
P.O. Box 800
9700 AV Groningen
The Netherlands
jdejong@astro.rug.nl

DI STEFANO Rosanne
Harvard-Smithsonian CfA
Theory Division
60 Garden Street
MA 02138 Cambridge
U.S.A.
rdistefano@cfa.harvard.edu

ELLIS Richard
Caltech
Astronomy 105-24
CA 91125 Pasadena
U.S.A.
rse@astro.caltech.edu

ERBEN Thomas
MPI für Astrophysik
P.O. Box 1523
85740 Garching
Germany
erben@mpa-garching.mpg.de

FISCHER Philippe
University of Michigan
Department of Astronomy
MI 48104 Ann Arbor
U.S.A.
philf@astro.lsa.umich.edu

GATES Evalyn
University of Chicago
Dept. of Astronomy
& Astrophysics
5640 S. Ellis Avenue
IL 60637 Chicago
U.S.A.
gates@oddjob.uchicago.edu

GHIGNA Sebastiano
Universita' di Milano
Bicocca
"V. Emanueli, 15"
20126 Milano
Italy
s.ghigna@durham.ac.uk

GLICENSTEIN Jean-François
CEA
DSM/DAPNIA/SPP
L'Orme des Merisiers
bâtiment 709
91191 Gif-sur-Yvette Cedex
France
glicens@hep.saclay.cea.fr

GOLDMAN Bertrand
Collège de France/IN2P3
LPCC
11 place Marcellin Berthelot
75231 Paris Cedex 05
France
goldman@cdf.in2p3.fr

GOLSE Ghislain
Observatoire Midi-Pyrénées
Laboratoire d'Astrophysique
UMR 5572
14 avenue Edouard Belin
31400 Toulouse
France
ggolse@obs-mip.fr

GORSKI Krzysztof
Warsaw Univ. Obs. & ESO
Karl-Schwarzschildstrasse 2
85748 Garching
Germany
kgorski@eso.org

GRAY Meghan
Institute of Astronomy
University of Cambridge
Madingley Road
CB3 0HA Cambridge
U.K.
meg@ast.cam.ac.uk

GREVE Thomas Rodriguez
Copenhagen University
Astronomical Observatory
Juliane Maries Vej. 30
2100 Copenhagen
Denmark
tgreve@astro.ku.dk

GRIFFITHS Richard
Carnegie Mellon University
Department of Physics Wean
Hall
5000 Forbes Avenue
PA 15213-3890 Pittsburgh
U.S.A.
griffith@astro.phys.cmu.edu

GUZIK Jacek
Jagiellonian University
Astronomical Observatory
Orla 171
30-244 Krakow
Poland
guzik@oa.uj.edu.pl

HAEMMERLE Hannelore
MPI für Astrophysik
P.O. Box 1523
85740 Garching
Germany
hanne@mpa-garching.mpg.de

HAMANA Takashi
Institut d'Astrophysique de Paris
CNRS
98bis boulevard Arago
75014 Paris
France
hamana@iap.fr

HAN Cheongho
Chungbuk National University
Dept. Astronomy & Space Science
361-763 Chongju
Korea
cheongho@astronomy.chungbuk.ac.kr

HATTORI Makoto
Tohoku University
Astronomical Institute
Graduate School of Science
980-8578 Sendai
Japan
hattori@astr.tohoku.ac.jp

HELBIG Phillip
Kaptein Institute
Rijksuniversiteit Groningen
P.O. Box 800
9700 AV Groningen
The Netherlands
helbig@astro.rug.nl

HERRANZ Diego
IFCA
Facultad de Ciencias
Avda. los Castros, s/n
39005 Santander
Spain
herranz@ifca.unican.es

HOEKSTRA Henk
Kaptein Institute
Rijksuniversiteit Groningen
P.O. Box 800
9700 AV Groningen
The Netherlands
hoekstra@astro.rug.nl

HUGHES John P.
CEA
Service d'Astrophysique
L'Orme des Merisiers
bâtiment 709
91191 Gif-sur-Yvette Cedex
France
jhughes@calix.saclay.cea.fr

IBATA Rodrigo
MPI für Astrophysik
Koenigstuhl 17
69117 Heidelberg
Germany
ribata@mpia-hd.mpg.de

IVISON Rob
University College London
Dept. of Physics & Astronomy
Gower Street
WC1E 6BT London
U.K.
rji@star.ucl.ac.uk

KERINS Eamonn
University of Oxford
Theoretical Physics
1 Keble Road
OX1 3NP Oxford
U.K.
e.kerins@physics.ox.ac.uk

KING Lindsay
MPI für Astrophysik
P.O. Box 1523
85740 Garching
Germany
lindsay@mpa-garching.mpg.de

KNEIB Jean-Paul
Observatoire Midi-Pyrénées
14 avenue Edouard Belin
31400 Toulouse
France
kneib@ast.obs-mip.fr

KOCHANEK Christopher
Center for Astrophysics
MS-51
60 Garden Street
MA 02138 Cambridge
U.S.A.
ckochanek@cfa.harvard.edu

KOOPMANS Leon
Kaptein Institute
Rijksuniversiteit Groningen
P.O. Box 800
9700 AV Groningen
The Netherlands
leon@astro.rug.nl

KRYVODUBSKYJ Valery
Kyiv National University
Astronomical Observatory
Observatorna Stret 3
04053 Kyiv – 53
Russia
krivod@aoku.freenet.kiev.ua

KUIJKEN Konrad
Kaptein Institute
Rijksuniversiteit Groningen
P.O. Box 800
9700 AV Groningen
The Netherlands
kuijken@astro.rug.nl

LARCHENKOVA Tanya
Astro Space Center
Profsoyuznaya 84/32
117810 Moscow
Russia
tanya@lukash.asc.rssi.ru

LARSEN Gerburg
European Commission
RTD F-1
200 rue de la Loi SDME-4-38
1049 Brussels
Belgium
gerburg.larsen@cec.eu.int

LASSERRE Thierry
CEA
L'Orme des Merisiers
bâtiment 709
91191 Gif-sur-Yvette Cedex
France
lasserre@hep.saclay.cea.fr

LE BORGNE Jean-François
Observatoire Midi-Pyrénées
Laboratoire d'Astrophysique
UMR 5572
14 avenue Edouard Belin
31400 Toulouse
France
leborgne@obs-mip.fr

LE DU Yann
Collège de France/IN2P3
LPCC
75231 Paris Cedex 05
France
ledu@cdf.in2p3.fr

LIDMAN Chris
ESO
Alonso de Cordova
P.O. Box 19001
19 Santiago
Chile
clidman@eso.org

LOMBARDI Marco
ESO
Karl-Schwarzschildstrasse 2
85748 Garching
Germany
mlombard@eso.org

MADAU Piero
Institute of Astronomy
University of Cambridge
Madingley Road
CB3 0HA Cambridge
U.K.
pmadau@ast.cam.ac.uk

MAOLI Roberto
Institut d'Astrophysique de
Paris
CNRS
98bis, boulevard Arago
75014 Paris
France
maoli@iap.fr

MARINONI Christian
University of Trieste
Department of Astronomy
via Tiepolo 11
34131 Trieste
Italy
marinonl@astro.uwaterloo.ca

MAYEN Christophe
Observatoire Midi-Pyrénées
Laboratoire d'Astrophysique
UMR 5572
14 avenue Edouard Belin
31400 Toulouse
France
cmayen@ast.obs-mip.fr

MELLIER Yannick
Institut d'Astrophysique de
Paris
CNRS
98bis, boulevard Arago
75014 Paris
France
mellier@iap.fr

MENEGHETTI Massimo
Università di Padova
Dipartimento di Astronomia
Vicolo dell'Osservatorio 5
35122 Padova
Italy
menegbetti@pd.astro.it

METCALF Ben
Institute of Astronomy
University of Cambridge
Madingley Road
CB3 0HA Cambridge
U.K.
bmetcalf@ast.cam.ac.uk

MONIEZ Marc
IN2P3 – LAL
Centre d'Orsay
bâtiment 200
BP. 34
91898 Orsay Cedex
France
moniez@lal.in2p3.fr

MORALES MERINO Carlos
MPI für Astrophysik
P.O. Box 1523
85740 Garching
Germany
carlos@mpa-garching.mpg.de

MORTLOCK Daniel
Institute of Astronomy
University of Cambridge
Madingley Road
CB3 0HA Cambridge
U.K.
mortlock@ast.cam.ac.uk

MUNOZ LOZANO Jose A.
Inst. Astrofisica de Canarias
C/Via Lactea s/n
38200 La Laguna
Spain
jmunoz@iac.es

NAKOS Theodoros
Observatoire Royal de
Belgique
Avenue Circulaire 3
1180 Bruxelles
Belgique
thodoris@oma.be

NARASIMHA Delampady
Tata Inst. of Fundamental
Research
Homi Bhabha Road Colaba
400 005 Mumbai
India
dna@astro.tifr.res.in

PARNOVSKY Serge
Kyiv National University
Astronomical Observatory
Observatorna Stret 3
04053 Kyiv – 53
Russia
par@aoku.freenet.kiev.ua

PELLO Roser
Observatoire Midi-Pyrénées
Laboratoire d'Astrophysique
UMR 5572
14 avenue Edouard Belin
31400 Toulouse
France
roser@obs-mip.fr

POGOSYAN Dmitri
CITA
University of Toronto
60 St George Street
M5S 3H8 Toronto
Canada
pogosyan@cita.utoronto.ca

PONTOPPIDAN Klaus M.
Copenhagen University
Astronomical Observatory
Juliane Maries Vej. 30
2100 Copenhagen
Denmark
pontop@astro.ku.dk

REBLINSKY Katrin
MPI für Astrophysik
P.O. Box 1523
85740 Garching
Germany
reblinsk@mpa-garching.mpg.de

REFREGIER Alexandre
Institute of Astronomy
University of Cambridge
Madingley Road
CB3 0HA Cambridge
U.K.
ar@ast.cam.ac.uk

SCHIRMER Michael
ESO
Karl-Schwarzschildstrasse 2
85748 Garching
Germany
mschirme@eso.org

SCHNEIDER Peter
MPI für Astrophysik
P.O. Box 1523
85740 Garching
Germany
peter@mpa-garching.mpg.de

SUTHERLAND Will
University of Oxford
Astrophysics
1 Keble Road
OX1 3RH Oxford
U.K.
w.sutherland@physics.ox.ac.uk

TAKADA Masahiro
Astronomical Institute
Graduate School of Science
Tohoku University
980-8578 Sendai
Japan
takada@astr.tohoku.ac.jp

THION Aurélien
Institut d'Astrophysique de Paris
CNRS
98bis boulevard Arago
75014 Paris France
thion@iap.fr

TOFT Sune
Copenhagen University
Astronomical Observatory
Juliane Maries Vej. 30
2100 Copenhagen
Denmark
toft@astro.ku.dk

UGLESICH Robert
Columbia University
Astronomy Dept.
Mailcode 5246
550W 120th Street
NY 10027 New York
U.S.A.
rru@astro.columbia.edu

VALAGEAS Patrick
CEA
Service de Physique Théorique
L'Orme des Merisiers
bâtiment 709
91191 Gif-sur-Yvette Cedex
France
valag@wasa.saclay.cea.fr

VAN WAERBEKE Ludovic
CITA
St George Street
M5S 3H8 Toronto
Canada
waerbeke@cita.utoronto.ca

WAMBSGANSS Joachim
Universität Potsdam
Institut für Physik
Am Neuen Palais 10
14469 Potsdam
Germany
jkw@astro.physik.uni-potsdam.de

WARREN Steve
Imperial College
Astrophysics-Blackett Labs
Prince Consort Road
SW7 2BZ London
U.K.
sjw4@ic.ac.uk

WIKLIND Tommy
Onsala Space Observatory
43992 Onsala
Sweden
tommy@oso.chalmers.se

WILLIS Jon
Institute of Astronomy
Madingley Road
CB3 0HA Cambridge
U.K.
jwillis@ast.cam.ac.uk

WYITHE Stuart
Princeton University
Observatory Peyton Hall
NJ 08544 Princeton
U.S.A.
swyithe@astro.princeton.edu

ZAKHAROV Alexander
Instit. The. & Exp. Physics
B. Cheremushkinskaya 25
117259 Moscow
Russia
zakharov@vitep5.itep.ru

ZEBRUN Karol Mikolaj
Warsaw University
Astronomical Observatory
Al. Ujazdowskie 4
00-478 Warsaw
Poland
zebrun@astrouw.edu.pl

ZHAO HongSheng
Huygens Laboratory
Niels-Bohrweg 2
2333 CA Leiden
The Netherlands
hsz@strw.leidenuniv.nl

Achevé d'imprimer sur les presses de l'Imprimerie BARNÉOUD
B.P. 44 - 53960 BONCHAMP-LÈS-LAVAL
Dépôt légal : avril 2001 – N° d'imprimeur : 12542